The evolution of the oceanic lithospheric mantle: experimental and observational constraints

by

Archana Shejwalkar
Master of Science, Goa University, 2003
Bachelor of Science, Dhempe College of Arts and Science, Goa University 2001

A Dissertation Submitted in Partial Fulfillment
of the Requirements for the Degree of

DOCTOR OF PHILOSOPHY

in the School of Earth and Ocean Sciences

© Archana Shejwalkar, 2016
University of Victoria

All rights reserved. This dissertation may not be reproduced in whole or in part, by photocopy or other means, without the permission of the author.

Supervisory Committee

The evolution of the oceanic lithospheric mantle: experimental and observational constraints

by

Archana Shejwalkar
Master of Science, Goa University, 2003
Bachelor of Science, Dhempe College of Arts and Science, Goa University 2001

Supervisory Committee

Dr. Laurence Coogan (School of Earth and Ocean Sciences)
Supervisor

Dr. Kathryn Gillis (School of Earth and Ocean Sciences)
Departmental Member

Dr. Dante Canil (School of Earth and Ocean Sciences)
Departmental Member

Dr. Tom Fyles (Department of Chemistry)
Outside Member

Abstract

Supervisory Committee
Dr. Laurence Coogan (School of Earth and Ocean Sciences)
Supervisor
Dr. Kathryn Gillis (School of Earth and Ocean Sciences)
Departmental Member
Dr. Dante Canil (School of Earth and Ocean Sciences)
Departmental Member
Dr. Tom Fyles (Department of Chemistry)
Outside Member

Abstract

The oceanic lithosphere forms as a residue of partial melting of the mantle beneath the mid-ocean ridge axis. Subduction of this residual layer has a profound impact on the Earth's thermal and geochemical cycles as the recycling of this layer facilitates heat loss from the Earth's interior and induces geochemical heterogeneities in the mantle. The goal of this study is to understand the thermal and geochemical evolution of the oceanic lithospheric mantle from a petrological perspective. An empirical geobarometer is calibrated for ocean island xenoliths in order to understand the thermal structure of the oceanic lithospheric mantle. The results of 0.1 MPa experiments from this study and high-pressure experiments from previous studies are used in the calibration. The uncertainties on pressures derived using the above geobarometer are high and hence could not be tested against thermal models for the oceanic lithosphere. The geochemical evolution of the oceanic lithospheric mantle involves post-melting geochemical modifications such as metasomatism. The geochemical evolution of the uppermost oceanic lithospheric mantle is studied using harzburgites from Hess Deep ODP Site 895, which are depleted in moderately incompatible elements relative to the global suite of abyssal peridotites. A comparison between Yb-abundances in Hess Deep harzburgites

and those of a model depleted MORB mantle (DMM) residue reveals that the harzburgites have undergone up to 25% melting, assuming 0.5% melt porosity. Higher light and middle rare earth elements in the Hess Deep harzburgites than the model DMM melting residue are interpreted as the result of plagioclase crystallisation from melts being extracted by diffuse porous flow through the upper mantle. The effect of plagioclase crystallisation does not affect the chemistry of residual mineral phases as evidenced from the depleted light rare earth element abundances in clinopyroxene relative to the bulk rock. Ocean island xenoliths are studied to understand when and where metasomatism occurs in the deeper portion of the oceanic lithosphere. The median values of measured and reconstructed bulk concentration of Al_2O_3 in most ocean island xenoliths is lower than in abyssal peridotites, which generally would be interpreted as indicating a higher extent of melting in the former. However, a comparison between Yb-abundances in ocean island xenoliths and abyssal peridotites with a model DMM melting residue suggests that the extents of melting in the suites of rocks are broadly similar. Although fewer in number than ocean island xenoliths, abyssal peridotites from several locations have low concentrations of moderately incompatible elements. Metasomatism is observed in both, ocean island xenoliths and abyssal peridotites in the form of higher bulk rock Ce and Nd concentration than the model DMM melting residue but the extent of metasomatism is higher in ocean island xenoliths. There is no correlation between the concentrations of bulk rock Ce, Nd, Sm and Eu of ocean island xenoliths and age of the oceanic lithosphere from which the xenoliths originate. It is interpreted that metasomatism in the lower oceanic lithospheric mantle occurs near the ridge axis above the wings of the melting column.

Table of Contents

Supervisory Committee ii
Abstract iii
Table of Contents v
List of Tables vii
List of Figures viii
Acknowledgments xviii
Dedication xx
1. The thermal and geochemical evolution of the oceanic lithospheric mantle 1
1.1. The oceanic lithospheric mantle 1
1.2. The oceanic lithosphere as a thermal boundary layer 3
1.3. The oceanic lithosphere as a mechanical boundary layer 5
1.4. Geochemistry of the oceanic lithospheric mantle 8
1.4.1. Abyssal peridotites 8
1.4.2. Mantle xenoliths from ocean islands 14
1.5. Scientific contribution of this thesis 18
2. Experimental calibration of the role of Fe in Ca exchange between olivine and clinopyroxene at 0.1 MPa 21
2.1. Introduction 21
2.2. Experimental Methods 28
2.3. Analytical Techniques 29
2.4. Results 32
2.4.1. Calcium content of pure forsterite as a function of temperature 33
2.4.2. The impact of iron on the Ca content of olivine 37
2.5. Discussion 42
2.5.1. Comparison to the previous geobarometer 42
2.5.2 Calibration of the olivine – low-Ca-pyroxene – clinopyroxene – melt saturation surface at 0.1 MPa. 45
2.5.3. Are current geothermobarometers sufficiently accurate to test thermal models of the oceanic lithosphere? 48
2.6. Summary 55
3. Evidence for pervasive melt-rock reaction within the uppermost mantle at Hess Deep 58
3.1. Introduction 58
3.2. Hess Deep and the Sample suite 61
3.3. Analytical methods 62
3.4. Results 68
3.4.1. Petrography 68
3.4.2. Bulk rock chemistry 70
3.4.3. Mineral chemistry 78
3.4.4. Alteration in Hess Deep harzburgites 79
3.5. Discussion 83
3.5.1. Depletion in Hess Deep Site 895 harzburgites 83

3.5.2. Light REE and trace element enrichment in Hess Deep harzburgites 86
3.5.3. Model history of Hess Deep harzburgites 101
3.6. Summary and Conclusions 102
4. Melt-rock reaction and compositional heterogeneity in the residual oceanic lithospheric mantle: insights from ocean island xenoliths 106
4.1. Introduction 106
4.2. Sampling and analytical methods 110
4.3. Results 113
4.3.1. Petrography 115
4.3.2. Mineral Chemistry 116
4.3.3. Bulk rock geochemistry 121
4.4. Late-stage geochemical modifications in ocean island xenoliths and abyssal peridotites 135
4.4.1. Emplacement related chemical changes in ocean island xenoliths 136
4.4.2. Hydrothermal alteration in abyssal peridotites 140
4.5. The geochemical evolution of the oceanic lithospheric mantle 141
4.5.1. Trace elements as indicators of metasomatism in the lower oceanic lithospheric mantle 145
4.5.2. When and where does metasomatism occur in the lower oceanic lithospheric mantle? 153
4.6. Summary and conclusion 156
5. Summary and Future Work 159
5.1. An empirical geobarometer for spinel peridotites 160
5.2. The geochemical evolution of the oceanic lithospheric mantle 161
5.2.1. A working model for the evolution of the oceanic lithospheric mantle 162
5.3. Future work 165
5.3.1. Future work on the Ca-in-olivine geothermobarometer 165
5.3.2. Future work on understanding the geochemical evolution of the oceanic lithospheric mantle. 167
Bibliography 169
Appendix A 196
Appendix B 333

List of Tables

Table 2.3. Coefficients describing best-fit parameters of linear regression for Eq. 2.14 . 49
Table 3.5. Average detection limits calculated for LA-ICP-MS data using Eq. 3.1. 71
Table 3.6. Mineral modes determined by point-counting..... 73
Table 3.7a. Mineral/melt partition coefficients (Kd) for trace elements used in construction of melting models for DMM composition (from Kelemen et al., 2003)..... 89
Table 3.7b. Mineral/melt partition coefficients (Kd) for trace elements used in construction of melting models for DMM composition (from Hellebrand et al., 2002). . 90
Table 3.8. Average REE concentrations in hydrothermal fluids from the EPR (Klinkhammer et al., 1994)..... 93

List of Figures

Figure 1.1. Cartoon cross section of the Earth. The innermost portion of the Earth consists of a solid inner core and a liquid outer core and is largely made up of the siderophile elements, Fe and Ni. The core is followed by the lower and upper mantle, which is largely made up of silicates. The asthenosphere (shown in yellow) is a low-viscosity layer that lies at the top of upper mantle and is overlain by the lithosphere (shown in red). The lithosphere is the outermost rigid layer of the Earth and is made up of the crust and the topmost part of the upper mantle. Figure modified from http://www.geology.sdsu.edu/how_volcanoes_work/Heat.html 2

Figure 1.2. Predicted distribution of isotherms in the oceanic lithosphere as a function of age for: (a) the half space model, (b) the plate model and (c) the CHABLIS model. (a) In the half space model, the oceanic lithosphere cools by conduction through the top of a semi-infinite half space of the underlying mantle (Davis and Lister, 1974). The thickness and isotherms for the half space model are calculated based on Turcotte and Schubert (2002). A thermal diffusivity of $1*10^{-6}$ m^2/s and initial temperature of 1400ºC is used in construction of the half space model above. (b) In the half space model, the P-T array varies with age for the entire lithosphere. In the plate model, the oceanic lithosphere forms with its full thermal thickness of 95 km and basal temperature of 1450 ± 250ºC (Stein and Stein, 1992) at the ridge axis. Based on the plate model, the P-T array in the lithosphere remains constant for lithosphere greater than ~80 Ma. In the CHABLIS model the oceanic lithosphere increases in thickness away from the ridge axis. (c) It has been hypothesised that small-scale mantle convection provides constant heat flux at the base of the oceanic lithosphere (Doin and Fleitout, 1996). The figures for the plate and CHABLIS models are drawn based on Doin and Fleitout (1996). 7

Figure 1.3. Illustration of the melting column at a MOR showing the process of decompression melting beneath the ridge axis and generation of mid-ocean ridge basalt that crystallises to form the oceanic crust. Partial melting in the melting column leaves behind a residue that is sampled as abyssal peridotites at the top and ocean island xenoliths in the lower portions of the oceanic lithospheric mantle. (a) Melting begins at the solidus, which is generally located at a depth of ~ 60 kms beneath the oceanic crust (Langmuir et al., 1992). The percentage of melting is highest at the axis of the melting column, with progressively lower percentages towards the sides. (b) The melting can extend up to greater depths beneath the oceanic crust if the mantle potential temperature is high. The crustal thickness associated with greater extent of melting is also higher and residual abyssal peridotites formed as a residue of partial melting are less likely to be exposed close to the ocean floor and are likely to be more depleted. (c) If the mantle is colder than average, melting begins at a shallower depth and the associated crustal thickness is lower than average and abyssal peridotites are likely to be exposed on the seafloor by tectonism. However, it was later suggested that the thickness of the crust in regions of slow spreading (cold mantle) could vary along the ridge axis. The crystallisation of basaltic melts in a cold mantle can take place below the crust resulting in a thicker crust composed of a mixture of gabbro, sheeted dykes and basaltic lava (Cannat, 1996). The above diagrams are based on Langmuir et al. (1992). 11

Figure 2.1. Results of experiments run at the same temperature but with either different durations or different starting compositions in the CMAS system. The 1322°C and 1277°C experiments are the same starting composition that was run for different durations whereas the 1305°C experiments are different starting compositions run for both the same and different duNote that two of the 1305°C experiments contain pigeonite and the other two orthopyroxene and there is no significant difference in the Ca content of the olivine crystals between these experiments. Error bars represent 1σ on electron microprobe analyses of Ca in olivine..... 34
Figure 2.2. Calcium content of olivine, expressed as $\ln(X_{Mo})$, versus reciprocal temperature for olivine of different forsterite contents from the experiments reported here. The Ca-content of olivine in lower temperature Fe-bearing experiments is much higher than that expected from extrapolation of Fe-free experiments. Also shown are model olivine Ca contents at different Fo content derived from Eq. 2.11 (dashed lines). Filled symbols are orthopyroxene-bearing experiments and open symbols are pigeonite-bearing experiments. 36
Figure 2.3. Relationship between the Fo-content of olivine and the difference ($\Delta\ln[X_{Mo}]$) between the measured Ca content of the olivine and that predicted from the experimental temperature using the relationship between temperature and X_{Mo} derived from the Fe-free experiments (Eq. 2.8a). The linear relationship between olivine Fo-content and $\Delta\ln[X_{Mo}]$ indicates that olivine Fo-content is critical in controlling the Ca-content of olivine. Whether the low-Ca-pyroxene is orthopyroxene or pigeonite makes no obvious difference to $\Delta\ln[X_{Mo}]$..... 39
Figure 2.4. Difference between the temperatures predicted using the geothermometer calibrated in this study (Eq. 2.11) versus experimental temperatures plotted as functions of (a) olivine Fo content and (b) experimental temperature. The misfits do not correlate with either parameter. The thermometer reproduces the experimental temperatures to within 20ºC. Whether the low-Ca-pyroxene is orthopyroxene (open diamonds) or pigeonite (red filled squares) makes no obvious difference. 41
Figure 2.5. Comparison of the results of 0.1 MPa experiments reported here and previous high-pressure experiments. (a) data from Fe-bearing experiments (Kohler and Brey, 1990; Adams and Bishop, 1986) with the 0.1 MPa data points (black symbols) calculated from the thermometer developed here (Eq. 2.11). The previous experiments are consistent with one another and with the results of this study provided the effect of Fe on the Ca contents of olivine is incorporated into the thermometer. (b) data from Fe-free experiments (Finnerty and Boyd, 1978; Adams and Bishop, 1982) with the 0.1 MPa data points calculated from the thermometer developed here (Eq. 2.11). The agreement is poor between the new data and those of these high-pressure studies except at 1300°C. Note that both increasing pressure and temperature apparently have a smaller effect on the Ca content of olivine in the Fe-free system..... 43
Figure 2.6. Misfit between calculated and experimental pressures for Fe-bearing (Adams and Bishop, 1986; Kohler and Brey, 1990) and Fe-free (Finnerty and Boyd, 1979; Adams and Bishop, 1982) experiments. The maximum misfit for Fe-bearing and Fe-free experiments is 0.7 GPa and 2.6 GPa respectively. 45
Figure 2.7. Concentrations of (a) SiO_2, (b) MgO and (c) CaO calculated using Eq. 2.14 plotted against measured experimental concentrations. (d) Temperatures calculated using Eq. 2.14 are plotted against experimental temperatures and are found to be within +/-

30ºC. The r-squared (R^2) values for each linear regression line are shown in the respective plots. The solid line in each figure represents X=Y on the plot. Eq. 2.14 can be used to calculate starting compositions for future studies that require modeling of the olivine-low-Ca-pyroxene-clinopyroxene saturated melts. 49
Figure 2.8. Comparison between temperatures calculated using different geothermometer pairs as indicated in the figures. Five samples in (a) are off the chart with temperatures greater than 1500°C calculated using Liermann and Ganguly (2003). Error bars indicate 1σ on the geothermometers. 53
Figure 2.9. Geotherms for the oceanic lithospheric mantle constructed using temperatures calculated by the olivine-spinel geothermometer (Ballhaus et al., 1991) and pressures calculated using Eq. 2.13 (red diamonds) and Kohler and Brey (1990; black squares). The depth is calculated using the relation $Depth = pressure/(density * gravity)$ and a density of 3.3 gm/cm^3. Error bars indicate 1σ uncertainty on the geobarometer. Three samples in (e) are outside the chart area with depths up to 300 km. The solid blue line is the geotherm for respective age of the oceanic lithosphere calculated for the half space model using the equation from Turcotte and Schubert (2002). 54
Figure 2.10. Geotherms for the oceanic lithospheric mantle constructed using temperatures calculated by the two-pyroxene geothermometer (Brey and Kohler, 1990) and pressures calculated using Eq. 2.13 (red diamonds) and Kohler and Brey (1990; black squares). The calculation of depth and error bars is as described in Fig. 2.9. The solid blue line is the geotherm for respective age of the oceanic lithosphere calculated for the half space model using the equation from Turcotte and Schubert (2002). 56
Figure 3.1 Comparison between (a) MgO/SiO_2 ratio and (b) FeO (wt%) analysed by ICP-OES (open diamonds) and XRF (red diamonds) plotted against Al_2O_3 (wt%). The MgO/SiO_2 ratio and FeO analysed by XRF are lower than ICP-OES analyses. For one sample (147-895D-002R-02W 33-38), the concentration of Al_2O_3 analysed by XRF is lower than that analysed by ICP-OES. 64
Figure 3.2 Photomicrographs of harzburgites from Hess Deep (ODP) Site 895 showing textural relationships between olivine (Ol), orthopyroxene (Opx), clinopyroxene (Cpx) and spinel (Sp) along with alterations (Alt) and exsolution lamellae (Ex). (a) 895E-007R-04W (86-94): Thin section of harzburgite showing highly cracked olivine crystals that are serpentinised along the cracks. The orthopyroxene in this sample is highly altered. (b) 895E-007R-04W (34-41): Highly serpentinised olivine and altered orthopyroxene along with serpentine veins cutting across olivine crystals. (c) 895D-005R-02W (127-135): Unaltered orthopyroxene crystal surrounded by highly cracked olivine crystals that are altered to chlorite. (d) 895D-005R-02W (103-112): Relatively fresh olivine and orthopyroxene crystals with minor alterations along the boundaries of crystals and along the cracks in olivine. (e) 895D-004R-03W (112-116): Typical spinel observed in harzburgites from ODP Site 895 of this study along with highly cracked olivine crystals with alterations along the cracks and borders of the crystals. (f) 895A-001R-02W (55-61): Relatively fresh part of the harzburgite with orthopyroxene showing exsolution blebs and surrounded by highly cracked olivine crystals. Also seen here is a clinopyroxene crystal analysed in this study. 72
Figure 3.3 Bulk rock compositions of Hess Deep peridotites (East Pacific Rise) reported on anhydrous basis as analysed in this study plotted alongside Hess Deep peridotites from previous studies (Gillis et al., 1993; Blum, 1990) and a global suite. The sources for data

for the global suite are as follows: Garrett Transform (EPR): Niu and Hekinian (1997); MAR: Casey et al. (1997), Aumento and Loubat (1971), Paulick et al. (2006), Godard et al. (2008), Cannat et al. (1995), Stephens (1997), Lee et al. (2003), Harvey et al. (2006); Pacific Antarctic Ridge: Niu (2004); CIR: Niu (2004); SWIR: Snow and Dick (1995), Niu (2004); American Antarctic Ridge: Niu (2004). The plots show bulk rock concentrations of (a) CaO, (b) SiO_2, (c) MgO and (d) FeO versus Al_2O_3 (all in weight percent). Samples from the Garrett Transform are shown as separate symbols since it is the only other sample suite from the EPR. Separate symbols are also shown for peridotites from 15º 20' N along MAR as the only suite that is more or as depleted as Hess Deep. The depleted nature of Hess Deep peridotites is apparent from the low Al_2O_3 and CaO concentrations of these rocks compared to the global suite. Higher CaO concentration (a) in one Hess Deep sample is the result of calcite precipitation. The star symbol at the base of the arrow in part (a) represents the carbonate-corrected concentration of CaO for this sample. The results of EPMA analyses of secondary minerals (recalculated to anhydrous basis; filled orange circles) are plotted for comparison with the bulk rock data in order to understand how alteration modifies the bulk rock composition. Also shown for comparison are compositions of ocean island xenoliths. It is observed that Hess Deep peridotites plot close to the depleted end of the ocean island xenoliths global array (References as in Fig. 4.4; Chapter 4). MgO variation diagrams are plotted for (e) FeO and (f) SiO_2; alteration is likely to have removed MgO in most of the harzburgites from this study while SiO_2 may have been added in some of the harzburgites. The differences between concentrations of some elements like CaO in Hess Deep harzburgites analysed in this study and the data from previous studies may be due to the differences the extent of alteration in the samples. For example, the higher concentration of CaO in Hess Deep harzburgites from previous studies (open red diamonds) may be due to calcite precipitation in these rocks. 76

Figure 3.4 Bulk rock trace element concentrations of Hess Deep peridotites for (a) Sc, (b) V, (c) Co and (d) Ti plotted on Al_2O_3 variation diagrams. Also shown are Hess Deep peridotites from previous studies (Gillis et al., 1993; Blum, 1990) along with the global sample suite (Sources as in Fig. 3.3). As in Figure 3.3, samples from the Garrett Transform are shown as separate symbols as a distinction of peridotites from the EPR. The depleted nature of Hess Deep peridotites is clearly observed with only samples from 15º 20' N (Paulick et al., 2006; Godard et al., 2008) along the MAR being similar to Hess Deep samples. 77

Figure 3.5 Chondrite-normalised bulk rock REE and trace element pattern for Hess Deep peridotites illustrated along with DMM composition (Workman and Hart, 2005). The grey shaded area represents the composition of the global sample suite. The sources for the global dataset are: Garrett Transform: Niu and Hekinian (1997); MAR: Casey et al. (1997); Brandon et al. (2000); Aumento and Loubat (1971); Paulick et al. (2006); Godard et al. (2008). Hess Deep peridotites, along with having more depleted REE concentrations than the global suite, display a weakly U-shaped pattern. Prominent positive Sr- and Eu-anomalies are observable in the Hess Deep peridotites. High field strength elements Zr and Hf variably display positive, negative or flat pattern relative to Nd and Sm for each Hess Deep sample. Three of the samples shown as dashed black lines have prominent Zr-Hf anomalies while the rest of the elements display nearly flat trace element pattern. One sample shown as a dotted line has the highest concentrations

most elements compared to the rest of the suite and is characterised by a flat trace element pattern. 80
Figure 3.6 Average mineral compositions of individual samples from Hess Deep (ODP) Site 895 harzburgites analysed in this study (filled red diamonds) and the global abyssal peridotite suite (green crosses) illustrated by (a) high Fo (Ol) and high spinel Cr# and (b) low Al_2O_3 in orthopyroxene and clinopyroxene. Hess Deep (previous studies; open red diamonds) samples refer to harzburgites from Hess Deep ODP Site 895 analysed previously by Dick and Natland (1996), Arai and Matsukage (1998) and Edwards and Malpas (1996). The global array represents analyses from previous studies on the SWIR and American Antarctic Ridge (Snow and Dick, 1995), MAR (Juteau, et al., 1990; Komor et al., 1990; Ross and Elthon, 1997; Brunelli et al., 2006), the American Antarctic Ridge (Dick, 1989) and the SWIR (Hamlyn and Bonatti, 1980). In part (a), the data plotted along the X-axis is the set of samples where Fo (Ol) data are missing and data along the Y-axis is the data for which spinel Cr# data are missing. In part (b), the data plotted along the X-axis is the data for which Al_2O_3 in orthopyroxene data are missing while data plotted along the Y-axis is the data for which Al_2O_3 in clinopyroxene data are missing. 81
Figure 3.7. Zr and Ti concentrations in clinopyroxenes from Hess Deep harzburgite analysed in this study along with the global array defining the melting trend as in Johnson et al. (1990). Data sources for the global dataset include: Dick (1984; 1989); Johnson et al. (1990); Johnson and Dick (1992); Hellebrand et al. (2002). It is observed that all except three clinopyroxenes from Hess Deep harzburgites are highly depleted to the point of Zr being below the detection limit. The Zr-depleted clinopyroxenes plot at the depleted end of the global spectrum. Error bars represent 1σ on clinopyroxene Zr analyses used to calculate averages for individual samples; since most of the Zr-concentrations are below the detection limit, the error bars are meaningless. 82
Figure 3.8 Compositions of altered minerals in Hess Deep ODP Site 895 harzburgites calculated as cations per 28 oxygens. The majority of alteration phases analysed are Serpentines or serpentine+smectite mixes. A few samples have slightly higher lower Si (which correspond to higher Al than the remaining samples) and are classified as serpentine+chlorite+smectite mixes. The high-Si and high-Ca+Na+K samples are identified as tremolite is visible as discernable crystals in thin sections. Fields marked in (a) are from Nozaka et al. (2008). 84
Figure 3.9 Bulk rock variations in MgO and SiO_2 shown in MgO/SiO_2 versus Al_2O_3/SiO_2 space. The global 'terrestrial array' (Jagoutz et al., 1979) is the melting trend defined by the global abyssal peridotite suite shown in the figure. Highest depletions are observed in harzburgites from Hess Deep along with those from 15º 20' N (MAR; Paulick et al., 2006; Godard et al., 2008) and the Garrett Transform (EPR; Niu and Hekinian, 1997). Also shown for comparison are harzburgite and lherzolite samples of ocean island xenoliths, most of which also plot at the depleted end of the global spectrum (data sources for ocean island xenoliths are cited in Fig. 4.4 of Chapter 4). 85
Figure 3.10. A comparison between observed chondrite-normalised bulk rock trace element concentrations with the model residue of 10, 15 and 25% melting of a DMM source composition (Workman and Hart, 2004). It is observed that the bulk rock trace element pattern is not what can be expected for melting of a DMM source composition, as the LREE and Sr concentrations are much lower in the model residue. 91

Figure 3.11. A comparison between observed chondrite-normalised bulk rock trace element concentrations with the model residue 25% melting of DMM, E-DMM and D-DMM source compositions source composition (Workman and Hart, 2004). The partition coefficients used in the construction of the melting are from Kelemen et al. (2003). Since the starting compositions have similar abundances of REEs, the resulting melting models do not differ from one another. A variation of the DMM-melting model is shown by replacing the partition coefficients of Kelemen et al. (2003) by those from Hellebrand et al., (2002). With the exception of Zr, no differences are observed between the models after 25% melting of DMM. The difference in Zr-abundances between melting models of varying partition coefficients is due the higher value of partition coefficient of Zr in orthopyroxene in Hellebrand et al., (2002) compared to Kelemen et al., (2003). Also shown are variations of 25% melting of DMM are 0.5, 1 and 2% porosities..... 92
Figure 3.12. (a) Composition of the residue of 25% melting of DMM after mixing REE concentrations measured for seawater (Elderfield and Greaves, 1982) to the residue. It is observed that extremely high water/rock ratios (10^9 to 10^{10}) are required to generate the observed LREE pattern for geochemical modification just by seawater alteration. (b) Composition of the residue of 25% melting after mixing the average REE concentrations of hydrothermal fluids from the EPR (Table 3.8; Klinkhammer et al., 1994) in a 1:1 proportion..... 93
Figure 3.13. Bulk rock Ce concentrations of Hess Deep peridotites normalised to chondritic values (McDonough and Sun, 1995) plotted against chondrite-normalised bulk rock (a) Li, (b) B and (c) Cu concentrations. No correlation is observed in either case. . 94
Figure 3.14. Bulk rock Ce concentrations of Hess Deep peridotites normalised to chondritic values (McDonough and Sun, 1995) plotted against chondrite-normalised bulk rock (a) Hf and (b) Zr concentrations. No correlation is observed in either case..... 95
Figure 3.15. Composition of the residue of 25% melting of DMM after mixing 0.1, 0.5 and 2% plagioclase to the residue. The plagioclase composition used is that of a gabbro from the Hess Deep region (Lissenberg et al., 2013), which was selected so it resembles melts that form the MORB in the Hess Deep region. It is observed that mixing 2% plagioclase to the residue of 25% melting of DMM is sufficient to reproduce the highest LREE, MREE and Sr abundances observed in most harzburgites from Hess Deep. Notable exceptions are the samples that are enriched in LREE compared to DMM (dotted and dashed black lines). Concentrations for Tb, Zr and Hf are not reported for plagioclase and hence these elements are not modeled. 96
Figure 3.16 Chondrite-normalised abundances of (a) Ce, (b) Nd, (c) Ti and (d) Zr in clinopyroxene from Hess Deep (ODP) Site 895 harzburgites plotted against bulk rock abundances for the same group of samples. For samples in which clinopyroxenes were absent or could not be analysed, only bulk rock compositions are plotted. Also shown for comparison are clinopyroxene compositions for Hess Deep harzburgites analysed by Dick and Natland (1996) and clinopyroxenes from the global suite. Clinopyroxenes from the global suite generally have higher concentrations of Nd, Ti and Zr compared to the Hess Deep clinopyroxenes. Compared to bulk rock compositions, the clinopyroxenes in Hess Deep harzburgites have similar or lower abundances of Ce, Nd and Zr and higher concentration of Ti. Error bars on clinopyroxene compositions are 1σ on multiple analyses of the same clinopyroxene crystal or multiple crystals from the same sample. High uncertainties on clinopyroxene data indicate highly depleted concentrations of Ce,

Nd and Zr in clinopyroxene. Data plotted along the X-axes is data with no clinopyroxene analysis while data plotted along the Y-axis is data with no bulk rock analysis. Sources for clinopyroxene data in the global dataset are as in Fig. 3.7..... 100
Figure 4.1. An illustration of a melting column at the MOR axis. The base of the triangular melting region represents the dry solidus above which melting begins and progresses towards the top. The extent of melting is lowest near the edges of the base of the triangular region and is higher towards the center. The black arrows indicate the direction of movement of the solid residue of the respective amounts of melting. Melts migrate through the melting column moving towards the top (green arrows). Melts erupting at the top of the melting column form MORBs that represent the top of the oceanic crust. The top of the melting column is the residue of highest extent of melting that forms abyssal peridotites, which are exposed on the surface of the oceanic crust due to faults (F). The lower portion represents residues of progressively lower extents of melting and is sampled as ocean island xenoliths. Melts generated in the wings (purple arrows) and at the base (red arrows) of the melting column can metasomatise the residual oceanic lithospheric mantle..... 108
Figure 4.2. Locations of global ocean island xenolith sample suite used in this study. . 114
Figure 4.3. Lithologies of ocean island xenoliths analysed in this study with number of samples represented as percentages for each ocean island. The number of samples for each ocean island is as follows: Kerguelen – 8, Tahiti – 10, Hawaii – 15, Cape Verde – 7, Madeira – 8, The Canary Islands – 20. The lithologies do not necessarily represent the percentages in which each rock type occurs in each ocean island..... 114
Figure 4.4. Photomicrographs showing the mineralogy and textures in ocean island xenoliths analysed in this study. (a) Harzburgite sample LEIUG 114018 from Lanzarote showing coarse-grained xenomorphic granular texture in olivine and orthopyroxene crystals. (b) Clinopyroxene crystal in the interstices of olivine crystals in harzburgite sample LEIUG 114031 from Lanzarote. (c) Basalt contact with the xenolith NI 120 F from Cape Verde with a basalt intrusion extending into the xenolith. (d) Basalt vein through dunite xenolith TAH-4 from Tahiti. (e) Pyroxenite vein cutting a spinel websterite xenolith BM 1964-737-11b from Madeira. (f) Xenomorphic granular texture in spinel harzburgite xenolith BM 64888 from Kerguelen..... 118
Figure 4.5. Histograms illustrating bulk and mineral compositions of harzburgites and lherzolites in ocean island xenoliths and abyssal peridotites. The frequency is expressed as a percentage of the number of samples in order to overcome the difference in number of ocean island xenolith and abyssal peridotite samples. Bulk compositions are shown on the left hand side while the mineral composition that most influences the respective oxide's bulk concentration is shown on the right hand side. Data sources in addition to ocean island xenoliths analysed in this study are as follows: Canary Islands: Siena et al. (1991); Neumann (1991); Wulff-Pedersen et al. (1996), Neumann et al. (2002, 2004), Abu El-Rus et al. (2006); Cape Verde: Bonadiman et al. (2005); Kerguelen: Gregoire et al. (1997; 2000a; 2000b); Delpech (2004); Azores: Johansen (1996); Grande Comore: Coltorti et al. (1999); Samoa: Hauri et al. (1993); Hawaii: Kuno (1969); Sen (1987); Jackson and Wright (1970); Goto and Yokoyama (1988); Sen and Leeman (1991); Tahiti: Qi et al. (1994); Ocean island xenolith data compilation from Simon et al. (2008). Abyssal peridotite data sources are as follows: MAR: Cannat et al. (1995); Stephens (1997); Casey et al. (1997); Brandon et al. (2000); Lee et al. (2003); Miyashiro et al.

(1969); Aumento and Loubat (1971); SWIR: Snow and Dick (1995); Godard et al. (2008); Hess Deep (EPR): Gillis et al. (1993); Blum (1990); Garret Transform (EPR): Niu and Hekinian (1997). Compilation of abyssal peridotite data from Johnson et al. (1990) and Niu (2004). 120
Figure 4.6. Measured and reconstructed bulk rock major element concentrations of ocean island xenoliths from Tahiti on an Al_2O_3 variation diagram. 123
Figure 4.7. Measured and reconstructed bulk rock major element concentrations of ocean island xenoliths from Cape Verde on an Al_2O_3 variation diagram. 124
Figure 4.8. Measured and reconstructed bulk rock major element concentrations of ocean island xenoliths from Lanzarote on an Al_2O_3 variation diagram. 125
Figure 4.9. Measured and reconstructed bulk rock major element concentrations of the global suite of ocean island xenoliths plotted on an Al_2O_3 variation diagram. 126
Figure 4.10. Measured and reconstructed bulk rock major element concentrations of abyssal peridotites plotted on an Al_2O_3 variation diagram. Bulk compositions are reconstructed from mineral chemistry and modal data for abyssal peridotites from the Central Indian Ridge (Hellebrand et al., 2002), Southwest Indian Ridge (Dick et al., 1984), American-Antarctic Ridge (Dick et al., 1984) and Hess Deep (Chapter 3; this study). Measured bulk compositions are from sources cited in Fig. 3.3 (Chapter 3). 127
Figure 4.11. Histogram showing measured bulk concentration of Al_2O_3 in (a) ocean island xenoliths and (b) abyssal peridotites. 130
Figure 4.12. Median and mean measured and reconstructed bulk rock major element concentrations of ocean island xenoliths and abyssal peridotites on an Al_2O_3 variation diagram. 131
Figure 4.13. Measured and reconstructed bulk rock concentrations of (a) Sc and (b) V plotted on an Al_2O_3 variation diagram. Error bars on reconstructed data represent the uncertainty propagated from the variance calculated for modal percentage of each mineral phase using the method of Solomon (1964). 133
Figure 4.14. Chondrite-normalised LREEs (a) Ce and (b) Nd, MREEs (c) Sm and (d) Eu and trace elements (e) Ti and (f) Zr in ocean island xenoliths and abyssal peridotites plotted against chondrite-normalised Yb concentrations. Error bars represent the uncertainty propagated from the variance calculated for modal percentage of each mineral phase using the method of Solomon (1964). The error bars for Ce and Nd and for Hess Deep reconstructed data are smaller than the symbols. Also shown is the concentration of DMM (Workman and Hart, 2004) in comparison with ocean island xenoliths and abyssal peridotites. The extent of melting in ocean island xenoliths and abyssal peridotites is estimated by comparing observed concentrations of the above elements with those of a model-melting curve. The concentrations from 5 to 25% melting of DMM (Workman and Hart, 2004) are calculated using equations shown in Chapter 3 (Section 3.5.2). Data sources in addition to ocean island xenoliths analysed in this study are as follows: Canary Islands: Siena et al. (1991); Neumann (1991); Wulff-Pedersen et al. (1996), Neumann et al. (2002, 2004); Cape Verde: Bonadiman et al. (2005); Kerguelen: Gregoire et al. (1997; 2000); Sen and Leeman (1991); Tahiti: Qi et al. (1994); Ocean island xenolith data compilation from Simon et al. (2008). Abyssal peridotite data sources are as follows: MAR: Stephens (1997); Casey et al. (1997); Aumento and Loubat (1971); SWIR: Snow and Dick (1995); Godard et al. (2008); Garret Transform (EPR):

Niu and Hekinian (1997) and Hess Deep data from Chapter 3. Compilation of abyssal peridotite data from Johnson et al. (1990) and Niu (2004). 134
Figure 4.15. Zoning profile for forsterite (Fo) in olivine for ocean island xenolith sample NI 120 C from Cape Verde measured from rim to core. A comparison with a model zoning profile indicates an Mg-Fe diffusion time of ~ 2 years for the observed Fo-zoning. 138
Figure 4.16. Model concentrations of Ce in clinopyroxene calculated using the diffusion coefficient of Van-Orman et al. (2001) at 1200ºC for time lengths of 2 (blue diamonds) and 83 years (red diamonds) time. The diffusion equation used in the calculation is for a semi-infinite plane (Crank, 1975). 140
Figure 4.17. Chondrite-normalised concentrations of (a) Ce, (b) Nd, (c) Sm, (d) Eu, (e) Ti and (f) Zr in clinopyroxene plotted against chondrite-normalised Yb in clinopyroxene from ocean island xenoliths and abyssal peridotites in comparison with concentrations of clinopyroxene in equilibrium with DMM (Workman and Hart, 2004). Also shown is the model-melting curve for DMM-clinopyroxene in equilibrium with the residue of 5 to 25% melting. The concentration of clinopyroxene is calculated in equilibrium with the residue of DMM-melting as in Figure 4.7. Mineral/melt partition coefficients (Kd) from Table 4.4 are used in the calculation. In addition to clinopyroxenes analysed in this study, the sources of clinopyroxene data are as follows: Kerguelen: Gregoire et al. (2000); The Canary Islands: Neumann et al. (1991); Siena et al. (1991); Neumann et al. (2002); Wulff-Pedersen et al. (1996); Cape Verde: Bonadiman et al. (2005); Grande Comore: Coltorti et al. (1999); Hawaii: Sen (1988); Sen et al. (1993); Sen and Jones (1988); Sen and Presnall (1996); Yang et al. (1998). Sources for abyssal peridotite clinopyroxene data are as follows: American-Antarctic Ridge: Dick (1989); SWIR: Dick (1989); Johnson et al. (1990); MAR: Tartorotti et al. (2002); Johnson and Dick (1992); CIR: Hellebrand et al. (2002); Workman and Hart (2004); Hess Deep (Dick and Natland, 1996); Chapter 3. 150
Figure 4.18. Chondrite normalised Ce-concentration in clinopyroxene from ocean island xenoliths and abyssal peridotites in comparison with clinopyroxene in equilibrium with a model melting residue of DMM in the spinel field. The model-melting residue represents melting in 5% increments. Also shown is the clinopyroxene composition in equilibrium with the model residue of melting of DMM in the garnet field followed by equilibration in the spinel field. 152
Figure 4.19. Orthopyroxene/Clinopyroxene REE ratios for harzburgite and lherzolite ocean island xenoliths compared with published partition coefficients for pyroxenes in equilibrium in spinel harzburgites (Hellebrand et al., 2005). 153
Figure 4.20. Chondrite-normalised reconstructed bulk rock abundances of (a) Ce, (b) Nd, (c) Sm and (d) Eu in ocean island xenoliths plotted against age of oceanic lithosphere beneath each ocean island. Also shown for comparison are chondrite-normalised bulk rock abundances of REEs in abyssal peridotites. No systematic variation is observed with age in both, measured and reconstructed, bulk rock concentrations of the REEs. 154
Figure 4.21. Chondrite-normalised reconstructed bulk rock abundances of (a) Ce, (b) Nd, (c) Sm and (d) Eu in ocean island xenoliths plotted against age of oceanic lithosphere beneath each ocean island. Also shown for comparison are chondrite-normalised bulk rock abundances of REEs in abyssal peridotites. No systematic variation is observed with age in both, measured and reconstructed, bulk rock concentrations of the REEs. 155

Figure 5.1. Illustration of the model for the geochemical evolution of the oceanic lithospheric mantle. 164
Figure 5.2. Schematic diagram of the experimental set up for high-pressure experiments. Holes will be drilled in an olivine crystal and experimental charges placed into these. The crystal will then be placed inside a platinum container. Since two samples can be run at a time, the reversal runs can be carried out at the same time and under the exact same conditions as the initial experiments. 166

Acknowledgments

First and foremost, I sincerely thank Laurence Coogan for his invaluable advice, his continuous support, patience and motivation. I could not have completed this thesis without him. Laurence's guidance has helped me throughout the duration of my doctoral studies and no words could express my immense gratitude toward him.

I thank Prof. Dante Canil for the valuable discussions on techniques in experimental petrology and for allowing me the use of his laboratory.

My supervisory committee Prof. Kathryn Gillis, Prof. Dante Canil and Prof. Tom Fyles have been very kind in extending their support and encouragement and for that I am truly thankful.

To my teachers, Prof. A. G. Dessai, Prof. T. A. Vishwanath, Prof. K. Mahinder, Prof. A. G. Agshikar, Prof. R. Gurav, Late Prof. O. A. Fernandes, Prof. A. Viegas, Prof. D. Parab and Prof. S. Sabnis: My gratitude towards you cannot be expressed in easy words. Thank you!

I extend my appreciation towards Prof. Mati Raudsepp and Edith Czech for their help during my sessions on the electron microprobe at UBC.

My sincere thanks to Prof. Eric Hellebrand for his encouraging words on my research and thesis and his invaluable advice on further improvements.

My special thanks to Jody Spence for all the help in conducting LA-ICP-MS analyses and for the solution ICP-MS analyses, which were performed most promptly and with so much consideration for my timeline.

I would like to thank Dr. Elaine Humphrey and Adam Schuetze for supporting me during sample analyses on the scanning electron miscroscope at the University of Victoria.

To Prashant: Thank you so much for standing by me all these years and for giving me the inspiration to pursue my ambition. My sincere thanks to Prashant for listening to me rambling on about the oceanic lithospheric mantle, a topic now quite well known to him.

My family has been most patient and supportive during the long years I have spent so far away from them. My gratitude for their presence in my life is beyond measure. To my family: Malati Shejwalkar, Rajaram Shejwalkar, Anodita Shejwalkar, Sureshchandra Shejwalkar, Shaila Shejwalkar, Abhijit and Akshata, thank you.

My sincere appreciation and thanks to my parents-in-law Mohan Pednekar and Satyavati Pednekar and my entire Pednekar family – Pradeep, Pradnya, Pravin, Sampada,

Sandeep, Shilpa, Smita and Nakul and all the youngsters in my family for believing in me and for the love you all have bestowed upon me.

For my family in Canada: Thank you so much Nirmala, Jerome, Jasleen and Vikram for always being by my side. I truly appreciate your support and encouragement. I extend my sincere thanks to Krishna for inspiring me in so many ways. I thank Subbarao for his friendship and for the afternoon walks in the sun and to Bidyut for the much-needed tea breaks. My sincere thanks to Jothir and Ilam for hosting innumerable potluck dinners and for all the fun and laughs and countless unforgettable moments.

I would also like to thank my friends Mayur and Niyati who have always been there for me. The long online chats were excellent companions in times of great stress.

Thanks to Patwin, Vijay, Mahadev, Nandakumar, Vaidehi, Puja and Chaitanya for being the best geology group ever. My interest in the subject would never have been fuelled if not for your company.

Dedication

For my grandparents,

Malati and Narayan Shejwalkar

1. The thermal and geochemical evolution of the oceanic lithospheric mantle

1.1. The oceanic lithospheric mantle

The geochemical evolution of the Earth takes place by the process of differentiation, which is related to the cooling of the planet as a whole. Extraction of heat from the Earth's interior controls large-scale processes such as plate motion and the Earth's magnetic field. Motion of oceanic plates involves the movement of the Earth's lithosphere (Fig. 1.1), the rigid outer layer of the Earth consisting of the crust and the top of the upper mantle over a weaker layer called the asthenosphere (Fig. 1.1). Although the asthenosphere is generally solid, it can partially melt due to decompression e.g. beneath mid-oceanic ridges (MOR; Langmuir et al., 1992; Phipps-Morgan, 1997). The oceanic lithosphere forms as a result of partial melting at the MOR axis. As it ages, the lithosphere that forms at MORs cools and moves away from the MOR axis. The subsequent subduction of cold plates at convergent margins is the principal component of the plate tectonics paradigm that facilitates heat loss from the Earth's interior.

The precise definition of the lithosphere depends on the property being considered. For example, in terms of the temperature structure, the oceanic lithosphere can be defined as a thermal boundary layer through which heat is lost by conduction as opposed to convection (Schubert et al., 2001). As a mechanical boundary layer, the oceanic lithosphere is defined by rocks that are mechanically rigid and may not be deformed more than 1% in 10^8 years at a given pressure (Schubert et al., 2001). The base of the mechanical boundary layer is defined by an isotherm since the mechanical rigidity depends on viscosity, which in turn is dependent on temperature (Schubert et al., 2001). It has been hypothesised that the

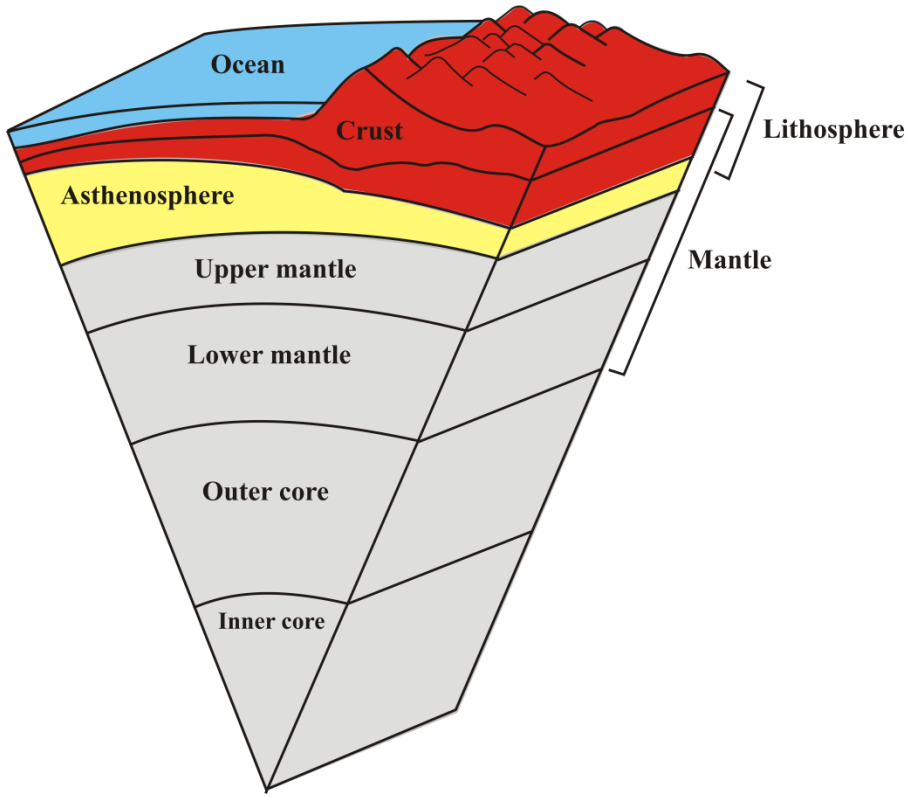

Figure 1.1. Cartoon cross section of the Earth. The innermost portion of the Earth consists of a solid inner core and a liquid outer core and is largely made up of the siderophile elements, Fe and Ni. The core is followed by the lower and upper mantle, which is largely made up of silicates. The asthenosphere (shown in yellow) is a low-viscosity layer that lies at the top of upper mantle and is overlain by the lithosphere (shown in red). The lithosphere is the outermost rigid layer of the Earth and is made up of the crust and the topmost part of the upper mantle. Figure modified from http://www.geology.sdsu.edu/how_volcanoes_work/Heat.html

mechanical boundary layer is underlain by the thermal boundary layer (McKenzie and Bickle, 1988), which separates the lithosphere from the underlying convecting asthenosphere (Fig. 1.1). The thickness of the thermal boundary layer is not well defined (e.g. Schubert, 2001), but since temperature and rheology generally are strongly coupled and the mechanical behaviour of a region controls whether it convects, the lithosphere, whether defined as a thermal or mechanical boundary layer, is broadly the same. In the following sections, the evolution of the thermal boundary layer (Section 1.2) is discussed separately from the mechanical boundary layer (Section 1.3).

Partial melting of the mantle beneath the MOR axis leaves a residual layer that forms the oceanic lithospheric mantle. After its formation at the MOR axis, the oceanic lithospheric mantle undergoes geochemical modifications prior to subduction at convergent margins. The only direct samples available for the geochemical study of the oceanic lithospheric mantle are (1) abyssal peridotites i.e. pieces of the upper oceanic lithospheric mantle exposed on the seafloor; (2) mantle xenoliths from ocean islands, which represent the deeper portions of the oceanic lithospheric mantle and (3) fragments of the oceanic lithosphere that have been obducted on to the edge of continental plates. This study focuses on abyssal peridotite and ocean island xenoliths and an introduction to the geochemistry of each is provided in Section 1.4.

1.2. The oceanic lithosphere as a thermal boundary layer

Models for the cooling of the oceanic lithosphere as a thermal boundary layer have been developed to explain observed surface heat flow and bathymetry of the oceanic lithosphere (McKenzie, 1967; Davis and Lister, 1974; Crough, 1975; Parsons and Sclatter, 1977; Stein and Stein, 1992; Doin and Fleitout, 1996). Surface heat flow over the ocean

floor decreases while water depth increases with increasing plate age. The three main types of models for cooling of the oceanic lithosphere are: (1) the half space-cooling model (Fig. 1.2a), (2) the plate cooling model (Fig. 1.2b) and (3) the CHABLIS (Constant Heat flux Applied at the Bottom Lithosphere ISotherm) model (Fig. 1.2c).

The half-space cooling model predicts cooling of the oceanic lithosphere by conduction through the top of a semi-infinite half space of the underlying mantle such that the depth varies as the square root of age of the oceanic lithosphere. The temperature at the top of the lithosphere is constant and the maximum thickness of the lithosphere resulting from cooling of the half space is unlimited (Davis and Lister, 1974). Figure 1.2a shows isotherms for the oceanic lithosphere as a function of depth and age as predicted by the half space model. Seafloor bathymetry can be predicted from the half space model if the (average) thermal expansivity of the lithosphere is known. The half-space model's approximation for the seafloor bathymetry is close to the observed topography for oceanic lithosphere younger than ~80 Ma (Parsons and Sclatter, 1977). For ages greater than 80 Ma, the observed depth varies slowly whereas the half-space model predicts deeper depths for oceanic lithosphere older than 80 Ma. Similarly, heat flow also varies slowly beyond ages of 65 Ma and it has been suggested that heat flow for oceanic lithosphere aged between 65 to 120 Ma may depend on deep lithosphere reheating (Lister et al., 1990). Additional heat flow from below the lithosphere to balance the heat loss from the seafloor can stop cooling of the older lithosphere as predicted by the half-space model, which causes flattening of the lithosphere older than ~80 Ma (e.g. McKenzie, 1967; Parsons and Sclatter, 1977; Stein and Stein, 1992; DeLaughter et al., 2005).

The plate model assumes a constant depth isotherm at the base of the oceanic lithosphere. Although the predictions of the half-space and plate models are similar for

oceanic lithosphere younger than ~80 Ma, they are different for older oceanic lithosphere (Fig. 1.2b). Small-scale convection in the underlying mantle is a hypothesised source of heat at the base of the lithosphere, which results in a heat flux into the base of older and colder oceanic lithosphere (McKenzie, 1967; Parsons and Sclatter, 1977; Stein and Stein, 1996). The Parsons and Sclatter (1977) model described a cooling plate that fit observed heat flow and bathymetry based on a basal temperature of 1350ºC +/-275ºC and a plate thickness of 125 km +/-10 km (Parsons and Sclatter, 1977). An improved heat flow data set used by Stein and Stein (1992) to model cooling of the oceanic lithosphere obtains a better fit to observed data by using a hotter (1450ºC +/-250ºC) and thinner (95 km +/-15 km) lithosphere.

A third model that describes the observed heat flow and bathymetry data is the CHABLIS model (Crough, 1975; Doin and Fleitout, 1996; Fig. 1.2c). This model assumes a lithosphere defined by a given isotherm and a constant heat flux at the base of the oceanic lithosphere at all ages resulting in a continuously thickening lithosphere (Doin and Fleitout, 1996). The CHABLIS model differs from the plate model in its boundary condition; i.e. a constant heat flow at the base of the lithosphere in the former versus a constant temperature at a given depth for the latter (Doin and Fleitout, 1996).

1.3. The oceanic lithosphere as a mechanical boundary layer

The oceanic lithosphere as a mechanical boundary layer begins to form as a residue of partial melting at MORs (Fig. 1.3a; e.g. Langmuir et al., 1992) where melting occurs due to decompression and mid-ocean ridge basalts (MORB) crystallize to form the oceanic

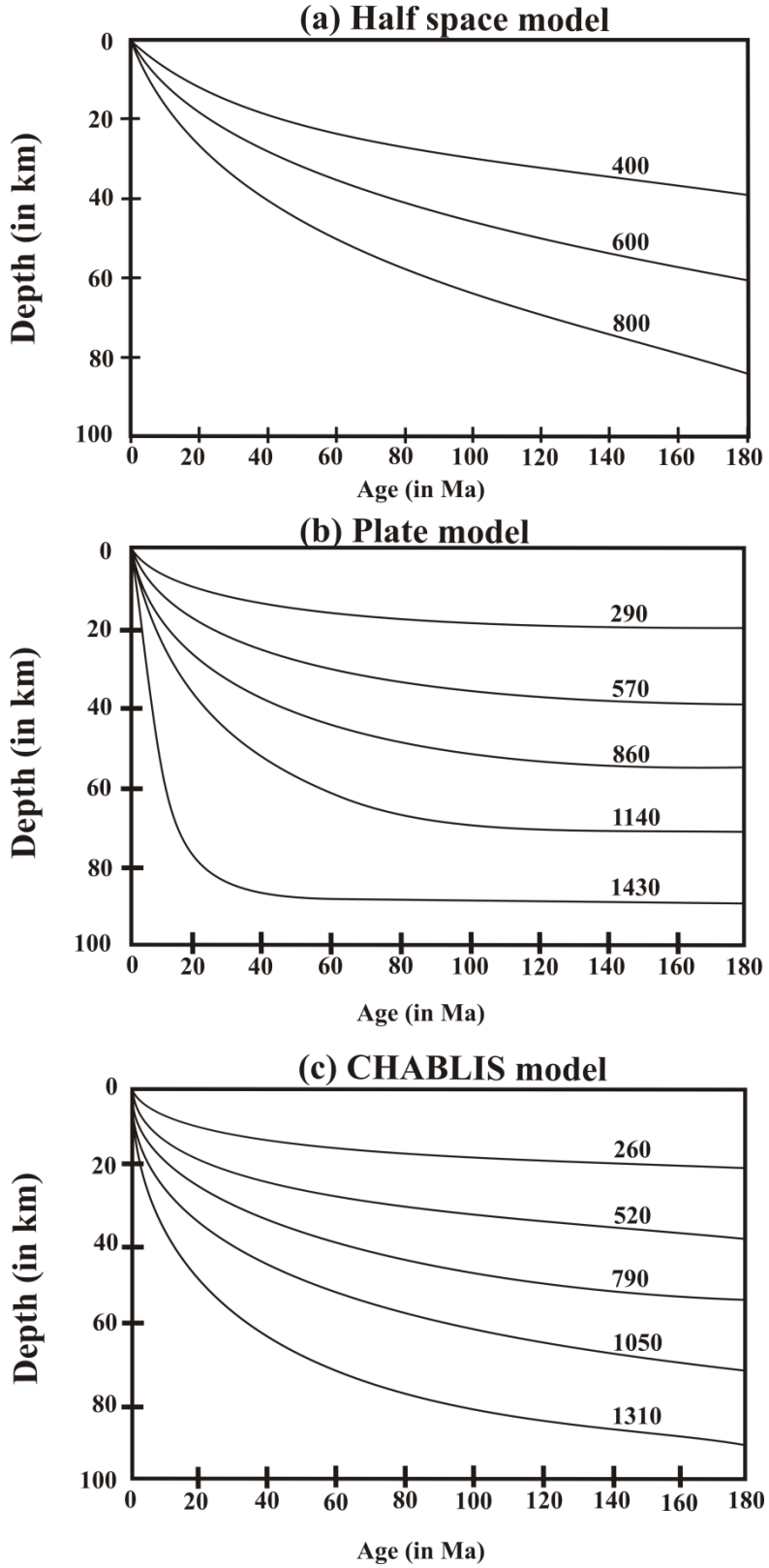

Figure 1.2. (Caption on following page)

Figure 1.2. Predicted distribution of isotherms in the oceanic lithosphere as a function of age for: (a) the half space model, (b) the plate model and (c) the CHABLIS model. (a) In the half space model, the oceanic lithosphere cools by conduction through the top of a semi-infinite half space of the underlying mantle (Davis and Lister, 1974). The thickness and isotherms for the half space model are calculated based on Turcotte and Schubert (2002). A thermal diffusivity of $1*10^{-6}$ m^2/s and initial temperature of 1400ºC is used in construction of the half space model above. (b) In the half space model, the P-T array varies with age for the entire lithosphere. In the plate model, the oceanic lithosphere forms with its full thermal thickness of 95 km and basal temperature of 1450 ± 250ºC (Stein and Stein, 1992) at the ridge axis. Based on the plate model, the P-T array in the lithosphere remains constant for lithosphere greater than ~80 Ma. In the CHABLIS model the oceanic lithosphere increases in thickness away from the ridge axis. (c) It has been hypothesised that small-scale mantle convection provides constant heat flux at the base of the oceanic lithosphere (Doin and Fleitout, 1996). The figures for the plate and CHABLIS models are drawn based on Doin and Fleitout (1996).

crust (Fig. 1.3a). The residue of melting remains behind to form the oceanic lithospheric mantle, which is largely made of peridotites.

The oceanic lithosphere is hypothesised as a compositionally distinct residue of partial melting of the mantle at ridge axes (Phipps-Morgan, 1997). During its formation and subsequent journey from the ridge axis to subduction zone, the oceanic lithospheric mantle cools and may be modified chemically. A combination of these processes influences its physical properties such as density and viscosity (Hirth and Kohlstedt, 1996; Afonso et al., 2007). Initially, melt extraction at ridge axes results in depletion of highly incompatible elements including H_2O, which leaves a residue with increased viscosity (Hirth and Kohlstedt, 1996). The extraction of Fe during melting decreases the density of the residual lithospheric mantle making it a buoyant layer above the asthenosphere. This can cause a 1-2% decrease in the density of the residual layer (Phipps-Morgan, 1997). This light or high viscosity layer generated by partial melting may act as a mechanical boundary layer and

define the "plate" in plate cooling models. As the oceanic lithosphere ages and moves away from the ridge axis, processes such as metasomatism can modify its composition.

The chemical composition of the residual layer that forms as a result of partial melting at ridge axes depends on the starting composition and degree of melt extraction. The density of the oceanic lithosphere can also vary due to the spinel to garnet transition (Wood and Yuen, 1983; Afonso et al. 2007), which in turn depends on the pressure-temperature-composition (P-T-X) structure of oceanic lithosphere. It has been suggested that the removal of water during melting beneath the mid-ocean ridges increases the viscosity of the residual layer (e.g. Phipps-Morgan, 1997). After the formation of the residual layer, small (< 1%) mantle melt fractions that are enriched in highly incompatible elements such as Ce can percolate into the oceanic lithosphere and change its composition (McKenzie, 1989). The H_2O/Ce ratio is uniform for mid-oceanic ridge basalts suggesting that the two have similar partition coefficients (Michael, 1995). The addition of Ce to the oceanic lithospheric mantle during metasomatism is likely to add H_2O in the amount proportional to that of Ce present in the metasomatising melts. The addition of water to the residual layer can cause a decrease in viscosity if the water is absorbed by minerals such as olivine in the residual layer (e.g. Hirth and Kohlstedt, 1996). Hence, metasomatism can potentially weaken the oceanic lithospheric mantle causing rheological changes (Phipps-Morgan, 1997).

1.4. Geochemistry of the oceanic lithospheric mantle

1.4.1. Abyssal peridotites

Abyssal peridotite samples are obtained by drilling into the oceanic lithosphere and dredging and submersible studies. The thickness of the oceanic crust varies as a function of

the extent of melting beneath the ridge axis, which in turn is a function of the temperature of the underlying mantle (e.g. Langmuir et al., 1992). At high mantle potential temperatures, melting begins at deeper levels and generates a thicker oceanic crust (Fig. 1.3b; Langmuir et al., 1992). Conversely, when the mantle temperature is low, melting begins at shallow depths thus resulting in less melt being generated and a thinner crust formed (Fig. 1.3c; Langmuir et al., 1992). As a consequence of the higher extent of melting associated with higher mantle potential temperatures, the residual oceanic lithosphere is highly depleted and is buried beneath a thick crust (Fig. 1.3b) as opposed to thinner crust where the extent of melting is low (Fig. 1.3c). In the latter scenario, the residual oceanic lithosphere is covered by thin or no crust and can be exposed at the seafloor by faulting (Fig. 1.3c). However, it has been suggested that some of the melt extracted in regions of thin crust may begin to crystallise below the crust and that the ridge segment may have thicker crust composed of gabbro, sheeted dykes and basalt (Cannat, 1996). Mantle peridotites can also be exposed at the seafloor at transform faults, which is where most samples studied to-date come from and along low-angle normal faults that exhume peridotites to crustal levels.

Abyssal peridotite studies provided the first direct information of the uppermost mantle (e.g. Miyashiro et al., 1969). However, upper mantle exposures are restricted to certain regions on the seafloor e.g. fracture zones (e.g. Dick et al., 1984), tectonic deeps (Niu, 1997), serpentine domes (Parkinson and Pearce, 1998) and some passive continental margins (Bodinier and Godard, 2003). Regions where abyssal peridotites have been sampled along the seafloor include slow spreading ridges such as the Mid-Atlantic Ridge and Indian Ridge system (e.g. Dick et al., 1984; Johnson et al., 1990; Elthon, 1992; Casey, 1997; Seyler and Bonatti, 1997; Hellebrand et al., 2002) and the ultra-slow South-West

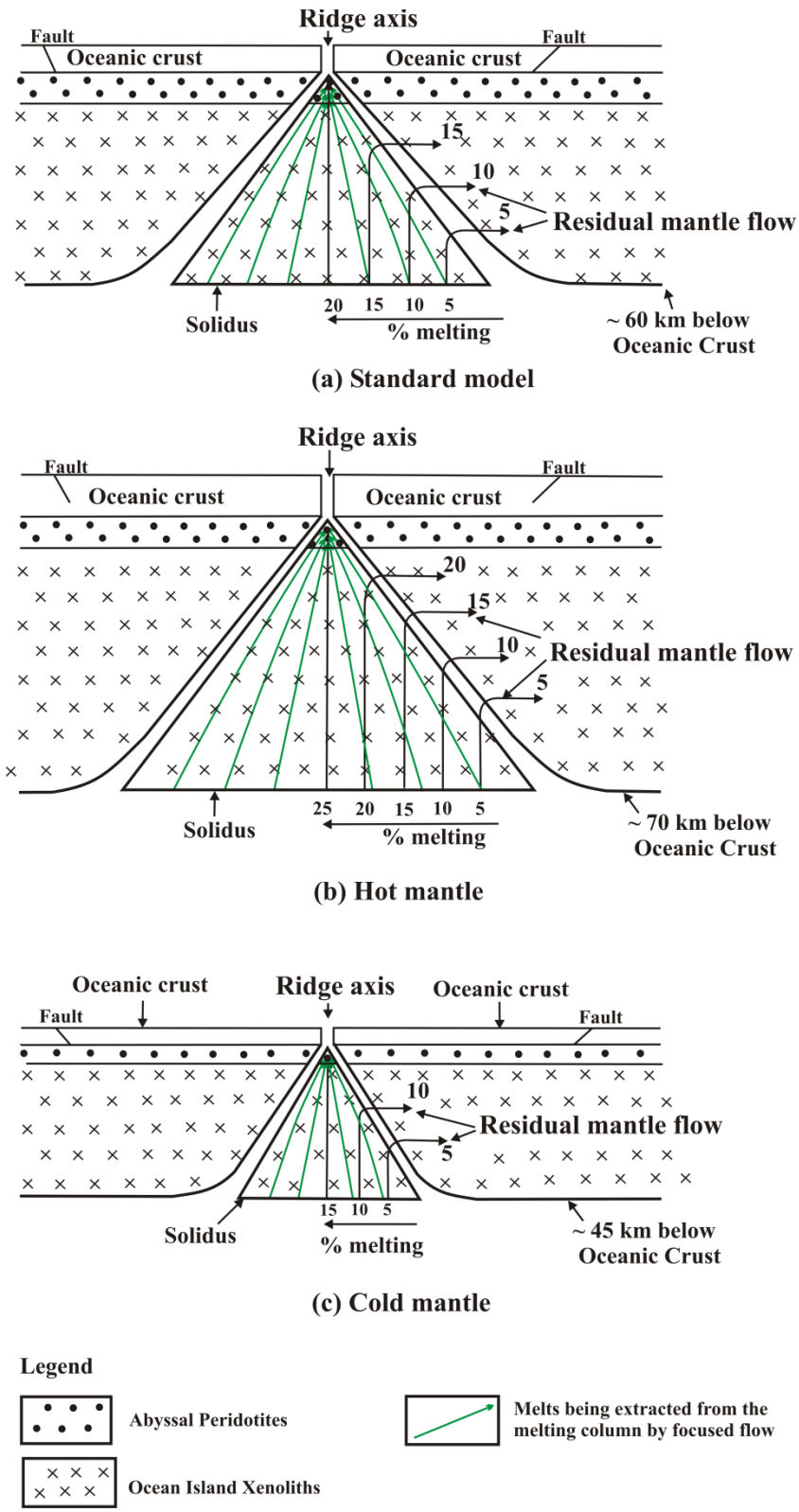

Figure 1.3. (Caption on following page)

Figure 1.3. Illustration of the melting column at a MOR showing the process of decompression melting beneath the ridge axis and generation of mid-ocean ridge basalt that crystallises to form the oceanic crust. Partial melting in the melting column leaves behind a residue that is sampled as abyssal peridotites at the top and ocean island xenoliths in the lower portions of the oceanic lithospheric mantle. (a) Melting begins at the solidus, which is generally located at a depth of ~ 60 kms beneath the oceanic crust (Langmuir et al., 1992). The percentage of melting is highest at the axis of the melting column, with progressively lower percentages towards the sides. (b) The melting can extend up to greater depths beneath the oceanic crust if the mantle potential temperature is high. The crustal thickness associated with greater extent of melting is also higher and residual abyssal peridotites formed as a residue of partial melting are less likely to be exposed close to the ocean floor and are likely to be more depleted. (c) If the mantle is colder than average, melting begins at a shallower depth and the associated crustal thickness is lower than average and abyssal peridotites are likely to be exposed on the seafloor by tectonism. However, it was later suggested that the thickness of the crust in regions of slow spreading (cold mantle) could vary along the ridge axis. The crystallisation of basaltic melts in a cold mantle can take place below the crust resulting in a thicker crust composed of a mixture of gabbro, sheeted dykes and basaltic lava (Cannat, 1996). The above diagrams are based on Langmuir et al. (1992).

Indian Ridge (e.g. Johnson and Dick, 1992) and Gakkel Ridge (e.g. Hellebrand et al., 2002). The only abyssal peridotite samples from the fast spreading Pacific Ridge system are from the Garrett transform and the Hess Deep (Gillis, Mevel et al., 1993; Dick and Natland, 1996; Niu, 1997; Niu and Hekinian, 1997). Other regions where abyssal peridotites were sampled include supra-subduction zone settings such as the Tyrrhenian Sea (Bonatti et al., 1990), Izu-Bonin-Mariana Forearc (Parkinson and Pearce, 1998) and the South Sandwich Arc (Pearce et al., 2000).

The most common lithology in abyssal peridotites is harzburgite followed by lherzolite along with rare occurrences of dunites, spinel wehrlites and pyroxenites. Plagioclase, when present, is seen in small proportions i.e. < 2% (e.g. Dick et al., 1984). It has been hypothesised that plagioclase is the product of melt infiltration and partial

crystallization (e.g. Dick et al., 1984). Abyssal peridotites are generally affected by hydrothermal and seawater alteration and their whole rock compositions are strongly modified by this. However, some minerals may remain unaltered and *in situ* mineral analyses of these crystals provide direct information on upper mantle melting and geochemistry (e.g. Johnson et al., 1990).

Abyssal peridotites have been interpreted as residues of partial melting of the mantle beneath the mid-oceanic ridges (e.g. Dick et al., 1984; Michael and Bonatti, 1985; Dick, 1989; Johnson et al., 1990). Different extents of melting of the mantle are suggested for abyssal peridotites, which correlate with MORB chemistry in the respective regions (e.g. Klein and Langmuir, 1987). However, it has also been suggested that abyssal peridotites may not be simple residues of partial melting (e.g. Elthon, 1992). Since the modal proportion of olivine in abyssal peridotites is higher than that predicted for model melting residues (Kinzler and Grove, 1992), it was suggested that abyssal peridotites are not the products of progressive melting of similar mantle sources (Niu et al., 1997). Instead Niu (1997) suggested that the excess olivine observed in abyssal peridotites is the result of olivine crystallisation during the ascent and cooling of mantle melts. Abyssal peridotites are thus suggested to be mixtures of melting residues and excess olivine (Niu, 1997). Although heterogeneities in the mantle sources have been inferred based on clinopyroxene veins and layers in mantle peridotites (e.g. Natland, 1989), the observed abyssal peridotite compositions require heterogeneities in olivine/orthopyroxene ratios in the source mineralogy (Niu et al., 1997). This interpretation of Niu et al. (1997) was based on comparison of abyssal peridotites compositions with experimental melting paths (Kinzler, 1997; Walter et al., 1995; Kinzler and Grove, 1992; Baker and Stolper, 1994).

In terms of major element compositions of abyssal peridotites, it was observed that reconstructed bulk compositions did not follow the trends of equilibrium or fractional melting (Niu et al., 1997). For example, the strong positive correlation between reconstructed bulk rock FeO and MgO could not be reproduced by model melting curves (Niu et al., 1997). It was also observed that abyssal peridotites tend to be enriched in MgO at a given Na_2O concentration relative to model melting residues (Niu et al., 1997). It was thus interpreted that abyssal peridotites are the residues of melting beneath the ridge axis followed by crystallisation of olivine in the rocks (Niu et al., 1997). However, implementing different methodologies than Niu et al. (1997) to reconstruct the bulk-rock compositions did not reproduce the above-mentioned positive correlation between FeO and MgO (e.g. Baker and Beckett, 1998). It was later hypothesised that a combination of polybaric near-fractional melting and equilibrium melting is more likely to produce the observed abyssal peridotite compositions (Asimow, 1999). Another hypothesis put forth to explain the excess olivine in abyssal peridotites is that of Niu et al. (1997), wherein melt extraction takes place by porous flow and crystallisation of olivine from cooling melts at the top of the residual melting column.

A contrasting hypothesis suggests that melts are extracted by diffuse porous flow followed by crystallisation of olivine from the melts (Kelemen et al., 1997). The above hypotheses are tested and discussed in detail in Chapter 3. Detailed examination of mineral and bulk rock trace element systematics of a global abyssal peridotite suite has proved useful in understanding the melt extraction process. For example, clinopyroxenes in abyssal peridotites have very low abundances of light rare earth elements (LREE) and it has been hypothesised that the melting process involved incremental extraction of melts from near-fractional melting of the source mantle (Johnson et al., 1990; Kelemen et al., 1997). The

melts from near-fractional melting are hypothesised as extracted through dunite channels that are not in equilibrium with the surrounding mantle.

1.4.2. Mantle xenoliths from ocean islands

Fragments of the oceanic lithospheric mantle are brought to the surface by basaltic lavas that erupt at intraplate volcanic islands in the form of xenoliths. The most geochemically well-studied mantle xenoliths are from the Canary Islands (Siena et al., 1991; Neumann, 1991; Neumann et al., 1995; Wulff-Pedersen et al., 1996; Neumann and Wulff-Pedersen, 1997; Andersen and Neumann, 2001; Neumann et al., 2002; Neumann et al., 2004; Andersen et al., 2005; El-Rus et al., 2006;), Hawaii (Sen and Presnall, 1986; Sen, 1988; Sen and Leeman, 1991; Sen et al., 1993; Sen et al., 1996; Yang et al., 1998; Ducea et al., 2002; Keshav and Sen, 2003; Sen et al., 2005;), Kerguelen (Matielli et al., 1996; Gregoire et al., 1997; 2000; Delpech et al., 2004; Bascou et al., 2008) and Cape Verde (Shaw et al., 2006; Bonadiman et al., 2005) followed by those from Tahiti (Tracy, 1980; Qi et al., 1994), French Polynesia (Tommasi et al., 2004), Grande Comore (Coltorti et al., 1999) and Samoa (Hauri et al., 1993; Hauri and Hart, 1994).

Studies on mantle xenoliths are useful in deciphering the processes that modify the geochemical composition of the mantle. A concept that gained the widest attention in the field of mantle studies using ocean island xenolith is metasomatism. Metasomatism has been documented in xenoliths from several ocean islands e.g. the Canary Islands (Wulff-Pedersen et al., 1996; Neumann et al., 2002; 2004), Kerguelen (Gregoire et al., 1997; 2000), Hawaii (Sen et al., 1993; Yang et al., 1998), Cape Verde (Bonadiman et al., 2005) and Grande Comore (Coltorti et al., 1999). Enrichment in highly incompatible elements relative to moderately incompatible elements in ocean island xenoliths is indicative of metasomatism in the xenoliths.

Mantle xenoliths that are interpreted to be metasomatised by alkali-silicate metasomatising agents are common (e.g. Wulff-Pedersen et al., 1996) but those metasomatised by carbonatitic melts have also been documented (e.g. Coltorti et al., 1999; Gregoire et al., 2000). The occurrence of silicic glass in ocean island xenoliths was initially interpreted to be the result of host magma infiltration (e.g. Garcia and Presti, 1987). However, it was later hypothesised that the silicate glass is the result of reaction between peridotite minerals and metasomatising melts (e.g. Siena et al., 1991; Hauri et al., 1993; Coltorti et al., 1999). For example, glass in peridotitic ocean island xenoliths from Grande Comore is inferred to be the product of metasomatic reactions between peridotite minerals and alkali-carbonatitic melt (Coltorti et al., 1999).

In situ geochemical analytical techniques such as laser ablation inductively coupled plasma mass spectrometry (LA ICP-MS), ion microprobe and electron probe micro analyser (EPMA) have been used to determine mineral compositions at multiple points within crystals and glasses. Clinopyroxene in ocean island xenoliths is found to be the major repository for incompatible elements in ocean island xenoliths followed by orthopyroxene (e.g. Neumann et al., 2002). The concave upward rare earth element (REE) pattern observed in clinopyroxene in xenoliths from various ocean islands is possibly due to enrichment in highly incompatible elements caused by metasomatism (e.g. Sen et al., 1993). The processes involved in the evolution of the oceanic lithosphere beneath ocean islands such as Hawaii and the Canary Islands have been inferred based on the study of metasomatism in ocean island xenoliths. For example, metasomatic enrichment of LREEs in clinopyroxenes from Hawaiian ocean island xenoliths is hypothesised as being due to reaction of the lithosphere with Honolulu volcanics (Sen et al., 1993). Similarly, it was inferred that the upper mantle beneath the Canary Islands is metasomatised by carbonatitic

melts (Neumann et al., 2002; 2004). The type of metasomatism in ocean island xenoliths is discussed in detail in Chapter 4.

Along with providing indications for metasomatism of the mantle as discussed above, the study of ocean island xenoliths is also useful in deciphering the melting history of the oceanic lithosphere. The extent of partial melting involved in the formation of the residual lithospheric mantle has been predicted using bulk rock and mineral-major and trace element concentrations in ocean island xenoliths. A comparison of the Mg# ($Mg^{2+}/[Mg^{2+}+Fe^{2+}]$) of the bulk rock, olivine and clinopyroxene in xenoliths from the Kerguelen Islands with that of experimental melting residues of Jacques and Green, (1980) indicates high extent of melting (15-25%) in the lithosphere (Gregoire et al., 1997). Xenoliths from La Palma in the Canary Islands are also inferred to have undergone high extents of melting compared to MORB-source mantle due to their low concentration of moderately incompatible elements relative to normal MORB-source (Wulff-Pedersen et al., 1996).

In addition to major and trace element concentrations, the study of Sm and Nd isotopic ratios is used to determine of the melting history of the oceanic lithosphere. For example, the high Sm/Nd and $^{143}Nd/^{144}Nd$ ratios of Hawaiian spinel peridotites (specifically from Pali in Hawaii) are interpreted as indications for the peridotites being residues of Cretaceous partial melting beneath the Pacific Ridge (Ducea et al., 2002). However, it has been suggested that metasomatising melts can reset the Nd (and Sr) isotopic ratios as observed in xenoliths from the Canary Islands (Neumann et al., 2002). In general, Sr and Nd isotope data for ocean island xenoliths indicate isotopic signatures similar to the respective ocean island basalt (e.g. Matielli et al., 1996; Sen et al., 2003; Neumann et al., 2004; Simon et al., 2008). Isotope studies of whole rock and clinopyroxene

in ocean island xenoliths from the Canary Islands suggests that metasomatism of the lithosphere beneath the Canary Islands reset the Sr-Nd isotopic ratios to values within those of the Canary Island basalts (Neumann et al., 2004). It was later hypothesised that low $^{87}Sr/^{86}Sr$ ratios obtained from *in situ* analyses of clinopyroxenes in some xenoliths from the Canary Islands are evidence against interaction with plume melts (Simon et al., 2008).

In a single study that combines the major and trace element geochemistry of a global ocean island xenolith suite, it was interpreted that the xenolith suites from most ocean islands are dominated by highly refractory harzburgites (Simon et al., 2008). This was suggested for a highly refractory xenoliths with no residual clinopyroxenes, low whole rock Al_2O_3, CaO and heavy rare earth element (HREE) concentrations, low Al_2O_3 in orthopyroxene (< 3 wt%) and high Fo in olivine (average > 91.5; Simon et al., 2008). Simon et al. (2008) showed that these highly refractory ocean island xenoliths are significantly more refractory than abyssal peridotites. The model Os-isotope age of some refractory harzburgite xenoliths from Cape Verde is of the order of ~3300 Ma (Bonadiman et al., 2005), implying that they formed significantly prior to the oceanic lithospheric mantle (Simon et al., 2008). Significantly old Os-isotope ages have also been reported for xenoliths from Kerguelen (1600 Ma; Delpech et al., 2004) and the Canary Islands (~650 Ma; Simon et al., 2008). Old Os-isotope ages (up to 2000 Ma) have also been reported for abyssal peridotites from various ridge segments (e.g. Snow and Reisberg, 1995; Brandon et al., 2000; Harvey et al., 2006).

Refractory harzburgites that are sampled as ocean island xenoliths and abyssal peridotites and have old Os-isotope ages are interpreted as residues of high extents of melting that occurred episodically over the Earth's melting history (Simon et al., 2008). It is hypothesised that Os-isotopic ages in ocean island xenoliths and abyssal peridotites older

than the respective oceanic lithosphere may represent ancient recycled continental or oceanic lithosphere that is not related to the local lithosphere (e.g. Simon et al., 2008; Liu et al., 2008; Coltorti et al., 2010). It is interpreted that fragments of ancient melt depletion residues may be preserved in the convecting mantle (Brandon et al., 2000) and may be incorporated into the oceanic lithosphere during passive advection along mid-oceanic ridges or by accumulating to the base of the lithosphere as it cools and moves away from the ridge axis (Simon et al., 2008).

The process of subduction of the oceanic lithospheric mantle also plays a dominant role in the influx of geochemical heterogeneities into the mantle (e.g. Pilet et al., 2005). Recycled oceanic lithosphere is widely believed to be an important component of mantle plumes (e.g. Hofmann and White, 1982; Hofmann, 1997). However, it has also been suggested that the oceanic crust may not be associated with the source of ocean island basalts (e.g. Niu and O'Hara, 2003). Instead, metasomatised oceanic lithospheric mantle that has been subducted and recycled is more likely a source of ocean island basalt lavas (e.g. Niu and O'Hara, 2003; Workman et al., 2004; Pilet et al., 2005; 2008).

1.5. Scientific contribution of this thesis

The thermal models for the oceanic lithosphere described in Section 1.2 have been tested against variations in global bathymetry and heat flow data. However, there have not been attempts to test the thermal models with actual samples of the oceanic lithosphere. In order to understand the thermal structure of the oceanic lithospheric mantle using geochemical data, I use ocean island xenolith samples to investigate the P-T evolution of the oceanic lithospheric mantle. To this end, mineral chemistries of xenolith samples that represent various ages of the oceanic lithospheric mantle (25-180 Ma) are analysed. This

data is used to calculate the pressures and temperatures at which the xenoliths equilibrated. Because of problems with existing geothermobarometers I undertook an experimental calibration of the Ca-in-olivine geobarometer performing experiments at a constant pressure (1 atmosphere). The experimental methodology and calibration of the Ca-in-olivine geobarometer is discussed in detail in Chapter 2 of this thesis.

The geochemical evolution of the oceanic lithospheric mantle can be studied using abyssal peridotite and ocean island xenolith samples described in Section 1.4. The extent of melting that abyssal peridotites have undergone has been studied extensively (e.g. Dick et al., 1984; Michael and Bonatti, 1985; Dick, 1989; Johnson et al., 1990; Dick and Natland, 1996; Hellebrand et al., 2002a). Based on the extent of depletion of REEs, Zr and Ti in clinopyroxene in abyssal peridotites, it has been inferred that abyssal peridotites undergo near-fractional melting (Johnson et al., 1990). The melts that are extracted from the melting column have been argued to be brought to the base of the crust by flow of melts towards the center of the melting column (Fig. 1.3a). The inflow of a large portion of the melts towards the center of the melting column may cause the residual rocks at the top of the melting column to react with the melts (Fig. 1.3a). If melts are extracted by pervasive porous flow, melt/rock reaction can modify the composition of the uppermost oceanic lithospheric mantle, which is the source region of abyssal peridotites. In order to test whether melts are being extracted from the melting column by pervasive flow, a group of abyssal peridotites from Hess Deep Ocean Drilling Program (ODP) Site 895 were analysed in this study. Peridotites from Hess Deep were selected as they sampled by drill core technique and are likely to be less chemically modified by seafloor alteration. The results of major and trace element analyses of major mineral phases and the bulk rock are detailed in Chapter 3.

While abyssal peridotites come from the upper portion of the oceanic lithospheric mantle, ocean island xenoliths may include fragments of the lower oceanic lithospheric mantle that are emplaced on the surface by ocean island volcanics. Thermobarometry suggests that most ocean island xenoliths are derived from moderate depths (up to 70 km; Neumann, 1991; Qi et al., 1994; Lassiter, 2011). A comparison between the geochemical characteristics of ocean island xenoliths and abyssal peridotites is made in Chapter 4 and it is shown that the former have more depleted compositions compared to the latter. Along with having lower bulk rock Al_2O_3 and CaO and higher bulk rock Mg# than abyssal peridotites, the ocean island xenoliths also have lower concentrations of moderately incompatible trace elements such as V and Sc.

Although ocean island xenoliths have lower bulk rock concentrations of moderately incompatible elements, the bulk rock concentrations of highly incompatible trace elements such as Ce, Nd and Sr are higher in ocean island xenoliths than abyssal peridotites. This suggests that ocean island xenoliths undergo enrichment in highly incompatible element abundances through metasomatism (e.g. Wulff-Pederson et al., 1996; Gregoire et al., 1997; 2000; Moine et al., 2000; Neumann et al., 2002; 2004; Bonadiman et al., 2005; Shaw et al., 2006; Simon et al., 2008). As mentioned previously, metasomatism may weaken the oceanic lithosphere. However, whether metasomatism evolves progressively as the oceanic lithosphere ages has not been investigated. In this study, the geochemical evolution of oceanic lithospheric mantle is investigated using ocean island xenoliths (Chapter 4).

2. Experimental calibration of the role of Fe in Ca exchange between olivine and clinopyroxene at 0.1 MPa

2.1. Introduction

Thermal models for the oceanic lithospheric mantle include the half space model, the plate model and the CHABLIS model which are discussed in Chapter 1. These models for the thermal state of the oceanic lithosphere could be tested using geothermobarometry on ocean island xenoliths if a reliable geobarometer was available. Geochemical reactions between minerals in the upper mantle during cooling are temperature- and pressure-dependent and can therefore, in principle, be used to determine the temperatures and pressures of equilibration of these rocks. While several geothermometers are available for the calculation of temperatures of equilibration for spinel peridotites (e.g. Brey and Kohler, 1990; Ballhaus et al., 1991; Liermann and Ganguly, 2003; Wan et al., 2008), only one geobarometer suitable for spinel peridotites exists: the Ca-in-olivine geobarometer (Kohler and Brey, 1990).

The formation of the monticellite ($CaMgSiO_4$) component of olivine, due to the partitioning of Ca from clinopyroxene to olivine (see Eq. 2.1) is associated with a large volume change of 4.98 cm^3/mol and is suitable as a geobarometer (Kohler and Brey, 1990). Because of the importance of having a well-calibrated geobarometer for spinel peridotites, numerous experiments have been performed to calibrate the temperature and pressure dependence of calcium partitioning into olivine in the presence of clinopyroxene and orthopyroxene. Finnerty and Boyd (1978) conducted experiments in the CaO-MgO-Al_2O_3-SiO_2 (CMAS) system between 1000-1400ºC but did not obtain successful reversals in their

experiments. Adams and Bishop (1982, 1986) conducted experiments in $CaO-MgO-SiO_2$ and $CaO-FeO-MgO-SiO_2$ systems at 1100-1300ºC. However, the experimental calibration of Finnerty and Boyd (1978) and Adams and Bishop (1982, 1986) did not yield satisfactory results when applied to natural systems when used with the well-calibrated Al in orthopyroxene geobarometer of Kohler and Brey (1990).

The experiments of Kohler and Brey (1990) cover a wide range of temperatures (900 to 1400ºC) and pressures (0.2 to 6 GPa). The experimental results of Kohler and Brey (1990) for partitioning of Ca between olivine and clinopyroxene at 1000ºC and 900ºC give higher concentration of Ca in olivine than would be expected by extrapolation from higher temperatures. This change in the solubility of Ca in olivine has been hypothesised to be associated with the hypothesised preferential partitioning of Ca into the M2 site of olivine at lower temperatures i.e. order-disorder phenomenon for Ca between M1 and M2 sites of olivine (Kohler and Brey, 1990). Adams and Bishop (1986) also observed a discontinuity in partition coefficient for Ca between forsterite and diopside between temperatures of 1100 and 1200ºC, which they too explained as a result of order-disorder phenomenon. The calibration of the Kohler and Brey (1990) geobarometer involved separate equations for temperatures above and below ~1100ºC (Fig. 2.5), which was calculated in iterative steps from their experimental calibrations. From these calculations, a ‘kinked’ non-linear correlation between Ca-in-olivine and temperature was introduced into the Kohler and Brey (1990) calibration.

Along with being temperature and pressure sensitive, the exchange of Ca between olivine and clinopyroxene has been suggested to depend on the Fe-content of the system (Adams and Bishop, 1986). However, the compositional dependence of Ca partitioning is not considered in the Kohler and Brey (1990) calibration. The experiments of Kohler and

Brey (1990) were all conducted on natural lherzolites with Mg# 88 to 92.8 for olivine and they suggested that no significant effect of Fe-content was observed. Kohler and Brey (1990) consider the effect of Fe to be negligible for Mg# values between 87-100. However, based on experimental data at 7.5 GPa and temperatures of 1100, 1300 and 1500ºC, Kawasaki (1995) found a positive correlation between the Ca distribution between olivine and clinopyroxene (D_{Ca}) and $Fe^{2+}/(Fe^{2+}+Mg^{2+})$ in olivine.

When comparing the results of various experimental studies, the methodologies used for analysis need due consideration. For example, during electron microprobe analyses a beam of high-energy electrons is fired on the mineral to be analysed. This causes ionisation of inner shell electrons in the mineral, which are filled by electrons from outer electron shells with the excess energy released as characteristic X-rays. The region within the mineral being analysed where the electron beam hits the mineral is known as the interaction volume, which can extend several micrometers deep into the mineral. Characteristic X-rays from the target crystal are emitted in all directions, with only a small fraction going to the detector; some of these X-rays can cross grain boundaries into adjacent crystals (Dalton and Lane, 1996). The interaction between characteristic X-rays from the target crystal with the adjacent crystal may induce ionisation and emission of characteristic X-rays in the latter phase. This process is called secondary fluorescence. The experimental results of Kawasaki (1995) are not consistent with the values predicted by the Kohler and Brey (1990) calibration. This inconsistency may be due to unaccounted secondary fluorescence in the data of Kawasaki (1995). While the effect of secondary fluorescence is negligible in most cases, it can have a profound impact if the element of interest occurs as a trace element in the crystal being analysed and as a major element in the interfering crystal such as in the case of Ca in an olivine crystal close to a

clinopyroxene crystal (Dalton and Lane, 1996). Elements such as Fe in olivine can cause fluorescence of Ca X-rays in adjoining high-Ca phases due to primary FeKα X-rays originating in olivine (Dalton and Lane, 1996). Kohler and Brey (1990) avoided interference due to secondary fluorescence by physically separating the olivine crystals prior to analyses but there was no check on secondary fluorescence in the study of Kawasaki (1995).

In order to decipher the role of Fe in the partitioning of Ca between olivine and clinopyroxene, more experiments were needed with a wider range of Fe-content. With this aim in mind, a series of experiments were conducted in the CMAS system and in the CMAS+FeO+TiO_2+Na_2O+K_2O system at 0.1 MPa pressure. The results of this experimental study are detailed in this chapter and a version of this study was published in *Lithos* as Shejwalkar and Coogan (2013). From the results of 21 experiments with varying Fe-content in the starting compositions and run at temperatures ranging from 1170ºC to 1322ºC, it was established that the addition of Fe to the system substantially increases the concentration of Ca in olivine in equilibrium with clinopyroxene and orthopyroxene at a given temperature and pressure. Analyses of the resulting mineral compositions led to the construction of a geothermometer that incorporates the effect of Fe in the system in calculating equilibration temperatures of spinel peridotites.

The solubility of Ca in olivine has long been known to be temperature and pressure sensitive (e.g., Simkin and Smith, 1970) and thus can provide important insights into geological processes in mafic and ultramafic rocks. Additionally, the temperature sensitivity of the solubility of Ca in olivine, coupled to its relatively high diffusion coefficient (Coogan et al., 2005), leads to large amounts of Ca diffusing out of olivine during cooling of mafic and ultramafic rocks. The extent of Ca-loss thus can be used as a

geospeedometer to determine the cooling rate of such rocks (e.g., Coogan et al., 2007). Finally, it has been suggested that the Ca content of olivine phenocrysts in basalts can be used to provide insight into the mineralogy of the basalts' mantle source (peridotite versus pyroxenite; Sobolev et al., 2007).

In many mafic and ultramafic rocks, olivine co-exists with clinopyroxene and low-Ca-pyroxene (including many situations where one pyroxene is exsolved from the other) and the activity of Ca in the system is buffered by the reaction (e.g., Finnerty and Boyd, 1978):

$$3Mg_2Si_2O_6 + 2CaO = 2Mg_2SiO_4 + 2CaMgSi_2O_6 \qquad \text{Eq. 2.1}$$

In nature, the mineral phases are all Mg-Fe solid solutions and thus the simplest possible realistic system to consider is CaO-FeO-MgO-SiO_2. In this system (with three degrees of freedom) the Ca content of olivine is controlled by the pressure, temperature and Mg# of the system which is well represented by the forsterite (Fo) content of the olivine. Under the assumption that minor elements in the olivine and pyroxenes are of second order importance in controlling the thermodynamics of Eq. 2.1, the same three parameters are expected to provide the main controls on the Ca content of natural olivine crystals. Alternatively stated, the Ca content of an olivine in equilibrium with low-Ca-pyroxene and clinopyroxene can provide information about pressure or temperature provided that the other is known and the effect of Mg# is accounted for.

Calcium, being larger than Fe and Mg, is thought to favour the larger, distorted, octahedral M2 site in olivine (Birle et al., 1968; Brown, 1980; Lumpkin et al., 1983; Mukhopadhyay and Lindsley, 1983; Davidson and Mukhopadhyay, 1984). However, there

is evidence that small, but potentially significant, amounts of Ca also partition onto the M1 site especially in Fo-rich compositions (Lumpkin et al., 1983; Adams and Bishop, 1985) and higher temperature than 900ºC. An increase in the amount of Ca on the M1 site with increasing temperature has been suggested as an explanation for an apparent non-linear change in Ca partitioning between clinopyroxene and olivine with increasing temperature (Kohler and Brey, 1990). However, existing thermodynamic models of Ca solubility in olivine only consider Ca incorporation on the M2 site (Davidson and Mukhopadhyay, 1984; Hirschmann, 1991; Kawasaki, 1995). These thermodynamic models are partially calibrated based on experimental studies of the olivine quadrilateral consisting of the end-members forsterite (Mg_2SiO_2), fayalite (Fe_2SiO_4), monticellite ($CaMgSiO_4$) and kirschsteinite ($CaFeSiO_4$). Limited miscibility between both forsterite and monticellite (Biggar and O'Hara, 1969; Warner and Luth, 1973) and between fayalite and kirschsteinite (Mukhopadhyay and Lindsley, 1983) is shown by these experimental studies. The miscibility gap between Ca-rich and Ca-poor end-members decreases with increasing temperature and with increasing Fe-content indicating a smaller Ca-Fe interaction energy (~21 kJ mol^{-1}) than Ca-Mg interaction energy (~33 kJ mol^{-1}; Davidson and Mukhopadhyay, 1984; Hirschmann, 1991). Likewise, the partition coefficient for calcium between olivine and melt increases substantially with increasing Fe-content of the olivine (Jurewicz and Watson, 1988; Libourel, 1999).

The Ca in olivine geothermobarometer has been experimentally investigated in both Fe-free and Fe-bearing systems at elevated pressure but has not been investigated at 0.1 MPa. This is largely because the assemblage olivine-clinopyroxene-low-Ca-pyroxene-melt is only stable across a relatively narrow temperature-composition range at 0.1 MPa. At elevated pressure, experiments in the CMAS system (Finnerty and Boyd, 1978) and CaO-

MgO-SiO_2 (CMS) system (Adams and Bishop, 1982) demonstrated an increase in the Ca content of olivine with increasing temperature and decreasing pressure as expected on crystal chemical grounds. Results of experiments in the CaO-FeO-MgO-SiO_2 (CFMS) system (~Fo_{84} – Adams and Bishop, 1986; ~Fo_{90} – Kohler and Brey, 1990) suggest that the addition of Fe to the system leads to larger changes in olivine Ca content with both pressure and temperature changes than in the Fe-free system. This means that, if all datasets are trusted, at low-pressure the addition of Fe to the system should increase the Ca content of olivine at fixed temperature – the inverse of the effect of Fe at high-pressure. However, some experiments in the olivine-clinopyroxene system, not buffered to lie along the orthopyroxene-clinopyroxene solvus, apparently show the inverse with the Ca content of olivine coexisting with clinopyroxene increasing with decreasing Fo-content and fixed temperature at 7.5 GPa (Kawasaki, 1995).

In this study, a series of one-atmosphere experiments have been undertaken to better quantify the temperature and Fo-content dependence of the Ca-in-olivine geothermometer at low-pressure. Experiments were designed to be olivine-low-Ca-pyroxene-clinopyroxene-melt saturated at 0.1 MPa and were performed between 1170 and 1322ºC in both the Fe-free CMAS system and in the Fe-bearing CMAS+FeO+TiO_2+Na_2O+K_2O system. These experiments demonstrate a substantial increase in the Ca content of olivine in this system with increasing temperature and increasing Fe-content (olivine Fo_{100} to Fo_{76}) at low pressure. Since a primary requirement of this calibration is the presence of olivine, low-Ca pyroxene, clinopyroxene and melt in the system, the experimental compositions that resulted in the co-crystallisation of these phases were used to calibrate an equation for their saturation surface.

2.2. Experimental Methods

The experiments were performed using synthetic starting compositions based on modifications to compositions published from previous 0.1 MPa experimental studies that reported the presence of coexisting liquid, olivine, orthopyroxene and clinopyroxene (Longhi, 1987; Grove and Juster, 1989; Draper and Johnston, 1992; Baker et al., 1994). All starting mixtures (Supplementary Table 2.1) were prepared using reagent grade oxides and carbonates (SiO_2, TiO_2, Al_2O_3, Fe_2O_3, $MgCO_3$, $CaCO_3$, Na_2CO_3 and K_2CO_3) that were dried at 120ºC for at least 24 hours prior to weighing out the starting compositions. Subsequently the powders were ground under ethanol in an agate mortar and then devolatilised at 850ºC for 24 hours and further homogenised by grinding under ethanol for 20-30 minutes. The homogenised starting mixtures were mixed in ethanol to form a paste and mounted on 0.2 mm diameter Pt-wire loops and fused on the loops. The experimental bead was homogenised by holding it at a temperature at least 50ºC higher than its liquidus for at least 1 hour. All beads were examined to ensure they were crystal free following this homogenization step prior to performing the experiment.

Experiments were performed in a vertical tube gas-mixing furnace with the temperature monitored by a type B thermocouple. Fe-bearing experiments were performed at conditions approximately one log unit more reducing than the Quartz-Fayalite-Magnetite (QFM) buffer and Fe-free experiments were performed in air. CO_2 and CO were mixed in the appropriate ratio to control the oxygen fugacity (fO_2) in the furnace and this was monitored using an EMF cell. The fO_2 in the furnace was checked against the Ni-NiO and Co-CoO buffers and was found to be within ±0.5 log units (Frost et al., 1988; Huebner and Sato, 1970). The temperature in the furnace was checked against the melting point of gold (1064ºC). In order to minimise Fe loss to the Pt-wire loop, the Fe-bearing starting

compositions were initially run on a Pt-wire loop under the same T-fO_2 conditions as would be used in the final experiment for at least 24 hours and the bead was then either dissolved in HF or crushed and separated from the wire loop. The resultant Pt-Fe wire alloy, now close to equilibrium with the starting compositions, was used for the final experiment. Experimental charges were quenched under a stream of air as soon as they were removed from the furnace and mounted in epoxy and polished for analysis. Fe-free experiments were run for up to 261 hours at temperatures between 1254 and 1322ºC, while iron bearing experiments were run at temperatures from 1170 to 1254ºC for durations up to 169 hours.

2.3. Analytical Techniques

Experimental run products were analysed using a Cameca SX-50 electron microprobe at the University of British Columbia. Olivine, low-Ca-pyroxene and clinopyroxene crystals were analysed using an acceleration voltage of 15 kV, a 40 nA beam current and ~1 µm beam diameter. Plagioclase and glass were analysed using an acceleration voltage of 15 kV, a 20 nA beam current and a 5 µm beam diameter. In all cases only crystals surrounded by glass were analysed. Peak counting time for all elements was 20 seconds with 10 seconds on each background, except for Ca in olivine with a peak counting time of 60 seconds and background counting times of 30 seconds. Data were reduced using the PAP/øρZ (Pouchou and Pichoir, 1985) approach. In most experiments two olivine crystals were analysed, with a range from one to four analyses, to check for homogeneity. In all cases a zoning profile was measured to check for homogeneity and to test for evidence of secondary fluorescence. Uncertainties on the average mineral compositions are calculated as one standard deviation of the analyses and are shown in

Supplementary Table 2.2. When fitting the data as a thermometer the data are weighted by the reciprocal of the standard deviation. No olivine standard with a similar Ca content to those of the experimentally grown olivine was available. However, as a check on data quality the following tests were performed: (i) a clinopyroxene standard was run with every analytical session and showed no variation in measured CaO content (1 standard deviation of 26 analyses of 0.13 wt% CaO); (ii) a nominally Ca-free olivine (Fo_{92}) was analysed to check the background in each analytical session giving a range of nominal values of 10-30 ppm Ca – i.e. indicating there is no significant background; and (iii) two experiments were analysed in different analytical sessions and the average olivine CaO contents differed by <0.01 wt%.

Secondary fluorescence is a well-known problem for the analysis of Ca in olivine by electron microprobe. The impact of this on the data is minimised in the CMAS experiments because only continuum X-ray fluorescence of Ca is possible in this Fe-free system. Dalton and Lane (1996) show empirically that for a pure forsterite crystal adjacent to diopside (25 wt% CaO) secondary fluorescence can lead to an increase in the apparent CaO content of the olivine of ~0.03 wt% CaO at 5 μm from the diopside and a maximum of ~0.04 wt% CaO at the rim of the olivine (their Fig. 4). Llovet and Galan (2003) simulated virtually identical apparent enrichments in Ca in olivine using a Monte Carlo approach to model the X-ray spectrum near such a boundary. The glass adjacent to the olivine in the CMAS experiments in this study contains ~16 wt% CaO meaning that the maximum increase in the apparent CaO content of the olivine would be approximately a third lower (~0.02 wt% at 5 μm from the rim). In the Fe-bearing system, in addition to continuum X-rays, characteristic X-rays generated by Fe in the olivine can excite Ca atoms in the surrounding glass. The data in Dalton and Lane (1996), and simulations of Llovet

and Galan (2003), show that the apparent Ca signal 5 μm from the rim due to secondary fluorescence is roughly linearly correlated with the Fe content of the olivine. Based on these studies, and using the maximum olivine Fe content from this study (22 wt% FeO), secondary fluorescence could lead to an increase in the apparent CaO content of the olivine of ~0.06 wt% CaO at 5 μm from a diopside. However, in this high Fe experiment the CaO content of the glass is only 10 wt% meaning that the maximum enhancement of the Ca signal due to secondary fluorescence would be ~40% of that adjacent to diopside (~0.025 wt% at 5 μm from the crystal rim).

To minimise the impact of secondary fluorescence on the data analyses <5 μm from the olivine rims were excluded when calculating average olivine compositions meaning a worst case scenario of 0.025 wt% CaO from secondary fluorescence. Additionally, zoning profiles were examined for evidence of increased measured CaO near the crystal rims; this was absent in most cases indicating that secondary fluorescence was insignificant. However, in four olivine crystals a small increase in the measured CaO content was observed at the crystal rims. This is interpreted to be due to secondary fluorescence and the following criteria was devised to exclude these: if the Ca content of analyses in the outer 15 μm of the crystal were >1σ (~0.01 wt% CaO based on counting statistics) higher than the average of the analyses of the crystal core then they were excluded in calculating the average olivine composition. As a further check that secondary fluorescence is not significantly impacting the thermometer calibration a fit is reported in which only analyses >20 μm from the rim of the olivine are included in calculating the average olivine composition. As discussed below, this makes little difference to the resulting thermometer calibration.

2.4. Results

All starting compositions used in the experiments for this study are basaltic to andesite in composition with Mg#s ranging from 1 to 0.6 (Supplementary Table 2.1). The experiments reported here all contain the assemblage olivine-clinopyroxene-low-Ca-pyroxene-melt with either orthopyroxene or pigeonite as the low-Ca pyroxene (Supplementary Table 2.2). Olivine crystals in the experimental charges range in size from 15 to 120 μm in diameter while low-Ca-pyroxene ranges from 25 to 105 μm in diameter and clinopyroxene are the smallest (~5 to 35 μm in diameter).

Low-Ca-pyroxenes were divided between pigeonite and orthopyroxene by comparison of their Ca contents with the Ca contents of low-Ca-pyroxene in the studies of similar bulk compositions by Longhi (1987; for CMAS experiments) and Grove and Juster (1989; for Fe-bearing experiments). In the CMAS experiments low-Ca-pyroxene containing >4.5 wt% CaO are interpreted to be pigeonite and those containing <3.6 wt% CaO are interpreted to be orthopyroxene (note, however, that Longhi (1987) reports a single pigeonite with 3.7 wt% CaO). In the Fe-bearing experiments low-Ca-pyroxene with >3.7 wt% CaO are interpreted to be pigeonite and those with <2.7 wt% CaO are interpreted to be orthopyroxene.

In an attempt to test for equilibrium two time series experiments were performed in the CMAS system at 1322ºC and 1277ºC and four experiments were performed in the CMAS system at 1305°C with three different starting compositions and two different durations. The results show no systematic change of Ca in olivine with either experiment duration or starting material (Fig. 2.1). This is consistent with the olivine Ca contents being close to equilibrium values. *A posteriori* the consistency of the results also supports this interpretation. Finally, although Mg-Fe equilibrium between olivine and melt does not

prove Ca equilibrium in the system it provides a useful further test of whether the system approached equilibrium. Olivine crystals are virtually unzoned in Fo content (maximum core-to-rim variation of 0.5% Fo). Further, application of the Ford et al. (1983) thermometer to the olivine-melt pairs predicts the Fo content in all cases to within 1.5% Fo and on average to within 0.7% Fo again supporting a close approach to equilibrium.

2.4.1. Calcium content of pure forsterite as a function of temperature

As expected based on previous studies, the Ca content of olivine in the CMAS experiments decreases strongly with decreasing temperature (Fig. 2.2). The incorporation of Ca into olivine in equilibrium with clinopyroxene and low-Ca-pyroxene can be described by the reaction (Eq. 2.2) forsterite + diopside (Di) = monticellite (Mo) + low-Ca-pyroxene (enstatite or pigeonite; En or Pig):

$$Mg_2SiO_4 + MgCaSi_2O_6 = MgCaSiO_4 + Mg_2Si_2O_6 \qquad \text{Eq. 2.2}$$

In the CMAS system Longhi (1987) showed that the assemblage olivine-diopside-enstatite is stable between ~1322°C and ~1250°C. At higher temperature the low-Ca pyroxene changes to pigeonite but metastable pigeonite is also commonly present at lower temperatures (Longhi, 1987). Because both pigeonite and orthopyroxene are observed in the experiments reported here we first consider whether this has a substantial effect on the activity of the monticellite (a_{Mo}) component as fixed by Equation 2.2.

The difference in a_{Mo} in the pigeonite and orthopyroxene bearing systems was calculated using the thermodynamic model for pyroxenes of Carlson and Lindsley (1988). In this model the activity of monticellite in the pigeonite bearing system is 1.04x higher than that in the enstatite bearing system at 1322°C and 1.10x higher at 1254°C. This is

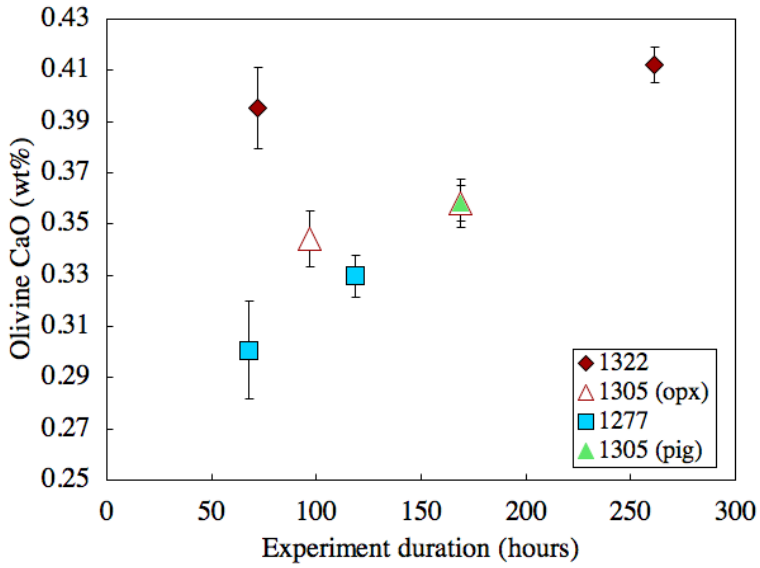

Figure 2.1. Results of experiments run at the same temperature but with either different durations or different starting compositions in the CMAS system. The 1322°C and 1277°C experiments are the same starting composition that was run for different durations whereas the 1305°C experiments are different starting compositions run for both the same and different duNote that two of the 1305°C experiments contain pigeonite and the other two orthopyroxene and there is no significant difference in the Ca content of the olivine crystals between these experiments. Error bars represent 1σ on electron microprobe analyses of Ca in olivine.

slightly inconsistent with the experimental data of Longhi (1987) that demonstrate that at 1322°C the equilibrium assemblage is pigeonite-orthopyroxene-diopside-forsterite-melt; this requires a_{Mo} to be the same in the pigeonite and orthopyroxene bearing systems at this temperature. This discrepancy may relate to Carlson and Lindsley's (1988) model being for the Al-free system. The maximum difference between a_{Mo} in the pigeonite and orthopyroxene bearing systems over this temperature range is thus estimated to be ~5%

which is only slightly greater than the standard deviation in the olivine Ca measurements (~0.01 wt% CaO). Thus, while the pigeonite-bearing experiments do contain olivine with slightly higher Ca contents than those that contain orthopyroxene (Fig. 2.2), both the observed and theoretical differences are sufficiently small that they are not accounted for in producing the thermometer calibration derived here. Writing Equation 2.2 in terms of the free energy of the reaction for the end-member components (ΔG_r^0) and the equilibrium constant for the reaction:

$$\Delta G_r^o = -RT\ln\left(\frac{a_{Mo}a_{En}}{a_{Fo}a_{Di}}\right) \qquad \text{Eq. 2.3}$$

where a is the activity of the component, T is the temperature (K) and R the gas constant (J mol^{-1} K^{-1}). Making the assumption that along the pyroxene solvus the ratio of a_{En} to a_{Di} is roughly constant, which is consistent with the thermodynamic model of Carlson and

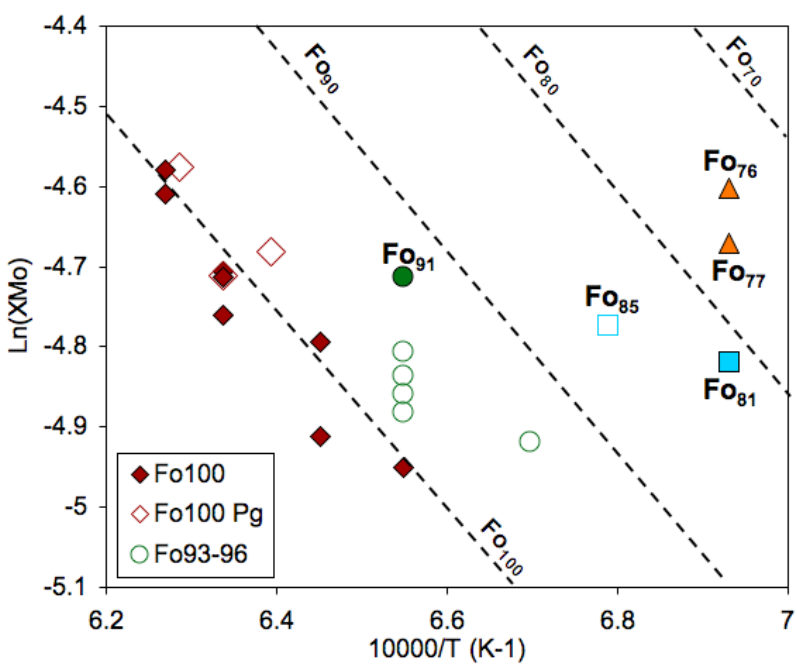

Figure 2.2. Caption on following page

Figure 2.2. Calcium content of olivine, expressed as ln(X_{Mo}), versus reciprocal temperature for olivine of different forsterite contents from the experiments reported here. The Ca-content of olivine in lower temperature Fe-bearing experiments is much higher than that expected from extrapolation of Fe-free experiments. Also shown are model olivine Ca contents at different Fo content derived from Eq. 2.11 (dashed lines). Filled symbols are orthopyroxene-bearing experiments and open symbols are pigeonite-bearing experiments.

Lindsley (1988) for the CMS system (a_{En}/a_{Di} is between 1.07 and 1.09 from 1000 and 1400°C), and considering only the CMAS experiments (a_{Fo}~1), this can be written:

$$\Delta H^o - T\Delta S^o = -RT\ln(a_{Mo}c) \qquad \text{Eq. 2.4}$$

where, H = enthalpy S = entropy and c is a constant approximating a_{En}/a_{Di}. Replacing a_{Mo} with $\gamma_{Mo}X_{Mo}$, where γ_{Mo} = activity coefficient of the monticellite component in olivine and X_{Mo} = mole fraction monticellite in olivine (which equals the number of Ca atoms per 4 oxygens) and rearranging we have:

$$\ln(X_{Mo}) = \frac{\Delta S^o}{R} - \frac{\Delta H^o}{RT} - \ln[c\gamma_{Mo}] \qquad \text{Eq. 2.5}$$

For the binary Mo-Fo system, assuming a symmetrical solution model (Warner and Luth, 1973), the activity coefficient for monticellite can be written:

$$\gamma_{Mo} = Exp\left(\frac{(1 - X_{Mo})^2 W}{RT}\right) \qquad \text{Eq. 2.6}$$

where W is a symmetrical interaction energy. With nearly pure forsterite ($1-X_{Mo} \cong 1$), combining the temperature dependence of the activity coefficient and entropy terms and

ignoring the temperature dependence of ΔH^o and W, Equations 2.5 and 2.6 can be combined and simplified to:

$$\ln(X_{Mo}) = \frac{a}{T} + b \qquad \text{Eq. 2.7}$$

where a and b are constants that can be fit from regressing $\ln(X_{Mo})$ against reciprocal temperature.

Figure 2.2 shows that at 0.1 MPa in the CMAS system, the Ca content of olivine in equilibrium with low-Ca-pyroxene and clinopyroxene increases strongly with increasing temperature and can be fit to Eq. 2.7 giving the empirical relationship:

$$\ln(X_{Mo}) = 2.59(1.73) - \frac{11442(2709)}{T(K)} \qquad \text{Eq. 2.8a}$$

or just using the orthopyroxene bearing experiments:

$$\ln(X_{Mo}) = 3.43(1.04) - \frac{12823(1636)}{T(K)} \qquad \text{Eq. 2.8b}$$

where the values in parentheses are the (highly correlated) standard errors on the fit.

2.4.2. The impact of iron on the Ca content of olivine

The Ca-content of olivine in equilibrium with low-Ca-pyroxene and clinopyroxene is markedly higher in the Fe-bearing experiments than predicted by the Fe-free experiments (Fig. 2.2) as expected based on previous studies. The difference in $\ln(X_{Mo})$ calculated using Eq. 2.8a, and the measured value, increases linearly with decreasing Fo content of the olivine (Fig. 2.3). This increase in the Ca content of olivine coexisting with clinopyroxene

and low-Ca-pyroxene in the Fe-bearing system is much larger than any possible contribution from secondary fluorescence and is not noticeably changed by considering only analyses >20 μm from the rim of olivine crystal. For example, at 1170ºC the Ca content of olivine predicted by extrapolation of the higher temperature CMAS data is half that measured in the olivine Fo_{76} (Fig. 2.2). The increase in Ca content of olivine, at a given temperature, with increasing olivine Fe content is consistent with previous experiments that suggested that addition of Fe to the system increases the Ca content of olivine at low-pressure (Adams and Bishop, 1986; Jurewicz and Watson, 1988; Libourel, 1999). How much of this reflects changes in the activity coefficient for Ca in olivine with changing composition, and how much reflects changes in a_{Mo} in the system defined by Eq. 2.2 with changing the bulk Mg/Fe of the system, cannot be unambiguously resolved with these data. However, the change in $\ln[X_{Mo}]$ with Fo content observed here is very similar to the change in olivine-melt Ca partition coefficient (corrected for changes in melt Ca activity coefficient) with Fo observed by Libourel (1999; his equation 14); this is most simply explained if changes in the activity coefficient for Ca in olivine are the dominant controlling factor. Figure 2.3 also shows that whether the low-Ca-pyroxene is orthopyroxene or pigeonite makes no significant difference in the offset between the measured and predicted olivine Ca content. This may reflect the experiments being performed at conditions very close to co-saturation of orthopyroxene and pigeonite or may reflect a small difference between the activity of monticellite in the orthopyroxene and pigeonite bearing assemblages. Whatever the explanation, the similarity in the Ca content of olivine in those experiments at the same temperature, and with a similar olivine Fo content, that contain orthopyroxene or pigeonite allow the data to be treated together.

Because the difference between the measured Ca content of an olivine and that predicted by Equation 2.8 (derived in the CMAS system) correlates linearly with the Fo content of the olivine (Fig. 2.3) a linear correction to Eq. 2.8 is applied for the Fe-bearing system. In reality, both changes in the activity coefficient of monticellite with changing Fo-content, and changes in the activity of the monticellite component with changing Fe content of the other phases, mean that this cannot be a linear relationship across the entire range of olivine compositions. However, for the temperature and composition range considered here this empirical linear correction is all that is warranted. Adding a linear correction term (d) to Equation 2.7 for the olivine Fo content we have:

$$\ln(X_{Mo}) = \frac{a}{T} + b + dFo \qquad \text{Eq. 2.9}$$

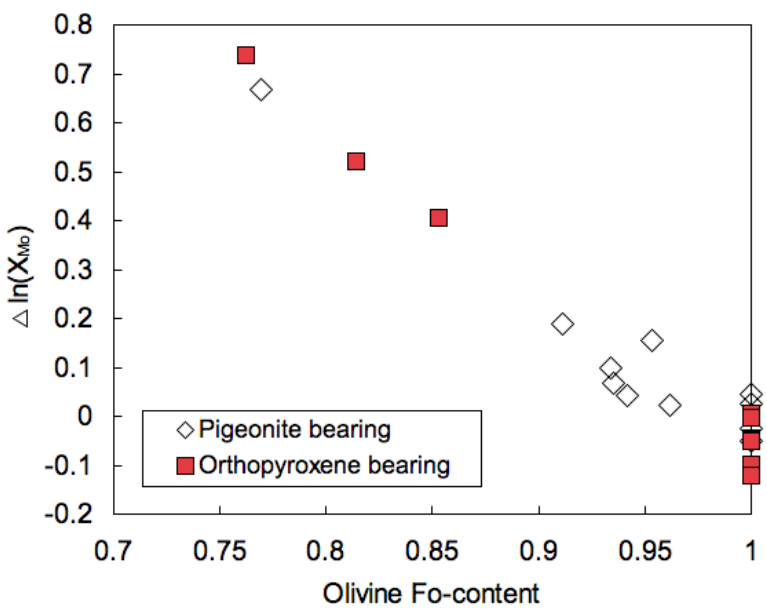

Figure 2.3. Relationship between the Fo-content of olivine and the difference ($\Delta\ln[X_{Mo}]$) between the measured Ca content of the olivine and that predicted from the experimental temperature using the relationship between temperature and X_{Mo} derived from the Fe-free experiments (Eq. 2.8a). The linear relationship between olivine Fo-content and $\Delta\ln[X_{Mo}]$ indicates that olivine Fo-content is critical in controlling the Ca-content of olivine. Whether the low-Ca-pyroxene is orthopyroxene or pigeonite makes no obvious difference to $\Delta\ln[X_{Mo}]$.

Which can be rearranged as a thermometer to:

$$T(°C) = \frac{a}{\ln(X_{Mo}) - b - dFo} - 273 \qquad \text{Eq. 2.10}$$

Fitting the entire dataset to Equation 2.10 gives:

$$T(°C) = \frac{-12368(2032)}{\ln(X_{Mo}) - 6.395(1.79) + 3.235(0.51)Fo} - 273 \qquad \text{Eq. 2.11}$$

Using only analyses of olivine crystals >20 µm from the crystal rim, the following best fit to the entire dataset is obtained:

$$T(°C) = \frac{-12201(1291)}{\ln(X_{Mo}) - 6.23(1.18) + 3.17(0.38)Fo} - 273 \qquad \text{Eq. 2.12}$$

This is almost identical to Equation 2.11, despite being based on a smaller number of analyses and one less experiment (in which the olivine were too small for any analyses to be performed >20 µm from the rim), providing further confidence that secondary fluorescence did not impact the results significantly. Using Equation 2.11 the experimental temperatures are reproduced to within 20ºC and the misfit between model and experimental temperature does not correlate with either the olivine Fo-content or experimental temperature (Fig 2.4). The relationship between inverse temperature and ln[XMo] for different olivine forsterite contents as derived from Eq. 2.11 is shown in Fig. 2.2. It should be clear from the discussion above that this thermometer should not be used outside of the compositional range over which it is calibrated.

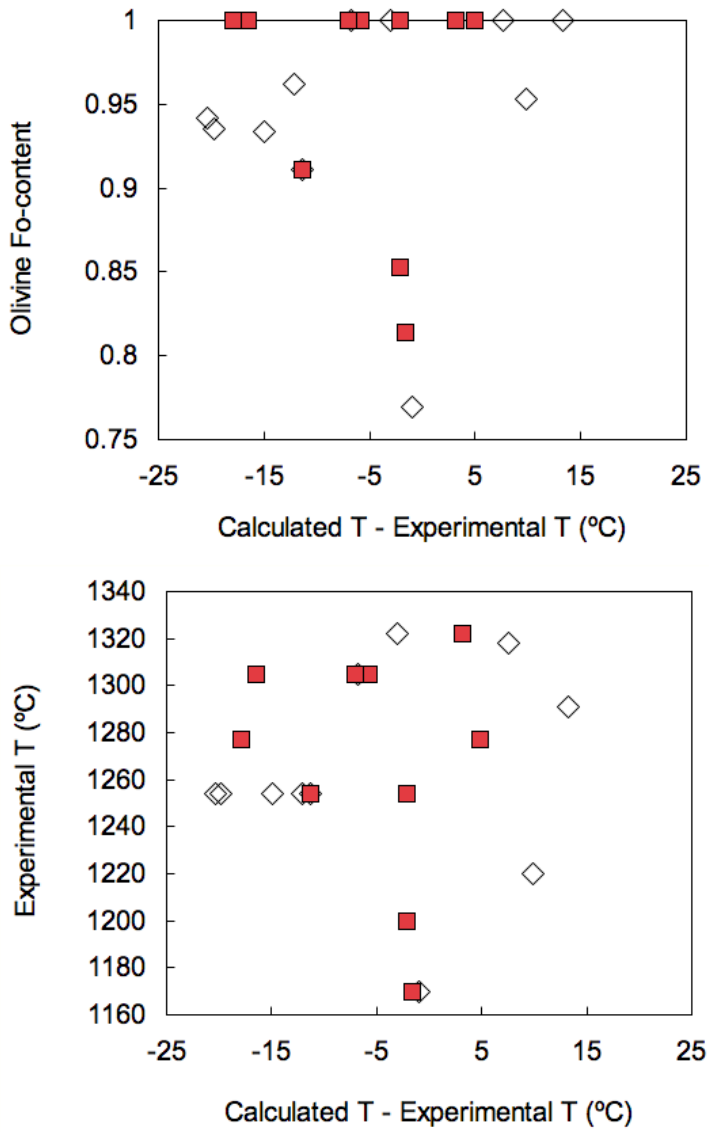

Figure 2.4. Difference between the temperatures predicted using the geothermometer calibrated in this study (Eq. 2.11) versus experimental temperatures plotted as functions of (a) olivine Fo content and (b) experimental temperature. The misfits do not correlate with either parameter. The thermometer reproduces the experimental temperatures to within 20ºC. Whether the low-Ca-pyroxene is orthopyroxene (open diamonds) or pigeonite (red filled squares) makes no obvious difference.

2.5. Discussion

2.5.1. Comparison to the previous geobarometer

There have been no previous studies of the Ca content of olivine coexisting with clinopyroxene and low-Ca-pyroxene at 0.1 MPa to compare with the results derived here. The closest that exists is a single experiment at 200 MPa and 1100°C reported by Kohler and Brey (1990); this is the lowest pressure experiment we know of to investigate the Ca content of olivine in equilibrium with two pyroxenes. They reversed this experiment with olivine Ca contents overlapping between ~1100 and 1270 ppm with a preferred value of 1170 ppm (Fo ~90). Ignoring the difference in pressure, Equation 2.11 recovers a temperature of 1110°C for this experiment which is in very good agreement with the experimental temperature.

As a further comparison of the thermometer reported here with previous studies Fig. 2.5 shows previous experimental data for this system as a function of pressure (Finnerty and Boyd, 1978; Adams and Bishop, 1982, 1986; Kohler and Brey, 1990). Comparison of the Fe-bearing experiments of Adams and Bishop (1986; $Fo_{\sim 84}$) and Kohler and Brey (1990; $Fo_{\sim 90}$) to the compositions predicted at 0.1 MPa by Eq. 2.11 shows good agreement (Fig. 2.5a). The compositional dependence determined here explains the offset of the Adams and Bishop (1986) data to slightly higher olivine Ca contents relative to those of Kohler and Brey (1990) for experiments performed at the same pressure and temperature. However, high-pressure experiments in the Fe-free system (Fig. 2.5b) show an apparently much weaker temperature dependence than observed either at 0.1 MPa in the Fe-free experiments reported here or in the high-pressure Fe-bearing experiments. Additionally, the decrease in Ca content of olivine with increasing pressure in the Fe-free system is much

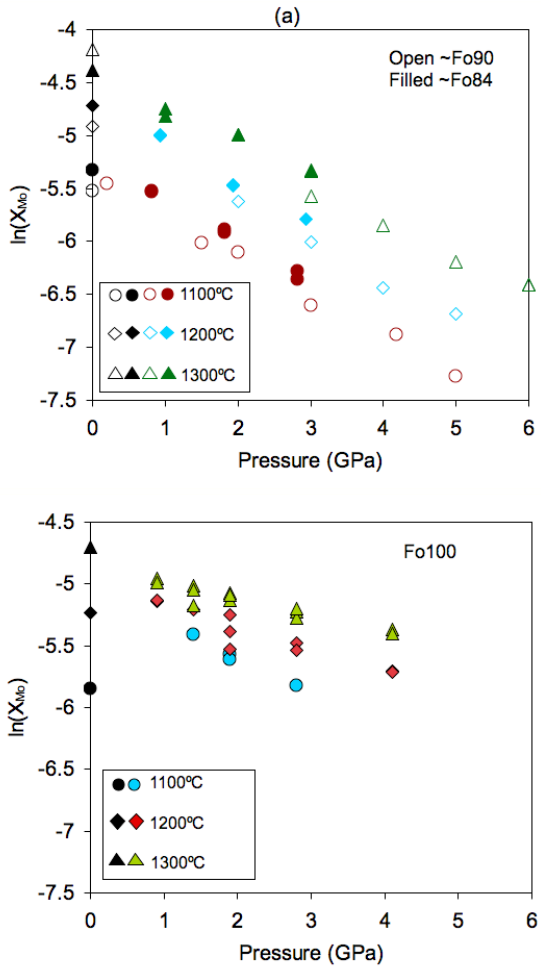

Figure 2.5. Comparison of the results of 0.1 MPa experiments reported here and previous high-pressure experiments. (a) data from Fe-bearing experiments (Kohler and Brey, 1990; Adams and Bishop, 1986) with the 0.1 MPa data points (black symbols) calculated from the thermometer developed here (Eq. 2.11). The previous experiments are consistent with one another and with the results of this study provided the effect of Fe on the Ca contents of olivine is incorporated into the thermometer. (b) data from Fe-free experiments (Finnerty and Boyd, 1978; Adams and Bishop, 1982) with the 0.1 MPa data points calculated from the thermometer developed here (Eq. 2.11). The agreement is poor between the new data and those of these high-pressure studies except at 1300°C. Note that both increasing pressure and temperature apparently have a smaller effect on the Ca content of olivine in the Fe-free system.

smaller than observed in the Fe-bearing experiments. The origin of this large discrepancy between the Fe-free and Fe-bearing high-pressure studies is unclear and requires future study.

Because the high-pressure Fe-bearing experiments of Kohler and Brey (1990) and Adams and Bishop (1986) are consistent with the low-pressure experimental data reported here they have been fit together as an empirical geothermobarometer. Within the scatter of the data a simple linear pressure dependence is all that is justified. It is clearly unwise to use this outside of a very limited range of Fo content (82-92). Because previous studies do not all report uncertainties on olivine Ca contents no weighting is used in the fitting. This gives:

$$\ln(X_{Mo}) = 3.64(0.24) - 2.328(0.20)Fo - \frac{9525(193)}{T(K)} - 0.0334(0.00065)P(kbar)$$

Eq. 2.13

The misfit between experimental pressure and calculated pressure using Eq. 2.13 is up to 0.7 GPa (1σ = 0.2 GPa) for Fe-bearing experiments and up to 2.6 GPa (1σ = 0.8 GPa) for Fe-free experiments (Fig. 2.6). In the case of Fe-bearing experiments, the misfit between experimental and calculated pressures is lowest at 900°C, progressively increases up to 1100°C and then begins to decrease from 1200°C to 1400°C (Fig. 2.6). The temperature dependence of the pressure misfit (Fig. 2.6) needs to be further evaluated. Applying Eq. 2.13 to the experiments reported here, the experimental temperatures are fit to within +17/-30°C. Clearly more work is required to produce a precise and accurate barometer based on the Ca content of olivine but this study shows that incorporating the effect of Mg/Fe substitution in olivine will be critical to this.

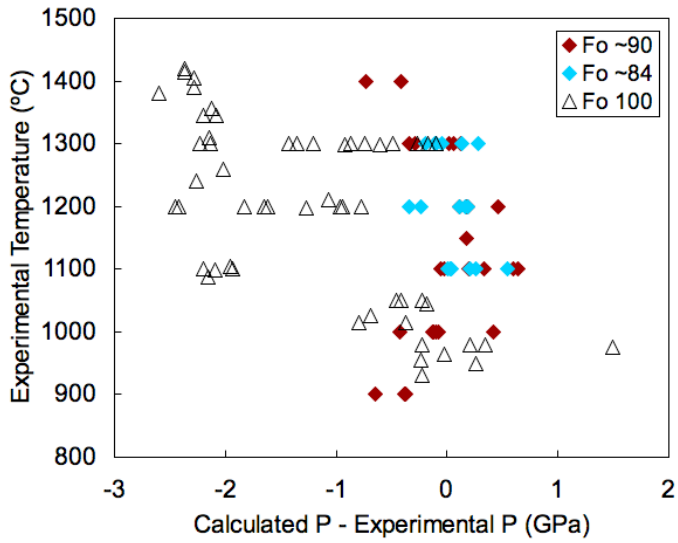

Figure 2.6. Misfit between calculated and experimental pressures for Fe-bearing (Adams and Bishop, 1986; Kohler and Brey, 1990) and Fe-free (Finnerty and Boyd, 1979; Adams and Bishop, 1982) experiments. The maximum misfit for Fe-bearing and Fe-free experiments is 0.7 GPa and 2.6 GPa respectively.

2.5.2 Calibration of the olivine – low-Ca-pyroxene – clinopyroxene – melt saturation surface at 0.1 MPa.

The melt phase in the experiments conducted in this study is saturated in olivine, low-Ca-pyroxene and clinopyroxene. An added advantage of the results of experiments performed in this study is to allow the calibration of the co-saturation surface of olivine-low-Ca-pyroxene-clinopyroxene saturated melts at 0.1 MPa, which will facilitate future studies of this system as well as modeling crystallisation of basaltic andesites. There have been few studies of this system at low-pressure (Longhi, 1987; Grove and Juster, 1989; Draper and Johnston, 1992; Baker et al., 1994). Longhi (1987) derived an equation for the olivine-clinopyroxene-orthopyroxene-melt saturation surface in the CMAS system. A similar model for the composition of melts in this system for more complex compositions, which include Na, K, Ti and Fe, is developed here. The experiments conducted in this

study along with published results of 0.1 MPa experiments saturated with the same assemblage (Longhi, 1987; Grove and Juster, 1989; Draper and Johnston, 1992; Baker et al., 1994 and Libourel, 1999) are used here to define the olivine-clinopyroxene-orthopyroxene-melt saturation surface at 0.1 MPa.

Earlier studies that describe olivine-plagioclase-augite-saturated melts have defined the saturation surface using CMAS-FeO (Shi, 1992) and CMAS-FeO-Na_2O-K_2O-TiO_2 (Yang et al., 1996) systems. It was demonstrated that accounting for minor components such as Na, K and Ti is necessary in order to make accurate predictions of melt compositions saturated in olivine-plagioclase-augite (Yang et al., 1996) and that the equations of Shi (1992) were insufficient to this regard. In this study with 8 components and 4 phases, the variance (F) of the system is 6. In order to evaluate the effect of changing composition on the olivine-clinopyroxene-low-Ca-pyroxene-melt saturation surface, six compositional parameters are selected as independent variables. Molar fractions (X) of six melt components: X_{Si}, X_{Ti}, X_{Fe2+}, X_{Fe3+}, X_{Na} and X_K are used to describe four dependent variables X_{Al}, X_{Ca}, X_{Mg} and T (K) for melts saturated with olivine-clinopyroxene-low-Ca-pyroxene. Since both, CMAS and Fe-bearing experiments were used in developing this equation the dependent variables were selected so that three components are common between the two sets of experiments.

The coefficients of linear regression for independent variables X_{Ti}, X_{Al}, X_{Fe2+}, X_{Fe3+}, X_{Na} and X_K that predict T (K), X_{Ca}, X_{Mg} and X_{Si} are derived by linear regression of the following equation:

$$V = a * X_{Ti} + b * X_{Al} + c * X_{Fe^{2+}} + d * X_{Na} + e * X_K + f * X_{Fe^{3+}} + g \quad \text{(Eq. 2.14)}$$

where V = dependent variables T (K), X_{Si}, X_{Ca} or X_{Mg} and a-g are regression coefficients.

The concentrations of Fe^{2+} and Fe^{3+} in the melt have been considered in order to derive suitable equations for the saturation surface. This is necessary since the crystallisation of low-Ca pyroxene at 0.1 MPa is sensitively controlled by oxygen fugacity because of the effect of changing fO_2 on Mg# (Grove and Juster, 1989). Changes in fO_2 at 0.1 MPa change the bulk composition by changing the Fe^{2+}/Fe^{3+} ratio. With increasing abundance of Fe^{3+} in a melt, an oxide phase is stabilised and hence the liquid is enriched in SiO_2. Increased SiO_2 activity in turn facilitates the crystallisation of orthopyroxene. This may be explained by the reaction:

$$2Fe_2SiO_4 + \tfrac{1}{2}O_2 = Fe_2O_3 + Fe_2Si_2O_6 \qquad \text{(Eq. 2.15)}$$

It has also been suggested that orthopyroxene may stabilise due to the partitioning of Fe^{3+} into its structure (Grove and Juster, 1989). The concentrations of Fe^{2+} and Fe^{3+} were calculated using the approach of Kress and Carmichael (1991).

The coefficients that describe best-fit parameters of linear regression for the saturation surface according to Eq. 2.14 are given in Table 2.3. Plots showing predicted versus observed compositions of melts saturated in olivine-clinopyroxene-low-Ca-pyroxene-melt are illustrated in Fig. 2.7.

Table 2.3. Coefficients describing best-fit parameters of linear regression for Eq. 2.14.

Eq. No	V	Constant (g)	X_{Ti} (a)	X_{Al} (b)	X_{Fe2+} (c)	X_{Na} (d)	X_K (e)	X_{Fe3+} (f)
1	XSi	0.520304	-0.540982	-0.0994304	-0.0780142	0.534183	1.48088	-1.00912
2	XCa	0.175181	0.0423548	-0.112616	-0.193298	-0.659389	-1.40171	-0.494312
3	XMg	0.303271	-0.504813	-0.779399	-0.74167	-0.739254	-1.74855	0.323304
4	T (K)	1665.65	-963.151	-778.518	-1008.17	-65.5667	-3850.77	1616.97

2.5.3. Are current geothermobarometers sufficiently accurate to test thermal models of the oceanic lithosphere?

In order to test whether the composition-dependent Ca-in-olivine geobarometer developed here (Eq. 2.13) can be successfully used on natural rocks, it has been applied to a suite of ocean island xenoliths, despite the large uncertainty (up to 0.7 GPa; Fig. 2.9) in calculated pressures. Two main criteria are considered prior to application of the geobarometer to the xenoliths. Firstly, since the calculation of accurate pressures requires a reasonably good temperature estimate, several potential geothermometers are considered and discussed below. Secondly, the Ca-content of olivine is sensitive to changes in temperature, which may include local heating e.g. during transport to the surface in a magma. Hence, only xenoliths that show no evidence of Ca-mobility in the form of zoned crystals are utilised in this test. The following geothermometers are considered for measurement of temperature:

1. Ca-exchange between orthopyroxene and clinopyroxene (Brey and Kohler, 1990): The temperature dependent partitioning of Ca between orthopyroxene and clinopyroxene requires an approximate value of pressure to calculate temperature. Hence, temperature and pressure values have to be calculated iteratively.
2. Fe-Mg exchange between orthopyroxene and spinel (Liermann and Ganguly, 2003; 2007): This geothermometer is sensitive to composition e.g. Fe^{3+} and Cr^{3+} of spinel for which necessary equations have been calibrated (Liermann and Ganguly, 2003).
3. Fe-Mg exchange between olivine and spinel (Ballhaus et al., 1991): A simplified version of the previous Fe-Mg exchange geothermometer involving olivine and spinel (Fabries, 1979; O'Neill and Wall, 1987).

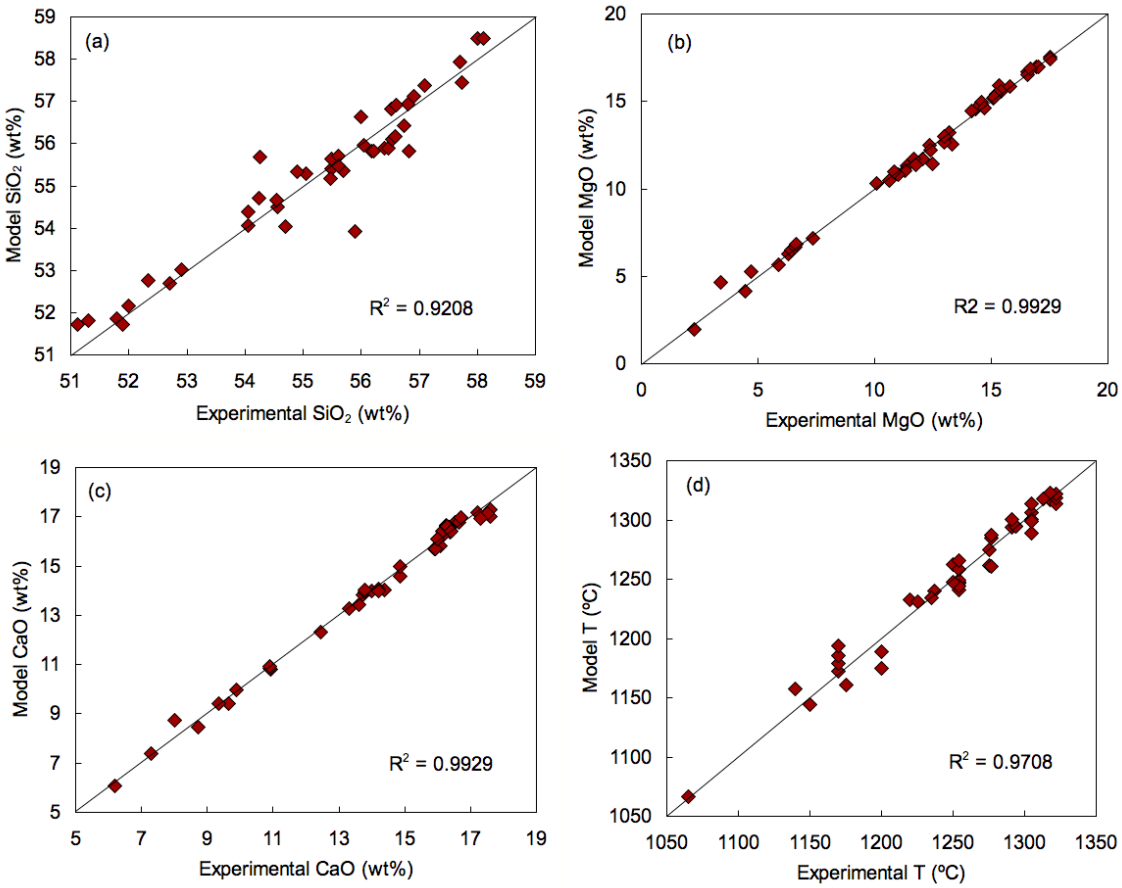

Figure 2.7. Concentrations of (a) SiO_2, (b) MgO and (c) CaO calculated using Eq. 2.14 plotted against measured experimental concentrations. (d) Temperatures calculated using Eq. 2.14 are plotted against experimental temperatures and are found to be within +/- 30ºC. The r-squared (R^2) values for each linear regression line are shown in the respective plots. The solid line in each figure represents X=Y on the plot. Eq. 2.14 can be used to calculate starting compositions for future studies that require modeling of the olivine-low-Ca-pyroxene-clinopyroxene saturated melts.

4. Exchange of Al between olivine and spinel (Wan et al. 2008): This geothermometer is applicable to xenoliths with spinel Cr# ($Cr^{3+}/[Cr^{3+}+Al^{3+}+Fe^{3+}]$) ranging between 0.07 and 0.69, which is commonly the Cr# range for spinel in the samples used in this research. Empirical testing of this geothermometer shows that

pressure does not play a significant role in controlling the partitioning of Al between olivine and spinel (Wan et al., 2008).

The results of applying the four geothermometers described above to harzburgites, lherzolites and olivine-bearing pyroxenites are plotted in Fig. 2.8. As the oceanic lithospheric mantle cools, the minerals equilibrate with the new conditions by the diffusion of elements between minerals. The difference in closure temperatures of different mineral pairs thus results in a wide range of temperatures being determined for the same sample if different geothermometers are applied (e.g. Fig. 2.8). It is observed that application of the orthopyroxene-spinel geothermometer (Liermann and Ganguly, 2003) results in higher temperatures than the olivine spinel geothermometer (Ballhaus et al., 1991) on the high temperature side while giving lower temperatures than the latter on the low-temperature side (Fig. 2.8a). A comparison between temperatures calculated using the Liermann and Ganguly (2003) and the Al-in-olivine geothermometer (Wan et al., 2008) shows a scatter in calculated temperatures (Fig. 2.8b). The Fe-Mg interdiffusion in orthopyroxene (Ganguly and Tazzoli, 1994), olivine (Chakraborty, 1997) and spinel (Liermann and Ganguly, 2002) indicates that the diffusion coefficient D (OPx) < D (Ol) < D (Sp), which may explain the higher temperature calculated using the orthopyroxene-spinel geothermometer (Liermann and Ganguly, 2003) compared to the olivine-spinel geothermometer (Ballhaus et al., 1991). The temperatures calculated using the above geothermometers are likely to be closure temperatures and are thus higher than actual temperatures. The temperatures derived from the Ballhaus et al. (1991) and Wan et al. (2008) geothermometers are scattered around the one-to-one correlation line (Fig. 2.8c).

As in the orthopyroxene-clinopyroxene geothermometer of Kohler and Brey (1990), the geothermometers of Ballhaus et al. (1991) and Liermann and Ganguly (2003) require

pressure for the calculation of temperature. Temperatures for the above two geothermometers are thus calculated iteratively with an assumed value for pressure to begin with. The calculations are repeated until a geothermometer pair calculates similar values for temperatures. Several iterations resulted in similar (within 20ºC) temperatures being derived for only 6 xenoliths between the two-pyroxene (Brey and Kohler, 1990) and orthopyroxene-spinel (Liermann and Ganguly, 2003, 2007; Fig. 2.8d) geothermometers. Temperatures derived using the two-pyroxene geothermometer (Brey and Kohler, 1990) are mostly lower than those derived using the Al-in-olivine (Wan et al., 2008) geothermometer (Fig. 2.8e). No geothermometer pair resulted in similar temperatures being calculated for all ocean island xenolith samples even when the same mineral pair was involved in the calibration (e.g. Fig. 2.8c). This may either be due to uncertainties in the geothermometer calibration and/or due to the differences in diffusion coefficients of different elements between the mineral pairs.

As discussed above, the results of applying different geothermometers do not show consistency between the derived temperatures for all the ocean island xenoliths. The choice of geothermometer for the calculation of pressures thus depends on the purpose for which pressures need to be calculated. If equilibration pressures need to be calculated for rapidly cooled rocks, a mineral pair with slowly diffusing elements e.g. Fe-Mg between orthopyroxene and spinel (Liermann and Ganguly, 2003) is unsuitable, as it would record higher temperatures and therefore result in greater calculated depths compared to the olivine-spinel geothermometer (Ballhaus et al., 1991; Fig. 2.8a). For the purpose of testing the geobarometer developed here (Eq. 2.13), the geothermometer that correlates best with more than one other geothermometer is applied to calculate temperatures. The olivine-spinel (Ballhaus et al., 1991) geothermometer is selected since it correlates fairly well with

the orthopyroxene-spinel (Liermann and Ganguly, 2003; Fig. 2.8a) and the Al-in-olivine (Wan et al., 2008; Fig. 2.8c). The choice of the geothermometer does not indicate that the temperature used is appropriate; i.e. the Ca in olivine may have equilibrated at a different temperature.

Depths calculated for xenoliths from oceanic lithosphere of different ages using Eq. 2.13 along with temperatures derived from the olivine-spinel geothermometer (Ballhaus et al., 1991) are shown (Fig. 2.9). Depths calculated pressures from the Kohler and Brey (1990) geobarometer are shown for comparison with depths calculated from Eq. 2.13 (Fig. 2.9). Also shown for comparison is the temperature and depth of the isotherm for the bottom of the oceanic lithosphere according to the half space model (Turcotte and Schubert, 2002). Along with the high uncertainties in calculated pressures the depths are largely scattered around the geotherm for the half space model (Fig. 2.9). For example, depths calculated for most xenoliths from the Kerguelen (25 Ma lithosphere) are up to 100 km deeper than the half-space model isotherm (Fig. 2.9a). There are multiple possible reasons for greater depths being calculated for ocean island xenoliths from the Kerguelen. For example, this may reflect uncertainty in the calibration of the geobarometer or the geothermometer used. Alternatively there may be a change in the partitioning mechanism of Ca into olivine with changes in temperature (e.g. ordering onto the M2 site at lower temperature; Kohler and Brey, 1990).

The depths calculated using pressures from the Kohler and Brey (1990) geobarometer are shallower than those calculated using Eq. 2.13 (Fig. 2.9). The two-pyroxene geothermometers of Brey and Kohler (1990) has been recommended for application with the Kohler and Brey (1990) geobarometer (Kohler and Brey, 1990). A comparison between temperatures calculated using the olivine-spinel (Ballhaus et al., 1991)

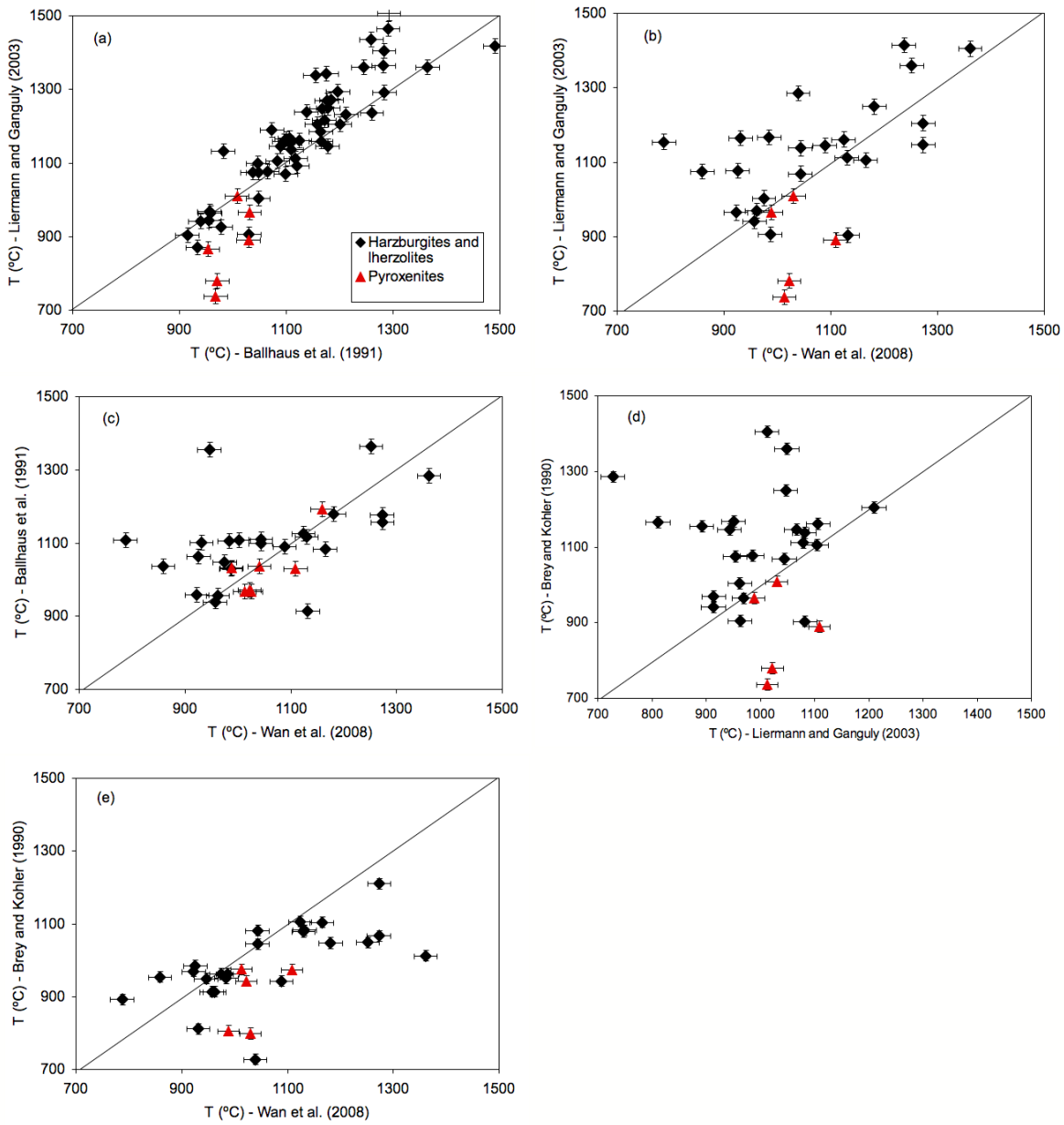

Figure 2.8. Comparison between temperatures calculated using different geothermometer pairs as indicated in the figures. Five samples in (a) are off the chart with temperatures greater than 1500°C calculated using Liermann and Ganguly (2003). Error bars indicate 1σ on the geothermometers.

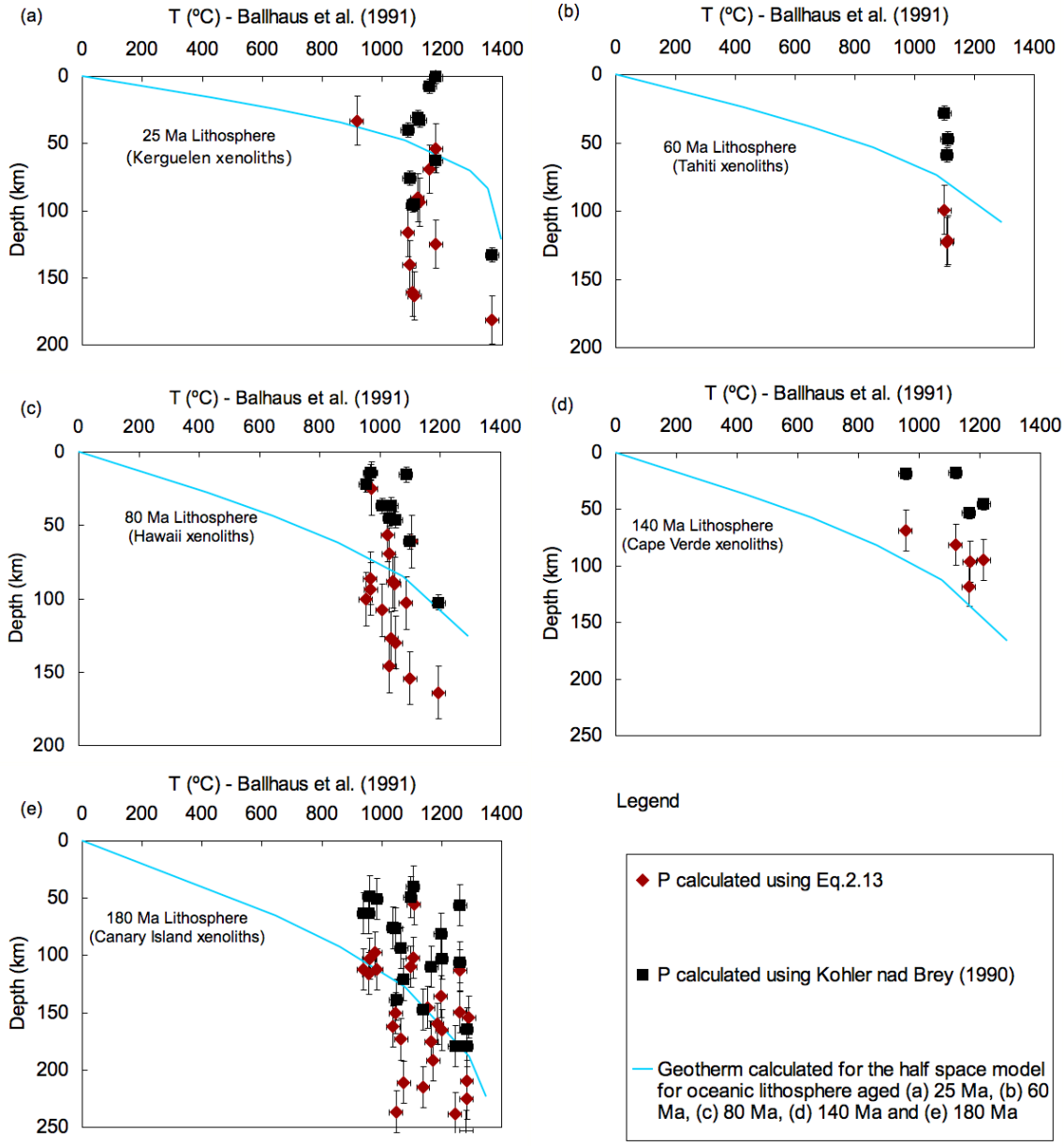

Figure 2.9. Geotherms for the oceanic lithospheric mantle constructed using temperatures calculated by the olivine-spinel geothermometer (Ballhaus et al., 1991) and pressures calculated using Eq. 2.13 (red diamonds) and Kohler and Brey (1990; black squares). The depth is calculated using the relation $Depth = pressure/(density * gravity)$ **and a density of 3.3 gm/cm^3. Error bars indicate 1σ uncertainty on the geobarometer. Three samples in (e) are outside the chart area with depths up to 300 km. The solid blue line is the geotherm for respective age of the oceanic lithosphere calculated for the half space model using the equation from Turcotte and Schubert (2002).**

and two-pyroxene (Brey and Kohler, 1990) geothermometers shows lower temperatures being calculated by the latter (Fig. 2.9). Depths calculated using pressures from the Kohler and Brey (1990) geobarometer and those from Eq. 2.13 with temperatures from the two-pyroxene geothermometer (Brey and Kohler, 1990) are compared (Fig. 2.10). There is no systematic difference between pressures calculated using temperatures from the olivine-spinel (Ballhaus et al., 1991; Fig. 2.9) and two-pyroxene (Brey and Kohler, 1990; Fig. 2.10) geothermometers. Although the pressures that are calculated using Eq. 2.13 are temperature-dependent, the large uncertainty (up to 0.7 GPa) associated with the calibration needs to be investigated before using the geobarometer to test between thermal models of the oceanic lithospheric mantle. As shown above, the use of two different geobarometers results in differences in calculated pressures but these differences are not systematic. As discussed before, the role of Fe in the partitioning of Ca between olivine and clinopyroxene at high pressure has not been evaluated experimentally. Future work on constraining the role of Fe in the partitioning of Ca between olivine and clinopyroxene at high pressure is suggested (Chapter 5).

2.6. Summary

An empirical Ca-in-olivine geothermometer, that incorporates the effect of olivine forsterite content, has been experimentally calibrated at 0.1 MPa. The geothermometer requires the presence of olivine in equilibrium with a low-Ca pyroxene and clinopyroxene in order to buffer the activity of Ca in the system. Accounting for the effect of Fo in olivine on the Ca content in this system helps to explain the difference between the results of previous high-pressure studies in the Fe-bearing system. Unresolved differences still exist in the Fe-free system at high-pressure.

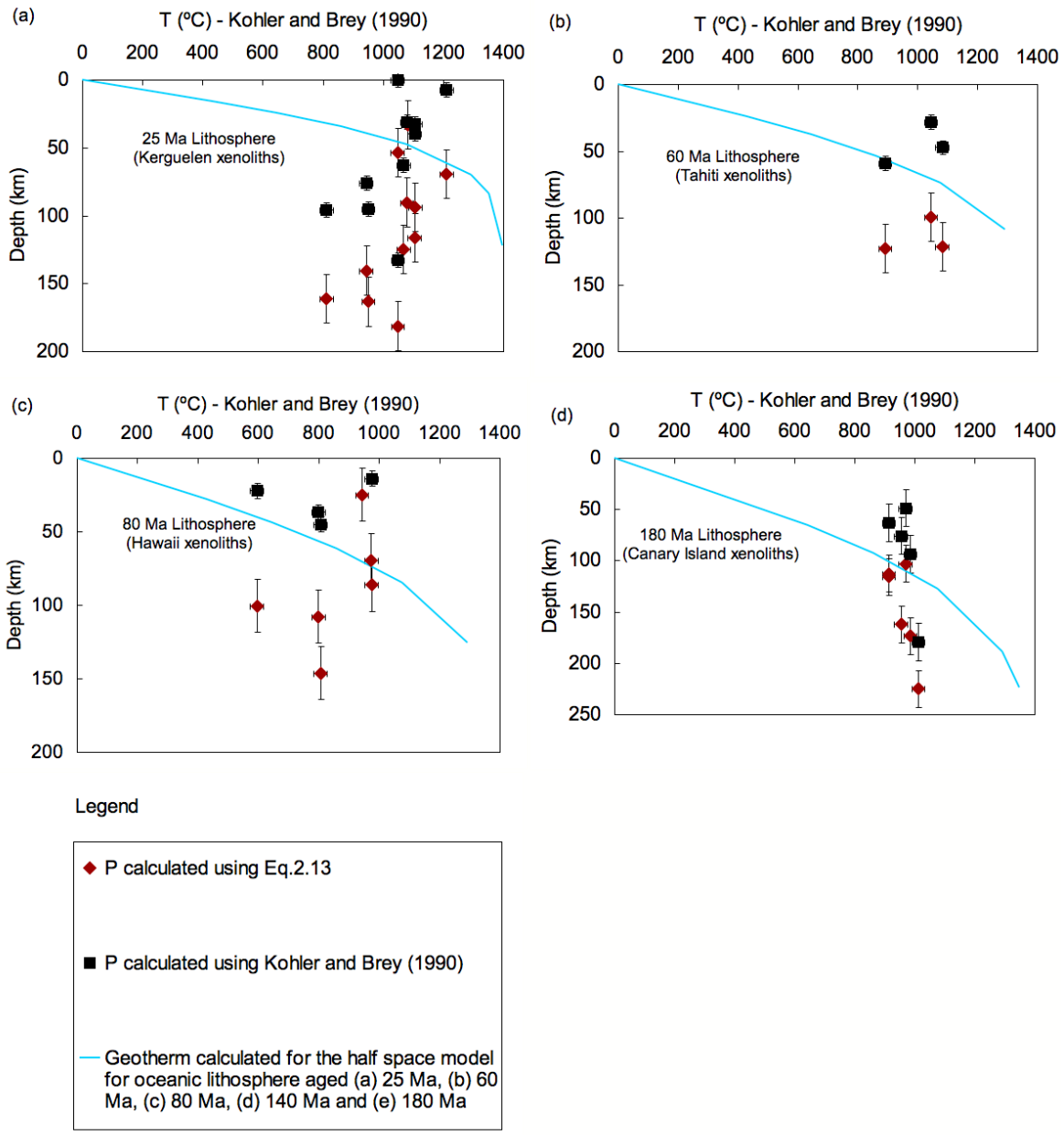

Figure 2.10. Geotherms for the oceanic lithospheric mantle constructed using temperatures calculated by the two-pyroxene geothermometer (Brey and Kohler, 1990) and pressures calculated using Eq. 2.13 (red diamonds) and Kohler and Brey (1990; black squares). The calculation of depth and error bars is as described in Fig. 2.9. The solid blue line is the geotherm for respective age of the oceanic lithosphere calculated for the half space model using the equation from Turcotte and Schubert (2002).

A saturation surface for the crystallisation of olivine, low-Ca pyroxene and clinopyroxene in equilibrium with a melt phase is calibrated. Experimental concentrations of SiO_2, MgO and CaO are reproduced within $\pm$ 2.8, $\pm$1.9 and $\pm$0.9 wt% respectively and experimental temperatures are reproduced within $\pm$ 30ºC. To facilitate the calibration of the olivine-low-Ca pyroxene-clinopyroxene-melt saturation surface at pressures greater than 0.1 MPa, an experimental study that includes varying Mg/Fe ratios in the starting compositions and conducted at higher pressures than 0.1 MPa is suggested.

The empirical geobarometer calibrated using the results of 0.1 MPa experiments from this study and previous high-pressure experiments (Kohler and Brey, 1990) is applied to ocean island xenoliths from different ages of the oceanic lithospheric mantle. The depths calculated using the pressures derived from Eq. 2.13 are compared with the half-space model geotherm for the respective age of oceanic lithosphere (Fig. 2.9). The choice of geothermometer is an important factor influencing the calculation of pressures using Eq. 2.13. The uncertainty in pressures derived from Eq. 2.13 arises from a combination of uncertainties in calculated temperatures and the error associated with calibrating the Ca-in-olivine geobarometer. Since the Ca-in-olivine geobarometer is highly sensitive to composition, a high-pressure experimental study involving the measurement of Ca in a wide range of Fo (Ol) at different pressures is suggested (Chapter 5).

3. Evidence for pervasive melt-rock reaction within the uppermost mantle at Hess Deep

3.1. Introduction

Mid-ocean ridge basalts (MORB) form by decompression melting of the mantle beneath the MOR axis (Fig. 1.3). The residue of melting beneath the ridge axis forms the oceanic lithospheric mantle. As discussed in Chapter 1, the uppermost oceanic lithospheric mantle can be sampled near the seafloor as abyssal peridotites; ocean island xenoliths, on the other hand, are likely to represent the deeper portion of the oceanic lithospheric mantle (Fig. 1.3). The mechanism of melt extraction from the mantle is debated. A fundamental constraint on melt extraction mechanisms is that abyssal peridotites are not in equilibrium with MORB. The clearest evidence of this comes from: (i) the observation that orthopyroxene is always present in abyssal peridotites but MORB are far from orthopyroxene saturation at low pressure (O'Hara, 1965; Stolper, 1980) and (ii) clinopyroxene in abyssal peridotites are commonly depleted in the highly incompatible elements relative to clinopyroxene in equilibrium with MORB (Johnson et al., 1990; Johnson and Dick, 1992; Dick and Natland, 1996).

The observed disequilibrium between upper mantle peridotites and MORB has generally been thought to provide evidence that mantle melting is "near-fractional" (Johnson et al., 1990; Johnson and Dick, 1992) with melts extracted through channels that are not in equilibrium with the surrounding mantle (e.g. Kelemen et al., 1997). The observation that dunite bodies within the upper mantle in the Oman ophiolite contain clinopyroxene that is in equilibrium with MORB has led to a widely accepted model that these represent the conduits through which MORB is extracted from the mantle (Kelemen et al., 1995). Because the olivine phase field expands with decreasing pressure (e.g.

Stolper, 1980) melt-rock reaction within a high melt flux conduit will cause the dissolution of pyroxenes and precipitation of olivine during melt ascent thus forming dunites (Kelemen et al., 1995).

The model of melt extraction from the mantle through dunite conduits (Kelemen et al., 1995) has been challenged based on evidence that abyssal peridotites have higher modal olivine abundances than predicted residues of melting (Niu, 1997) and have higher whole-rock incompatible element abundances than expected for residues of near fractional melting (Niu, 2004). These observations suggest that most abyssal peridotites have been modified by pervasive reaction with melts migrating by diffuse porous flow. Based on these observations it has been suggested that "diffuse porous flow is the primary mode of melt migration" (Niu, 1997) and that the melts are able to remain out of equilibrium with the cores of the clinopyroxene crystals (Niu, 2004). Niu (2004) suggests that disequilibrium can be maintained between the migrating melts and surrounding harzburgites because the upper mantle is conductively cooled.

There is evidence that some of the melts extracted from the mantle are in equilibrium with abyssal peridotites. Some melt inclusions in olivine and plagioclase phenocrysts have very depleted LREE contents relative to MORB and similar to those in equilibrium with clinopyroxene in abyssal peridotites (Sobolov and Shimizu, 1993; Nielsen et al., 1995). These have been interpreted as being frozen melts that entered the crust and were trapped in crystallising olivine. Additionally, sampling of the lower (plutonic) crust at Hess Deep has shown that primitive plutonic rocks can contain cumulus orthopyroxene inconsistent with the crystallisation order of typical MORB (Gillis et al., 2014) i.e. olivine-plagioclase-clinopyroxene-orthopyroxene (Ghiorso and Sack, 1995). These have been interpreted to indicate crystallisation of melts that had equilibrated with upper mantle

orthopyroxene during melt extraction and hence orthopyroxene was a near-liquidus phase in their parental melts (Coogan et al., 2002; Gillis et al., 2014). Thus, it seems that while typical MORB may be far from equilibrium with the upper mantle (i.e. abyssal peridotites) some melts added to the crust may be in equilibrium with the upper mantle.

This chapter tests the hypothesis that abyssal peridotites experienced large fluxes of diffuse porous melt migration during melt extraction at the top of the melting column. To this end, a sample suite consisting of spinel harzburgites from the Hess Deep region that formed at the East Pacific Rise (EPR) were selected and analysed for both whole-rock and mineral major and trace element compositions. Hess Deep, in the equatorial Pacific, provides a unique view into the upper mantle. Here, peridotites formed at the fast-spreading EPR are exposed at the seafloor due to rifting associated with the propagation of the Cocos-Nazca ridge towards the EPR. Thus, peridotites that would not normally be exposed are accessible to sampling.

Harzburgites were sampled from Hess Deep by drilling on ODP Leg 147 and were studied here for their major and trace element compositions in both bulk-rock and minerals. It is shown that the bulk-rock compositions are highly depleted in Al_2O_3, CaO and moderately incompatible trace elements such as Ti, V, Sc and HREEs lying at the most depleted end of the global spectrum of abyssal peridotites. However, the highly incompatible elements are enriched in the bulk-rock relative to expected melting residues. Strikingly, the Ce content of clinopyroxene is similar to the bulk-rock Ce content demonstrating that the clinopyroxene is far from equilibrium with the bulk-rock. Since the partition coefficient of Ce is higher in clinopyroxene than any other primary mineral phase in the harzburgite (i.e. olivine, orthopyroxene and spinel), the concentration of Ce in clinopyroxene is expected to be higher and not similar to the bulk rock. The bulk-rock

incompatible element abundances in most samples can be explained by melt-rock reaction by pervasive diffuse melt flow during which plagioclase crystallises from the melts that percolate along grain boundaries. Pervasive diffuse melt transport appears to have played an important role in controlling the composition of the Hess Deep abyssal peridotites.

3.2. Hess Deep and the Sample suite

Drilling at ODP Site 895 of the Hess Deep region recovered a suite of rocks consisting predominantly of harzburgites and dunites along with gabbro, olivine-gabbro and troctolite (Gillis, Mevel et al., 1993). The harzburgites from Hess Deep have been described as having minor amounts of plagioclase (0.1%) in addition to olivine (83.6%), orthopyroxene (14.6%), clinopyroxene (1%) and spinel (0.7%; Dick and Natland, 1996). The thickness of the crust at Hess Deep is about 5.6 km (Gillis et al., 2014), which is at the low end of the typical thickness for the crust formed at the EPR, possibly due to formation of the Hess Deep crust at a segment end where the magma supply is expected to be below average. The abyssal peridotites in Hess Deep were exposed due to the westward propagation of the Cocos-Nazca spreading center (Gillis, Mevel et al., 1993; Dick and Natland, 1996). The Hess Deep region has been selected for this study primarily since the sampling was done by drilling and the samples were described as being ~80% altered (Gillis, Mevel et al., 1993) and are therefore likely to have at least ~20% material fresh enough for mineral and whole rock analyses. Secondly, the crustal section overlying the peridotites is the best studied crustal section formed at a fast-spreading ridge providing context for this study. Finally, the occurrence of primitive cumulus orthopyroxene in the

overlying crust has been interpreted as indicative of melts in equilibrium with the upper mantle being extracted into the lower crust (Gillis et al., 2014).

The area at Hess Deep where the samples for this study were drilled is located along the southern slope of the intra-rift ridge where ultramafic rocks had previously been recovered using the *Nautile* submersible (Francheteau et al., 1990). Eighteen samples were selected based on descriptions of core samples and thin sections made on-board and published in IODP volume 147 (Gillis, Mevel et al., 1993). Only those samples that were described as less than 80% altered were selected. The cores recovered from ODP Site 895 are largely harzburgitic but they are cut by dunites and gabbros, which have been interpreted as regions of focused melt flow (Dick and Natland, 1996). Some evolved olivines (Mg# ~89.5) have been reported in Hess Deep peridotites associated with these gabbros and dunites. To avoid, as best as possible, chemical effects related to this focussed melt extraction, only regions of the core described as harzburgitic and far from any described dunites or gabbroic bodies were selected. However, poor recovery (average of 23.5%; Gillis, Mevel et al., 1993) means that dunites and gabbroic bodies that were not sampled may have existed close to the samples studied here.

3.3. Analytical methods

The samples, which were ~ 64 cm^3 in volume, were cleaned of sample number labels and glue residues and after cutting off a thin section billet, crushed. Initial crushing was by hand, using a steel hammer with the rock separated from the hammer by double plastic bags. The coarse crush was then washed in deionised (DI) water, dried and then pulverised in an agate planetary mill. The bulk rock major element composition of the powders were analysed using Inductively Coupled Plasma Optical Emission Spectroscopy

(ICP-OES) at Acme Laboratories in Vancouver. The concentrations are reported on both, hydrous and anhydrous basis (Supplementary Table 3.1). The MgO/SiO_2 ratio reported from ICP-OES analysis was found to be lower (average 0.85; Supplementary Table 3.1) than previously reported for Hess Deep Site 895 harzburgites (average 1.1; Gillis, Mevel et al., 1993). As a check on data quality, the samples were re-analysed at Bureau Veritas Mineral Laboratories (Vancouver) using X-Ray Fluorescence (XRF) technique and the results are included in Supplementary Table 3.1. In all of the XRF-analysed samples, the bulk MgO/SiO_2 ratios are higher than ICP-OES-analyses (Fig. 3.1a; Supplementary Table 3.1) and similar to previously reported Hess Deep harzburgites. The concentration of FeO is higher by ~ 0.5 wt% when analysed by XRF compared to ICP-OES analysis for the same sample (Fig. 3.1b; Supplementary Table 3.1).

The bulk rock concentrations of all elements analysed using XRF are comparable to those previously reported for harzburgites from Hess Deep Site 895 (Gillis, Mevel et al., 1993). The results of XRF analyses on seventeen samples are used to apply a mathematical correction to the ICP-OES data for sample (147-895D-004R-01W 54-60), which is not analysed by XRF due to lack of sample, using the following methodology. The XRF and ICP-OES data for the same element were plotted against each other and a best fit line was constructed through the points using least squares linear regression. Further, this line was forced through the origin and the slope of this line was multiplied with the ICP-OES-measured concentration of the respective element. The corrected compositions are given in Supplementary Table 3.1.

Bulk rock trace element abundances were analysed on a Thermo X-Series 2 quadrupole ICP-MS at the University of Victoria. Rock powders were digested in HF and HNO_3 using a microwave pressure vessel to ensure dissolution of spinel; that this occurred

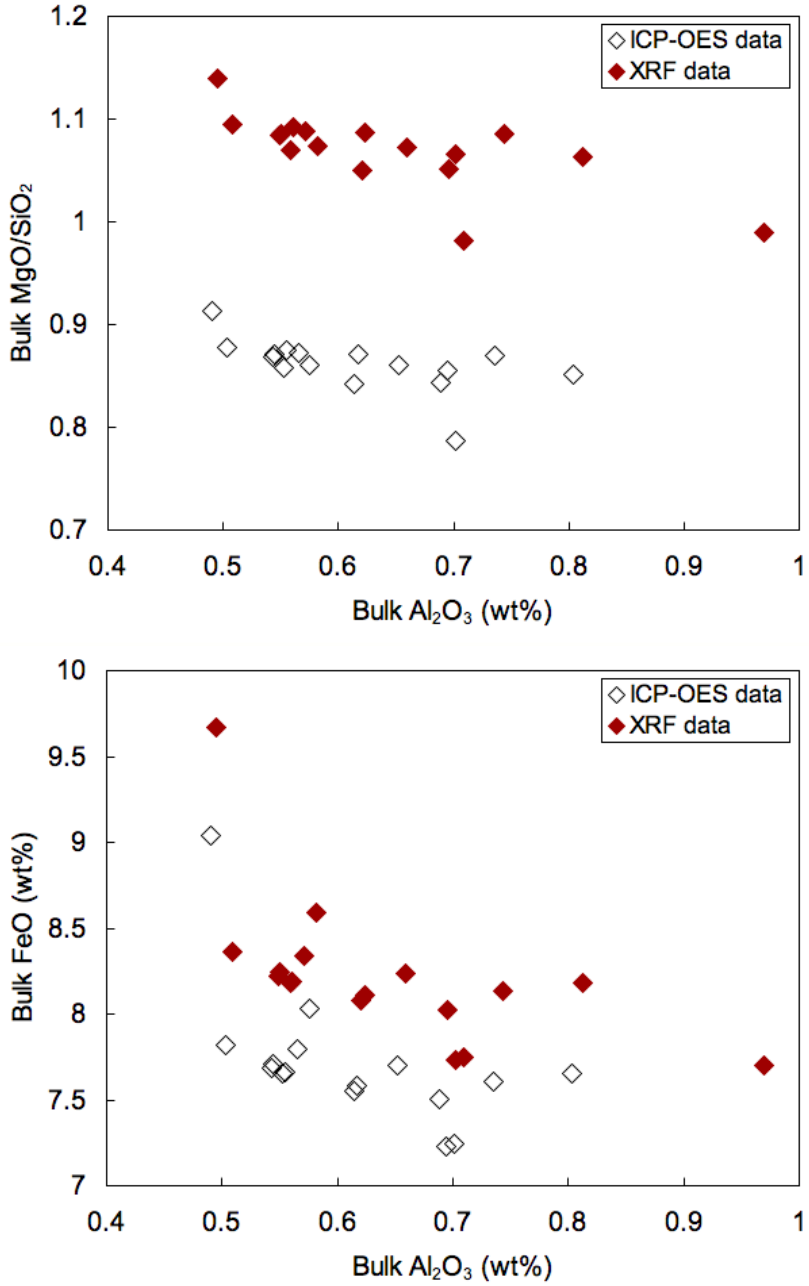

Figure 3.1 Comparison between (a) MgO/SiO_2 ratio and (b) FeO (wt%) analysed by ICP-OES (open diamonds) and XRF (red diamonds) plotted against Al_2O_3 (wt%). The MgO/SiO_2 ratio and FeO analysed by XRF are lower than ICP-OES analyses. For one sample (147-895D-002R-02W 33-38), the concentration of Al_2O_3 analysed by XRF is lower than that analysed by ICP-OES.

was subsequently confirmed by the close agreement of the Cr contents determined by the XRF and ICP-MS analytical techniques. The acids were then evaporated on a hot plate at ~150ºC. When nearly dry, 2 mL of 1:1 HNO_3 and DI water was added to the vials and refluxed overnight at ~130ºC. The last two steps were repeated until the sample had completely dissolved. The solutions were then diluted to give an average dilution factor of 0.0004 prior to analysis. Internal standards (30 ppb of Rh, In, Re) were added on-line during analysis.

The final results of trace element concentrations were calculated by data reduction (explained in detail below) and calibrating the analytical results against peridotite standard JP-1, serpentinite UB-N and basalt BIR-1 (using the values given in Supplementary Table 3.2). Duplicate analyses of samples gave results that were within analytical uncertainty of each other. Following is the step by step procedure used for the calculation of final trace element concentrations:

1. The materials run in the ICP-MS along with the samples whose concentrations are to be determined include the standards JP-1, UB-N and BIR-1, 2% nitric acid blank, a drift solution to monitor instrument drift through the course of analysis during the day and procedure blanks.
2. The raw data which is obtained as counts per second of the mass of the respective isotope was first normalised to the concentration of the internal standard.
3. The drift solution is run at multiple times during the course of the day. Instrument drift was checked by normalising the counts per second of each element for the drift solution to the first reading of the day. The normalised data were plotted against the run number and a second order polynomial line

($Y = Ax^2 + Bx + C$) was fit through the data. The values of A, B and C obtained by fitting the data to the polynomial line were used to calculate drift factors by substituting the run number for the value of x in the above equation. The internal standard corrected counts per second were then normalised by the respective drift factors thus correcting for instrument drift.

4. The average of procedure blanks was subtracted from the internal standard- and drift-corrected counts per second. If the results of this subtraction were less than three times the standard deviation on the average of procedure blanks, the element was considered to be below the detection limit of the ICP-MS analyses. Elements that were below the detection limit were thus filtered out prior to further processing.
5. The data for elements that were determined to be detectable in the above step were corrected for the dilution factor by normalising the internal standard- and drift-corrected counts per second for each sample by the dilution factors.
6. Finally the concentrations of each element in the samples were calculated by using coefficients from least squares linear regression of known concentrations of standards (Table 3.2) against internal standard normalised concentrations. Supplementary Table 3.3 shows the data reduction techinque used for solution ICP-MS analyses.

Major elements in minerals were analysed by electron microprobe at the University of British Columbia using an automated CAMECA SX-50. All phases were analysed using an excitation voltage of 15 kV with a 40 nA beam current and 5 μm beam diameter. Peak

and background counting time for all elements was 20 seconds, except for Ni and Ca in olivine where 60 seconds was used. Data reduction was carried out using the PAP/ΦρZ method (Pouchou and Pichoir, 1985).

In-situ trace element mineral analyses were performed on olivine and pyroxenes in the harzburgites. Mineral trace element concentrations were analysed by Laser Ablation Inductively Coupled Plasma Mass Spectrometer (LA-ICP-MS) at the University of Victoria. Only crystals with little or no signs of optically observable alteration were analysed. In all minerals, zoning profiles were measured across crystals to test for homogeneity. Continuous profiles across adjacent olivine, pyroxene and spinel were obtained where possible in order to examine the possible change in composition along crystal borders due to exchange of elements between the various mineral phases. A 213 nm New Wave laser with a 40 μm beam diameter and a pulse frequency of 10 Hz was rastered along lines ~150 to 250 μm long parallel to the crystal edges. After collection of a gas blank that was used to determine the background, the laser was fired for ~30 seconds. The ablated sample was transported for analysis to a Thermo X-Series 2 quadrupole ICP-MS by a helium carrier gas flowing at ~1.18 litres per minute. Peak time slices for the acquired data were selected manually based on the time resolved spectra. The data was calibrated against MPI-DING standards GOR128, GOR132, KL-2G and ML-3B (Jochum et al., 2005; Supplementary Table 3.1). These standards were analysed before and after each sample. San Carlos olivine was used as the external standard for Al and Cr in olivine using the concentrations reported by Wan et al. (2008); this was analysed in the beginning of the day of analysis. Electron microprobe analyses of Ni and Ca were used as internal standards for calibration of LA-ICP-MS data for olivine and pyroxene respectively. Electron microprobe data was collected for the same crystals that were analysed on the ICP-MS and data points

for both analysis were selected to be as close to one another as possible. When exsolution lamellae were present in orthopyroxenes, LA-ICP-MS analyses that gave anomalously high raw counts per second values for Ca in comparison to orthopyroxenes with no exsolution lamellae were discarded. Supplementary Table 3.4 is a sample spreadsheet showing LA-ICP-MS data processing technique for some Hess Deep harzburgites.

Detection limits for elements in minerals were calculated for LA-ICP-MS analyses and are given in Table 3.5. The detection limit for each element was calculated as the concentration the phase would have, using a measured background counts per second (cps) of 3 times the standard deviation on the background for each element and the measured cps on the internal standard. The equation used for the detection limit in ppm is as follows:

$$\text{Detection Limit (ppm)} = \frac{\text{Measured concentration (ppm)} * 3\sigma \text{ on background cps}}{\text{Measured cps on internal standard}} \quad \text{Eq. 3.1}$$

Calcium was selected as the internal standard since detection limits were calculated for trace element concentrations in pyroxenes and olivine. The concentrations of Ce, Nd and Zr in orthopyroxenes and clinopyroxene were found to be close to detection limits in many samples (Table 3.5). The locations of electron probe and LA-ICP-MS analysis spots on minerals analysed in this study are shown in Appendix A.

3.4. Results

3.4.1. Petrography

All Hess Deep rocks from this study are medium-coarse grained, protogranular harzburgites with olivine and orthopyroxene crystals ranging from 2-5 mm across (Fig. 3.2a-f). Trace

amounts of clinopyroxene and accessory spinel, usually ranging in size from 0.25 to 1 mm (Fig. 3.2e-f) occur as interstitial grains (Dick and Natland, 1996; Gillis, Mevel et al. 1993; Arai and Matsukage, 1996). While all rocks are ~25-70% altered, they contain fresh phases suitable for analysis (Fig. 3.2). The percentages of altered phases for each sample are

Table 3.5. Average detection limits calculated for LA-ICP-MS data using Eq. 3.1.

Element	Detection limit in pyroxene (ppm)	Detection limit in olivine (ppm)
Li	0.02	0.02
Sc	0.34	0.8
Ti	0.003	0.01
V	0.78	2.9
Cr	58	79
Co	0.08	0.16
Ni	4	2
Zn	0.2	0.5
Sr	0.15	0.9
Y	0.01	0.1
Zr	0.04	0.6
Ba	0.04	0.7
Ce	0.01	0.2
Nd	0.01	0.05
Yb	0.001	0.005

given in Table 3.6 and Supplementary Table 3.1. Detailed analyses of the alteration in Hess Deep harzburgites from this study is given in Section 3.4.4. Olivine crystals are subhedral, highly cracked and serpentinised (Figs. 3.2a-f). Orthopyroxenes are relatively fresh in most

samples and many have exsolution lamellae or blebs of clinopyroxene (Fig. 3.2f). Exsolution is also observed in clinopyroxene and the lamellae are sometimes as close as 10 μm apart. Olivine and orthopyroxene generally have interlocking boundaries but are sometimes entirely surrounded by an altered matrix obscuring the primary textural relationships (Fig. 3.2a-b). In some cases, pyroxenes are partially to completely replaced by amphibole and chlorite by hydrothermal alteration. Calcite occurs as veins in some samples.

3.4.2. Bulk rock chemistry

Hess Deep peridotites recovered from ODP Site 895 have low Al_2O_3 concentrations (<1 wt%) and are located at the depleted end of the global spectrum of abyssal peridotite compositions (Fig. 3.3a-d). With the exception of one sample that has a high CaO content (4.6 wt%; Fig. 3.3a), the generally low CaO (<1.25 wt %) matches that expected for the low Al_2O_3 content (Fig. 3.3a; Supplementary Table 3.1). The high-CaO is interpreted as a result of calcite precipitation since this sample also has a higher percentage of C relative to other samples (Supplementary Table 3.1). The percentage of CaO corrected after subtracting Ca in calcite is similar to the rest of the harzburgites (star symbol in Fig. 3.3a). The concentrations of SiO_2, CaO, Al_2O_3 and MgO measured here for Hess Deep harzburgites are similar to previous analyses of abyssal peridotites from this region (Fig. 3.3; Gillis, Mevel et al., 1993; Blum, 1990).

The low concentrations of the moderately incompatible trace elements Ti, V and Sc in the ODP Site 895 harzburgites, in comparison with the global abyssal peridotite suite (Fig. 3.4), also indicate that they are more depleted than most abyssal peridotites. The Ti concentrations of the ODP Site 895 harzburgites analysed in this study are lower than

in the depleted peridotites recovered from the Garrett Transform (Niu and Hekinian, 1997) and similar in composition to the highly depleted peridotites from the 15º 20’ N

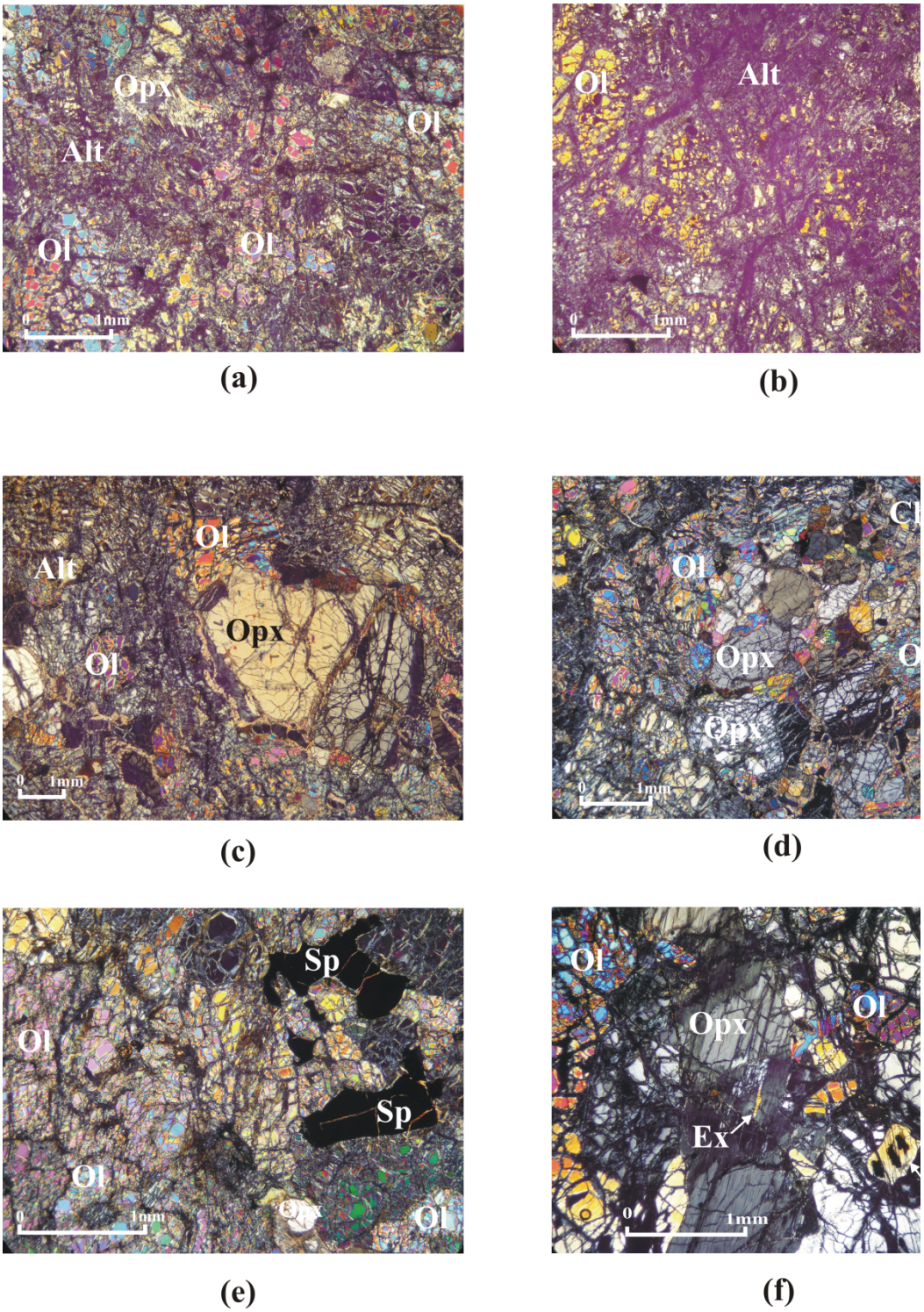

Figure 3.2. (Caption on following page)

Figure 3.2 Photomicrographs of harzburgites from Hess Deep (ODP) Site 895 showing textural relationships between olivine (Ol), orthopyroxene (Opx), clinopyroxene (Cpx) and spinel (Sp) along with alterations (Alt) and exsolution lamellae (Ex). (a) 895E-007R-04W (86-94): Thin section of harzburgite showing highly cracked olivine crystals that are serpentinised along the cracks. The orthopyroxene in this sample is highly altered. (b) 895E-007R-04W (34-41): Highly serpentinised olivine and altered orthopyroxene along with serpentine veins cutting across olivine crystals. (c) 895D-005R-02W (127-135): Unaltered orthopyroxene crystal surrounded by highly cracked olivine crystals that are altered to chlorite. (d) 895D-005R-02W (103-112): Relatively fresh olivine and orthopyroxene crystals with minor alterations along the boundaries of crystals and along the cracks in olivine. (e) 895D-004R-03W (112-116): Typical spinel observed in harzburgites from ODP Site 895 of this study along with highly cracked olivine crystals with alterations along the cracks and borders of the crystals. (f) 895A-001R-02W (55-61): Relatively fresh part of the harzburgite with orthopyroxene showing exsolution blebs and surrounded by highly cracked olivine crystals. Also seen here is a clinopyroxene crystal analysed in this study.

fracture zone on the MAR (Paulick et al., 2006; Godard et al., 2008). As with Al_2O_3 and CaO, the only sample suite with as low concentrations of the transition metal V is that from the 15º 20' N fracture zone on the MAR (Paulick et al., 2006; Godard et al., 2008; Fig. 3.4b). A positive correlation is observed between bulk concentrations of V and Al_2O_3 in Hess Deep harzburgites. The bulk concentration of Sc does not show any correlation with Al_2O_3 (Fig. 3.4a) and is similar to the remaining abyssal peridotite samples. Similarly, the bulk rock concentration of Co in the ODP Site 895 harzburgites from this study is similar to the global suite and does not show any correlation with Al_2O_3 (Fig. 3.4c). The bulk concentration of Ti is scattered on the Al_2O_3 variation diagram (Fig. 3.4d). The concentration of Ti is not well resolved for most samples from the global sample suite as seen in Fig. 3.4d and is likely due to most of the previous data being analysed by XRF, which is less precise.

Table 3.6. Mineral modes determined by point-counting.

Sample No	Ol	OPx	CPx	Sp	Chl	Serp after olivine	Alt OPx	Alt CPx	Trm	Serp/ Chl Vein	Ox	Exs CPx	Total
147-895D-005R-02W (103-112)	48.41	3.29	2.35	2.35	2.94	28.67	8.11	2.11	1.06	0	0.12	0.58	99.99
147-895D-005R-01W (48-54)	34.85	4.76	0	0.41	0.99	47.01	7.96	0	2.75	1.46	0	0.26	100
147-895D-003R-01W (34-39)	32.15	12.52	0.91	1.77	0.27	42.96	6.93	0.38	0	1.45	0	0.65	99.99
147-895D-007R-02W (127-135)	25.47	10.84	3.68	2	1.05	44.95	8.53	0	0	2.84	0.63	0	99.99
147-895E-007R-04W (34-41)	26.73	1.26	0	3.3	2.2	41.19	16.67	0	1.88	6.76	0	0	99.99
147-895D-004R-05W (11-18)	24.67	2.07	1.96	2.17	1.74	38.04	19.13	2.28	3.48	3.69	0.54	0.22	99.99
147-895D-004R-03W (52-58)	35.35	4.51	2.25	1.9	0.83	37.49	13.04	0.47	0.24	3.44	0.47	0	99.99
147-895D-004R-01W (54-60)	37.24	3.31	2.21	0.77	1.1	35.03	15.36	1.1	0.99	1.77	0.22	0.88	99.98
147-895C-001R-01W (103-107)	34.85	4.76	0	0.41	0.99	47.01	7.96	0	2.75	1.46	0	0.26	100
147-895C-003R-01W (135-143)	46.61	0.48	2.62	1.03	2.97	31.39	8.16	2.35	0.2	3.52	0	0.62	99.95
147-895D-002R-02W (33-38)	38.37	8.13	1.37	1.92	0.43	40.57	6.76	0.54	0.1	0.87	0.38	0.49	99.93
147-895A-002R-01W (5-10)	50.85	7.3	2.48	0.78	0.56	30.7	4.1	0.07	0	2.48	0	0.63	99.95
147-895A-001R-02W (55-61)	34.04	11.01	1.06	1.06	0.66	37.75	5.24	0	0	3.78	3.51	1.85	99.96
147-895D-003R-01W (61-70)	50.03	8.63	2.74	1.47	0.8	26.89	5.62	1.27	0	1.74	0	0.8	99.99
147-895B-001R-01W (65-72)	49.24	5.84	1.92	1.58	0.82	24.69	9.49	0.13	0.34	4.95	0.89	0.06	99.95

Table 3.6 continued on next page

Table 3.6 continued

Sample No	Ol	OPx	CPx	Sp	Chl	Serp after olivine	Alt OPx	Alt CPx	Trm	Serp/ Chl Vein	Ox	Exs CPx	Total
147-895E-007R-04W (86-94)	34.55	2.71	0.82	1.94	1.88	36.55	15.01	0	0.71	5.83	0	0	100
147-895D-004R-03W (112-116)	58.61	9.06	3.32	4.83	0.6	22.05	1.51	0	0	0	0	0	99.98

Abreviations used: Ol – olivine, OPx – orthopyroxene, CPx – clinopyroxene, Sp – spinel, Serp – serpentine, Alt Opx – alteration after orthopyroxene, Alt CPx – alteration after clinopyroxene, Trm – tremolite, Serp/Chl – serpentine/chlorite, Ox – oxide, Exs CPx – exsolved clinopyroxene.

Within the Hess Deep suite, three distinct REE patterns are observed (Fig. 3.5). Most samples have weakly U-shaped REE patterns (solid black lines in Fig. 3.5) with nearly flat chondrite normalised (subscript 'n') LREE/MREE ($(La/Sm)_n$ ~1 to 3) but high HREE/MREE ($(Lu/Tb)_n$ ~3 to 26). These samples have small but notable positive Zr and Hf anomalies and large positive Ti anomalies (Fig. 3.5). The LREE abundances in the samples with weakly U-shaped REE pattern are lower than in the depleted MORB mantle (DMM) initial composition (Workman and Hart, 2005). Three samples are generally similar to the main group of abyssal peridotites, but have much stronger LREE enrichment and higher LREE/MREE ($(La/Sm)_n$ ~5) than the remaining samples (Fig. 3.5; dashed black lines) and these samples are characterised by strong negative Zr and Hf anomalies. Finally, one sample has a nearly flat REE pattern at much higher MREE and LREE abundances than the other samples (Fig. 3.5; dotted blacklines) and does not show any negative Zr and Hf anomaly. The abundances of La in the LREE-enriched and flat REE pattern samples are higher than DMM. The difference in concentrations of LREE between the most enriched and the most depleted of the Hess Deep harzburgites is about two orders of magnitude. Such a large variation in LREE content suggests that the Hess Deep harzburgites have been subject

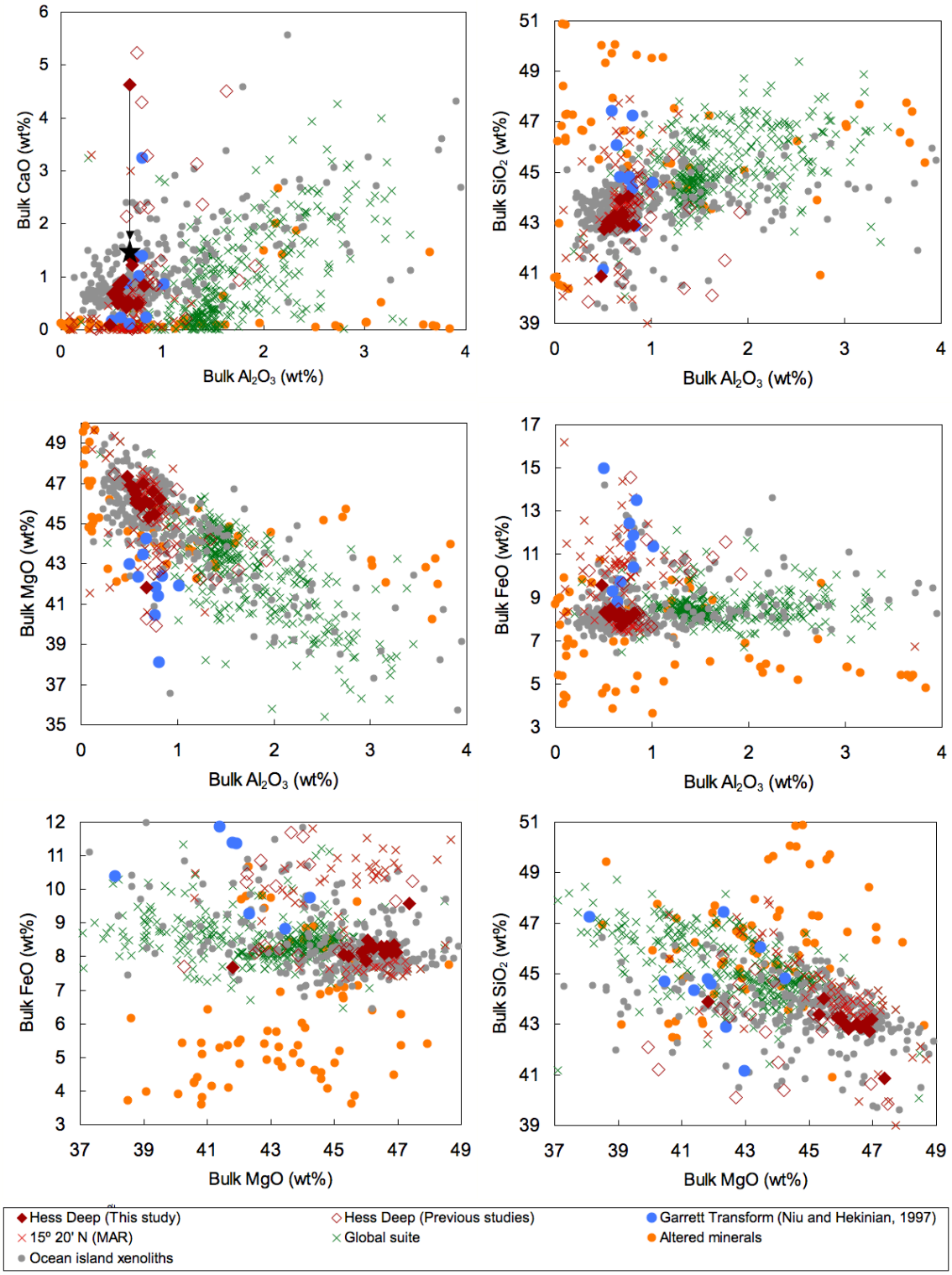

Figure 3.3 (Caption on following page)

Figure 3.3 Bulk rock compositions of Hess Deep peridotites (East Pacific Rise) reported on anhydrous basis as analysed in this study plotted alongside Hess Deep peridotites from previous studies (Gillis et al., 1993; Blum, 1990) and a global suite. The sources for data for the global suite are as follows: Garrett Transform (EPR): Niu and Hekinian (1997); MAR: Casey et al. (1997), Aumento and Loubat (1971), Paulick et al. (2006), Godard et al. (2008), Cannat et al. (1995), Stephens (1997), Lee et al. (2003), Harvey et al. (2006); Pacific Antarctic Ridge: Niu (2004); CIR: Niu (2004); SWIR: Snow and Dick (1995), Niu (2004); American Antarctic Ridge: Niu (2004). The plots show bulk rock concentrations of (a) CaO, (b) SiO_2, (c) MgO and (d) FeO versus Al_2O_3 (all in weight percent). Samples from the Garrett Transform are shown as separate symbols since it is the only other sample suite from the EPR. Separate symbols are also shown for peridotites from 15º 20' N along MAR as the only suite that is more or as depleted as Hess Deep. The depleted nature of Hess Deep peridotites is apparent from the low Al_2O_3 and CaO concentrations of these rocks compared to the global suite. Higher CaO concentration (a) in one Hess Deep sample is the result of calcite precipitation. The star symbol at the base of the arrow in part (a) represents the carbonate-corrected concentration of CaO for this sample. The results of EPMA analyses of secondary minerals (recalculated to anhydrous basis; filled orange circles) are plotted for comparison with the bulk rock data in order to understand how alteration modifies the bulk rock composition. Also shown for comparison are compositions of ocean island xenoliths. It is observed that Hess Deep peridotites plot close to the depleted end of the ocean island xenoliths global array (References as in Fig. 4.4; Chapter 4). MgO variation diagrams are plotted for (e) FeO and (f) SiO_2; alteration is likely to have removed MgO in most of the harzburgites from this study while SiO_2 may have been added in some of the harzburgites. The differences between concentrations of some elements like CaO in Hess Deep harzburgites analysed in this study and the data from previous studies may be due to the differences the extent of alteration in the samples. For example, the higher concentration of CaO in Hess Deep harzburgites from previous studies (open red diamonds) may be due to calcite precipitation in these rocks.

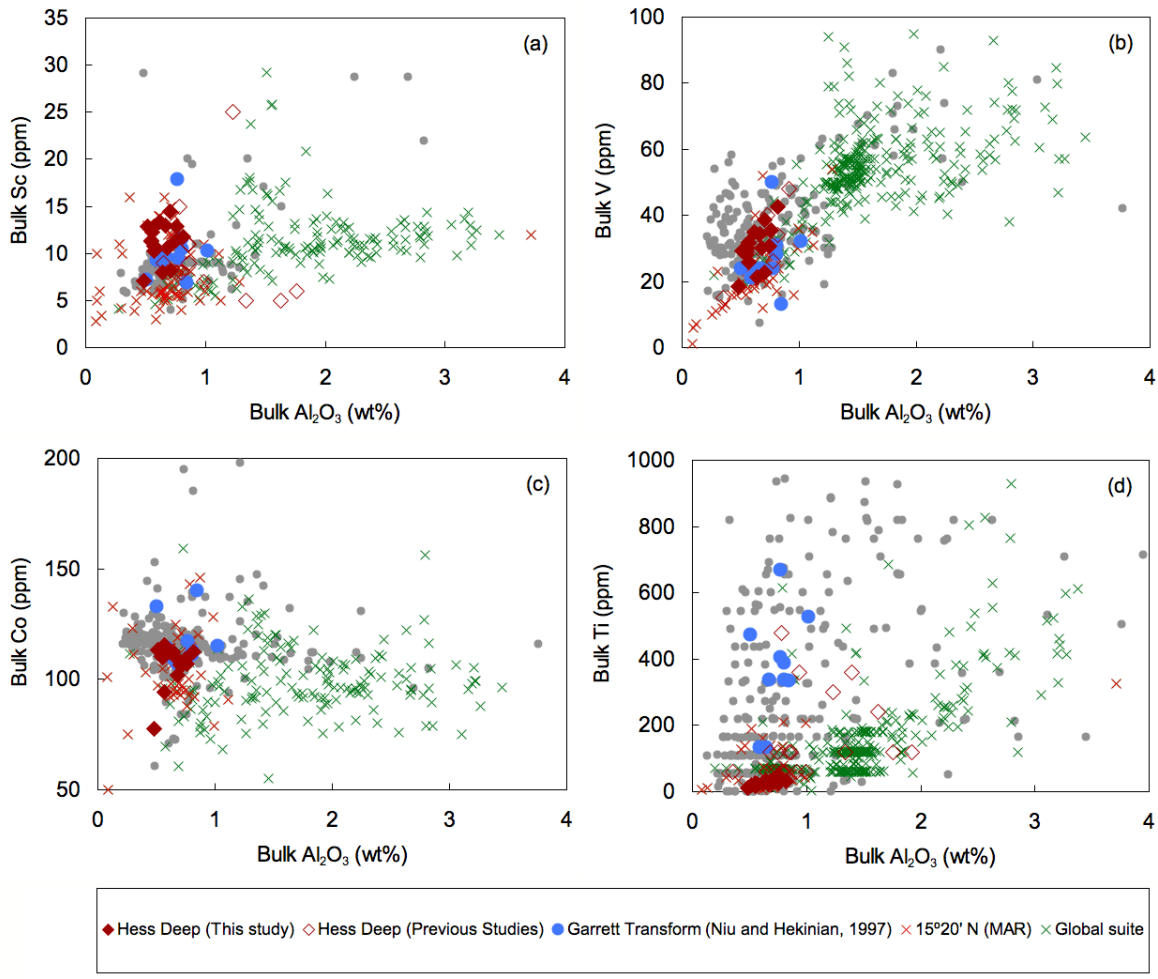

Figure 3.4 Bulk rock trace element concentrations of Hess Deep peridotites for (a) Sc, (b) V, (c) Co and (d) Ti plotted on Al_2O_3 variation diagrams. Also shown are Hess Deep peridotites from previous studies (Gillis et al., 1993; Blum, 1990) along with the global sample suite (Sources as in Fig. 3.3). As in Figure 3.3, samples from the Garrett Transform are shown as separate symbols as a distinction of peridotites from the EPR. The depleted nature of Hess Deep peridotites is clearly observed with only samples from 15º 20' N (Paulick et al., 2006; Godard et al., 2008) along the MAR being similar to Hess Deep samples.

to a wide range of post-melting modifications. There is no observable correlation between REE concentrations and weight loss on ignition (LOI) and the modifications in REE are unlikely to be related to hydrothermal alteration (further discussed in Section 3.5.2).

3.4.3. Mineral chemistry

The major and trace element mineral compositions of Hess Deep peridotites (Supplementary Table 3.1), like the whole-rock compositions, reflect the highly depleted characteristics of the Site 895 harzburgites (Fig. 3.6; Dick and Natland, 1996; Edwards and Malpas, 1996; Allan and Dick, 1996; Arai and Matsukage, 1998). In terms of major element geochemistry, the average olivine forsterite content of the samples studied here is 90.9 and the average spinel Cr# is 54.5 (Fig. 3.6a). The Hess Deep samples have high Cr# in spinel (i.e. 40-60; Fig. 3.6a) compared to the global suite (i.e. 15 to 55). The concentration of Al_2O_3 in orthopyroxene is at the low end (1.8-2.6 wt%; Fig. 3.6b) of the global array (3 to 6 wt%). Low Al_2O_3 concentrations are also observed in clinopyroxene from the Hess Deep suite (2 to 4 wt%; Fig. 3.6b) compared to those in the global suite (3.5 to 7 wt%).

Clinopyroxene is present in fifteen of the seventeen samples that were analysed for mineral chemistry in this study. Of these, only nine samples had clinopyroxenes that were large enough to be analysed for trace elements by LA-ICP-MS (Supplementary Table 3.1). Compared to the global dataset, clinopyroxenes from Hess Deep harzburgites are highly depleted in incompatible elements such as Zr and Ti (Fig. 3.7). The global dataset of mineral trace element compositions defines the melting trend for abyssal peridotite samples (Fig. 3.7). Most clinopyroxenes analysed in this study are highly depleted in Zr and Ti with some Zr contents being below the detection limits of the LA-ICP-MS analyses (Table 3.5;

Section 3.3). Clinopyroxene in the Hess Deep harzburgites from a previous study (Dick and Natland, 1996) plot away from the melting trend defined by the global suite at high Zr/Ti (Fig. 3.7). It has been suggested that this is an analytical artefact resulting from a background spike for Zr in clinopyroxene rather than from high Zr contents (Dick and Natland, 1996). With the exception of three samples, the clinopyroxenes in most harzburgites from ODP Site 895 are highly depleted in Zr and Ti (Fig. 3.7). The three clinopyroxenes with higher concentrations of Zr and Ti analysed in this study plot at the depleted end of the global melting trend (Fig. 3.7). Like Zr, the LREE concentrations in clinopyroxenes are also close to their detection limits in LA-ICP-MS analysis (Supplementary Table 3.1). Such low LREE concentrations in clinopyroxene have previously been reported for Hess Deep Site 895 harzburgites (Dick and Natland, 1996; Fig. 3.7a and 3.7b). The concentration of Yb in clinopyroxenes in the harzburgites from Hess Deep is higher than the bulk rock (Fig. 3.7c), while that of Ce and Nd are similar to bulk rock (Fig. 3.7a and 3.7b). The higher LREE abundances in the bulk-rocks than clinopyroxene (Fig. 3.7) indicate that the clinopyroxenes are not in equilibrium with the bulk-rock and that there must be another repository for LREEs in these samples.

3.4.4. Alteration in Hess Deep harzburgites

Alteration minerals in Hess Deep ODP Site 895 harzburgites were identified based on microscopic observations followed by electron probe analyses. Alteration in each major mineral phase (i.e. olivine, orthopyroxene and clinopyroxene) was analysed by electron microprobe and the results are reported in Supplementary Table 3.1. The analyses show that the altered phases have oxide weight percent totals ranging from 82 to 88%, which suggests the presence of water in the mineral structure such as in serpentine and clay minerals.

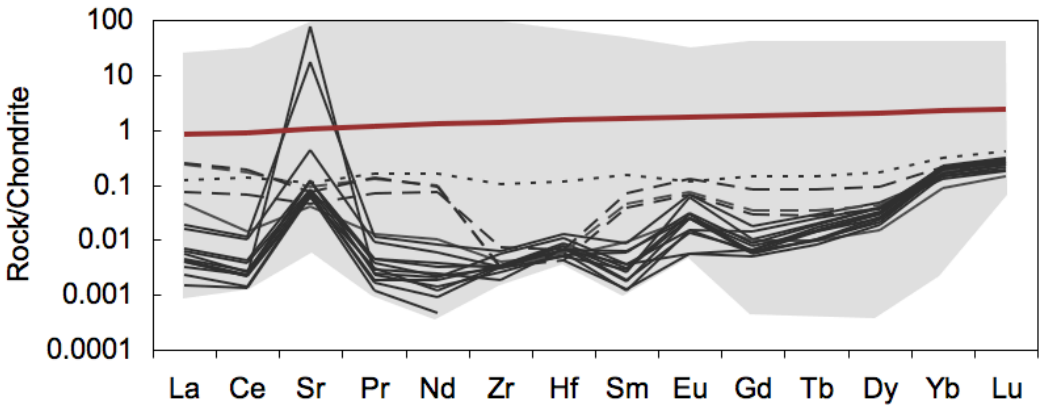

Figure 3.5 Chondrite-normalised bulk rock REE and trace element pattern for Hess Deep peridotites illustrated along with DMM composition (Workman and Hart, 2005). The grey shaded area represents the composition of the global sample suite. The sources for the global dataset are: Garrett Transform: Niu and Hekinian (1997); MAR: Casey et al. (1997); Brandon et al. (2000); Aumento and Loubat (1971); Paulick et al. (2006); Godard et al. (2008). Hess Deep peridotites, along with having more depleted REE concentrations than the global suite, display a weakly U-shaped pattern. Prominent positive Sr- and Eu-anomalies are observable in the Hess Deep peridotites. High field strength elements Zr and Hf variably display positive, negative or flat pattern relative to Nd and Sm for each Hess Deep sample. Three of the samples shown as dashed black lines have prominent Zr-Hf anomalies while the rest of the elements display nearly flat trace element pattern. One sample shown as a dotted line has the highest concentrations most elements compared to the rest of the suite and is characterised by a flat trace element pattern.

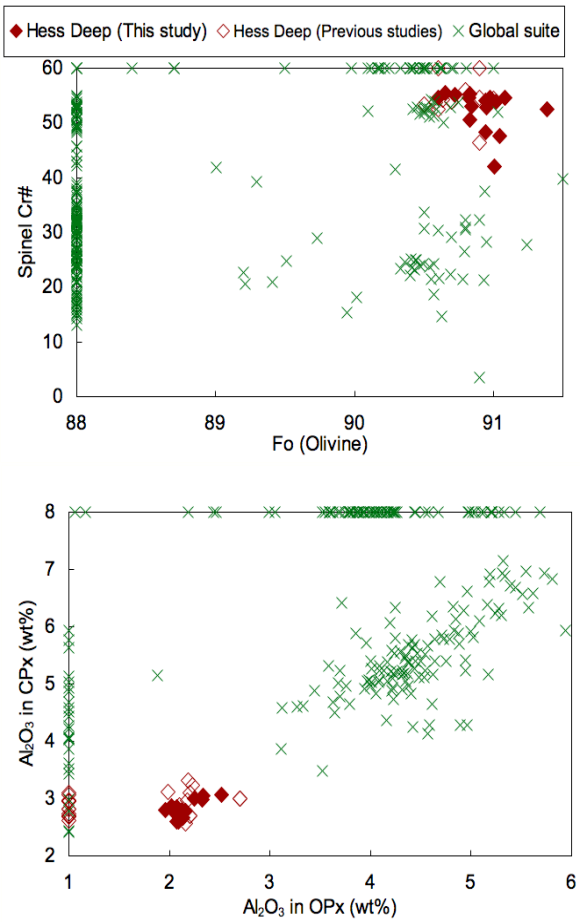

Figure 3.6 Average mineral compositions of individual samples from Hess Deep (ODP) Site 895 harzburgites analysed in this study (filled red diamonds) and the global abyssal peridotite suite (green crosses) illustrated by (a) high Fo (Ol) and high spinel Cr# and (b) low Al_2O_3 in orthopyroxene and clinopyroxene. Hess Deep (previous studies; open red diamonds) samples refer to harzburgites from Hess Deep ODP Site 895 analysed previously by Dick and Natland (1996), Arai and Matsukage (1998) and Edwards and Malpas (1996). The global array represents analyses from previous studies on the SWIR and American Antarctic Ridge (Snow and Dick, 1995), MAR (Juteau, et al., 1990; Komor et al., 1990; Ross and Elthon, 1997; Brunelli et al., 2006), the American Antarctic Ridge (Dick, 1989) and the SWIR (Hamlyn and Bonatti, 1980). In part (a), the data plotted along the X-axis is the set of samples where Fo (Ol) data are missing and data along the Y-axis is the data for which spinel Cr# data are missing. In part (b), the data plotted along the X-axis is the data for which Al_2O_3 in orthopyroxene data are missing while data plotted along the Y-axis is the data for which Al_2O_3 in clinopyroxene data are missing.

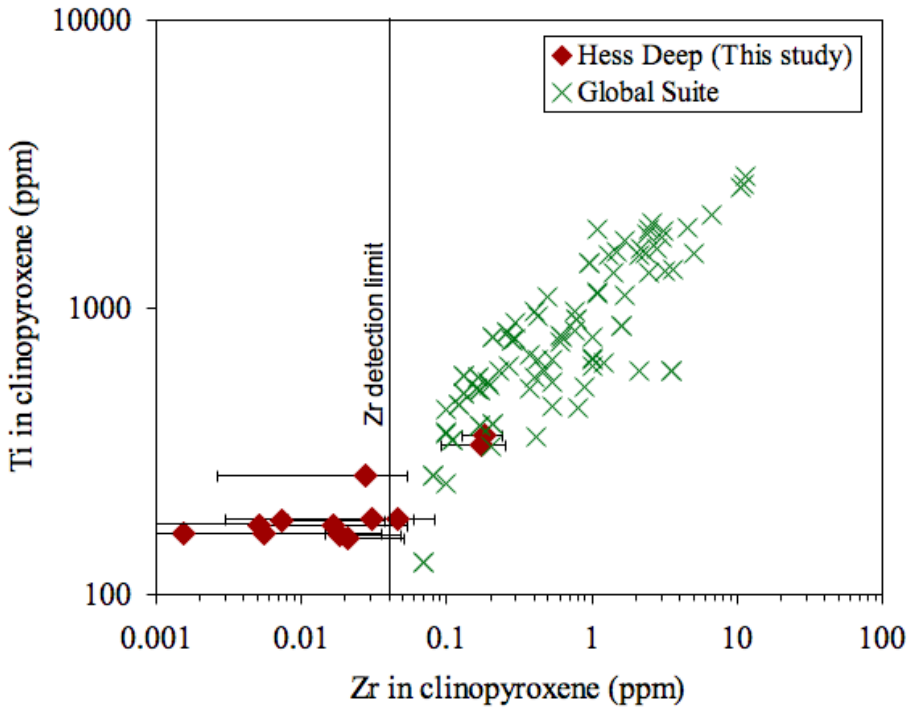

Figure 3.7. Zr and Ti concentrations in clinopyroxenes from Hess Deep harzburgite analysed in this study along with the global array defining the melting trend as in Johnson et al. (1990). Data sources for the global dataset include: Dick (1984; 1989); Johnson et al. (1990); Johnson and Dick (1992); Hellebrand et al. (2002). It is observed that all except three clinopyroxenes from Hess Deep harzburgites are highly depleted to the point of Zr being below the detection limit. The Zr-depleted clinopyroxenes plot at the depleted end of the global spectrum. Error bars represent 1σ on clinopyroxene Zr analyses used to calculate averages for individual samples; since most of the Zr-concentrations are below the detection limit, the error bars are meaningless.

Initial identification of altered minerals was done by comparing analysed compositions of minerals in harzburgites, expressed as cation proportions calculated to 28 oxygens, with the results of Alt and Bach (2001). The low-Fe/(Fe+Mg) minerals correspond to serpentine analyses and the Type A alteration of Nozaka et al. (2008), which is described as a mixture of serpentine, talc and a fine-grained mixture of clay minerals. The mixture of altered minerals was not discernible under the microscope and was too

fineto be separated on the electron probe. Since Ca+Na+K and Fe/(Fe+Mg) are both similar to serpentine and Si and Si/(Si+Al) are both similar to talc and clay minerals, the altered material analysed here is likely to be a combination of serpentine and chlorite/smectite mixtures. In Ca+Na+K versus Si/(Si+Al) space, most alteration products are similar to the compositions of chlorite/smectite mixtures but with lower Ca+Na+K for a given Si/(Si+Al) compared to the results of Alt and Bach (2001; Fig. 3.8). Also, in Fe/(Fe+Mg) versus Si space, the Hess Deep harzburgites from this study have lower Fe/(Fe+Mg) for a given Si (Fig. 3.8a) than the chlorite/smectite analyses of Alt and Bach (2001). The high Ca+Na+K mineral is identified as tremolite both from microscopic as well as electron probe analyses. Serpentine forms as an alteration product of orthopyroxene in addition to olivine while the mixtures of clay minerals and serpentine form as alteration products of pyroxenes.

3.5. Discussion

3.5.1. Depletion in Hess Deep Site 895 harzburgites

Melting of primitive mantle compositions leads to a characteristic depletion trend that can be represented by a so-called 'terrestrial array' in MgO/SiO_2 versus Al_2O_3/SiO_2 space (Jagoutz et al., 1979). In this array, low Al_2O_3/SiO_2 and high MgO/SiO_2 values are characteristic of residues of large extents of melt extraction. Hess Deep harzburgites from this study fall near the depleted end of this terrestrial array (Fig. 3.9), as do the Hess Deep samples from previous studies (Gillis et al., 1993; Blum, 1990). Some samples from the Garrett Transform have similar Al_2O_3/SiO_2 ratios as Hess Deep harzburgites (Fig. 3.9), but have lower MgO/SiO_2 ratios, which has been interpreted as being due to seafloor alteration (Niu and Hekinian, 1997). Peridotites from the Garrett Transform are seafloor samples and

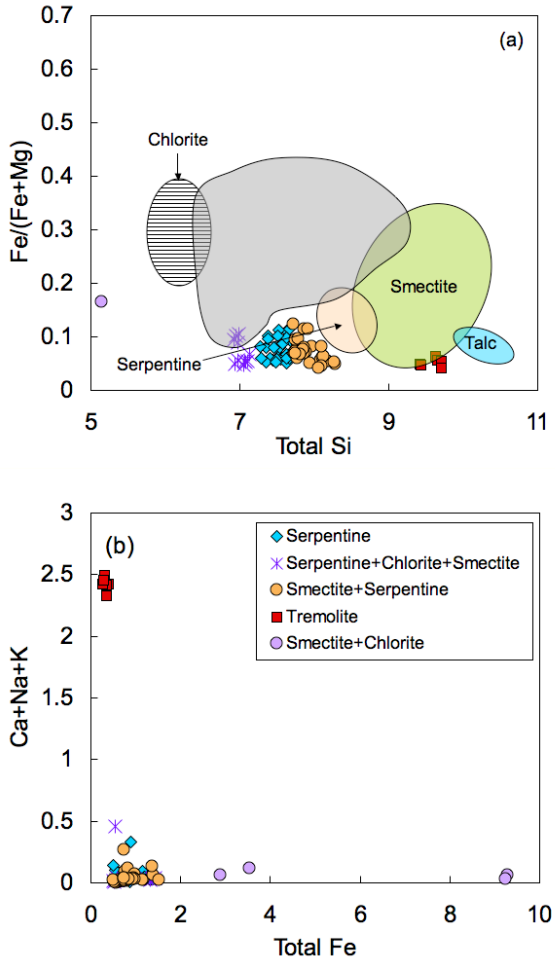

Figure 3.8 Compositions of altered minerals in Hess Deep ODP Site 895 harzburgites calculated as cations per 28 oxygens. The majority of alteration phases analysed are Serpentines or serpentine+smectite mixes. A few samples have slightly higher lower Si (which correspond to higher Al than the remaining samples) and are classified as serpentine+chlorite+smectite mixes. The high-Si and high-Ca+Na+K samples are identified as tremolite is visible as discernable crystals in thin sections. Fields marked in (a) are from Nozaka et al. (2008).

are different from Hess Deep as alteration by seawater plays a major role in compositional modifications in peridotites from the Garrett Transform. The other sample suite that has similar Al_2O_3/SiO_2 but lower MgO/SiO_2 ratios than Hess Deep Site 895 harzburgites is

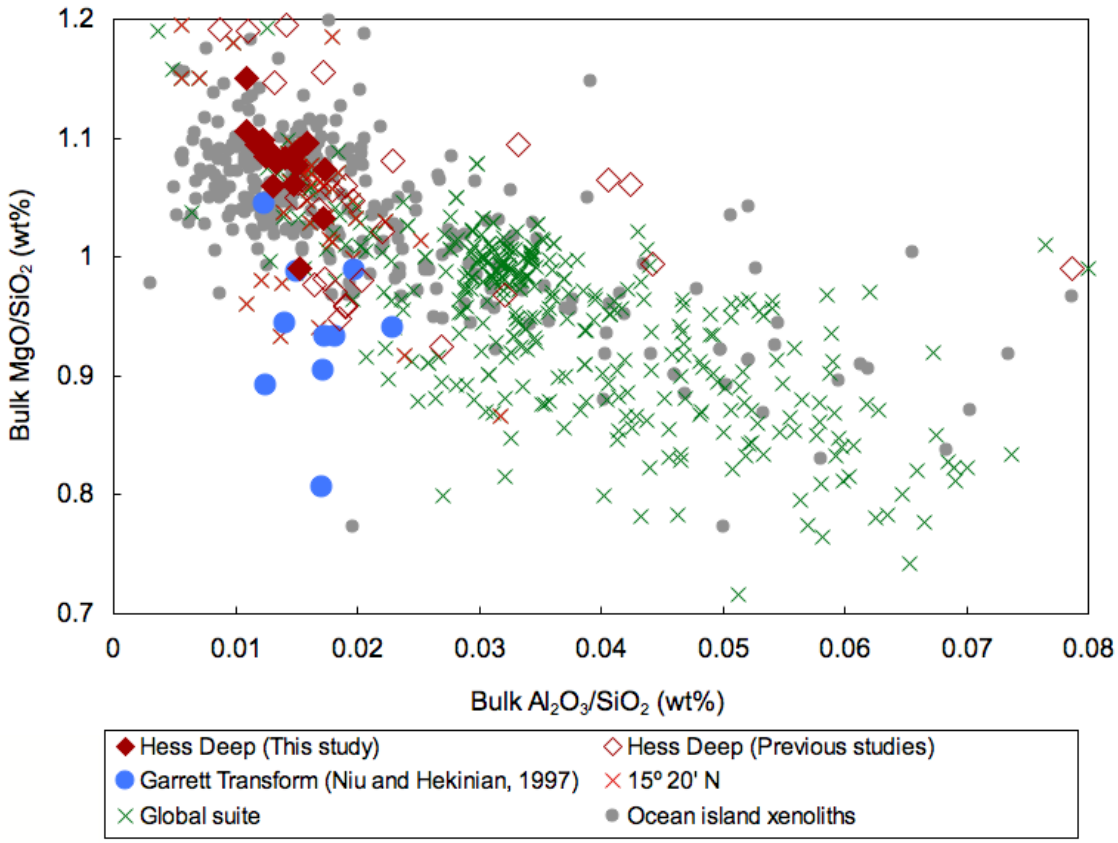

Figure 3.9 Bulk rock variations in MgO and SiO_2 shown in MgO/SiO_2 versus Al_2O_3/SiO_2 space. The global 'terrestrial array' (Jagoutz et al., 1979) is the melting trend defined by the global abyssal peridotite suite shown in the figure. Highest depletions are observed in harzburgites from Hess Deep along with those from 15º 20' N (MAR; Paulick et al., 2006; Godard et al., 2008) and the Garrett Transform (EPR; Niu and Hekinian, 1997). Also shown for comparison are harzburgite and lherzolite samples of ocean island xenoliths, most of which also plot at the depleted end of the global spectrum (data sources for ocean island xenoliths are cited in Fig. 4.4 of Chapter 4).

from 15º 20' N along the MAR (Fig. 3.9), which may be due to addition of silica during alteration to talc (Paulick et al., 2006; Fig. 3.9). Talc is not observed in the Hess Deep thin sections from this study. The sizes of analysed samples may influence the bulk rock geochemistry since alteration runs unevenly through the samples. Unfortunately, the sample sizes of MAR peridotites are not available to compare with the Hess Deep harzburgites from this study.

3.5.2. Light REE and trace element enrichment in Hess Deep harzburgites

In order to establish the melting history of harzburgites from Hess Deep, the whole rock trace element compositions were compared with those of a melting model. The melting model is constructed using equations outlined below with the partition coefficients from Kelemen et al. (2003; Table 3.7a). The DMM composition of Workman and Hart (2005) is used as the starting composition for this model (Fig. 3.10) and an intergranular melt porosity of 0.5% (after Johnson and Dick, 1992) is used to simulate 10, 20 and 25% near-fractional melting (Figure 3.10). The following equations were used to construct the melting models:

Equation for calculating the concentration of an element *i* in the melt for non-modal fractional melting as given by Shaw (1970) is as follows:

$$C^{i}_{Solid} = \frac{C^{i}_{Initial}}{(1-F)} * \left(1 - \frac{P * F}{Kd^{i}}\right)^{(\frac{1}{P}-1)} \qquad \text{(Eq. A1)}$$

C^{i}_{Solid} is the concentration of element *i* in the residual solid.

$C^{i}_{initial}$ is the initial concentration of element *i* (i.e. concentration of *i* in the DMM).

F is the fraction of melt formed.

K_d is the bulk partition coefficient calculated using mineral/melt partition coefficients from Kelemen et al. (2003) and the initial modal proportions.

P is the average of individual partition coefficients weighted according to which minerals enter the melt. Since minerals do not enter the melt phase in the proportion in which they are present in the rock, the parameter P is incorporated in order to acquire realistic values for the concentration of an element in the residue. The following equation is used to calculate P:

$$Pi = \sum p_{\phi} Kd_i^{\phi/l} \qquad \text{(Eq. A2)}$$

where p is the proportion in which phase ϕ (i.e. olivine, orthopyroxene, clinopyroxene and spinel) enters the melt phase. In case of the equation used in the melting models in Chapters 3 and 4, the proportions of mineral phases entering the melt are based on Niu (1997) and are as follows:

Olivine: -9%

Orthopyroxene: 28%

Clinopyroxene: 70%

Spinel: 11%

The parameter $Kd_i^{\phi/l}$ is the mineral/melt partition coefficient for element *i* in the phases olivine, orthopyroxene, clinopyroxene and spinel.

The initial modes used in constructing the melting equations are as follows:

Olivine: 54.5%

Orthopyroxene: 25%

Clinopyroxene: 18%

Spinel: 2%

Melt: 0.5%

(The model parameters such as partition coefficients and melt porosity are varied to test between various models and the results are described below).

Table 3.7a. Mineral/melt partition coefficients (Kd) for trace elements used in construction of melting models for DMM composition (from Kelemen et al., 2003).

Element	Kd Olivine/Melt	Kd Orthopyroxene/Melt	Kd Clinopyroxene/Melt	Kd Spinel/Melt
Ce	0.00001	0.003	0.0858	0.0006
Nd	0.00007	0.009	0.1873	0.0006
Zr	0.004	0.04	0.1234	0.07
Sm	0.0007	0.02	0.291	0.0006
Eu	0.00095	0.03	0.33	0.0006
Ti	0.015	0.14	0.384	0.15
Er	0.009	0.07	0.387	0.003
Yb	0.023	0.1	0.43	0.0045

Table 3.7b. Mineral/melt partition coefficients (Kd) for trace and REEs used in construction of melting models for DMM composition (from Hellebrand et al., 2002).

Element	Kd Olivine/Melt	Kd OPx/Melt	Kd CPx/Melt	Kd CPx/Melt(2) (Blundy et al., 1998)	Kd Spinel/Melt
Ce	0.00001	0.005	0.1	0.16	0.0006
Nd	0.00007	0.01	0.2	0.36	0.0006
Zr	0.004	0.024	0.12	0.27	0.07
Sm	0.001	0.02	0.3	0.67	0.001
Eu	0.001	0.03	0.37	0.8	0.001
Ti	0.015	0.1	0.35	0.71	0.15
Er	0.009	0.07	0.43	1.44	0.003
Yb	0.014	0.09	0.41	1.43	0.005

Abbreviations used: Kd – Partition coefficient; OPx – orthopyroxene, CPx – clinopyroxene.

It is observed that the HREE concentration of the model-melting curve matches that of Hess Deep harzburgites at 25% melting of DMM with a 0.5% melt porosity. Varying the starting composition to depleted or enriched DMM (D-DMM and E-DMM respectively) does not change the resulting melting model significantly (Fig. 3.11). Using DMM as the starting composition, the mineral/melt partition coefficients of Kelemen et al. (2003; Table 3.4a) are substituted by those from Hellebrand et al. (2002; Table 3.7b). With the exception of Zr, no other element shows a major variation in the composition of the residue after 25%

melting of the DMM (Fig. 3.11). The difference in Zr-abundance in the melting residue is due to the different $Kd^{OPx/Melt}$ for Zr as given in Kelemen et al. (2003) and Hellebrand et al. (2002). A major difference in the abundances of LREE and MREE in the DMM-melting residue is observed when the melt porosity is changed from 0.5% to 1% and 2% (Fig. 3.11). However, previous studies have indicated that the melt porosity in mid oceanic ridge environments is of the order of 0.1% (Johnson et al., 1990; Lundstrom et al., 1995; Johnson and Dick, 1992) to 0.5% (e.g. Johnson and Dick, 1992). For the purpose of this study the models will be discussed for a melt porosity of 0.5%. At 25% melting of the DMM, the abundances of Lu and Yb in the model melting residue match the average abundances of the Hess Deep harzburgites, but the abundances of LREE, MREE and Sr are lower in the model melting residue than the observed whole rock abundances of these elements in Hess Deep harzburgites (Fig. 3.10 and Fig. 3.11).

One hypothesis to explain the increased bulk LREE concentrations and the positive Sr and Eu-anomalies in Hess Deep harzburgites is alteration caused by seawater. In a model testing this hypothesis, REE concentrations of seawater (Elderfield and Greaves, 1982) are mixed with the model residue of 25% melting of the DMM using the equation:

$$C_{mix} = (M_{SW} * X_{SW}) + (M_{Rock} * X_{Rock}) \qquad \text{(Eq. 3.2)}$$

where C_{mix} = composition of residue after mixing, M_{SW} and $M_{Rock}(=1)$ are the masses of seawater from which the REE's are removed and rock respectively while X_{SW} and X_{Rock} represent concentrations of elements in seawater and rock respectively. Assuming 100% of the REEs are removed from seawater into the rock, extremely high water/rock mass ratios of the order of 10^9 to 10^{10} are required to match the LREE concentrations of the model residue of melting of DMM with the observed lowest LREE

concentration of Hess Deep harzburgites (Fig. 3.12a). Since the heat required for fluid flow is not sufficient for such extreme water/rock mass ratios, it is unlikely that seawater alteration can result in the observed LREE and MREE concentrations in the Hess Deep harzburgites.

A second hypothesis is the contribution of hydrothermal fluids in adding LREE and MREE to the residual harzburgites from ODP Site 895. The REE composition of seawater in Eq. 3.2 is replaced by the average REE composition of hydrothermal fluids from the EPR region (Klinkhammer et al., 1994; Table 3.8). It is observed that mixing of the average hydrothermal fluid REE composition with the model DMM-melting residue (0.5% porosity) in a 1:1 proportion reproduces the observed abundances of REEs in the harzburgites from ODP Site 895 (Fig. 3.12b). Moreover, the positive Eu-anomaly is also reproduced in the resulting model (Fig. 3.12b). The increased LREE abundances relative to HREEs in ODP Site 895 harzburgites by hydrothermal alteration may thus be a plausible hypothesis. One of the tests for this hypothesis is a correlation between elements such as Li, B and Cu, which are known to be mobile during hydrothermal processes (e.g. Humphris and Thompson, 1978). However, it is observed that Ce does not show any correlation with Li, B and Cu (Fig. 3.13) and hence hydrothermal fluids are not a convincing source of LREE enrichment in the harzburgites.

Table 3.8. Average REE concentrations in hydrothermal fluids from the EPR (Klinkhammer et al., 1994).

Element	La	Ce	Pr	Nd	Sm	Eu	Gd	Tb	Dy	Ho
Average concentration in EPR hydrothermal fluid (ppm)	0.0003	0.0005	0.0007	0.0003	0.000068	0.0003	0.00006	0.000009	0.00004	0.000007

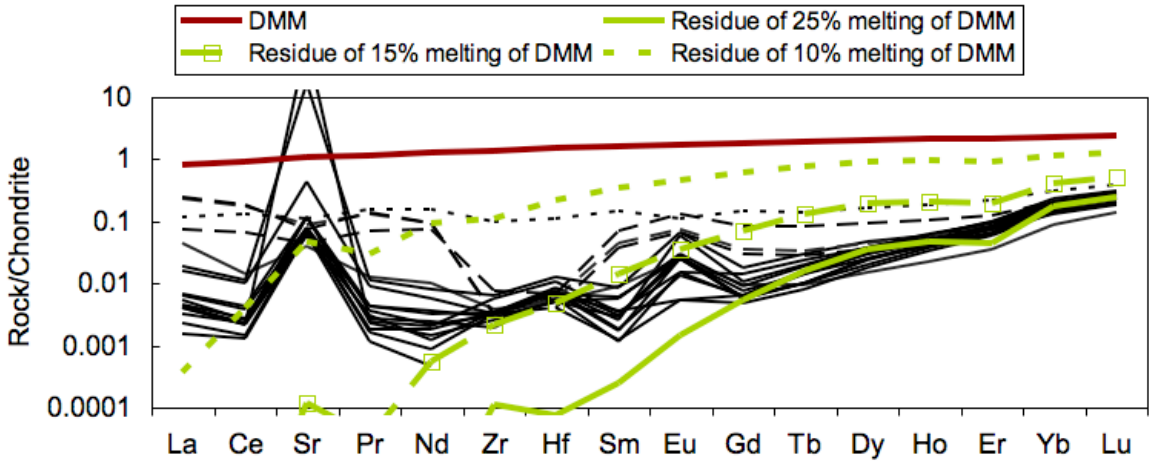

Figure 3.10. A comparison between observed chondrite-normalised bulk rock trace element concentrations with the model residue of 10, 15 and 25% melting of a DMM source composition (Workman and Hart, 2004). It is observed that the bulk rock trace element pattern is not what can be expected for melting of a DMM source composition, as the LREE and Sr concentrations are much lower in the model residue.

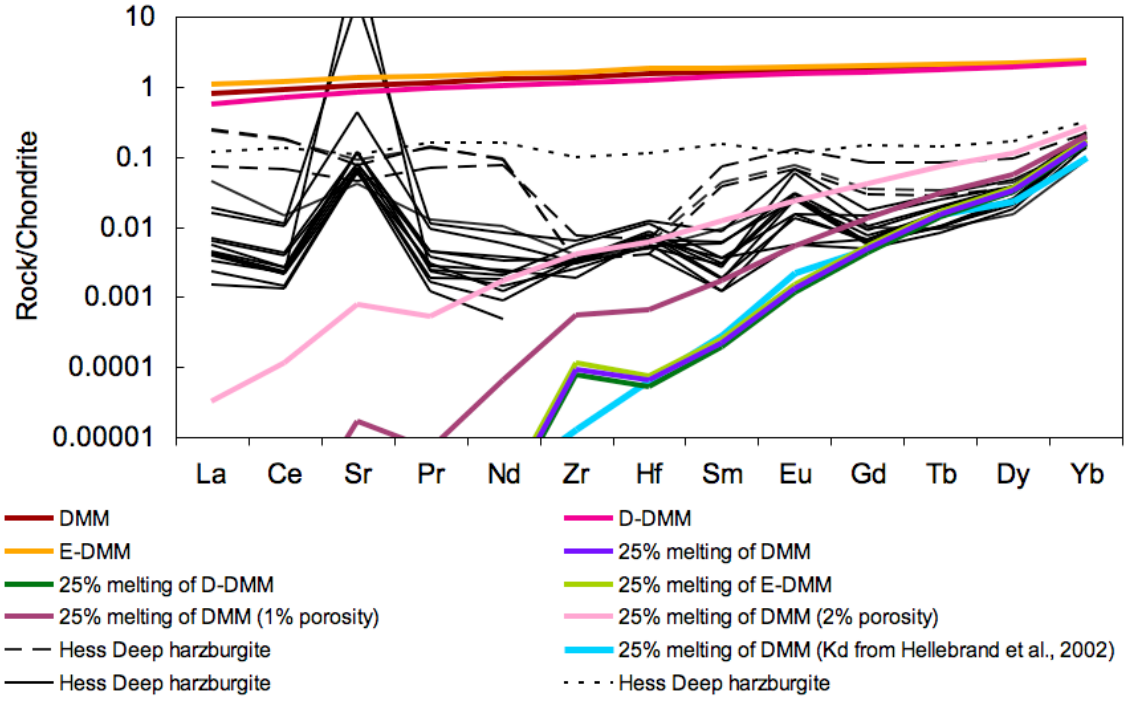

Figure 3.11. A comparison between observed chondrite-normalised bulk rock trace element concentrations with the model residue 25% melting of DMM, E-DMM and D-DMM source compositions source composition (Workman and Hart, 2004). The partition coefficients used in the construction of the melting are from Kelemen et al. (2003). Since the starting compositions have similar abundances of REEs, the resulting melting models do not differ from one another. A variation of the DMM-melting model is shown by replacing the partition coefficients of Kelemen et al. (2003) by those from Hellebrand et al., (2002). With the exception of Zr, no differences are observed between the models after 25% melting of DMM. The difference in Zr-abundances between melting models of varying partition coefficients is due the higher value of partition coefficient of Zr in orthopyroxene in Hellebrand et al., (2002) compared to Kelemen et al., (2003). Also shown are variations of 25% melting of DMM are 0.5, 1 and 2% porosities.

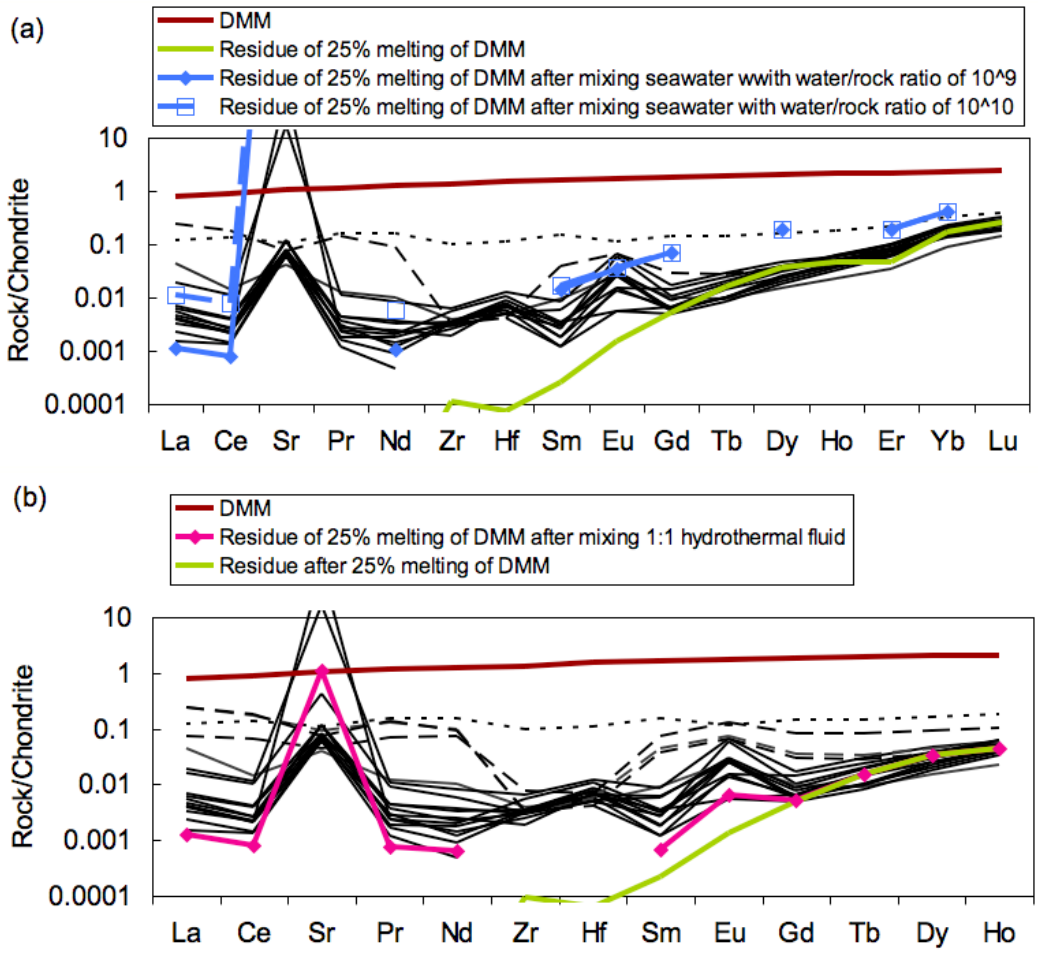

Figure 3.12. (a) Composition of the residue of 25% melting of DMM after mixing REE concentrations measured for seawater (Elderfield and Greaves, 1982) to the residue. It is observed that extremely high water/rock ratios (10^9 to 10^{10}) are required to generate the observed LREE pattern for geochemical modification just by seawater alteration. (b) Composition of the residue of 25% melting after mixing the average REE concentrations of hydrothermal fluids from the EPR (Table 3.8; Klinkhammer et al., 1994) in a 1:1 proportion.

It has been suggested that the hypothesis for magmatic processes increasing the LREE abundances in abyssal peridotites is supported by the positive correlation between LREEs and elements such as Zr and Hf, which are not mobile during hydrothermal processes (Niu, 2004). In the case of ODP Site 895 harzburgites, there is no correlation between Zr or Hf with LREEs (Fig. 3.14). A source other than seawater and hydrothermal

fluids for LREE enrichment in ODP Site 895 harzburgites is magmatic. Our final hypothesis to explain the elevated bulk rock concentrations of LREE and MREE, the positive Sr and Eu anomalies and the negative Zr and Hf anomalies is the precipitation of plagioclase in the rocks. This hypothesis is based on the partition coefficients for LREE in plagioclase being similar to those for clinopyroxene but the partition coefficients for Zr and Hf are very small (e.g. Bindeman et al., 1998).

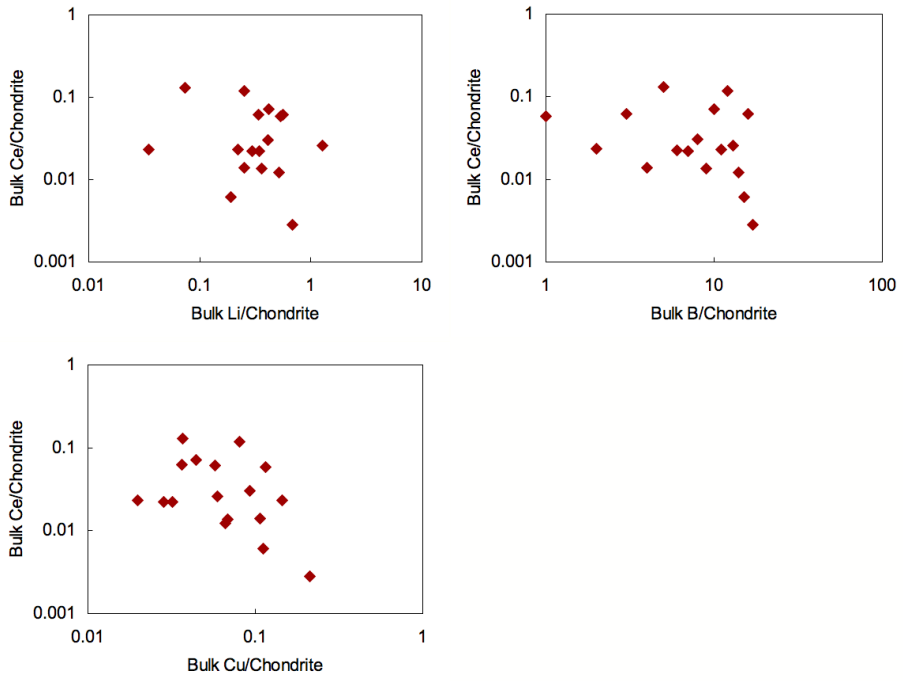

Figure 3.13. Bulk rock Ce concentrations of Hess Deep peridotites normalised to chondritic values (McDonough and Sun, 1995) plotted against chondrite-normalised bulk rock (a) Li, (b) B and (c) Cu concentrations. No correlation is observed in either case.

Additionally, Eu preferentially partitions into plagioclase (e.g. Blundy and Wood, 2003) and precipitation of plagioclase will lead to positive Eu anomaly.

To test the hypothesis for plagioclase precipitation as a mechanism for higher REEs than the melting model, a plagioclase-mixing model similar to the seawater-mixing model

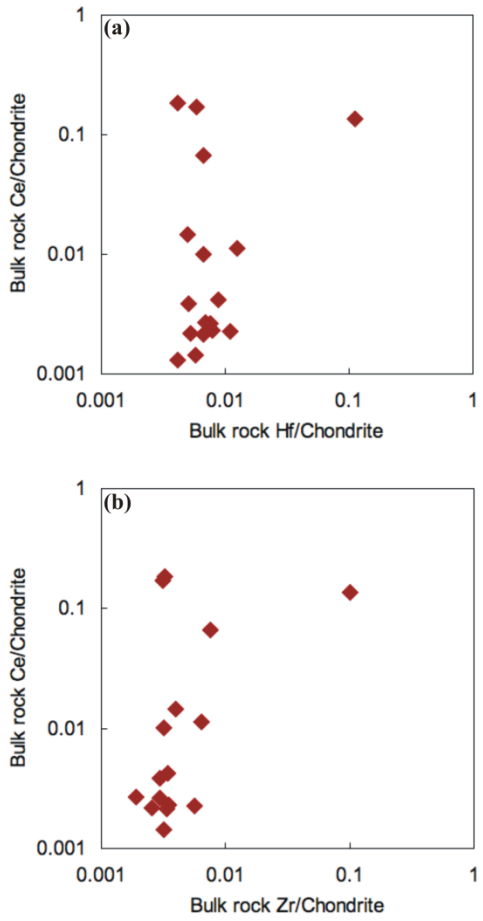

Figure 3.14. Bulk rock Ce concentrations of Hess Deep peridotites normalised to chondritic values (McDonough and Sun, 1995) plotted against chondrite-normalised bulk rock (a) Hf and (b) Zr concentrations. No correlation is observed in either case.

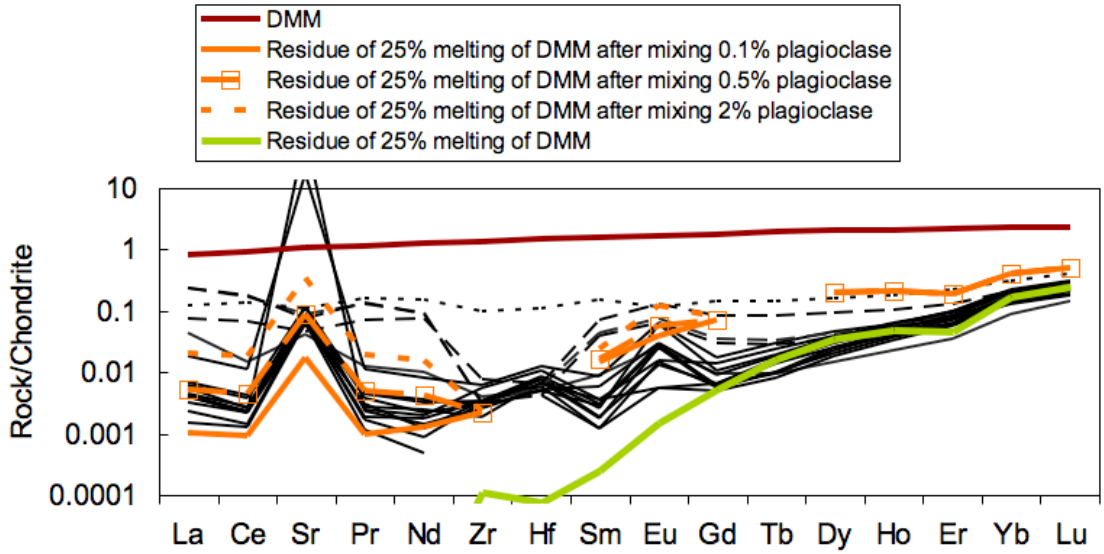

Figure 3.15. Composition of the residue of 25% melting of DMM after mixing 0.1, 0.5 and 2% plagioclase to the residue. The plagioclase composition used is that of a gabbro from the Hess Deep region (Lissenberg et al., 2013), which was selected so it resembles melts that form the MORB in the Hess Deep region. It is observed that mixing 2% plagioclase to the residue of 25% melting of DMM is sufficient to reproduce the highest LREE, MREE and Sr abundances observed in most harzburgites from Hess Deep. Notable exceptions are the samples that are enriched in LREE compared to DMM (dotted and dashed black lines). Concentrations for Tb, Zr and Hf are not reported for plagioclase and hence these elements are not modeled.

described above is developed. The concentration of the most REE depleted plagioclase crystal from the overlying lower crustal gabbroic rocks from Hess Deep (Lissenberg et al., 2013) was mixed with the model concentrations of the residue of 25% melting of the DMM. This plagioclase composition was selected so that it resembles the plagioclase likely to precipitate from a Hess Deep parental MORB. Mixing of only 0.1% plagioclase is sufficient to generate approximately the observed minimum enrichment of LREE over a model DMM melting residue (Fig. 3.15). Moreover, the observed Eu-anomaly is also reproduced in the plagioclase mixing model (Fig. 3.15). Adding 0.5% plagioclase to the residue of 25% melting of the DMM reproduces approximately the average LREE

abundances in the Hess Deep harzburgites (Fig. 3.15). The addition of 2% plagioclase to the DMM melting residue generates the moderately high LREE and MREE concentrations observed in Hess Deep harzburgites (Fig. 3.15). At only 0.5% plagioclase mixing, the positive Eu anomalies also resemble those in Hess Deep harzburgites. The lack of correlation between LREE concentrations with Hf (Fig. 3.14a) and Zr (Fig. 3.14b) is also consistent with the model of plagioclase precipitation, since Hf and Zr are incompatible in plagioclase. With the exception of two samples that have higher Sr-concentration (122 and 540 ppm; Supplementary Table 3.1), the positive Sr-anomaly observed in bulk rocks is also reproduced in the plagioclase mixing model (Fig. 3.15).

Previous studies have interpreted the association of gabbroic rocks with the Hess Deep harzburgites as a progressive melt-peridotite reaction where orthopyroxene in refractory harzburgites was dissolved to form olivine + spinel and clinopyroxene ± plagioclase (Edwards and Malpas, 1996). However, a problem with the plagioclase-mixing hypothesis is that no plagioclase is observed in any thin section that was analysed in this study. The possibility that all plagioclase formed by melt-rock reaction may have been completely altered was tested by analysing altered mineral phases in the thin sections. As described in Section 3.4.4, this was investigated by analysing only the alteration observed around spinel crystals since the formation of plagioclase is likely to be in the vicinity of aluminous phases such as spinel in harzburgites. The alteration phase highest in aluminium (~10 wt%) is identified as a chlorite/smectite mixture, which is likely to form as a result of alteration of orthopyroxene and/or clinopyroxene. The phase most likely to be the product of plagioclase alteration is chlorite, but only trace amounts of chlorite could be identified as mixed with serpentine and smectite. Since only trace amounts (0.5%) of plagioclase are required to bring the LREE abundances in the model DMM melting residue to match the

average LREE in ODP Site 895 harzburgites, it is possible that small amounts of plagioclase were present in the harzburgites and were completely altered to chlorite-smectite mixtures. The crystallisation of plagioclase from percolating melts is thus a possible explanation for the higher LREE and MREE abundances relative to the DMM-melting model. However, the geochemical characteristics of residual mineral phases in the ODP Site 895 harzburgites analysed in this study show no indication of the presence of plagioclase in their vicinity. For example, the spinels in the harzburgites are homogeneous on the scale of a thin section and are characterised by low-TiO_2, indicating that reactive melt transport could not have crystallised plagioclase. Evidence for the presence of plagioclase exists in the form of plagioclase-bearing dunites and harzburgites that were also recovered at ODP Site 895 (Gillis, Mevel et al., 1993; Dick and Natland, 1996).

The plagioclase precipitation model does explain LREE and MREE enrichment in most harzburgites from this study (Fig. 3.15), but four samples have higher LREE and MREE than can be explained by trace amounts of plagioclase (dashed lines in Figs. 3.10, 3.11, 3.12 and 3.15). The four harzburgites with higher LREE than the rest of the harzburgites are the ones that contain clinopyroxene with similar or slightly higher abundances of these elements than the bulk rock (Fig. 3.16a and 3.16b). A hypothesis that can explain the increased bulk rock LREE and MREE concentrations in Hess Deep Site 895 harzburgites is the metasomatic enrichment of clinopyroxene grain boundaries. Hence, the highest LREE concentrations recorded in the Hess Deep Site 895 harzburgites from this study are likely to represent samples that are enriched by processes not related to plagioclase precipitation. It has been previously observed that multiple thin sections from the same rock sample show different degrees of LREE enrichment in clinopyroxene thus indicating extremely localised enrichment (Ross et al., 2005). The evidence for melt-rock

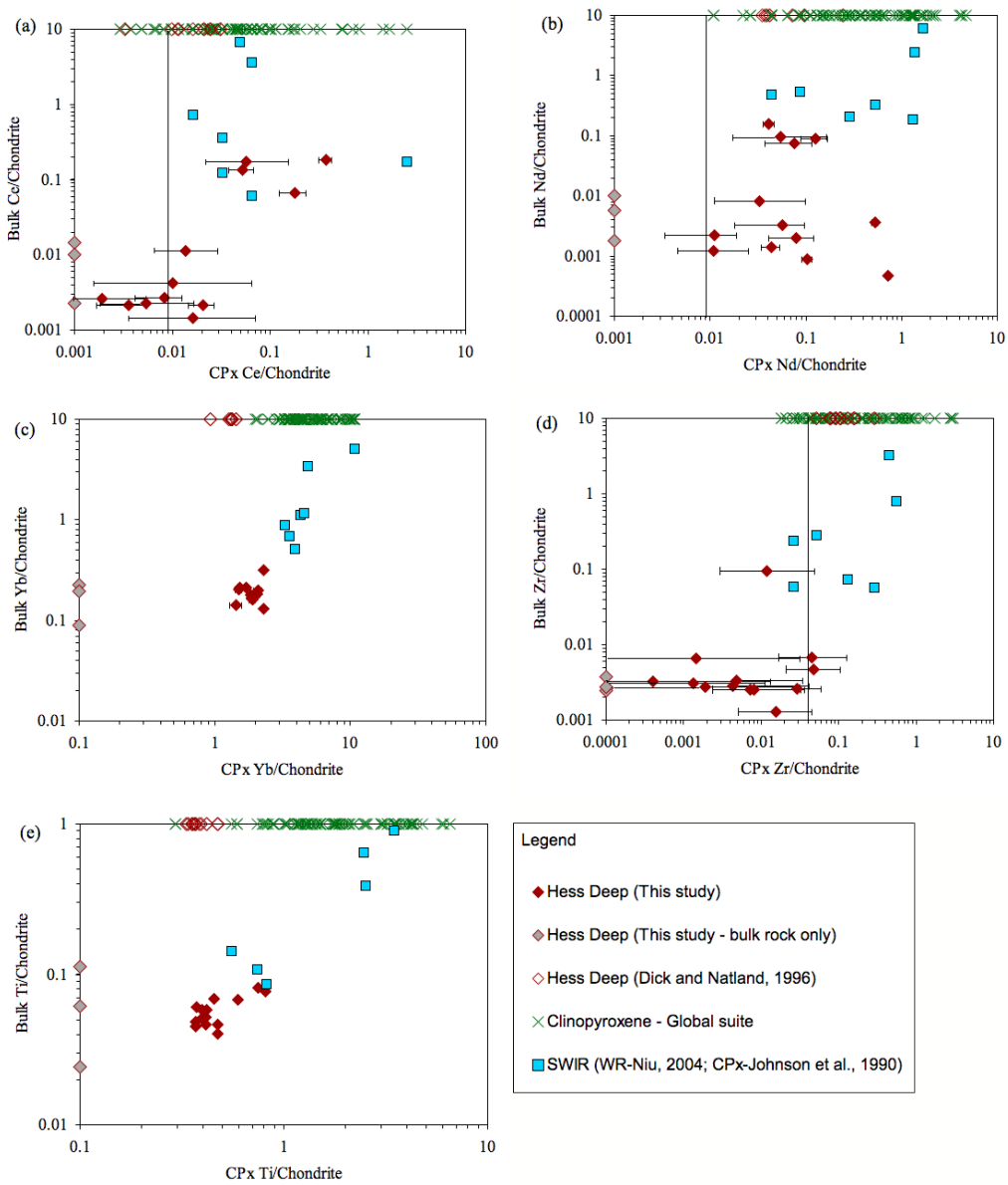

Figure 3.16. (Figure Caption on following page)

Figure 3.16 Chondrite-normalised abundances of (a) Ce, (b) Nd, (c) Ti and (d) Zr in clinopyroxene from Hess Deep (ODP) Site 895 harzburgites plotted against bulk rock abundances for the same group of samples. For samples in which clinopyroxenes were absent or could not be analysed, only bulk rock compositions are plotted. Also shown for comparison are clinopyroxene compositions for Hess Deep harzburgites analysed by Dick and Natland (1996) and clinopyroxenes from the global suite. Clinopyroxenes from the global suite generally have higher concentrations of Nd, Ti and Zr compared to the Hess Deep clinopyroxenes. Compared to bulk rock compositions, the clinopyroxenes in Hess Deep harzburgites have similar or lower abundances of Ce, Nd and Zr and higher concentration of Ti. Error bars on clinopyroxene compositions are 1σ on multiple analyses of the same clinopyroxene crystal or multiple crystals from the same sample. High uncertainties on clinopyroxene data indicate highly depleted concentrations of Ce, Nd and Zr in clinopyroxene. Data plotted along the X-axes is data with no clinopyroxene analysis while data plotted along the Y-axis is data with no bulk rock analysis. Sources for clinopyroxene data in the global dataset are as in Fig. 3.7.

reaction is seen in ODP Site 895 harzburgites as elevated LREE in both, bulk rock and clinopyroxene. The residence of Ce along crystal borders is highly probable and crystallisation of trace amounts of plagioclase is not the only mechanism for high LREEs in the bulk rock.

In summary, plagioclase precipitation is not the only mechanism for bulk rock LREE enrichment in ODP Site 895 harzburgites as suggested by the presence of high-LREE in clinopyroxenes from four samples relative to clinopyroxenes from the remaining harzburgites (Fig. 3.16a and 3.16b). While some evidence for the presence of trace amounts of plagioclase exists in altered mineral phases as chlorite/smectite mixtures, the major mineral phases do not show any evidence for plagioclase precipitation from melt-rock reaction. It is still possible that plagioclase crystallised from cooling of melts percolating along grain boundaries since plagioclase bearing dunites and harzburgites have been

reported in the Hess Deep region (Gillis, Mevel et al., 1993; Dick and Natland, 1996). Melt-rock reaction is likely to have occurred in the form of diffusive LREE enrichment of clinopyroxene borders but the small size of clinopyroxenes in the samples makes it difficult to detect increased concentrations of LREE along the rims. Melt-rock reactions and melt trapping may both be significant processes that led to enrichments in LREE and MREE in the Hess Deep harzburgites.

3.5.3. Model history of Hess Deep harzburgites

At slow-spreading ridges, mantle melts ascending through the oceanic lithospheric mantle react with residual rocks, thereby causing post-melting refertilisation and the precipitation of plagioclase and olivine (e.g. Niu, 2004). The region around Hess Deep formed towards the end of the fast-spreading Galapagos Ridge segment where cooler temperatures are expected relative to the segment center. Melts ascending by intergranular or porous flow can react with the residual rocks and can precipitate plagioclase ± olivine at lower pressures (Dick and Natland, 1996). It has been suggested that in regions of focussed flow in the Hess Deep region, the crystallisation of plagioclase proceeded up to the point of formation of plagioclase dunites, troctolites and gabbros, which are associated with drilled harzburgite samples from ODP Site 895 (Gillis, Mevel et al., 1993; Dick and Natland, 1996; Arai and Matsukage, 1996, 1998). One harzburgitic sample found in contact with a gabbroic segregation has been attributed to melt/rock reaction during transport in the shallower, cooler regions of the oceanic lithospheric mantle (Dick and Natland, 1996). In this study, evidence for the presence of plagioclase in harzburgites from ODP Site 895 is observed in the form of higher bulk rock LREE and MREE relative to the DMM melting model along with positive Eu- and Sr-anomalies in the trace element pattern (Fig. 3.15). Based on the mixing models discussed above, only a trace amount of plagioclase is

sufficient to reproduce the observed LREE and MREE abundances in the ODP Site 895 harzburgites (Fig. 3.15). Since some harzburgites from this study have higher LREE abundances than can be explained by mixing trace amounts of plagioclase, it is hypothesised that melt-rock reaction causes diffusive transfer of LREEs into clinopyroxene crystal borders. Low temperatures in the oceanic lithospheric mantle reduce the extent of reaction between ascending melts and clinopyroxenes (Niu, 2004), which results in clinopyroxene cores retaining depleted compositions. The melts thus end up reacting with crystal borders and precipitating olivine and plagioclase in the residual rocks.

Primitive orthopyroxene is identified in crustal gabbros that were drilled along with harzburgites from ODP Site 895 (e.g. Gillis et al., 2014). The melts from which this orthopyroxene crystallised are hypothesised to have formed by dissolution of orthopyroxene during melt extraction by diffuse porous flow through the upper mantle (Coogan et al., 2002; Gillis et al., 2014) and is evidence for melt-rock reaction in the Hess Deep region. Melt-rock reaction does not affect mineral geochemistry as inferred from low LREE in most clinopyroxenes (Fig. 3.16). Since clinopyroxenes exhibit highly refractory compositions (Fig. 3.16), the processes that affect the bulk rock chemistry have not affected the cores of clinopyroxenes as also suggested for peridotites from the SWIR and AAR by Niu (2004).

3.6. Summary and Conclusions

The aim of this study was to test the hypothesis that abyssal peridotites interact with melts that are being extracted at the top of the melting column by porous flow. A suite of rocks from Hess Deep were analysed for major and trace elements in the major mineral phases and in the bulk rock. The ODP Site 895 harzburgites analysed in this study are

medium to coarse-grained protogranular harzburgites consisting of olivine, orthopyroxene, clinopyroxene and spinel as major mineral phases. Mineral and bulk rock analyses of these harzburgites reveal that they are depleted in moderately incompatible elements Al_2O_3, CaO, V and Sc. A comparison between the HREE abundances in ODP Site 895 harzburgites and those of a model DMM-melting residue reveals that the harzburgites have undergone up to 25% melting assuming 0.5% melt porosity (Fig. 3.10). In contrast to HREEs, the abundances of LREE and MREE are higher than those of the model DMM-melting residue. Moreover, a positive Eu-anomaly is observed in the trace element pattern (Figs. 3.5 and 3.10, 3.11, 3.12 and 3.15). This increase in LREE and MREE in the Hess Deep harzburgites is interpreted as being due to the precipitation of plagioclase from the melts being extracted by diffuse porous flow through the upper mantle. The effect of plagioclase precipitation and addition of LREE to the bulk rock does not affect the chemistry of residual mineral phases as evidenced from the depleted LREE abundances in clinopyroxene relative to the bulk rock (Fig. 3.16). This is interpreted to record pervasive diffuse porous flow through a cool thermal boundary layer as suggested by Niu (1997; 2004).

Although the elevation in bulk rock trace element abundances in ODP Site 895 harzburgites is interpreted as being due to plagioclase precipitation from a melt migrating through the rocks on a grain scale, the mineral chemistry of residual phases in most samples does not appear to have been modified by this; instead they are highly depleted. For example, the clinopyroxene compositions in harzburgites from ODP Site 895 have extremely low LREE contents in most samples (Fig. 3.16a and 3.16b). Since the partition coefficients of LREEs are higher in clinopyroxene than any other phase in residual mantle peridotites, the abundances of these elements in samples with elevated bulk LREE

abundances are expected to be higher in clinopyroxene than in the bulk rock. However, it is observed that the abundances of incompatible elements in clinopyroxene are lower than or close to the bulk rock abundances of these elements. Harzburgites from Hess Deep have undergone up to 25% melting. In the models described in this study, the addition of trace amounts of plagioclase to a model DMM residue of up to 25% melting reproduces the trace element pattern observed in the LREE-enriched and Zr-Hf-depleted harzburgites (Fig. 3.15). The elevated LREE, MREE and positive Eu anomaly are interpreted as being due to the crystallisation of plagioclase from melts percolating along grain boundaries within the upper mantle at Hess Deep. Mixing of 0.5% plagioclase (Lissenberg et al., 2013) with the composition of a model DMM-melting residue (DMM from Workman and Hart, 2004) is sufficient to match the LREE and MREE abundances with the observed abundances in the harzburgites analysed in this study (Fig. 3.15). Moreover, the observed positive Eu anomaly is also reproduced in the mixing model (Fig. 3.15). It has been hypothesised that reaction between harzburgitic residues and melts in the oceanic lithospheric mantle resulted in the precipitation of high-Ca plagioclase and clinopyroxene, thus giving rise to gabbroic segregations (Dick and Natland, 1996).

In the case of harzburgites from ODP Site 895, the effects of melt-rock interaction do not extend into residual mineral geochemistry as inferred from the low LREE in most clinopyroxenes from these rocks (Fig. 3.16). It is also possible that melts percolating through mineral grain boundaries only affect the rims of clinopyroxene crystals (Niu, 2004). This suggests that a significant amount of melt extraction from the mantle occurs by porous flow and that the melts maintain disequilibrium with the residual rocks due to conductive cooling of the oceanic lithospheric mantle, as previously suggested by Niu (2004) for slow-spreading ridges.

Although the above discussion suggests trace element disequilibrium between MORB and residual phases in mantle peridotites, melts transported by diffuse porous flow would be forced towards saturation in the phases found in the upper mantle; i.e. they would move to, or close to, orthopyroxene saturation. This is consistent with the hypothesis that the orthopyroxene-bearing gabbroic rocks from the lower crust at Hess Deep are indicative of melts being forced towards orthopyroxene saturation during transport through the upper mantle (Coogan et al., 2002; Gillis et al., 2014).

4. Melt-rock reaction and compositional heterogeneity in the residual oceanic lithospheric mantle: insights from ocean island xenoliths

4.1. Introduction

As discussed in Chapter 1, the oceanic lithosphere begins to form at mid-oceanic ridges where new oceanic crust is generated by partial melting of the mantle. In the simplest model of passive upwelling and a dry mantle source, melting begins at the solidus and progresses toward the top of the melting column (Figs. 1.3 and 4.1; Langmuir et al., 1992) leaving a residue with lower abundances of highly incompatible elements at the top compared to the bottom of the melting column (Figs. 1.3 and 4.1). Over time, the older, solid residual lithosphere moves away from the ridge axis to finally subduct at convergent margins.

After its formation beneath the ridge axis, the composition of the residual oceanic lithospheric mantle is suggested to be modified by metasomatism (Andersen et al., 1995; Andersen and Neumann, 2001; Neumann et al., 1997, 2002; Gregoire et al., 2000; Pilet, 2008). During metasomatism, incompatible elements are added to the residual oceanic lithospheric mantle. The source of the metasomatic melts is debated and may include:

(i) Melts from the wings of the melting column beneath the ridge axis (Fig. 4.1). Melts generated in the wings of the melting column may not be focused to the ridge axis and instead may migrate upwards into the overlying lithosphere and metasomatise it (e.g. Workman et al., 2004). Due to their low volume, the melts from the wings of the melting column are enriched in highly incompatible elements such as LREEs relative to the surrounding residual oceanic lithospheric mantle that has undergone melt extraction. The

interaction of these melts with the residual lithospheric mantle thus results in the addition of highly incompatible elements to the residue (e.g. Workman et al., 2004).

(ii) Small melt fractions (~1% melt) derived from the asthenosphere beneath the oceanic lithospheric mantle away from the ridge axis (e.g. due to small-scale convection; Fig. 4.1): Small-scale convection cells at the base of the lithosphere can give rise to small melt fractions that are rich in LREE and can react with the residual oceanic lithospheric mantle to cause metasomatism (Niu and O'Hara, 2003; Pilet et al., 2008; Niu et al., 2011). This process could occur throughout the lifetime of a piece of oceanic lithospheric mantle (Fig. 4.1). The continuous reaction of small melt fractions with the melting residues that make up the oceanic lithosphere will result in progressive metasomatic enrichment of the highly incompatible elements with increasing age of the oceanic lithosphere i.e. increasing distance from the ridge axis.

(iii) Melts produced beneath ocean islands that traverse the oceanic lithosphere in the middle of the tectonic plate prior to eruption at ocean islands: The reaction between hot ocean island basalts and cool wall rocks of the oceanic lithosphere can result in metasomatism. Some ocean island xenoliths are interpreted to have undergone metasomatism during emplacement by ocean island lavas (e.g. Klugel, 1998, Shaw et al., 2006). Metasomatism related to emplacement is thus a late-stage modification that only xenolith fragments undergo and hence does not affect the bulk of the oceanic lithospheric mantle.

Metasomatism of the residual oceanic lithospheric mantle by sources i and/or ii listed above may result in the addition of highly incompatible elements to much of the

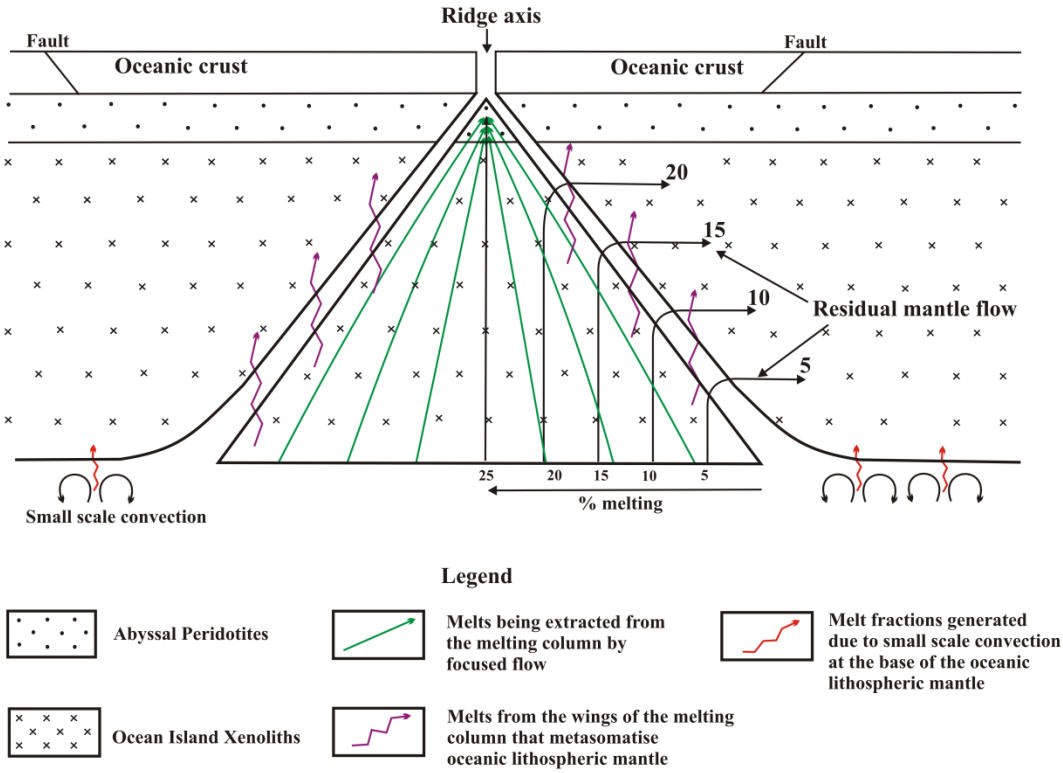

Figure 4.1. An illustration of a melting column at the MOR axis. The base of the triangular melting region represents the dry solidus above which melting begins and progresses towards the top. The extent of melting is lowest near the edges of the base of the triangular region and is higher towards the center. The black arrows indicate the direction of movement of the solid residue of the respective amounts of melting. Melts migrate through the melting column moving towards the top (green arrows). Melts erupting at the top of the melting column form MORBs that represent the top of the oceanic crust. The top of the melting column is the residue of highest extent of melting that forms abyssal peridotites, which are exposed on the surface of the oceanic crust due to faults (F). The lower portion represents residues of progressively lower extents of melting and is sampled as ocean island xenoliths. Melts generated in the wings (purple arrows) and at the base (red arrows) of the melting column can metasomatise the residual oceanic lithospheric mantle.

oceanic lithospheric mantle, thus making it an important geochemical reservoir (e.g. Niu and O'Hara, 2003; Workman et al., 2004); this has been proposed as an origin for the so-called EM2 (enriched mantle) reservoir (e.g. Workman et al., 2004), which is hypothesised as a component in the source of some ocean island basalts. With increasing distance away from the ridge axis, the lithosphere cools and becomes dense as it nears the convergent margins where it eventually subducts (Molnar and Atwater, 1978). The subducted oceanic lithospheric mantle is recycled through the mantle and has been suggested as a likely source material for ocean island basalts (e.g. Niu and O'Hara, 2003).

In this chapter, the evolution of the lower portion of the oceanic lithosphere is considered from a petrological point of view. The oceanic lithospheric mantle can be sampled in the form of ocean island xenoliths and abyssal peridotites (Figs. 1.3 and 4.1). While abyssal peridotites represent the upper oceanic lithospheric mantle that is exposed near the seafloor by tectonic processes, ocean island xenoliths may be fragments of a wide range of depths within oceanic lithospheric mantle beneath ocean islands. The uppermost oceanic lithospheric mantle can be sampled from tectonic exposures or faults on the seafloor (e.g. Dick, et al., 1984; Fig. 4.1). Abyssal peridotites exhibit a wide range of mineral modes and chemical compositions (e.g. Dick, et al., 1984; Cannat et al., 1995; Snow and Dick, 1995; Dick and Natland, 1996; Stephens, 1997; Casey, 1997; Niu, 1997; 2004; Hellebrand et al., 2002a). Ocean island xenoliths have been recovered from ocean islands such as Kerguelen, Tahiti, Hawaii, Grande Comore, The Canary Islands, Samoa, The Azores, Cape Verde and Madeira. A wide variety of lithologies such as harzburgites, lherzolites, dunites and pyroxenites have been sampled as ocean island xenoliths (Gregoire et al., 1997, 2000; Moine et al., 2001; Neumann et al., 2002, 2004; Delpech, 2004; Bonadiman et al., 2005; Shaw et al., 2006; Simon et al., 2008).

This chapter includes new modes and mineral major and trace element analyses for a suite of 72 mantle xenoliths from various ocean islands. The xenoliths represent oceanic lithospheric mantle of varying age (i.e. varying distance from the ridge axis) from the Atlantic, Pacific and Indian Ocean basins. Significant differences in the geochemical characteristics of abyssal peridotites and ocean island xenoliths are observed. The majority of ocean island xenoliths have lower abundances of moderately incompatible elements (Al_2O_3, V, Sc and HREE) compared to abyssal peridotites. The lower abundances of moderately incompatible elements in ocean island xenoliths may either be due to the greater extent of refertilisation of abyssal peridotites during melt-rock reaction or due to the uncommon exposure of depleted abyssal peridotites since these are covered by thick crust. In contrast, the concentrations of highly incompatible trace elements are higher in ocean island xenoliths than abyssal peridotites suggesting that post-melting metasomatic addition of these elements is higher in the former.

4.2. Sampling and analytical methods

The sampling strategy for ocean island xenoliths involved selecting ocean islands located on oceanic lithospheric mantle of different ages. The modal proportions of the phases in the xenoliths were determined by point counting at least 1000 points per thin section (typical thin section sizes are about 3 cm x 1.5 cm). Errors on the modal data were calculated using the method of Solomon (1964) and are presented in Supplementary Table 4.1.

In-situ mineral analyses were performed on fresh xenolith samples with little or no signs of alteration. In xenoliths with basalt veins cutting through them, the analysed crystals were selected to be as far away from the basalt as possible and were not embayed

by the basalt. In all cases, zoning profiles were measured across crystals to test for heterogeneity. Continuous profiles across adjacent olivine, pyroxene and spinel were obtained to examine the possible change in composition along crystal borders due to exchange of elements between the various mineral phases. Major elements were analysed by electron microprobe at the University of British Columbia using an automated CAMECA SX-50. Olivine, orthopyroxene and clinopyroxene crystals were analysed using an excitation voltage of 15 kV with a 40 nA beam current and 5 µm beam diameter. Peak and background counting time for all elements were 20 seconds, except for Ni and Ca in olivine where the counting time was 60 seconds. Spinel analyses were carried out under the same conditions as the silicate phases but with a 1 µm beam diameter.

Trace elements were analysed by Laser Ablation Inductively Coupled Plasma Mass Spectrometer (LA-ICP-MS) at the University of Victoria. A 213 nm laser with a 40 µm beam diameter and pulse frequency of 20 Hz was rastered along lines ~200 to 250 µm long, parallel to the crystal edges. After collection of a gas blank that was used to correct the background, the laser was fired for ~30 seconds. The ablated sample was transported for analysis to a PQ II S+ series ICP-MS by a helium carrier gas flowing at 1.18 litres per minute. Peak time slices for the acquired data were selected manually. The data was calibrated against NIST glasses 611, 613 and 615. These standards were analysed after every 5-6 analysis of the samples as well as before and after sample changes. San Carlos (SC) olivine (Wan et al., 2008) was used as an external standard for Al and Cr in olivine and was analysed at the beginning of the day of analysis. The quality of the data was assessed by analysing MPI-DING (Jochum et al., 2005) reference glasses KL2-G (basalt), ML3B-G (basalt), GOR 128-G (komatiite) and GOR 132-G (komatiite) that were also run at the beginning of the day. All elements measured by replicate analysis of MPI-DING

glasses are within analytical uncertainty of their recommended values (Supplementary Table 4.1 – LA-ICP-MS Standards). Phosphorous and sodium gave anomalously high concentrations and hence the concentration of these elements analysed by LA-ICP-MS will not be used in this study. Electron microprobe analyses of Ni and Ca were used as internal standards for the calibration of LA-ICP-MS data for olivine and pyroxene respectively. Electron microprobe data was collected for the same crystals that were analysed on the ICP-MS and data points for both analysis were selected to be as close to one another as possible.

Volume weighted averages were calculated for trace element concentrations in the minerals in order to minimise the error due to possible zoning in the minerals. The crystals were assumed to have spherical geometry and since trace element data were collected in the form of profiles across the crystals, the crystals were divided as concentric shells within the sphere and the volume for each shell was calculated. The volume of each shell was normalised by the volume of the sphere (entire crystal) to give a volume fraction and the concentration of each element measured in the respective shell was multiplied by the volume fraction. The sum of each resulting volume concentration is the volume weighted average for the element. The volume weighted averages combined with the modal data were used to determine the xenolith bulk-rock compositions. Uncertainties on bulk compositions are determined by propagating the uncertainties on the modal proportions and on the mineral compositions. As will be discussed further in this Chapter, it is possible that the bulk rock geochemistry of ocean island xenoliths is modified during emplacement. Trace element enrichment may be restricted to a narrow zone where basalt intrusions are observed along crystal boundaries. In order to reduce the influence of possible chemical modification along crystal boundaries, this study uses reconstructed bulk chemistry of

ocean island xenoliths that is calculated using mineral analyses of points that are carefully selected at least 10 μm away from crystal boundaries. The locations of electron probe and LA-ICP-MS analysis spots on minerals analysed in this study are shown in Appendix B.

4.3. Results

Mantle xenoliths hosted by basalts from six ocean islands/island groups: Kerguelen (25 Ma), Tahiti (60 Ma), Hawaii (80 Ma), Cape Verde (130 Ma), Madeira (140 Ma) and the Canary Islands (i.e. Lanzarote, Gran Canaria, Fuertventura and Tenerife; 150 to 180 Ma) were studied here (Fig. 4.2). Sources of ocean island xenolith samples along with average major and trace element concentrations of minerals are given in Supplementary Table 4.2. All the samples were studied only in the form of thin sections with xenolith areas ranging from 200-940 mm^2 for most xenoliths (Supplementary Table 4.1), while the smallest xenoliths vary from ~70-100 mm^2 in area. Some thin sections that cover an area of 30-70 mm^2 are more likely to be large phenocrysts or cumulates; modal data and geochemical analyses for these thin sections are shown in Supplementary Table 4.1, but the data are not included in any further discussions. The lithology of the sample suite consists of harzburgites, lherzolites, dunites and pyroxenites (Fig. 4.3). A wide variety of textural and mineralogical characteristics are observed in the xenoliths. The sample suite was analysed for petrographic and mineral geochemical data, the results of which are presented in this section. Detailed analytical results of major mineral phases in the xenolith samples are provided in Supplementary Table 4.1. Published abyssal peridotite and ocean island xenolith composition data are incorporated as an integral part of this study (Fig. 4.2). A

compilation of all data used in this study along with the references is provided in Supplementary Table 4.3.

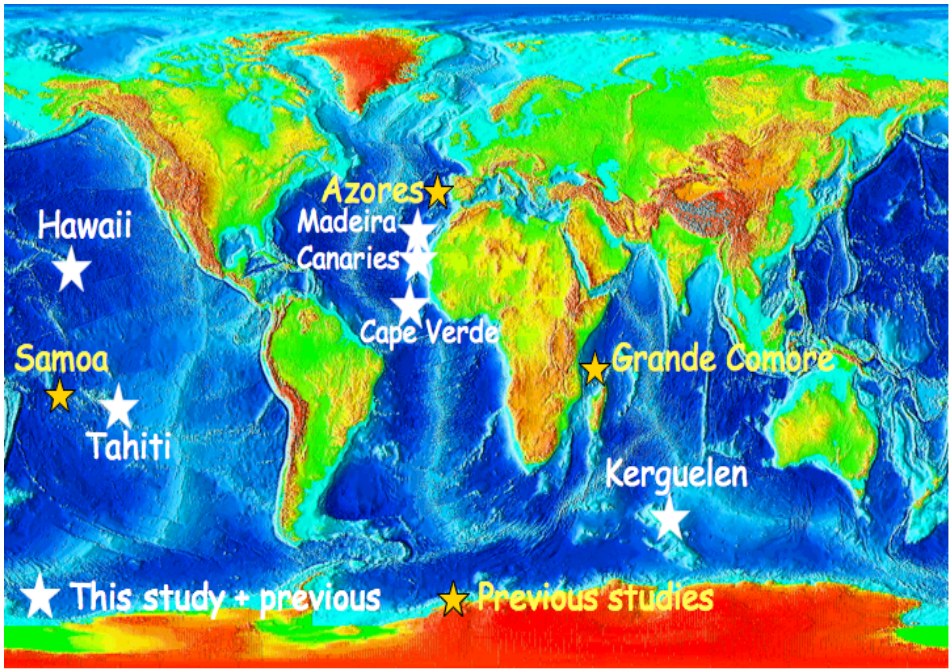

Figure 4.2. Locations of global ocean island xenolith sample suite used in this study.

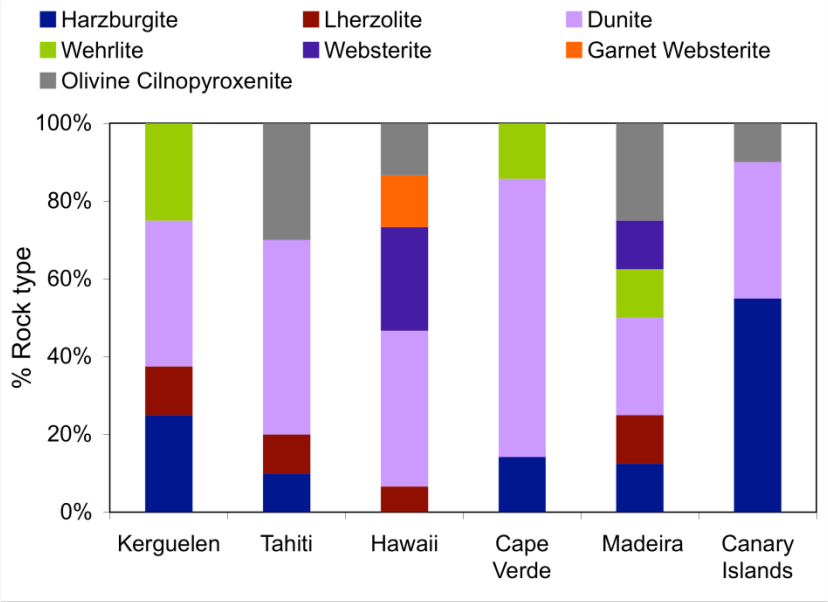

Figure 4.3. Lithologies of ocean island xenoliths analysed in this study with number of samples represented as percentages for each ocean island. The number of samples for each ocean island is as follows: Kerguelen – 8, Tahiti – 10, Hawaii – 15, Cape Verde – 7, Madeira –

8, The Canary Islands – 20. The lithologies do not necessarily represent the percentages in which each rock type occurs in each ocean island.

4.3.1. Petrography

Key petrographic characteristics such as grain size, presence of secondary minerals, veins etc. for individual samples are given in Supplementary Table 4.2. The harzburgite and lherzolite xenoliths generally exhibit equilibrated xenomorphic granular texture (Fig. 4.4a-f). Olivine and orthopyroxene crystals are subhedral with crystal sizes ranging from 2-4 mm for medium grained xenoliths and from 5-6 mm for coarse xenoliths. The largest crystals observed are ~8 mm long and are usually olivines. After spinel, clinopyroxene is the smallest mineral phase (~0.5-2 mm; Fig. 4.4) in harzburgites and low-clinopyroxene dunites and is usually subhedral to anhedral. Clinopyroxene exsolution is observed in orthopyroxene in some ocean island xenoliths (details in Supplementary Table 4.2). Spinel is present in most xenoliths with the exception of six samples (see Supplementary Tables 4.1 and 4.2). Minor mineral phases such as phlogopite, plagioclase and calcite are also present in trace amounts in some ocean island xenoliths (Supplementary Table 4.1).

Basalt veins cut across ~80% of the xenoliths and range in thickness from 40 μm to ~1 mm (Fig. 4.4c-d). When the margins of the xenoliths are visible, the basalt veins merge with the host basalt and have the same texture and mineralogy as the host basalt suggesting they are the same material. Basalt veins are more common near the contact of the xenolith with the host basalt (e.g. Fig. 4.4c) than in the interior of the xenolith. The host basalt also intrudes the xenolith along crystal boundaries forming embayed crystal borders. Crystals surrounded by basalt veins sometimes exhibit sieve-textured rims that are 50 to 100 μm thick (as also described by Bonadiman et al., 2005; Shaw et al., 2006; Shaw and Dingwell, 2008). Minerals in the smaller xenoliths (≤ 2 cm^2) are generally highly cracked and are

traversed by basalt veins (Fig. 4.4c). In order to avoid contamination from basalt veins, this study utilises mineral compositions and modes to calculate the bulk composition. Intrusion of host basalts into xenoliths during emplacement (Fig. 4.4c-d) can alter the composition of minerals in ocean island xenoliths. Emplacement-related metasomatism can be cryptic and may not alter the textural characteristics of the xenolith. Since emplacement-related chemical changes are not part of lithospheric mantle processes, ocean island xenoliths that are chemically altered by cryptic metasomatism during emplacement are filtered out in this study (Section 4.3.4).

4.3.2. Mineral Chemistry

Major element zoning is observed in very few xenoliths as given in Supplementary Table 4.1 and discussed in detail in Section 4.4.1. Olivine in harzburgite and lherzolite xenoliths has Mg# ($Mg^{2+}/[Mg^{2+}+Fe^{2+}]*100$) ranging from 89 to 92 and one lherzolite from Tenerife has olivine Mg# 84. One harzburgite xenolith from Cape Verde contains olivine zoned with Mg# ranging from 69 to 89. The Mg#s of pyroxenes in harzburgite and lherzolite xenoliths range from 91 to 94 (Supplementary Table 4.1). The lherzolite from Tenerife that has low olivine Mg# and the harzburgite from Cape Verde with zoned olivine are likely to have been modified by metasomatic processes to a greater extent than the rest of the suite and are hence not examined in detail for the purpose of this study. Filtering out these samples, the number of harzburgite and lherzolite xenoliths used for further interpretations in this study is eighteen. The concentration of Al_2O_3 in orthopyroxenes in harzburgites and lherzolites ranges from 0.2 to 5 wt%, while that in clinopyroxene is between 4.6 to 7 wt% (Supplementary Table 4.1). The Cr# ($Cr^{3+}/[Cr^{3+}+Al^{3+}]*100$) of spinels in harzburgite and lherzolite xenoliths ranges from 16 to 73 (Supplementary Table 4.1).

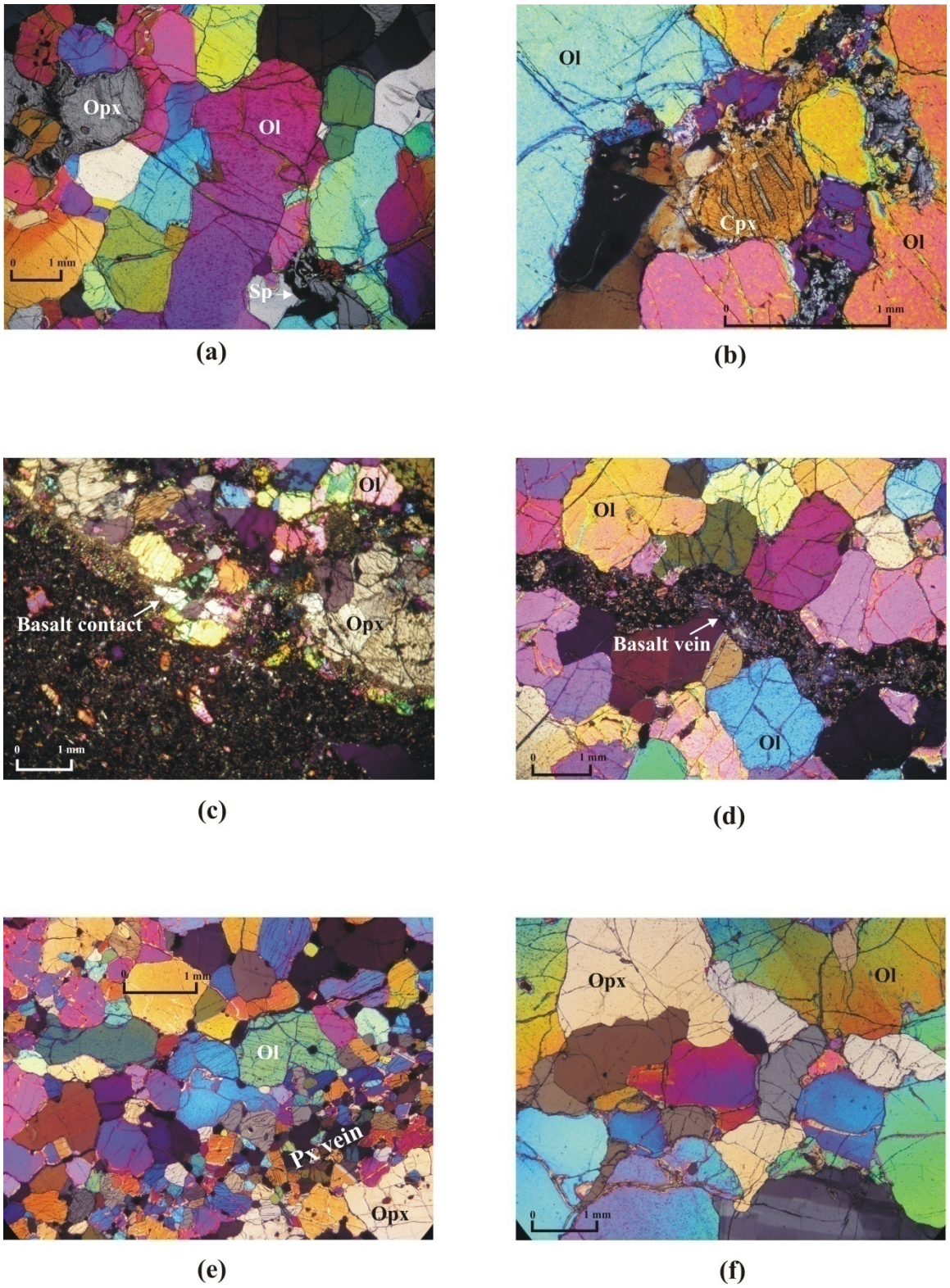

Figure 4.4. (Caption on following page)

Figure 4.4. Photomicrographs showing the mineralogy and textures in ocean island xenoliths analysed in this study. (a) Harzburgite sample LEIUG 114018 from Lanzarote showing coarse-grained xenomorphic granular texture in olivine and orthopyroxene crystals. (b) Clinopyroxene crystal in the interstices of olivine crystals in harzburgite sample LEIUG 114031 from Lanzarote. (c) Basalt contact with the xenolith NI 120 F from Cape Verde with a basalt intrusion extending into the xenolith. (d) Basalt vein through dunite xenolith TAH-4 from Tahiti. (e) Pyroxenite vein cutting a spinel websterite xenolith BM 1964-737-11b from Madeira. (f) Xenomorphic granular texture in spinel harzburgite xenolith BM 64888 from Kerguelen.

Dunites contain olivine with Mg# ranging from 81 to 91, while in pyroxenite xenoliths, olivine Mg# ranges from 80 to 90. Between ~1 to 4 modal volume of clinopyroxene is observed in dunite xenoliths, with Mg# ranging from 80 to 94, which correlates with the Mg# of coexisting olivines. Dunite xenoliths have spinel with Cr# ranging from 16 to 64 (Supplementary Table 4.1).

Clinopyroxene in pyroxenite xenoliths has Mg# ranging from 81 to 87 with the exception of a websterite sample from Madeira in which both pyroxenes have Mg# ~92. Orthopyroxene Mg#s in pyroxenite xenoliths range from 82 to 84 and match that of co-existing clinopyroxenes (Supplementary Table 4.1). Spinels in pyroxenite xenoliths span a wide range of Cr# ranging from 5 to 50 (Supplementary Table 4.1).

The forsterite content of olivine in 70% of the harzburgite and lherzolite xenoliths is higher (91-92) compared to most (70%) abyssal peridotites (90-91; Fig. 4.5b). The concentration of Al_2O_3 in orthopyroxene spans a wide range (0.4 to 4.3 wt%) in harzburgite and lherzolite xenoliths that extends to lower concentrations than in abyssal peridotites (1.7 to 6.1 wt%; Fig. 4.5d). The Cr# of spinel is between 0.3 to 0.9 in harzburgite and lherzolite xenoliths and is generally higher than in abyssal peridotites (0.12 to 0.57; Fig. 4.5f).

Overall, although there is substantial overlap, mineral major element compositions are more depleted in harzburgite and lherzolite xenoliths than abyssal peridotites.

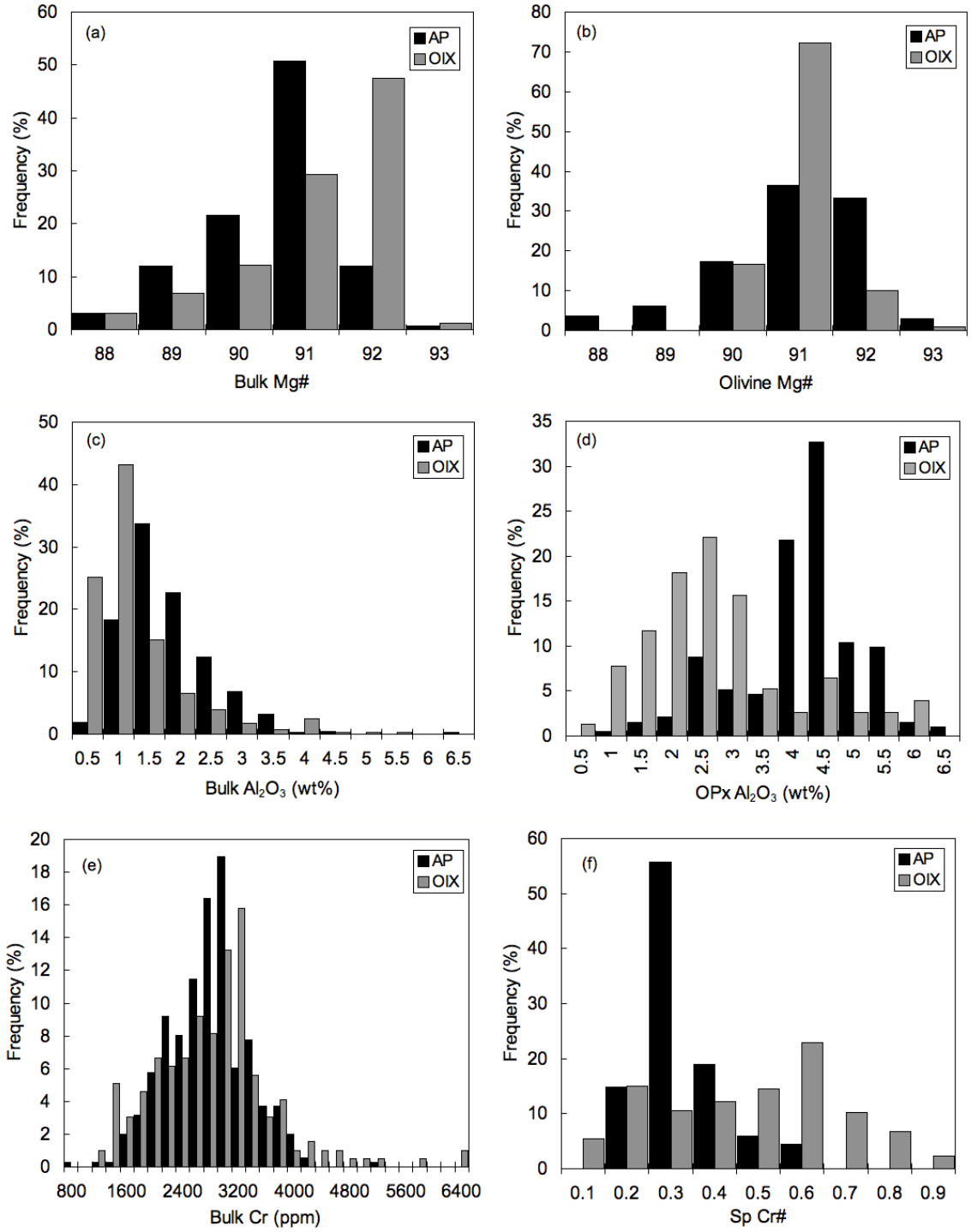

Figure 4.5. (Caption on next page)

Figure 4.5. Histograms illustrating bulk and mineral compositions of harzburgites and lherzolites in ocean island xenoliths and abyssal peridotites. The frequency is expressed as a percentage of the number of samples in order to overcome the difference in number of ocean island xenolith and abyssal peridotite samples. Bulk compositions are shown on the left hand side while the mineral composition that most influences the respective oxide's bulk concentration is shown on the right hand side. Data sources in addition to ocean island xenoliths analysed in this study are as follows: Canary Islands: Siena et al. (1991); Neumann (1991); Wulff-Pedersen et al. (1996), Neumann et al. (2002, 2004), Abu El-Rus et al. (2006); Cape Verde: Bonadiman et al. (2005); Kerguelen: Gregoire et al. (1997; 2000a; 2000b); Delpech (2004); Azores: Johansen (1996); Grande Comore: Coltorti et al. (1999); Samoa: Hauri et al. (1993); Hawaii: Kuno (1969); Sen (1987); Jackson and Wright (1970); Goto and Yokoyama (1988); Sen and Leeman (1991); Tahiti: Qi et al. (1994); Ocean island xenolith data compilation from Simon et al. (2008). Abyssal peridotite data sources are as follows: MAR: Cannat et al. (1995); Stephens (1997); Casey et al. (1997); Brandon et al. (2000); Lee et al. (2003); Miyashiro et al. (1969); Aumento and Loubat (1971); SWIR: Snow and Dick (1995); Godard et al. (2008); Hess Deep (EPR): Gillis et al. (1993); Blum (1990); Garret Transform (EPR): Niu and Hekinian (1997). Compilation of abyssal peridotite data from Johnson et al. (1990) and Niu (2004).

The average trace element concentrations of mineral phases in all ocean island xenoliths studied here (Supplementary Table 4.1) were calculated using 2-7 analyses for olivines and orthopyroxenes and 2-5 analyses for clinopyroxenes (Supplementary Table 4.1). Some clinopyroxene crystals were too small for multiple laser analyses and the result of a single analysis of two or more crystals were therefore used to calculate average compositions (Supplementary Table 4.1). Trace element zoning was not observed even in the largest (5 mm) crystals analysed in this study and hence the minerals are considered to be homogeneous. Variations in trace element concentrations have been reported for

multiple crystals of the same phase within single xenoliths (e.g. Neumann et al., 2004), but such variations are not observed in any of the samples in this study.

4.3.3. Bulk rock geochemistry

The following section only describes the bulk rock geochemistry of harzburgites and lherzolites. As discussed above, to ensure no contamination from the host basalt, the bulk rock compositions of the ocean island xenoliths studied here were calculated based onmeasured mineral compositions and modal percentages. The equation used in the calculation of bulk rock compositions is:

$$Bulk\ composition\ XOxide = XOl * FOl + XOPx * FOPx + XCPx * FOPx + XSp * FSp \quad \text{Eq. 4.1}$$

where F represents the modal fraction of each mineral in the xenoliths, as determined by point counting. Since the major discussions in this study are based on harzburgite and lherzolite lithologies, trace element data is not reported for all phases in other lithologies and hence bulk rock trace element concentrations are not calculated for these samples. The errors associated with point counting were calculated as variance on each mineral fraction (Solomon, 1964). The area of the thin sections varies widely covering a range from 200 to 940 mm^2 (Supplementary Table 4.1) and coupled with varying grain sizes contributes to large uncertainties in calculated bulk rock compositions in samples with smaller areas. The uncertainties on calculated bulk rock compositions associated with point counting errors were propagated by substituting the calculated variance on each mineral in place of the fraction of the mineral in Eq. 4.1. In case of abyssal peridotites, the bulk concentrations of CaO, SiO_2 and MgO can change due to seafloor alteration (e.g. Niu, 2004). The bulk concentrations of major elements in some abyssal peridotites were also reconstructed using previously measured mineral compositions and modal percentages (Dick et al., 1984; Hellebrand et al., 2002a; Chapter 3).

The following paragraphs in this section discuss comparisons of measured and reconstructed bulk rock compositions of ocean island xenoliths and abyssal peridotites. It is important to note here that the number of samples used to calculate reconstructed bulk rock compositions (31 for ocean island xenoliths and 32 for abyssal peridotites) is much smaller than the available dataset of measured bulk rock compositions (Supplementary Table 4.3). Measured and reconstructed bulk rock CaO, Na_2O, SiO_2, TiO_2, MgO and FeO in xenoliths from Tahiti, Cape Verde and Lanzarote are plotted on Al_2O_3 variation diagrams (Figs. 4.6, 4.7 and 4.8 respectively). Xenoliths from these ocean islands were selected to compare reconstructed and measured bulk rock compositions since the number of samples with reconstructed data was higher than the remaining ocean islands. The concentration of measured bulk rock Na_2O at a given bulk rock Al_2O_3 is slightly higher than the reconstructed bulk rock Na_2O in ocean island xenoliths from Cape Verde (Fig. 4.7b) and Lanzarote (Fig. 4.8b), but this is not observed in case of Tahiti (Fig. 4.6b). Higher bulk Na_2O in xenoliths from some ocean islands has been attributed to enrichment by basaltic melts e.g. the Canary Islands (Neumann et al., 1991; Siena et al., 1991; Simon et al., 2008). On Al_2O_3 variation diagrams, the measured and reconstructed bulk compositions of major oxides other than Na_2O in the global suite of ocean island xenoliths are similar to one another (Fig. 4.9). In the case of abyssal peridotites, the measured bulk concentrations of Al_2O_3, Na_2O (Fig. 4.10b), SiO_2 (Fig. 4.10c) and TiO_2 (Fig. 4.10d) are higher than the reconstructed bulk compositions for some of the samples. On the other hand, the measured bulk concentrations of CaO and MgO are lower than their respective reconstructed bulk concentrations for a given bulk rock Al_2O_3 concentrations (Fig. 4.10a and Fig. 4.10e

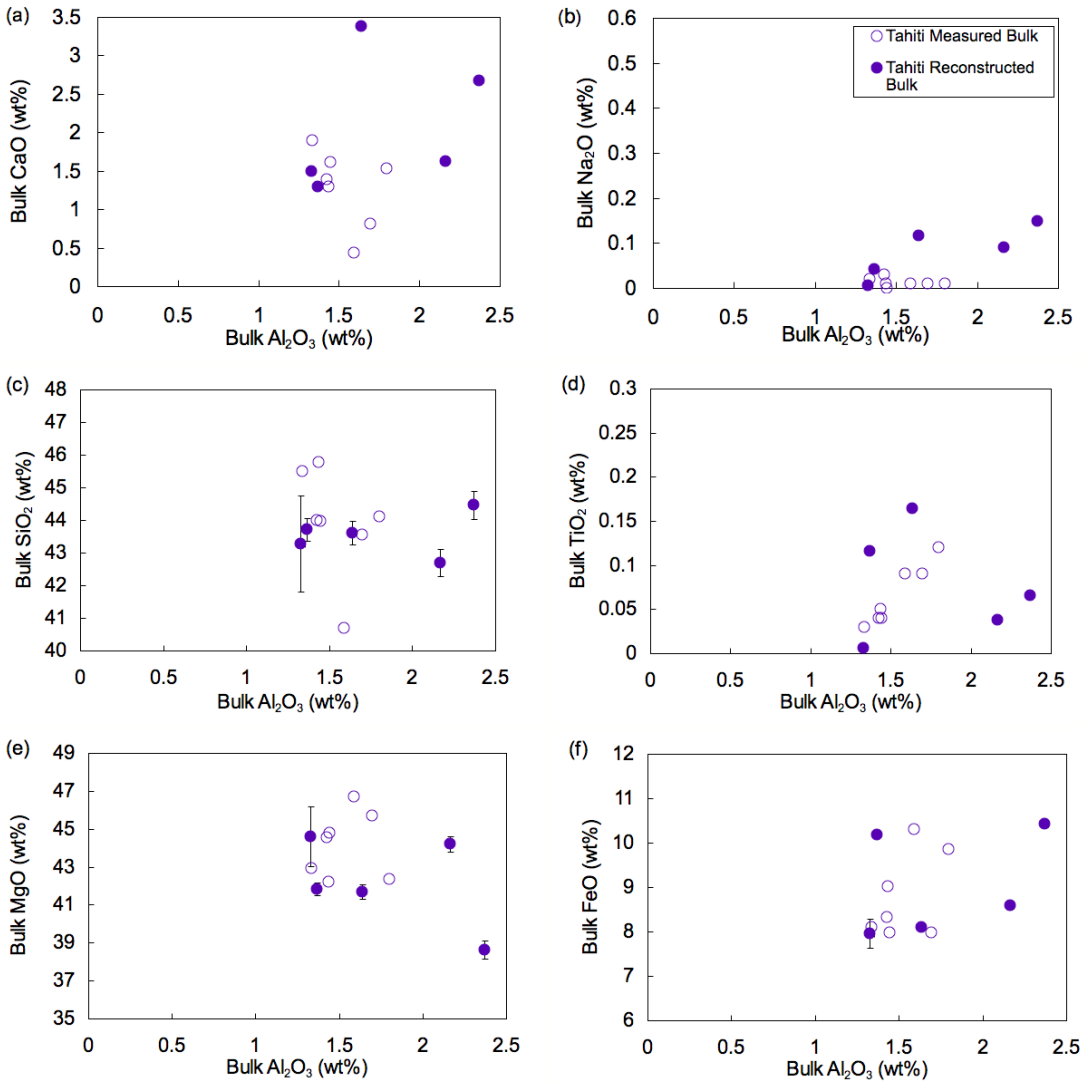

Figure 4.6. Measured and reconstructed bulk rock major element concentrations of ocean island xenoliths from Tahiti on an Al_2O_3 variation diagram.

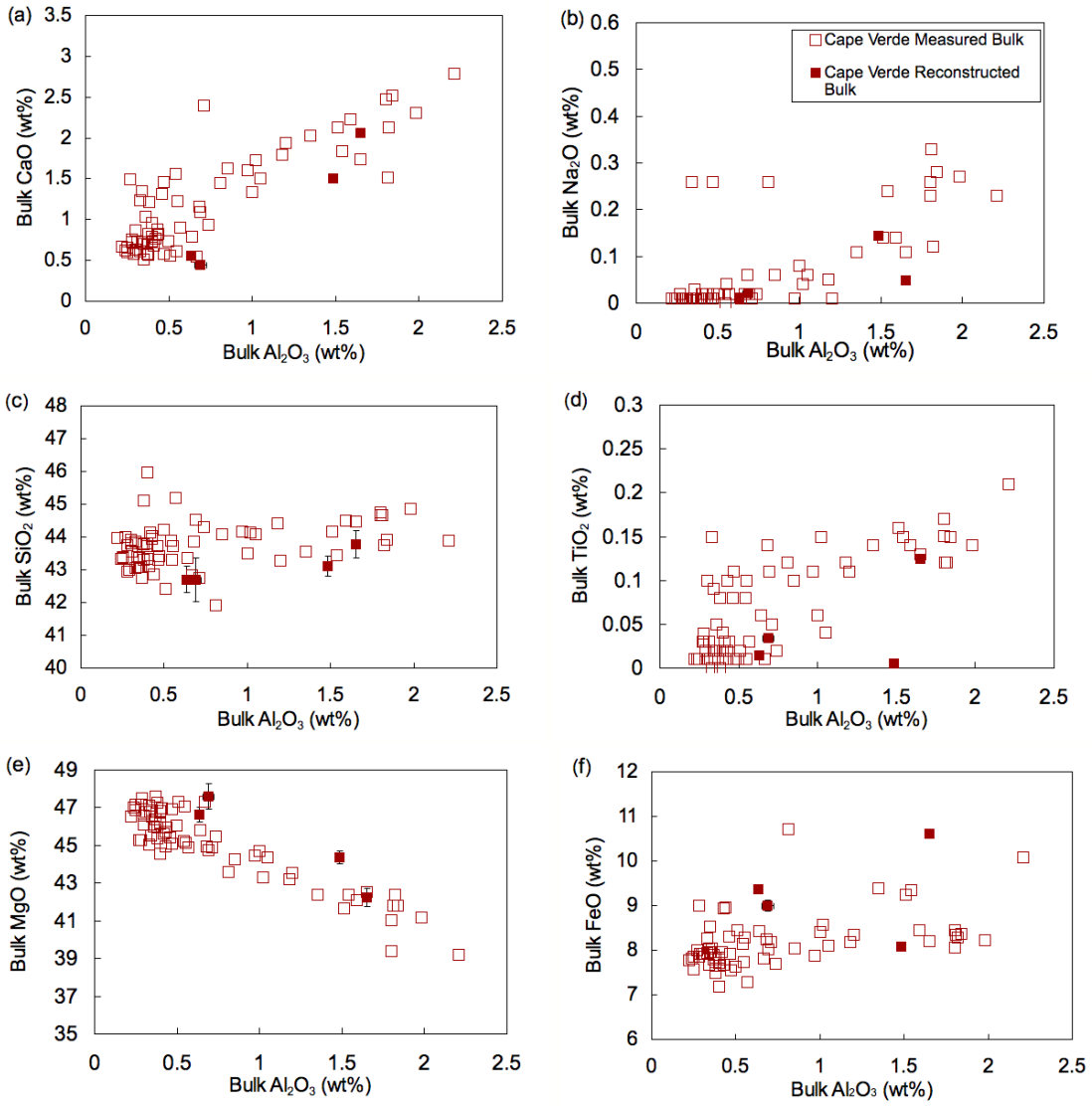

Figure 4.7. Measured and reconstructed bulk rock major element concentrations of ocean island xenoliths from Cape Verde on an Al_2O_3 variation diagram.

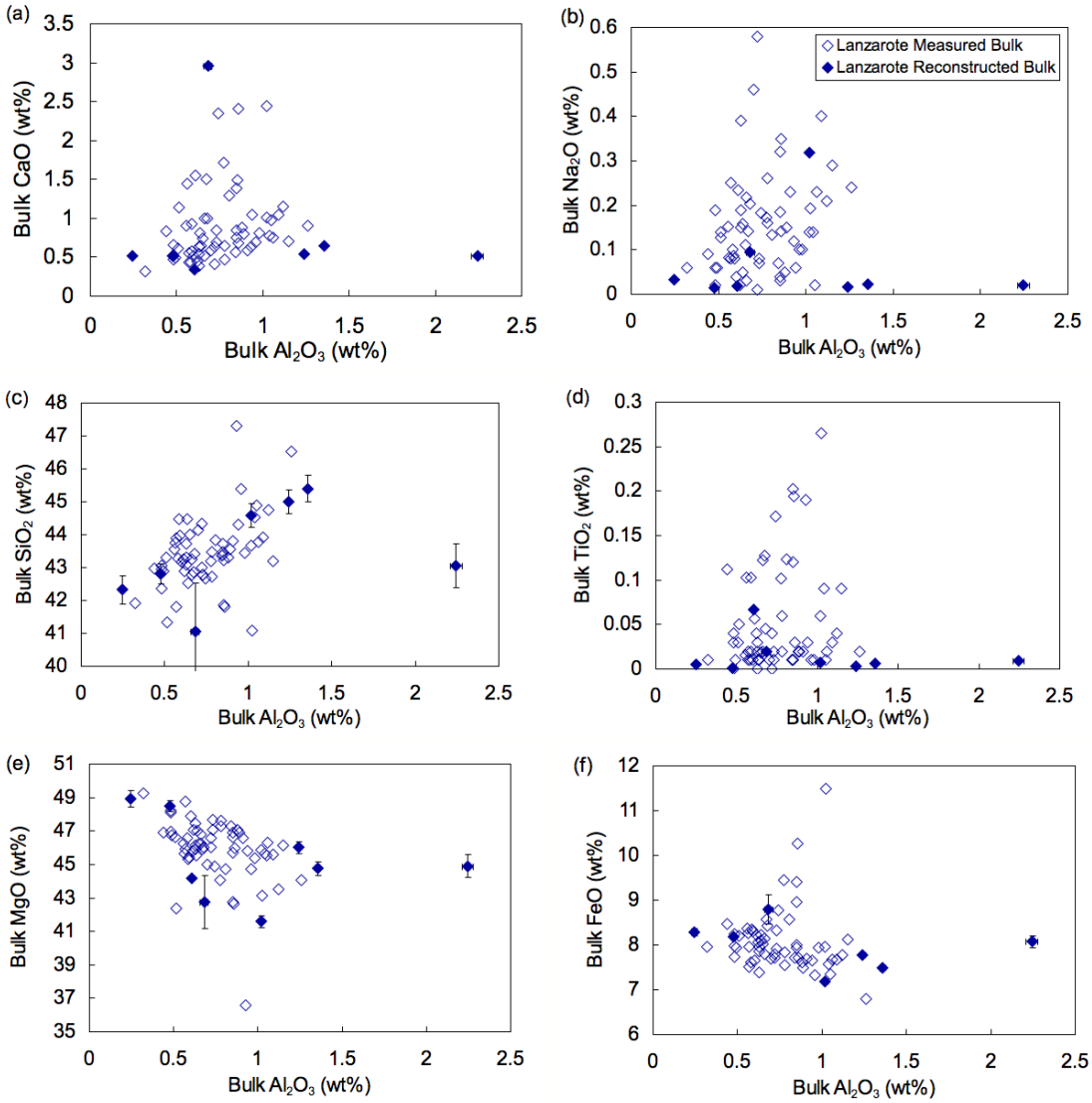

Figure 4.8. Measured and reconstructed bulk rock major element concentrations of ocean island xenoliths from Lanzarote on an Al_2O_3 variation diagram.

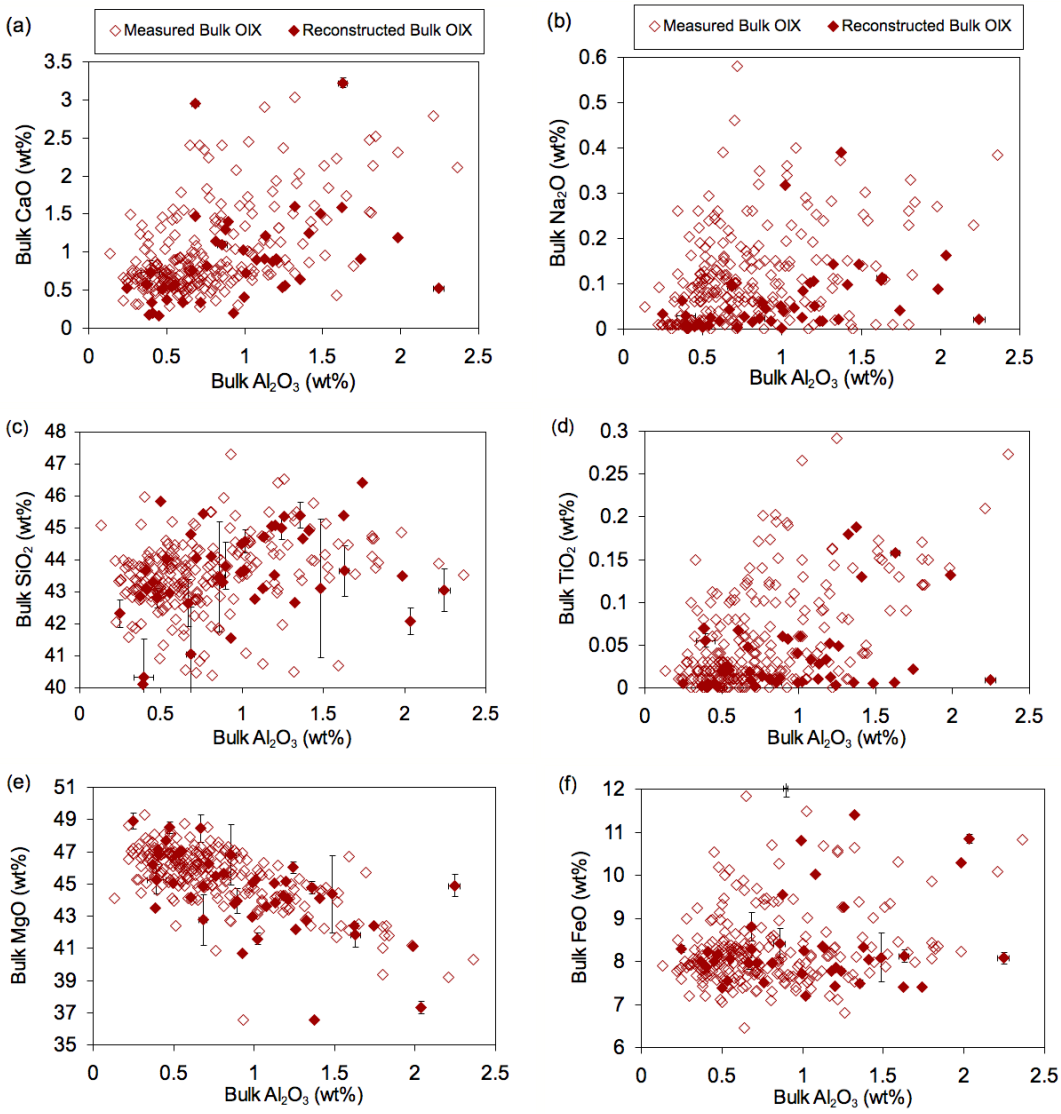

Figure 4.9. Measured and reconstructed bulk rock major element concentrations of the global suite of ocean island xenoliths plotted on an Al_2O_3 variation diagram.

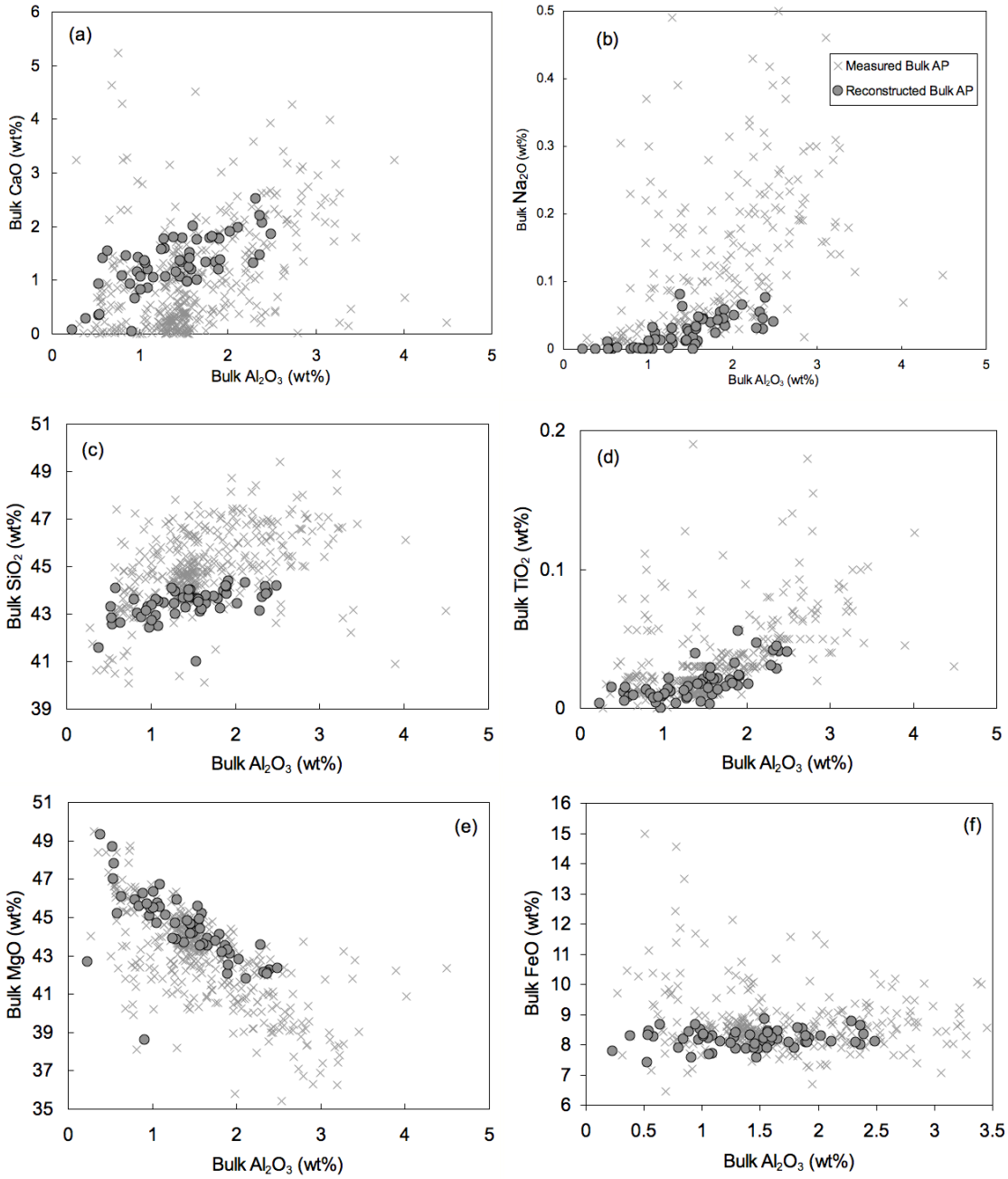

Figure 4.10. Measured and reconstructed bulk rock major element concentrations of abyssal peridotites plotted on an Al_2O_3 variation diagram. Bulk compositions are reconstructed from mineral chemistry and modal data for abyssal peridotites from the Central Indian Ridge (Hellebrand et al., 2002), Southwest Indian Ridge (Dick et al., 1984), American-Antarctic Ridge (Dick et al., 1984) and Hess Deep (Chapter 3; this study). Measured bulk compositions are from sources cited in Fig. 3.3 (Chapter 3).

respectively). As discussed in Chapter 3, the increased concentrations of SiO_2 and decreased concentration of MgO in abyssal peridotites from 15°20' N (MAR) relative to the global abyssal peridotite suite are due to alteration and formation of Si-rich phases such as smectite/chlorite, talc etc. Since each suite studied here has a few outliers in the compositional array, the median values were calculated in order to quantify the observed differences in the compositions of abyssal peridotites and ocean island xenoliths. For example, the measured bulk rock concentration of Al_2O_3 in 98% of the ocean island xenoliths is between 0.5 to 3.5 wt% with some samples containing up to 4 wt% bulk rock Al_2O_3 (Fig. 4.11; Supplementary Table 4.1). Although there is a significant overlap between the measured and reconstructed bulk compositions of ocean island xenoliths and abyssal peridotites, the median value of Al_2O_3 shows considerable difference between the two suites (Fig. 4.12). The median of the measured bulk-rock Al_2O_3 contents of abyssal peridotites (1.4 wt %) is higher than that of ocean island xenoliths (0.84 wt %). The same is true for the median reconstructed bulk rock Al_2O_3, which is higher in abyssal peridotites (1.58 wt %) than in ocean island xenoliths (0.99 wt %) and both these are higher than their respective measured bulk rock concentrations (Fig. 4.12). The measured and reconstructed bulk rock concentrations of CaO and TiO_2 in abyssal peridotites and ocean island xenoliths show broad positive correlations with Al_2O_3, while that of MgO correlates negatively with Al_2O_3 (Fig. 4.9 and Fig. 4.10).

The median value of both, measured and reconstructed bulk concentrations of CaO in ocean island xenoliths is ~0.8 wt%, but that of abyssal peridotites varies considerably with higher reconstructed bulk concentration (1.38 wt%) than the measured concentration (0.7 wt%; Fig. 4.12a); the higher CaO is likely due to calcite precipitation as discussed in

Chapter 3. Median values of measured and reconstructed bulk rock compositions of Na_2O in abyssal peridotites and ocean island xenoliths vary by ~0.05 wt%; the median values of measured bulk composition being higher than median values of reconstructed bulk composition (Fig. 4.12b) for both suites. For SiO_2, the median measured and reconstructed bulk compositions in ocean island xenoliths is ~43.6 wt% and for abyssal peridotites, it is 44.7 wt% for measured and 43.6 wt% for reconstructed bulk concentration (Fig. 4.12c).

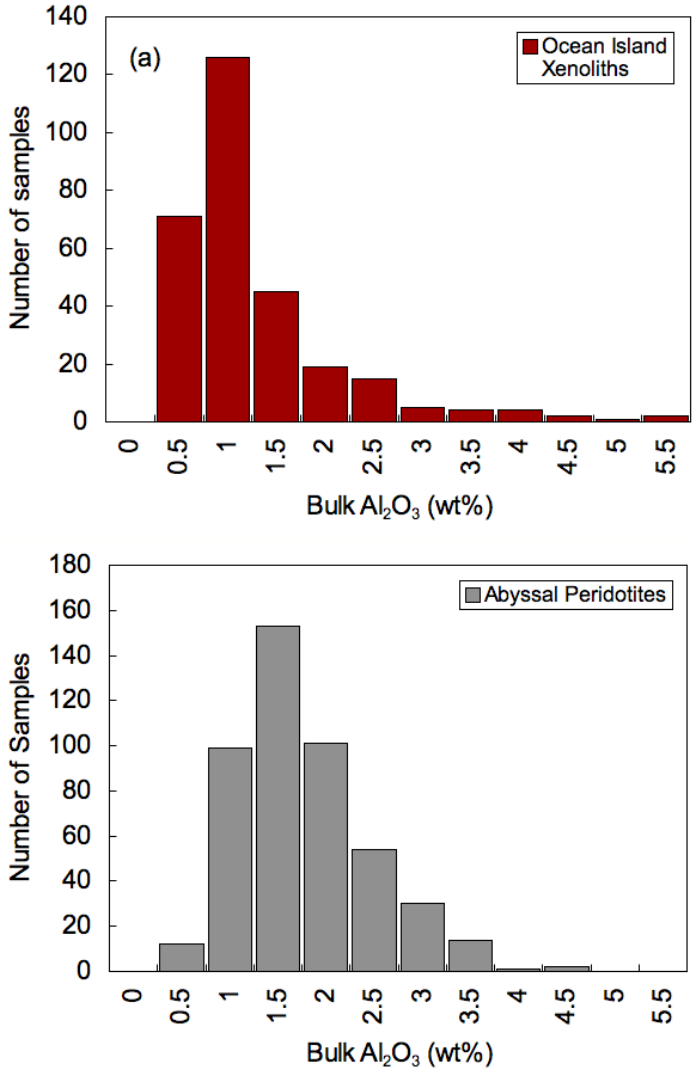

Figure 4.11. Histogram showing measured bulk concentration of Al_2O_3 in (a) ocean island xenoliths and (b) abyssal peridotites.

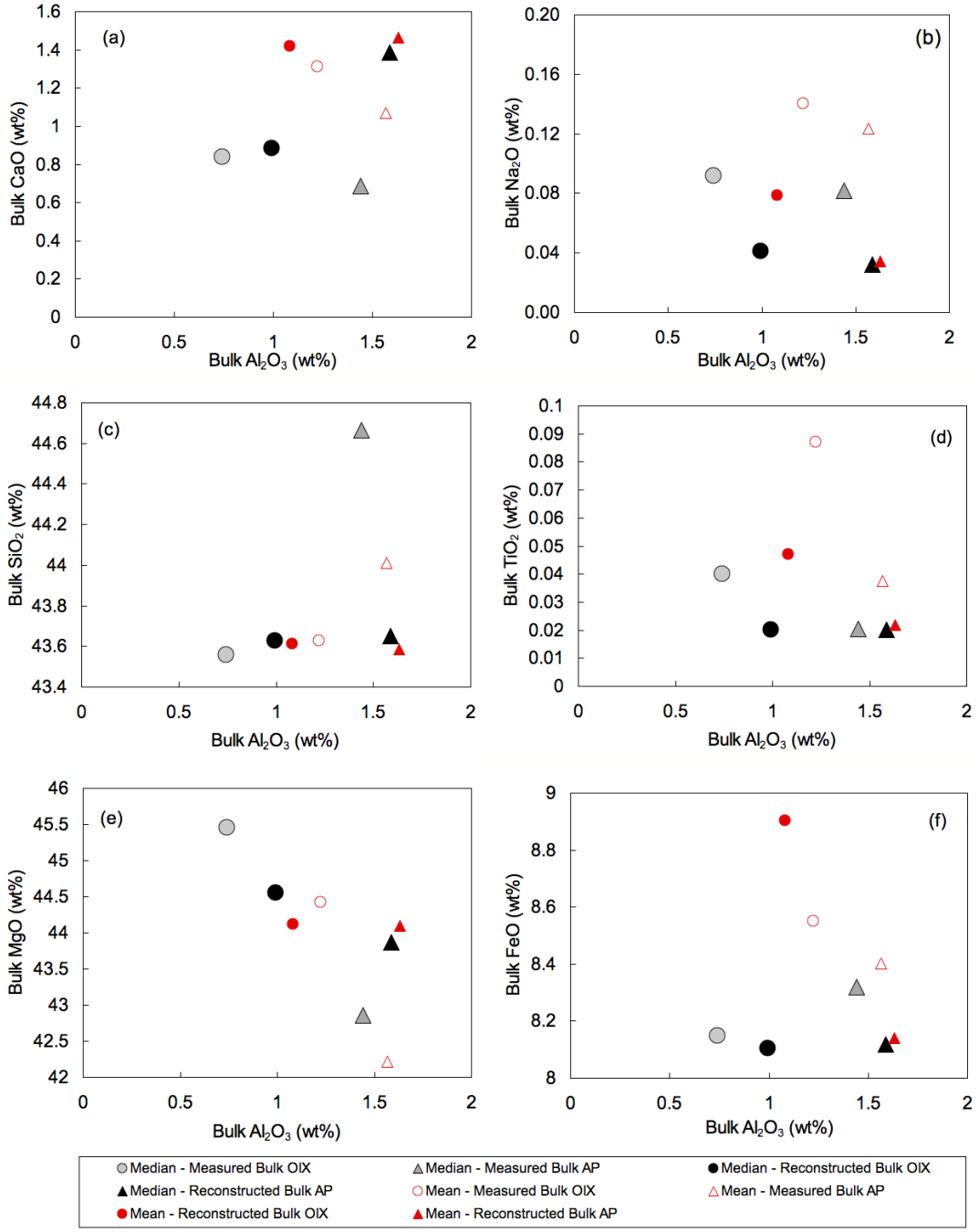

Figure 4.12. Median and mean measured and reconstructed bulk rock major element concentrations of ocean island xenoliths and abyssal peridotites on an Al_2O_3 variation diagram.

Harzburgite and lherzolite xenoliths generally have bulk Mg# ranging from 89 to 92 (Fig. 4.5a; Supplementary Table 4.1). Combined with the global harzburgite and lherzolite

suite of ocean island xenoliths, almost 72% of harzburgite and lherzolite xenoliths have bulk Mg# ranging from 90 to 92 with nearly 15% having a bulk Mg# of 92. In comparison, the measured bulk Mg# of 62% of the harzburgite and lherzolite abyssal peridotites ranges between 90 and 92 (Fig. 4.5; Supplementary Table 4.3). The bulk Mg#s of ocean island xenoliths are thus skewed to higher bulk Mg# than abyssal peridotites (Fig. 4.5a).

The bulk rock concentrations of the moderately incompatible trace elements Sc and V are generally lower in ocean island xenoliths than abyssal peridotites (Fig. 4.13). Since abyssal peridotites are commonly exposed in slow-spreading environments, the samples from Hess Deep are perhaps the only samples that could be considered from "normal" MOR environments and are thus shown as separate symbols. The concentration of V is higher in ocean island xenoliths from Cape Verde and Hawaii compared to the rest of the xenoliths and correlates to the higher bulk Al_2O_3 in these xenoliths (Supplementary Table 4.2). Mantle xenoliths from Hawaii and Cape Verde have previously been described as being fertile compared to the remaining ocean islands (e.g. Sen, 1988; Sen and Leeman, 1991; Sen et al., 1993; Simon et al., 2008).

The bulk rock concentrations of REEs, Ti and Zr are normalised against chondritic abundances (McDonough and Sun, 1995) and plotted in Yb-variation diagrams in Figure 4.14. The bulk-rock Ce and Nd abundances of ocean island xenoliths and abyssal peridotites vary from ~0.01 to ~10 times chondritic values (Figs. 4.14a and 4.14b). The bulk rock Zr-abundance varies from ~0.03 to ~1 times chondrite for ocean island xenoliths and from 0.05 to 8 times chondrite for abyssal peridotites (Fig. 4.14f). Most abyssal peridotites have Yb abundances ranging from ~0.2 to ~8 times chondrite and is the same as in ocean island xenoliths (Fig. 4.14). Overall, the abundances of the more incompatible elements (Ce, Nd and Zr) in ocean island xenoliths are higher than those of abyssal

peridotites at any given bulk-rock Yb-abundance (Figs. 4.14a, 4.14b and 4.14f). The bulk rock abundance of the moderately incompatible elements Sm, Eu and Ti in ocean island xenoliths is similar to abyssal peridotites with identical Yb-abundances (Fig. 4.14c, 4.14d and 4.14e).

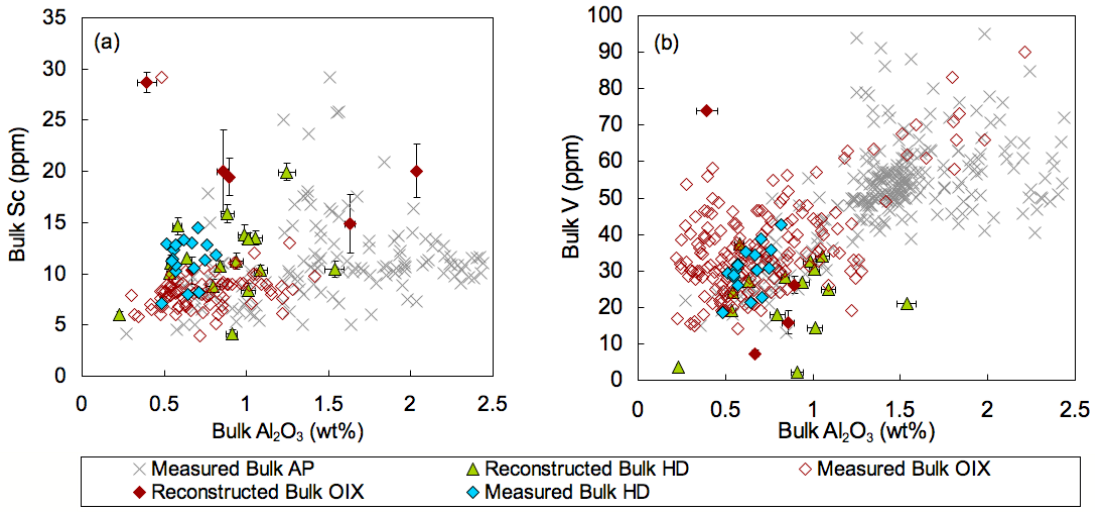

Figure 4.13. Measured and reconstructed bulk rock concentrations of (a) Sc and (b) V plotted on an Al_2O_3 variation diagram. Error bars on reconstructed data represent the uncertainty propagated from the variance calculated for modal percentage of each mineral phase using the method of Solomon (1964).

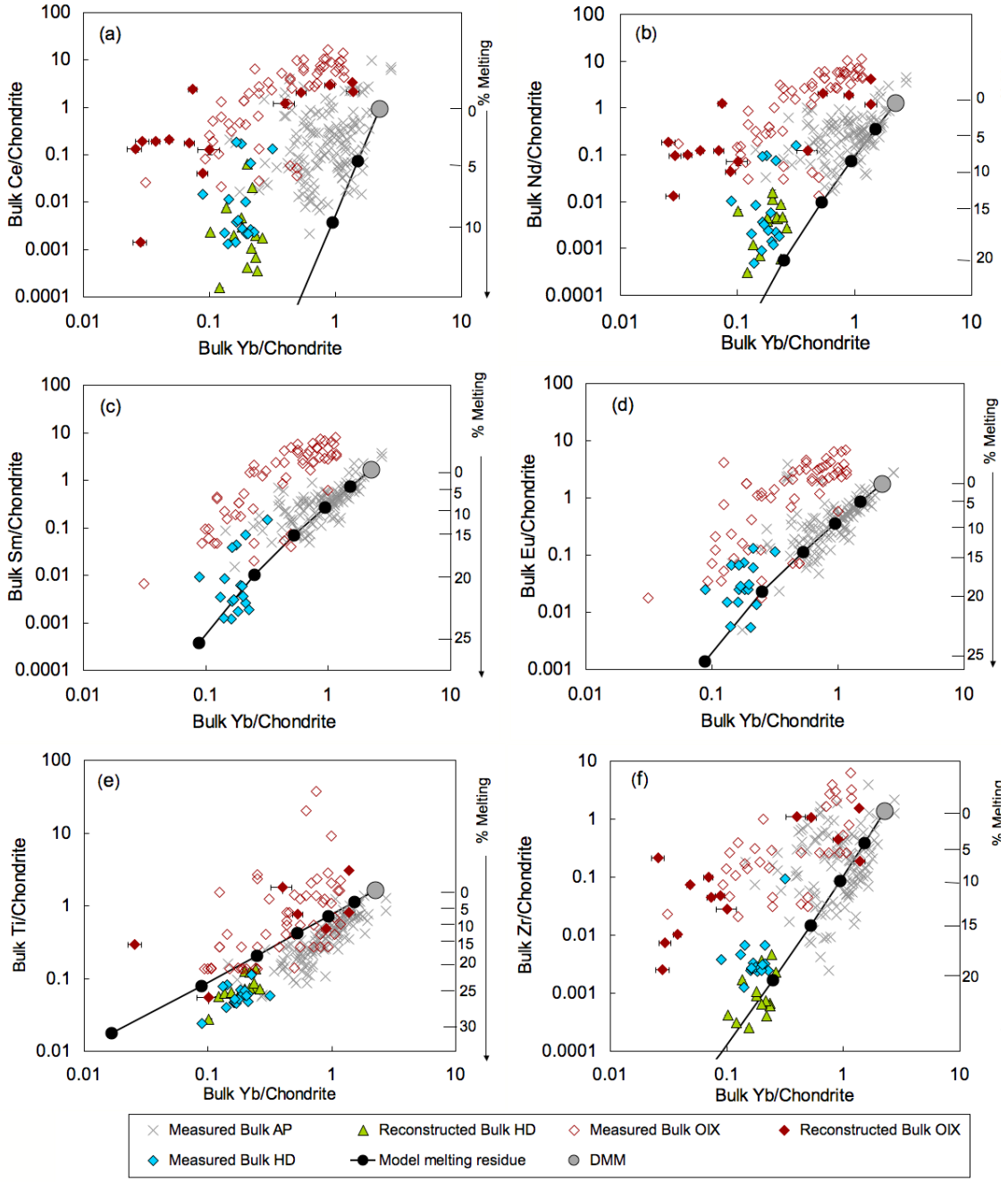

Figure 4.14 (Caption on following page)

Figure 4.14. Chondrite-normalised LREEs (a) Ce and (b) Nd, MREEs (c) Sm and (d) Eu and trace elements (e) Ti and (f) Zr in ocean island xenoliths and abyssal peridotites plotted against chondrite-normalised Yb concentrations. Error bars represent the uncertainty propagated from the variance calculated for modal percentage of each mineral phase using

the method of Solomon (1964). The error bars for Ce and Nd and for Hess Deep reconstructed data are smaller than the symbols. Also shown is the concentration of DMM (Workman and Hart, 2004) in comparison with ocean island xenoliths and abyssal peridotites. The extent of melting in ocean island xenoliths and abyssal peridotites is estimated by comparing observed concentrations of the above elements with those of a model-melting curve. The concentrations from 5 to 25% melting of DMM (Workman and Hart, 2004) are calculated using equations shown in Chapter 3 (Section 3.5.2). Data sources in addition to ocean island xenoliths analysed in this study are as follows: Canary Islands: Siena et al. (1991); Neumann (1991); Wulff-Pedersen et al. (1996), Neumann et al. (2002, 2004); Cape Verde: Bonadiman et al. (2005); Kerguelen: Gregoire et al. (1997; 2000); Sen and Leeman (1991); Tahiti: Qi et al. (1994); Ocean island xenolith data compilation from Simon et al. (2008). Abyssal peridotite data sources are as follows: MAR: Stephens (1997); Casey et al. (1997); Aumento and Loubat (1971); SWIR: Snow and Dick (1995); Godard et al. (2008); Garret Transform (EPR): Niu and Hekinian (1997) and Hess Deep data from Chapter 3. Compilation of abyssal peridotite data from Johnson et al. (1990) and Niu (2004).

In summary, it is apparent from Figure 4.13 that ocean island xenoliths and abyssal peridotites have similar ranges of Yb concentration and that ocean island xenoliths are strongly enriched in Ce, Zr and Nd and similar in Ti; i.e. ocean island xenoliths are strongly enriched in the most incompatible elements compared to abyssal peridotites.

4.4. Late-stage geochemical modifications in ocean island xenoliths and abyssal peridotites.

The above data was collected and collated in order to understand the geochemical processes in the oceanic lithospheric mantle. As discussed in Section 4.1, late-stage modifications in ocean island xenoliths can take place during emplacement of the xenoliths by ocean island basalts. Since emplacement-related geochemical modifications are not a part of typical lithospheric evolution, all xenoliths that show any signs of such

modifications need to be identified and then excluded from further discussion. In this section, late stage chemical modification during emplacement (for xenoliths) and by hydrothermal alteration (for abyssal peridotites) is considered.

4.4.1. Emplacement related chemical changes in ocean island xenoliths

Emplacement-related geochemical modifications in ocean island xenoliths are known to modify mineral chemistry. For example, Fe-Mg zoning is observed in olivines in mantle xenoliths from Cape Verde and is accompanied by textural evidence such as reaction rims around olivines as well as pyroxenes in the xenoliths (Shaw et al., 2006). The zoning profiles are used to calculate residence times of the xenoliths in the host lavas, as will be discussed below. The bulk rock trace element compositions discussed above (Fig. 4.14) may be also have been modified by interaction between the xenoliths and the host lavas. The hypothesis that the higher concentrations of highly incompatible elements such as Ce are due to modifications during emplacement can be modelled if the residence times of the xenoliths in the host lavas are known. Residence times for xenoliths in host lavas can also be calculated using Stoke's law, which takes into account the average settling rates of xenoliths based on their density and the rheological behaviour of the host lava (e.g. Spera, 1984). However, the calculation of residence times of xenoliths using Stoke's law have been argued to have large errors associated with them (e.g. Klugel, 1998; Shaw. 2004; Shaw et al, 2006). Thus, zoning profiles are used to derive residence times for xenoliths in host lavas.

Only two xenolith thin sections from Cape Verde (one websterite sample NI 120 C and one harzburgite sample NI 120 F), which are about 300 mm^2 in area (Supplementary Table 4.1), are traversed by basaltic veins (Fig. 4.4c; sample NI 120 C) up to 1 mm thick and show evidence for emplacement related metasomatism. Basalt veins surround most

minerals in these xenoliths unlike the rest of the suite analysed in this study. The forsterite content of olivines surrounded by host lava in these Cape Verde xenoliths is observably modified. The difference in forsterite content between rim and core is ~ 20 for sample NI 120 C (Fo 69.9 at rim and 89.9 at the core; Fig. 4.15; Supplementary Table 4.1) and ~17 for sample NI 120 F (Fo 71.41 at the rim and 89.06 in the core; Supplementary Table 4.1). Shaw et al. (2006) have calculated residence times of spinel bearing peridotite mantle xenoliths in basalts from Sal Island (Cape Verde) based on Fe-Mg interdiffusion between olivine from the xenolith and the host lava. The forsterite content of olivine is found to decrease through diffusive exchange of Mg and Fe with the host lava. Using the diffusion coefficient of Mg/Fe in olivine, the residence times of xenoliths in host lavas during ascent have been calculated to be ~ 4 years for mantle xenoliths (Shaw et al., 2006). The calculation uses a comparison between the measured Mg/Fe zoning profile in olivine and the compositional gradient acquired by modeling diffusive exchange of Mg/Fe in olivine. Using the mathematical model for diffusion in a semi-infinite plane (Crank, 1975) and the Mg-Fe diffusion coefficient for olivine (Chakraborty, 1997) for Mg# 80 (average Mg# of the zoned crystal) at 1200°C, a residence time of 2 years was calculated for Cape Verde xenoliths NI 120 C and NI 120 F from this study (Fig. 4.15). These samples are not considered in further discussions.

Unlike major elements, the REEs, Zr and Ti do not show zoning in any mineral on the scale of a thin section. To understand whether trace elements have been added to the mineral phases during emplacement, the residence times of the xenoliths in the host lavas can be used to model the maximum diffusion distances for REEs and other trace elements during emplacement. Since the measured and reconstructed bulk rock abundances of Ce in ocean island xenoliths are higher than abyssal peridotites (Fig. 4.14a) a model is

constructed to calculate diffusion distances for Ce in clinopyroxene, a major reservoir for Ce (Fig. 4.16). Using the diffusion coefficient for Ce in clinopyroxene (Van Orman et al., 2001) and the mathematical model for diffusion in a semi-infinite plane (Crank, 1975), a

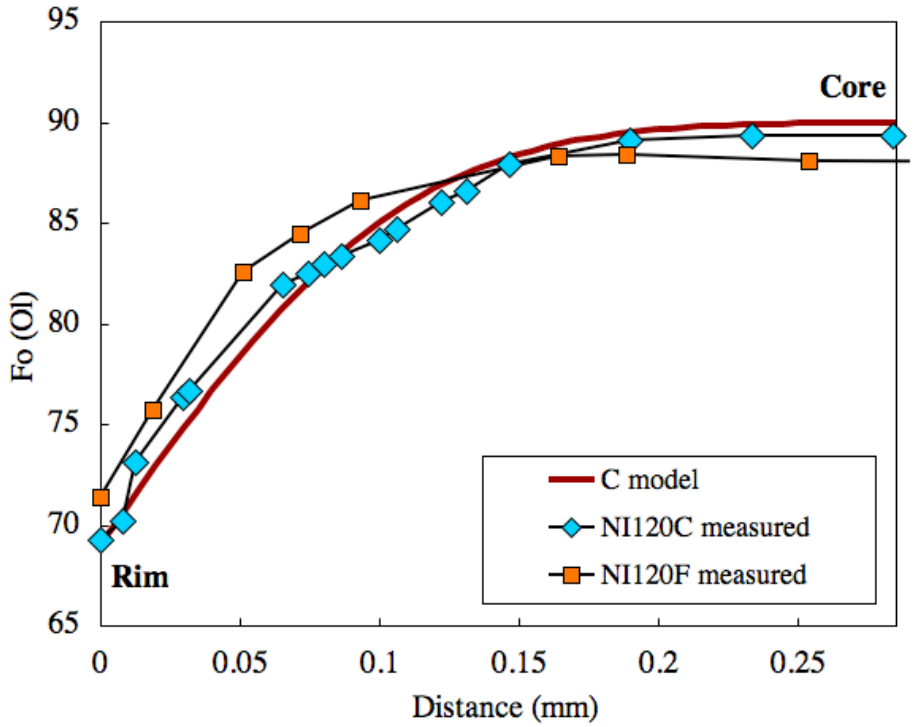

Figure 4.15. Zoning profile for forsterite (Fo) in olivine for ocean island xenolith sample NI 120 C from Cape Verde measured from rim to core. A comparison with a model zoning profile indicates an Mg-Fe diffusion time of ~ 2 years for the observed Fo-zoning.

model diffusion profile is constructed for Ce in clinopyroxene with an initial Ce-concentration of ~3 ppm (clinopyroxene in DMM; Workman and Hart, 2005) and a final concentration of 10 ppm (average Ce-concentration of clinopyroxene from this study). In a period of two years and assuming a temperature of 1200ºC, the diffusion distance for Ce in clinopyroxene is ~0.15 µm (Fig. 4.16). Residence times ranging from a few days to 7 years have been calculated for xenoliths from the Canary Islands (Klugel, 1998) and Cape Verde

(Shaw et al., 1998) based on Fe-Mg diffusion profiles in olivine. Considering a seven-year residence time, the diffusion of Ce into clinopyroxene increases up to a disctance of ~ 0.7 µm; i.e. only restricted to the rims of clinopyroxene crystals.

While xenoliths with young fractures have residence times ranging from a few days to 6 years, a residence time of 83 years has been suggested for mantle xenoliths from the Canary Islands due to stagnation of the xenoliths in the host lavas during ascent (Klugel, 1998). Increasing the residence time in the Ce-diffusion model to 83 years results in Ce concentration increasing by 1 ppm at a distance of ~5 µm from the rim of the crystal (Fig. 4.16). At this rate, the concentration of the core of a 20 µm clinopyroxene crystal increases by 1 ppm after 1000 years. The maximum time for xenoliths residing in host magmas being 83 years for old fractures (Klugel, 1998), any Ce diffusion from the host magma into clinopyroxene would only be restricted to the outermost rim (< 10 µm from the rim) of the crystal. Characteristics of old fractures such as pyroxenite veins are only observed in some pyroxenite xenoliths (e.g. Fig. 4.4e) and are not seen in any harzburgites or lherzolites analysed in this study. The zoning of Ce in clinopyroxene in xenoliths affected by short residence times in magmas during emplacement is not observed in any of the harzburgites and lherzolites in this study.

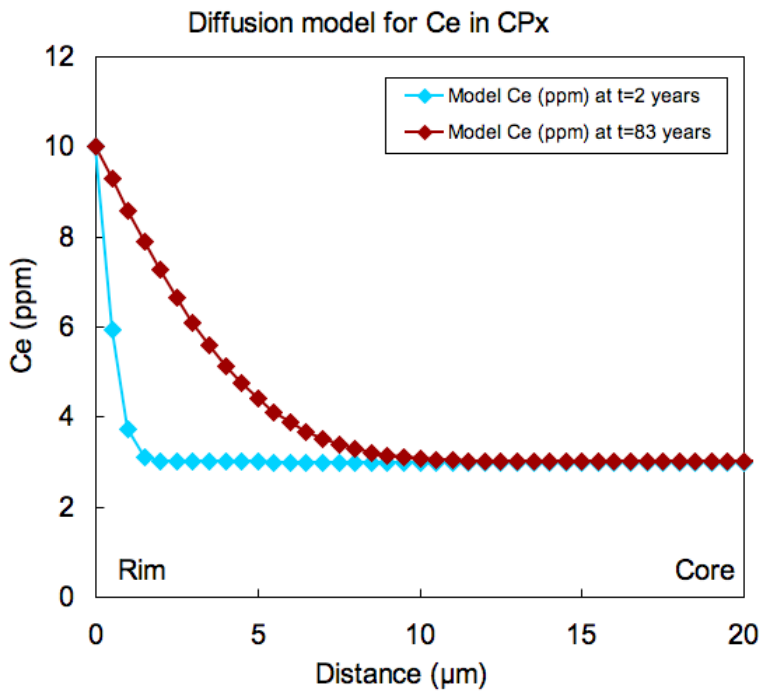

Figure 4.16. Model concentrations of Ce in clinopyroxene calculated using the diffusion coefficient of Van-Orman et al. (2001) at 1200ºC for time lengths of 2 (blue diamonds) and 83 years (red diamonds) time. The diffusion equation used in the calculation is for a semi-infinite plane (Crank, 1975).

4.4.2. Hydrothermal alteration in abyssal peridotites

The ocean island xenolith compositions are compared with abyssal peridotite compositions and therefore, understanding the effect of hydrothermal alteration on the latter is important to this study. The measured bulk concentration of CaO in abyssal peridotites is less than the reconstructed bulk concentration (Fig. 4.10a) and suggests loss of CaO during alteration in these samples (e.g. Godard et al., 2008). The measured bulk concentration of Na_2O in abyssal peridotites is higher than the reconstructed bulk concentration (Fig. 4.10b), which can be due to metasomatic enrichment of Na by melts (e.g. Seyler et al., 2003) or due to alteration by seawater. The reconstructed bulk composition of MgO is slightly higher than the measured bulk concentration (Fig. 4.10e).

A decrease in measured bulk MgO has been hypothesised as being due to MgO-loss during weathering (e.g. Snow and Dick, 1995; Niu, 2004). All abyssal peridotites undergo some hydrothermal alteration prior to being sampled and hence altered samples cannot be filtered out. Hence, any interpretations related to concentrations of fluid mobile elements that may be modified during alteration (e.g. CaO and MgO) must take into account geochemical modifications of abyssal peridotites during alteration.

4.5. The geochemical evolution of the oceanic lithospheric mantle

The above results outline a comparison of bulk rock major and trace element concentrations between all ocean island xenoliths and abyssal peridotites and some important geochemical differences are observed between the two suites of rocks. This study focuses on post-melting geochemical modifications in the oceanic lithospheric mantle and on just the main harzburgite / lherzolite lithologies, not the vein samples (dunites / pyroxenites). Henceforth, the terms ocean island xenoliths and abyssal peridotites include only harzburgite and lherzolite lithologies.

The concentrations of Al_2O_3 in ocean island xenoliths are lower than those of abyssal peridotites (Figs. 4.10 and 4.11), which could be interpreted either as indicating higher extents of melting in the xenoliths compared to the abyssal peridotites or that abyssal peridotites have undergone refertilisation causing an increase in Al_2O_3 in the bulk rock. The bulk rock concentrations of moderately incompatible trace elements Sc and V correlate positively with bulk rock Al_2O_3 in ocean island xenoliths and abyssal peridotites (Fig. 4.13) and support the hypothesis that the former could have undergone slightly greater extents of melting, or less refertilisation, than the latter. A comparison between mineral compositions of ocean island xenoliths with abyssal peridotites shows that the ocean island xenoliths

have higher olivine Mg# (Fig. 4.5b) and spinel Cr# (Fig. 4.5f) and lower Al_2O_3 in orthopyroxene (Fig. 4.5d) than abyssal peridotites, which also indicates higher extent of melting in ocean island xenoliths than abyssal peridotites.

Considering the model for melting beneath the ridge axis as shown in Figs. 1.3 and 4.1, the rocks that form the lower oceanic lithospheric mantle i.e. ocean island xenoliths should be less depleted than the abyssal peridotites. Three hypotheses are considered here in an attempt to explain the apparent higher extent of depletion in ocean island xenoliths than abyssal peridotites. One hypothesis is that fewer highly depleted abyssal peridotites are exposed on the ocean floor. The high extent of melting associated with fast-spreading ridges and that leaves behind a residue of highly depleted oceanic lithosphere are likely to have generated a large volume of basaltic crust i.e. a thicker crust above the depleted residue (Fig. 1.3b). Abyssal peridotites buried beneath a thicker crust may not be sampled close to the ocean floor, the only exception being peridotites from Hess Deep that are near the seafloor due to the rifting of the Cocos-Nazca Ridge toward the EPR (Chapter 3). The crustal thickness in the Hess Deep region is indicated to be ~5.6 km (Gillis et al., 2014). Although, highly depleted abyssal peridotites have been recovered along regions of low crustal thickness; e.g. along 15º 20’ N fracture zone (Godard et al., 2008) and along the Gakkel Ridge (Hellebrand et al., 2002a), these samples may represent local variations in such slow-spreading environments. For example, the highly refractory peridotites along the 15º20’ N fracture zone are interpreted as the result of an actively convecting mantle within a slow-spreading environment (Godard et al., 2008).

A second hypothesis is that abyssal peridotites initially undergo a similar extent of melting as ocean island xenoliths but their compositions have been modified by reaction with the high volume of melts ascending and converging into a narrow region at the top the

melting column. Although abyssal peridotites are considered as highly depleted residues of melting (e.g. Johnson et al., 1990), a small group of abyssal peridotites are interpreted to have undergone refertilisation with enrichment in incompatible elements and formation of interstitial clinopyroxene and amphiboles (e.g. Seyler et al., 2004; Hellebrand et al., 2002a; Brunelli et al., 2006; Warren and Shimizu, 2010). The formation of interstitial plagioclase in abyssal peridotites has been interpreted to follow trace element metasomatism, thus indicating that melt infiltration occurs in multiple stages beneath the ridge axis (Warren and Shimizu, 2010). The above processes can increase the concentrations of highly incompatible elements in abyssal peridotites. However, there is no data available on the mobility of moderately incompatible elements during refertilisation processes. Hence, the higher concentration of moderately incompatible trace elements in abyssal peridotites than ocean island xenoliths cannot be explained by refertilisation.

It is observed that the concentration of moderately incompatible elements in the Hess Deep sample suite analysed in Chapter 3 is identical to ocean island xenoliths (Figs. 4.13 and 4.14). As discussed in Chapter 3, trace element depletion in Hess Deep harzburgites is caused by high extent of melting that these rocks have undergone (up to 25%), which is also identical to ocean island xenoliths (Fig. 4.14). Hess Deep peridotites thus represent the rare samples of highly depleted residues that were sampled beneath normal crustal thickness and can thus be representative of the highest extent of depletion due to melting that the rocks from the oceanic lithospheric mantle can undergo. Interstitial, enriched clinopyroxenes or amphiboles are not observed in Hess Deep harzburgites analysed in Chapter 3. Melt-rock reaction in most Hess Deep harzburgites has not modified the compositions of mineral cores (Chapter 3) and hence, reconstructed bulk peridotite compositions represent unmodified depleted residues of melting. The similarity in the

composition of Hess Deep peridotites and ocean island xenoliths indicates that depletion during melting is the most likely reason for the low moderately incompatible elements in ocean island xenoliths.

A third hypothesis to explain the greater extent of depletion in the ocean island xenoliths relative to abyssal peridotites is that some of the highly refractory xenoliths from ocean islands may be fragments of ancient lithosphere that are spatially unrelated to the formation of the oceanic plate and the host plume (e.g. Simon et al., 2008). The low bulk rock Al_2O_3, CaO and HREEs in ocean island xenoliths are hypothesised to be the result of melting at potential temperatures above those normally observed at mid-oceanic ridges (Simon et al., 2008). Evidence for residues of ancient melt depletion events trapped as fragments in the oceanic lithospheric mantle is presented in the form of high Os-isotope ages of up to 3300 Ma for ocean island xenoliths (e.g. Cape Verde; Bonadiman et al., 2005). The old Os-isotope age fragments may also represent recycled continental lithosphere or sub-arc mantle wedge material (e.g. Simon et al., 2008). Model melting ages of up to 1700 Ma have been suggested for abyssal peridotites using Re-Os isotopes and are interpreted as evidence for ancient melt depletion events being preserved over time in the convecting mantle (Brandon et al., 2000). While the hypothesis that highly depleted ocean island xenoliths and abyssal peridotites may be fragments of ancient continental lithosphere has been investigated in several studies (e.g. Brandon et al., 2000; Bonadiman et al., 2005; Harvey et al., 2006; Simon et al., 2008; O'Reilly et al., 2009; Coltorti et al., 2010), the possibility that some of the highly depleted harzburgites formed as residues of melting at mid-oceanic ridges has not been excluded (Simon et al., 2008). The percentage of harzburgite formed as residues of melting at mid-ocean ridges has never been clearly

defined. In this study, the origin of depleted harzburgites as melting residues is investigated.

The ocean island xenolith sample suite that is unmodified during emplacement is used to decipher the post-melting geochemical processes in the lower portion of the oceanic lithospheric mantle. Based on the above results, a discussion leading to a model for the evolution of the lower oceanic lithospheric mantle is presented below. The following subsection discusses the post-melting geochemical modifications affecting the lower portion of the oceanic lithospheric mantle; i.e. the source region of ocean island xenoliths. Metasomatic enrichment in highly incompatible elements resulting in a geochemically evolved lower oceanic lithospheric mantle is highlighted. Finally, a model that reconciles post-melting geochemical processes such as metasomatism in the lower oceanic lithospheric mantle is described.

4.5.1. Trace elements as indicators of metasomatism in the lower oceanic lithospheric mantle

In order to determine the extent of melting in the oceanic lithospheric mantle, a melting model is constructed for comparison with ocean island xenoliths and abyssal peridotites. The composition of the depleted MORB mantle (DMM; Workman and Hart, 2005) is used as a starting point for the melting model. The concentration of an element *i* in the residue is calculated using the equation for non-modal fractional melting derived by Shaw (1970). Details of the calculation are given in Chapter 3. The partition coefficients used in the calculation of the concentration of an element in the residue are as in Kelemen et al. (2003) and are given in Table 3.7a. A melting porosity of 0.5% is considered based on Johnson and Dick (1992). Among the REEs, the LREEs are most incompatible while HREEs are moderately incompatible during melting. For example, the chondrite

normalised ratio of Ce/Yb changes from 0.39 in the DMM to 0.00039 in the residue after 15% melting and to $9.5*10^{-9}$ at 30% melting. Middle REEs such as Sm are extracted less rapidly from the solid residue than LREE and the Sm/Yb ratio changes from 0.71 in the DMM to 0.16 in the residue after 15% melting and to 0.009 in the residue at 30% melting. Since LREEs are incorporated into the melt phase, melt fractions that traverse the residual oceanic lithospheric mantle are enriched in LREEs compared to the residual mantle column. Such LREE-enriched melts are hypothesised to metasomatise residual rocks within the oceanic lithospheric mantle, which results in an increase in LREE abundances in the residual rocks (e.g. Johnson et al., 1990; Neumann et al., 2002, 2004).

The concentration of HREEs and Ti are less affected by metasomatism than the LREE due to their higher partition coefficients. Hence, the Yb or Ti abundance in residual rocks is a good indicator of the extent of melting. A comparison between the bulk rock concentrations of REE in ocean island xenoliths and abyssal peridotites shows that the concentration of Yb spans a wide range in both suites of rocks (Fig. 4.14). Some ocean island xenoliths from the Canary Islands (Lanzarote and Tenerife) and from the Kerguelen Islands exhibit lower abundance of Yb (0.015 to 0.15 times chondrite) than most abyssal peridotites (0.1 to 5 times chondrite; Fig. 4.14). When compared to the expected abundance as seen in the model DMM-melting residue (with a 0.5% melt porosity), the bulk concentration of Yb in ocean island xenoliths can be explained with a range of 0 to 25% melting (See Fig. 4.14c for the full range of melting extent model). The only exceptions are ocean island xenoliths from Lanzarote (Canary) and Kerguelen that resemble the residue of 27-30% DMM melting with respect to Yb-abundances (Fig. 4.14). It has been suggested that the upper mantle from the Canary Islands may have undergone a second period of melting and depletion due to heating of the lithosphere by the Canary Island plume

(Neumann et al., 2002). As discussed in Section 4.5 above, some of these highly refractory xenoliths from ocean islands are hypothesised as fragments of ancient lithosphere that are spatially unrelated to the formation of the oceanic plate and the host plume (Simon et al., 2008). Such extreme extents of melting are therefore not modeled in this study.

Bulk rock Yb concentrations in abyssal peridotites indicate 0-20% melting for most samples, with the exception of some examples that are similar to the low bulk Yb ocean island xenoliths (Fig. 4.14). The abyssal peridotite samples that have low bulk Yb concentration are not from a single locality, but are recovered from Hess Deep (Chapter 3), Garrett Transform (EPR; Niu and Hekinian, 1997); Kane Transform (MAR; Stephens et al., 1997); the 15º 20’ N Fracture Zone (MAR; Godard et al., 2008); SWIR and CIR (Niu, 2004). Although several locations around the globe are reported to have abyssal peridotites with low-Yb concentrations, the proportion of such samples of abyssal peridotites is far less than ocean island xenoliths with low Yb concentrations (Fig. 4.14).

Although highly incompatible elements are rapidly extracted from the residue as melting proceeds, the bulk rock concentrations of Ce, Nd, Sm and Eu in ocean island xenoliths are much higher than those expected for residues of DMM melting (Figs. 4.14a-d). Additionally, at a given Yb content the ocean island xenoliths have much higher LREE and MREE abundances than abyssal peridotites. In abyssal peridotites, the bulk concentrations of Ce and Nd are higher than the model DMM melting residue (Fig. 4.14), but the bulk concentrations of Sm and Eu for most abyssal peridotites match the concentrations predicted by the simple melting model based on the measured bulk Yb concentrations (Fig. 4.14). Higher than expected abundances of LREE in melting residues have been reported for ocean island xenoliths which have low Yb-abundances and are

postulated to be due to mantle metasomatism (Wulff-Pederson et al., 1996; Gregoire et al., 1997; 2000; Moine et al., 2000; Neumann et al., 2002; 2004; Bonadiman et al., 2005; Shaw et al., 2006; Simon et al., 2008). Light REE enrichment is also observed in rare abyssal peridotites (e.g. Johnson et al., 1990; Warren and Shimizu, 2010), but the extent of LREE enrichment for similar Yb concentrations is less in abyssal peridotites than that observed in ocean island xenoliths (Fig. 4.14).

A comparison between trace element concentrations of clinopyroxenes in ocean island xenoliths and the model concentrations of clinopyroxene in a melting residue indicates that LREE abundances in clinopyroxene from ocean island xenoliths are higher than those in clinopyroxene in equilibrium with the model DMM-melting residue (Fig. 4.17). Conversely, clinopyroxenes from abyssal peridotites have similar to lower LREE abundances than clinopyroxene in equilibrium with the model DMM-melting residue (Fig. 4.17). Since the bulk rock LREE abundances of both, ocean island xenoliths and abyssal peridotites are higher than the model DMM-melting residue, it can be said that while metasomatism affects both groups of rocks, the clinopyroxenes in ocean island xenoliths are affected by metasomatism to greater extent. As discussed in Chapter 3, the bulk rock LREE abundances in abyssal peridotites increases during metasomatism but the cores of clinopyroxenes in most samples retain their residual chemistry. With the exception of some xenoliths from Hawaii (Yang et al., 1998), the clinopyroxenes in all other ocean island xenoliths are enriched in Ce and Nd compared to the DMM-melting model and compared to abyssal peridotites with the same Yb content (Fig. 4.17). The higher Ce and Nd relative to abyssal peridotites and the melting model are interpreted as the result of diffusive transfer of these elements into the clinopyroxene from metasomatising melts. The low Ce and Nd clinopyroxene xenoliths from Hawaii (Figs. 4.17a-b) are interpreted as residues of

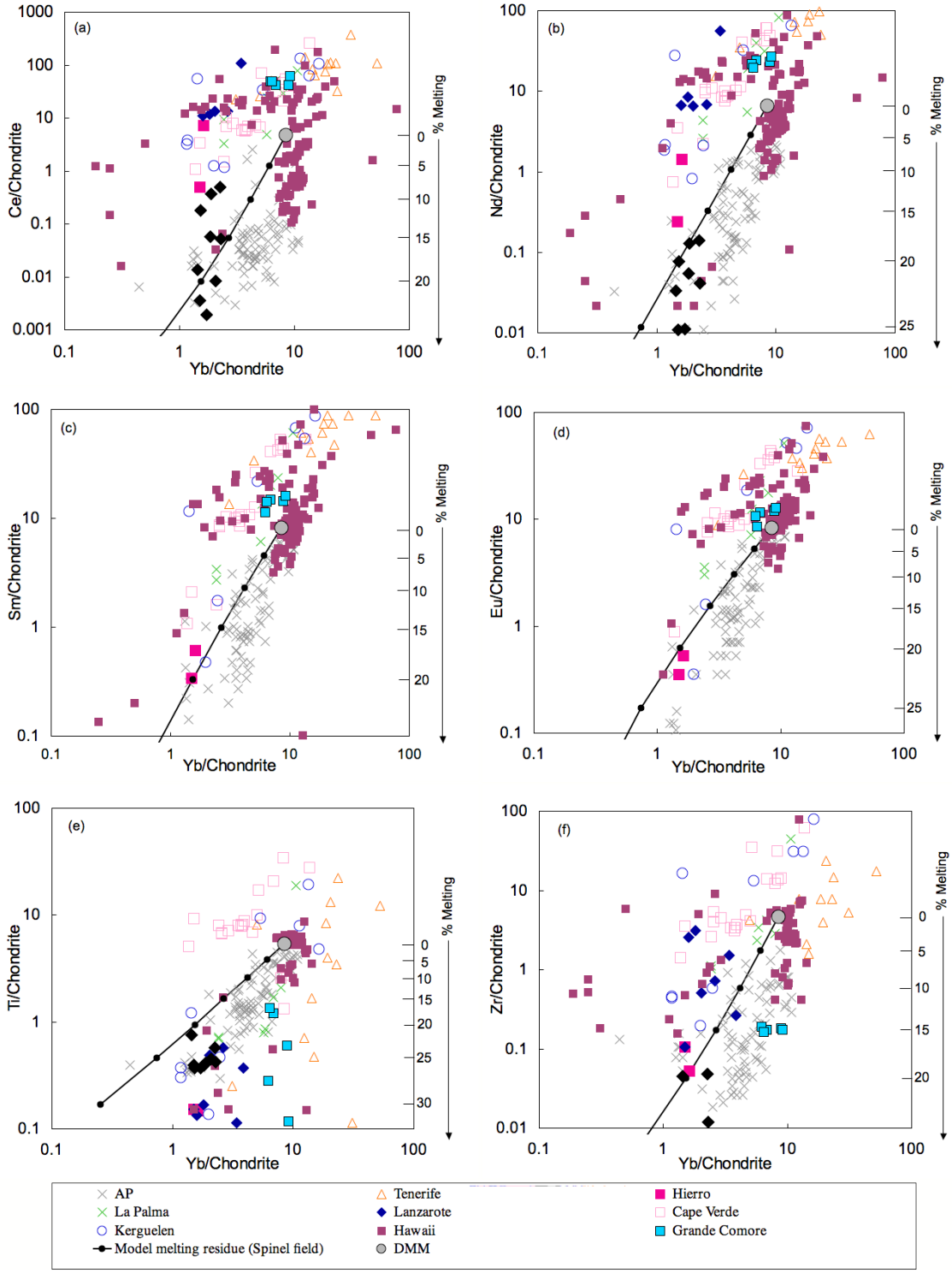

Figure 4.17 (Caption on next page)

Figure 4.17. Chondrite-normalised concentrations of (a) Ce, (b) Nd, (c) Sm, (d) Eu, (e) Ti and (f) Zr in clinopyroxene plotted against chondrite-normalised Yb in clinopyroxene from ocean island xenoliths and abyssal peridotites in comparison with concentrations of clinopyroxene in equilibrium with DMM (Workman and Hart, 2004). Also shown is the model-melting curve for DMM-clinopyroxene in equilibrium with the residue of 5 to 25% melting. The concentration of clinopyroxene is calculated in equilibrium with the residue of DMM-melting as in Figure 4.7. Mineral/melt partition coefficients (Kd) from Table 4.4 are used in the calculation. In addition to clinopyroxenes analysed in this study, the sources of clinopyroxene data are as follows: Kerguelen: Gregoire et al. (2000); The Canary Islands: Neumann et al. (1991); Siena et al. (1991); Neumann et al. (2002); Wulff-Pedersen et al. (1996); Cape Verde: Bonadiman et al. (2005); Grande Comore: Coltorti et al. (1999); Hawaii: Sen (1988); Sen et al. (1993); Sen and Jones (1988); Sen and Presnall (1996); Yang et al. (1998). Sources for abyssal peridotite clinopyroxene data are as follows: American-Antarctic Ridge: Dick (1989); SWIR: Dick (1989); Johnson et al. (1990); MAR: Tartorotti et al. (2002); Johnson and Dick (1992); CIR: Hellebrand et al. (2002); Workman and Hart (2004); Hess Deep (Dick and Natland, 1996); Chapter 3.

MORB melting, which have not been modified by metasomatism (Yang et al., 1998). The concentrations of Sm and Eu are also higher in clinopyroxenes from most ocean island xenoliths compared to those in the model DMM-melting residue and in abyssal peridotites; this is with the exception of two xenoliths each from Kerguelen and Hierro in which the concentrations of Sm and Eu in clinopyroxene are similar to the DMM-melting residue (Figs. 4.17c-d).

The abundance of Yb in clinopyroxenes in some ocean island xenoliths and abyssal peridotites is higher than in clinopyroxene in DMM (Fig. 4.17). High Yb-concentrations in clinopyroxenes in abyssal peridotites from the CIR relative to clinopyroxene in DMM has been hypothesised to be a result of melting in the garnet field where Yb is compatible and remains in the solid (Hellebrand et al., 2002b). Similarly, ocean island xenoliths from

Hawaii and Cape Verde are also interpreted as having undergone melting in the garnet field followed by re-equilibration in the spinel field (Yang et al., 1998; Bonadiman et al., 2005). Hellebrand et al. (2002b) constructed a melting model that calculates the composition of clinopyroxene in equilibrium with the residue of melting of a depleted mantle source composition in the garnet field. Using the approach of Hellebrand et al. (2002b), a model is constructed here to calculate the composition of a clinopyroxene in equilibrium with DMM (Workman and Hart, 2005) that has undergone melting in the garnet field followed by equilibration in the spinel field (Fig. 4.18). The maximum extent of melting shown in the garnet-field melting model in Fig. 4.18 is 12% followed by equilibration in the spinel field. From Figure 4.18, the higher Yb-concentration in clinopyroxene in some abyssalperidotites compared to that in DMM can be interpreted as up to 2% melting of the DMM source in the garnet field followed by equilibration in the spinel field. However, the higher Yb-concentrations in clinopyroxenes in ocean island xenoliths from Hawaii and Tenerife compared to that in DMM indicate up to 12% melting in the garnet field (Fig. 4.18). Melting of more than 2% in the garnet field is not thought to be plausible since the MORcrustal thickness generated by >2% melting in the garnet field exceeds the normal MOR thickness of ~7 km (e.g. Yang et al., 1998).

A comparison between partition coefficients for REEs between orthopyroxene and clinopyroxene in ocean island xenoliths with published values (Hellebrand et al., 2005) indicates that clinopyroxenes in ocean island xenoliths are enriched in REEs relative toorthopyroxene (Fig. 4.19) and is interpreted as disequilibrium between the two pyroxenes (e.g. Simon et al., 2008). The higher Yb-concentration in clinopyroxene from Tenerife and Hawaiian ocean island xenoliths compared to that in DMM may be due to precipitation of

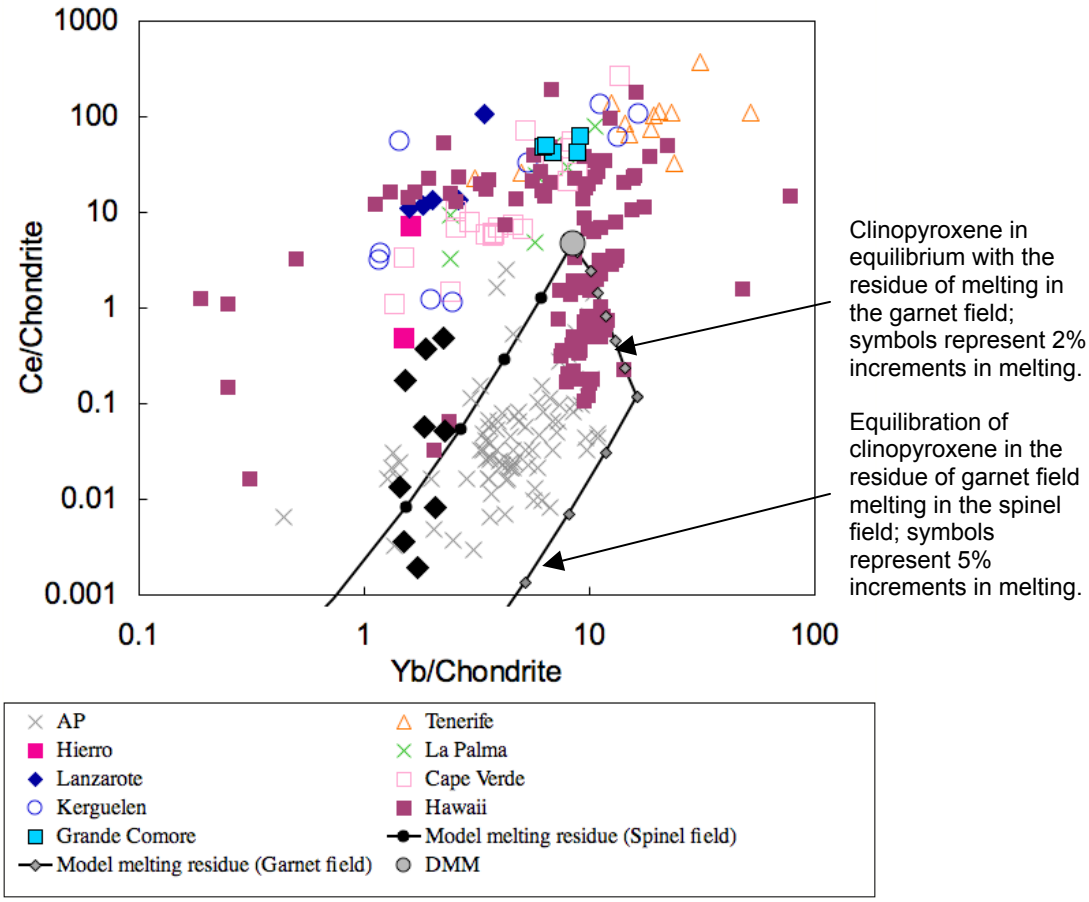

Figure 4.18. Chondrite normalised Ce-concentration in clinopyroxene from ocean island xenoliths and abyssal peridotites in comparison with clinopyroxene in equilibrium with a model melting residue of DMM in the spinel field. The model-melting residue represents melting in 5% increments. Also shown is the clinopyroxene composition in equilibrium with the model residue of melting of DMM in the garnet field followed by equilibration in the spinel field.

secondary clinopyroxene from melts rich in Yb along with other REEs. Recent studies suggest that down-temperature, subsolidus exchange between orthopyroxene and clinopyroxene can increase the HREE abundances in clinopyroxene (Sun and Liang, 2014).

The hypothesis for melting in the garnet field resulting in higher HREE in clinopyroxene from abyssal peridotites than in clinopyroxene in equilibrium with the model DMM-melting residue may not be valid.

4.5.2. When and where does metasomatism occur in the lower oceanic lithospheric mantle?

It has been suggested that small melt fractions from the asthenosphere at the base of the oceanic lithosphere metasomatise the oceanic lithospheric mantle repeatedly as the lithosphere ages (e.g. Pilet et al., 2008; Niu et al., 2011; Figs. 1.4b and 4.1). The interaction between the residual lithosphere and melts percolating from the base of the lithosphere has been modeled as the process leading to the formation of the enriched mantle (EM2) reservoir giving rise to the Samoan ocean island basalts (Workman and Hart, 2004). In order to test the model for metasomatism of the oceanic lithospheric mantle by small-scale

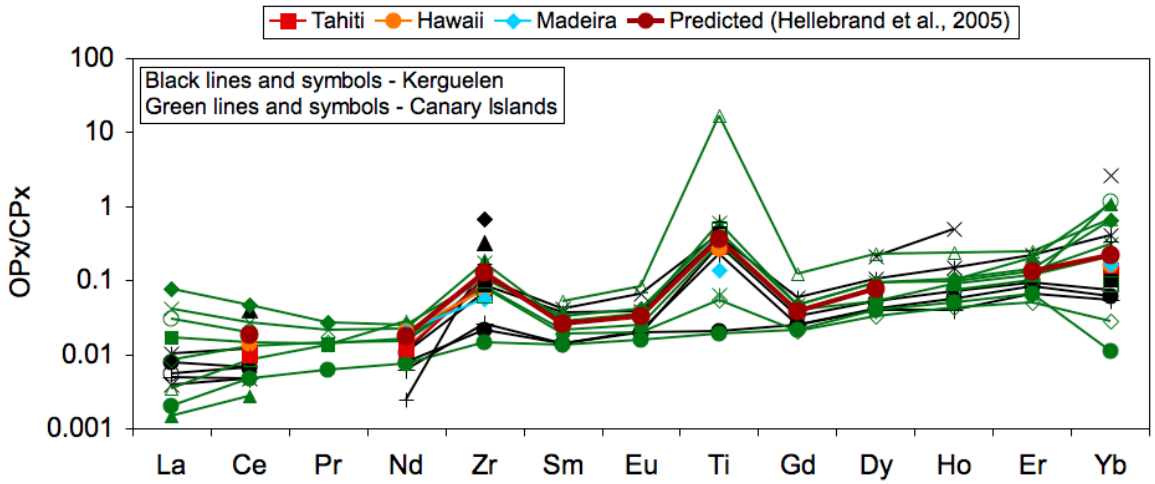

Figure 4.19. Orthopyroxene/Clinopyroxene REE ratios for harzburgite and lherzolite ocean island xenoliths compared with published partition coefficients for pyroxenes in equilibrium in spinel harzburgites (Hellebrand et al., 2005).

convection, the concentrations of incompatible elements Ce, Nd, Sm and Eu in bulk rock harzburgites and lherzolite are plotted as a function of lithospheric age. As mentioned earlier in this chapter, the concentration of incompatible elements may be modified due to emplacement-related metasomatism affecting the boundaries of crystals. To overcome this issue, bulk rock trace element concentrations are reconstructed (Fig. 4.20) using available mineral composition and modal data from this study and plotted along with measured bulk rock concentrations (Fig. 4.21) against age of the oceanic lithosphere for the respective ocean island. With the limited number of reconstructed bulk rock data available for each ocean island, it is not convincing that any correlation exists between the extent of metasomatism and age of the oceanic lithosphere (Fig. 4.20). No systematic correlation is observed between measured bulk rock abundances of REEs with age of the oceanic lithosphere (Fig. 4.21).

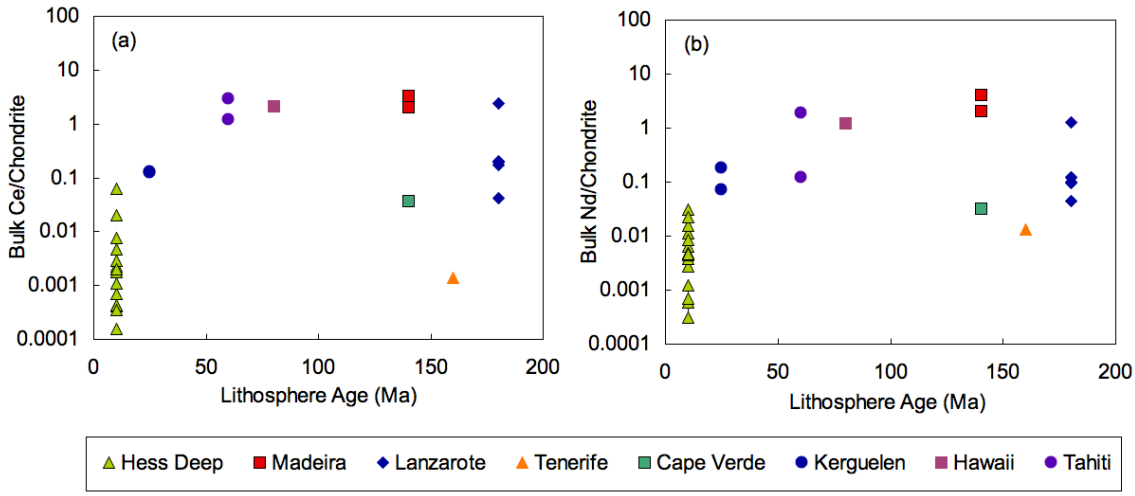

Figure 4.20. Chondrite-normalised reconstructed bulk rock abundances of (a) Ce, (b) Nd, (c) Sm and (d) Eu in ocean island xenoliths plotted against age of oceanic lithosphere beneath each ocean island. Also shown for comparison are chondrite-normalised bulk rock abundances of REEs in abyssal peridotites. No systematic variation is observed with age in both, measured and reconstructed, bulk rock concentrations of the REEs.

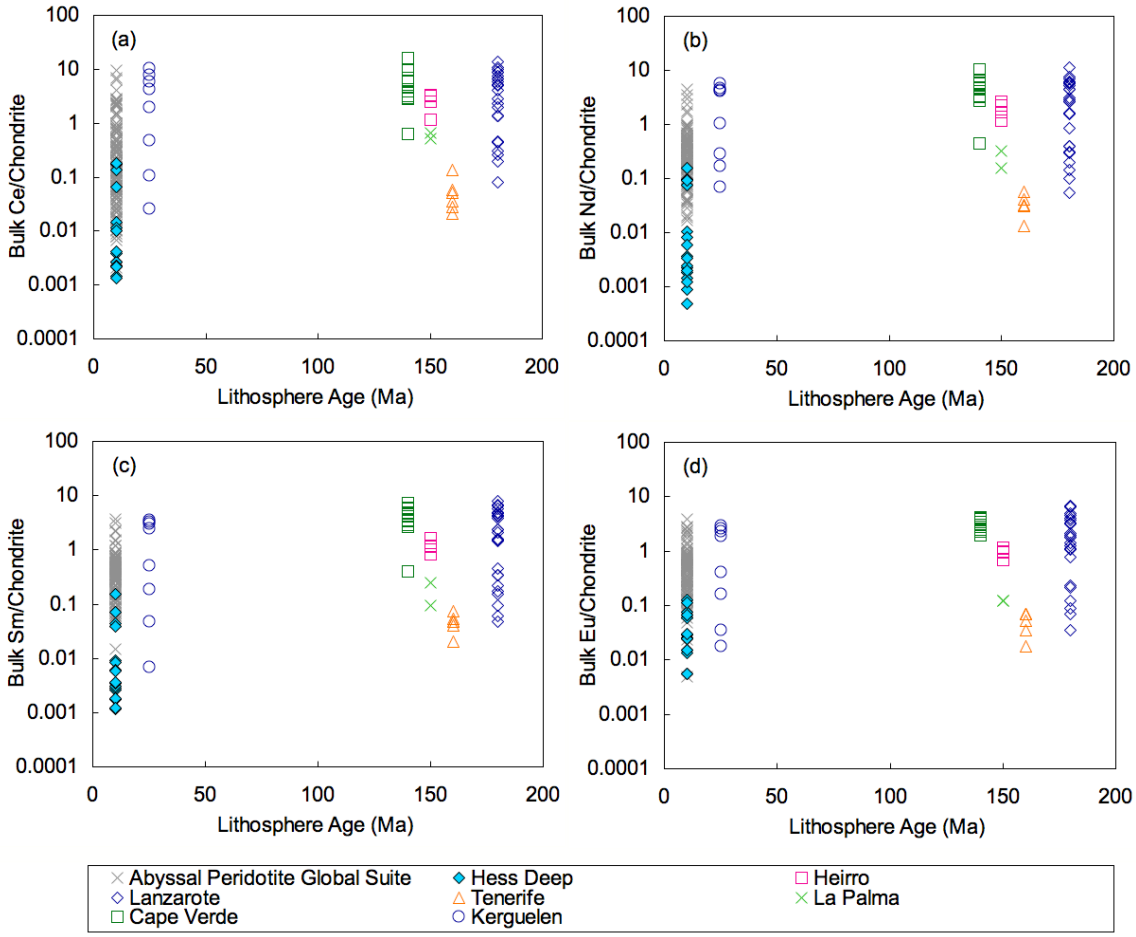

Figure 4.21. Chondrite-normalised reconstructed bulk rock abundances of (a) Ce, (b) Nd, (c) Sm and (d) Eu in ocean island xenoliths plotted against age of oceanic lithosphere beneath each ocean island. Also shown for comparison are chondrite-normalised bulk rock abundances of REEs in abyssal peridotites. No systematic variation is observed with age in both, measured and reconstructed, bulk rock concentrations of the REEs.

A second model that can explain the enrichment of incompatible elements involves all or most metasomatic enrichment occurring in the young oceanic lithospheric mantle.

The simplest source of metasomatising melts for young oceanic lithosphere is within the wings of the melting column (Fig. 4.1). If these melts are not focused to the ridge axis but instead migrate vertically into the overlying lithosphere, they could metasomatise it (Fig. 4.1). It has been suggested that metasomatic veins within the lithospheric mantle originate as small degree melts in the asthenosphere and in the vicinity of the melting column (Pilet et al., 2008). As described in Section 4.1, the melts generated in the wings of the melting column are likely to be enriched in highly incompatible elements compared to the residual oceanic lithospheric mantle. These small degree-melts may concentrate near the base of the oceanic lithospheric mantle due to their buoyancy and metasomatise the overlying lithosphere (Niu, 2008).

4.6. Summary and conclusion

The following points summarise the results and interpretations of this chapter:

- The concentration of moderately incompatible oxide Al_2O_3 and elements such as Sc, V and Yb in most ocean island xenoliths is lower than abyssal peridotites.
- A comparison between the chondrite-normalised bulk rock Yb-concentration in ocean island xenoliths and abyssal peridotites with a model residue of DMM melting suggests that the majority of ocean island xenoliths represent the residue of 0 to 25% melting of DMM. Although a majority of abyssal peridotites resemble the residue of 0-20% melting of DMM (Fig. 4.14), a small subset of samples from several locations around the globe are as depleted as ocean island xenoliths with respect to Yb-abundances (Fig. 4.14; Section 4.5.1). Thus the extents of melting is ~5% higher for ocean island xenoliths in general.

- Indications of metasomatism are observed in both, ocean island xenoliths and abyssal peridotites in the form of higher bulk rock Ce and Nd concentration than the model-melting residue of DMM, but the extent of metasomatism is much higher in ocean island xenoliths.
- The small number of reconstructed bulk rock Ce and Nd concentrations of ocean island xenoliths do not show a clear correlation with age of the oceanic lithosphere from which the xenoliths are derived (Fig. 4.20). This is interpreted as indicating that small melt fractions that are generated at the base of the lithosphere, for example by small scale convection, do not continually metasomatise the residual lithosphere. Instead, it is interpreted that most of the metasomatism occurs in a young oceanic lithosphere closer to the vicinity of the ridge axis.
- The measured and reconstructed bulk concentration of Al_2O_3 in ocean island xenoliths is lower than in abyssal peridotites (Fig. 4.10), which generally would be interpreted as indicating a higher extent of melting in the former compared to the latter. This is counter-intuitive to the expected scenario as shown in Figures 1.3 and 4.1 where the upper portion of the oceanic lithospheric mantle represents the residue of higher extents of melting than the lower portion. The most depleted suite of abyssal peridotites studied here i.e. Hess Deep harzburgites (Chapter 3) that form in “normal” MOR environment are as depleted as ocean island xenoliths (Fig. 4.14). Hess Deep harzburgites are exposed as a result of tectonic processes and are a rare example of peridotites that are viable for comparison in terms of the extent of melting. It is thus interpreted that abyssal peridotites are generally as depleted as ocean island

xenoliths but the most depleted abyssal peridotites have not been recovered due to the thick crust overlying them.

- The higher concentration of moderately incompatible elements such as Al_2O_3, Sc and V in abyssal peridotites relative to ocean island xenoliths may be attributed to lower extent of melting of the former. This is supported by the observation that peridotites from Hess Deep, which exhibit greater extent of melting than most abyssal peridotites have similar concentrations of Al_2O_3, Sc and V as ocean island xenoliths.

- Abyssal peridotites and ocean island xenoliths are both affected by post-melting metasomatism but in very different ways. In the case of abyssal peridotites from Hess Deep, the bulk rock abundances of LREEs increase but the clinopyroxenes retain their residual mineral chemistry while clinopyroxenes in ocean island xenoliths are enriched in LREEs relative to clinopyroxene in equilibrium with the model DMM-melting residue (Figs. 4.17a and 4.17b). Metasomatism in abyssal peridotites may thus be restricted to grain boundaries but extends into mineral crystals in ocean island xenoliths.

5. Summary and Future Work

The goal of this thesis was to understand the thermal and geochemical evolution of the oceanic lithospheric mantle from a petrological point of view. The thermal models for the oceanic lithospheric mantle i.e. the half space model, the plate model and the CHABLIS model were to be tested using petrological samples i.e. ocean island xenoliths. Understanding the thermal structure of the oceanic lithospheric mantle using xenoliths required the determination of equilibration temperatures and pressures for the xenoliths. While several geothermometers are available for the determination of temperatures, only the Ca-in-olivine geobarometer (Kohler and Brey, 1990) is suitable for the calculation of pressures of spinel peridotites. The limitations of the Ca-in-olivine geobarometer of Kohler and Brey (1990) are discussed in Chapter 2 and a new geobarometer (Eq. 2.13) is calibrated using results of 0.1 MPa experiments conducted in this study. A summary of the experimental results and the calibration of the new Ca-in-olivine geobarometer are presented in Section 5.1.

The geochemical evolution of the oceanic lithospheric mantle is studied with respect to compositional changes associated with melting and post-melting geochemical modifications. Mineral and bulk rock major and trace element data are collected and compiled for abyssal peridotites (Table 3.1) and ocean island xenoliths (Table 4.3). The results of this study are summarised in Section 5.2 and a model for the geochemical evolution of the oceanic lithospheric mantle is constructed (Section 5.2.1).

5.1. An empirical geobarometer for spinel peridotites

The partitioning of Ca between olivine and clinopyroxene in the presence of a low-Ca pyroxene has been calibrated as a geobarometer (Kohler and Brey, 1990). However, the previously hypothesised (Adams and Bishop, 1986) effect of the Fe-content of the system on the Ca-in-olivine geobarometer was not accounted for in the Kohler and Brey (1990) calibration. Since a wide range of Fo (Ol) was observed in ocean island xenoliths, a geobarometer that took the compositional parameter into account was required. To this end, a series of experiments were conducted at 0.1 MPa with a wide range of Fe-contents in the starting compositions (Table 2.1) and a geothermometer that incorporates the effect of Fo (Ol) on the partitioning of Ca between olivine and clinopyroxene was calibrated (Eq. 2.11). The Ca-in-olivine geothermometer calibrated in Chapter 2 successfully demonstrates the dependence of the Ca-content of olivine on the Fe-content of the system (Fig. 2.2). Whether the low-Ca pyroxene is pigeonite or orthopyroxene does not noticeably affect the partitioning of Ca into olivine and a linear relationship between Fo (Ol) and Ca-in-olivine is demonstrated (Fig. 2.3).

The results of the 0.1 MPa experiments conducted in this study were combined with the high-pressure experiments of Kohler and Brey (1990) and an empirical geobarometer (Eq. 2.13) for spinel peridotites is calibrated. In addition to studying metasomatism in the lower oceanic lithospheric mantle, an attempt is made to study the thermal structure of the oceanic lithospheric mantle using mantle xenoliths. However, it is observed that the xenoliths are largely scattered in the temperature-depth (pressure) space (Fig. 2.8). No correlation is observed between temperature and depth derived for the ocean island xenoliths with the isotherm constructed for the half space model of the respective age of oceanic lithosphere (Figs. 2.8). The large uncertainties in calculated pressures render the

current Ca-in-olivine geobarometer unsuitable for use on ocean island xenoliths for the purpose of testing thermal models for the oceanic lithospheric mantle.

Mineral major element data necessary for geothermobarometry was collected for mantle xenoliths from the ocean islands of Kerguelen, Tahiti, Hawaii, Cape Verde, Madeira and the Canary Islands (Supplementary Table 4.1). A dataset was compiled with mineral chemistry of xenoliths analysed previously (Table 4.3; Kuno, 1969; Sen, 1987; Goto and Yokoyama, 1988; Siena et al., 1991; Neumann, 1991; Neumann et al., 1995; 2002; 2004; Hauri et al., 1993; Hauri and Hart, 1994; Qi et al., 1994; Johansen, 1996; Wulff-Pedersen et al., 1996; Yang et al., 1998; Coltorti et al., 1999; Gregoire et al., 2000; Deplech et al., 2004; Tommasi et al., 2004; El Rus et al., 2005; Bonadiman et al., 2005). The gaps in the mineral chemistry data are realised as a majority of previous studies focus on bulk rock chemistry.

5.2. The geochemical evolution of the oceanic lithospheric mantle

The oceanic lithospheric mantle forms as the residue of partial melting beneath the ridge axis. The extraction of incompatible elements during melting decreases the density and increases the viscosity of the residual layer, which forms the mechanical boundary layer at the top of the less viscous asthenosphere. However, post-melting metasomatism significantly modifies the composition of the residual oceanic lithospheric mantle by the addition of highly incompatible elements from melts from the wings of the melting column. Subduction of this oceanic lithospheric mantle makes it an important geochemical reservoir that recycles elements into the Earth's mantle thus driving an important component of the global geochemical cycle. A study of the geochemical evolution of the oceanic lithospheric mantle is thus important to understand the global geochemical cycle.

In an attempt to investigate the geochemical evolution of the upper oceanic lithospheric mantle, a suite of "depleted" harzburgites from Hess Deep ODP Site 895 were analysed for mineral and bulk rock geochemistry. The logic behind analysing both, mineral and bulk composition was to understand geochemical changes on a mineral and bulk rock basis. It was inferred that the residual mineral chemistry is not affected by metasomatism even when the bulk-rock is. Evidence for plagioclase precipitation was also observed in the harzburgites from Hess Deep ODP Site 895 analysed here.

The geochemical evolution of the lower oceanic lithospheric mantle is investigated using ocean island xenoliths in Chapter 4. In addition to facilitating geothermobarometric analyses in Chapter 2, mineral chemistry was also utilised in the calculation of bulk rock geochemistry of ocean island xenoliths in combination with modal percentages of minerals in the xenoliths. This methodology for calculating bulk rock composition was adapted in order to avoid contamination by basalt veins that traverse the ocean island xenoliths. Unlike abyssal peridotites, the minerals in ocean island xenoliths are affected by geochemical modifications during metasomatism i.e. clinopyroxene in ocean island xenoliths show elevated concentrations of LREE relative to HREE (Fig. 4.17). Metasomatism in ocean island xenoliths does not correlate with age of the oceanic lithosphere (Figs. 4.20 and 4.21). This suggests that geochemical modifications due to metasomatism occur in the younger oceanic lithosphere.

5.2.1. A working model for the evolution of the oceanic lithospheric mantle

The model proposed for the chemical evolution of the oceanic lithosphere is illustrated in Figure 5.1. The oceanic lithospheric mantle in this model represents a residue of 0 to ~25% melting in the melting column. The lower portion of the residual melting column, as represented by ocean island xenoliths (Figs. 1.3, 4.1 and 5.1), is metasomatised

by melts generated in the wings of the melting column. Such metasomatism is indicated by LREE enrichment in both clinopyroxene and in measured bulk-rocks in ocean island xenoliths relative to abyssal peridotites and model melting residues. The lack of correlation between LREE abundances in ocean island xenoliths and age of the oceanic lithosphere indicates that metasomatism is not a significant process in the aging oceanic lithospheric mantle.

The upper portion of the residual oceanic lithospheric mantle represented by abyssal peridotites (Figs. 1.3, 4.1 and 5.1) undergoes melt-rock reaction resulting in LREE enrichment of only the rims of clinopyroxene. Melts traversing through the oceanic lithospheric mantle interact with the residual rocks and crystallise plagioclase in regions where the upper mantle is cool enough for melts to become plagioclase saturated (Fig. 5.1). The precipitation of plagioclase increases the concentration of LREE in the bulk rock along with generating a positive Eu anomaly in it (Fig. 3.11). There is no evidence for substantial chemical modification of the oceanic lithosphere after it migrates out of the axial region.

A comparison between the median values of the concentrations of moderately incompatible elements such as Al_2O_3, CaO, V and Sc between abyssal peridotites and ocean island xenoliths indicates that most ocean island xenoliths are depleted in these elements compared to abyssal peridotites (Figs. 4.10 and 4.13). Considering the model for melting beneath the ridge axis, the perception would be that the lower oceanic lithospheric mantle is less depleted than the upper oceanic lithospheric mantle (Figs. 1.3, 4.1 and 5.1). The apparent higher concentrations of moderately incompatible elements in abyssal peridotites than ocean island xenoliths are interpreted to be due to melt-rock reaction in the upper oceanic lithospheric mantle during melt extraction at the top of the melting column. Elevated concencentrations of moderately incompatible in abyssal peridotites are not

accompanied by elevations in highly incompatible elements compared to ocean island xenoliths. Higher concentrations of moderately incompatible elements such as Al_2O_3 may be the result of plagioclase precipitation in the upper oceanic lithospheric mantle (Chapter 3).

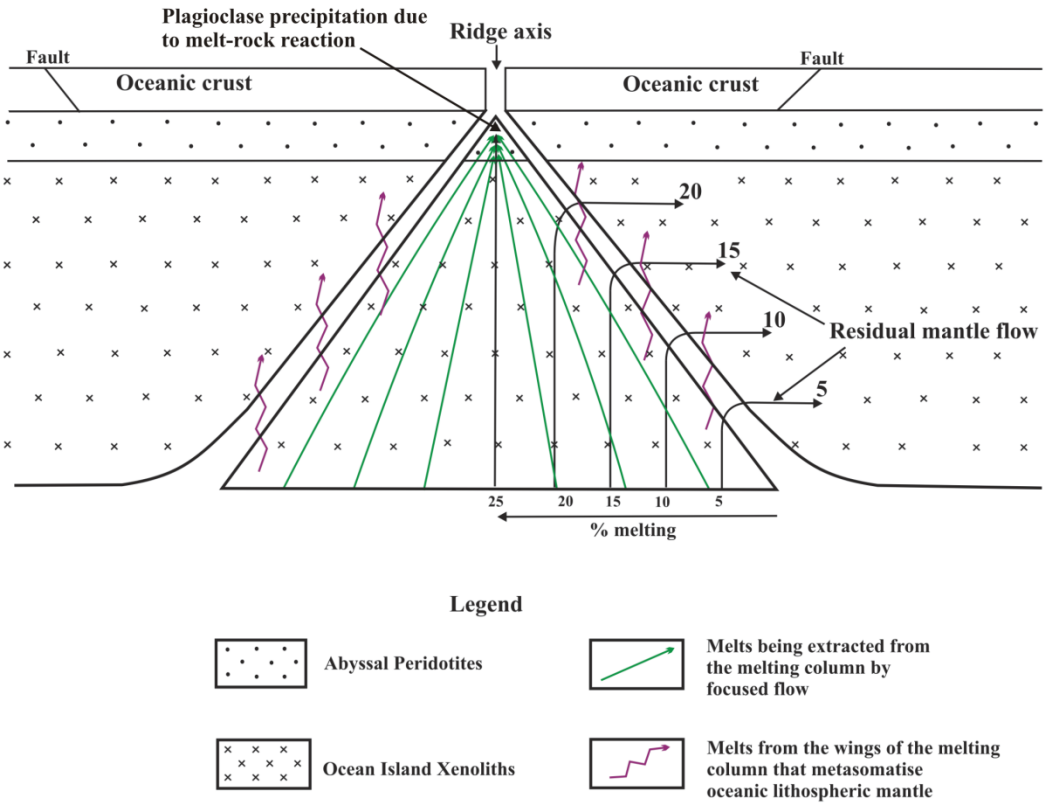

Figure 5.1. Illustration of the model for the geochemical evolution of the oceanic lithospheric mantle.

5.3. Future work

5.3.1. Future work on the Ca-in-olivine geothermobarometer

As mentioned in Chapter 2, high-P experiments need to be run with a wide range of Mg# of olivine in order to better constrain the Ca-in-olivine geobarometer. The following experimental approach is proposed for future work for the calibration of the Ca-in-olivine geobarometer. Following Kohler and Brey (1990) the experiments can be conducted using natural spinel lherzolite samples. The experimental methodology of Kohler and Brey (1990) i.e. using a single olivine crystal as the sample container in carrying out experiments for the calibration of the Ca in olivine geobarometer can be adopted (Fig. 5.2). This has proved very efficient in minimizing the problem of Fe loss to Pt sample containers. In the experimental set-up suggested in Figure 5.2, the experimental charges can be placed into holes drilled into the olivine crystal and covered with olivine lids drilled out of the same material as the sample container (Fig 5.2). In this way, experiments for increasing and decreasing Ca in olivine can be run at the same time in one container.

Olivine in starting materials for these experiments can be mantle-derived low-Ca-olivine, selected from localities that are known to consist of mantle rocks with low Ca-olivines that have cooled slowly and are therefore in equilibrium with orthopyroxene and clinopyroxene. For reversal experiments (where olivines lose Ca), olivines from volcanic rocks can be used since they have higher Ca-contents than plutonic rocks (Simkin and Smith, 1970). The rates of reactions can be increased by adding 2-5% water to the starting composition as previously done by Kohler and Brey (1990) although some experiments should be run dry to test whether this changes the solution mechanism of Ca in olivine.

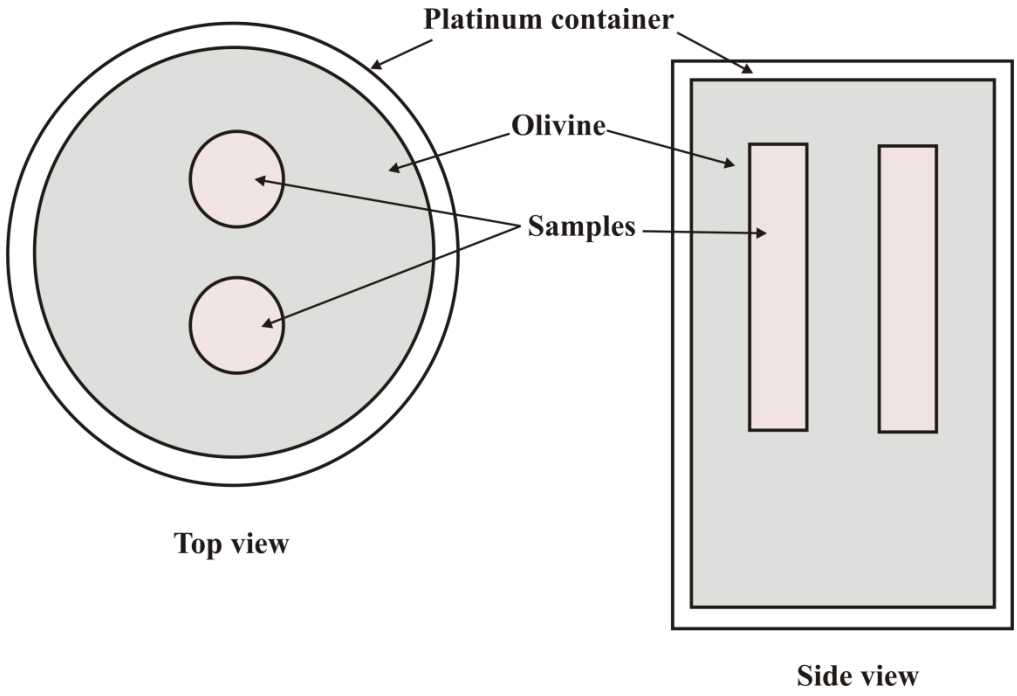

Figure 5.2. Schematic diagram of the experimental set up for high-pressure experiments. Holes will be drilled in an olivine crystal and experimental charges placed into these. The crystal will then be placed inside a platinum container. Since two samples can be run at a time, the reversal runs can be carried out at the same time and under the exact same conditions as the initial experiments.

Once the temperature and pressure conditions at which the xenolith equilibrated are determined, the results of the above-discussed experiments on the Ca in olivine geobarometer can be used to determine equilibrium pressure conditions for the mantle xenoliths. Accurate determination of temperature is of absolute necessity for using this geobarometer. Uncertainties in determination of equilibrium temperature can be minimised by using a variety of existing geothermometers. Elements used in exchange reactions for different geothermometers have a minimum temperature, called the closure temperature, below which elemental exchange nearly ceases. Equilibrium temperatures measured using

exchange thermometers should be well above the predicted closure temperature for each system. The use of multiple geothermometers is essential to test the reproducibility of the results. By combining temperature and pressure for mantle xenoliths derived from different ages of the oceanic lithosphere, multiple geotherms can be constructed for oceanic lithosphere of different ages, which can then be compared with thermal models e.g. the half-space model, the plate model and the CHABLIS model (Fig. 1.2).

The successful calibration of a geobarometer can be used to test existing geophysical models for the thermal structure of the oceanic lithospheric mantle. Models for various ages of the oceanic lithosphere can be constructed and P-T conditions for xenoliths of the corresponding age can be compared to these. The chronological evolution of the depth of the isotherms in the oceanic lithospheric mantle can thus be constructed using a petrological model.

5.3.2. Future work on understanding the geochemical evolution of the oceanic lithospheric mantle.

It is suggested that future work needs to focus on collecting bulk rock and mineral data for the same group of samples for both, ocean island xenoliths and abyssal peridotites from around the globe. This dataset must include the measurement of major and trace elements, both in the bulk rock and in minerals as well as mineral modes determined by point counting large thin sections or multiple thin sections of the same rock, were possible. Mineral analyses by measurement of zoning profiles across crystals will serve two purposes: First, measurement of zoning profiles will enable us to check for variations in the concentrations of elements within the crystals. As demonstrated in Chapter 4, Mg/Fe zoning is measured in olivines that are affected by emplacement-related geochemical changes. Ascertaining the homogeneity in crystals will enable us to examine samples that

do not incorporate late-stage geochemical modifications. Secondly, the availability of several points of analysed data will be suitable for the calculation of averages for statistically sufficient data points. Further, these data can then be used in geothermobarometric studies.

The elements to be analysed in each rock type will be selected with due consideration for use in geochemical and geothermobarometric analyses i.e. akin to the data compiled in this study. In order to enable the reconstruction of bulk trace element concentrations, it is advisable to analyse the same set of elements for all mineral phases. With the dataset described above, the hypothesis that differences exist between measured and reconstructed bulk compositions can be rigorously tested. A compilation of this dataset combined with the calibration of the Ca-in-olivine geobarometer will enable us to use xenolith geochemical data to determine temperatures and pressures of equilibration for the xenoliths, which in turn can be used to build a comprehensive model for the thermal and chemical evolution of the oceanic lithospheric mantle.

Bibliography

Adams, G. E. and Bishop, F. C. (1982). Experimental investigation of Ca-Mg exchange between olivine, orthopyroxene and clinopyroxene – potential for geobarometry. Earth and Planetary Science Letters 57, 241-250.

Adams, G. E. and Bishop, F. C. (1986). The olivine clinopyroxene geobarometer – experimental results and CaO-FeO-MgO-SiO_2 system. Contributions to Mineralogy and Petrology 94, 230-237.

Adams, G.E. and Bishop, F.C. (1985). An experimental investigation of the thermodynamic mixing properties and unit cell parameters of forsterite-monticellite solid solutions. Am. Min., 70, 714-722.

Allan, J. F. and Dick, H. J. (1996). Cr-rich spinel as a tracer for melt migration and melt-wall rock interaction in the mantle: Hess Deep, Leg 147. In Proceedings – Ocean Drilling Program Scientific Results (pp. 157-172). National Science Foundation.

Alt, J. C. And Bach, W. (2001). Data Report: Low-grade hydrothermal alteration of uplifted lower oceanic crust, Hole 735B: Mineralogy and isotope geochemistry. Proceedings of the Ocean Drilling Program, Scientific Results, Volume 176.

Andersen, T. and Neumann, E. R. (2001). Fluid inclusions in mantle xenoliths. Lithos 55, 301-320.

Andersen, T., Burke, E. A. J., and Neumann, E. R. (1995). Nitrogen-rich fluid in the upper mantle – fluid inclusions in spinel dunite from Lanzarote, Canary Islands. Contributions to Mineralogy and Petrology 120, 20-28.

Arai, S. and Matsukage, K. (1996). Petrology of gabbro-troctolite-peridotite complex from Hess Deep, equatorial Pacific: implications for mantle-melt interaction within the

oceanic lithosphere. Proceedings of the Ocean Drilling Program, Scientific Results. (Mevel, C., Gillis, M., and Meyer, P.S. – Editors). Volume 147, 135-156.

Arai, S. and Matsukage, K. (1998). Petrology of a chromitite micropod from Hess Deep, equatorial Pacific: a comparison between abyssal and alpine-type podiform chromitites. Lithos, 43 (1), 1-14.

Asimow, P. D. (1999). A model that reconciles major-and trace-element data from abyssal peridotites. Earth and Planetary Science Letters, 169 (3), 303-319.

Aumento, F., and Loubat, H. (1971). The Mid-Atlantic ridge near 45 N. XVI. Serpentinized ultramafic intrusions. Canadian Journal of Earth Sciences, 8 (6), 631-663.

Baker, M. B. and Stolper, E. M. (1994). Determining the composition of high-pressure mantle melts using diamond aggregates. Geochimica et Cosmochimica Acta, 58 (13), 2811-2827.

Baker, M. B., and Beckett, J. R. (1999). The origin of abyssal peridotites: a reinterpretation of constraints based on primary bulk compositions. Earth and Planetary Science Letters, 171 (1), 49-61.

Baker, M.B., Grove, T.L. and Price, R. (1994). Primitive basalts and andesites from Mt. Shasta region, N California – Products of varying melt fraction and water-content. Contributions to Mineralogy and Petrology, 118, 111-129.

Ballhaus, C., Berry, R. F. and Green, D. H. (1991). High pressure experimental calibration of the olivine-orthopyroxene-spinel oxygen geobarometer: implications for the oxidation state of the upper mantle. Contributions to Mineralogy and Petrology, 107 (1), 27-40.

Bascou, J., Delpech, G., Vauchez, A., Moine, B. N., Cottin, J. Y., and Barruol, G. (2008). An integrated study of microstructural, geochemical, and seismic properties of the

lithospheric mantle above the Kerguelen plume (Indian Ocean). Geochemistry, Geophysics, Geosystems, 9 (4).

Biggar, G.M. and O'Hara, M.J. (1969). Monticellite and Forsterite Crystalline Solutions. Journal of the American Ceramic Society, 52 (5): 249-252.

Bindeman, I. N., Davis, A. M. and Drake, M. J. (1998). Ion microprobe study of plagioclase-basalt partition experiments at natural concentration levels of trace elements. Geochimica et Cosmochimica Acta, 62 (7), 1175-1193.

Birle, J.D., Gibbs, G.V., Moore, P.B. and Smith, J.V., (1968). Crystals structures of natural olivines. American Mineralogist 53, 807-824.

Bizimis, M., Sen, G. and Salters, V. J. (2004). Hf–Nd isotope decoupling in the oceanic lithosphere: constraints from spinel peridotites from Oahu, Hawaii. Earth and Planetary Science Letters, 217 (1), 43-58.

Blundy, J. and Wood, B. (2003). Partitioning of trace elements between crystals and melts. Earth and Planetary Science Letters, 210 (3), 383-397.

Bodinier, J. L., and Godard, M. (2003). Orogenic, ophiolitic, and abyssal peridotites. Treatise on geochemistry, 2, 103-170.

Bonadiman, C., Beccaluva, L., Coltorti, M. and Siena, F. (2005). Kimberlite-like metasomatism and 'garnet signature' in spinel-peridotite xenoliths from Sal, Cape Verde Archipelago: relics of a subcontinental mantle domain within the Atlantic Oceanic lithosphere. Journal of Petrology, 46 (12), 2465-2493.

Bonatti, E., Peyve, A., Kepezhinskas, P., Kurentsova, N., Seyler, M., Skolotnev, S. and Udintsev, G. (1992). Upper mantle heterogeneity below the Mid-Atlantic Ridge, 0º15' N. Journal of Geophysical Research, 97, 4461-4476.

Brandon, D.A., Snow, J.E., Walker, R.J., Morgan, J.W. and Mock, T.D. (2000). ^{190}Pt-^{186}Os

and ^{187}Re-^{187}Os systematics of abyssal peridotites. Earth and Planetary Science Letters, 177, 319-335.

Brey, G. P. and Köhler, T. (1990). Geothermobarometry in four-phase lherzolites II. New thermobarometers, and practical assessment of existing thermobarometers. Journal of Petrology, 31 (6), 1353-1378.

Brown, G.E., (1980). Olivines and Silicate Spinels. In: P.H. Ribbe (Editor), Orthosilicates. Reviews in Mineralogy. Bookcrafters, pp. 275-381.

Brunelli, D., Seyler, M., Cipriani, A., Ottolini, L., and Bonatti, E. (2006). Discontinuous melt extraction and weak refertilization of mantle peridotites at the Vema lithospheric section (Mid-Atlantic Ridge). Journal of Petrology, 47 (4), 745-771.

Canil, D. (1997). Vanadium partitioning and the oxidation state of Archaean komatiite magmas. Nature, 389 (6653), 842-845.

Cannat, M. (1996). How thick is the magmatic crust at slow spreading oceanic ridges? Journal of Geophysical Research: Solid Earth (1978–2012), 101 (B2), 2847-2857.

Cannat, M. and Seyler, M. (1995). Transform tectonics, metamorphic plagioclase and amphibolitization in ultramafic rocks of the Vema transform fault (Atlantic Ocean). Earth and Planetary Science Letters, 133 (3), 283-298.

Carlson, W.D. and Lindsley, D.H., (1988). Thermochemistry of pyroxenes on the join $Mg_2Si_2O_6$-$CaMgSi_2O_6$. American Mineralogist, 73, 242-252.

Casey, J. F. (1997). Comparison of major-and trace-element geochemistry of abyssal peridotites and mafic plutonic rocks with basalts from the MARK region of the Mid-Atlantic Ridge. In Proceedings of the Ocean Drilling Program. Scientific Results Vol. 153, 181-241. Ocean Drilling Program.

Chakraborty S. (1997). Rates and mechanisms of Fe–Mg interdiffusion in olivine at 980º–

1,300 ºC. Journal of Geophysical Research 102:12317– 12331.

Chakraborty, S. (1997). Rates and mechanisms of Fe-Mg interdiffusion in olivine at 980 degrees-1300 degrees C. Journal of Geophysical Research-Solid Earth 102, 12317-12331.

Cherniak, D. J. and Liang, Y. (2007). Rare earth element diffusion in natural enstatite. Geochimica et Cosmochimica Acta, 71 (5), 1324-1340.

Coltorti, M., Bonadiman, C., Hinton, R. W., Siena, F., and Upton, B. G. J. (1999). Carbonatite metasomatism of the oceanic upper mantle: evidence from clinopyroxenes and glasses in ultramafic xenoliths of Grande Comore, Indian Ocean. Journal of Petrology, 40 (1), 133-165.

Coltorti, M., Bonadiman, C., O'Reilly, S. Y., Griffin, W. L., and Pearson, N. J. (2010). Buoyant ancient continental mantle embedded in oceanic lithosphere (Sal Island, Cape Verde Archipelago). Lithos, 120 (1), 223-233.

Coogan, L. A., Gillis, K. M., MacLeod, C. J., Thompson, G. M. and Hékinian, R. (2002). Petrology and geochemistry of the lower ocean crust formed at the East Pacific Rise and exposed at Hess Deep: A synthesis and new results. Geochemistry, Geophysics, Geosystems, 3 (11), 1-30.

Coogan, L.A., Hain, A., Stahl, S. and Chakraborty, S. (2005). Experimental determination of the diffusion coefficient for calcium in olivine between 900°C and 1500°C. Geochim. Cosmochim. Acta, 69 (14), 3683-3694.

Coogan, L.A., Jenkin, G.R.T. and Wilson, R.N. (2007). Contrasting cooling rates in the oceanic lithosphere at fast- and slow-spreading mid-ocean ridges derived from geospeedometry. Journal of Petrology, 48, 2211-2231.

Crank, J. (1975). The Mathematics of Diffusion: 2d Ed. Clarendon Press.

Crough, S. T. (1975). Thermal model of oceanic lithosphere. Nature, 256, 388-390.

Dalton, J.A. and Lane, S.J. (1996). Electron microprobe analysis of Ca in olivine close to grain boundaries: the problem of secondary X-ray fluorescence. Am. Min., 81, 194-201.

Davidson, P.M. and Mukhopadhyay, D.K. (1984). Ca-Fe-Mg olivines: phase relations and a solution model. Contrib. Mineral. Petrol., 86, 256-263.

Davis, E. E. and Lister, C. R. B. (1974). Fundamentals of ridge crest topography. Earth and Planetary Science Letters, 21 (4), 405-413.

DeLaughter, J. E., Stein, C. A., and Stein, S. (2005). Hotspots: A view from the swells. Geological Society of America Special Papers, 388, 257-278.

Delpech, G., Grégoire, M., O'Reilly, S. Y., Cottin, J. Y., Moine, B., Michon, G. and Giret, A. (2004). Feldspar from carbonate-rich silicate metasomatism in the shallow oceanic mantle under Kerguelen Islands (South Indian Ocean). Lithos, 75 (1), 209-237.

Dick, H. J. and Natland, J. H. (1996). Late-stage melt evolution and transport in the shallow mantle beneath the East Pacific Rise. In Proceedings – Ocean Drilling Program Scientific Results. (103-134). National Science Foundation.

Dick, H. J. B. (1989). Abyssal peridotites, very slow spreading ridges and ocean ridge magmatism. Geological Society, London, Special Publications, 42 (1), 71-105.

Dick, H. J. B., Fisher, R. L. and Bryan, W. B. (1984). Mineralogic variability of the uppermost mantle along Mid-Ocean Ridges. Earth and Planetary Science Letters 69, 88-106.

Dick, H. J. B., Tivey, M. A. and Tucholke, B. E. (2008). Plutonic foundation of a slow-spreading ridge segment: Oceanic core complex at Kane Megamullion, 23 degrees

30 ' N, 45 degrees 20 ' W. Geochemistry Geophysics Geosystems 9.

Doin, M. P. and Fleitout, L. (1996). Thermal evolution of the oceanic lithosphere: an alternative view. Earth and Planetary Science Letters, 142 (1), 121-136.

Draper, D.S. and Johnston, A.D. (1992). Anhydrous P-T phase relations of an Aleutian high-MgO basalt – An investigation of the role of olivine-liquid reaction in the generation of arc high-alumina basalts. Contributions to Mineralogy and Petrology, 112, 501-519.

Ducea, M., Sen, G., Eiler, J., and Fimbres, J. (2002). Melt depletion and subsequent metasomatism in the shallow mantle beneath Koolau volcano, Oahu (Hawaii). Geochemistry, Geophysics, Geosystems, 3 (2).

Edwards, S. J. and Malpas, J. (1996). Melt-peridotite interactions in shallow mantle at the East Pacific Rise: evidence from ODP Site 895 (Hess Deep). Mineralogical Magazine, 60 (398), 191-206.

Ehlers, K., Grove, T. L., Sisson, T. W., Recca, S. I. and Zervas, D. A. (1992). The effect of oxygen fugacity on the partitioning of nickel and cobalt between olivine, silicate melt, and metal. Geochimica et cosmochimica acta, 56 (10), 3733-3743.

Elderfield, H., and Greaves, M. J. (1982). The rare earth elements in seawater. Nature, 296 (3), 214-218.

El-Rus, M. A., Neumann, E. R. and Peters, V. (2006). Serpentinization and dehydration in the upper mantle beneath Fuerteventura (eastern Canary Islands): Evidence from mantle xenoliths. Lithos, 89 (1), 24-46.

Elthon, D. (1992). Chemical trends in abyssal peridotites: refertilization of depleted suboceanic mantle. Journal of Geophysical Research: Solid Earth (1978–2012), 97 (B6), 9015-9025.

Finnerty, A. A., and Boyd, F. R. (1978). Pressure-dependent solubility of Ca in forsterite coexisting with diopside and enstatite. Yearbook: Carnegie Institute of Washington 77, 713-717.

Ford, C.E., Russell, D.G., Craven, J.A. and Fisk, M.R. (1983). Olivine-liquid equilibria: temperature, pressure and composition dependence of the crystal/liquid cation paritition coefficients for Mg, Fe^{2+}, Ca and Mn. Journal of Petrology, 24 (3), 256-265.

Francheteau, J., Armijo, R., Cheminee, J.L., Hekinian, R., Lonsdale, P. and Blum,N., (1990).1 Ma East Pacific Rise oceanic crust and uppermost mantle exposed by rifting in Hess Deep (equatorial Pacific Ocean). Earth Planet. Sci. Lett., 101, 281-295.

Frost, B.R., Lindsley, D.H. and Andersen, D.J., (1988). Fe-Ti oxide silicate equilibria – assemblages with fayalitic olivine. American Mineralogist 73, 727-740.

Früh-Green, G. L., Plas, A. and Lécuyer, C. (1996). Petrologic and stable isotope constraints on hydrothermal alteration and serpentinization of the EPR shallow mantle at Hess Deep (Site 895). In Proceedings – Ocean Drillig Program Scientific Results. (pp. 255-292). National Science Foundation.

Ganguly J. and Tazzoli V. (1994) Fe^{2+}–Mg interdiffusion in orthopyroxene: Retrieval from the data on intracrystalline exchange reaction. American Mineralogist 79:930–937.

Garcia, M. O., and Presti, A. A. (1987). Glass in garnet pyroxenite xenoliths from Kaula Island, Hawaii: Product of infiltration of host nephelinite. Geology, 15 (10), 904-906.

Gillis, K. M. and Mével, C. (1993). ODP leg 147 Scientific party. Pacific lower crustal and shallow mantle sections recovered, EOS Trans. AGU, 74 (27), 297.

Gillis, Kathryn M., Jonathan E. Snow, Adam Klaus, Natsue Abe, Álden B. Adrião, Norikatsu Akizawa, Georges Ceuleneer, Michael J. Cheadle, Kathrin Faak, Trevor J. Falloon, Sarah A. Friedman, Marguerite Godard, Gilles Guerin, Yumiko Harigane, Andrew J. Horst, Takashi Hoshide, Benoit Ildefonse, Marlon M. Jean, Barbara E. John, Juergen Koepke, Sumiaki Machi, Jinichiro Maeda, Naomi E. Marks, Andrew M. McCaig, Romain Meyer, Antony Morris, Toshio Nozaka, Marie Python, Abhishek Saha and Robert P. Wintsch (2014). Primitive layered gabbros from fast-spreading lower oceanic crust. Nature 505 (7482), 204-207.

Godard, M., Lagabrielle, Y., Alard, O. and Harvey, J. (2008). Geochemistry of the highly depleted peridotites drilled at ODP Sites 1272 and 1274 (Fifteen-Twenty Fracture Zone, Mid-Atlantic Ridge): Implications for mantle dynamics beneath a slow spreading ridge. Earth and Planetary Science Letters 267, 410-425.

Gregoire, M., Lorand, J. P., Cottin, J. Y., Giret, A., Mattielli, N. and Weis, D. (1997). Xenoliths evidence for a refractory oceanic mantle percolated by basaltic melts beneath the Kerguelen archipelago. European Journal of Mineralogy 9, 1085-1100.

Gregoire, M., Moine, B. N., O'Reilly, S. Y., Cottin, J. Y., and Giret, A., (2000). Trace element residence and partitioning in mantle xenoliths metasomatised by highly alkaline, silicate- and carbonate-rich melts (Kerguelen Islands, Indian Ocean). Journal of Petrology 41, 477-509.

Grove, T. L., Kinzler, R. J., and Bryan, W. B. (1993). Fractionation of mid-ocean ridge basalt (MORB). Mantle flow and melt generation at mid-ocean ridges, 281-310.

Grove, T.L. and Juster, T.C., (1989). Experimental Investigations of Low-Ca Pyroxene Stability and Olivine Pyroxene Liquid Equilibria at 1-Atm in Natural Basaltic and Andesitic Liquids. Contributions to Mineralogy and Petrology, 103 (3), 287-305.

Hamlyn, P. R., and Bonatti, E. (1980). Petrology of mantle-derived ultramafics from the Owen Fracture Zone, northwest Indian Ocean: implications for the nature of the oceanic upper mantle. Earth and Planetary Science Letters, 48 (1), 65-79.

Harvey, J., Gannoun, A., Burton, K.W., Rogers, N.W., Alard, O. and Parkinson, I.J. (2006). Ancient melt extraction from the oceanic upper mantle revealed by Re-Os isotopes in abyssal peridotites from the Mid-Atlantic Ridge. Earth and Planetary Science Letters, 244(3), 606-621.

Hauri, E. H. and Hart, S. R. (1994). Constraints on melt migration from mantle plumes – A trace element study of peridotite xenoliths from Savaii, Western-Samoa. Journal of Geophysical Research-Solid Earth 99, 24301-24321.

Hauri, E. H., Shimizu, N., Dieu, J. J., and Hart, S. R. (1993). Evidence for hotspot-related carbonatite metasomatism in the oceanic upper mantle. Nature, 365, 221-227.

Hellebrand, E., Snow, J. E., and Mühe, R. (2002a). Mantle melting beneath Gakkel Ridge (Arctic Ocean): abyssal peridotite spinel compositions. Chemical Geology, 182(2), 227-235.

Hellebrand, E., Snow, J. E., Hoppe, P. and Hofmann, A. W. (2002b). Garnet-field melting and late-stage refertilization in 'residual' abyssal peridotites from the Central Indian Ridge. Journal of Petrology 43, 2305-2338.

Hellebrand, E., Snow, J. E., Mostefaoui, S. and Hoppe, P. (2005). Trace element distribution between orthopyroxene and clinopyroxene in peridotites from the Gakkel Ridge: a SIMS and NanoSIMS study. Contributions to Mineralogy and Petrology 150, 486-504.

Hermann, J., O'Neill, H. S. C., and Berry, A. J. (2005). Titanium solubility in olivine in the system TiO_2–MgO–SiO_2: no evidence for an ultra-deep origin of Ti-bearing olivine.

Contributions to Mineralogy and Petrology, 148 (6), 746-760.

Hervig, R. L., and Smith, J. V. (1982). Temperature-dependent distribution of Cr between olivine and pyroxenes in lherzolite xenoliths. Contributions to Mineralogy and Petrology, 81 (3), 184-189.

Hirschmann, M. (1991). Thermodynamics of multicomponent olivines and the solution properties of $(Ni,Mg,Fe)_2SiO_4$ and $(Ca,Mg,Fe)_2SiO_4$ olivines. American Mineralogist 76, 1232-1248.

Hirth, G., and Kohlstedt, D. L. (1996). Water in the oceanic upper mantle: implications for rheology, melt extraction and the evolution of the lithosphere. Earth and Planetary Science Letters, 144 (1), 93-108.

Hofmann, A. W. (1997). Mantle geochemistry: the message from oceanic volcanism. Nature, 385 (6613), 219-229.

Hofmann, A. W., and White, W. M. (1982). Mantle plumes from ancient oceanic crust. Earth and Planetary Science Letters, 57 (2), 421-436.

Huebner, J.S. and Sato, M. (1970). Oxygen fugacity-temperature relationships of manganese oxide and nickel oxide buffers. American Mineralogist 55, 934-952.

Jagoutz, Emile, H. Palme, Hildegard Baddenhausen, K. Blum, M. Cendales, Gerlind Dreibus, B. Spettel, H. Waenke, and V. Lorenz. (1979). The abundances of major, minor and trace elements in the earth's mantle as derived from primitive ultramafic nodules. Lunar and Planetary Science Conference Proceedings, Volume 10, 2031-2050.

Jochum, K. P., Nohl, U., Herwig, K., Lammel, E., Stoll, B. and Hofmann, A. W. (2005). GeoReM: a new geochemical database for reference materials and isotopic standards. Geostandards and Geoanalytical Research, 29 (3), 333-338.

Johnson, K. and Dick, H. J. (1992). Open system melting and temporal and spatial variation of peridotite and basalt at the Atlantis II fracture zone. Journal of Geophysical Research: Solid Earth (1978–2012), 97 (B6), 9219-9241.

Johnson, K., Dick, H. J. and Shimizu, N. (1990). Melting in the oceanic upper mantle: an ion microprobe study of diopsides in abyssal peridotites. Journal of Geophysical Research: Solid Earth (1978–2012), 95(B3), 2661-2678.

Jurewicz, A.J.G. and Watson, E.B. (1988). Cations in olivine, Part 1: Calcium partitioning and calcium-magnesium distribution between olivines and coexisting melts, with petrological applications. Contrib. Mineral. Petrol., 99, 176-185.

Juteau, T., Berger, E. and Cannat, M. (1990). Serpentinized, residual mantle peridotites from the MAR Median Valley, ODP hole 670A (21 10′ N, 45 02′ W, Leg 109): primary mineralogy and geothermometry. In Proceedings of Ocean Drilling Program. Scientific Results (Vol. 106, p. 109).

Kawasaki, T. (1995). Empirical formulation for the distribution of Ca^{2+} between olivine and Ca-rich clinopyroxene at 7.5 Gpa pressure. In: T. Yukutake (Editor), The Earth's central part: It structure and dynamics. Terra Scientific Publishing, Tokyo, pp. 45-55.

Kelemen, P. B. (1990). Reaction between ultramafic rock and fractionating basaltic magma. 1. Phase relations, the origin of calc-alkaline magma series and the formation of discordant dunite. Journal of Petrology 31, 51-98.

Kelemen, P. B., Dick, H. J. and Quick, J. E. (1992). Formation of harzburgite by pervasive melt/rock reaction in the upper mantle. Nature, 358 (6388), 635-641.

Kelemen, P. B., Hirth, G., Shimizu, N., Spiegelman, M. and Dick, H. J. (1997). A review of melt migration processes in the adiabatically upwelling mantle beneath oceanic

spreading ridges. Philosophical Transactions of the Royal Society of London A: Mathematical, Physical and Engineering Sciences, 355 (1723), 283-318.

Kelemen, P. B., Shimizu, N. and Salters, V. J. (1995). Extraction of mid-ocean-ridge basalt from the upwelling mantle by focused flow of melt in dunite channels.

Kelemen, P. B., Yogodzinski, G. M. and Scholl, D. W. (2003). Along-Strike Variation in the Aleutian Island Arc: Genesis of High Mg# Andesite and Implications for Continental Crust. Inside the subduction factory, 223-276.

Keshav, S., and Sen, G. (2003). A rare composite xenolith from Salt Lake Crater, Oahu: high-pressure fractionation and implications for kimberlitic melts in the Hawaiian mantle. Contributions to Mineralogy and Petrology, 144 (5), 548-558.

Kinzler, R. J. (1997). Melting of mantle peridotite at pressures approaching the spinel to garnet transition: Application to mid–ocean ridge basalt petrogenesis. Journal of Geophysical Research: Solid Earth (1978–2012), 102 (B1), 853-874.

Kinzler, R. J. and Grove, T. L. (1992). Primary magmas of mid-ocean ridge basalts 1. Experiments and methods. Journal of Geophysical Research, 97 (B5), 6885-6906.

Klinkhammer, G.P., Elderfield, H., Edmond, J.M. and Mitra, A. (1994). Geochemical implications of rare earth element patterns in hydrothermal fluids from mid-ocean ridges. Geochimica et Cosmochimica Acta, 58(23), 5105-5113.

Klugel, A. (1998). Reactions between mantle xenoliths and host magma beneath La Palma (Canary Islands): constraints on magma ascent rates and crustal reservoirs. Contributions to Mineralogy and Petrology 131, 237-257.

Köhler, T. P. and Brey, G. (1990). Calcium exchange between olivine and clinopyroxene calibrated as a geothermobarometer for natural peridotites from 2 to 60 kb with applications. Geochimica et Cosmochimica Acta, 54 (9), 2375-2388.

Komor, S. C., Grove, T. L. and Hébert, R. (1990). Abyssal peridotites from ODP Hole 670A (21 10'N, 45 02'W): residues of mantle melting exposed by non-constructive axial divergence. In Proceedings of Ocean Drilling Program, Scientific Results 85-101.

Kress, V. C. and Carmichael, I. S. (1991). The compressibility of silicate liquids containing Fe_2O_3 and the effect of composition, temperature, oxygen fugacity and pressure on their redox states. Contributions to Mineralogy and Petrology, 108 (1-2), 82-92.

Langmuir, C. H., Klein, E. M. and Plank, T. (1992). Petrological systematics of mid-ocean ridge basalts: Constraints on melt generation beneath ocean ridges. Geophysical Monograph Series, 71, 183-280.

Lassiter, J. C. (2011). Multi-stage melting history of the depleted mantle recorded in major element-Os isotope variations of abyssal peridotites and ocean island xenoliths. AGU Fall Meeting Abstracts (Vol. 1, p. 2553).

Lee, C. T. A., Brandon, A. D. and Norman, M. (2003). Vanadium in peridotites as a proxy for paleo-fO 2 during partial melting: prospects, limitations, and implications. Geochimica et Cosmochimica Acta, 67 (16), 3045-3064.

Libourel, G. (1999). Systematics of calcium partitioning between olivine and silicate melt: implications for melt structure and calcium content of magmatic olivines. Contrib. Mineral. Petrol., 136: 63-80.

Liermann, H. P. and Ganguly, J. (2002). Diffusion kinetics of Fe 2+ and Mg in aluminous spinel: experimental determination and applications. Geochimica et Cosmochimica Acta, 66 (16), 2903-2913.

Liermann, H. P. and Ganguly, J. (2003). Fe^{2+}–Mg fractionation between orthopyroxene and spinel: experimental calibration in the system $FeO–MgO–Al_2O_3–Cr_2O_3–SiO_2$, and applications. Contributions to Mineralogy and Petrology, 145 (2), 217-227.

Lissenberg, C. J. and Dick, H. J. (2008). Melt–rock reaction in the lower oceanic crust and its implications for the genesis of mid-ocean ridge basalt. Earth and Planetary Science Letters, 271 (1), 311-325.

Lissenberg, C. J., MacLeod, C. J., Howard, K. A. and Godard, M. (2013). Pervasive reactive melt migration through fast-spreading lower oceanic crust (Hess Deep, equatorial Pacific Ocean). Earth and Planetary Science Letters, 361, 436-447.

Lister, C. R. B., J. G. Sclater, E. E. Davis, H. Villinger, S. Nagihara. (1990). Heat flow maintained in ocean basins of great age: Investigations in the north-equatorial west Pacific, Geophys. J. Int., 102, 603–630.

Llovet, X. and Galan, G. (2003). Correction of secondary X-ray fluorescence near grain boundaries in electron microprobe analysis: applications to thermobarometry of spinel lherzolites. American mineralogist, 88, 121-130.

Longhi, J. (1987). Liquidus equilibria and solid solution in the system $CaAl_2SiO_8$-Mg_2SiO_4-$CaSiO_3$-SiO_2 at low pressure. Am. Jour. Sci., 287, 265-331.

Lumpkin, G.R., Ribbe, P.H. and Lumpkin, N.E. (1983). Composition, order-disorder and lattice-parameters of olivines – determinative methods for Mg-Mn and Mg-Ca silicate olivines. American Mineralogist 68, 1174-1182.

Lundstrom, C.C., Gill, J., Williams, Q. and Perfit, M.R. (1995). Mantle melting and basalt extraction by equilibrium porous flow. Science, New Series, 270 (5244), 1958-1961.

Mallmann, G. and O'Neill, H. S. C. (2013). Calibration of an Empirical Thermometer and

Oxybarometer based on the Partitioning of Sc, Y and V between Olivine and Silicate Melt. Journal of Petrology, egt001.

Mattielli, N., Weis, D., Grégoire, M., Mennessier, J. P., Cottin, J. Y., and Giret, A. (1996). Kerguelen basic and ultrabasic xenoliths: evidence for long-lived Kerguelen hotspot activity. Lithos, 37 (2), 261-280.

McDonough, W. F. and Sun, S. S. (1995). The composition of the Earth. Chemical Geology, 120 (3), 223-253.

McKenzie, D. (1989). Some remarks on the movement of small melt fractions in the mantle. Earth and Planetary Science Letters 95, 53-72.

McKenzie, D. and Bickle, M. J. (1988). The volume and composition of melt generated by extension of the lithosphere. Journal of petrology, 29 (3), 625-679.

McKenzie, D. P. (1967). Some remarks on heat flow and gravity anomalies. Journal of Geophysical Research, 72 (24), 6261-6273.

McKenzie, D., Jackson, J. and Priestley, K. (2005). Thermal structure of oceanic and continental lithosphere. Earth and Planetary Science Letters, 233 (3), 337-349.

Menzies, M. A., Rogers, N., Tindle, A. G. and Hawkesworth, C. J. (1987). Metasomatic and enrichment processes in lithospheric peridotites, an effect of asthenosphere-lithosphere interaction. Mantle Metasomatism. London, UK: Academic Press, pp. 313–361.

Michael, P. J. and Bonatti, E. (1985). Peridotite composition from the North Atlantic: regional and tectonic variations and implications for partial melting. Earth and Planetary Science Letters, 73 (1), 91-104.

Miyashiro, A., Shido, F. and Ewing, M. (1969). Composition and origin of serpentinites from the Mid-Atlantic Ridge near 24 and 30 north latitude. Contributions to Mineralogy and Petrology, 23 (2), 117-127.

Miyashiro, A., Shido, F., and Ewing, M. (1969). Composition and origin of serpentinites from the Mid-Atlantic Ridge near 24 and 30 north latitude. Contributions to Mineralogy and Petrology, 23 (2), 117-127.

Moine, B. N., Grégoire, M., O'Reilly, S. Y., Sheppard, S. M. F. and Cottin, J. Y. (2001). High field strength element fractionation in the upper mantle: evidence from amphibole-rich composite mantle xenoliths from the Kerguelen Islands (Indian Ocean). Journal of Petrology, 42 (11), 2145-2167.

Molnar, P. and Atwater, T. (1978). Interarc spreading and Cordilleran tectonics as alternates related to the age of subducted oceanic lithosphere. Earth and Planetary Science Letters, 41 (3), 330-340.

Mukhopadhyay, D.K. and Lindsley, D.H. (1983). Phase relations in the join kirschsteinite ($CaFeSiO_4$)-fayalite (Fe_2SiO_4). American Mineralogist, 68, 1089-1094.

Natland, J. H. (1989). Partial melting of a lithologically heterogeneous mantle: inferences from crystallization histories of magnesian abyssal tholeiites from the Siqueiros Fracture Zone. Geological Society, London, Special Publications, 42(1), 41-70.

Neilsen R. L., Crum J., Bourgeois R., Hascall K., Forsythe L. M., Fisk M. R. and Christie D. M. (1995). Melt inclusions in high-An plagioclase from the Gorda Ridge: an example of the local diversity of MORB parental magmas. Contrib. Miner. Pet. 122, 34–50.

Neumann, E. R. (1991). Ultramafic and mafic xenoliths from Hierro, Canary Islands: evidence for melt infiltration in the upper mantle. Contributions to Mineralogy and Petrology, 106 (2), 236-252.

Neumann, E. R. and Wulff-Pedersen, E. (1997). The origin of highly silicic glass in mantle xenoliths from the Canary Islands. Journal of Petrology 38, 1513-1539.

Neumann, E. R., Griffin, W. L., Pearson, N. J. and O'Reilly, S. Y. (2004). The evolution of the upper mantle beneath the Canary Islands: Information from trace elements and Sr isotope ratios in minerals in mantle xenoliths. Journal of Petrology 45, 2573-2612.

Neumann, E. R., Wulff-Pedersen, E., Johnsen, K., Andersen, T. and Krogh, E. (1995). Petrogenesis of spinel harzburgite and dunite suite xenoliths from Lanzarote, eastern Canary Islands: implications for the upper mantle. Lithos, 35 (1), 83-107.

Neumann, E. R., Wulff-Pedersen, E., Pearson, N. J. and Spencer, E. A. (2002). Mantle xenoliths from Tenerife (Canary Islands): Evidence for reactions between mantle peridotites and silicic carbonatite melts inducing Ca metasomatism. Journal of Petrology 43, 825-857.

Niida, K. (1997). Mineralogy of Mark peridotites: replacement through magma channelling examined from Hole 920D, Mark area. Proc. Ocean Dril. Prog, 153.

Niu, Y. (2004). Bulk-rock major and trace element compositions of abyssal peridotites: implications for mantle melting, melt extraction and post-melting processes beneath mid-ocean ridges. Journal of Petrology, 45 (12), 2423-2458.

Niu, Y. and Hékinian, R. (1997). Basaltic liquids and harzburgitic residues in the Garrett Transform: a case study at fast-spreading ridges. Earth and Planetary Science Letters, 146 (1), 243-258.

Niu, Y. and O'Hara, M. J. (2003). Origin of ocean island basalts: A new perspective from petrology, geochemistry, and mineral physics considerations. Journal of Geophysical Research: Solid Earth (1978–2012), 108(B4).

Niu, Y. L. (1997). Mantle melting and melt extraction processes beneath ocean ridges: Evidence from abyssal peridotites. Journal of Petrology 38, 1047-1074.

Niu, Y. L., Langmuir, C. H., and Kinzler, R. J. (1997). The origin of abyssal peridotites: a new perspective. Earth and Planetary Science Letters 152, 251-265.

Niu, Y., Wilson, M., Humphreys, E. R. and O'Hara, M. J. (2011). The origin of intra-plate ocean island basalts (OIB): the lid effect and its geodynamic implications. Journal of Petrology, 52 (7-8), 1443-1468.

Nozaka, T., Fryer, P. and Andreani, M. (2008). Formation of clay minerals and exhumation of lower-crystal rocks at Atlantis Massif, Mid-Atlantic Ridge. Geochemistry, Geophysics, Geosystems, 9 (11).

O'Hara, M. J. (1965). Primary magmas and the origin of basalts. Scottish Journal of Geology, 1 (1), 19-40.

O'Nions, K. (1992). The Continents. Brown, G., Hawkesworth, C., and Wilson, R. C. L. (Editors). Understanding the Earth, 145-164.

O'Reilly, S.Y., Zhang, M., Griffin, W.L., Begg, G and Hronsky, J. (2009). Ultradeep continental roots and their oceanic remnants: a solution to the geochemical "mantle reservoir" problem? Lithos, 2115, 1043-1054.

O'Donnell, T. H., and Presnall, D. C. (1980). Chemical variations of the glass and mineral phases in basalts dredged from 25–30 N along the Mid-Atlantic Ridge. Am. J. Sci, 280, 845-68.

O'Neill, H. S. C., and Wall, V. J. (1987). The Olivine-Orthopyroxene-Spinel oxygen geobarometer, the nickel precipitation curve, and the oxygen fugacity of the Earth's Upper Mantle. Journal of Petrology, 28 (6), 1169-1191.

Parkinson, I. J., and Pearce, J. A. (1998). Peridotites from the Izu–Bonin–Mariana forearc (ODP Leg 125): evidence for mantle melting and melt–mantle interaction in a supra-subduction zone setting. Journal of Petrology, 39 (9), 1577-1618.

Parsons, B. and Sclater, J. G. (1977). An analysis of the variation of ocean floor bathymetry and heat flow with age. Journal of geophysical research, 82 (5), 803-827.

Paulick, H., Bach, W., Godard, M., De Hoog, J. C. M., Suhr, G. and Harvey, J. (2006). Geochemistry of abyssal peridotites (Mid-Atlantic Ridge, 15 20′ N, ODP Leg 209): implications for fluid/rock interaction in slow spreading environments. Chemical Geology, 234 (3), 179-210.

Phipps Morgan, J. (1997). The generation of a compositional lithosphere by mid-ocean ridge melting and its effect on subsequent off-axis hotspot upwelling and melting. Earth and Planetary Science Letters, 146 (1), 213-232.

Pilet, S., Baker, M. B. and Stolper, E. M. (2008). Metasomatized lithosphere and the origin of alkaline lavas. Science, 320 (5878), 916-919.

Pilet, S., Hernandez, J., Sylvester, P. and Poujol, M. (2005). The metasomatic alternative for ocean island basalt chemical heterogeneity. Earth and Planetary Science Letters, 236 (1), 148-166.

Pouchou, J. L. and Pichoir, F. (1985): PAP $\phi(\rho Z)$ procedure for improved quantitative microanalysis. Microbeam Analysis, 104-106.

Qi, Q., Beard, B. L., Jin, Y. and Taylor, L. A. (1994). Petrology and geochemistry of Al-augite and Cr-diopside group mantle xenoliths from Tahiti, Society Islands. International Geology Review, 36 (2), 152-178.

Quick, J. E. (1981). Petrology and Petrogenesis of the Trinity Peridotite, an upper mantle diapir in the Eastern Klamath Mountains, Northern California. Journal of Geophysical Research 86, 1837-1863.

Reiners, P. W. (1998). Reactive melt transport in the mantle and geochemical signatures of mantle-derived magmas. Journal of Petrology, 39 (5), 1039-1061.

Ross, K. and Elthon, D. (1997). 13. Extreme incompatible trace-element depletion of diopside in residual mantle from south of the Kane Fracture Zone. In Proc. ODP, Sci. Results (Vol. 153).

Ross, K., Elthon, D., Hellebrand, E. and Snow, J. (2005). Melt refertilisation in Hess Deep Peridotites. Ofioliti, 30 (2), 253-254.

Schubert, G., Turcotte, D. L. and Olson, P. (2001). Mantle Convection in the Earth and Planets 2 Volume Set. Cambridge University Press.

Sen, G. (1988). Petrogenesis of spinel lherzolite and pyroxenite suite xenoliths from the Koolau shield, Oahu, Hawaii: implications for petrology of the post-eruptive lithosphere beneath Oahu. Contributions to Mineralogy and Petrology, 100 (1), 61-91.

Sen, G. and Jones, R. (1989). Experimental equilibration of multicomponent pyroxenes in the spinel peridotite field: implications for practical thermometers and a possible barometer. Journal of Geophysical Research: Solid Earth (1978–2012), 94 (B12), 17871-17880.

Sen, G. and Presnall, D. C. (1986). Petrogenesis of dunite xenoliths from Koolau volcano, Oahu, Hawaii: implications for Hawaiian volcanism. Journal of Petrology, 27 (1), 197-217.

Sen, G., and Leeman, W. P. (1991). Iron-rich lherzolitic xenoliths from Oahu: origin and implications for Hawaiian magma sources. Earth and Planetary Science Letters, 102 (1), 45-57.

Sen, G., Frey, F. A., Shimizu, N. and Leeman, W. P. (1993). Evolution of the lithosphere beneath Oahu, Hawaii: rare earth element abundances in mantle xenoliths. Earth and Planetary Science Letters, 119 (1), 53-69.

Sen, G., Frey, F. A., Shimizu, N. and Leeman, W. P. (1993). Evolution of the lithosphere beneath Oahu, Hawaii: rare earth element abundances in mantle xenoliths. Earth and Planetary Science Letters, 119 (1), 53-69.

Sen, G., Keshav, S., and Bizimis, M. (2005). Hawaiian mantle xenoliths and magmas: Composition and thermal character of the lithosphere. American Mineralogist, 90 (5-6), 871-887.

Sen, G., Macfarlane, A. and Srimal, N. (1996). Significance of rare hydrous alkaline melts in Hawaiian xenoliths. Contributions to Mineralogy and Petrology, 122 (4), 415-427.

Seyler, M., and Bonatti, E. (1997). Regional-scale melt-rock interaction in lherzolitic mantle in the Romanche Fracture Zone (Atlantic Ocean). Earth and Planetary Science Letters, 146 (1), 273-287.

Seyler, M., Cannat, M. and Mevel, C. (2003). Evidence for major-element heterogeneity in the mantle source of abyssal peridotites from the Southwest Indian Ridge (52º to 68º E). Geochemistry, Geophysics, Geosystems, 4 (2).

Seyler, M., Lorand, J. P., Toplis, M. J. and Godard, G. (2004). Asthenospheric metasomatism beneath the mid-ocean ridge: Evidence from depleted abyssal peridotites. Geology, 32 (4), 301-304.

Shaw, C. S. and Dingwell, D. B. (2008). Experimental peridotite–melt reaction at one atmosphere: a textural and chemical study. Contributions to Mineralogy and Petrology, 155, 199-214.

Shaw, D. M. (1970). Trace element fractionation during anatexis. Geochimica et Cosmochimica Acta, 34 (2), 237-243.

Shaw, S. J., Heidelbach, F. and Dingwell, D. B. (2006). The origin of reaction textures in mantle peridotite xenoliths from Sal Island, Cape Verde: the case for "metasomatism" by the host lava. Contributions to Mineralogy and Petrology 151, 681-697.

Shejwalkar, A., and Coogan, L. A. (2013). Experimental calibration of the roles of temperature and composition in the Ca-in-olivine geothermometer at 0.1 MPa. Lithos, 177, 54-60.

Shi, P. (1992). Basalt evolution at low pressure: implications from an experimental study in the system CaO-FeO-MgO-Al_2O_3-SiO_2. Contributions to Mineralogy and Petrology, 110 (2-3), 139-153.

Siena, F., Beccaluva, L., Coltorti, M., Marchesi, S. and Morra, V. (1991). Ridge to hot-spot evolution of the Atlantic lithospheric mantle: evidence from Lanzarote peridotite xenoliths (Canary Islands). Journal of Petrology, (2), 271-290.

Simkin, T. and Smith, J.V., 1970. Minor-element distribution in olivine. Journal of Geology, 78, 304-325.

Simon, N. S. C., Neumann, E. R., Bonadiman, C., Coltorti, M., Delpech, G., Gregoire, M.

and Widom, E. (2008). Ultra-refractory domains in the oceanic mantle lithosphere sampled as mantle xenoliths at ocean islands. Journal of Petrology 49, 1223-1251.

Snow, J. E. and Dick, H. J. (1995). Pervasive magnesium loss by marine weathering of peridotite. Geochimica et Cosmochimica Acta, 59 (20), 4219-4235.

Snow, J. E. and Reisberg, L. (1995). Erratum of "Os isotopic systematics of the MORB mantle: results from altered abyssal peridotites". Earth Planet. Sci. Lett. 133 (1995) 411–421. Earth and Planetary Science Letters, 136 (3), 723-733.

Sobolev A. V. and Shimizu N. (1993). Ultra-depleted primary inclusions in an olivine from the Mid-Atlantic Ridge. Nature 363, 151-154.

Sobolev, A.V., Hofmann, A.W., Kuzmin, D.V., Yaxley, G.M., Arndt, N.T., Chung, S.L., Danyushevsky, L.V., Elliott, T., Frey, F.A., Garcia, M.O., Gurenko, A.A., Kamenetsky, V.S., Kerr, A.C., Krivolutskaya, N.A., Matvienkov, V.V., Nikogosian, I.K., Rocholl, A., Sigurdsson, I.A., Sushchevskaya, N.M. and Teklay, M. (2007). The amount of recycled crust in sources of mantle-derived melts. Science, 316 (5823): 412-417.

Solomon, M. (1963). Counting and sampling errors in modal analysis by point counter. Journal of Petrology 4, 367-384.

Spandler, C. and O'Neill, H. S. C. (2010). Diffusion and partition coefficients of minor and trace elements in San Carlos olivine at 1,300º C with some geochemical implications. Contributions to Mineralogy and Petrology, 159 (6), 791-818.

Stein, C. A. and Stein, S. (1992). A model for the global variation in oceanic depth and heat flow with lithospheric age. Nature 359, 123-129.

Stein, C. A. and Stein, S. (1994). Constraints on hydrothermal heat flux through the oceanic lithosphere from global heat flow. Journal of Geophysical Research: Solid Earth (1978–2012), 99(B2), 3081-3095.

Stephens, C. J. (1997). Heterogeneity of oceanic peridotite from the western canyon wall at MARK: results from site 920. In Proceedings of the Ocean Drilling Program. Scientific Results (Vol. 153, pp. 285-303). Ocean Drilling Program.

Stolper, E. (1980). A phase diagram for mid-ocean ridge basalts: preliminary results and implications for petrogenesis. Contributions to Mineralogy and Petrology, 74 (1), 13-27.

Sun, C. And Liang, Y. (2014). An assessment of subsolidus re-equilibration on REE distribution among mantle minerals olivine, orthopyroxene, clinopyroxene and garnet in peridotites. Chemical Geology, 372, 80-91.

Tartarotti, P., Susini, S., Nimis, P. and Ottolini, L. (2002). Melt migration in the upper mantle along the Romanche Fracture Zone (Equatorial Atlantic). Lithos, 63 (3), 125-149.

Tommasi, A., Godard, M., Coromina, G., Dautria, J. M., and Barsczus, H. (2004). Seismic anisotropy and compositionally induced velocity anomalies in the lithosphere above mantle plumes: a petrological and microstructural study of mantle xenoliths from French Polynesia. Earth and Planetary Science Letters, 227 (3), 539-556.

Tracy, R. J. (1980). Petrology and genetic significance of an ultramafic xenolith suite from Tahiti. Earth and Planetary Science Letters, 48 (1), 80-96.

Turcotte, D. L. and Schubert, G. (2002). Geodynamics.

Walter, M. J., Sisson, T. W. and Presnall, D. C. (1995). A mass proportion method for calculating melting reactions and application to melting of model upper mantle lherzolite. Earth and Planetary Science Letters, 135 (1), 77-90.

Wan, Z. H., Coogan, L. A. and Canil, D. (2008). Experimental calibration of aluminum partitioning between olivine and spinel as a geothermometer. American Mineralogist 93, 1142-1147.

Warner, R. D. and Luth, W. C. (1973). Two-Phase Data for Join Monticellite (Camgsio4)-Forsterite (Mg_2SiO_4) – Experimental Results and Numerical-Analysis. American Mineralogist, 58 (11-1): 998-1008.

Warren, J. M. and Shimizu, N. (2010). Cryptic variations in abyssal peridotite compositions: evidence for shallow-level melt infiltration in the oceanic lithosphere. Journal of Petrology, egp096.

Witt-Eickschen, G. and O'Neill, H. S. C. (2005). The effect of temperature on the equilibrium distribution of trace elements between clinopyroxene, orthopyroxene, olivine and spinel in upper mantle peridotite. Chemical Geology, 221 (1), 65-101.

Workman, R. K. and Hart, S. R. (2005). Major and trace element composition of the depleted MORB mantle (DMM). Earth and Planetary Science Letters, 231 (1), 53-72.

Workman, R. K., Hart, S. R., Jackson, M., Regelous, M., Farley, K. A., Blusztajn, J., Kurz, M. and Staudigel, H. (2004). Recycled metasomatized lithosphere as the origin of the Enriched Mantle II (EM2) end-member: Evidence from the Samoan Volcanic Chain. Geochemistry, Geophysics, Geosystems, 5 (4).

Wulff-Pedersen, E., Neumann, E. R. and Jensen, B. B. (1996). The upper mantle under La Palma, Canary Islands: formation of Si− K− Na-rich melt and its importance as a metasomatic agent. Contributions to Mineralogy and Petrology, 125 (2-3), 113-139.

Xu, W., Yang, D., Gao, S., Pei, F. and Yu, Y. (2010). Geochemistry of peridotite xenoliths in Early Cretaceous high-Mg# diorites from the Central Orogenic Block of the North China Craton: the nature of Mesozoic lithospheric mantle and constraints on lithospheric thinning. Chemical Geology, 270 (1), 257-273.

Yang, H. J., Kinzler, R. J. and Grove, T. L. (1996). Experiments and models of anhydrous, basaltic olivine-plagioclase-augite saturated melts from 0.001 to 10 kbar. Contributions to Mineralogy and Petrology, 124 (1), 1-18.

Yang, H. J., Sen, G. and Shimizu, N. (1998). Mid-ocean ridge melting: constraints from lithospheric xenoliths at Oahu, Hawaii. Journal of Petrology, 39 (2), 277-295.

Yu, J. H., O'Reilly, S. Y., Zhang, M., Griffin, W. L. and Xu, X. (2006). Roles of melting and metasomatism in the formation of the lithospheric mantle beneath the Leizhou Peninsula, South China. Journal of Petrology, 47 (2), 355-383.

Appendix A

Content description

This appendix contains photomicrographs of olivine, pyroxenes, spinel and alteration phases showing the locations of *in situ* electron microprobe (shown as dots) and LA-ICP-MS (shown as lines) analyses for ODP Site 895 harzburgites discussed in Chapter 3. The symbols are colour-coded to match the analysis number. The number in the label for each photomicrograph is included with the analyses results for the respective mineral in Supplementary Table 3.1.

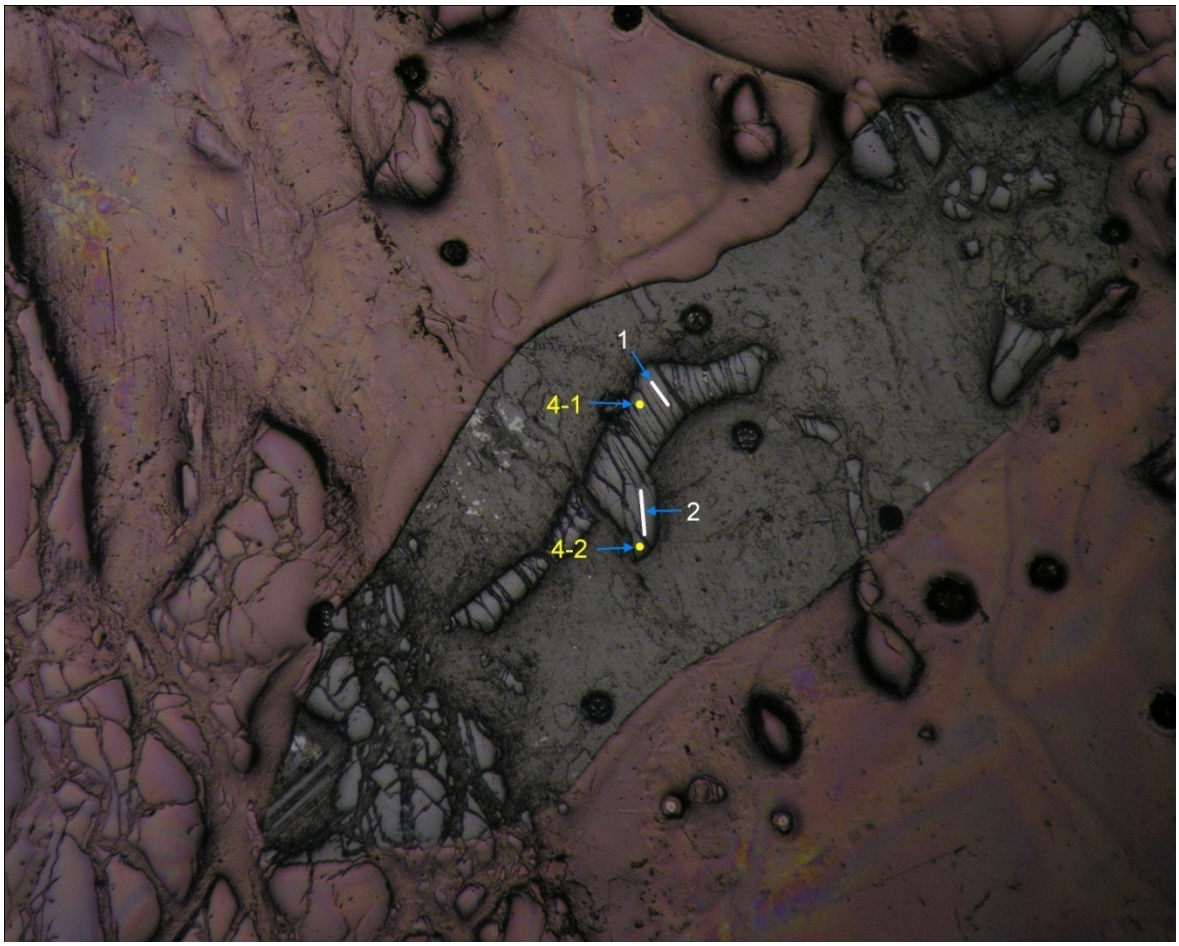

Photomicrograph 1

Sample No. 147-895A-001R-02W (55-61)

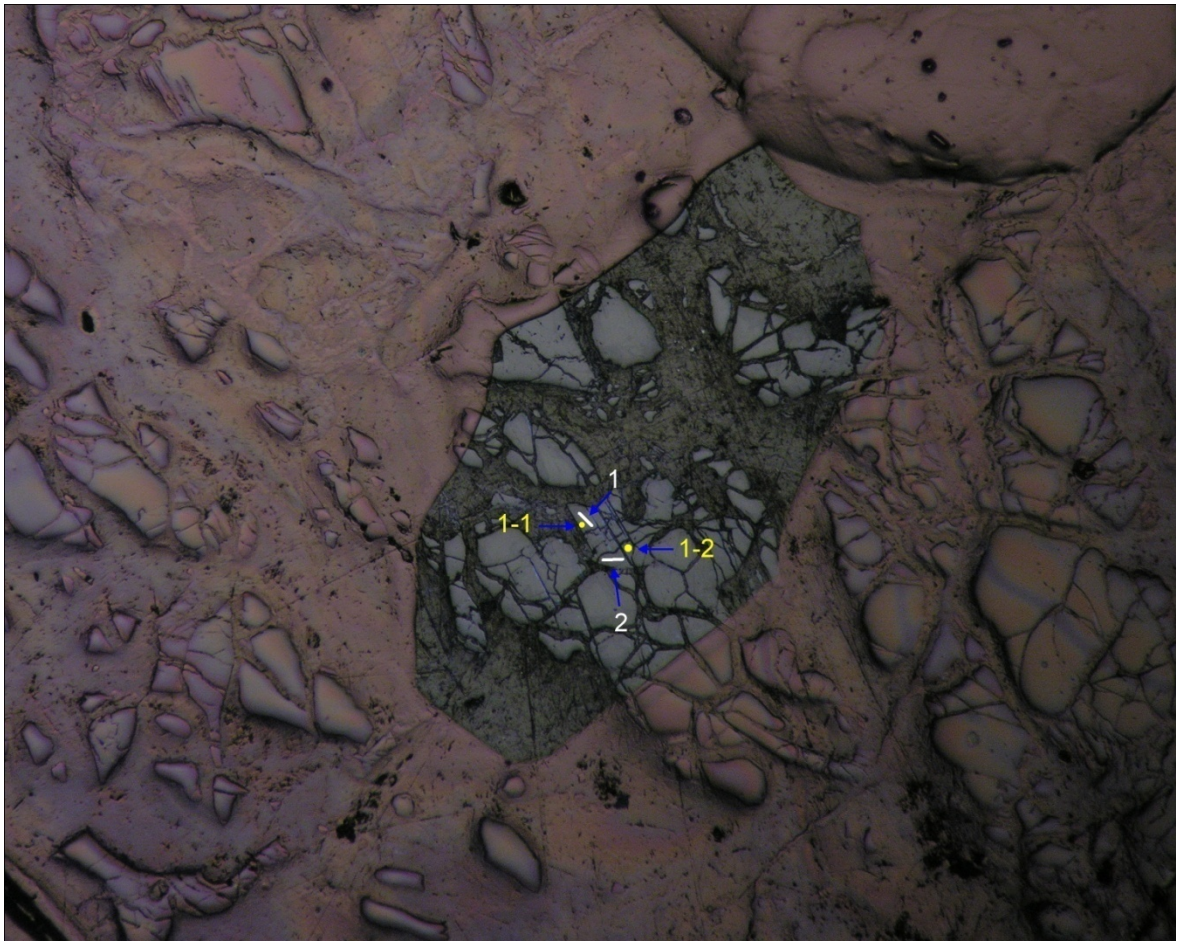

Photomicrograph 2

Sample No. 147-895A-001R-02W (55-61)

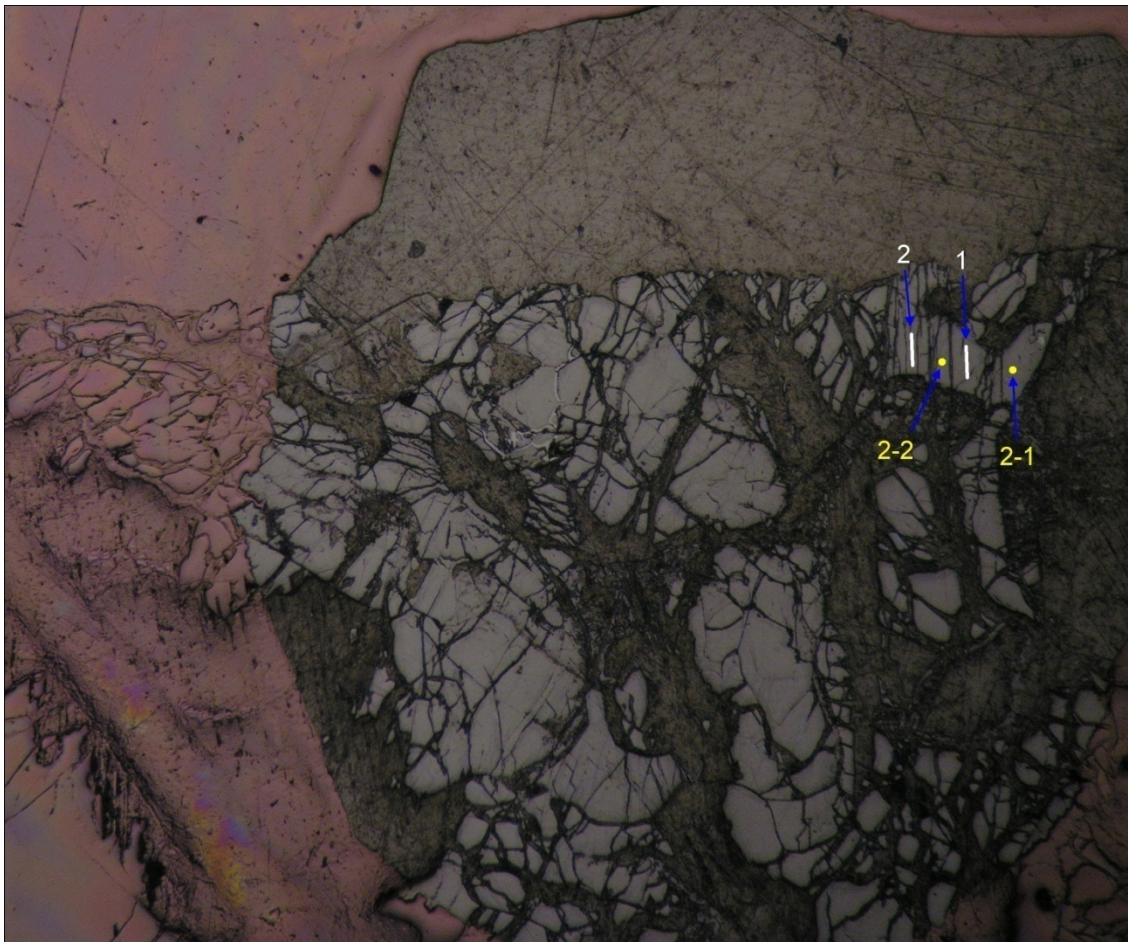

Photomicrograph 3

Sample No. 147-895A-001R-02W (55-61)

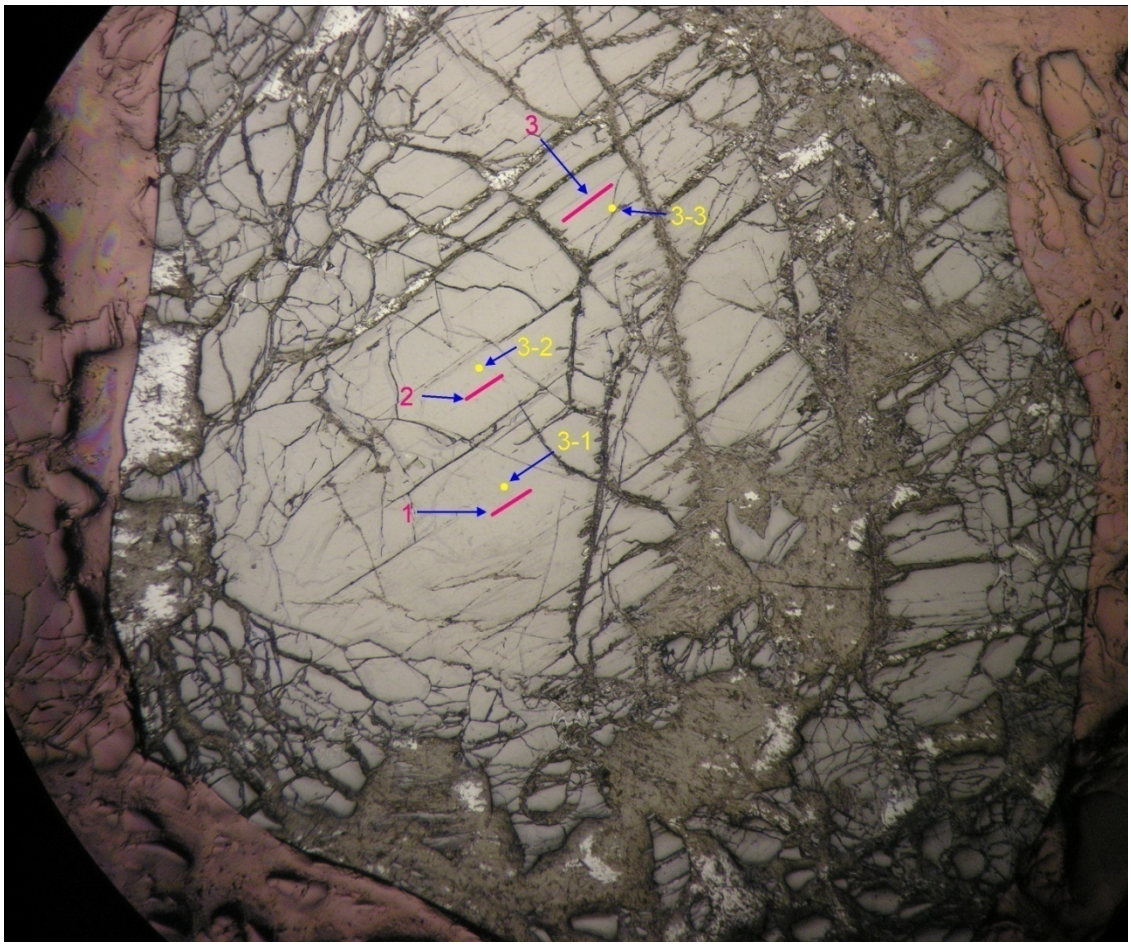

Photomicrograph 4

Sample No. 147-895A-001R-02W (55-61)

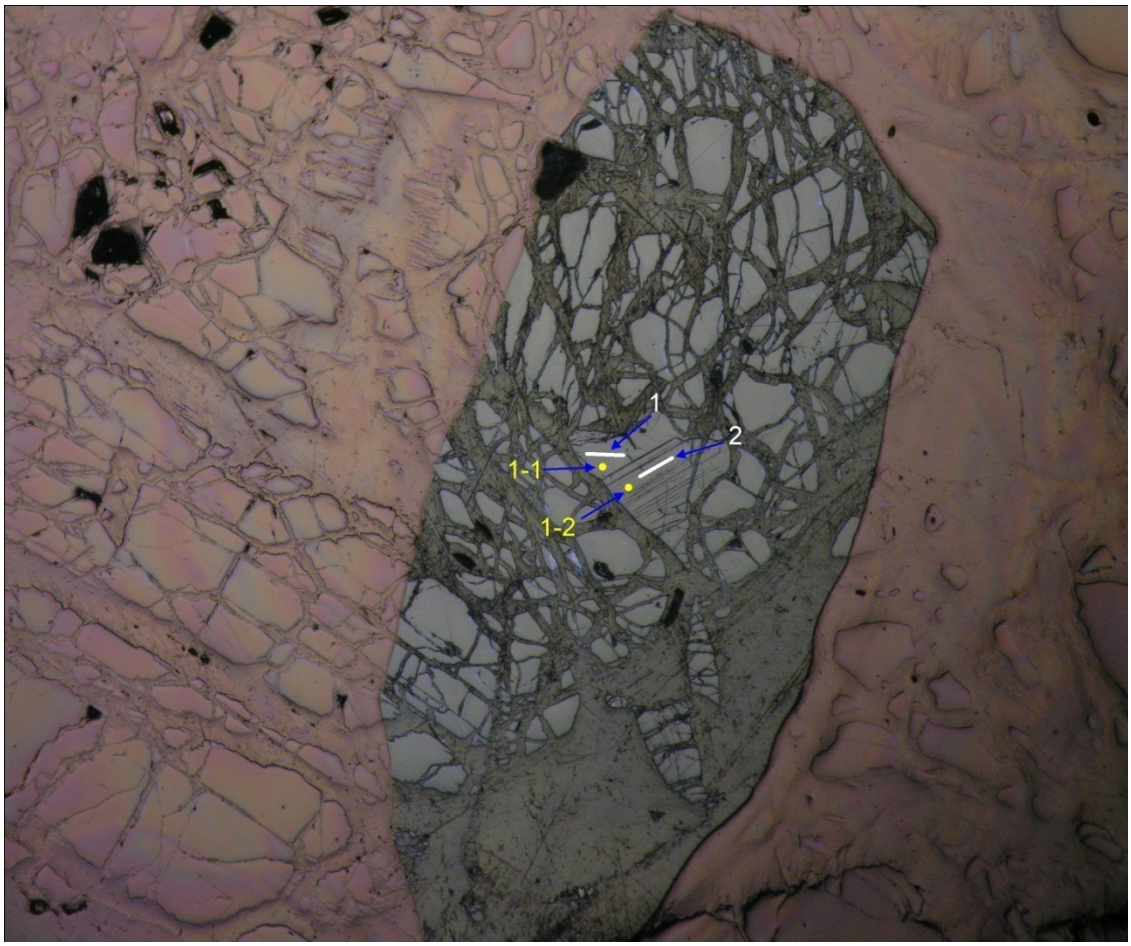

Photomicrograph 5

Sample No. 147-895A-002R-01W (5-10)

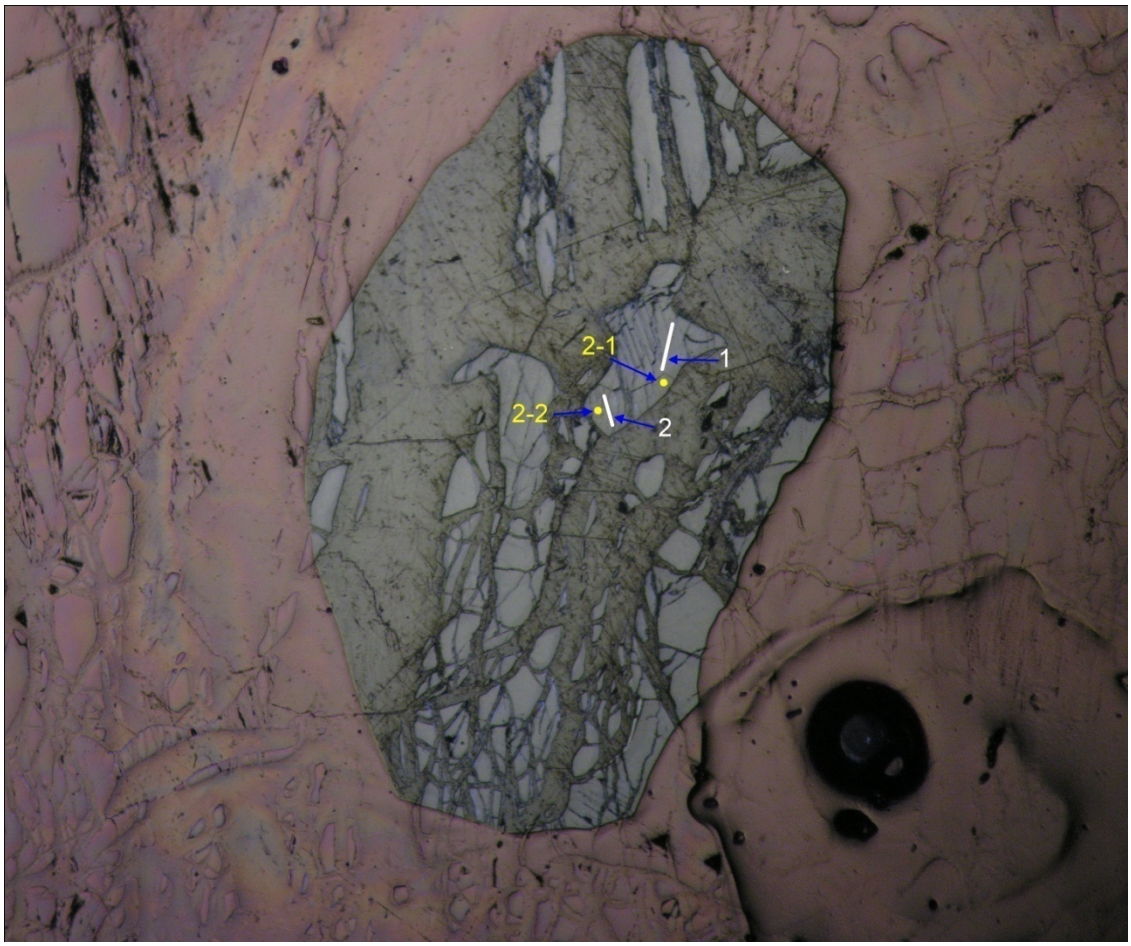

Photomicrograph 6

Sample No. 147-895A-002R-01W (5-10)

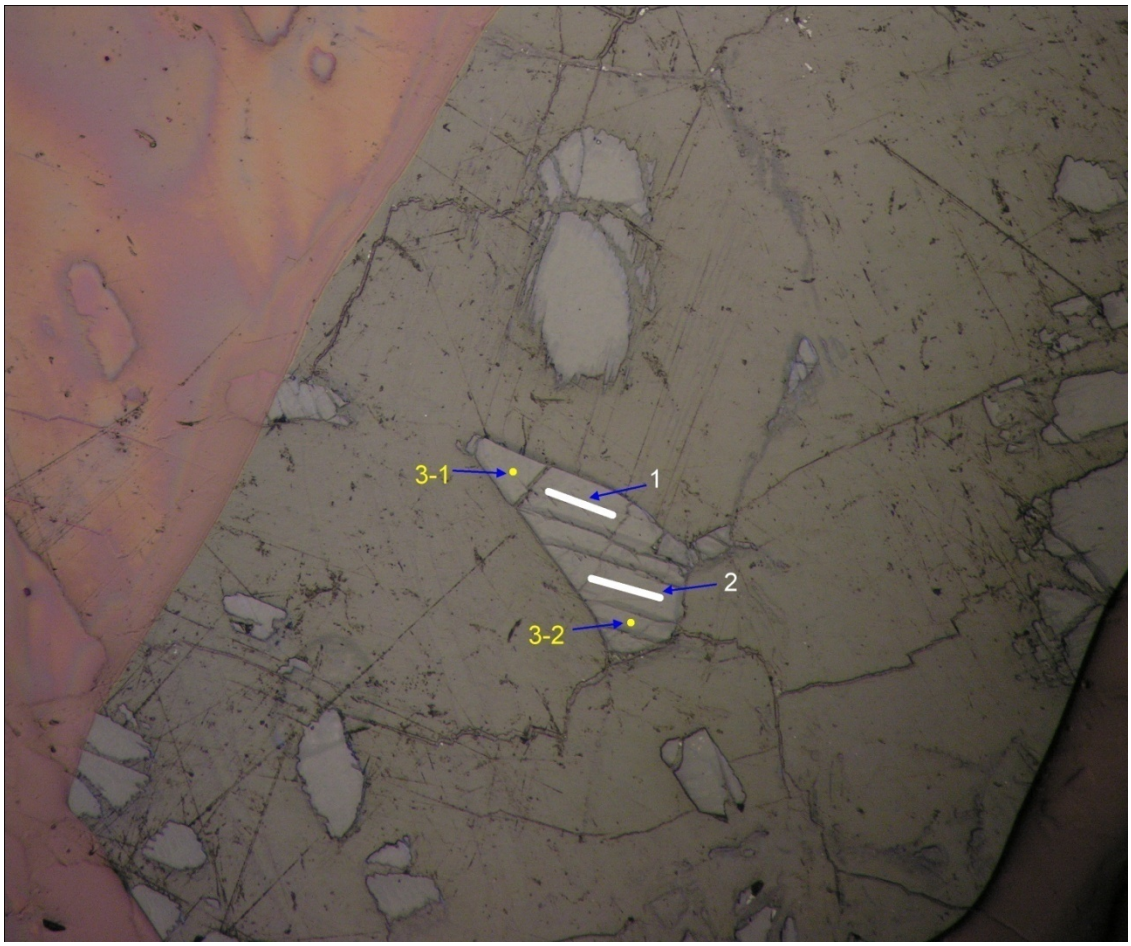

Photomicrograph 7

Sample No. 147-895A-002R-01W (5-10)

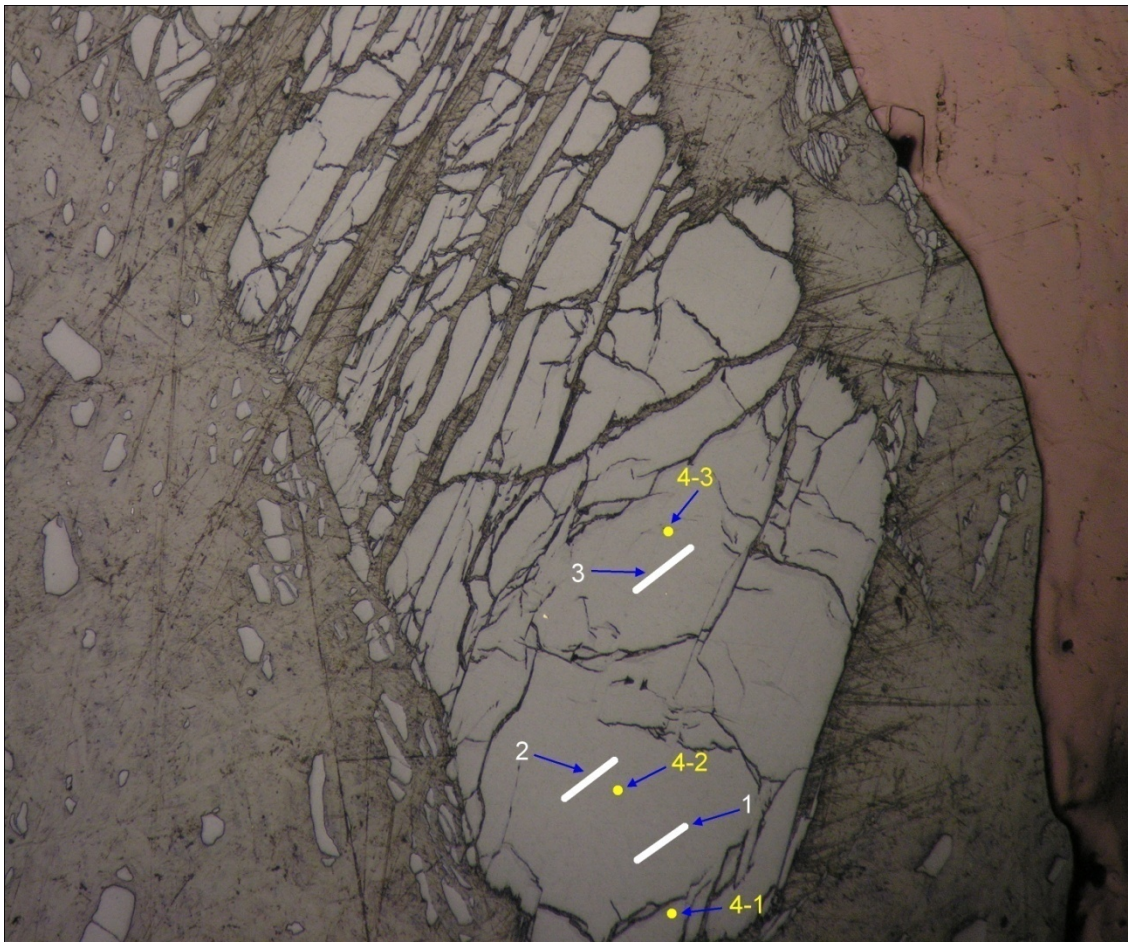

Photomicrograph 8

Sample No. 147-895A-002R-01W (5-10)

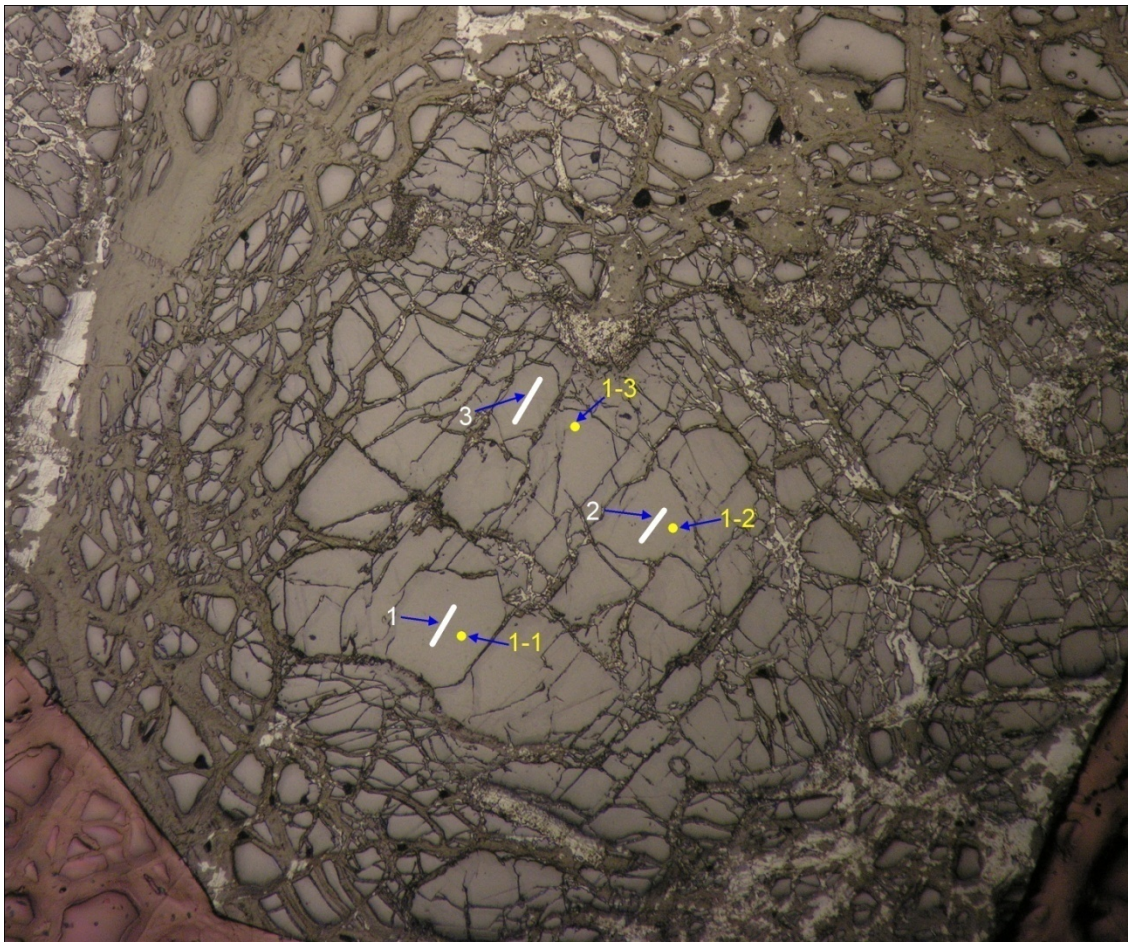

Photomicrograph 9

Sample No. 147-895B-001R-01W (65-72)

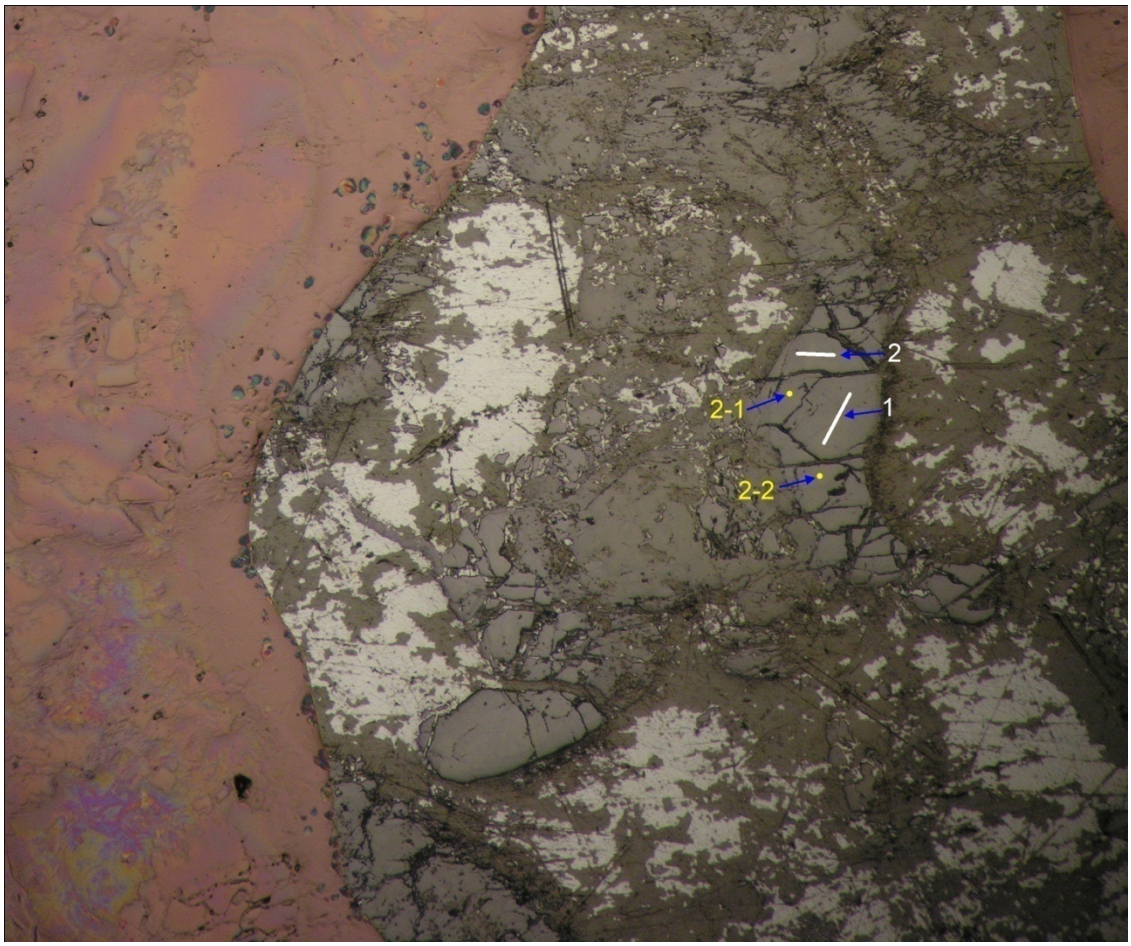

Photomicrograph 10

Sample No. 147-895B-001R-01W (65-72)

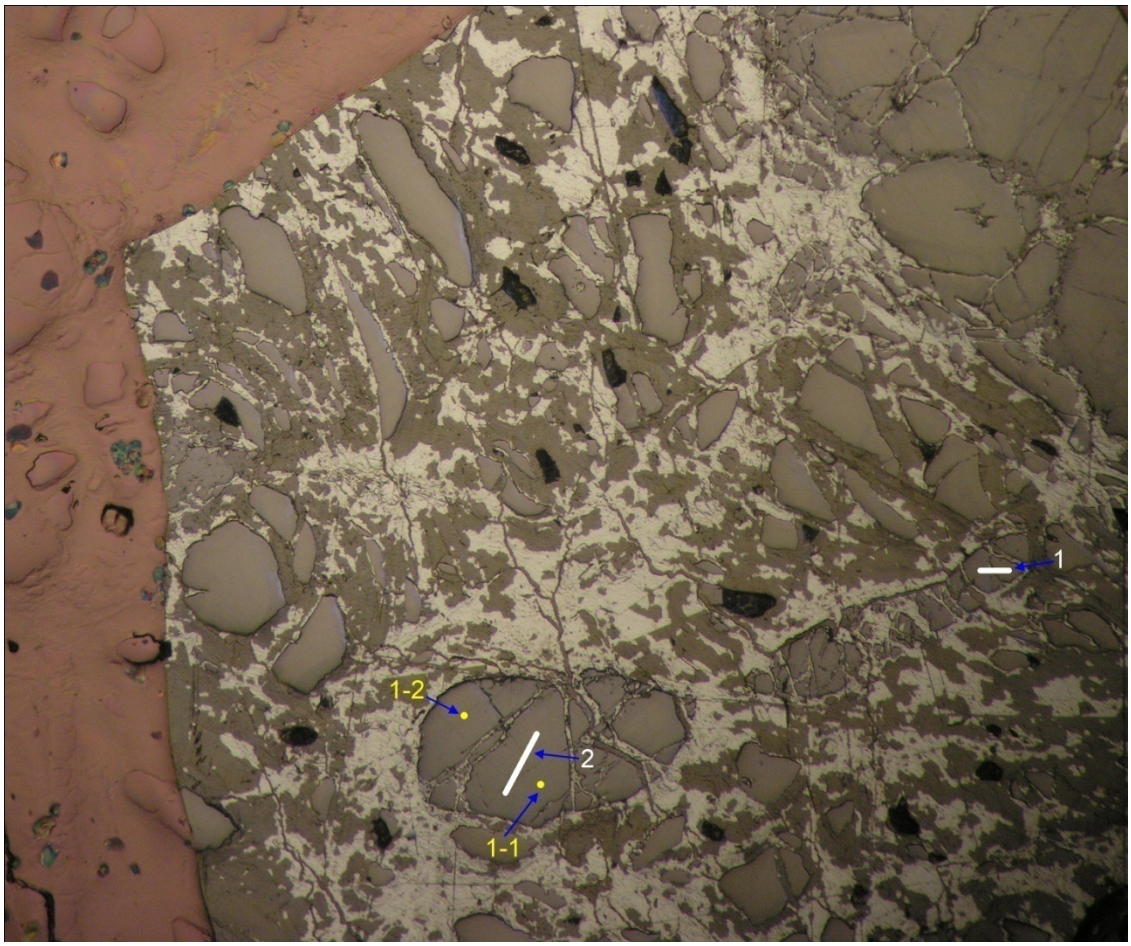

Photomicrograph 11

Sample No. 147-895B-001R-01W (65-72)

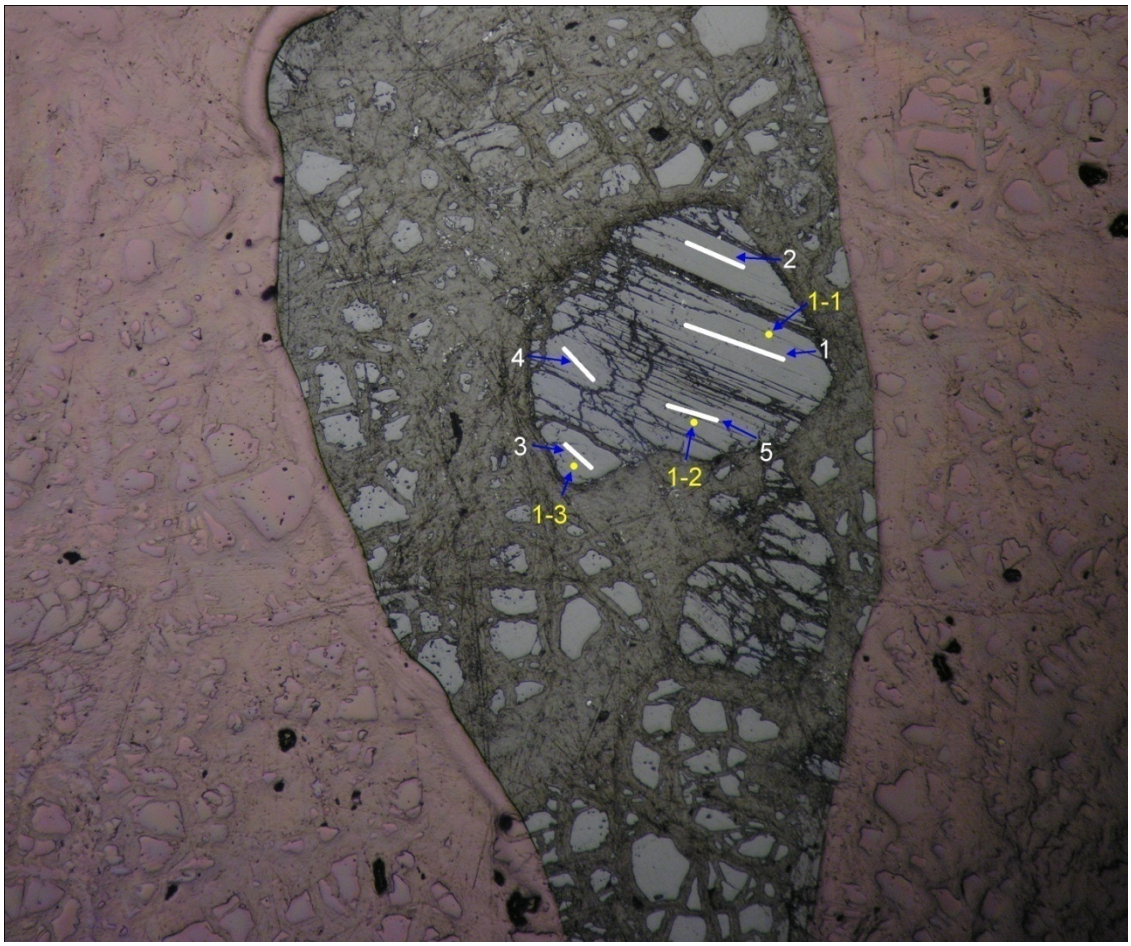

Photomicrograph 12

Sample No. 147-895C-003R-01W (135-143)

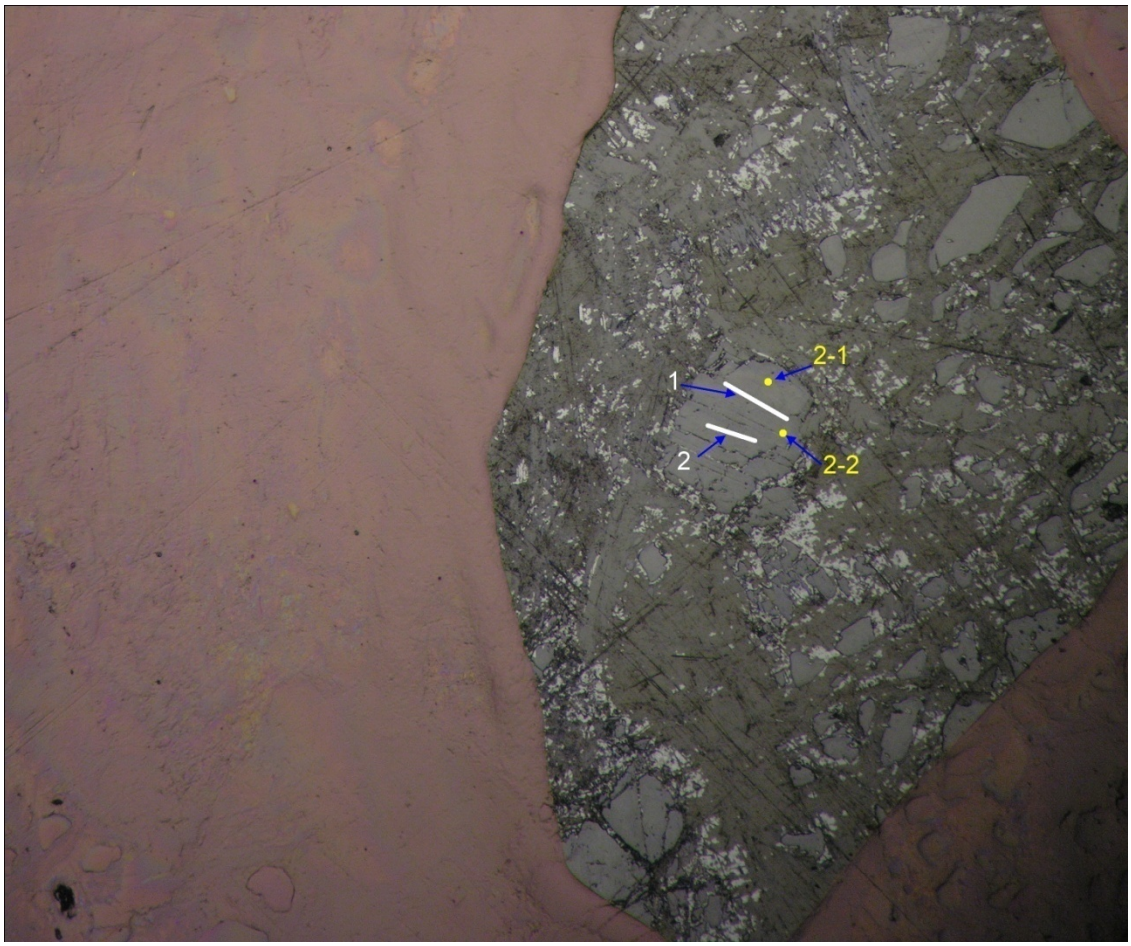

Photomicrograph 13

Sample No. 147-895C-003R-01W (135-143)

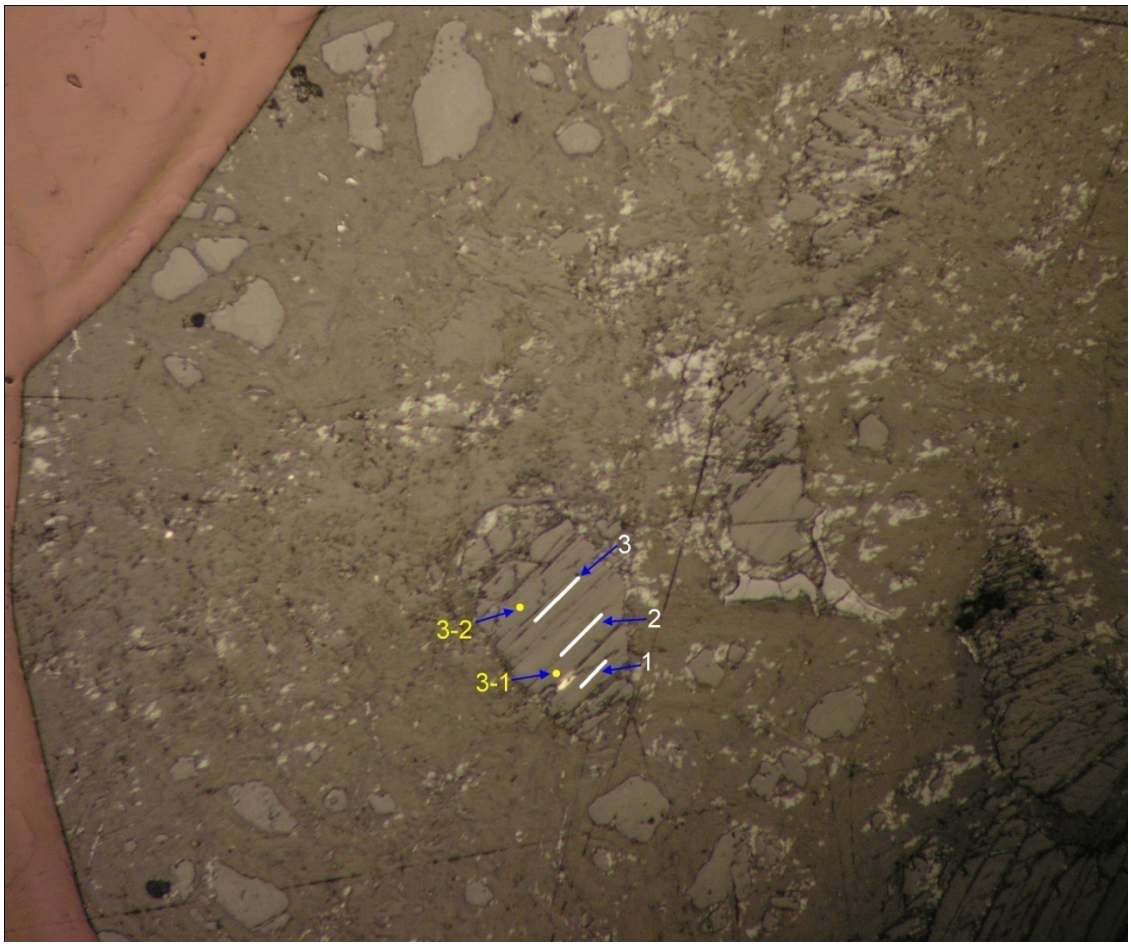

Photomicrograph 14

Sample No. 147-895C-003R-01W (135-143)

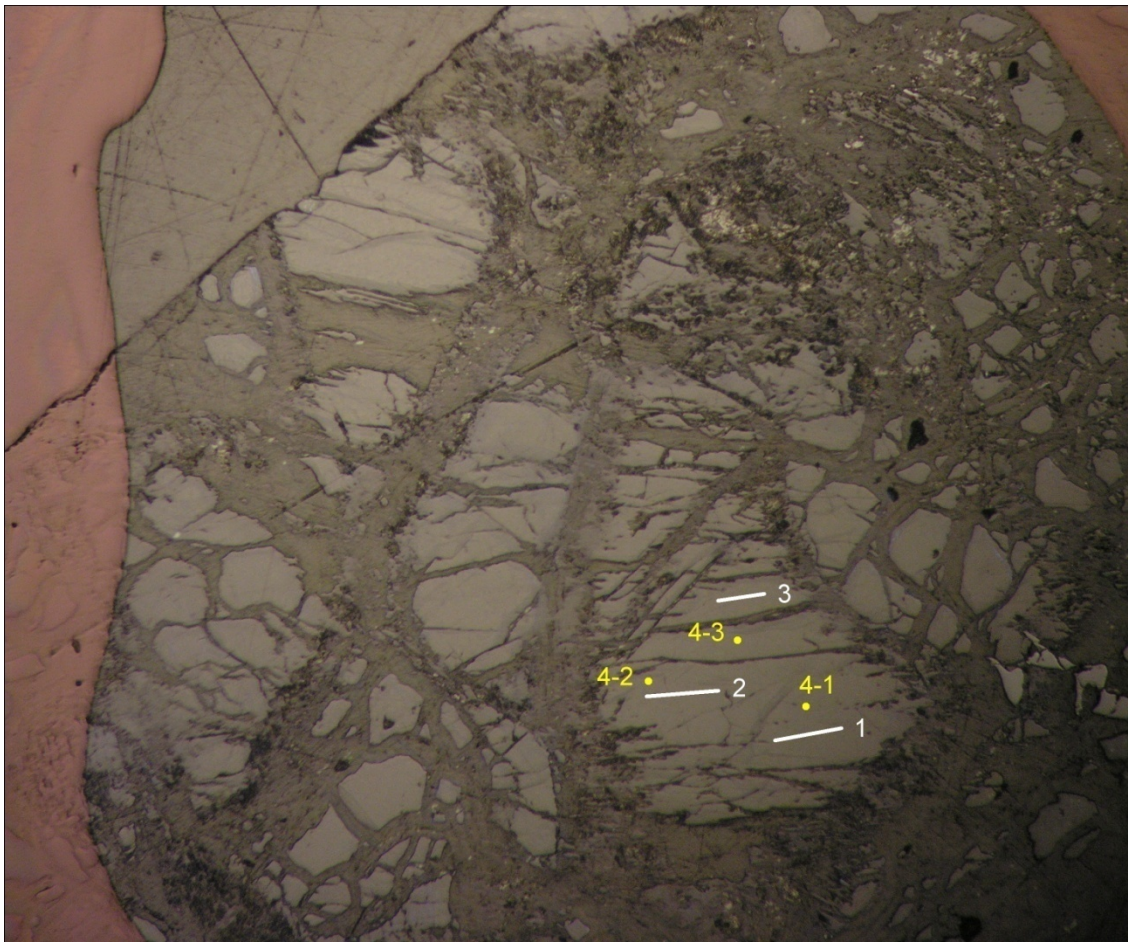

Photomicrograph 15

Sample No. 147-895C-003R-01W (135-143)

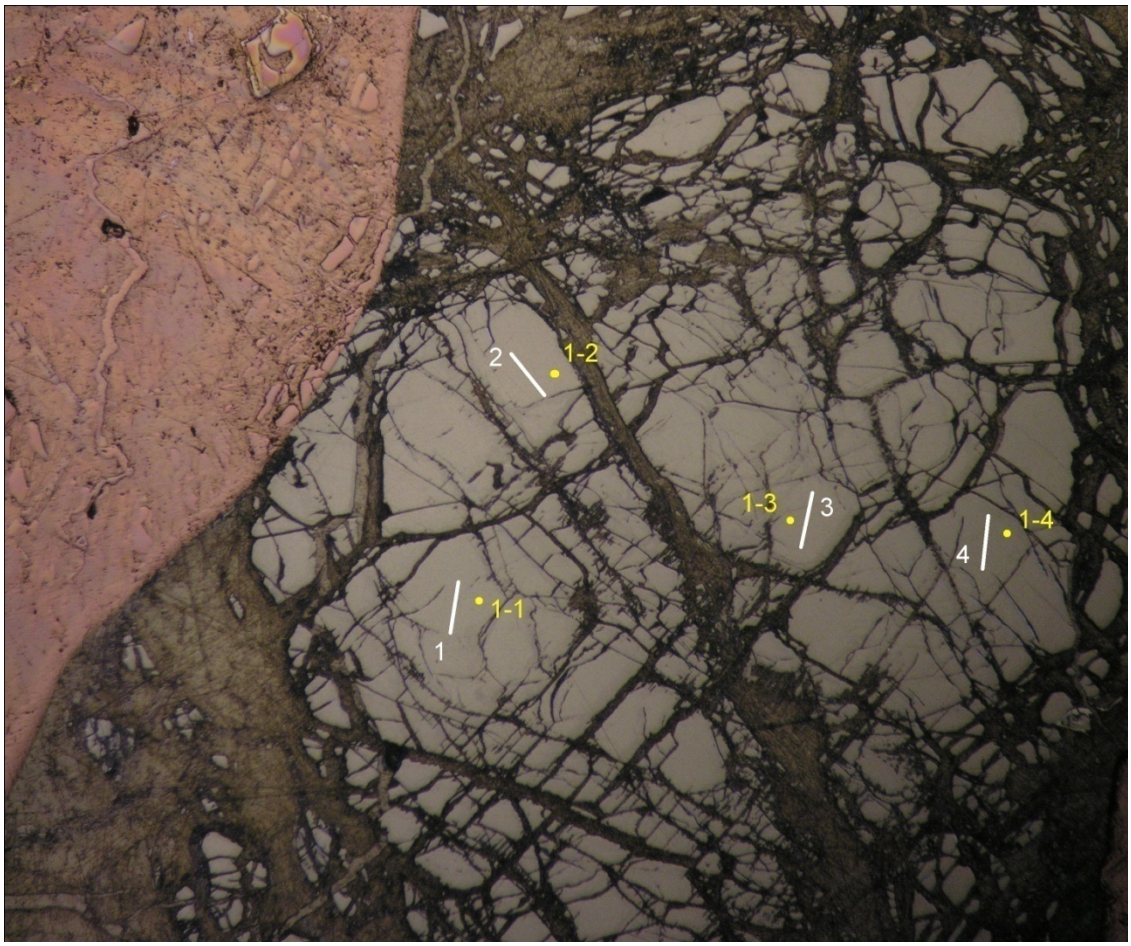

Photomicrograph 16

Sample No. 147-895D-002R-02W (33-38)

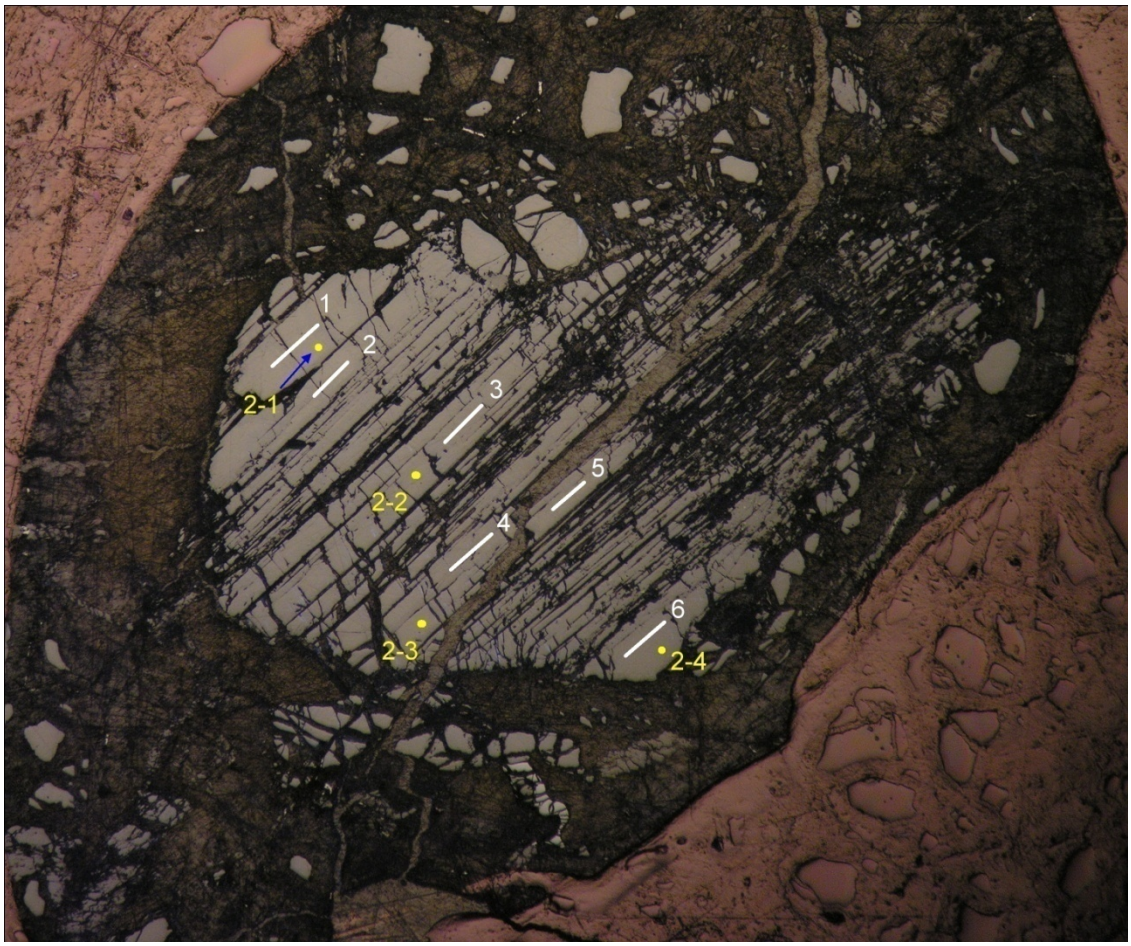

Photomicrograph 17

Sample No. 147-895D-002R-02W (33-38)

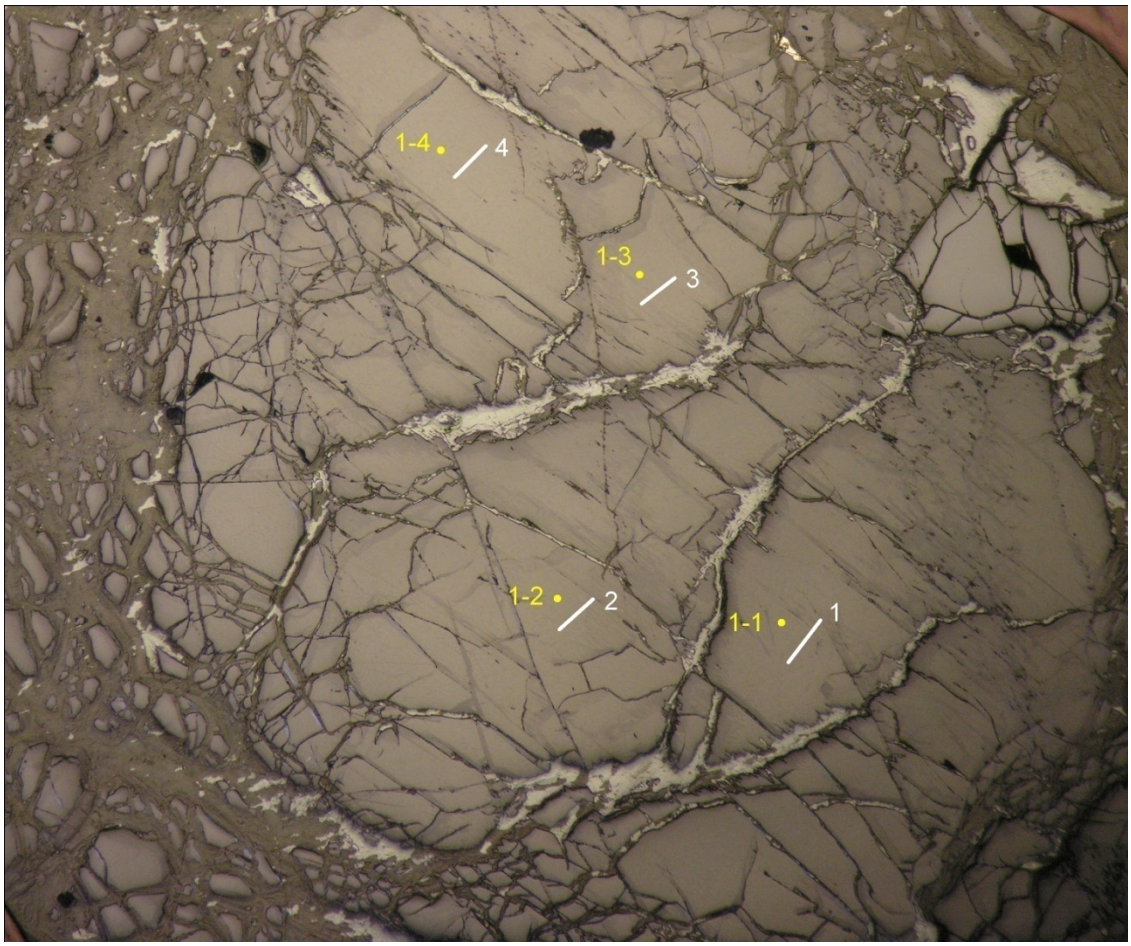

Photomicrograph 18

Sample No. 147-895D-003R-01W (34-39)

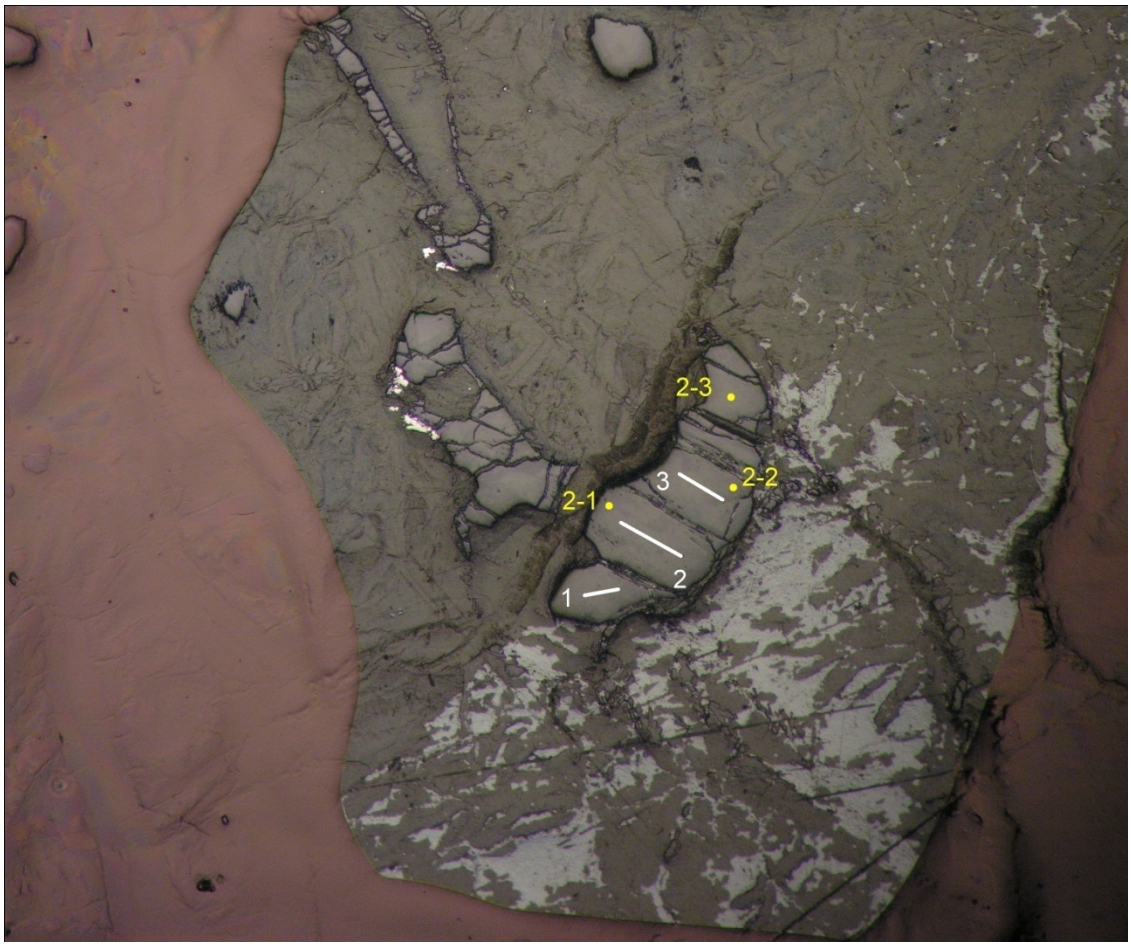

Photomicrograph 19

Sample No. 147-895D-003R-01W (34-39)

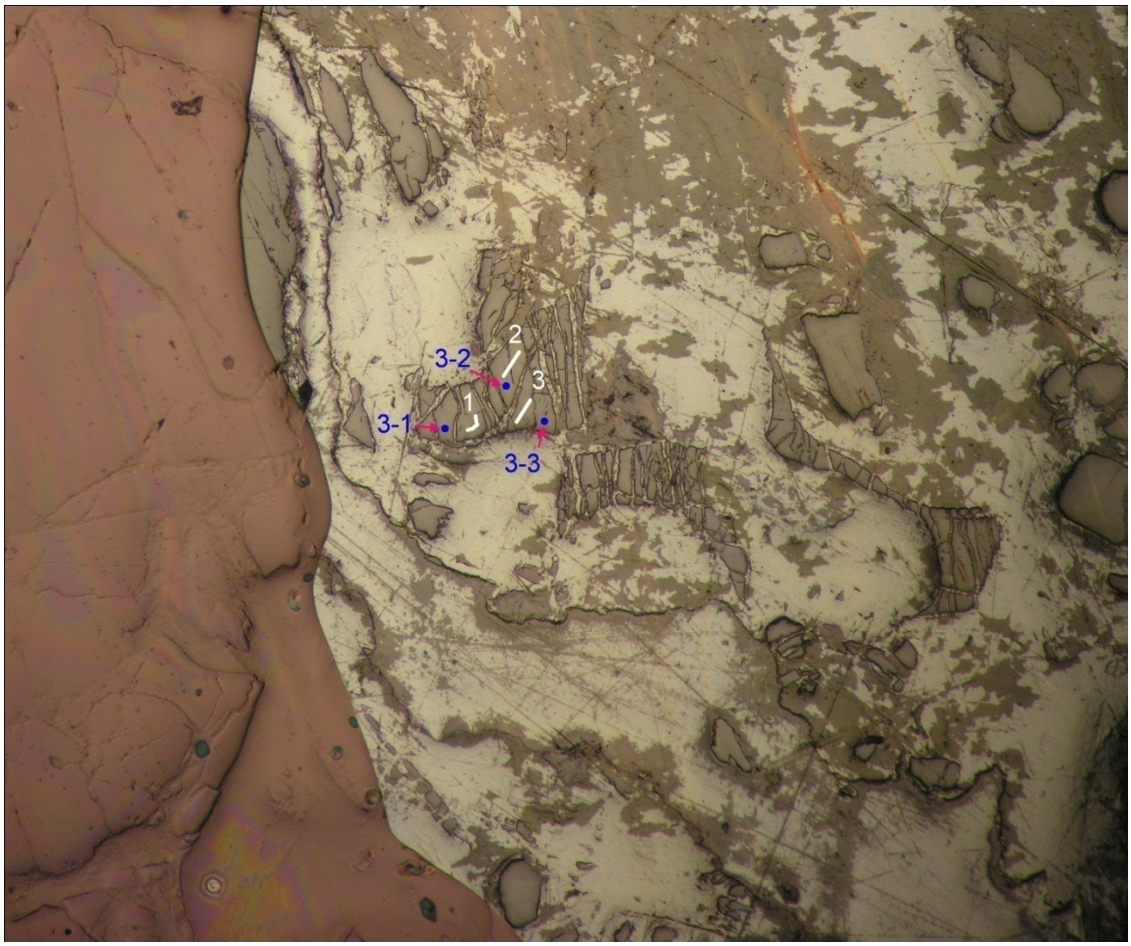

Photomicrograph 20

Sample No. 147-895D-003R-01W (34-39)

Photomicrograph 21

Sample No. 147-895D-003R-01W (61-70)

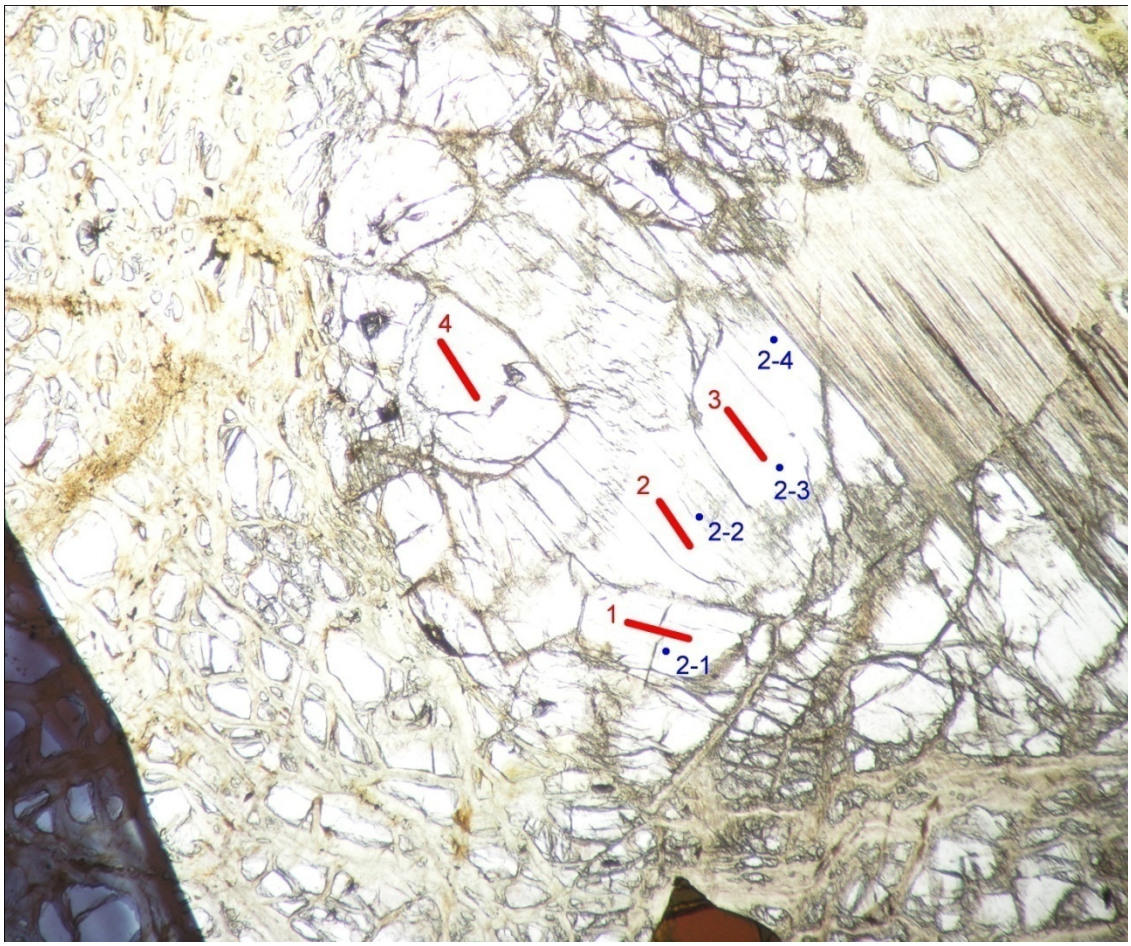

Photomicrograph 22

Sample No. 147-895D-003R-01W (61-70)

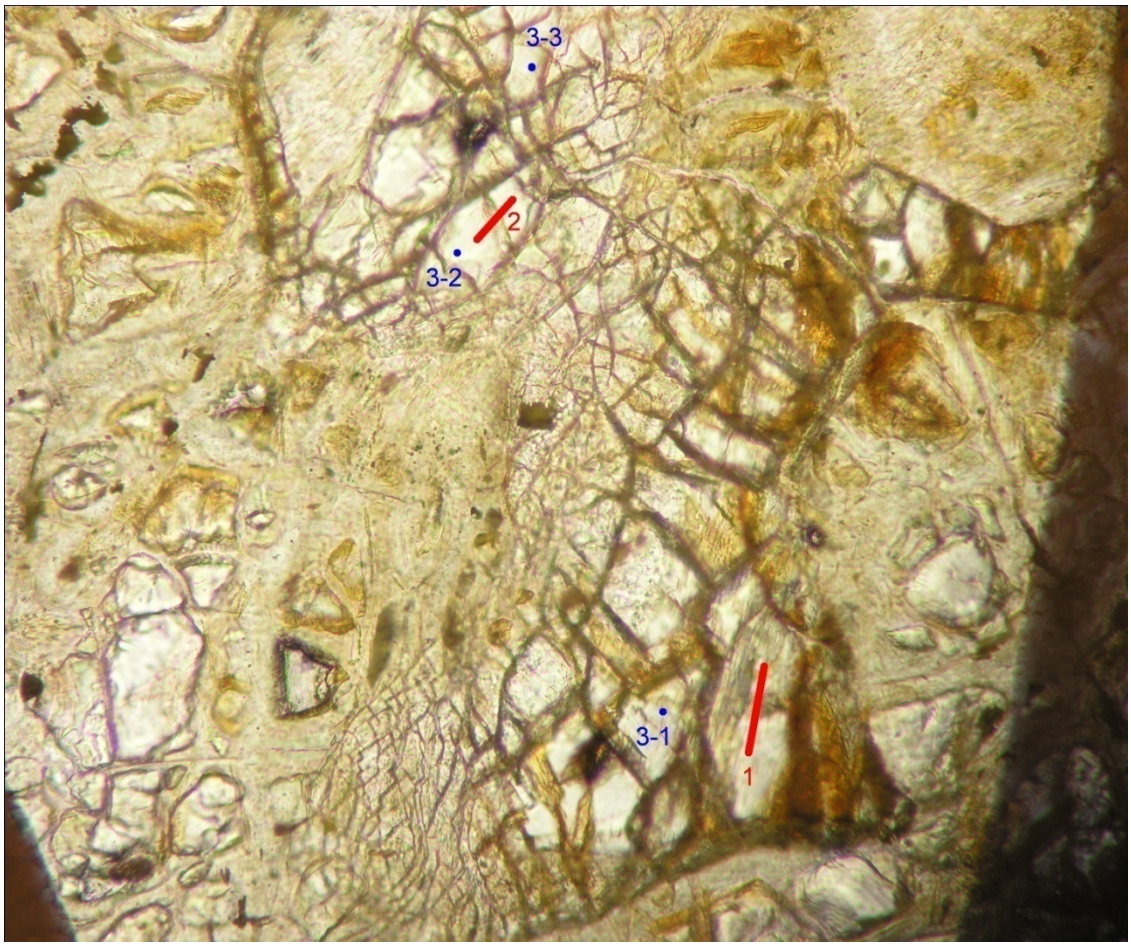

Photomicrograph 23

Sample No. 147-895D-003R-01W (61-70)

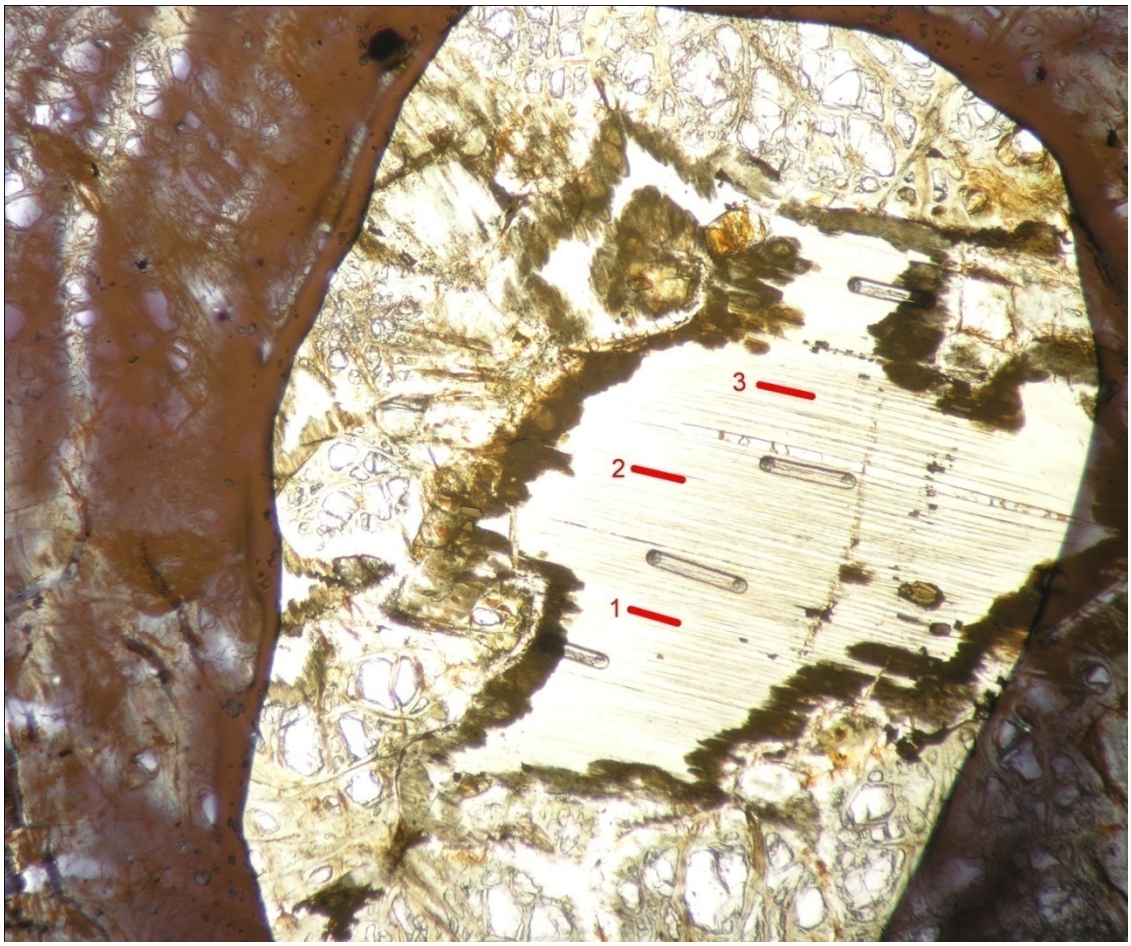

Photomicrograph 24

Sample No. 147-895D-004R-01W (54-60)

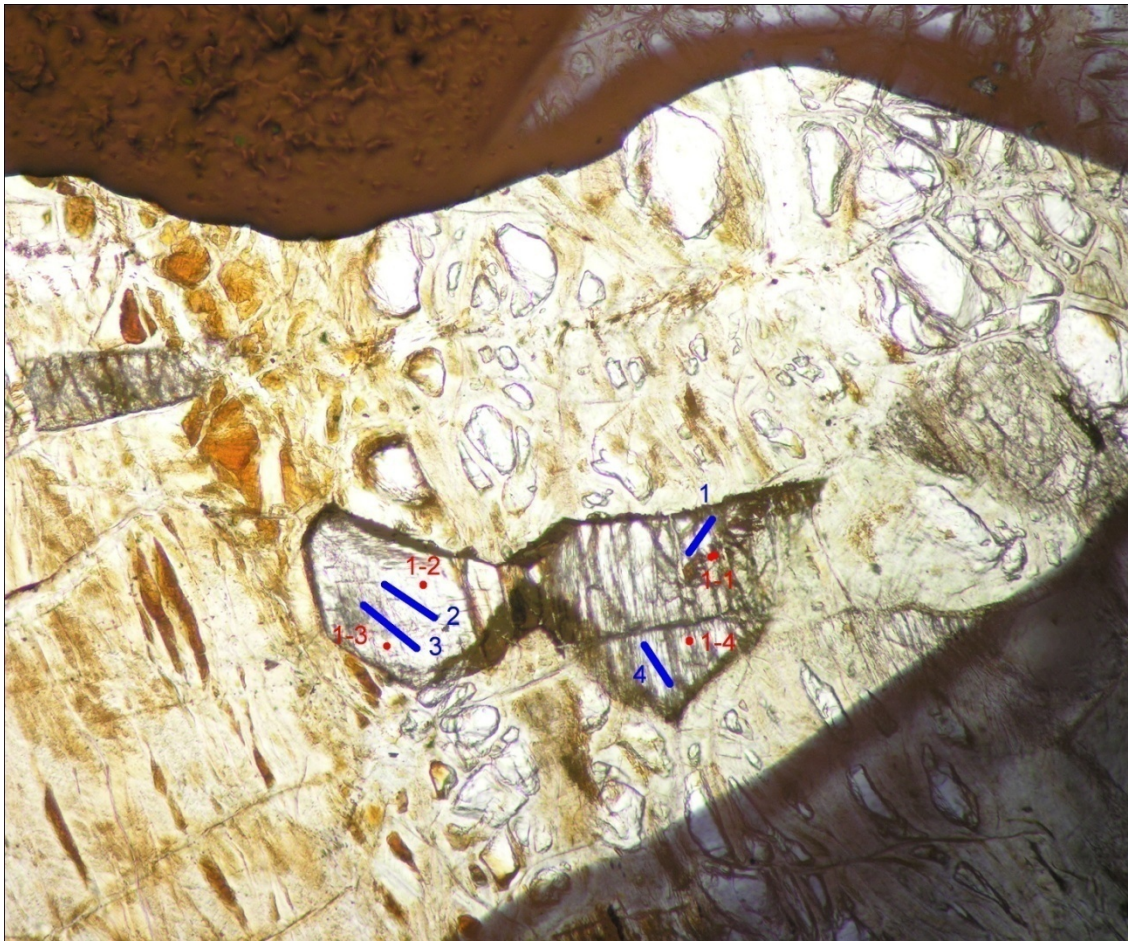

Photomicrograph 25

Sample No. 147-895D-004R-01W (54-60)

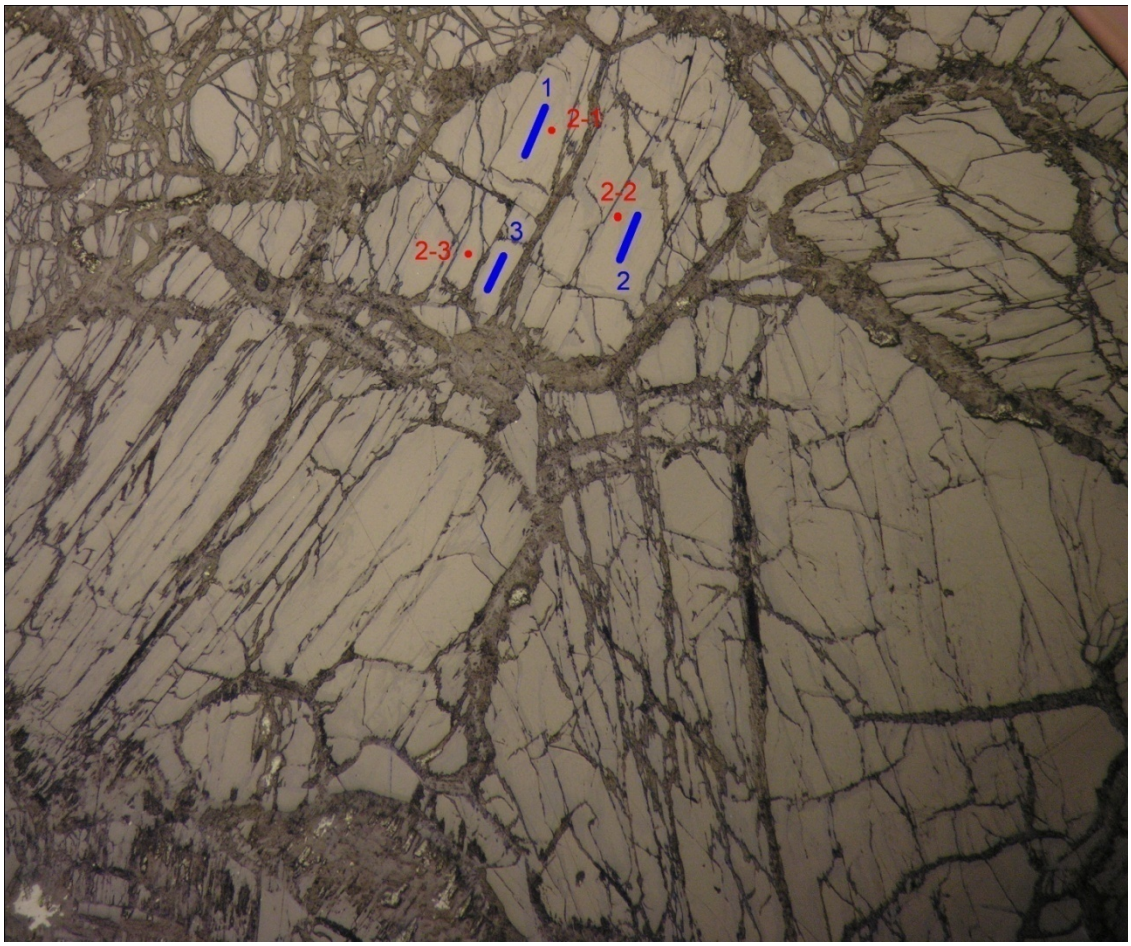

Photomicrograph 28

Sample No. 147-895D-004R-01W (54-60)

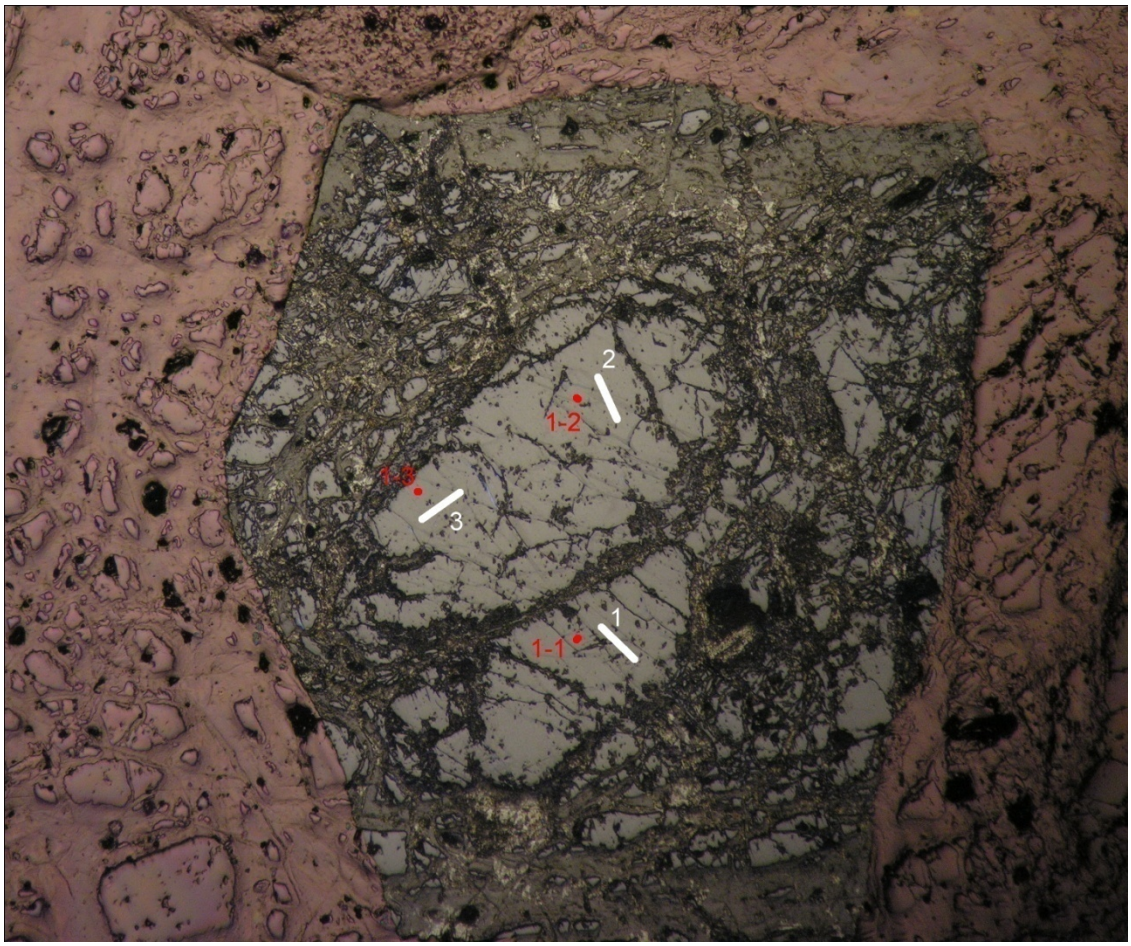

Photomicrograph 29

Sample No. 147-895D-004R-03W (52-58)

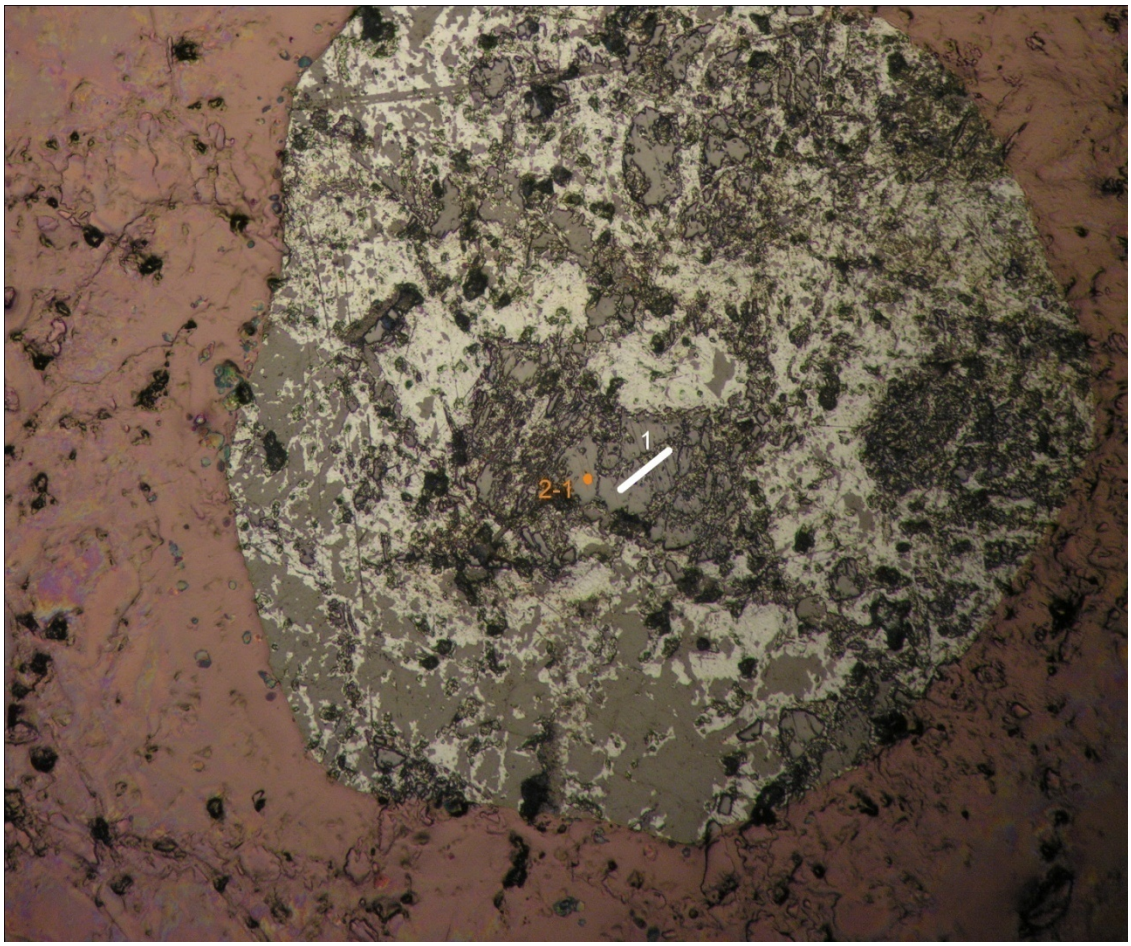

Photomicrograph 31

Sample No. 147-895D-004R-03W (52-58)

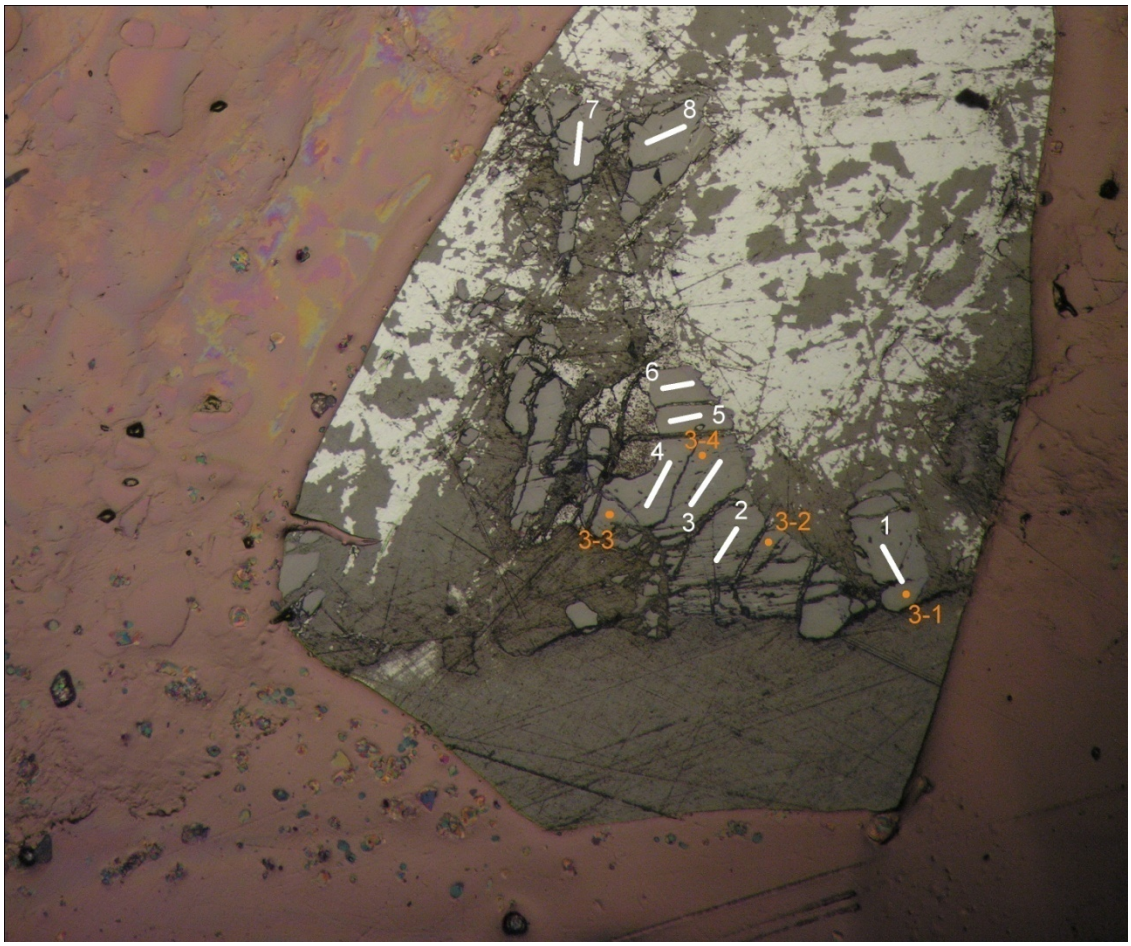

Photomicrograph 34

Sample No. 147-895D-004R-03W (52-58)

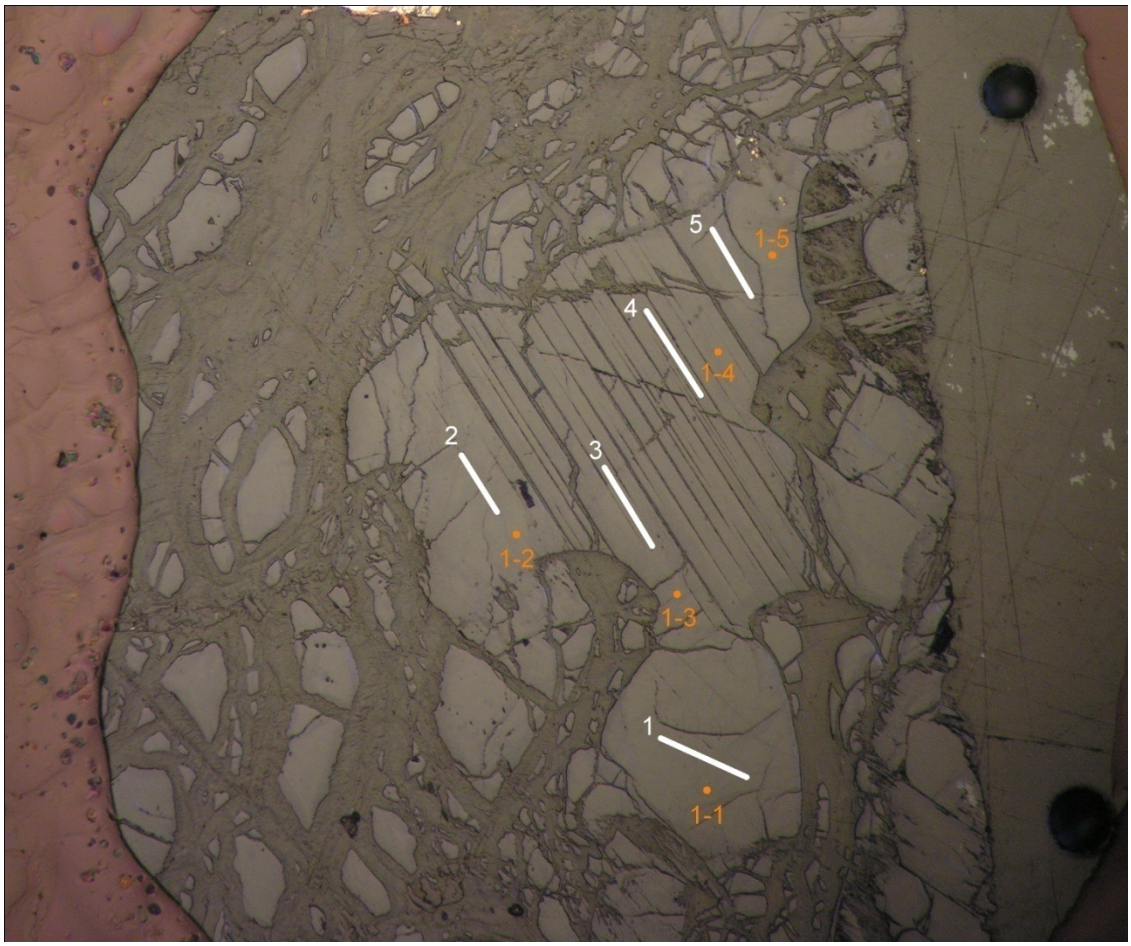

Photomicrograph 35

Sample No. 147-895D-004R-03W (112-116)

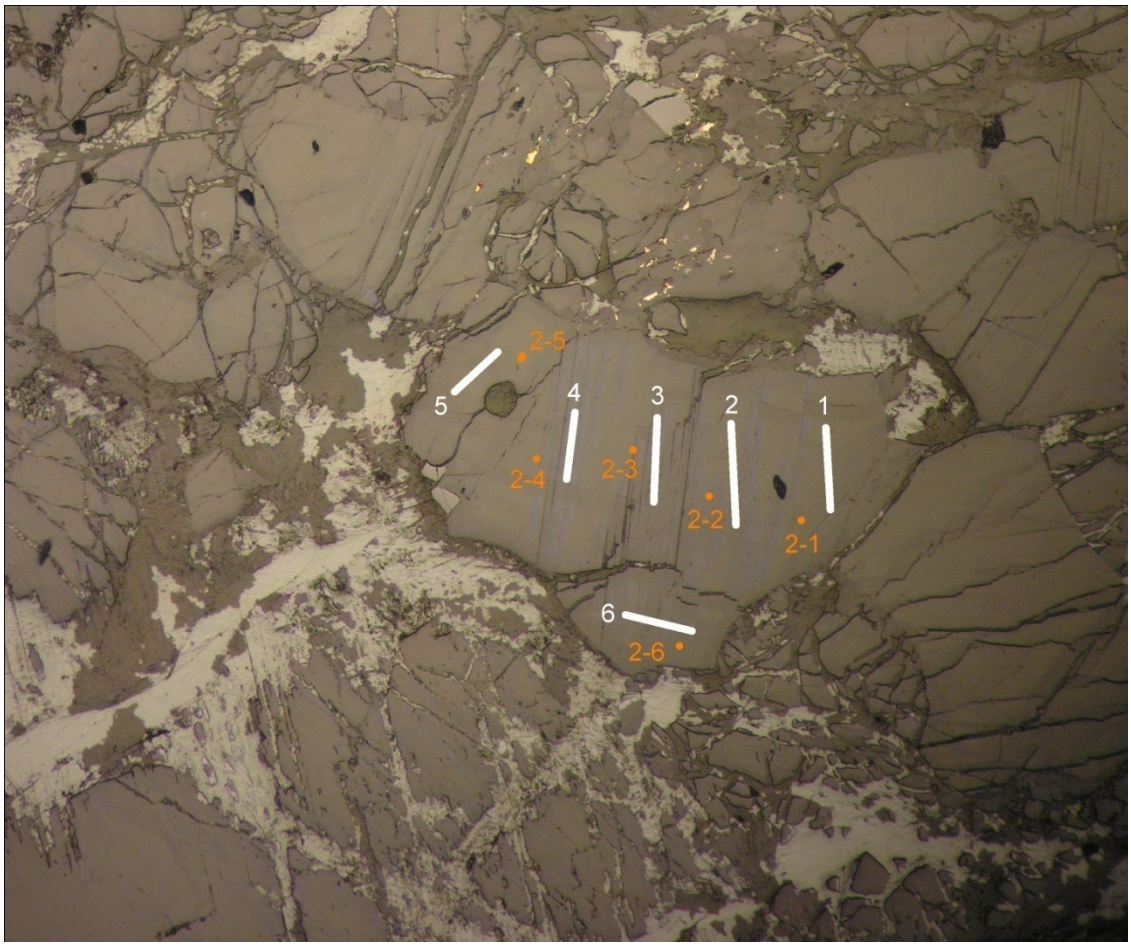

Photomicrograph 26

Sample No. 147-895D-004R-03W (112-116)

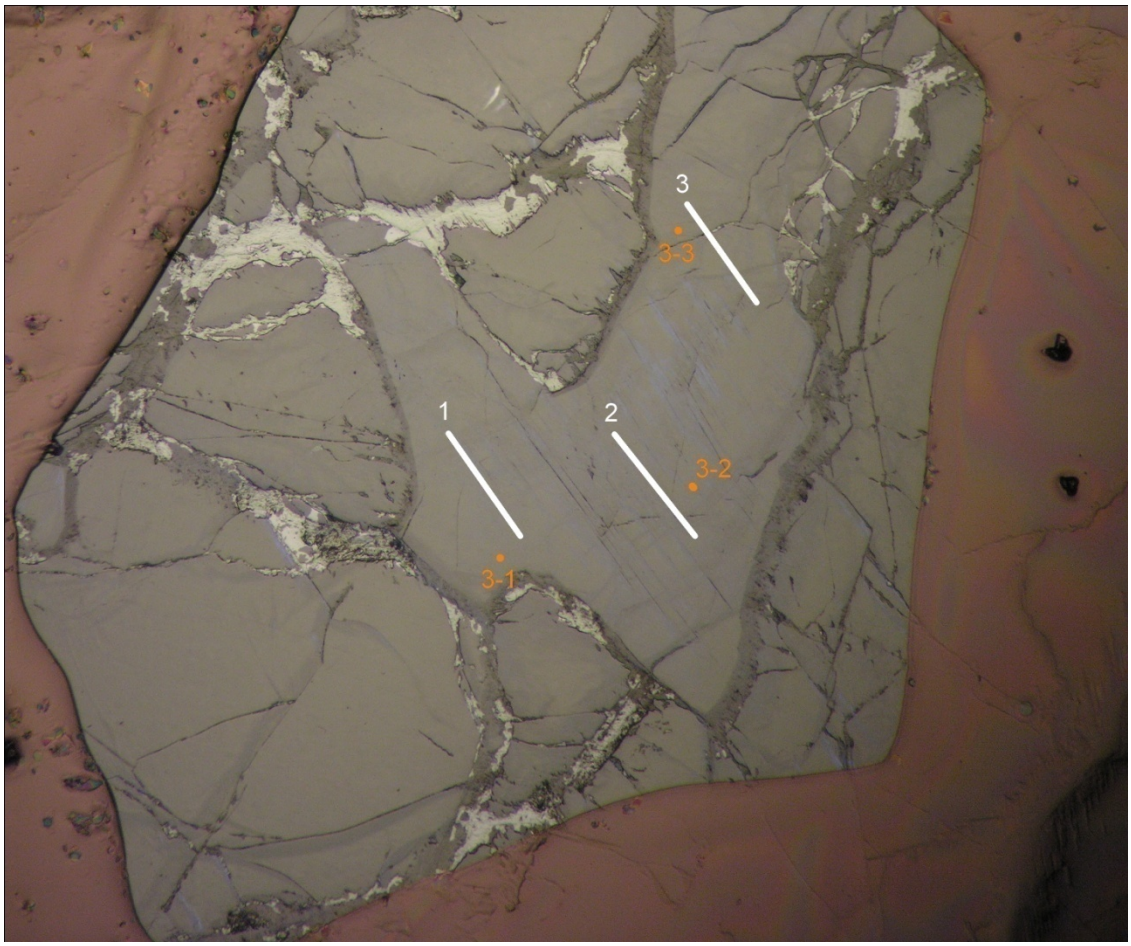

Photomicrograph 37

Sample No. 147-895D-004R-03W (112-116)

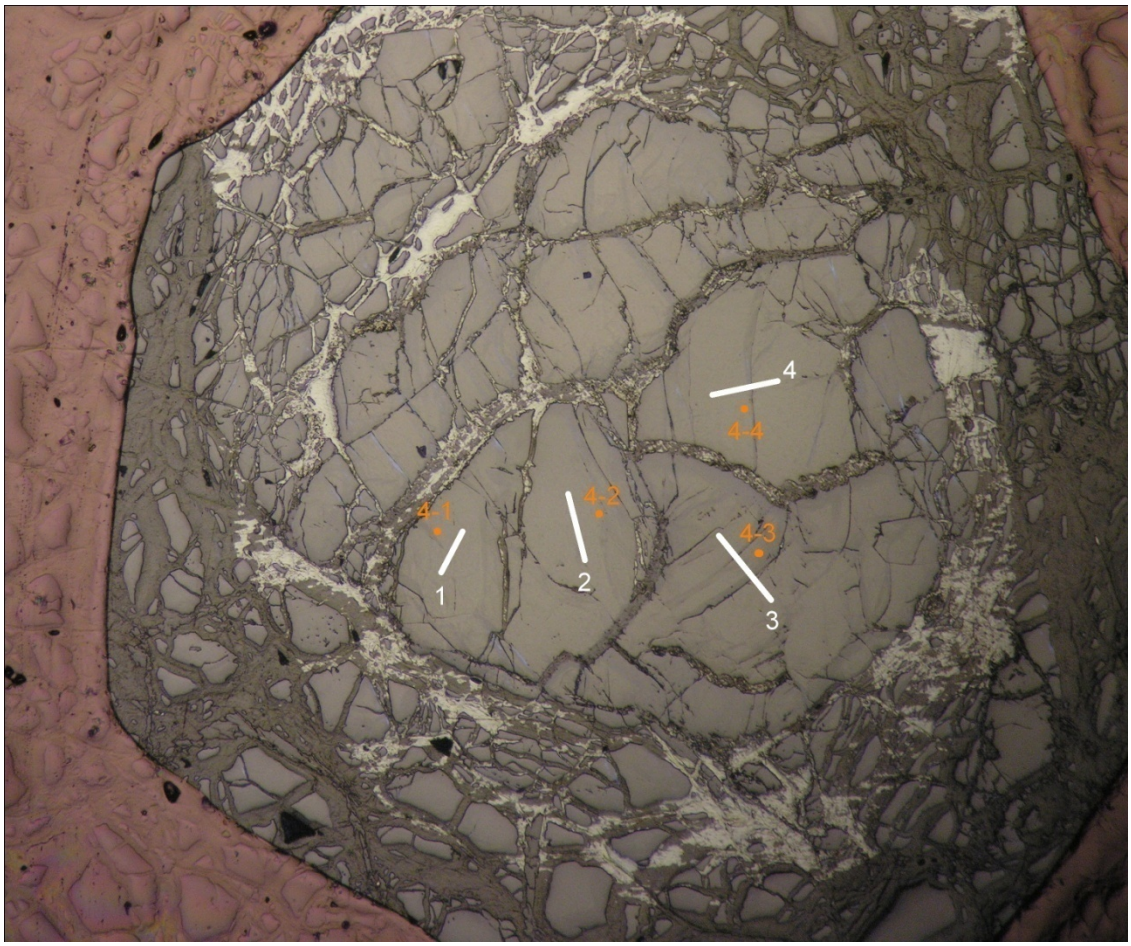

Photomicrograph 38

Sample No. 147-895D-004R-03W (112-116)

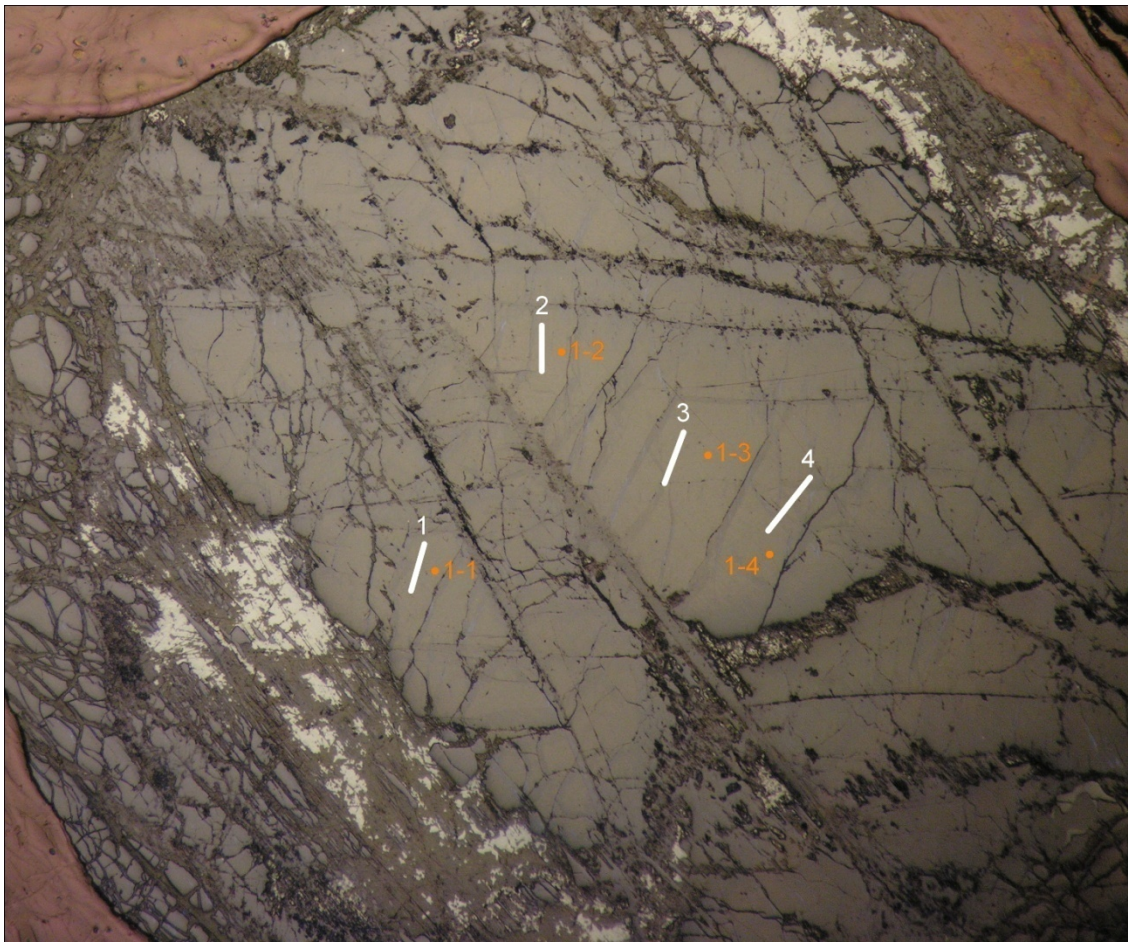

Photomicrograph 39

Sample No. 147-895D-004R-05W (11-18)

Photomicrograph 40

Sample No. 147-895D-004R-05W (11-18)

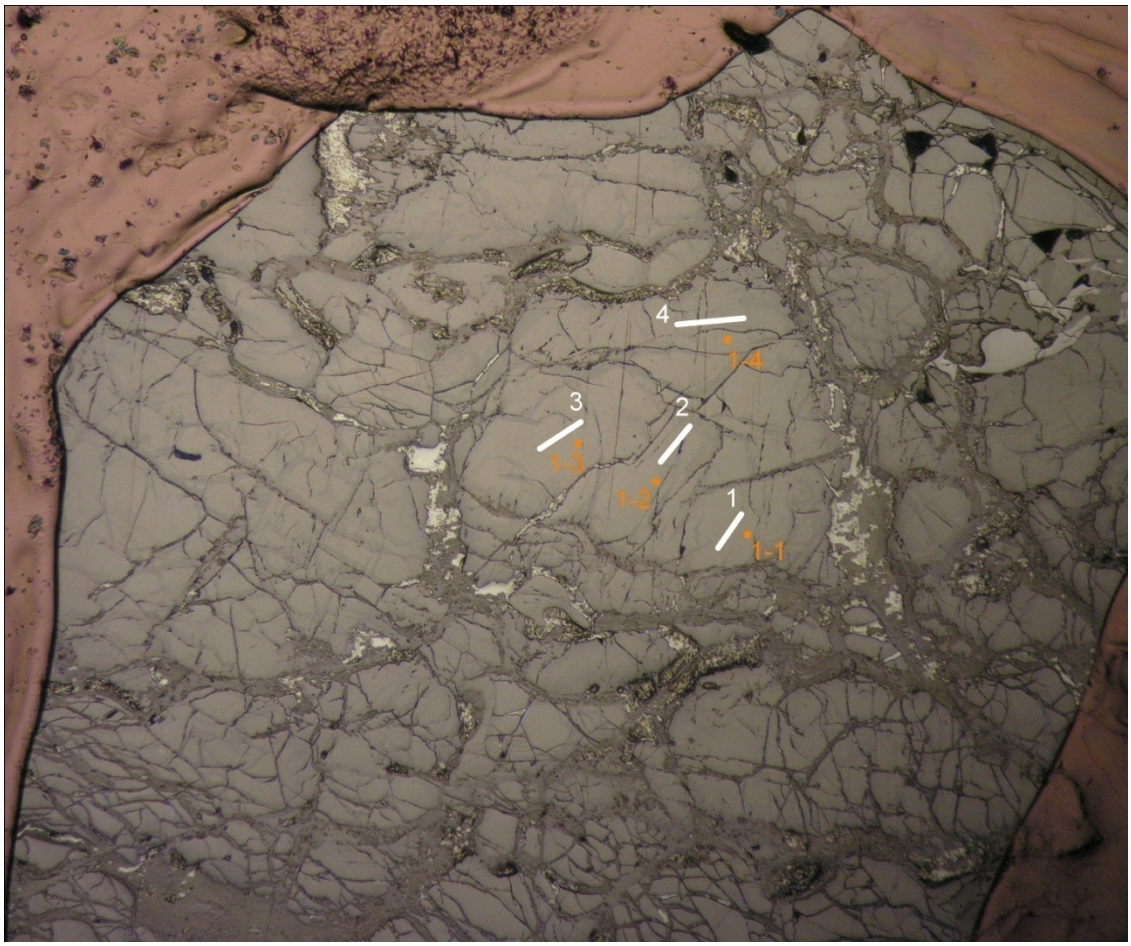

Photomicrograph 42

Sample No. 147-895D-005R-02W (103-112)

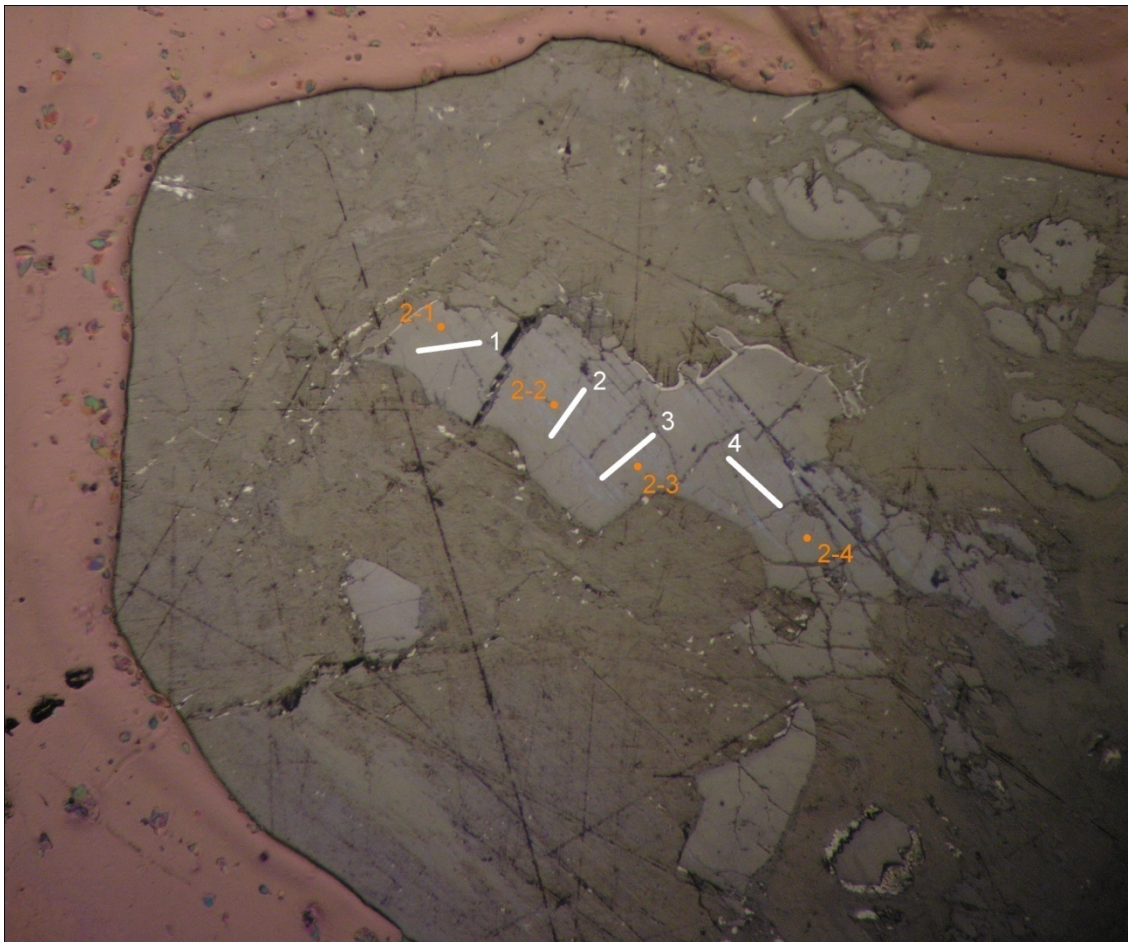

Photomicrograph 43

Sample No. 147-895D-005R-02W (103-112)

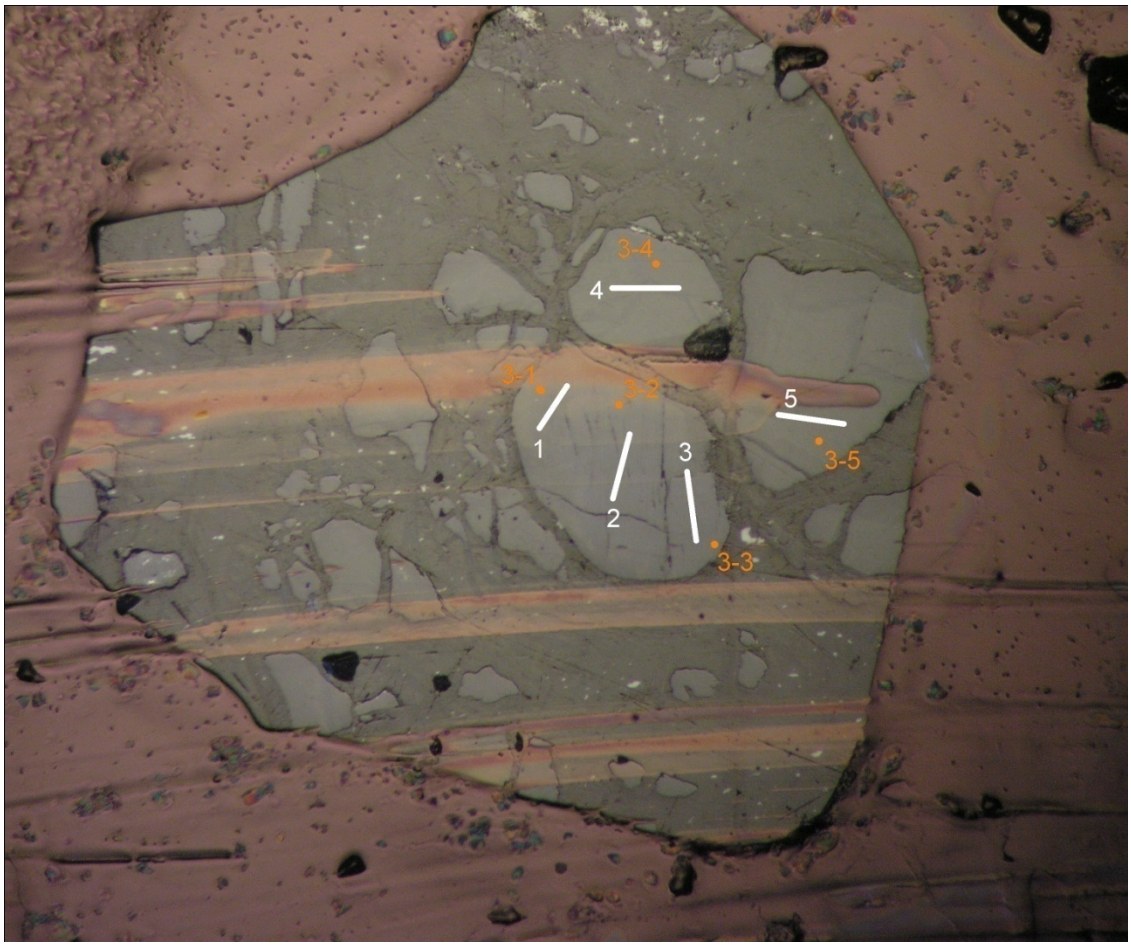

Photomicrograph 45

Sample No. 147-895D-005R-02W (103-112)

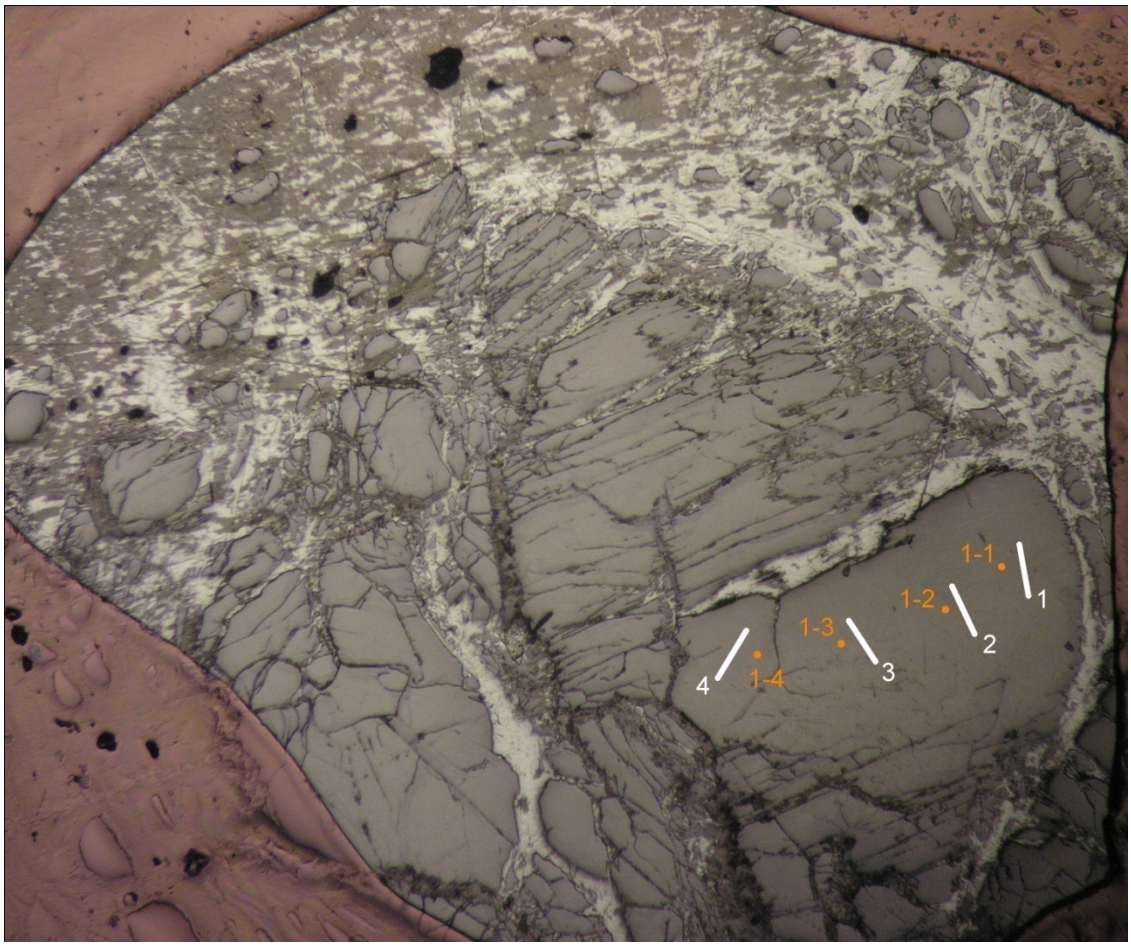

Photomicrograph 46

Sample No. 147-895D-007R-02W (127-135)

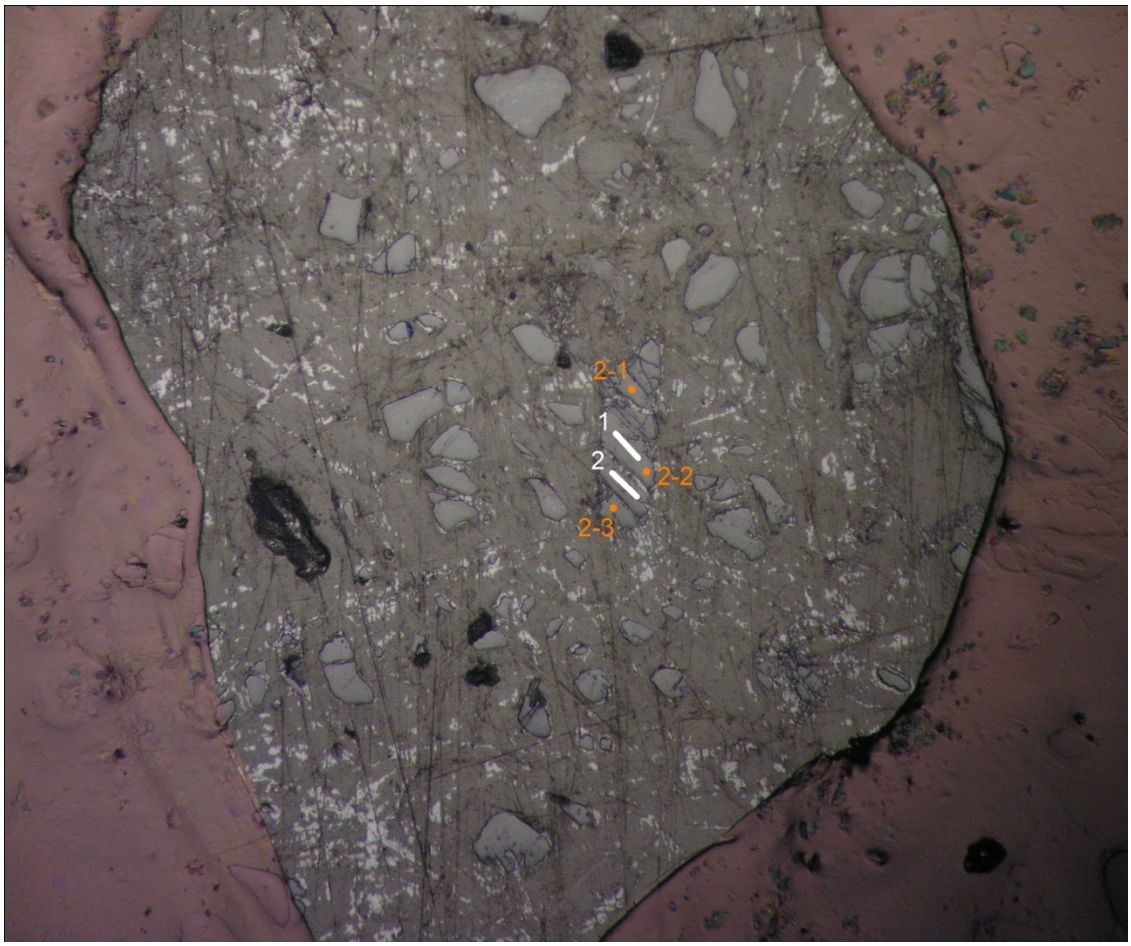

Photomicrograph 47

Sample No. 147-895D-007R-02W (127-135)

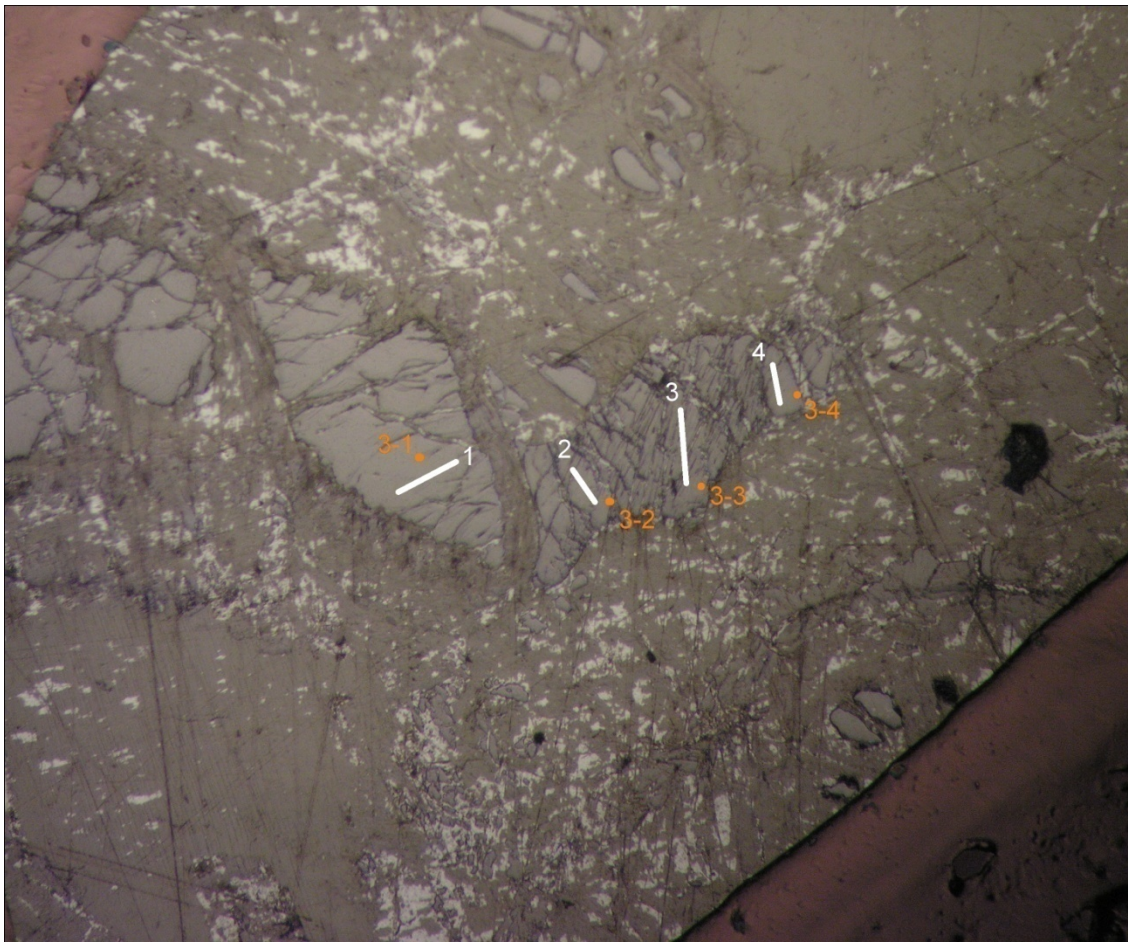

Photomicrograph 48

Sample No. 147-895D-007R-02W (127-135)

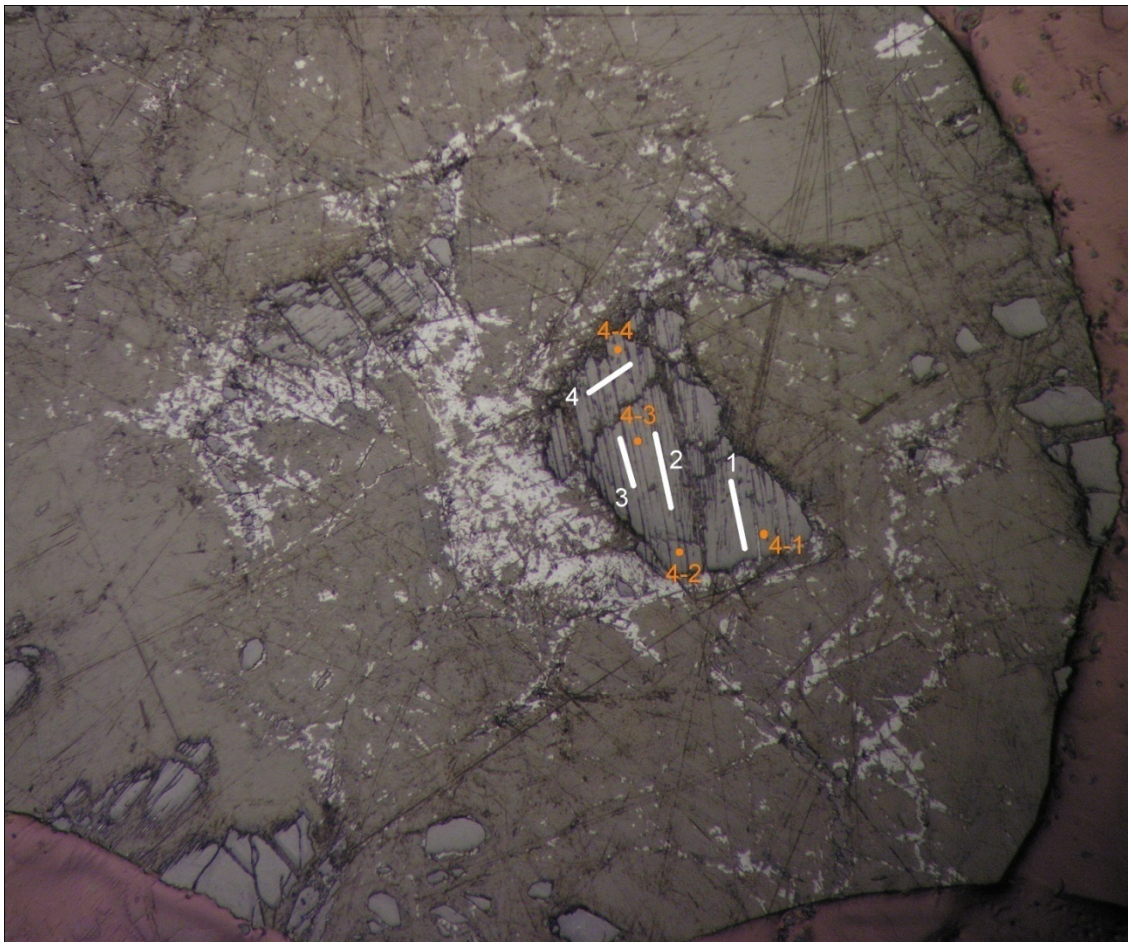

Photomicrograph 49

Sample No. 147-895D-007R-02W (127-135)

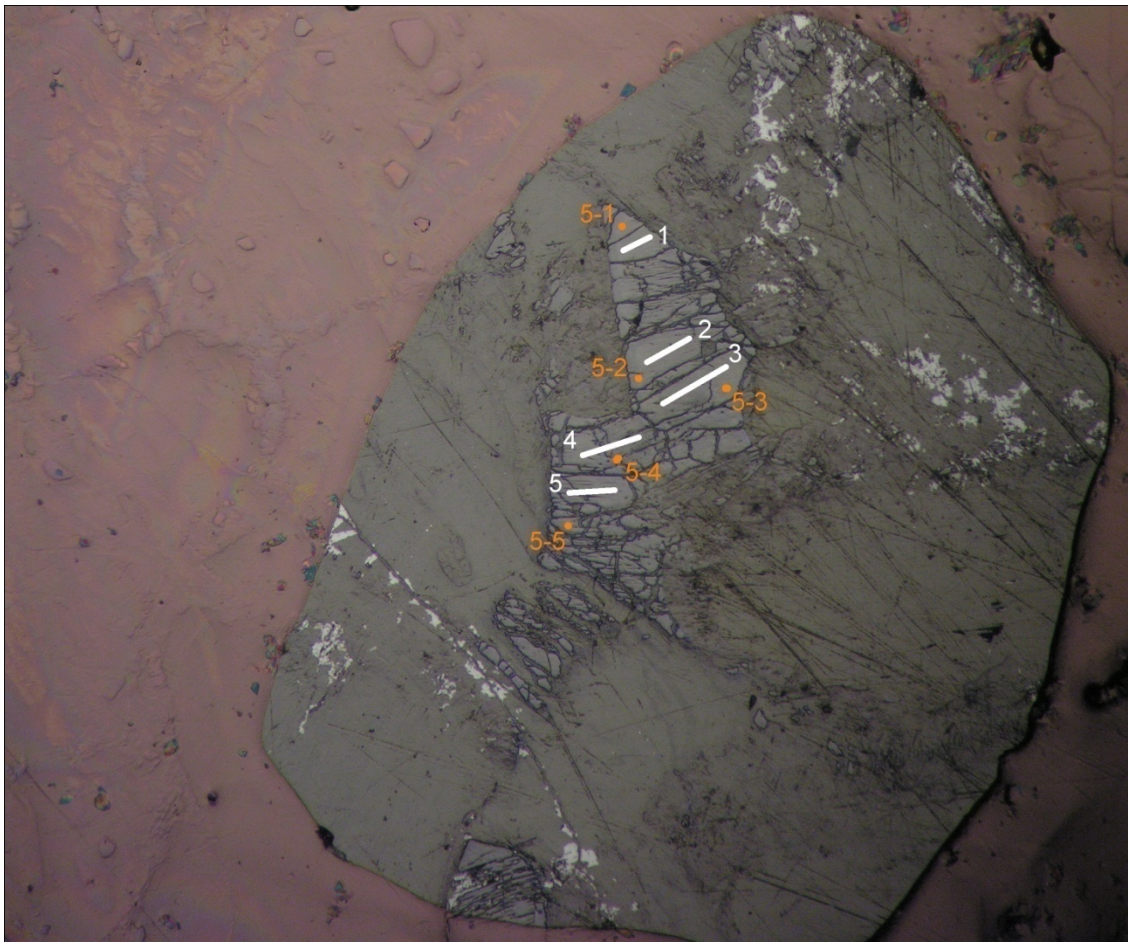

Photomicrograph 50

Sample No. 147-895D-007R-02W (127-135)

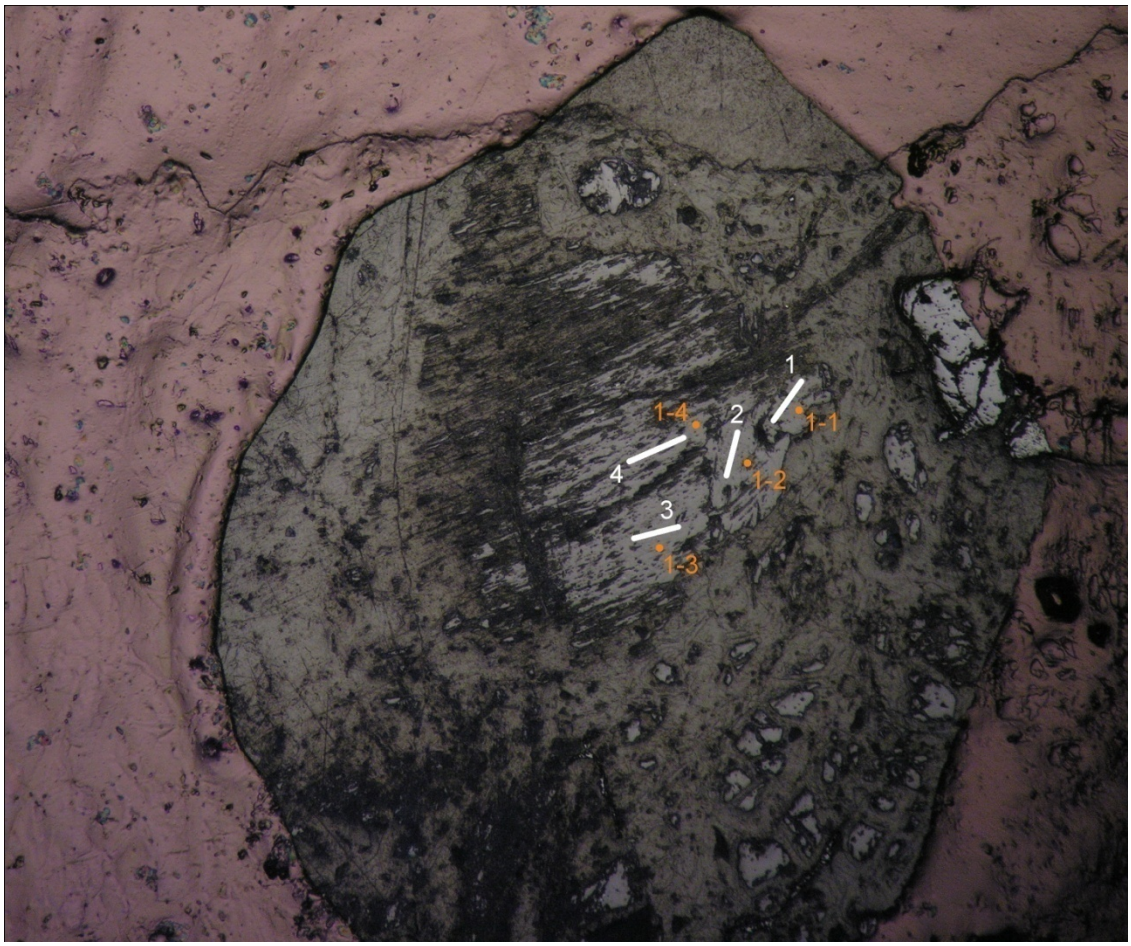

Photomicrograph 51

Sample No. 147-895E-007R-04W (37-41)

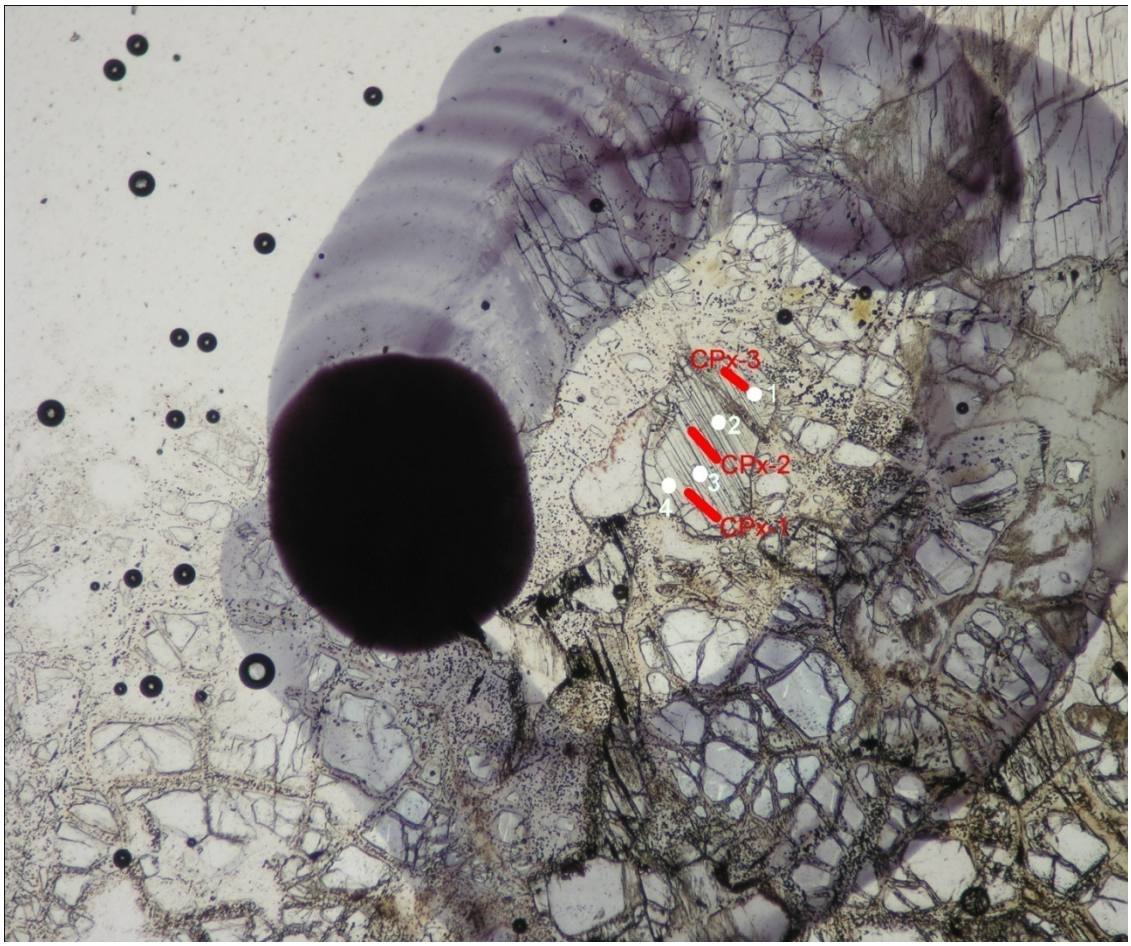

Photomicrograph 52
147-895A-001R-02W (55-61)

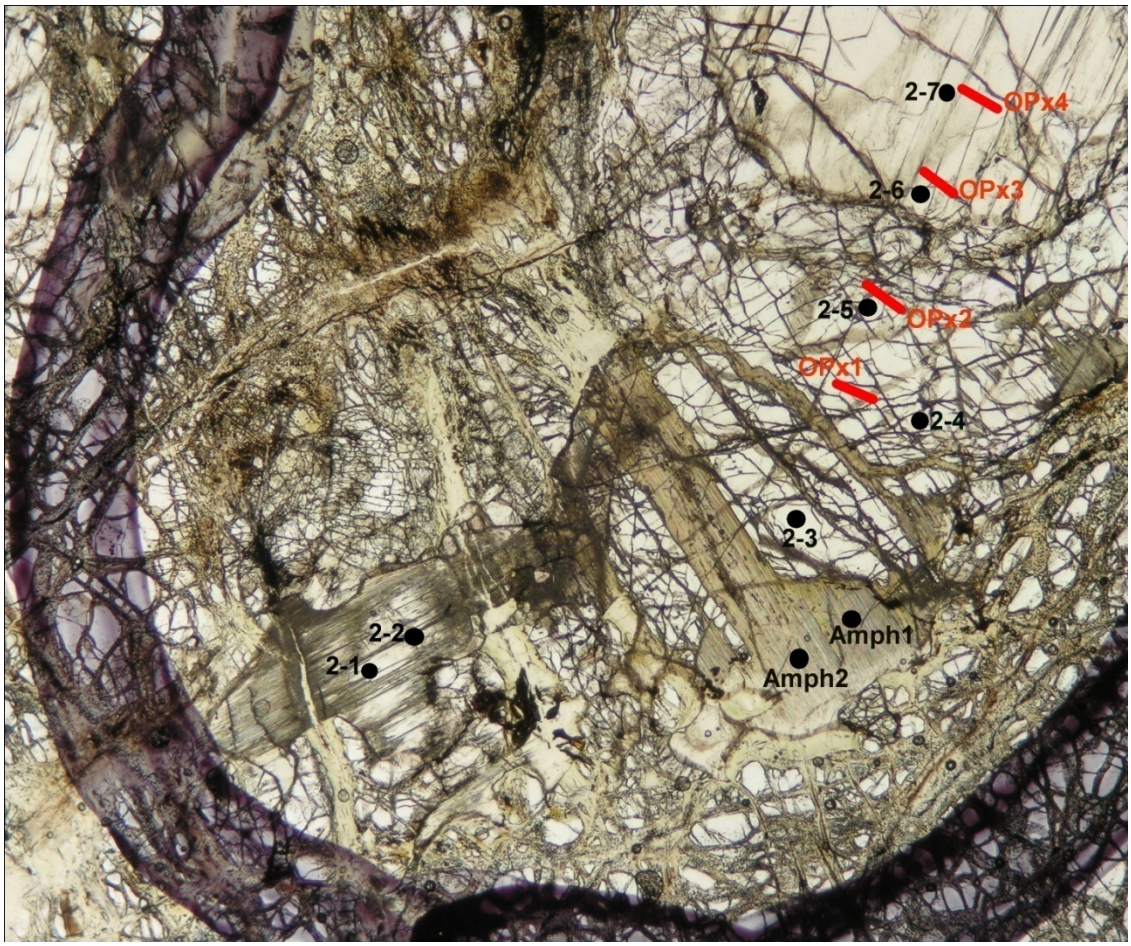

Photomicrograph 53
147-895A-001R-02W (55-61)

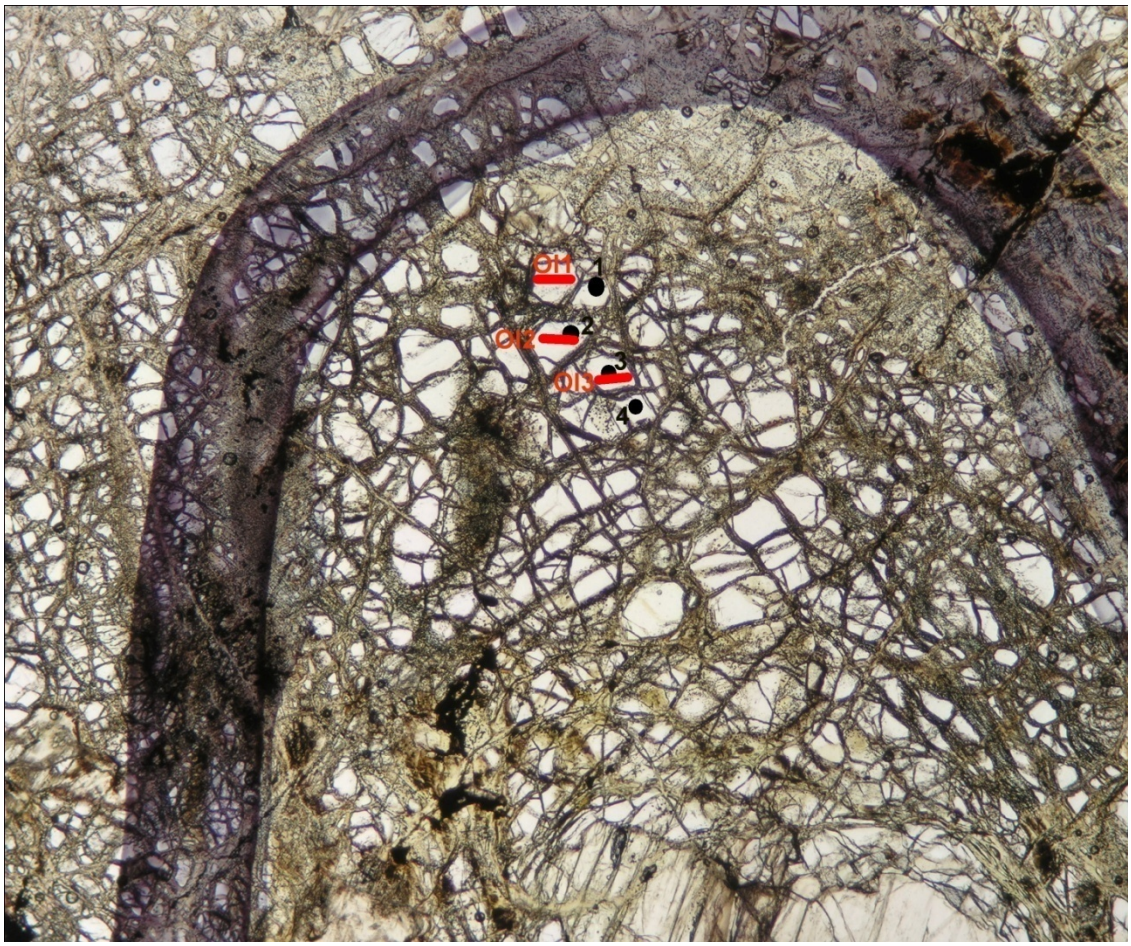

Photomicrograph 54
147-895A-001R-02W (55-61)

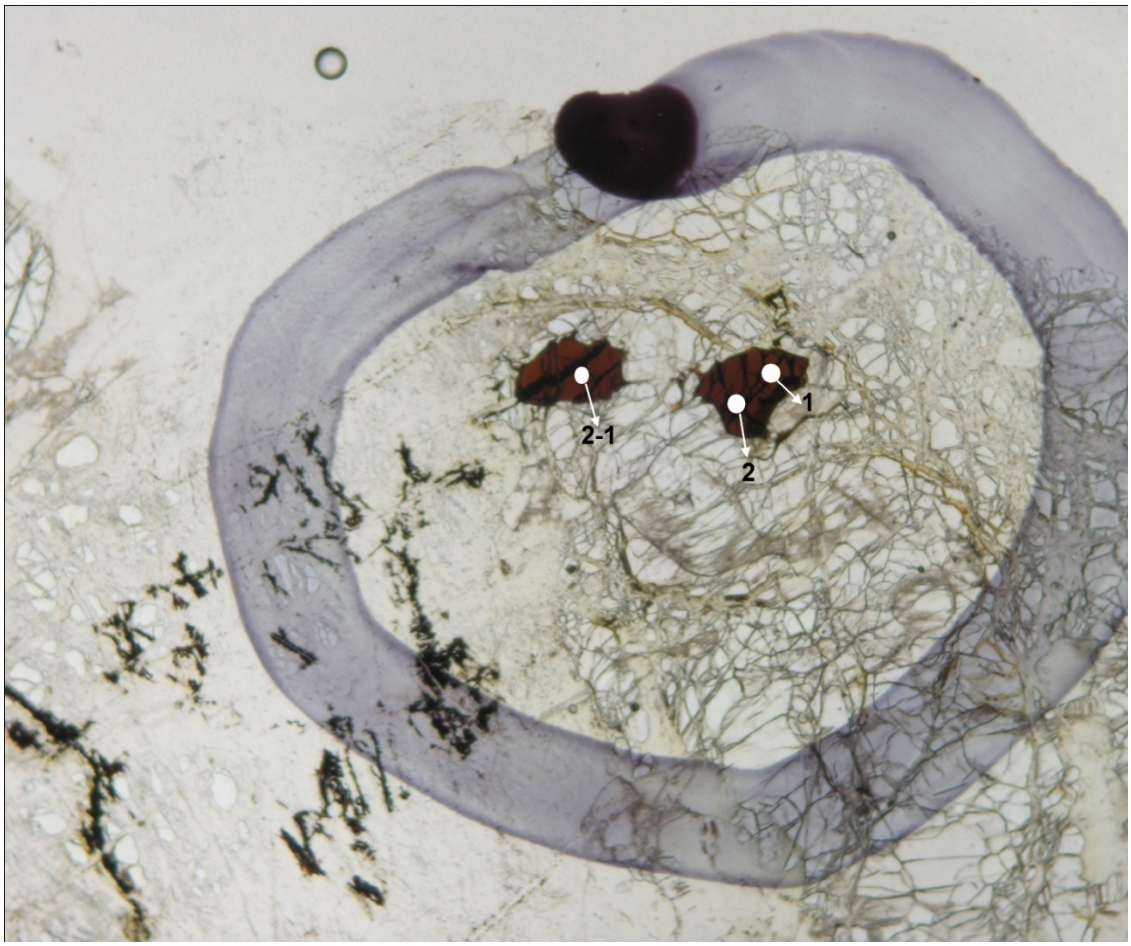

Photomicrograph 55
147-895A-001R-02W (55-61)

Photomicrograph 56
147-895A-001R-02W (55-61)

Photomicrograph 57
147-895A-002R-01W (5-10)

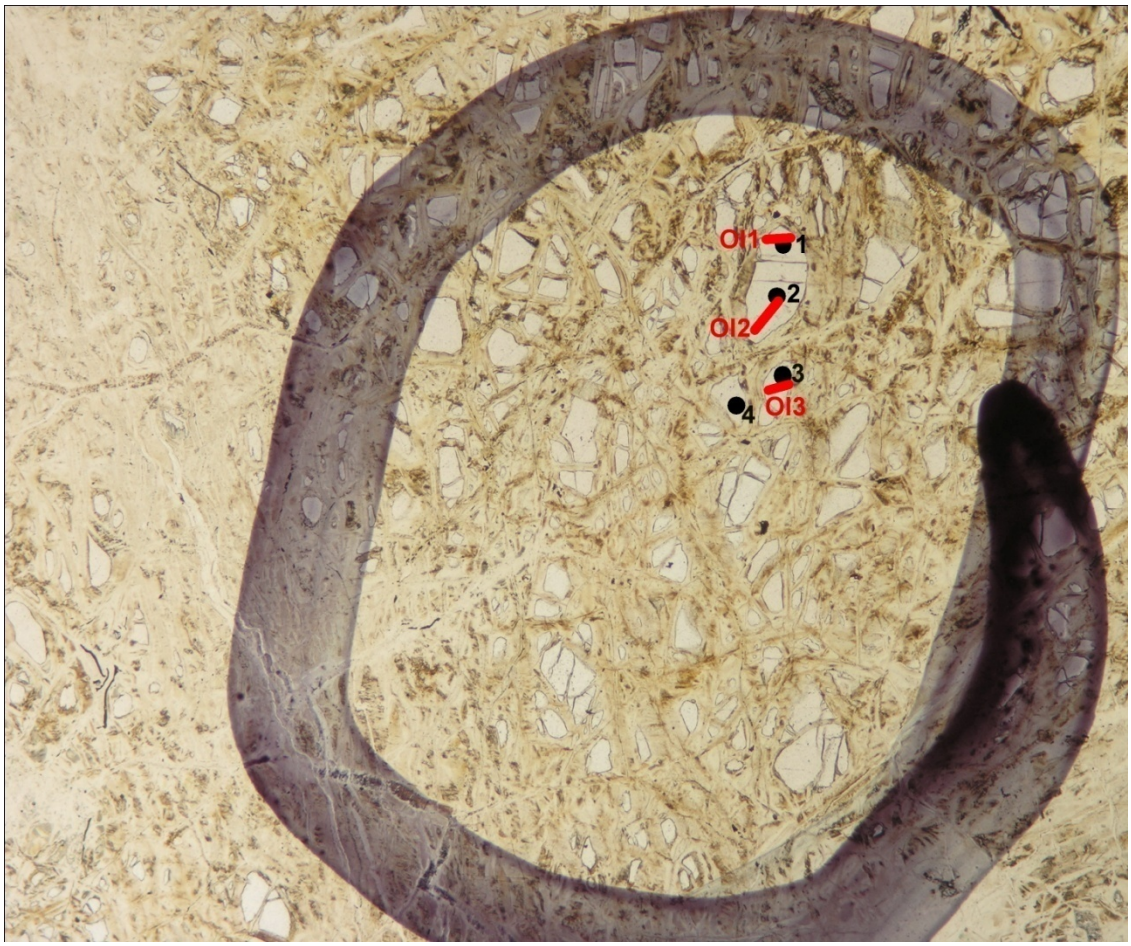

Photomicrograph 58
147-895A-002R-01W (5-10)

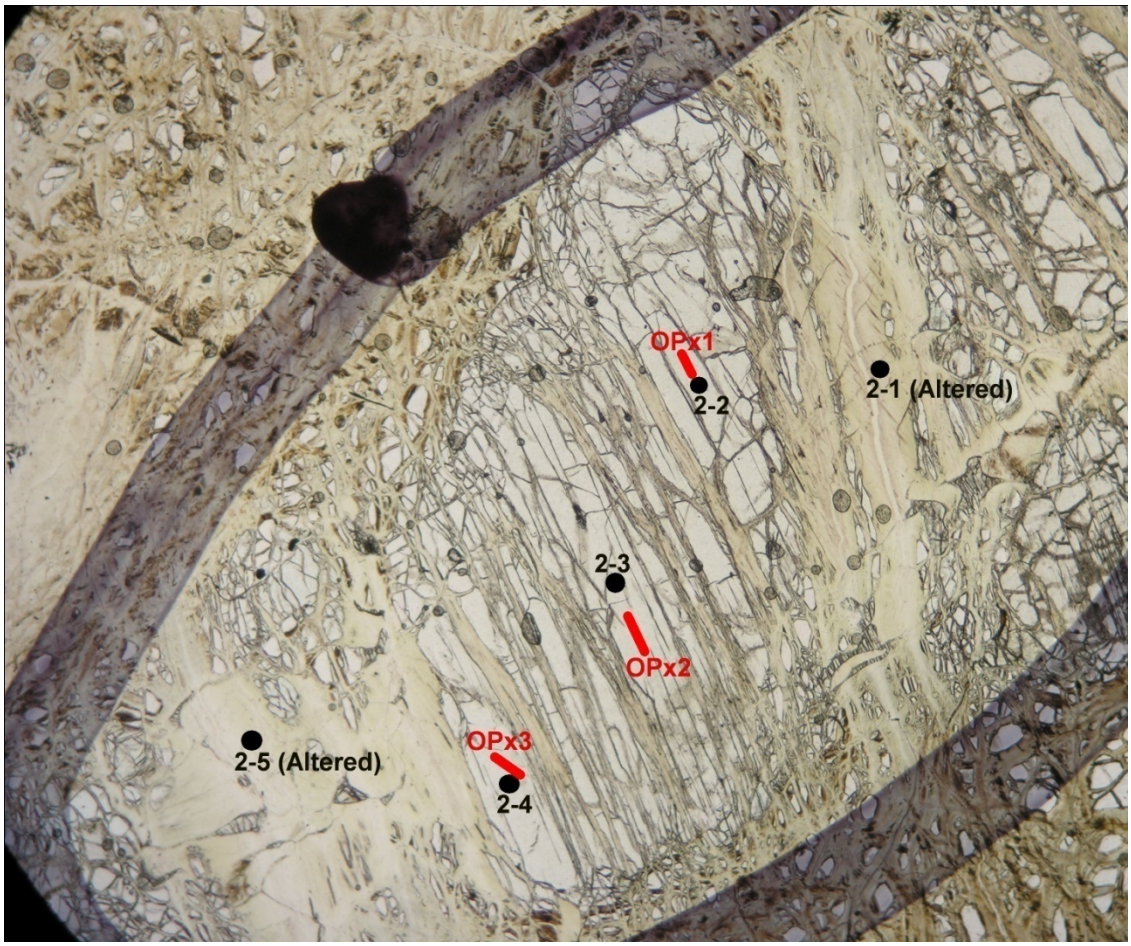

Photomicrograph 59
147-895A-002R-01W (5-10)

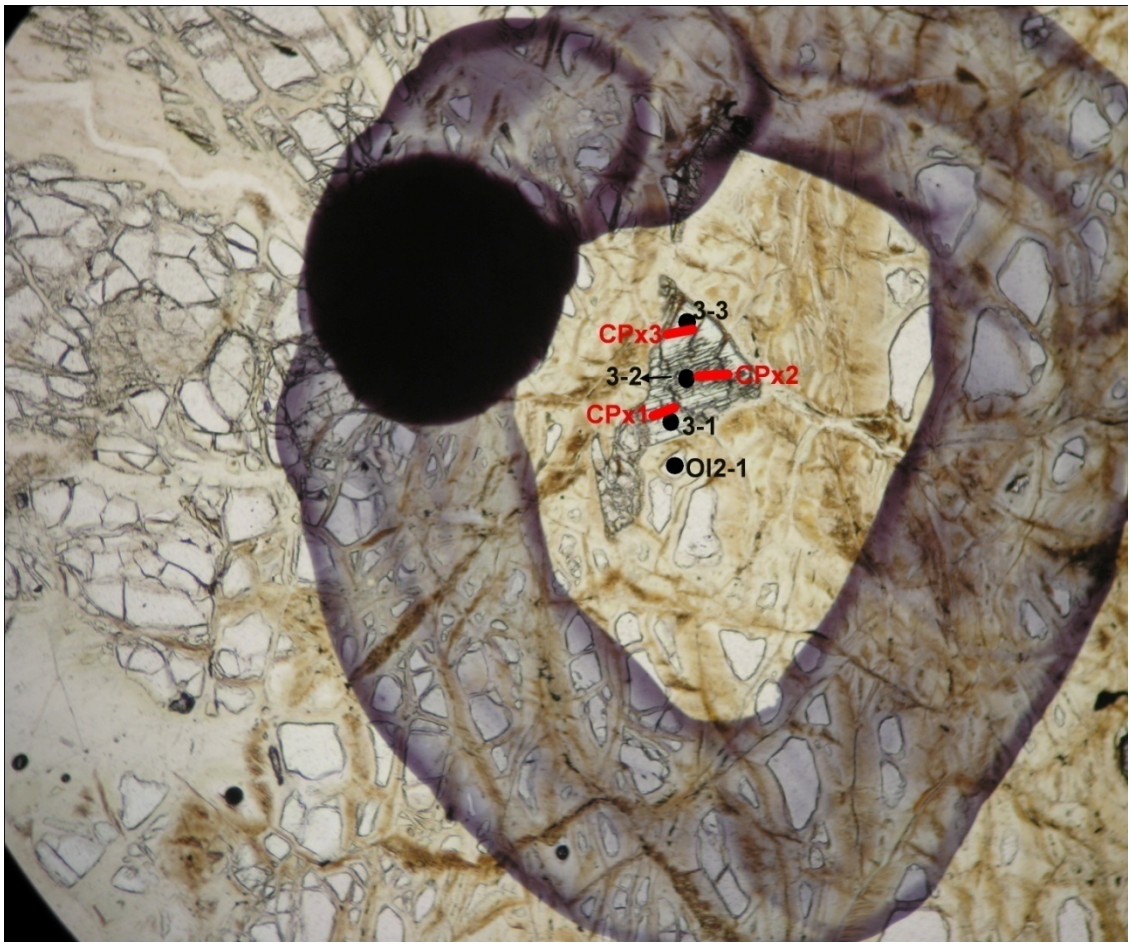

Photomicrograph 60
147-895A-002R-01W (5-10)

Photomicrograph 61
147-895A-002R-01W (5-10)

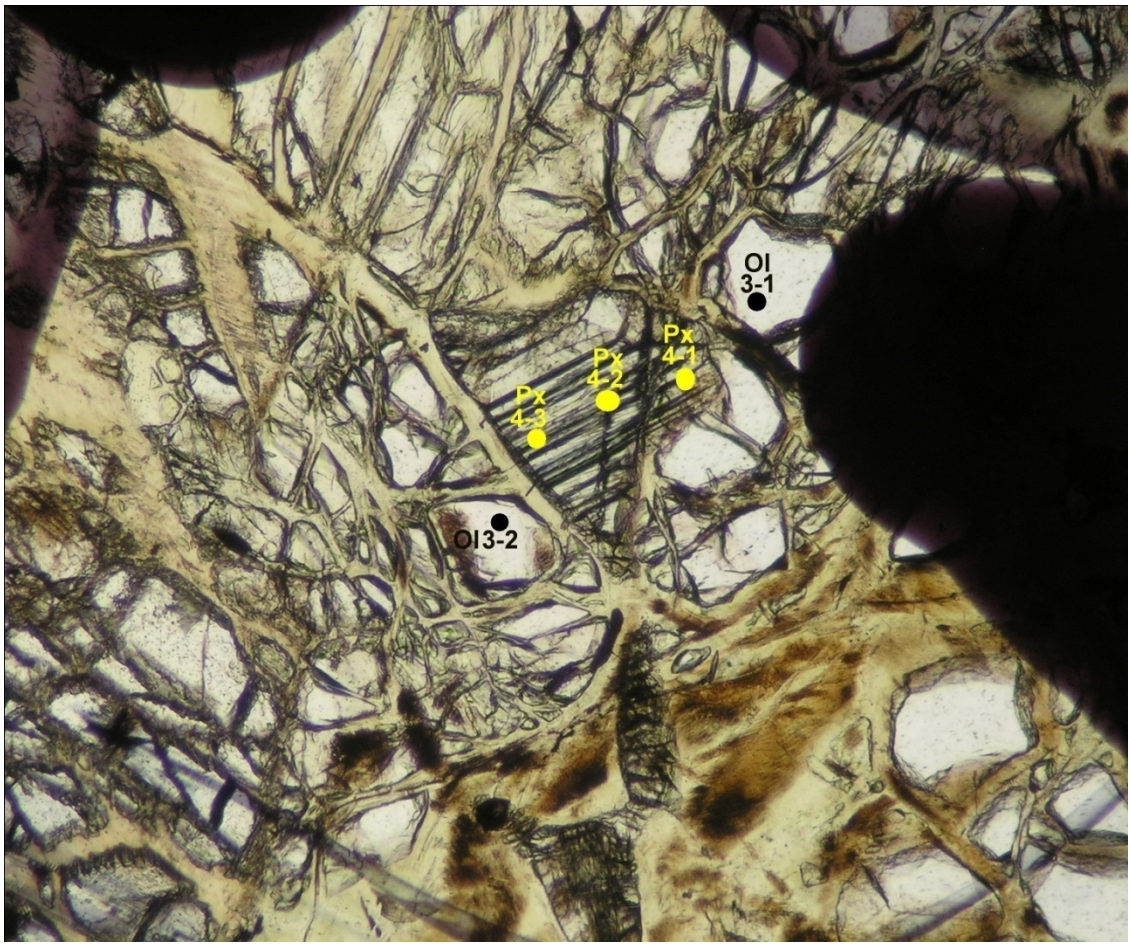

Photomicrograph 62
147-895A-002R-01W (5-10)

Photomicrograph 63
147-895B-001R-01W (65-72)

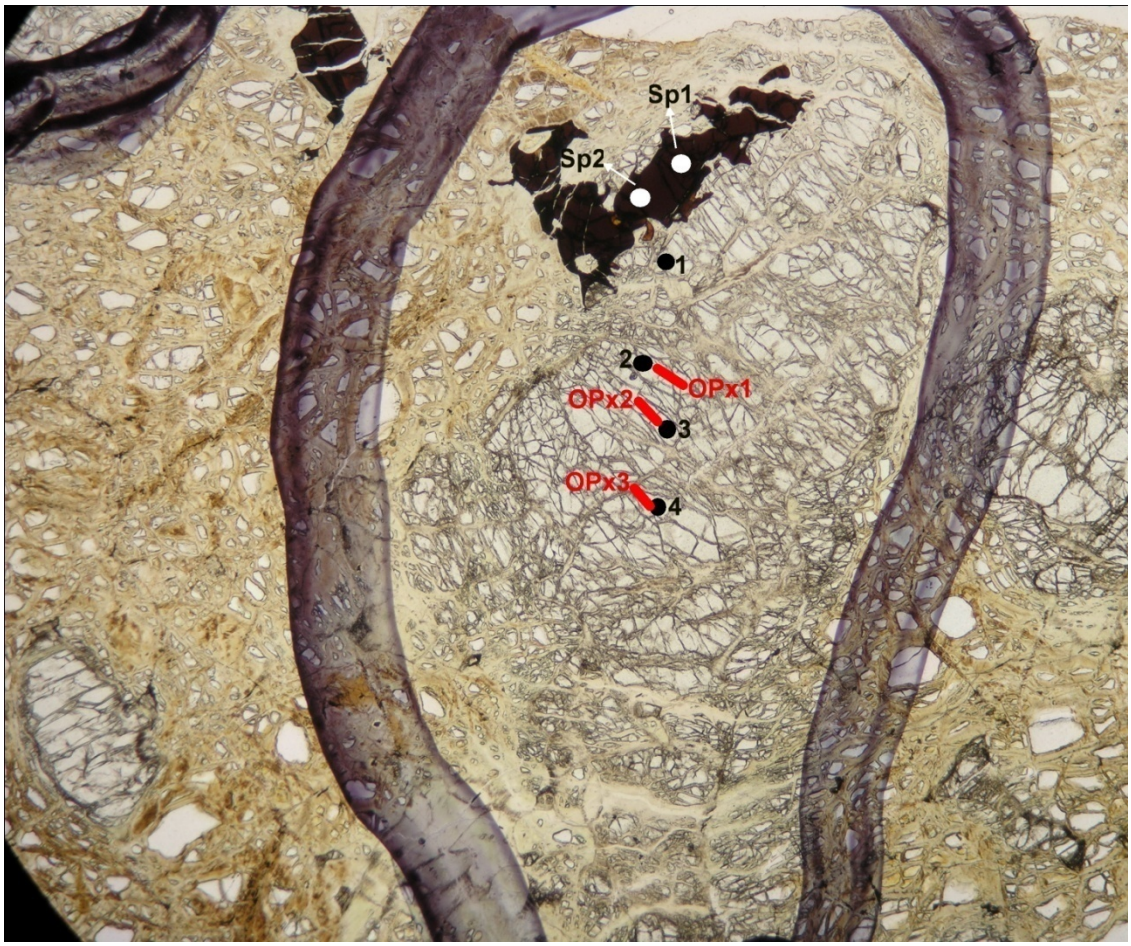

Photomicrograph 64
147-895B-001R-01W (65-72)

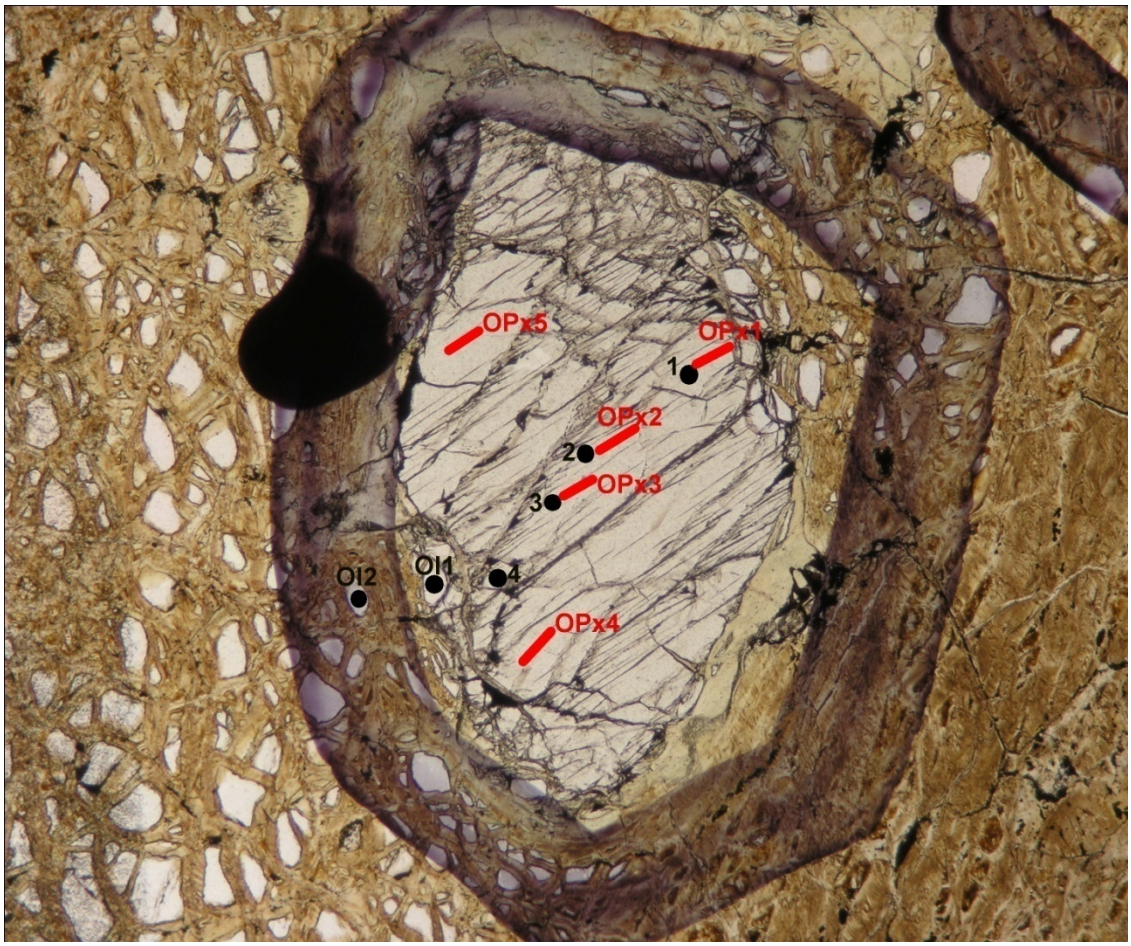

Photomicrograph 65
147-895C-001R-01W (103-112)

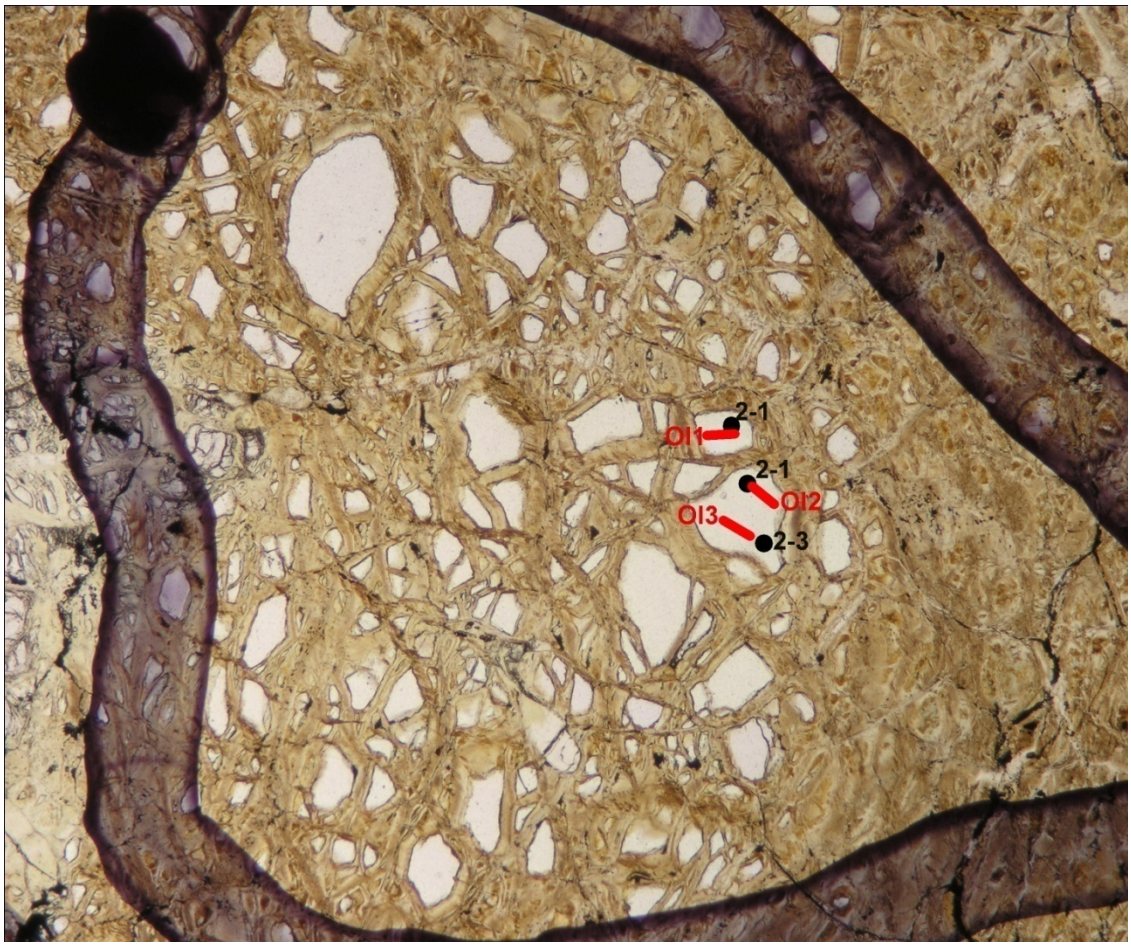

Photomicrograph 66
147-895C-001R-01W (103-112)

Photomicrograph 67
147-895C-001R-01W (103-112)

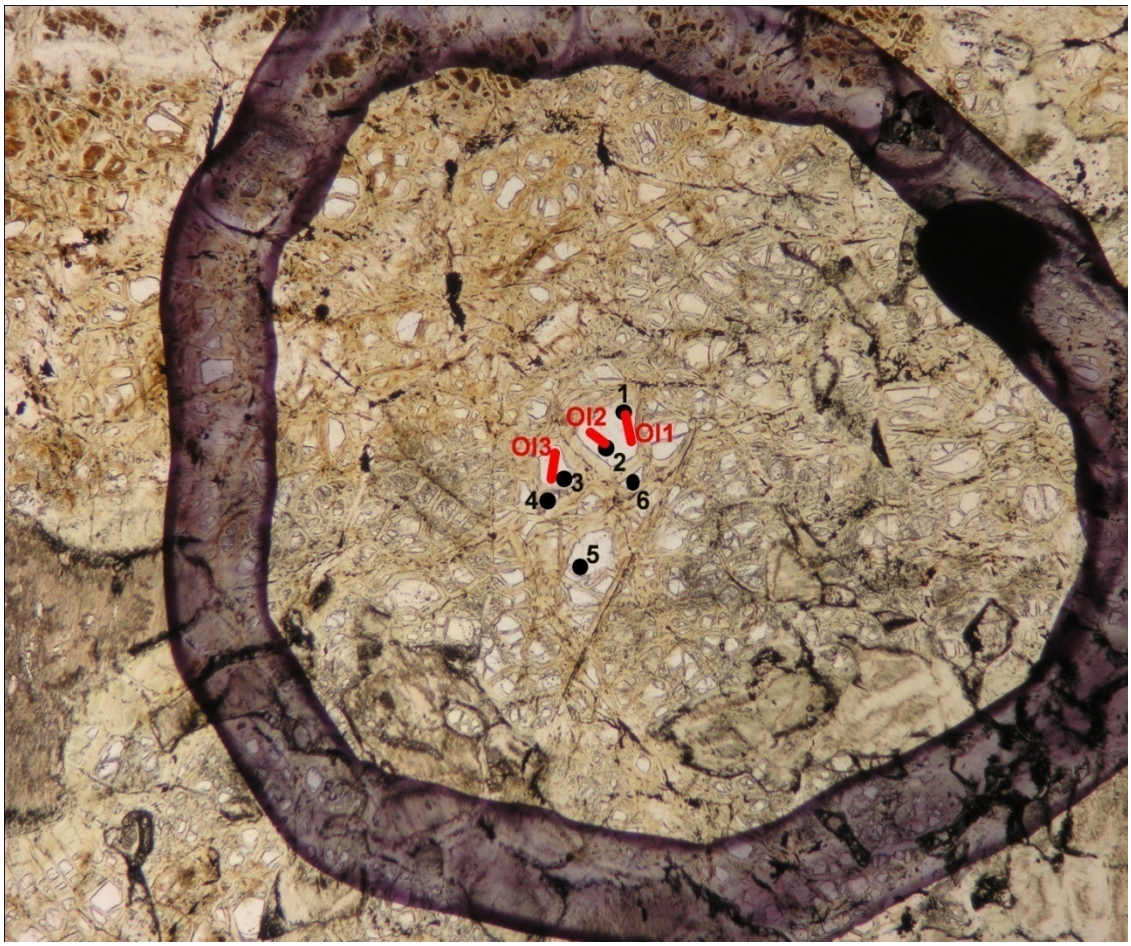

Photomicrograph 68
147-895C-003R-01W (135-143)

Photomicrograph 69
147-895C-003R-01W (135-143)

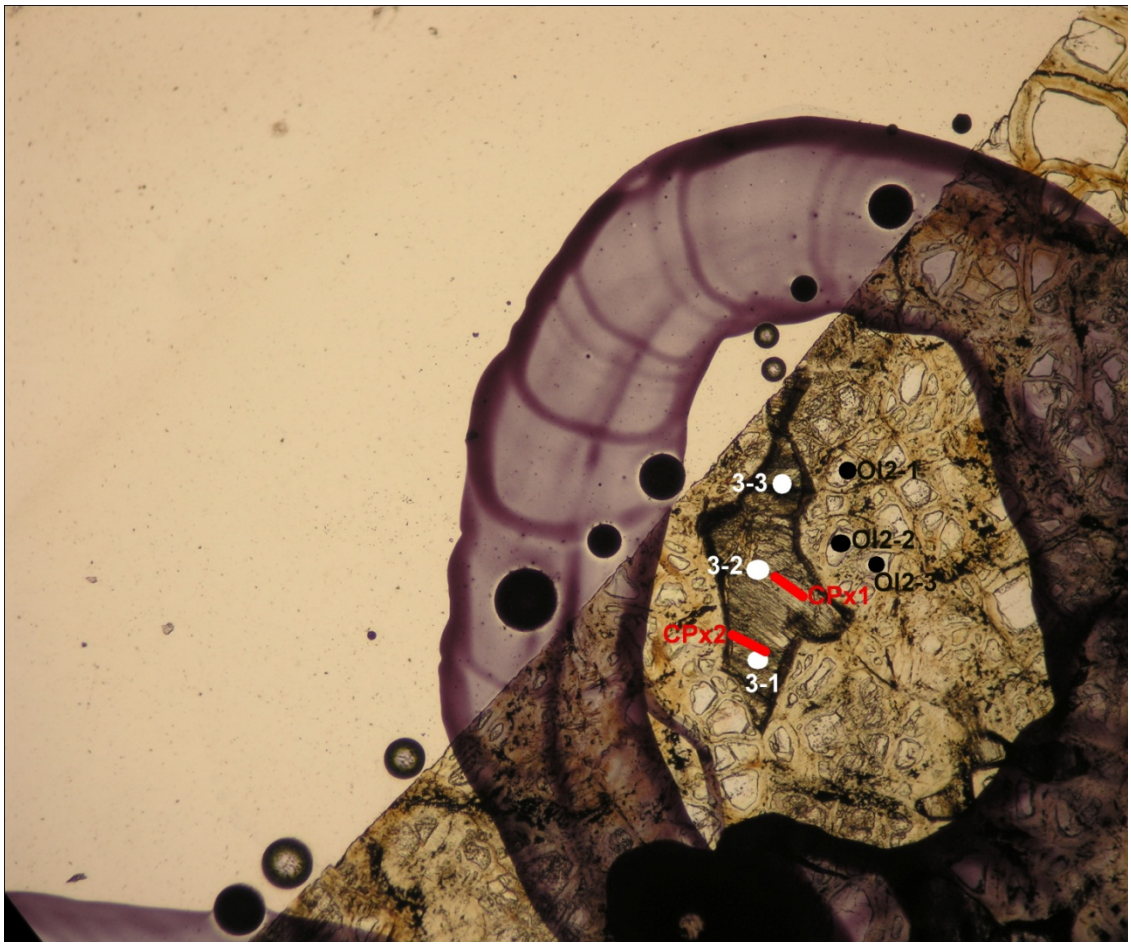

Photomicrograph 70
147-895C-003R-01W (135-143)

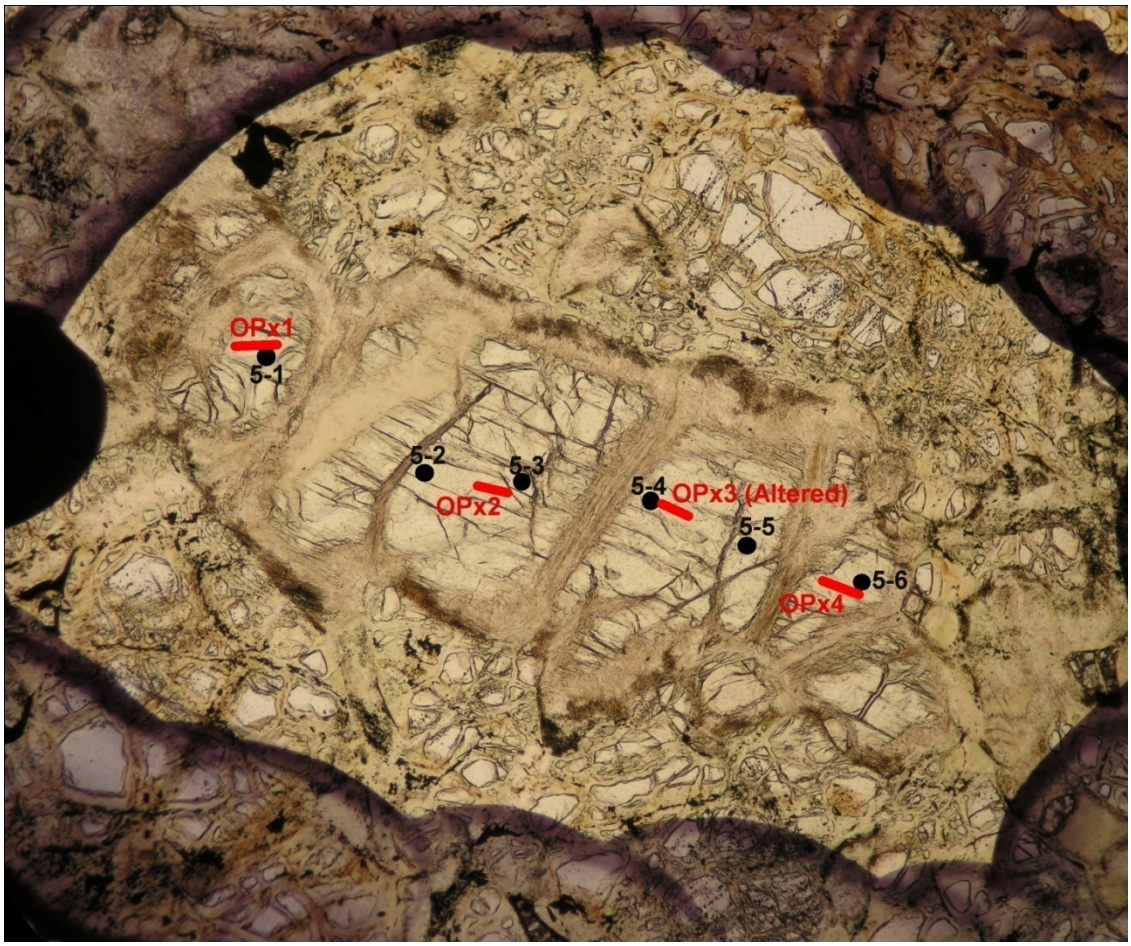

Photomicrograph 71
147-895C-003R-01W (135-143)

Photomicrograph 72
147-895C-003R-01W (135-143)

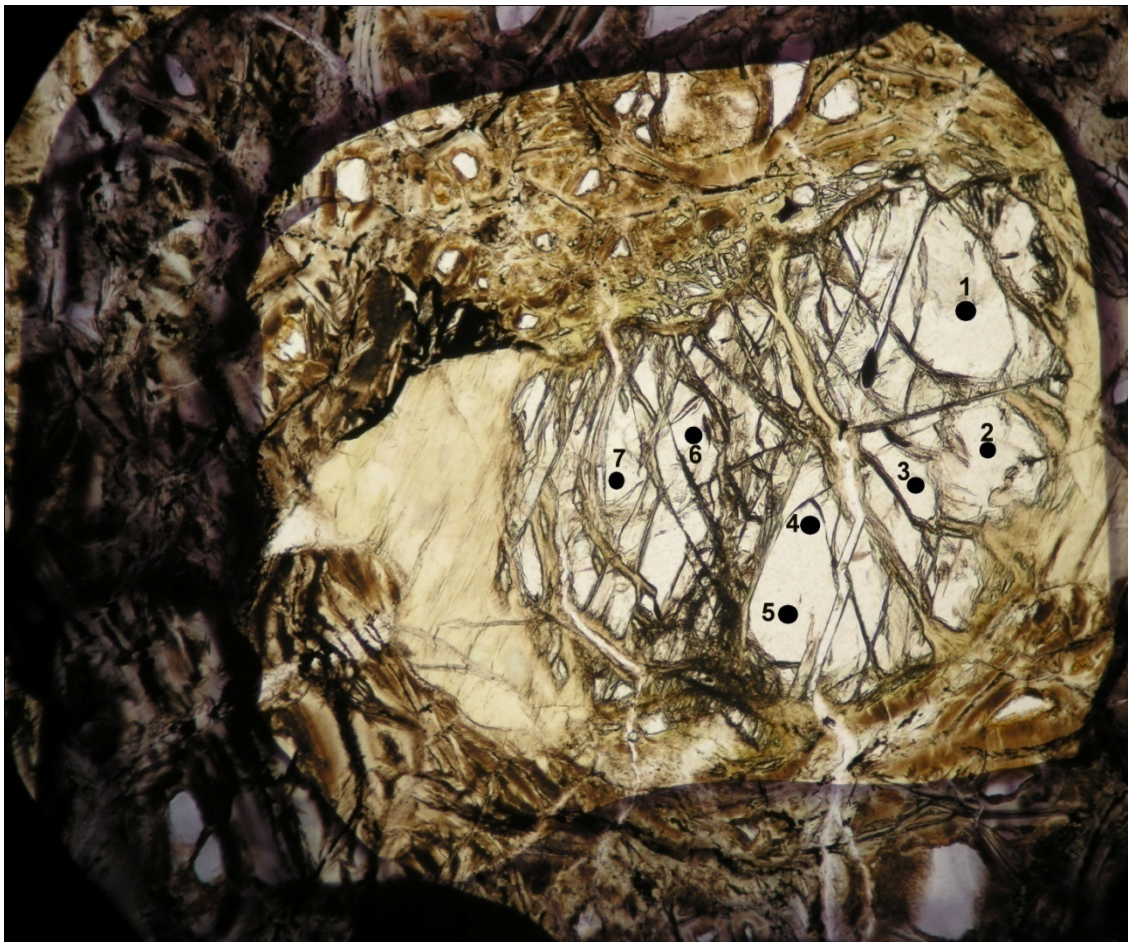

Photomicrograph 73
147-895D-002R-02W (33-38)

Photomicrograph 74
147-895D-002R-02W (33-38)

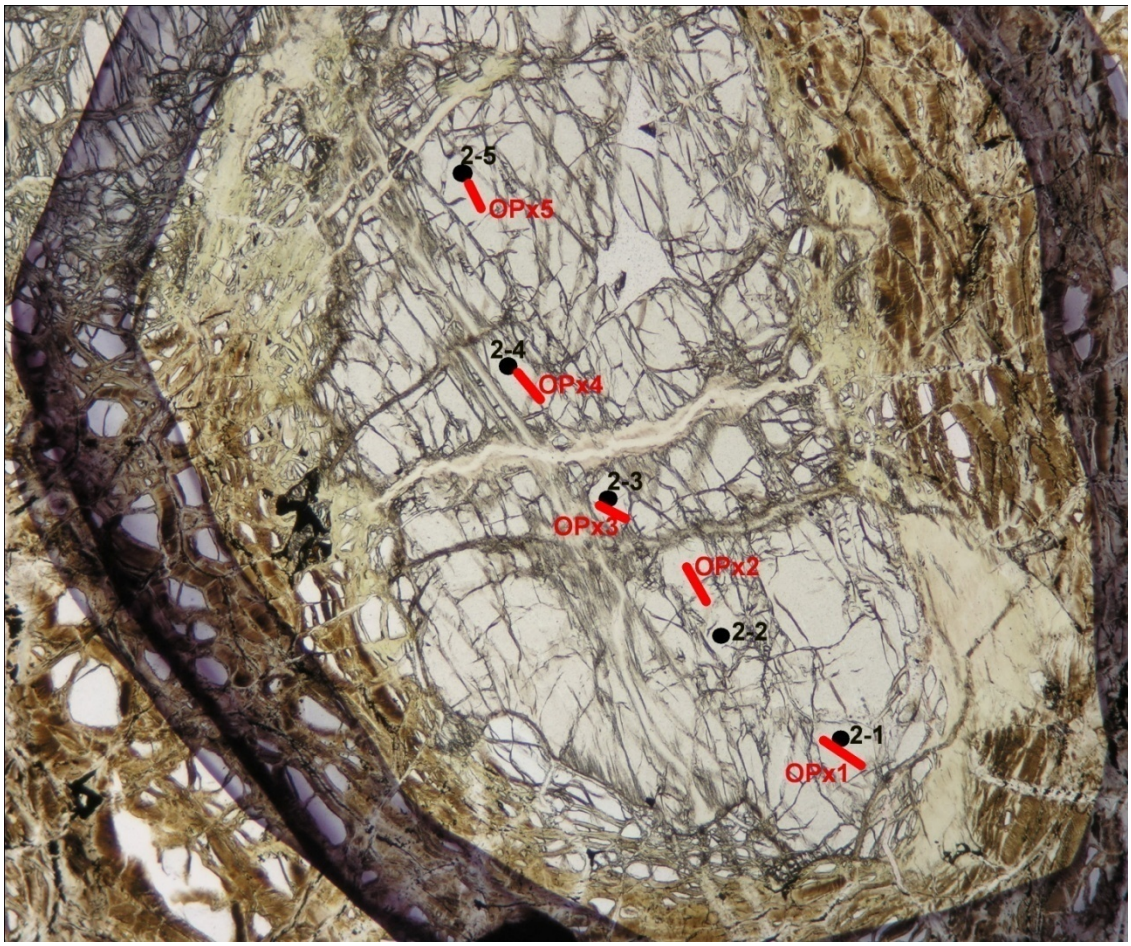

Photomicrograph 75
147-895D-002R-02W (33-38)

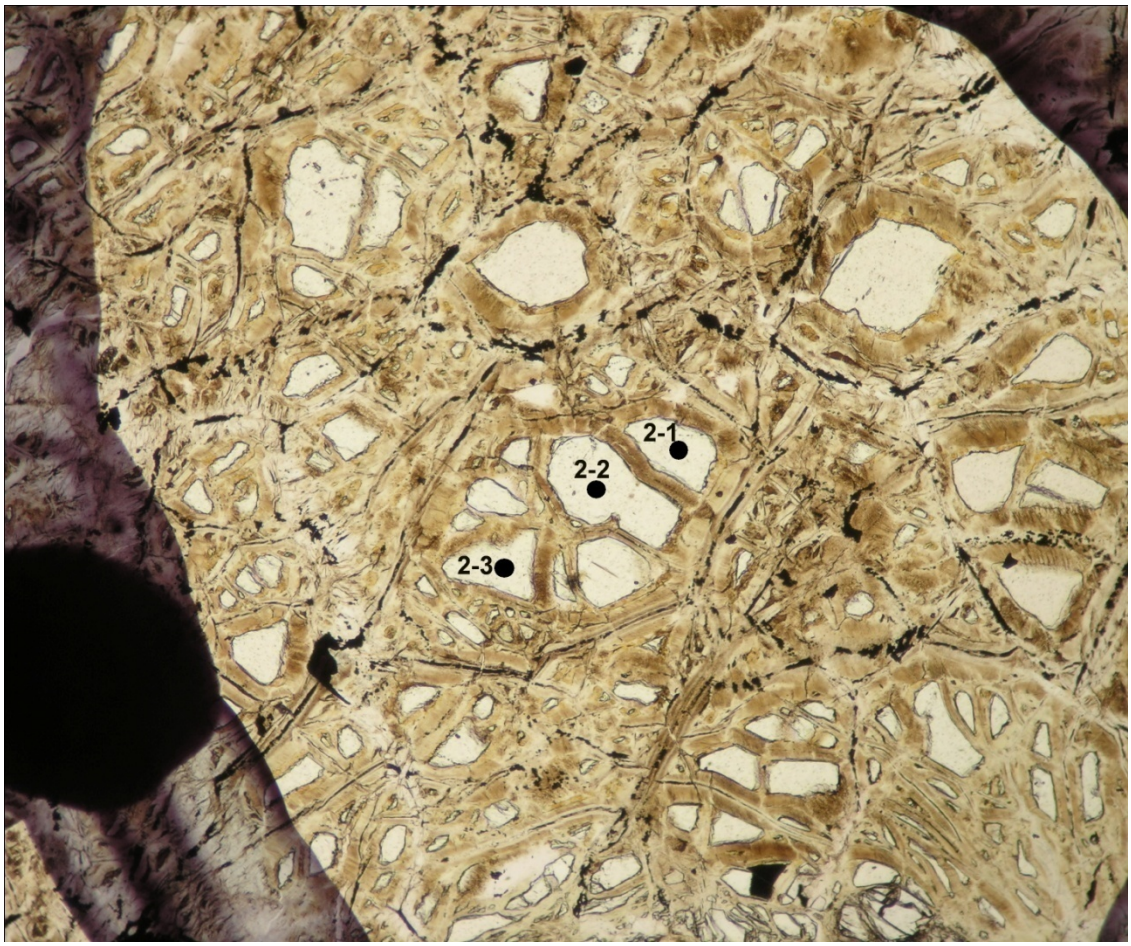

Photomicrograph 76
147-895D-002R-02W (33-38)

Photomicrograph 77
147-895D-002R-02W (33-38)

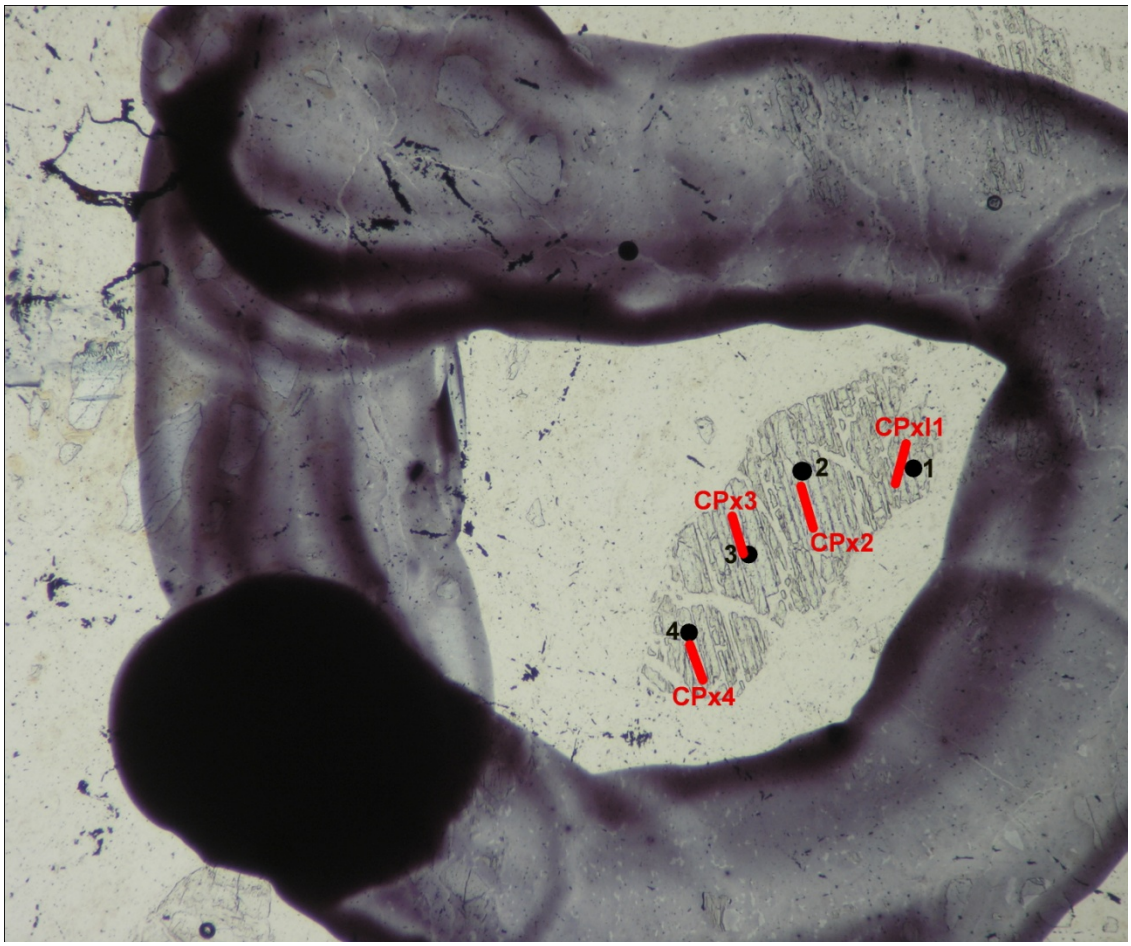

Photomicrograph 78
147-895D-002R-02W (33-38)

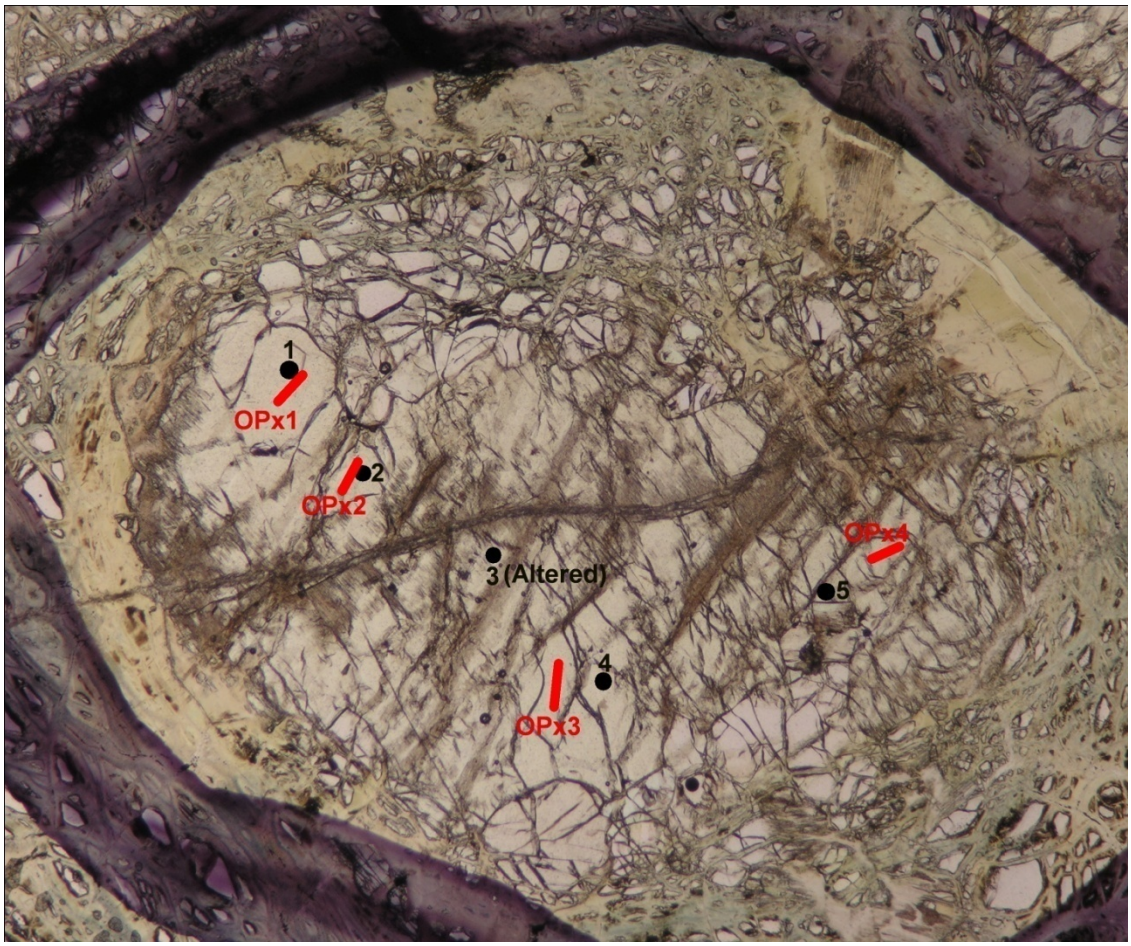

Photomicrograph 79
147-895D-003R-01W (34-39)

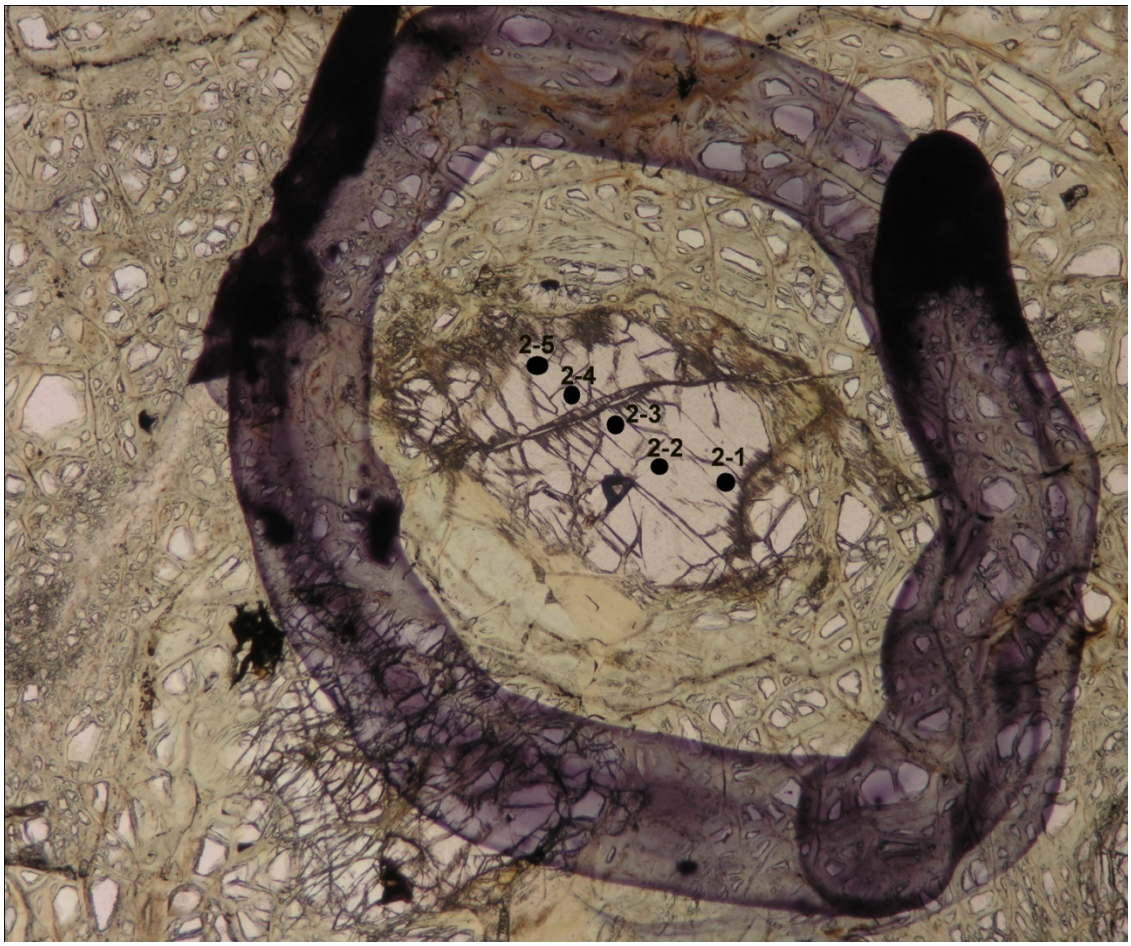

Photomicrograph 80
147-895D-003R-01W (34-39)

Photomicrograph 81
147-895D-003R-01W (34-39)

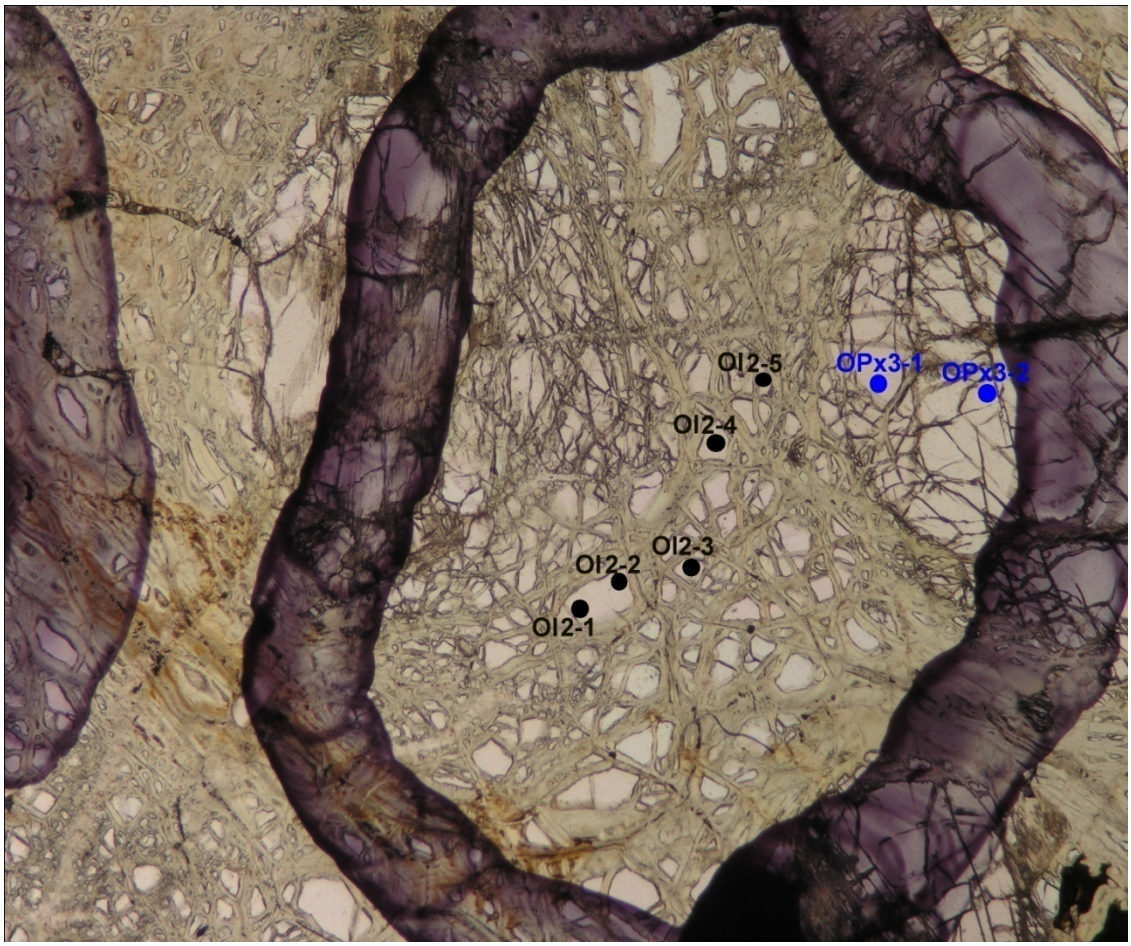

Photomicrograph 82
147-895D-003R-01W (34-39)

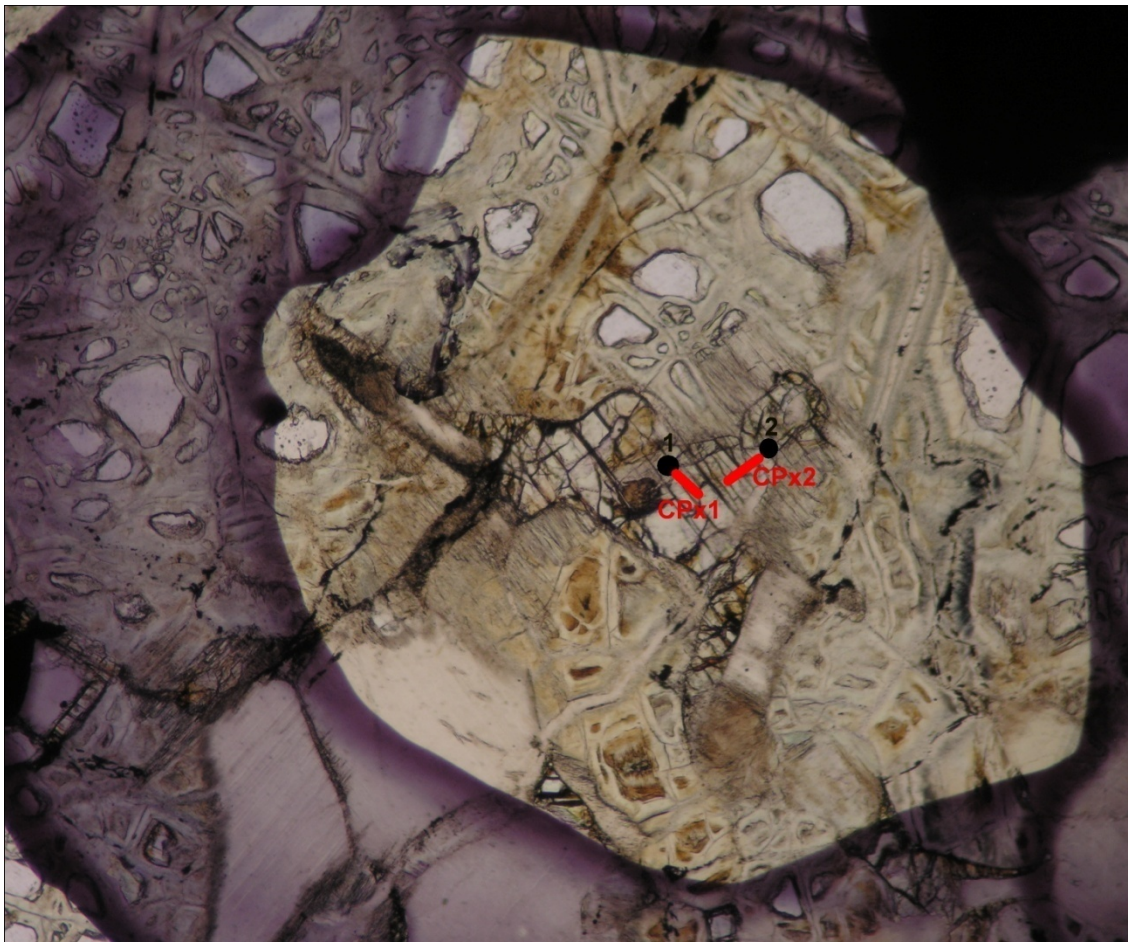

Photomicrograph 83
147-895D-003R-01W (34-39)

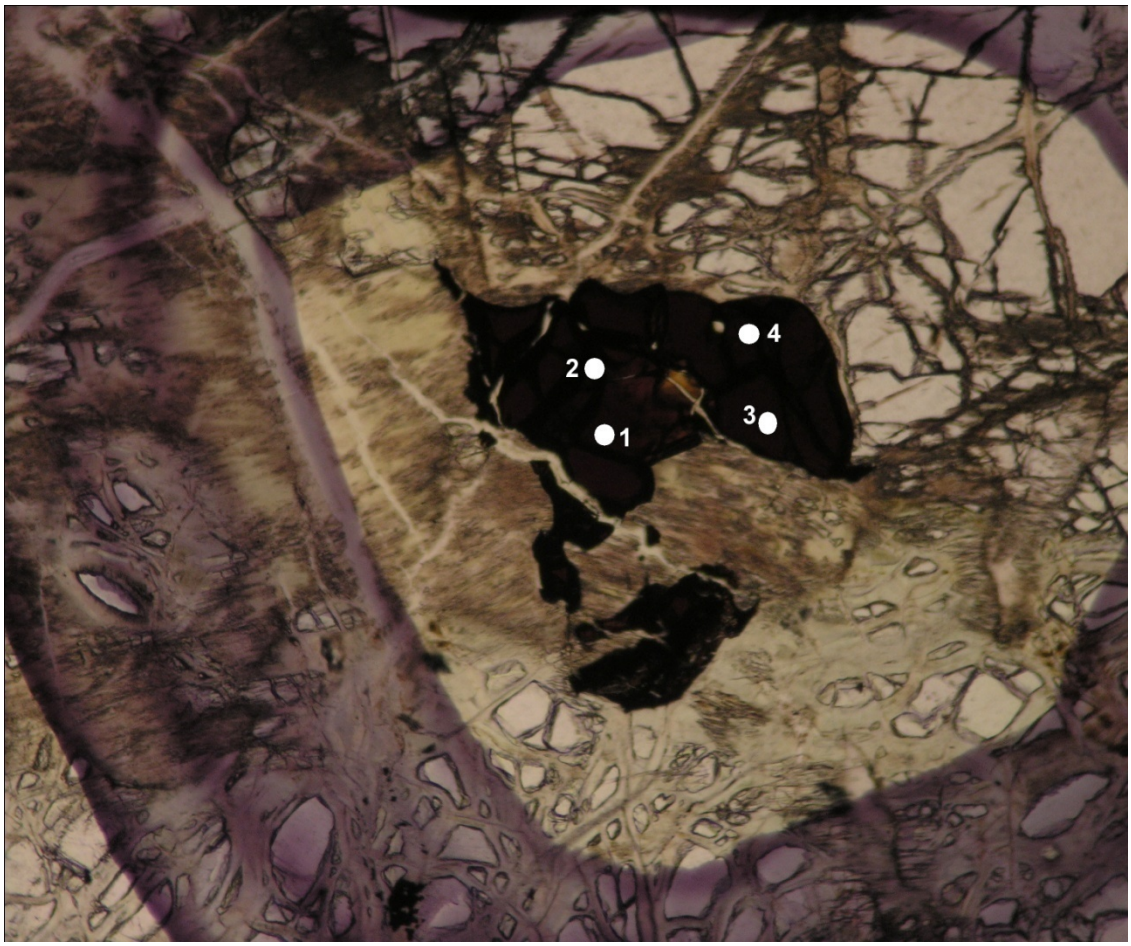

Photomicrograph 84
147-895D-003R-01W (34-39)

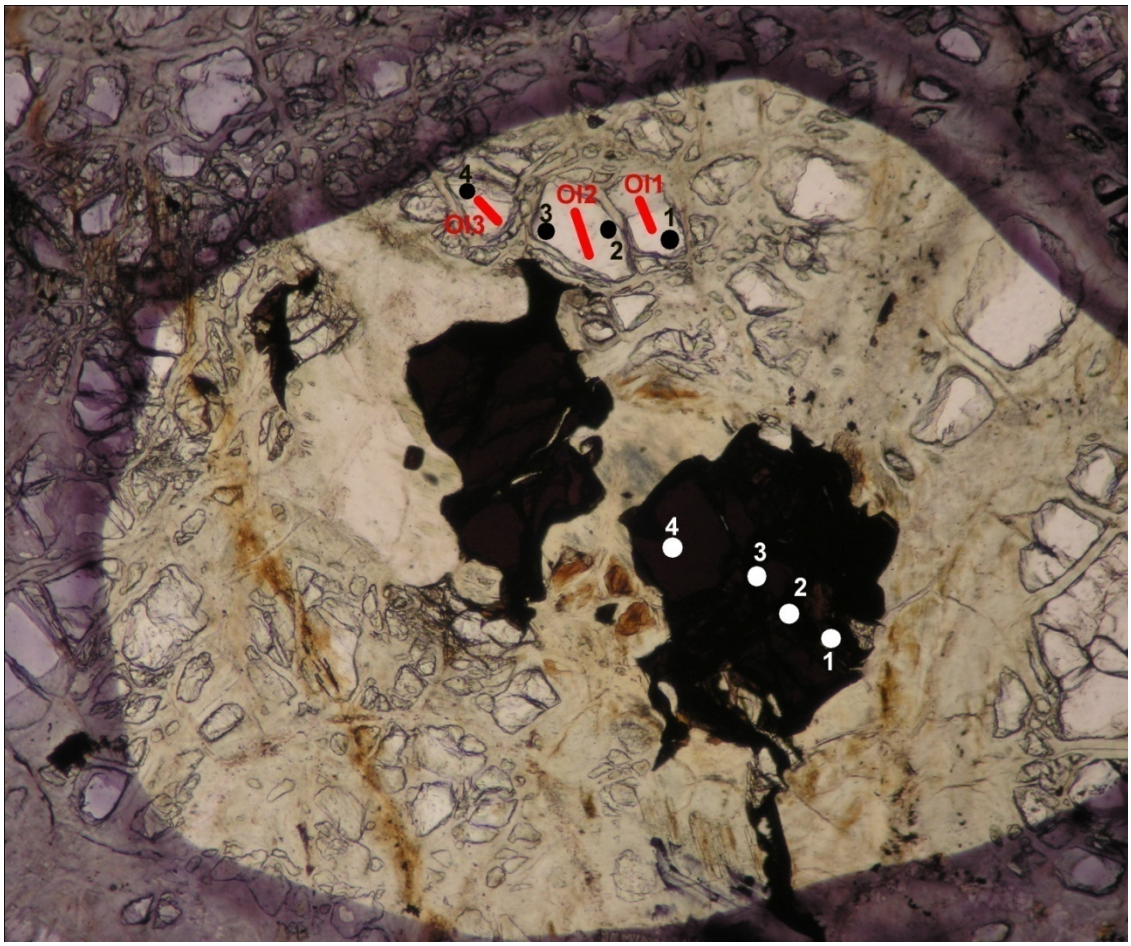

Photomicrograph 85
147-895D-003R-01W (61-70)

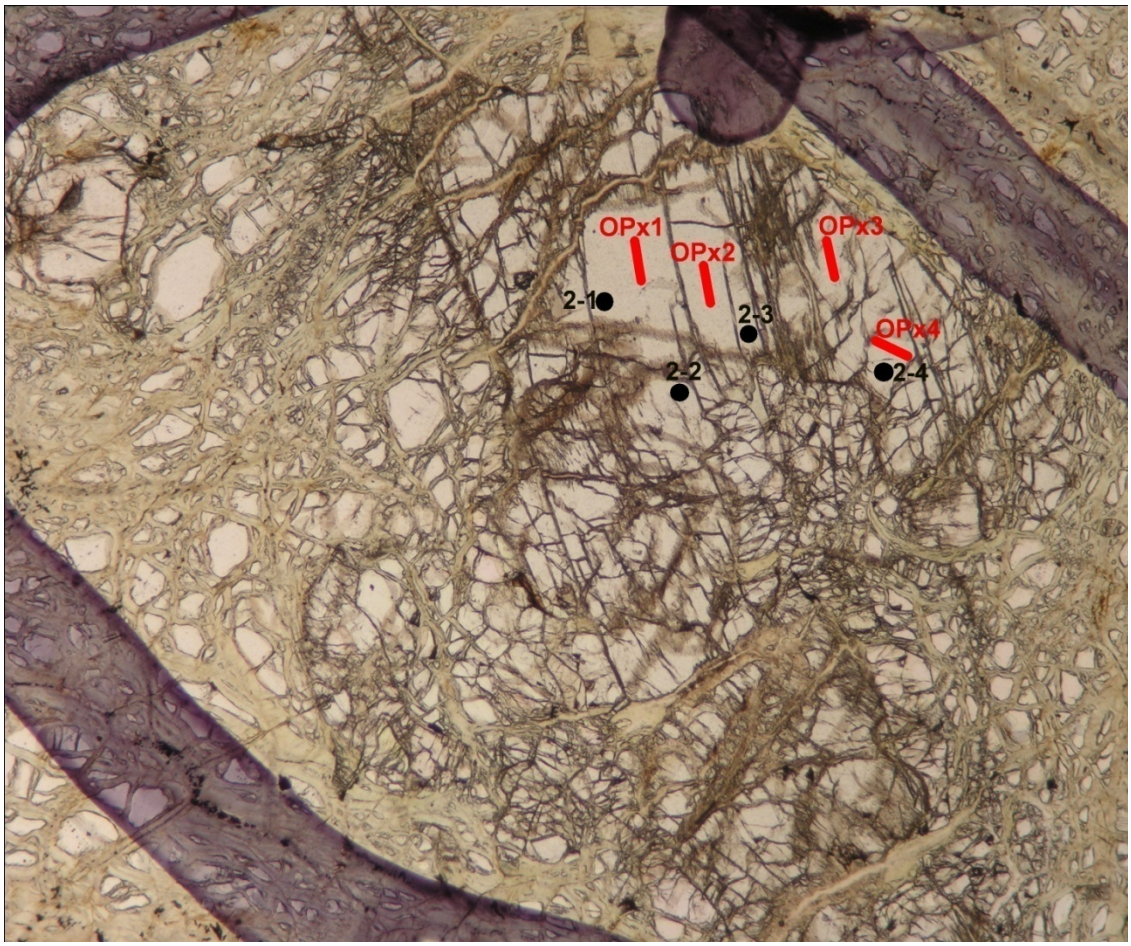

Photomicrograph 86
147-895D-003R-01W (61-70)

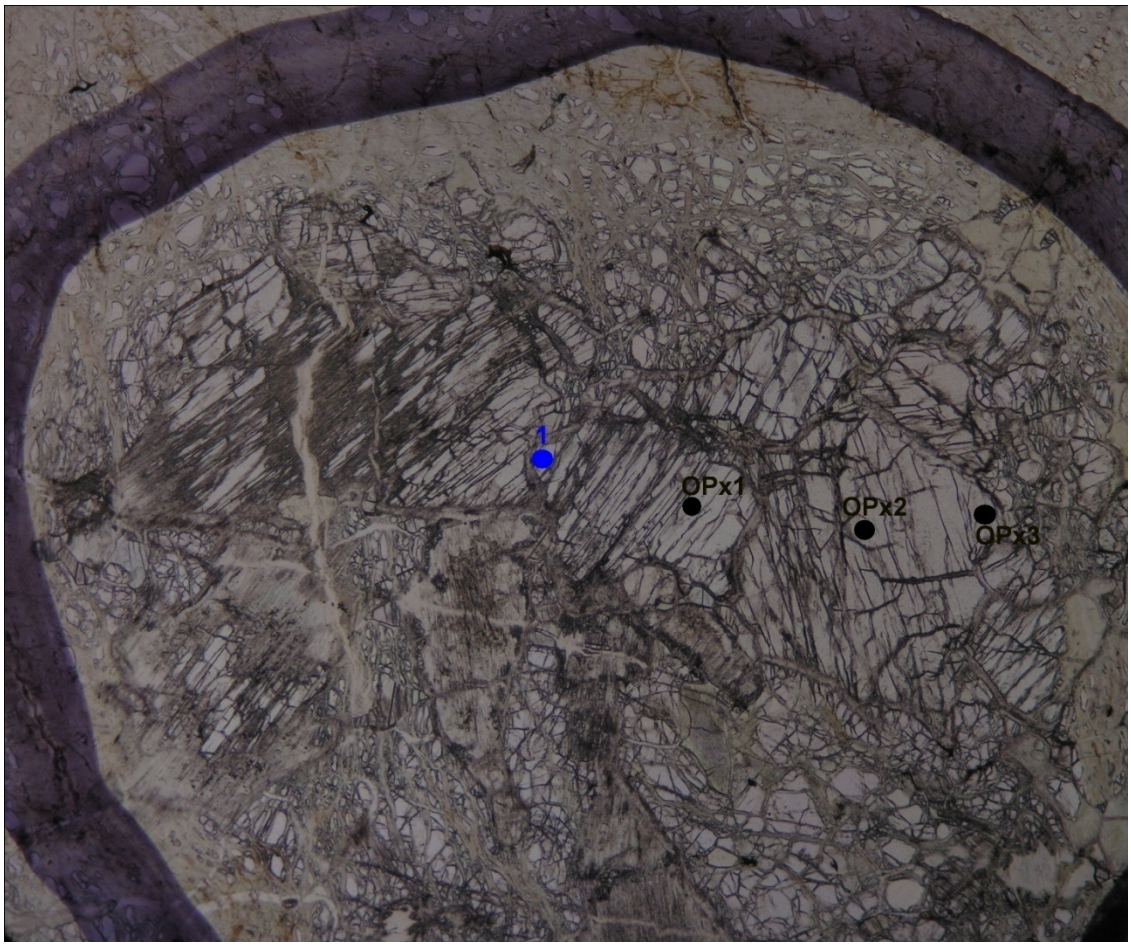

Photomicrograph 87
147-895D-004R-01W (54-60)

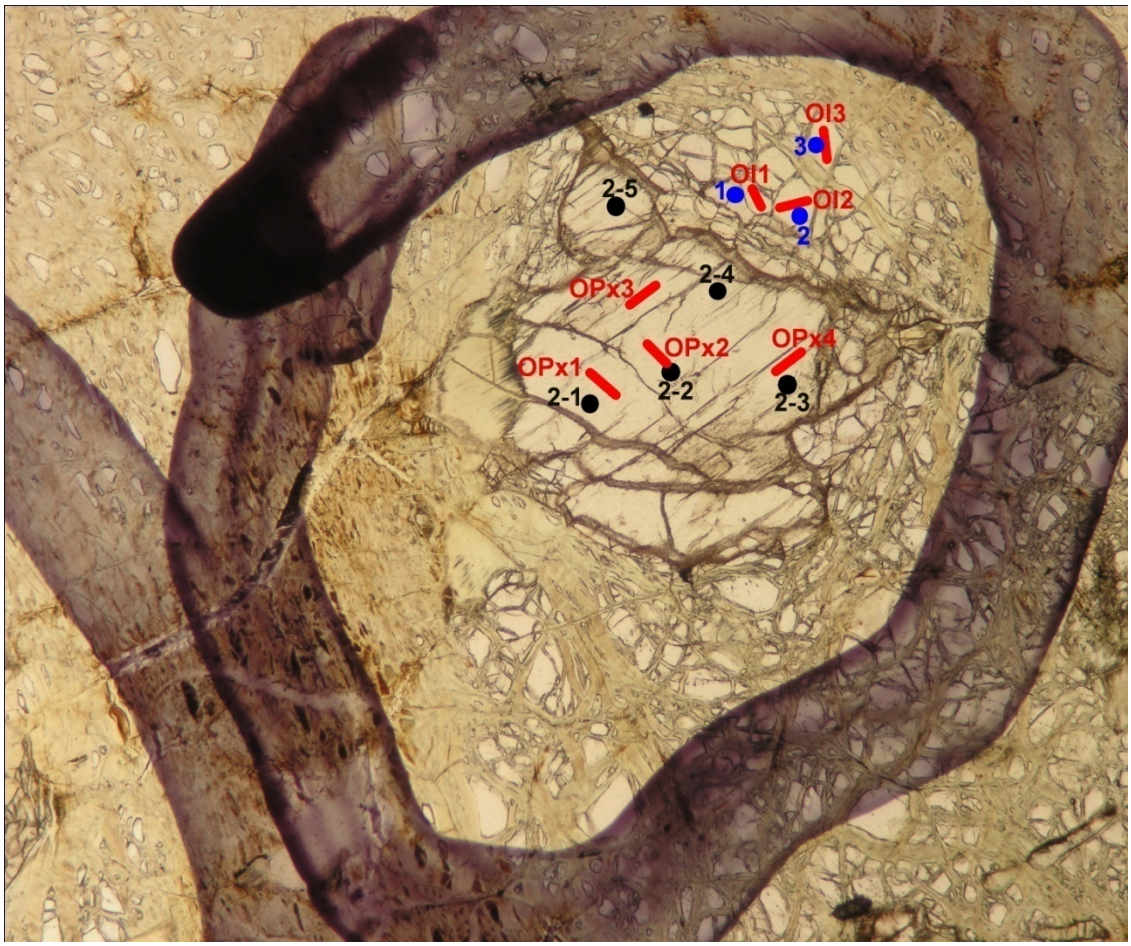

Photomicrograph 88
147-895D-004R-01W (54-60)

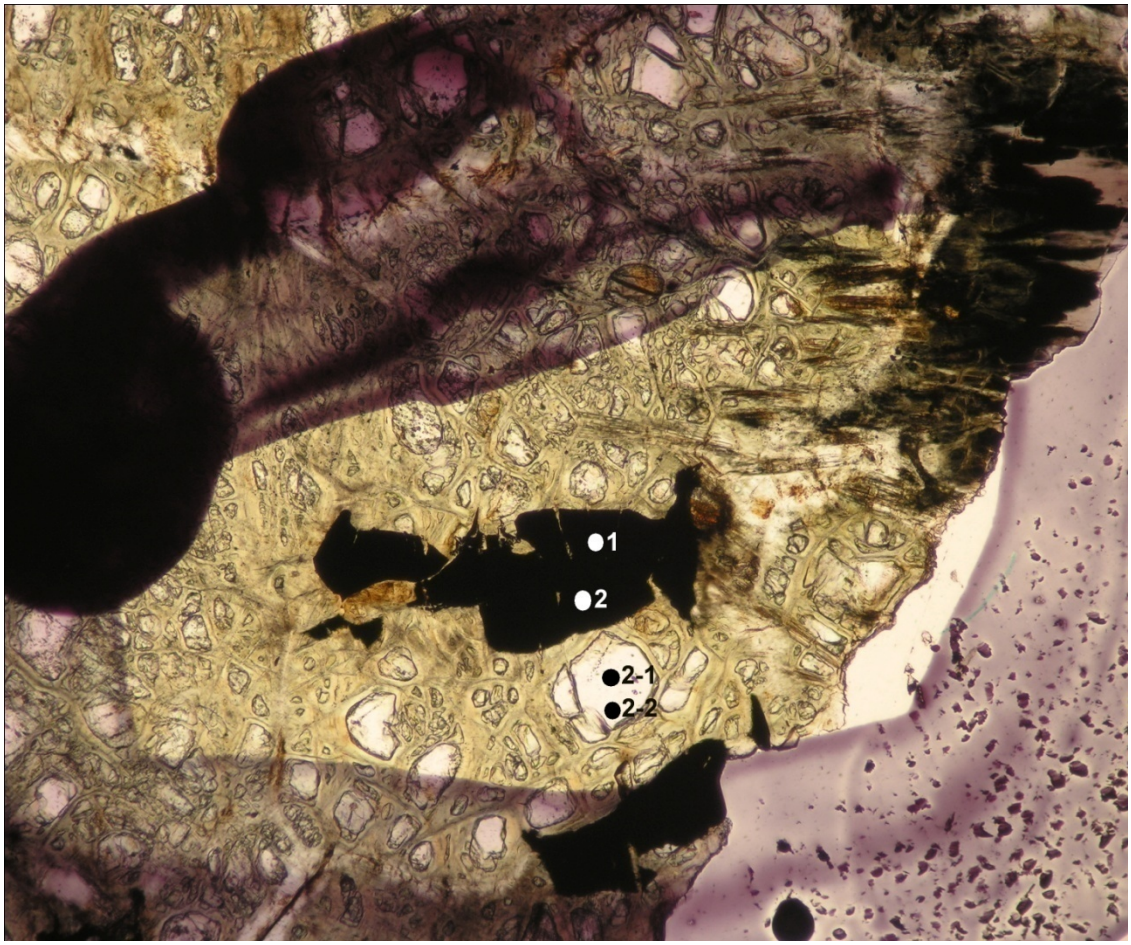

Photomicrograph 89
147-895D-004R-01W (54-60)

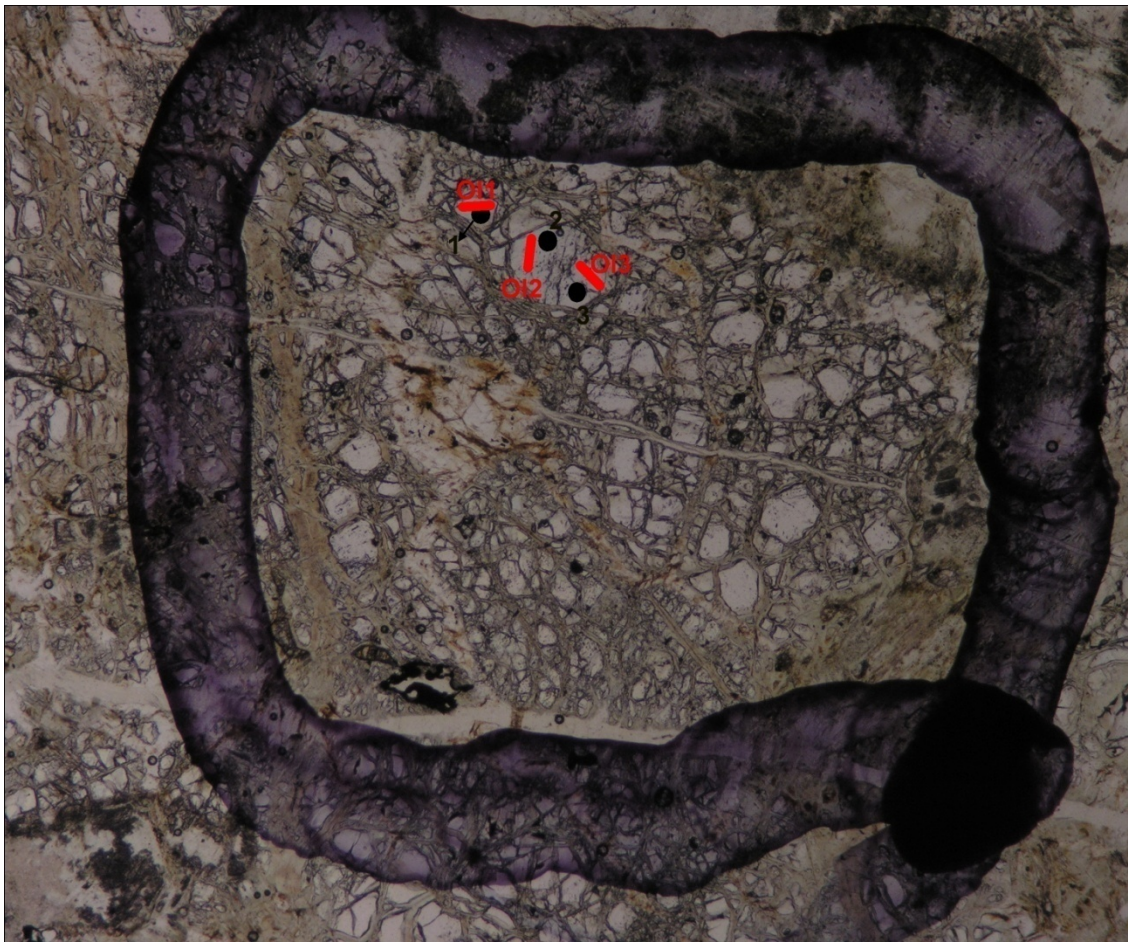

Photomicrograph 90
147-895D-004R-03W (52-58)

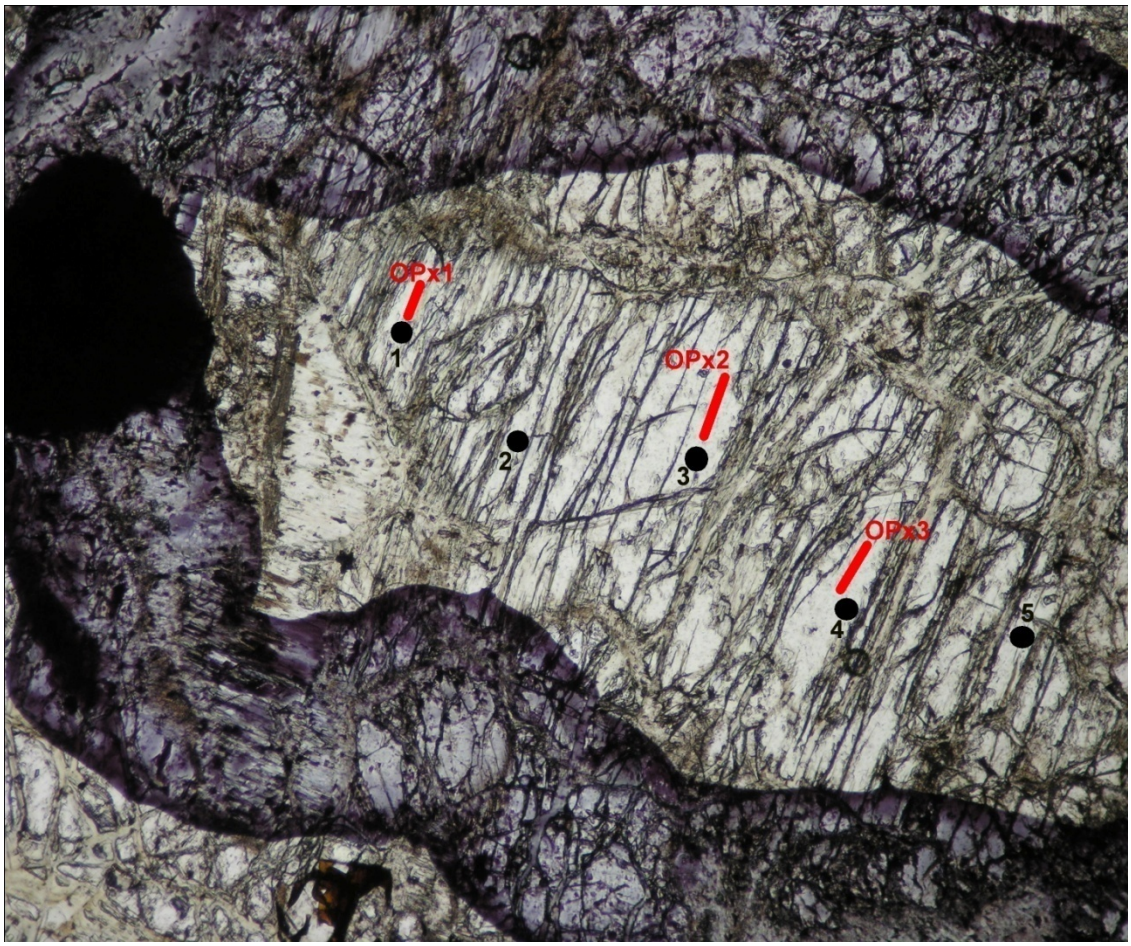

Photomicrograph 91
147-895D-004R-03W (52-58)

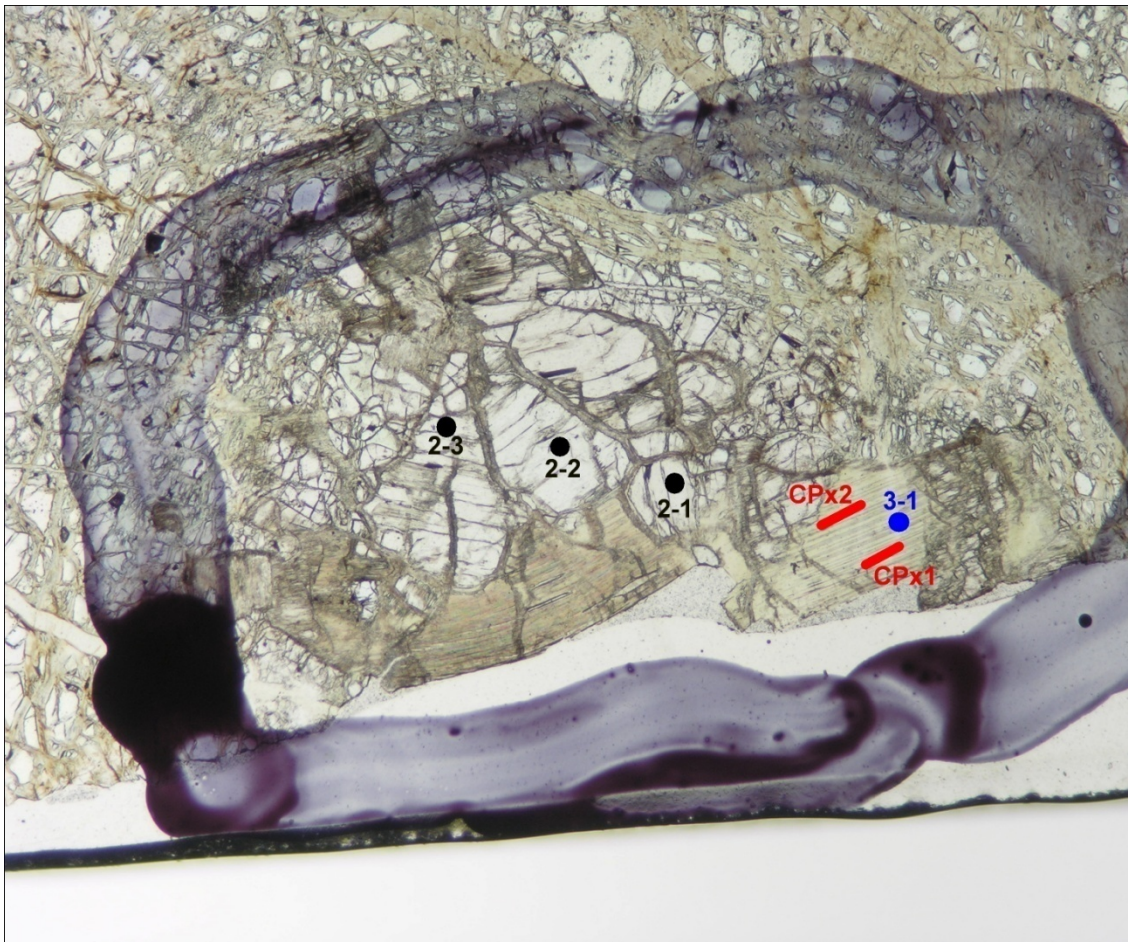

Photomicrograph 92
147-895D-004R-03W (52-58)

Photomicrograph 93
147-895D-004R-03W (52-58)

Photomicrograph 94
147-895D-004R-03W (112-116)

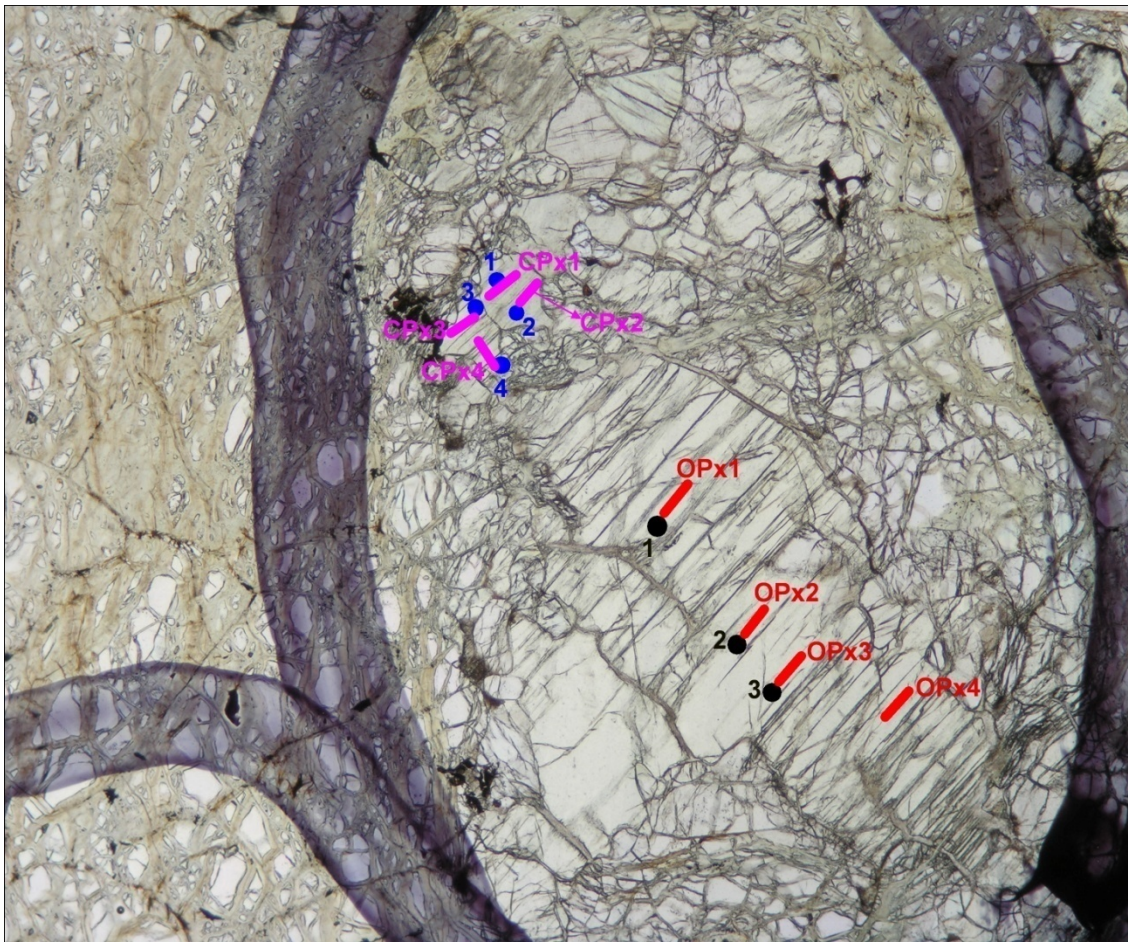

Photomicrograph 95
147-895D-004R-03W (112-116)

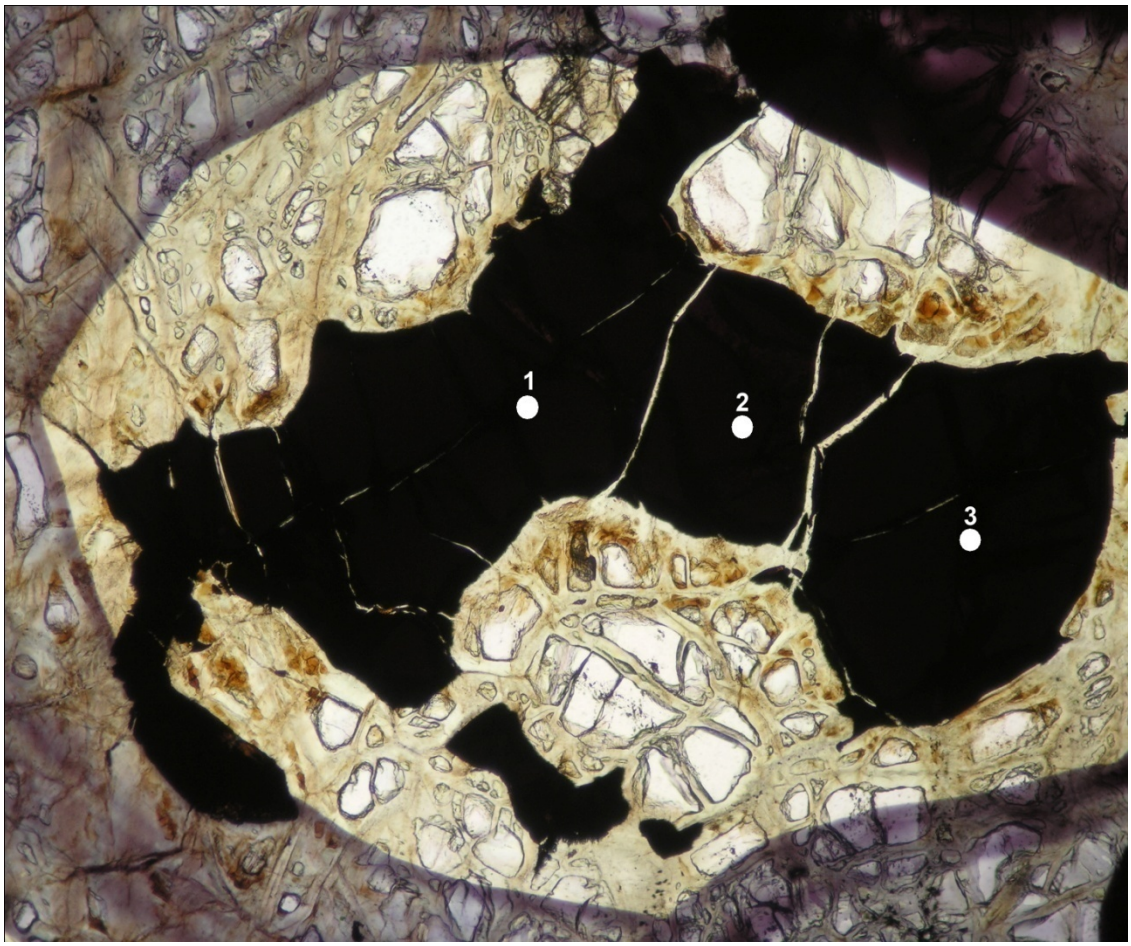

Photomicrograph 96
147-895D-004R-03W (112-116)

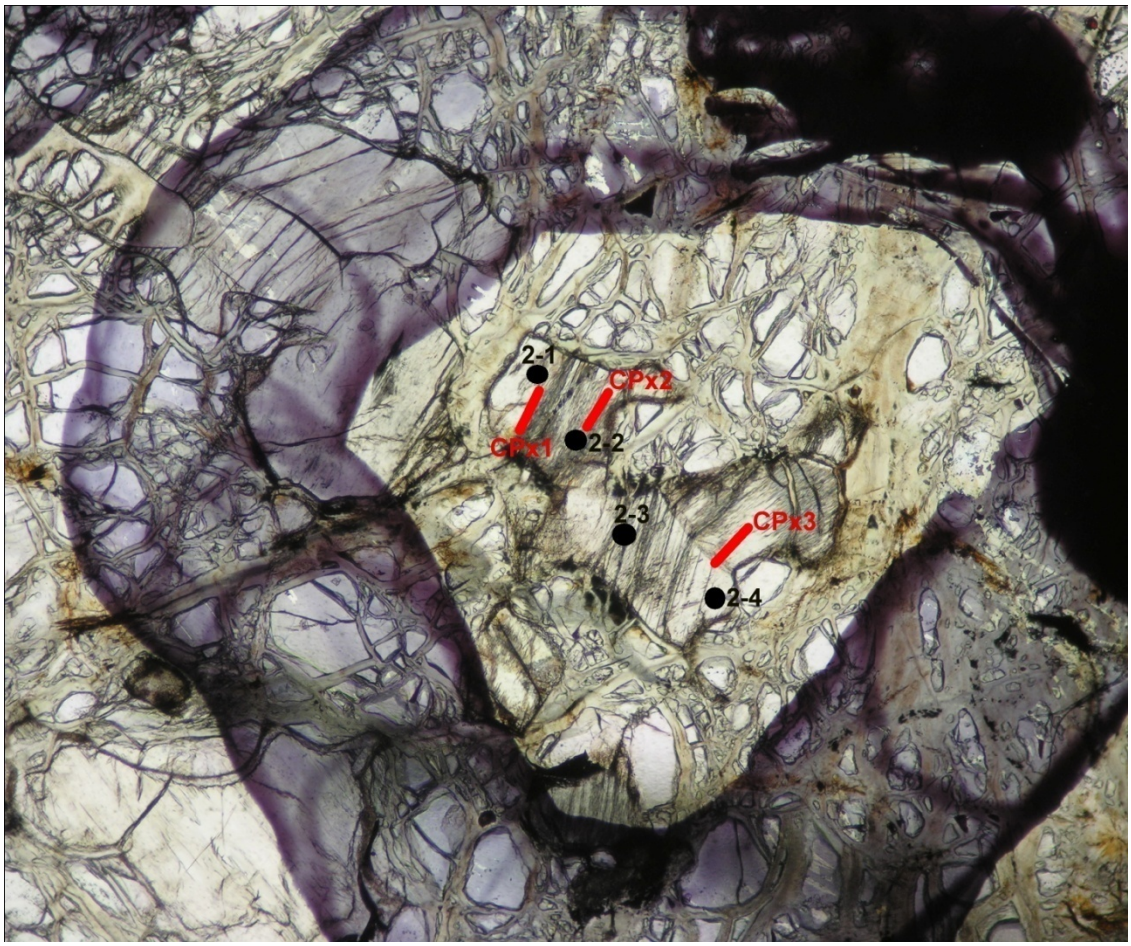

Photomicrograph 97
147-895D-004R-03W (112-116)

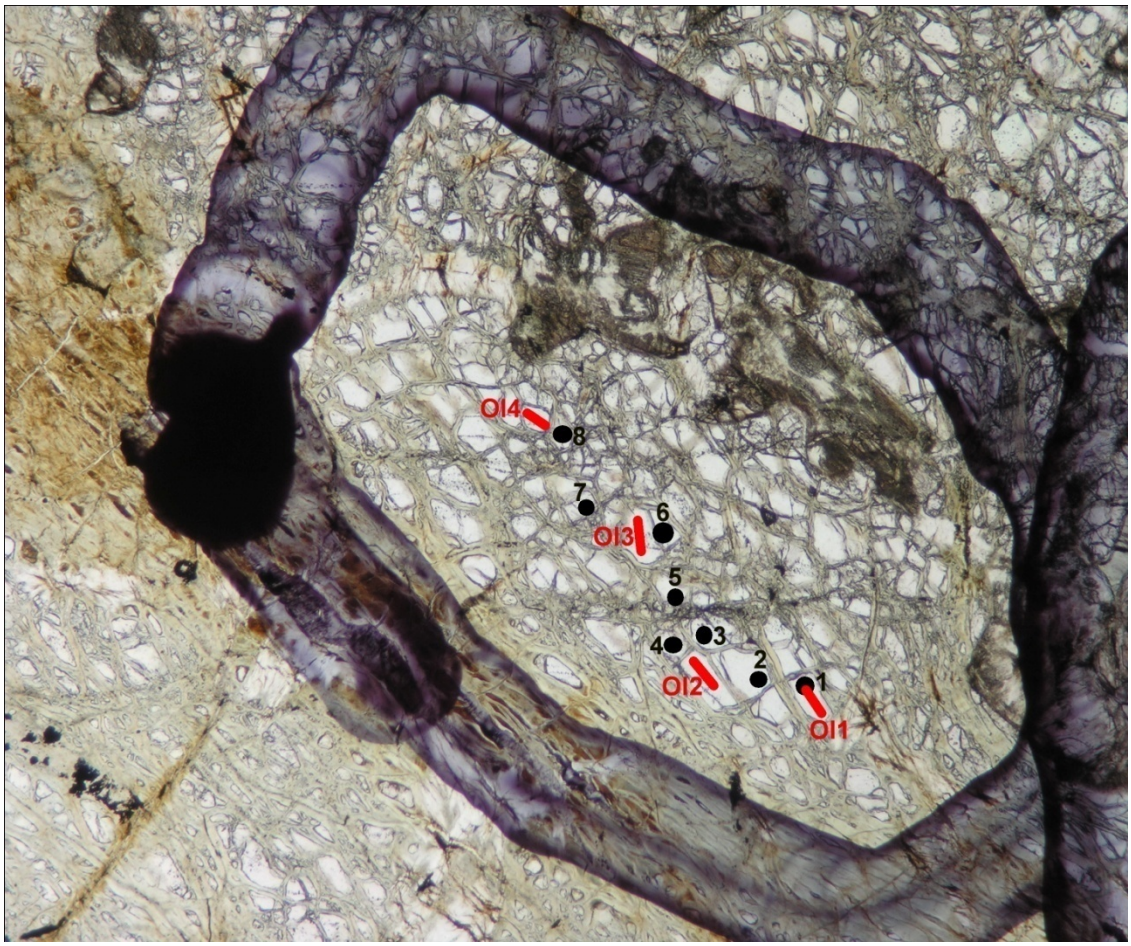

Photomicrograph 98
147-895D-004R-05W (11-18)

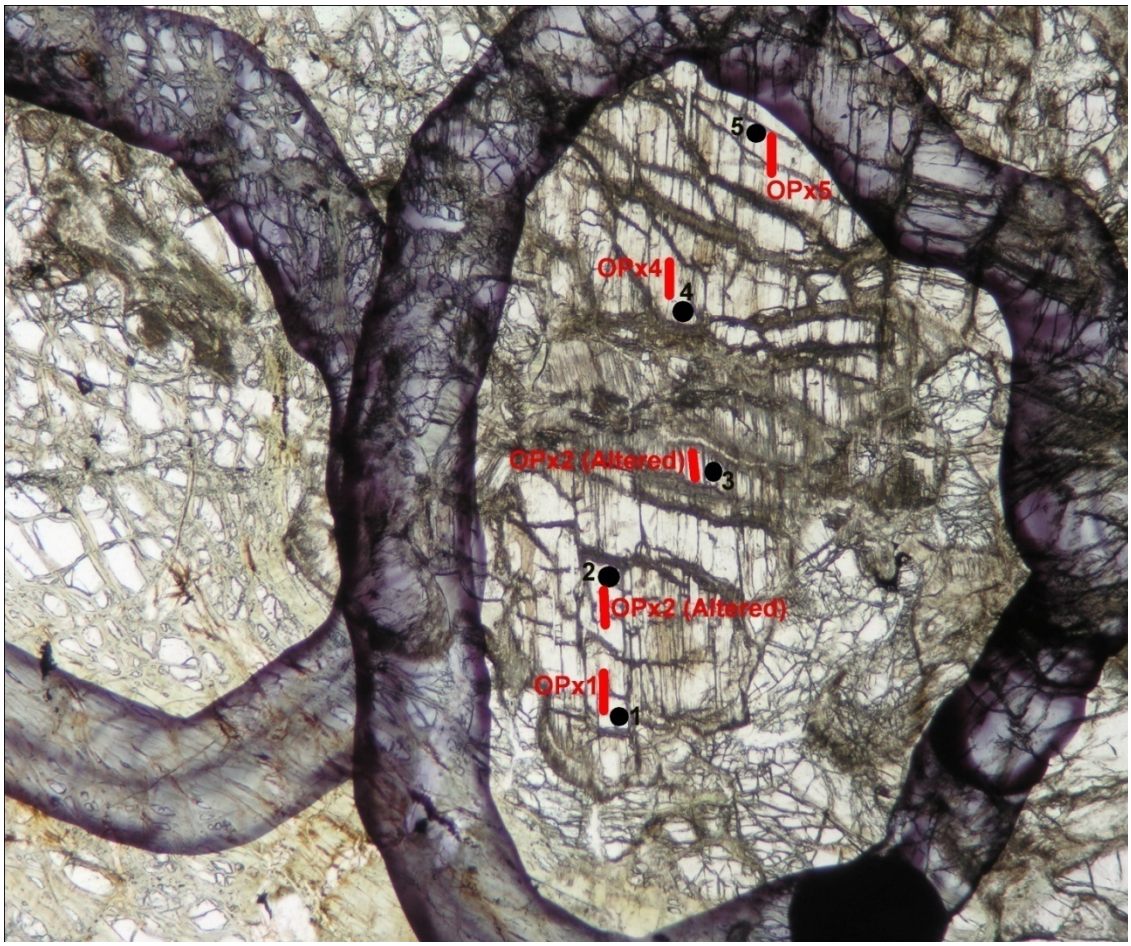

Photomicrograph 99
147-895D-004R-05W (11-18)

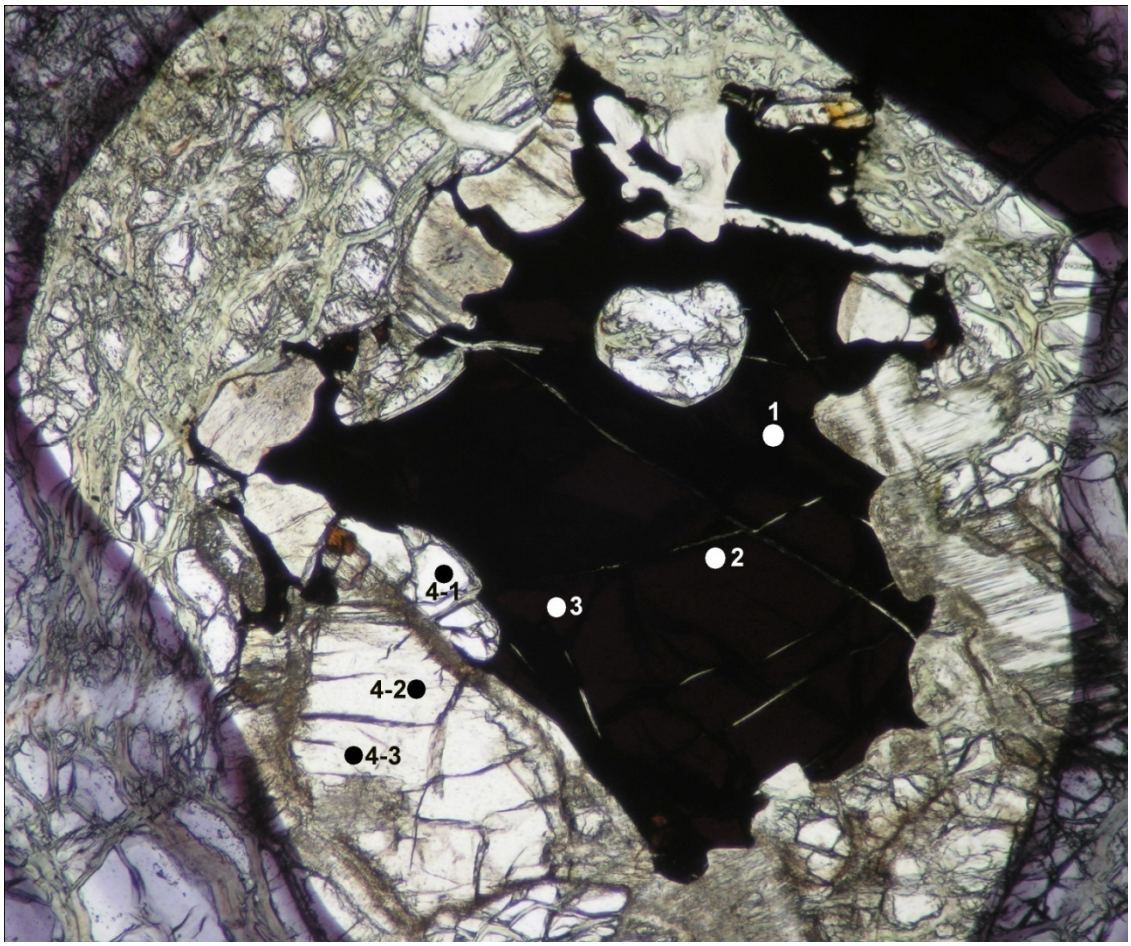

Photomicrograph 100
147-895D-004R-05W (11-18)

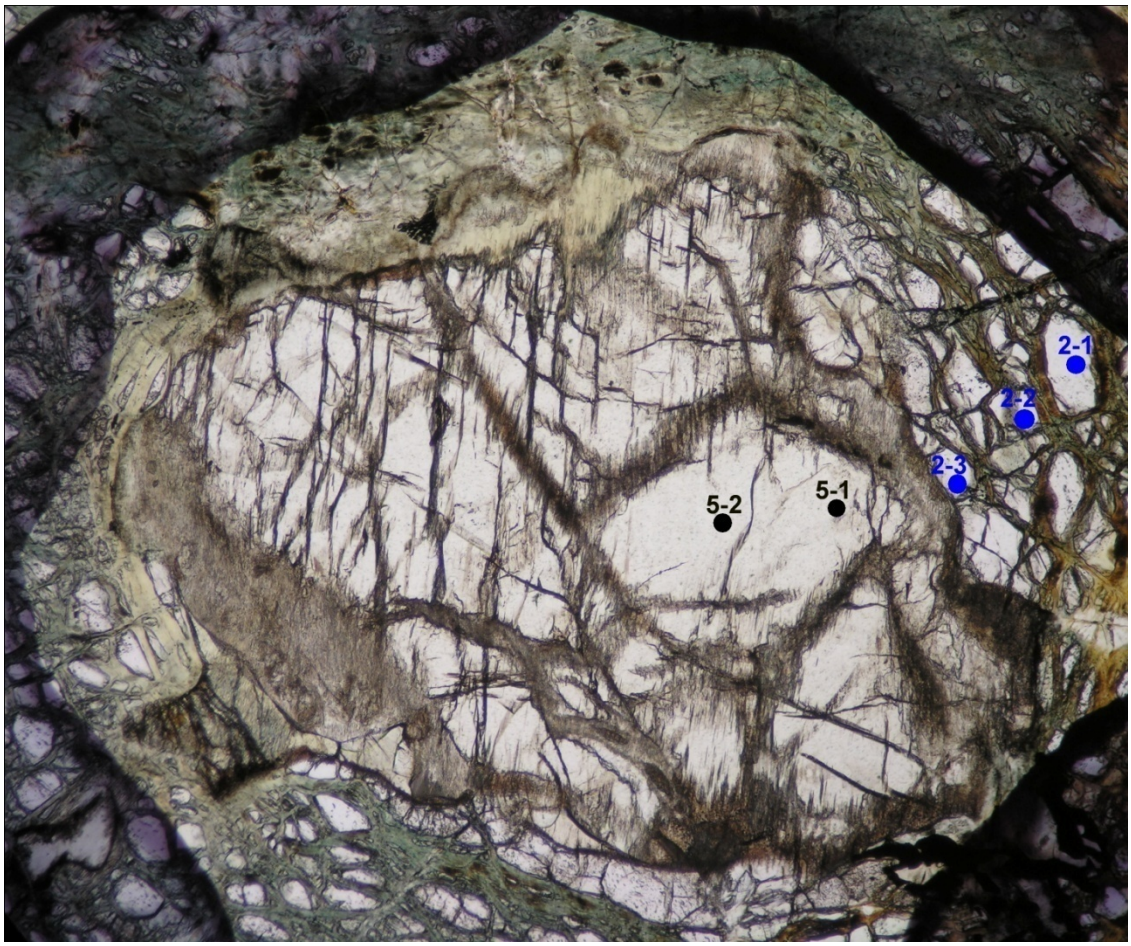

Photomicrograph 101
147-895D-004R-05W (11-18)

Photomicrograph 102
147-895D-005R-01W (48-54)

Photomicrograph 103
147-895D-005R-01W (48-54)

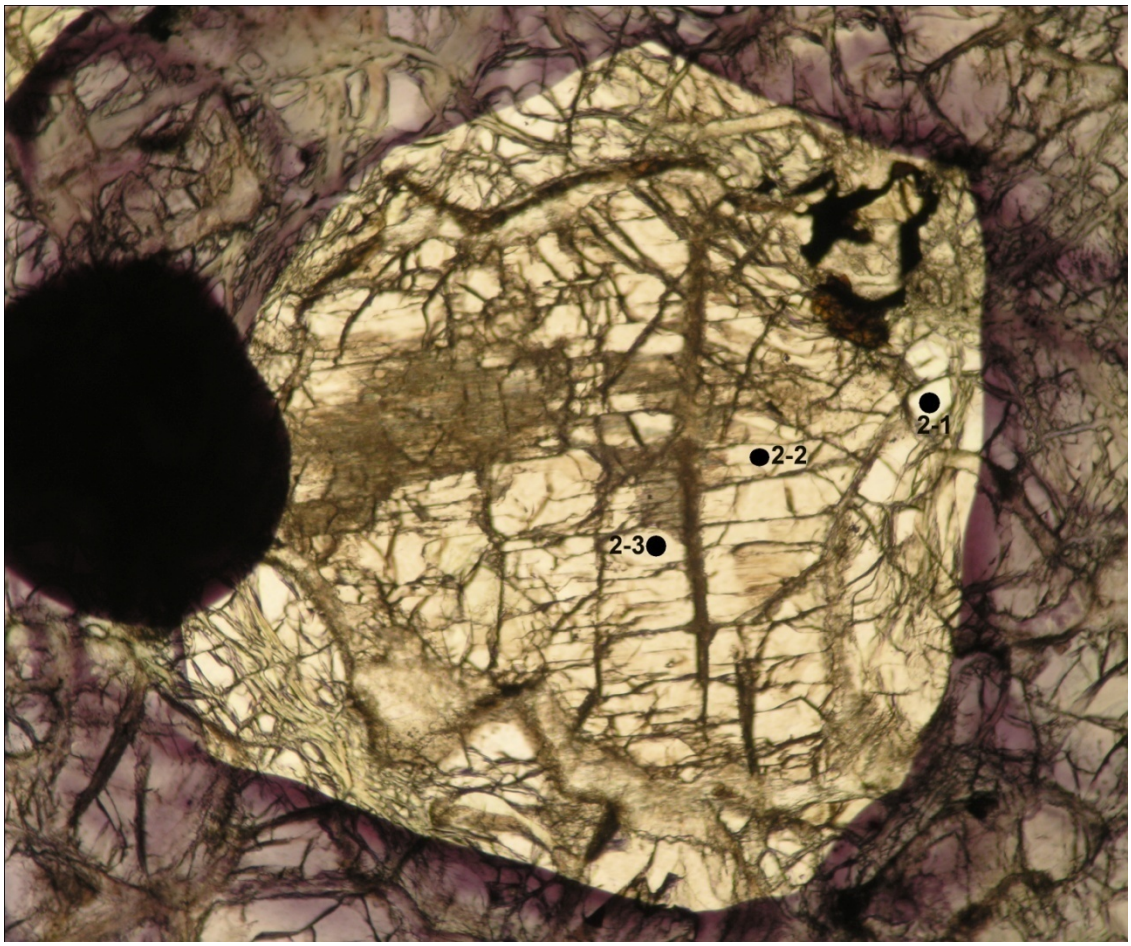

Photomicrograph 104
147-895D-005R-02W (103-112)

Photomicrograph 105
147-895D-005R-02W (103-112)

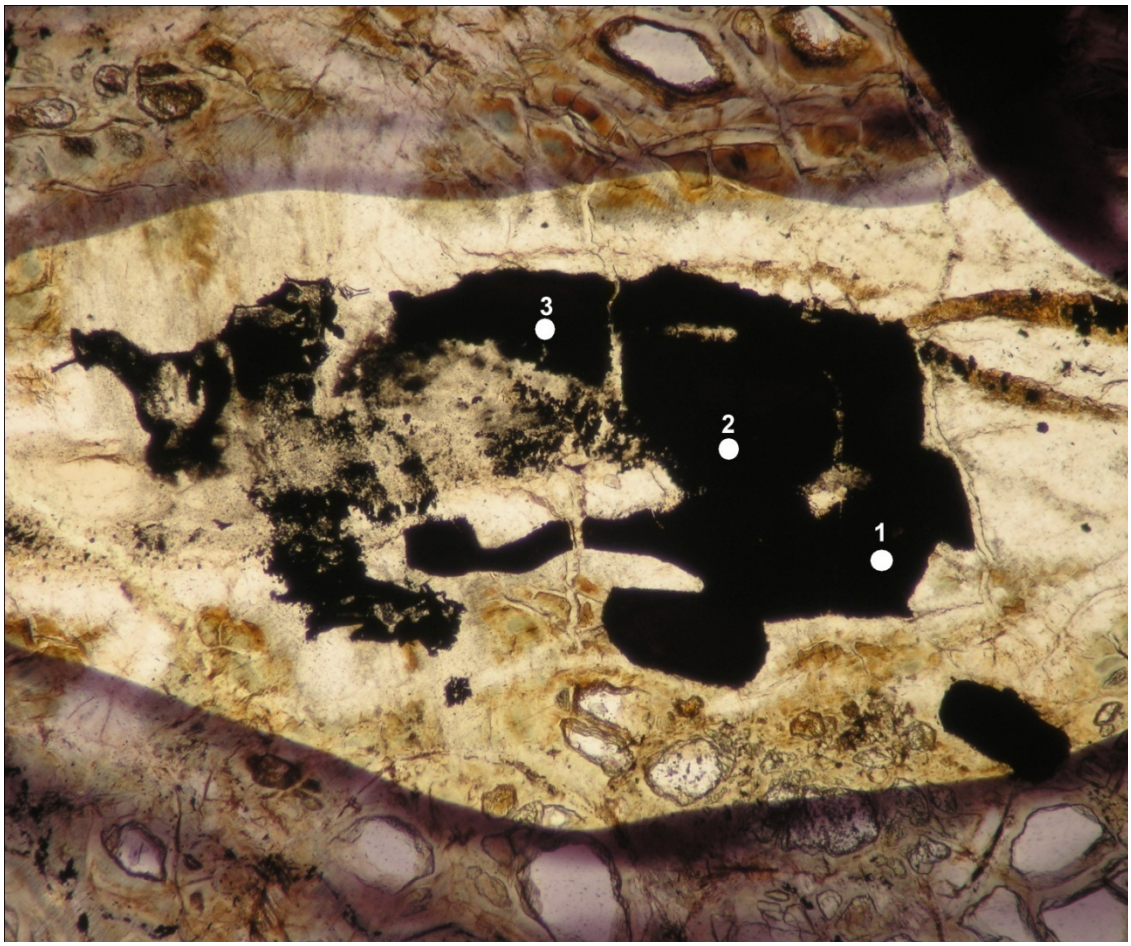

Photomicrograph 106
147-895D-005R-02W (103-112)

Photomicrograph 107
147-895D-005R-02W (103-112)

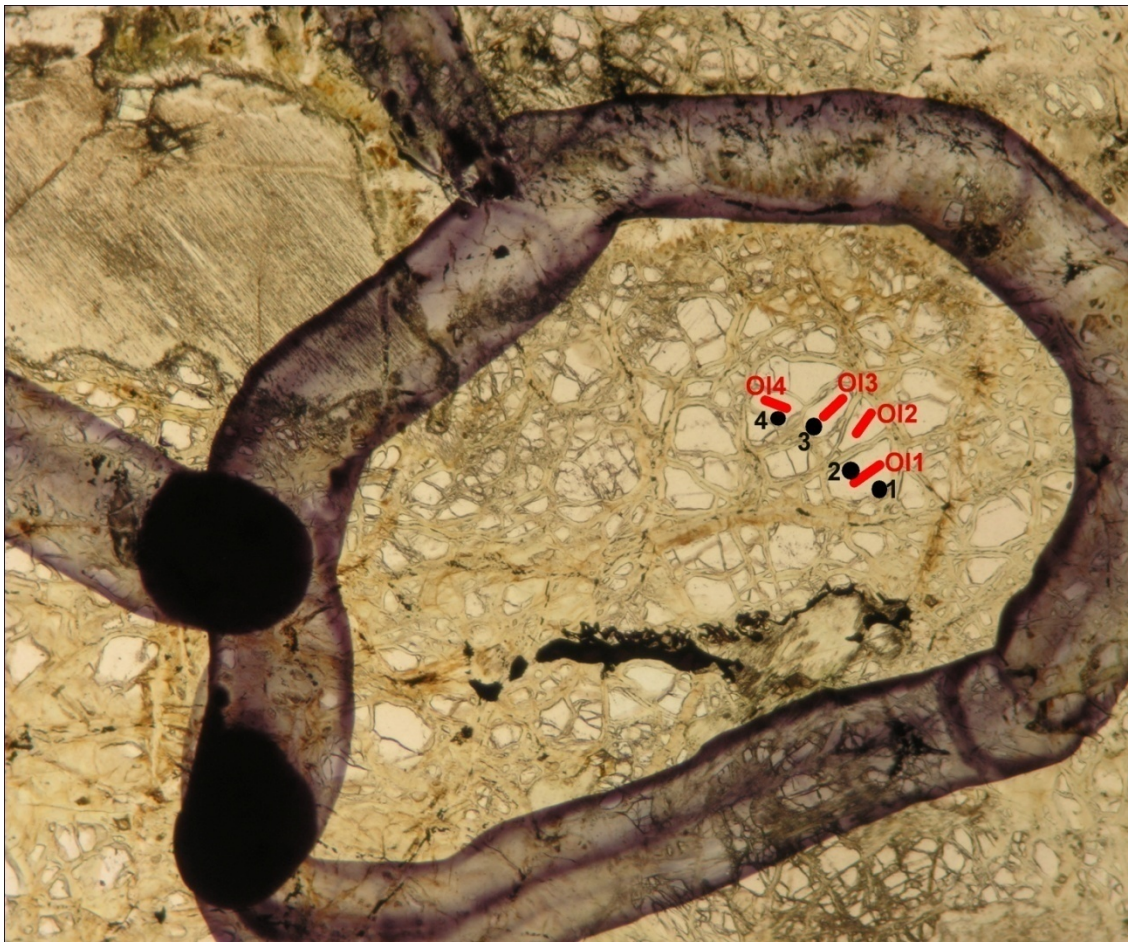

Photomicrograph 108
147-895D-005R-02W (103-112)

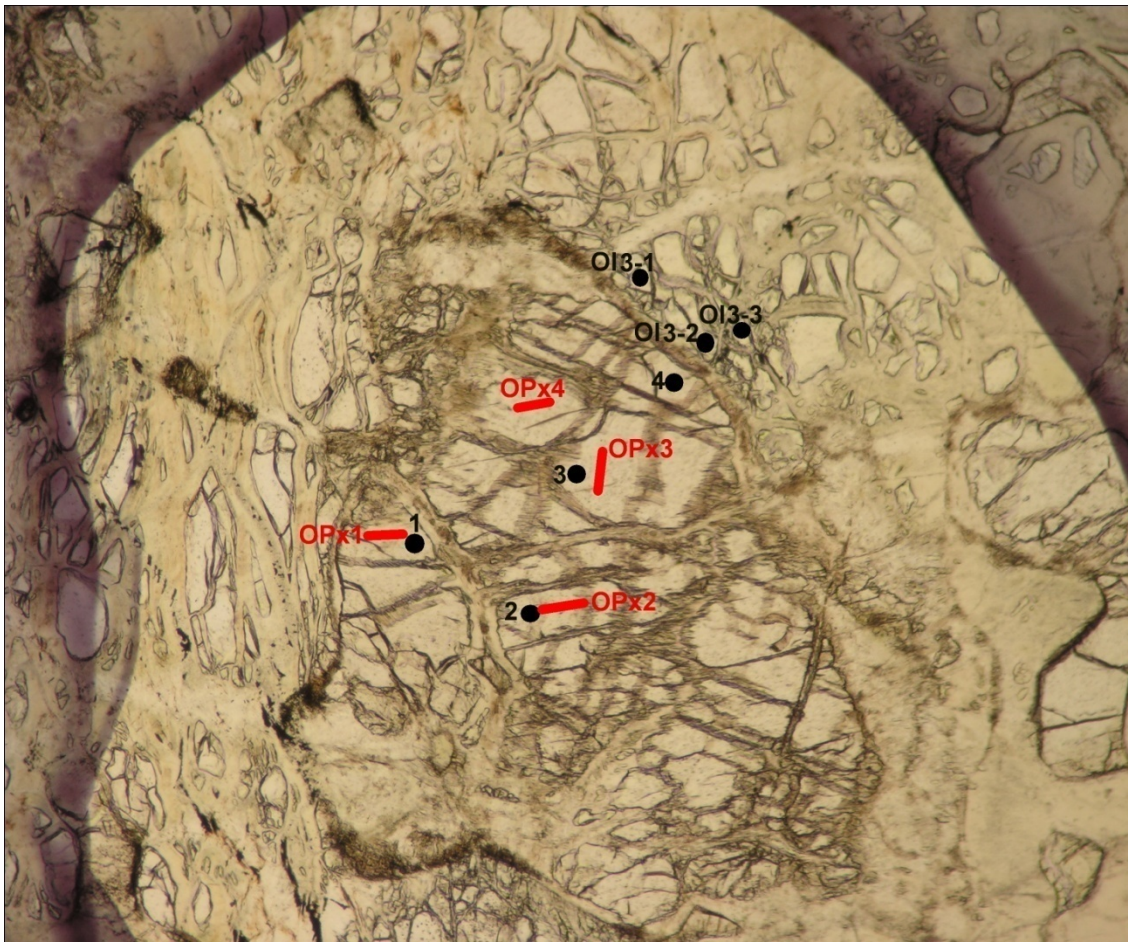

Photomicrograph 109
147-895D-005R-02W (103-112)

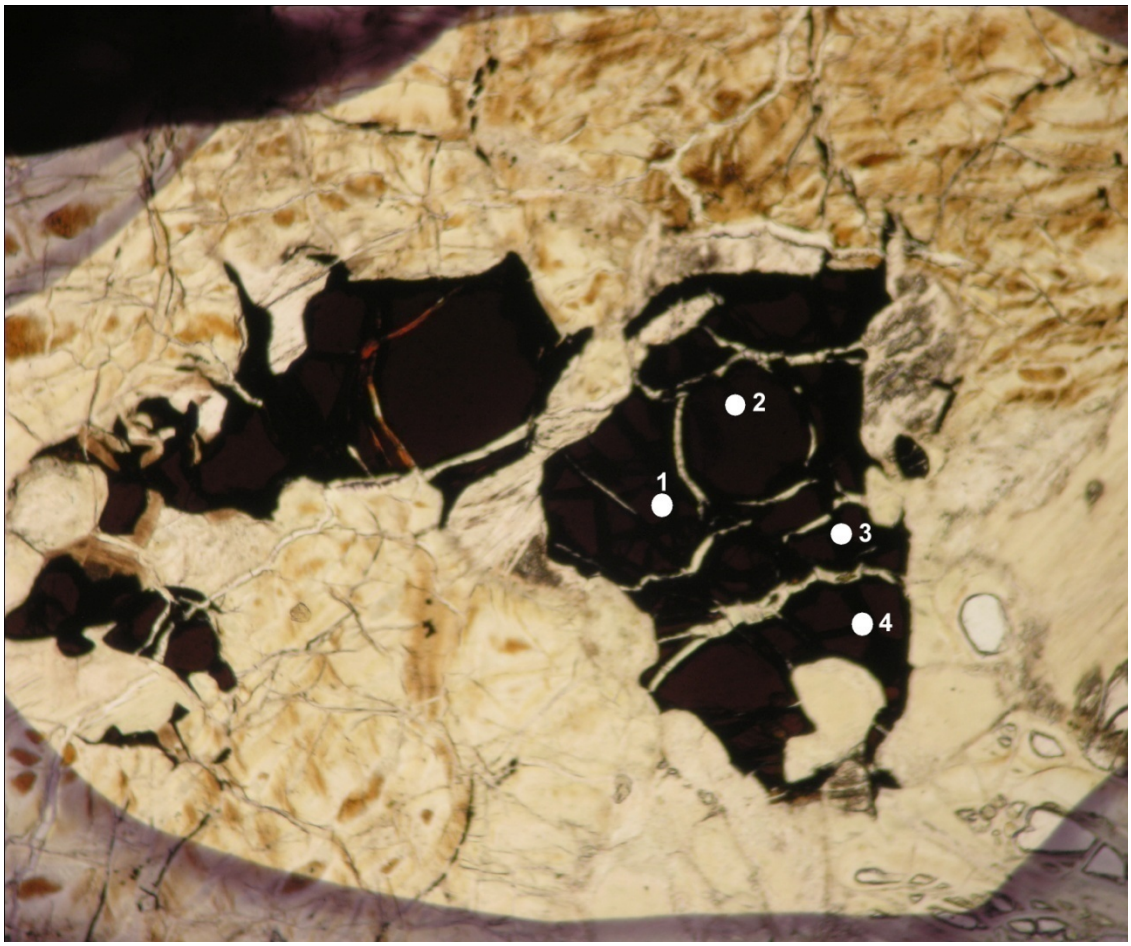

Photomicrograph 110
147-895D-007R-02W (127-135)

Photomicrograph 111
147-895D-007R-02W (127-135)

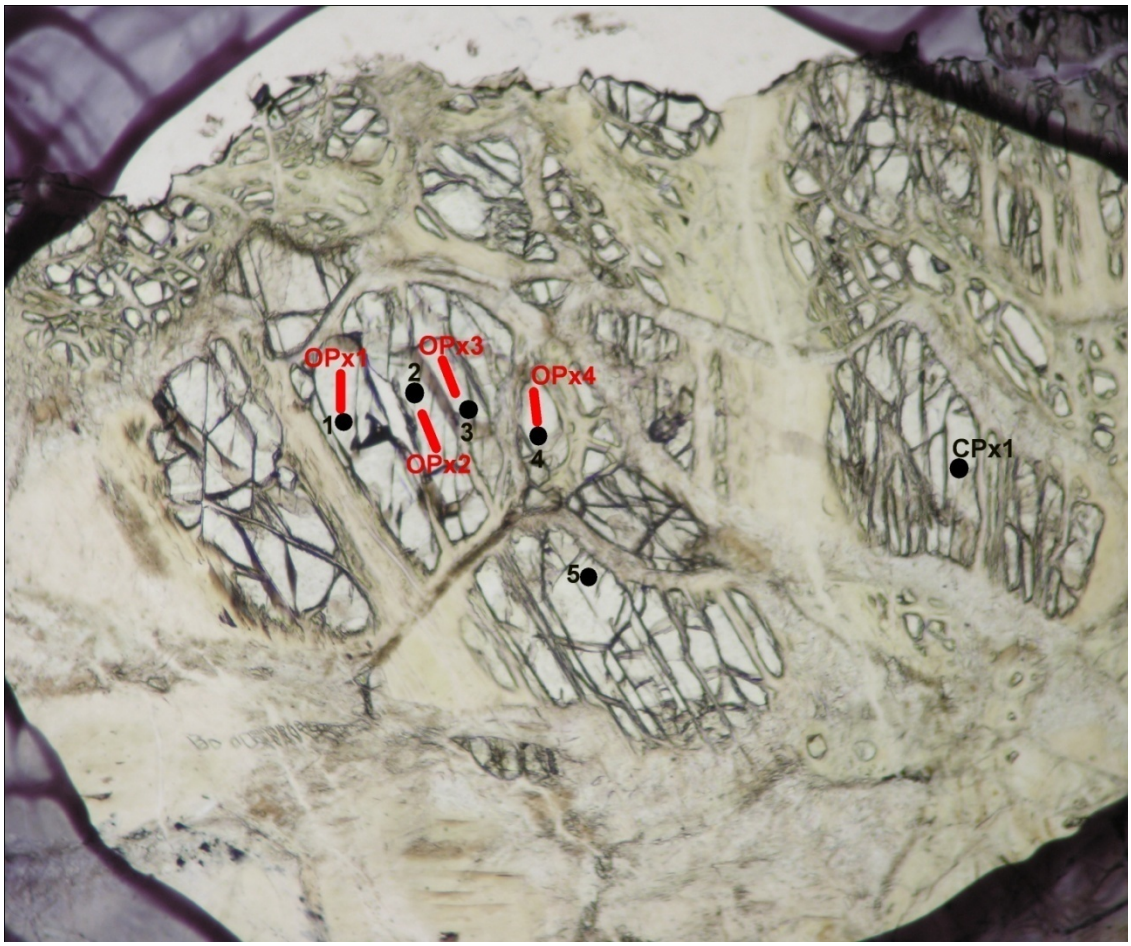

Photomicrograph 112
147-895D-007R-02W (127-135)

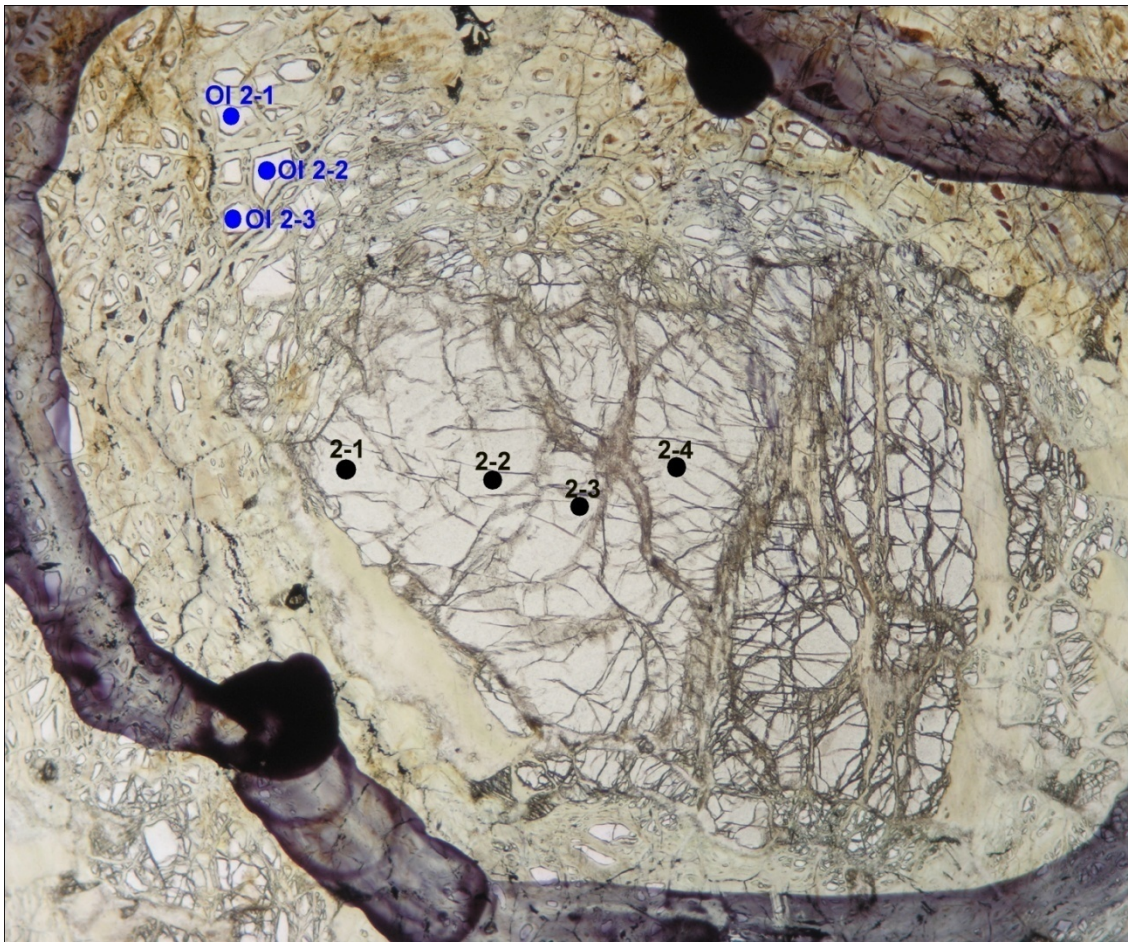

Photomicrograph 113
147-895D-007R-02W (127-135)

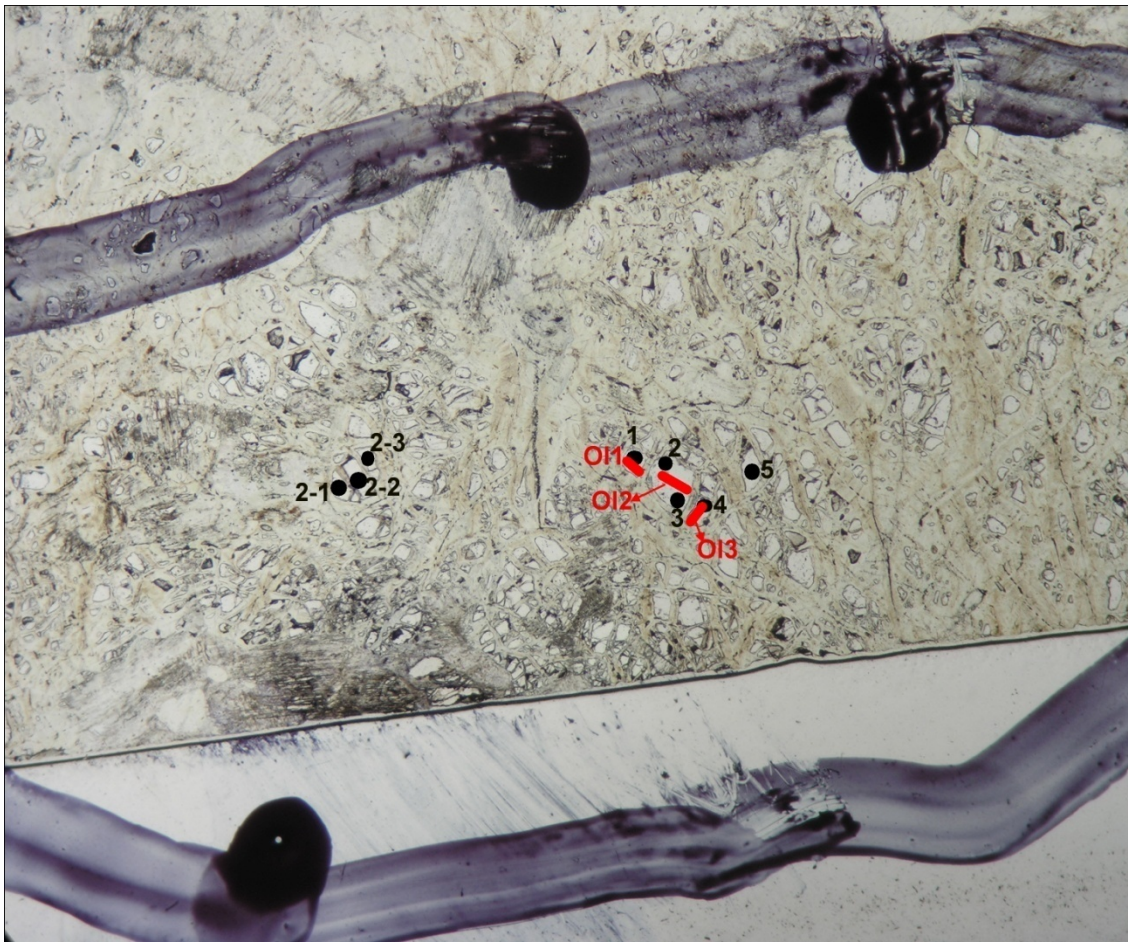

Photomicrograph 114
147-895E-007R-04W (37-41)

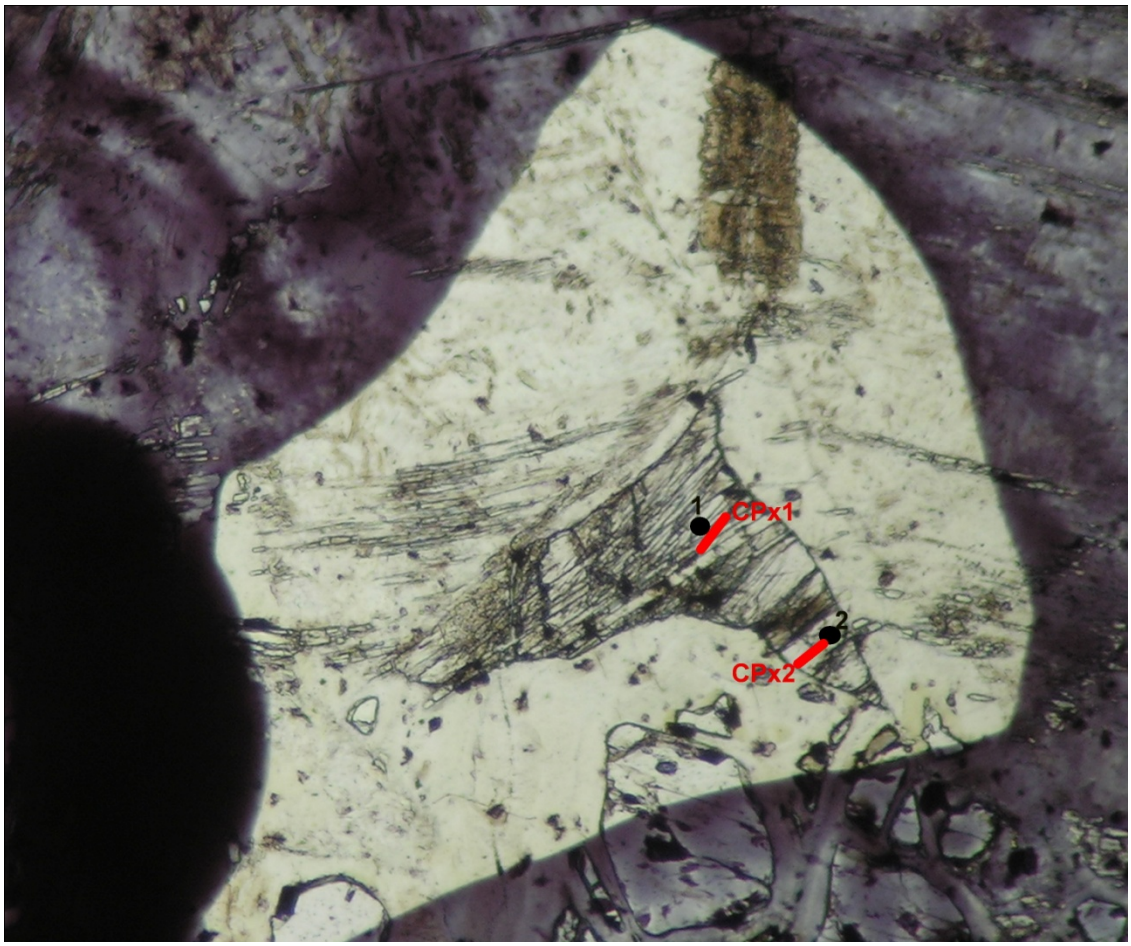

Photomicrograph 115
147-895E-007R-04W (37-41)

Photomicrograph 116
147-895E-007R-04W (37-41)

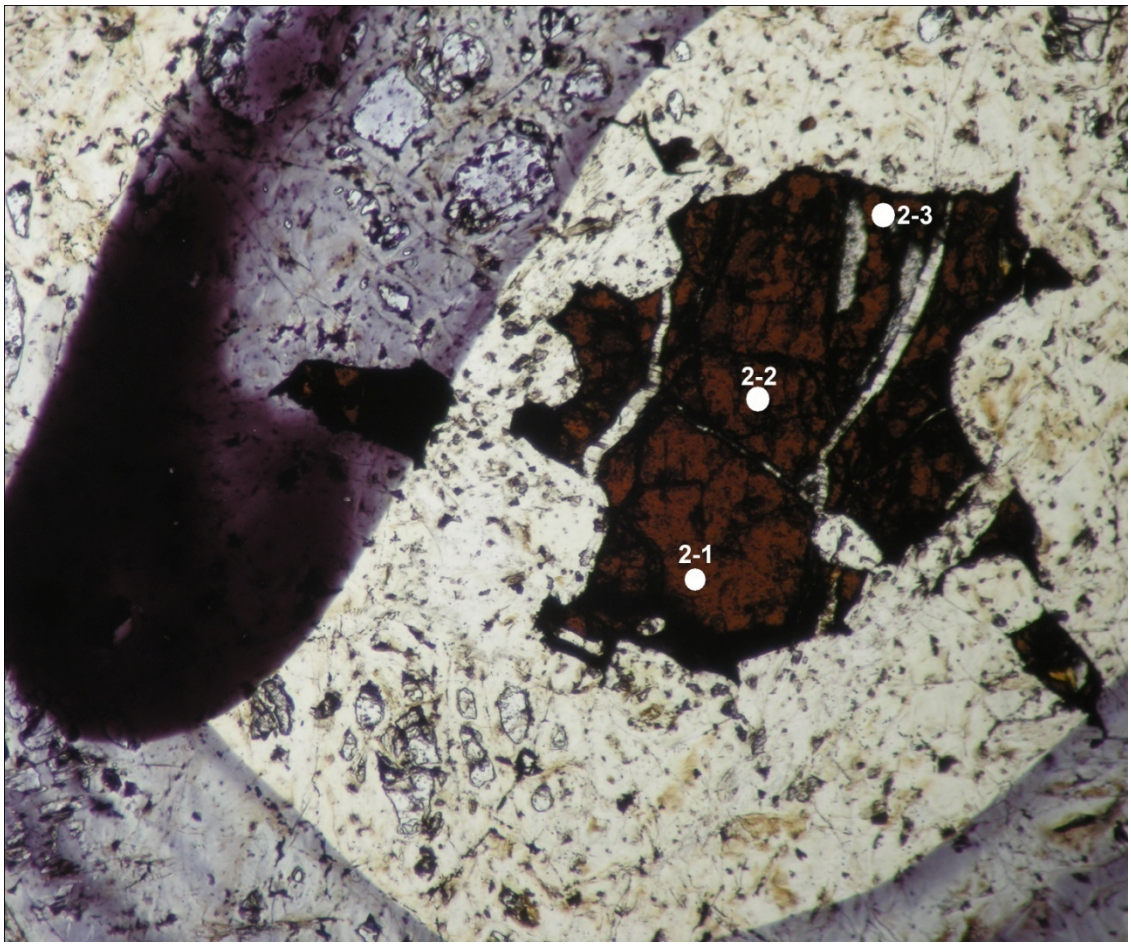

Photomicrograph 117
147-895E-007R-04W (37-41)

Photomicrograph 118
147-895E-007R-04W (37-41)

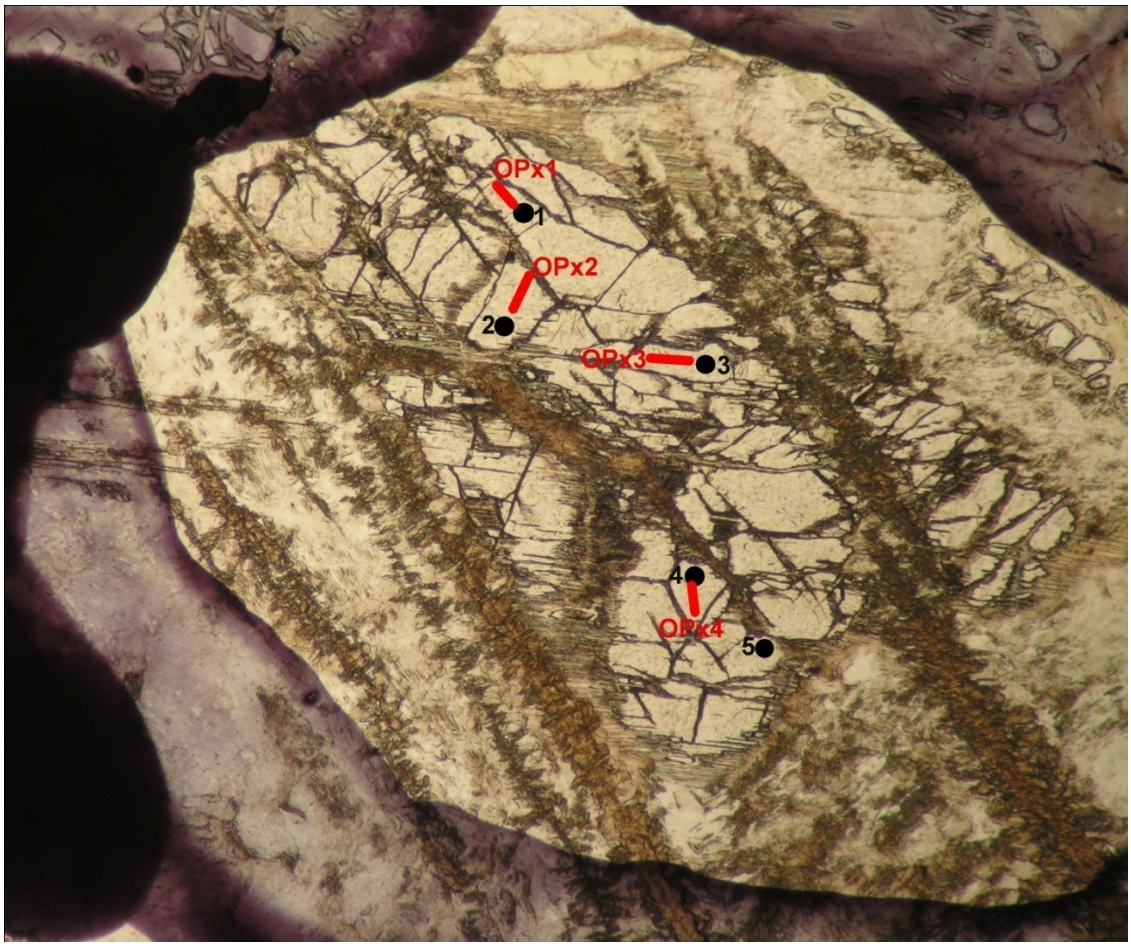

Photomicrograph 119
147-895E-007R-04W (86-94)

Photomicrograph 120
147-895E-007R-04W (86-94)

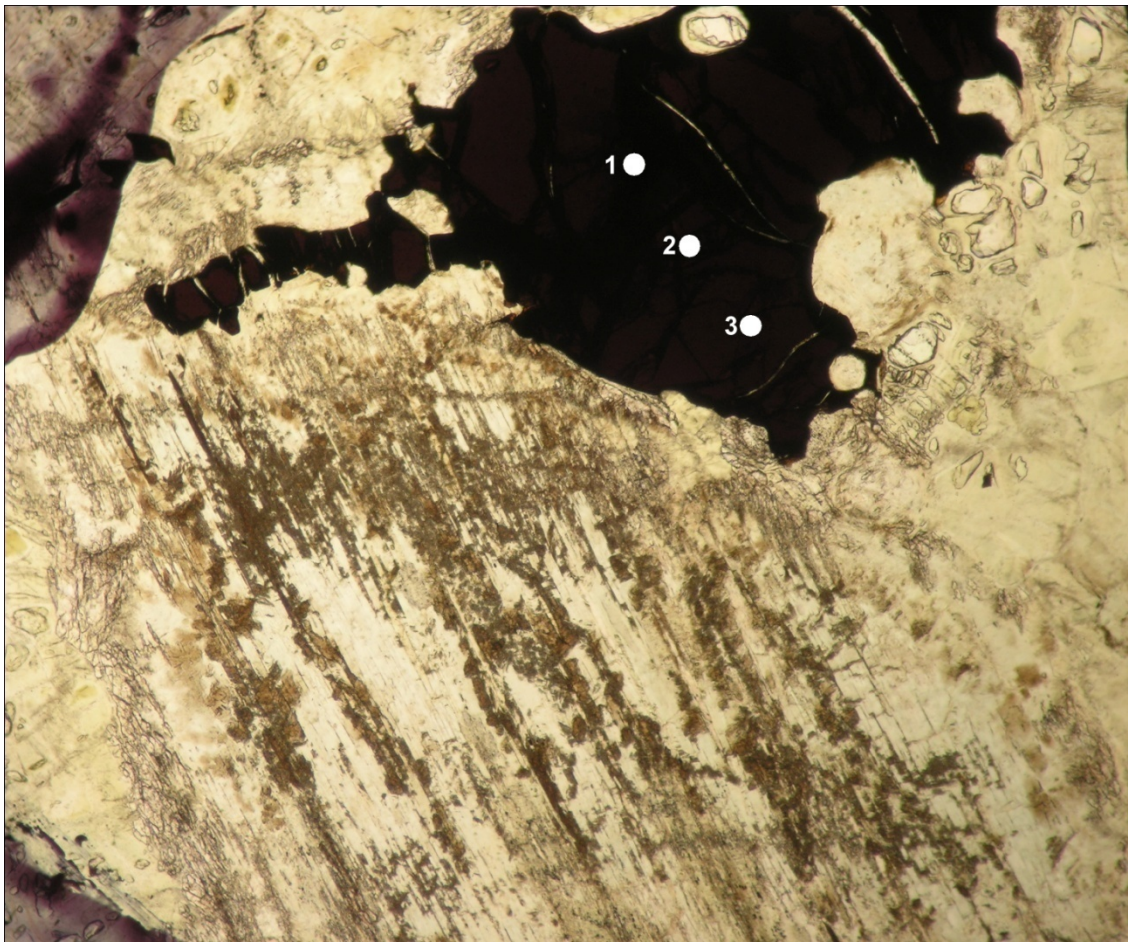

Photomicrograph 121
147-895E-007R-04W (86-94)

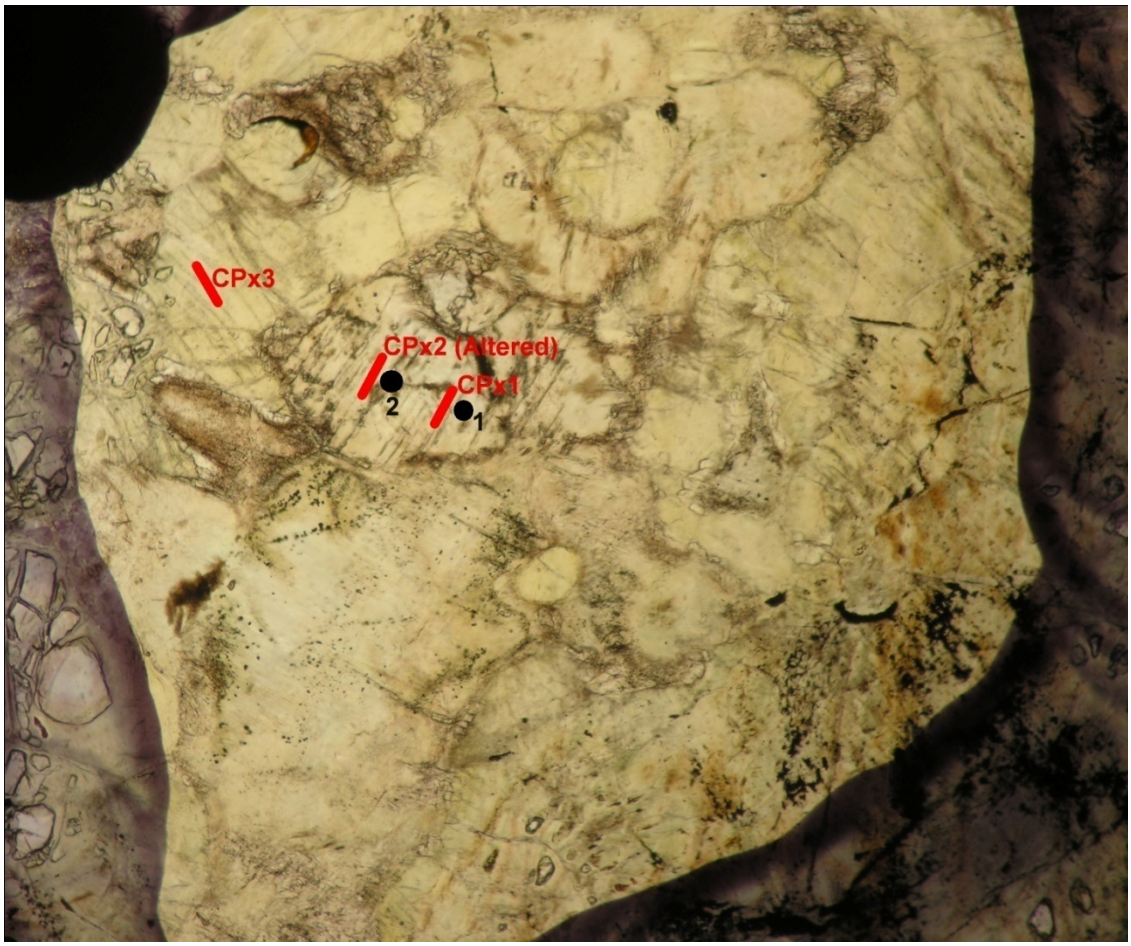

Photomicrograph 122
147-895E-007R-04W (86-94)

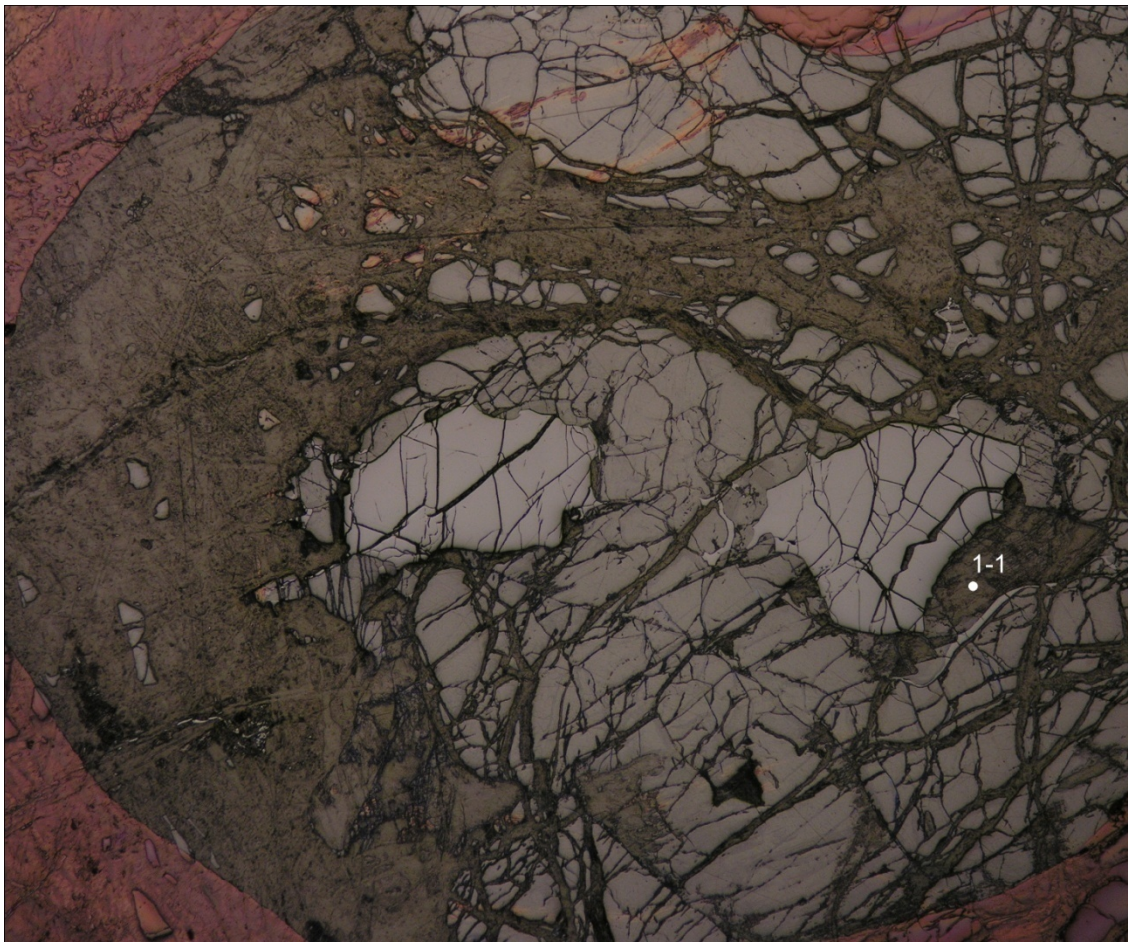

Photomicrograph 2a

Sample No. 147-895A-001R-02W (55-61)

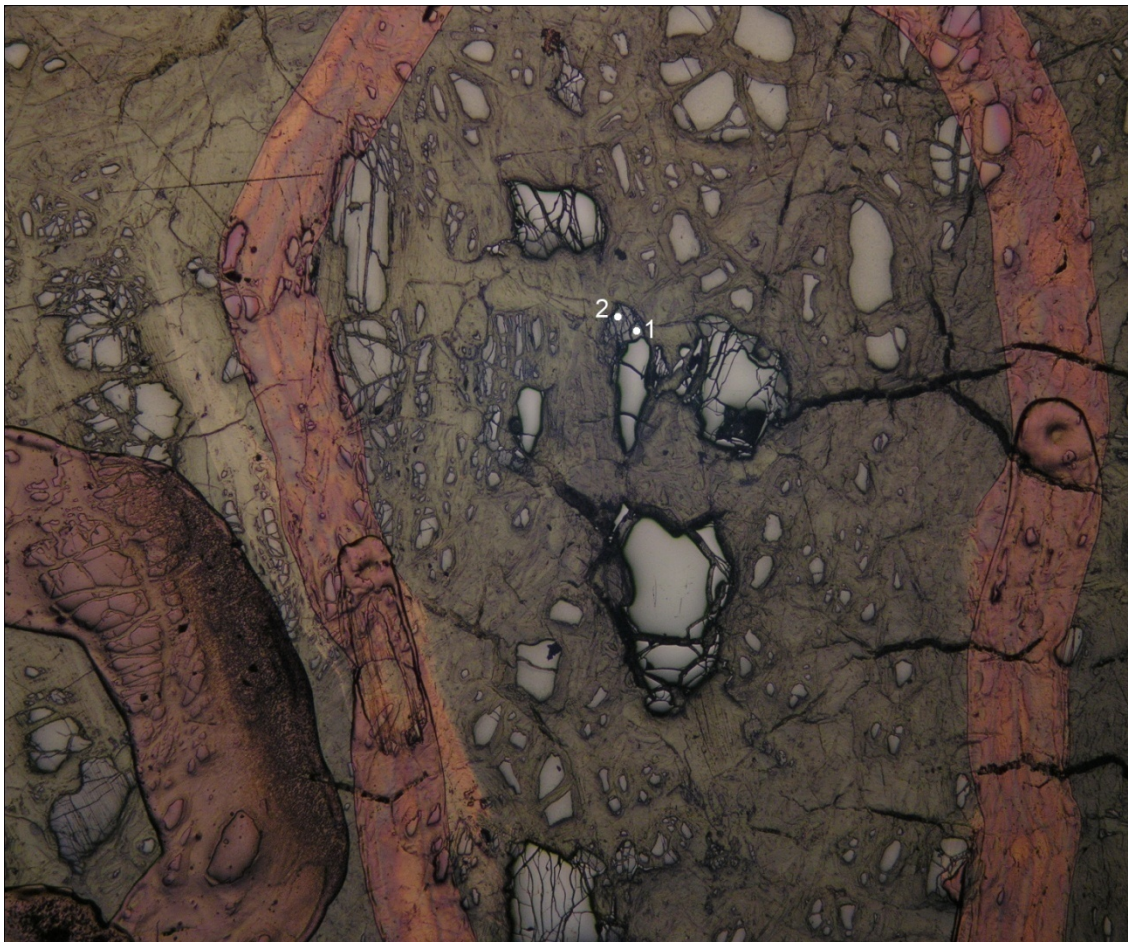

Photomicrograph 3a

Sample No. 147-895A-002R-01W (5-10)

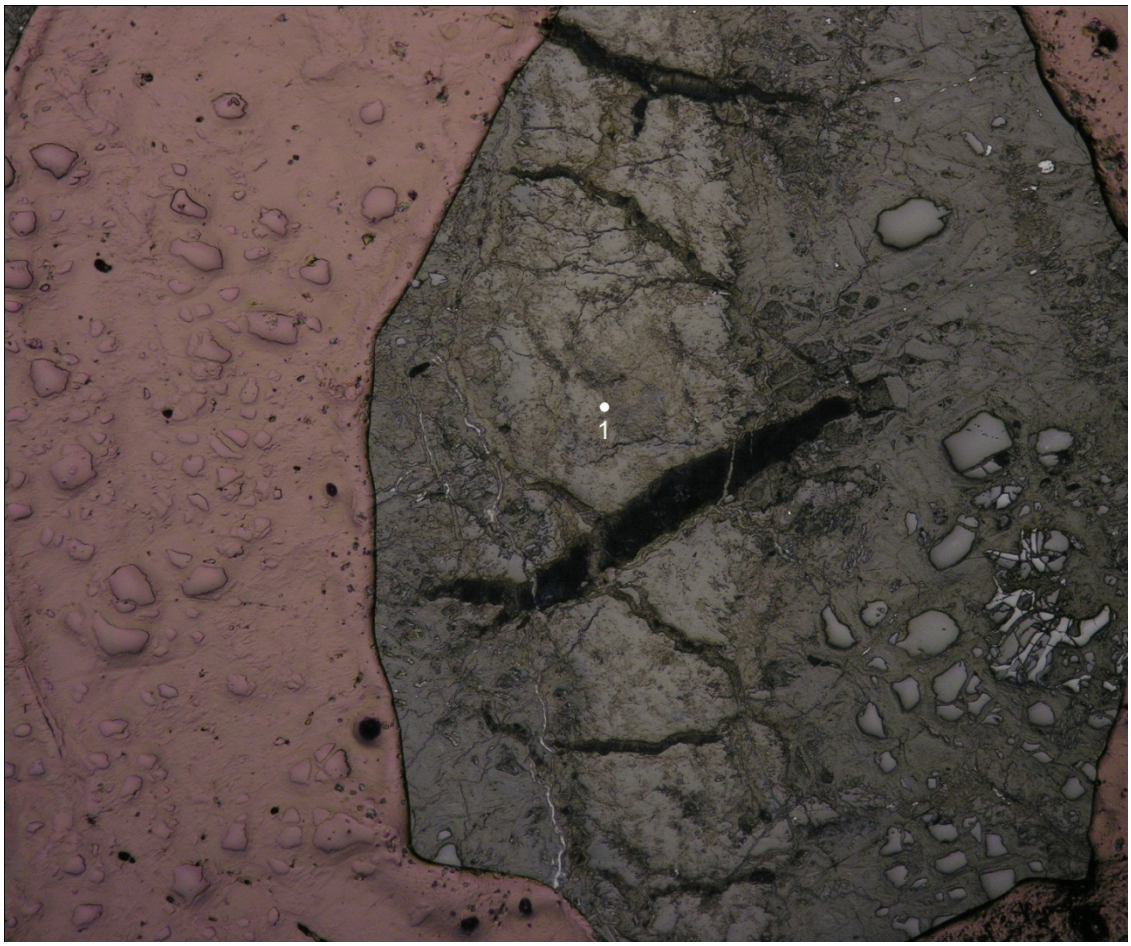

Photomicrograph 6a

Sample No. 147-895B-001R-01W (65-72)

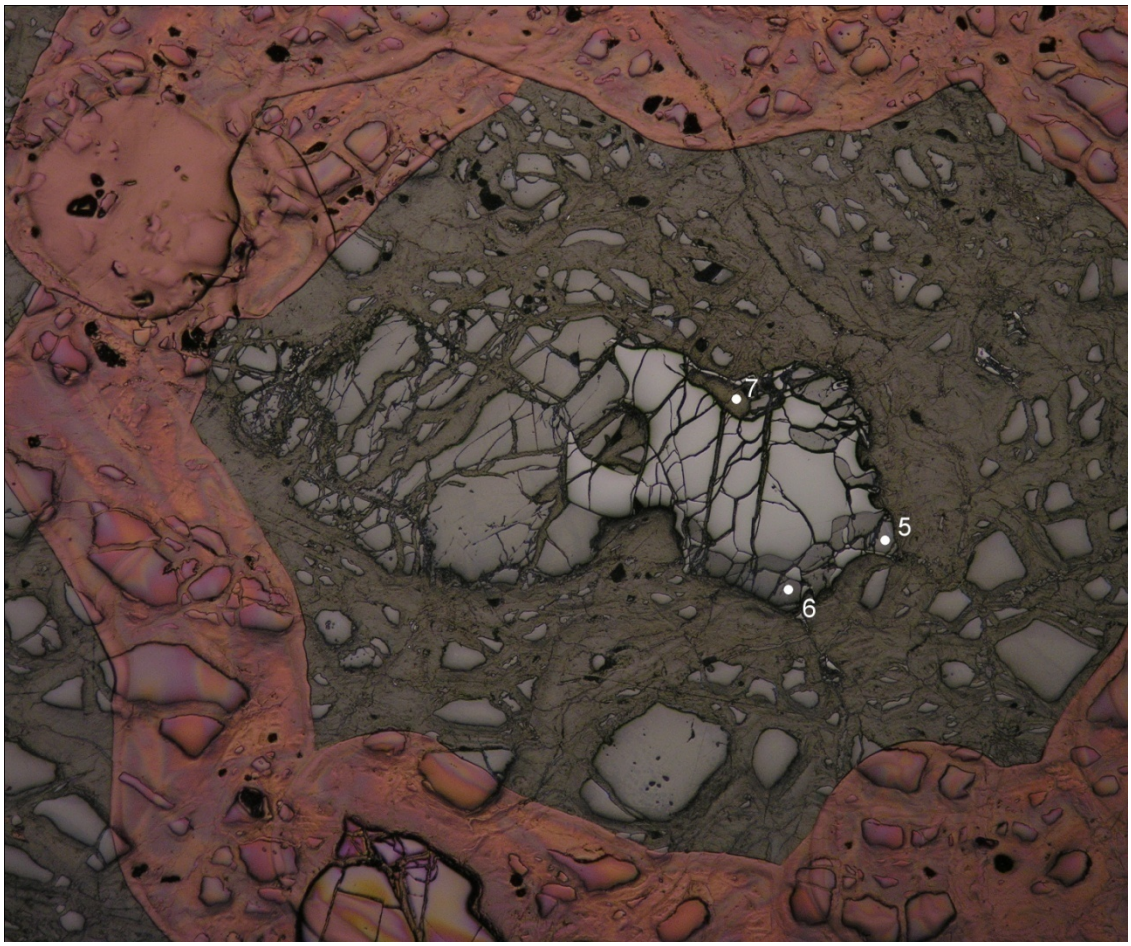

Photomicrograph 7a

Sample No. 147-895B-001R-01W (65-72)

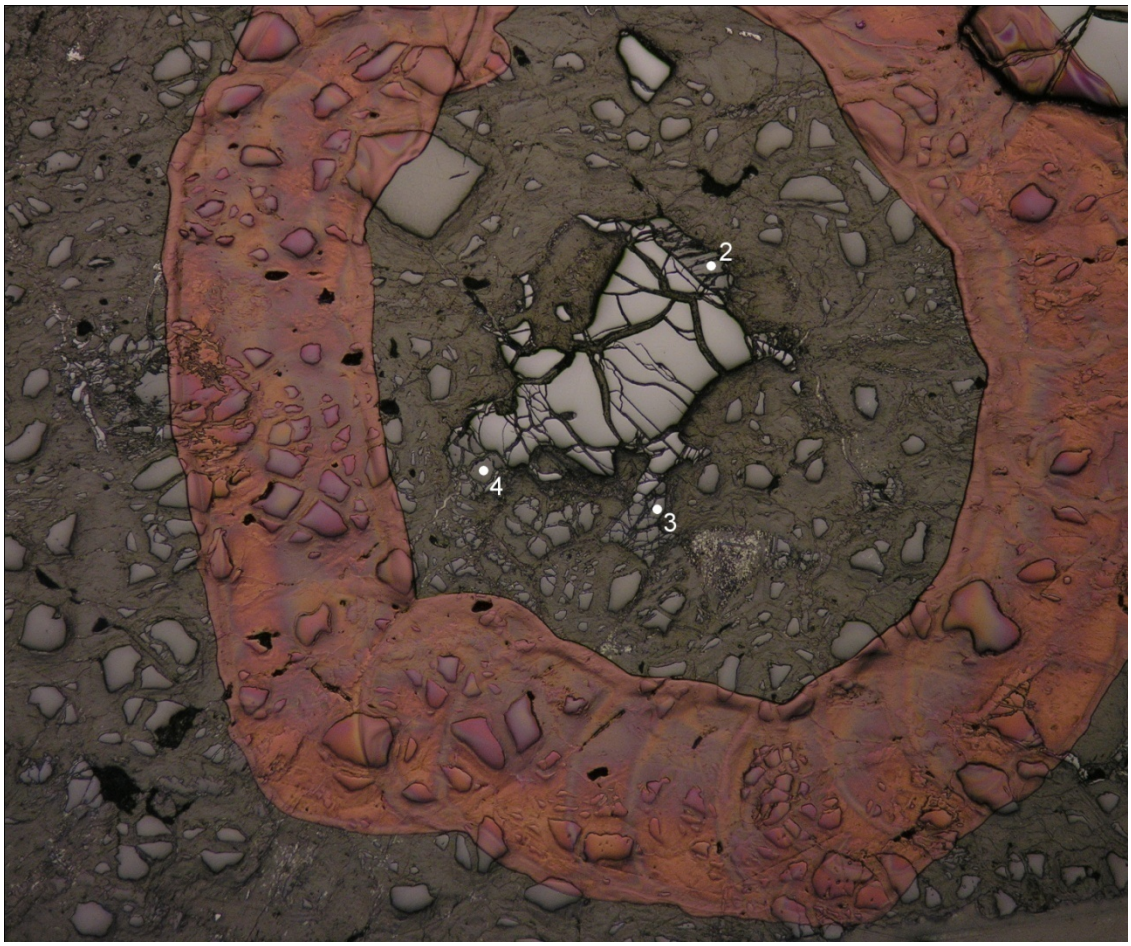

Photomicrograph 8a

Sample No. 147-895B-001R-01W (65-72)

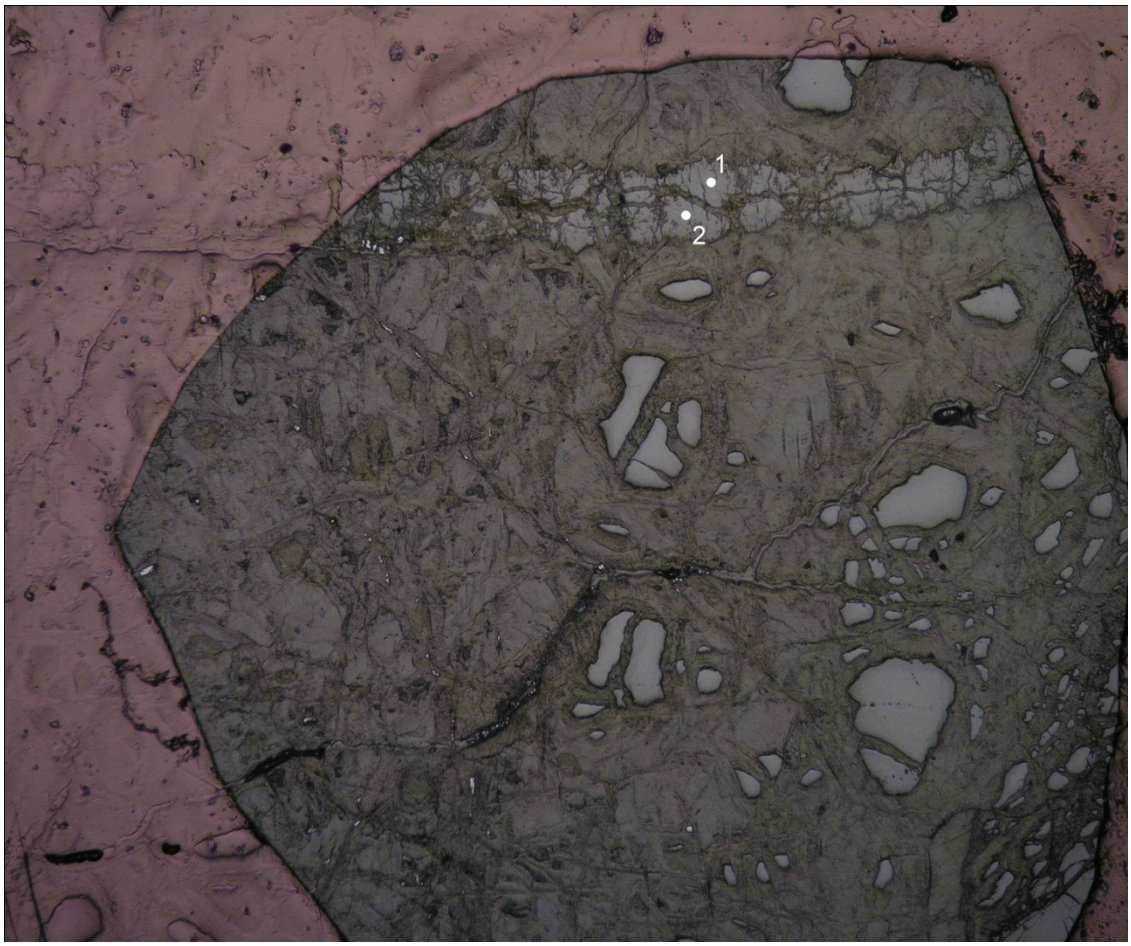

Photomicrograph 9a

Sample No. 147-895C-001R-01W (103-107)

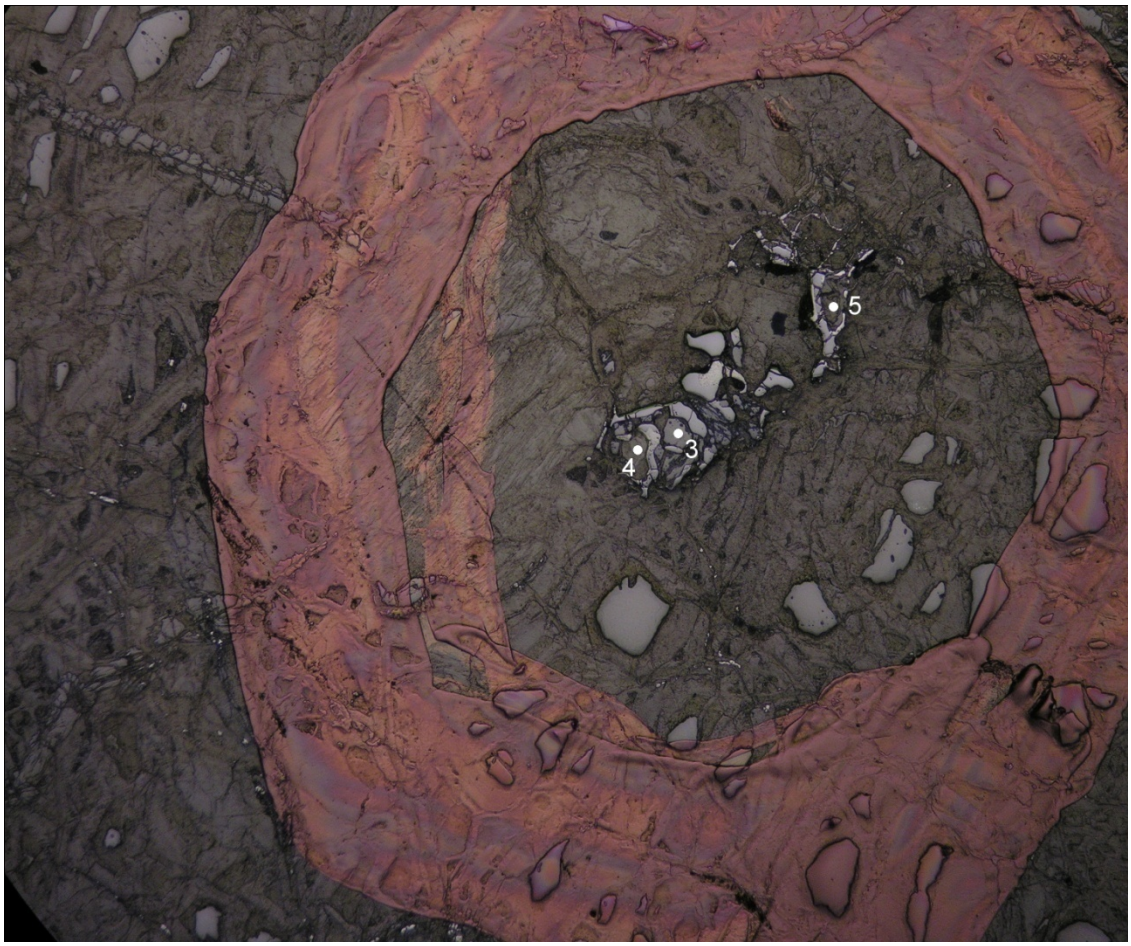

Photomicrograph 11a

Sample No. 147-895C-001R-01W (103-107)

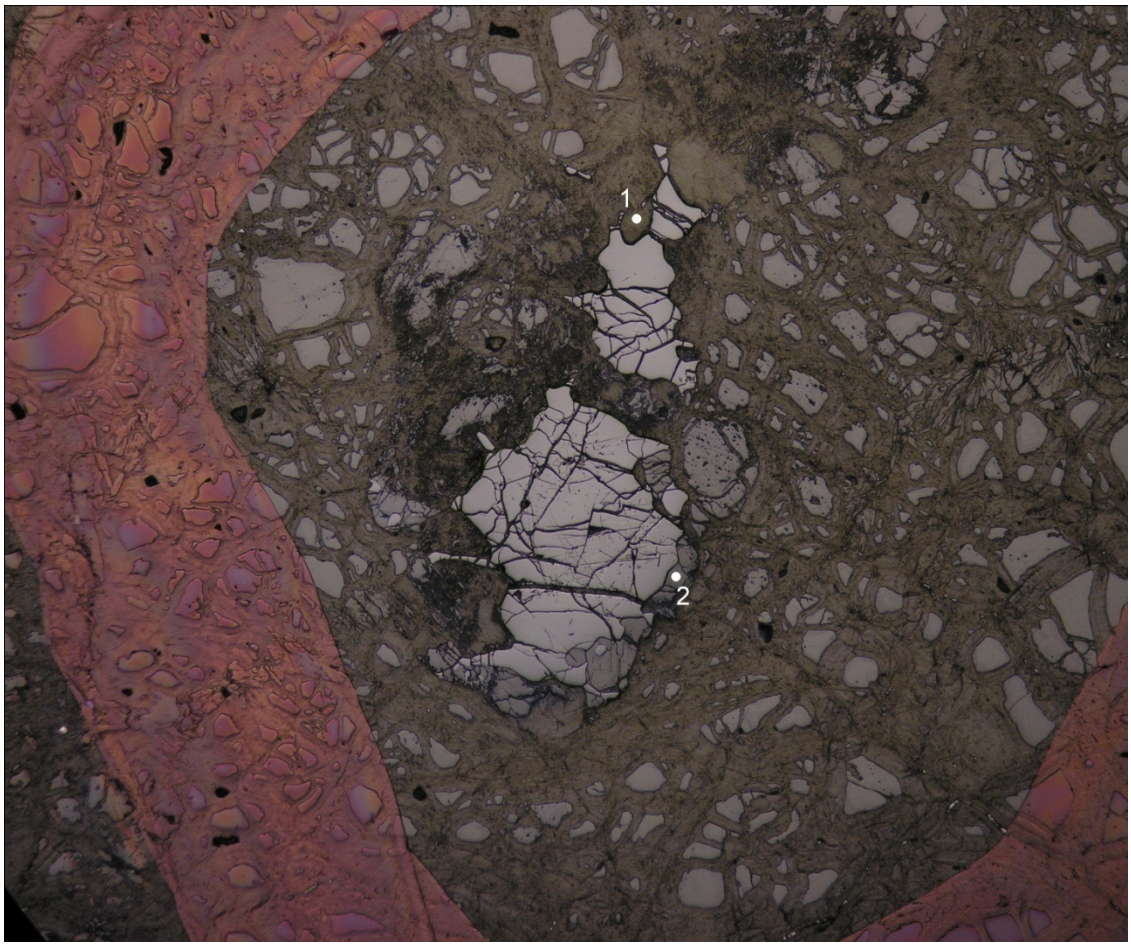

Photomicrograph 12a

Sample No. 147-895C-003R-01W (135-143)

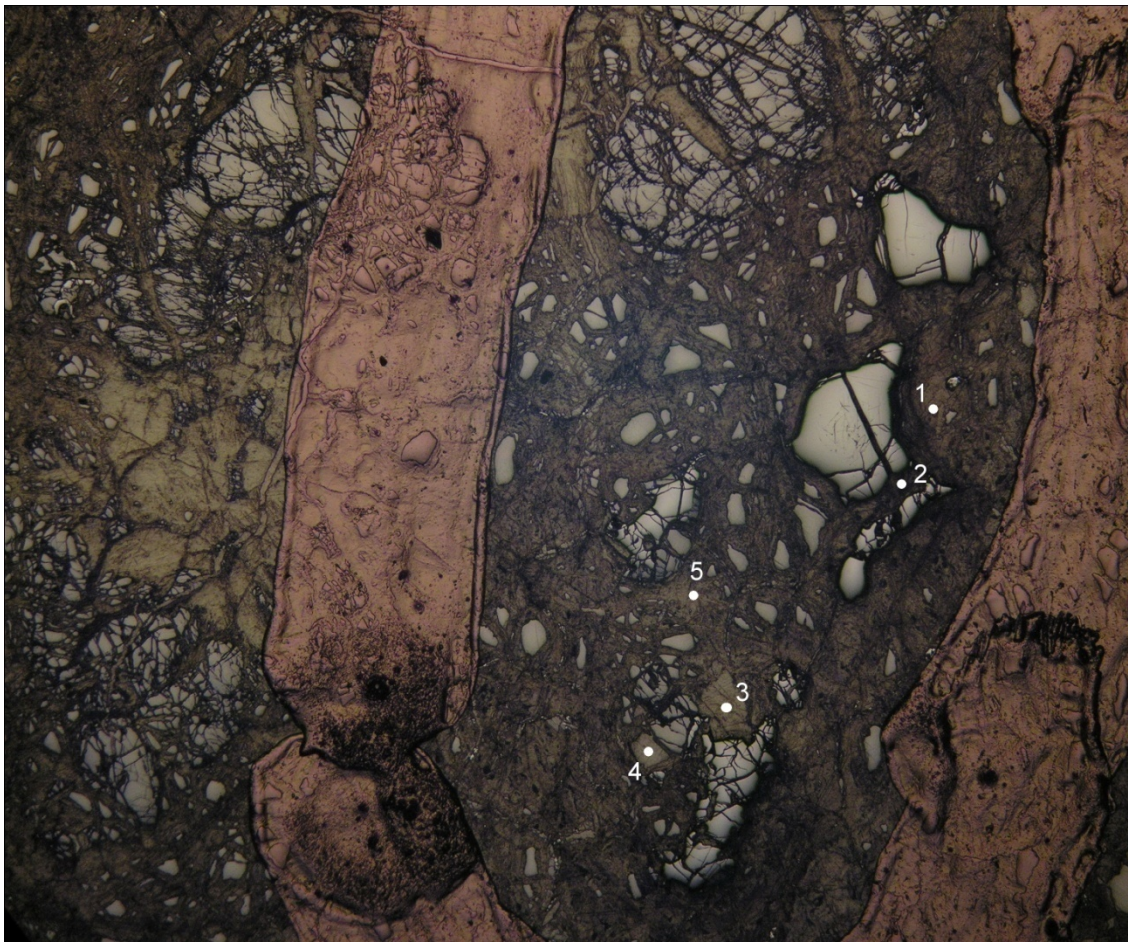

Photomicrograph 13a

Sample No. 147-895D-002R-02W (33-38)

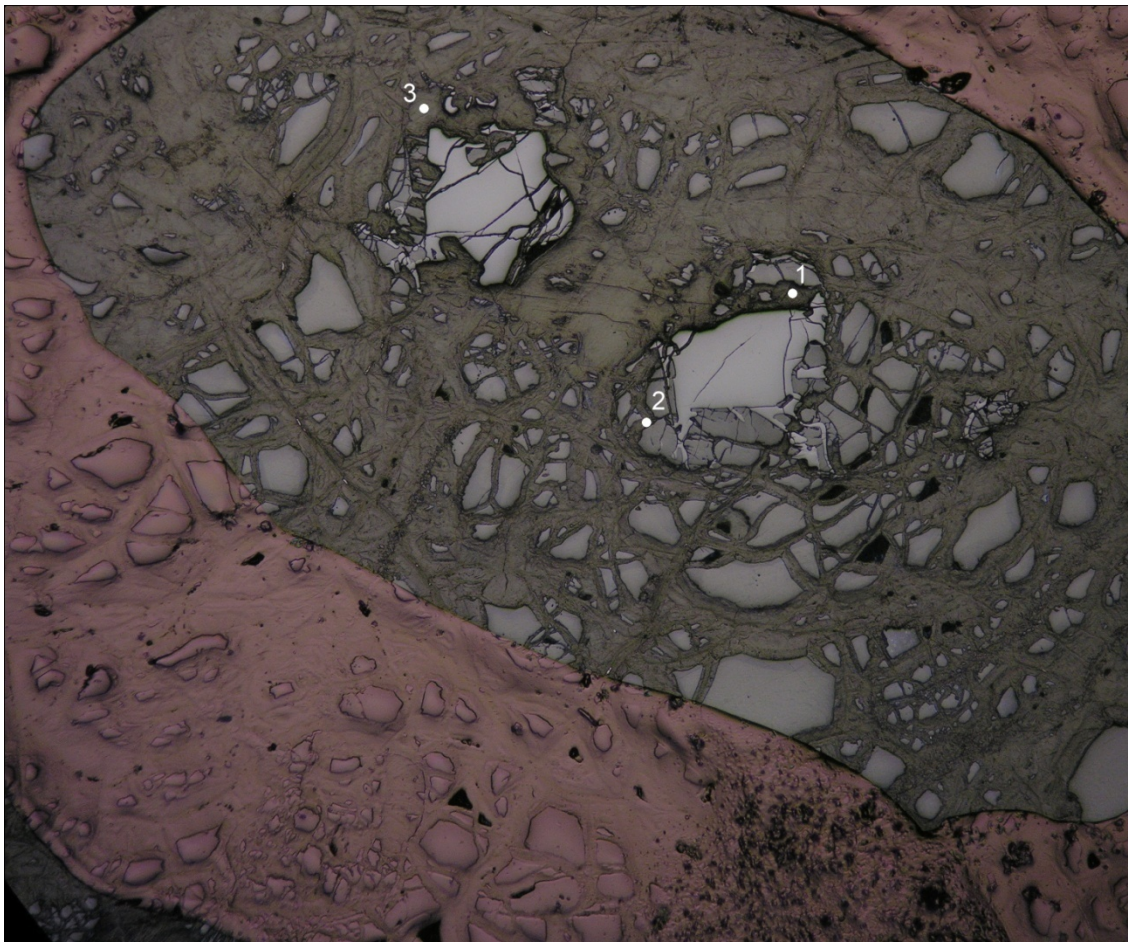

Photomicrograph 14a

Sample No. 147-895D-003R-01W (34-39)

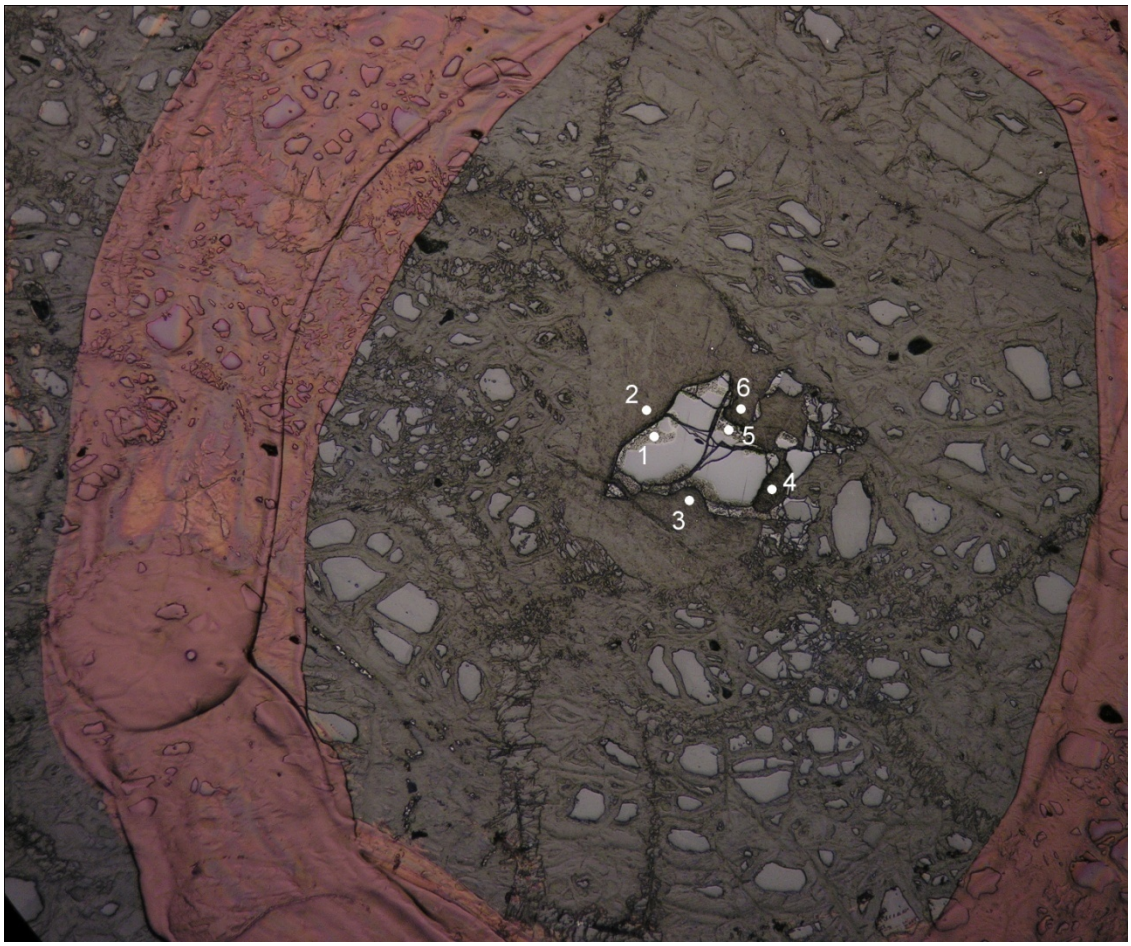

Photomicrograph 15a

Sample No. 147-895D-003R-01W (61-70)

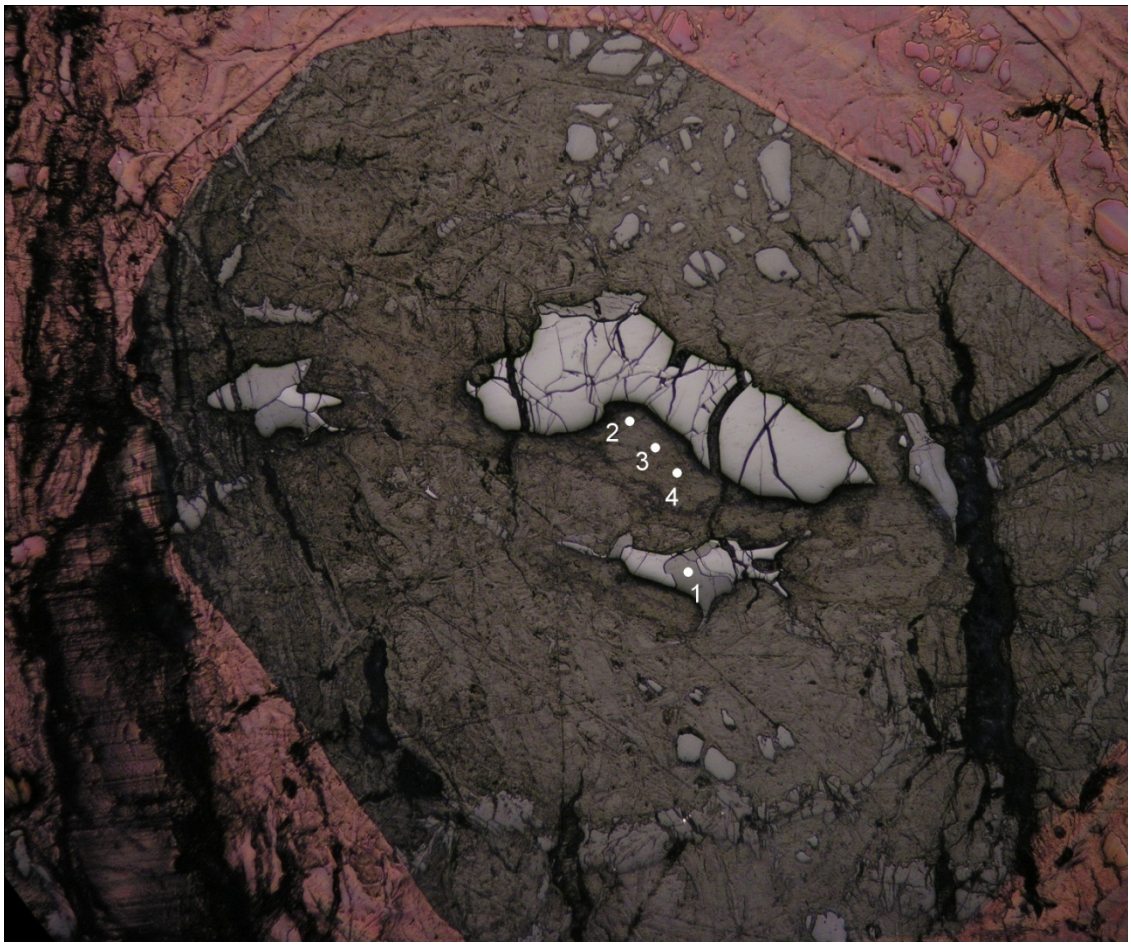

Photomicrograph 16a

Sample No. 147-895D-004R-01W (54-60)

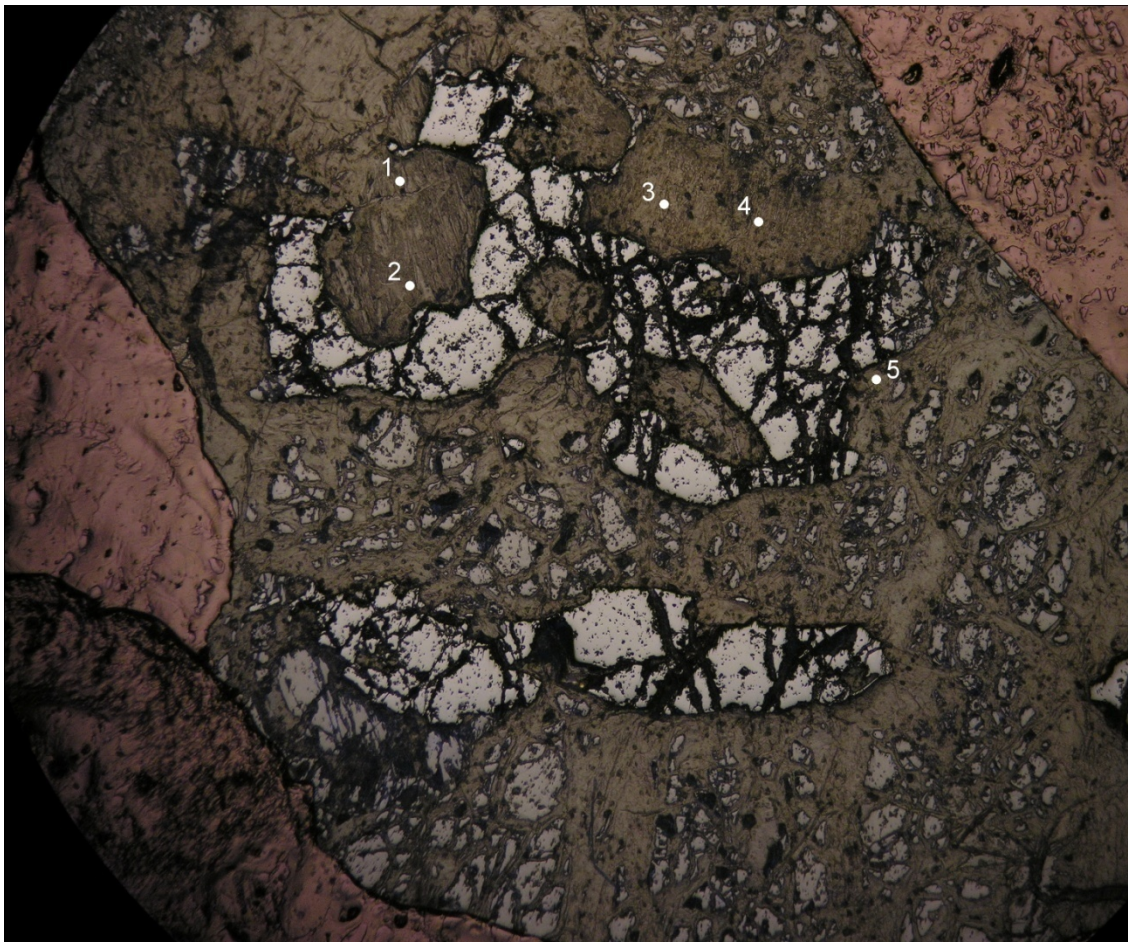

Photomicrograph 17a

Sample No. 147-895D-004R-03W (52-58)

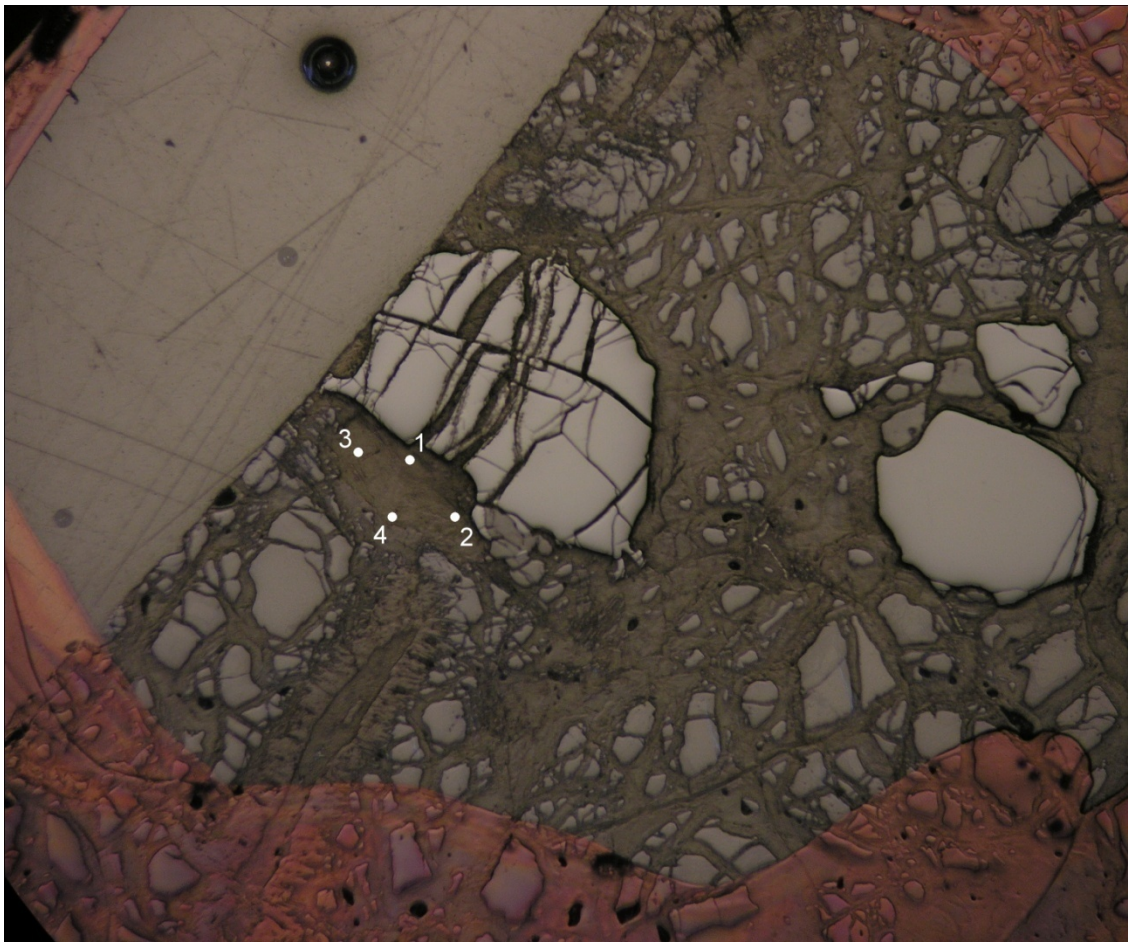

Photomicrograph 18a

Sample No. 147-895D-004R-03W (112-116)

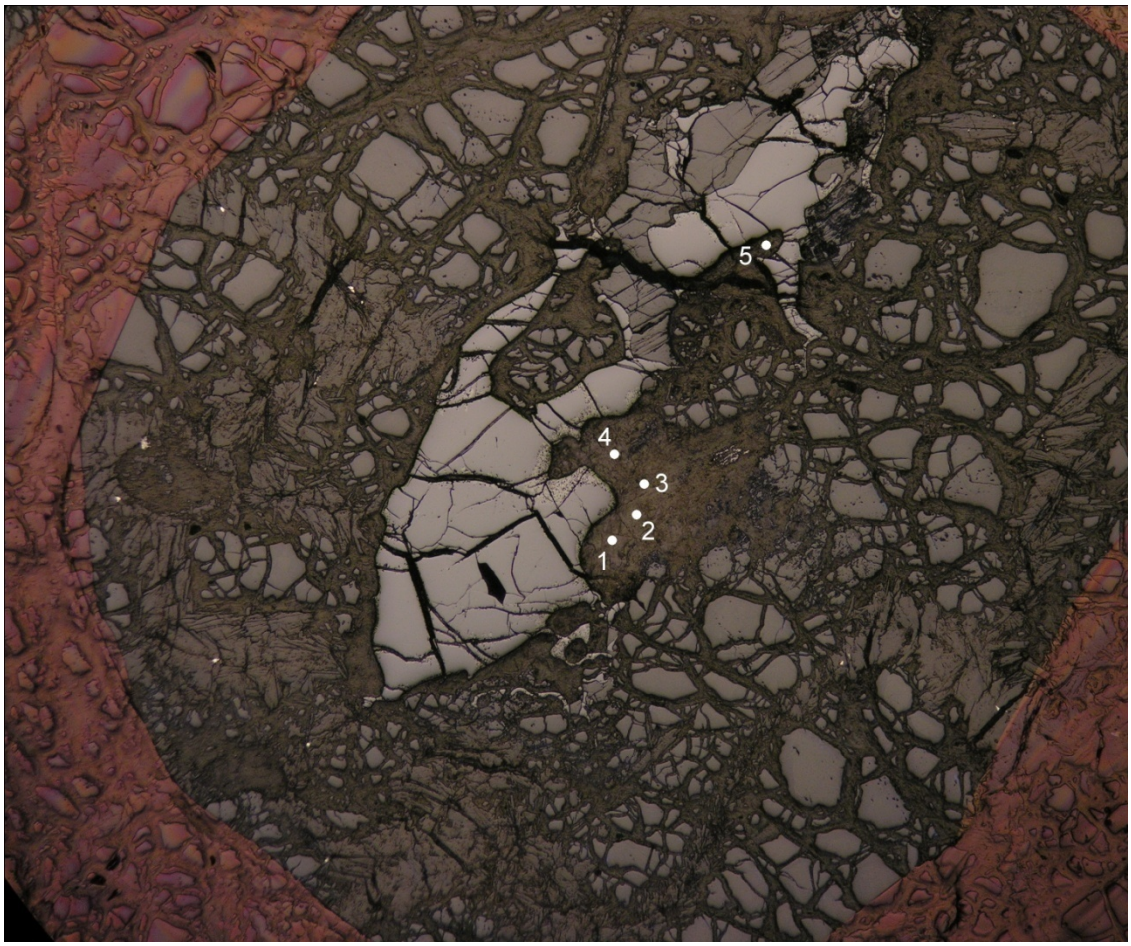

Photomicrograph 19a

Sample No. 147-895D-004R-05W (11-18)

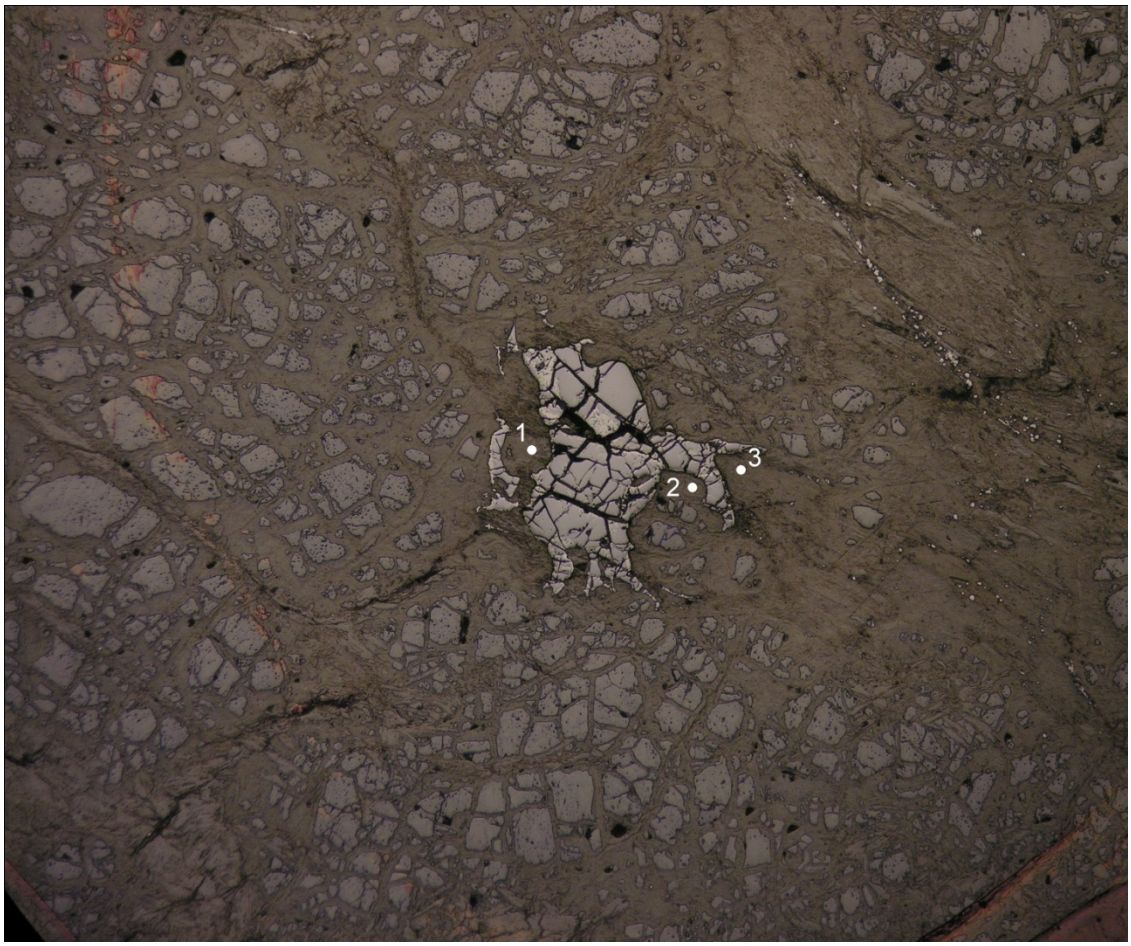

Photomicrograph 20a

Sample No. 147-895D-005R-01W (48-54)

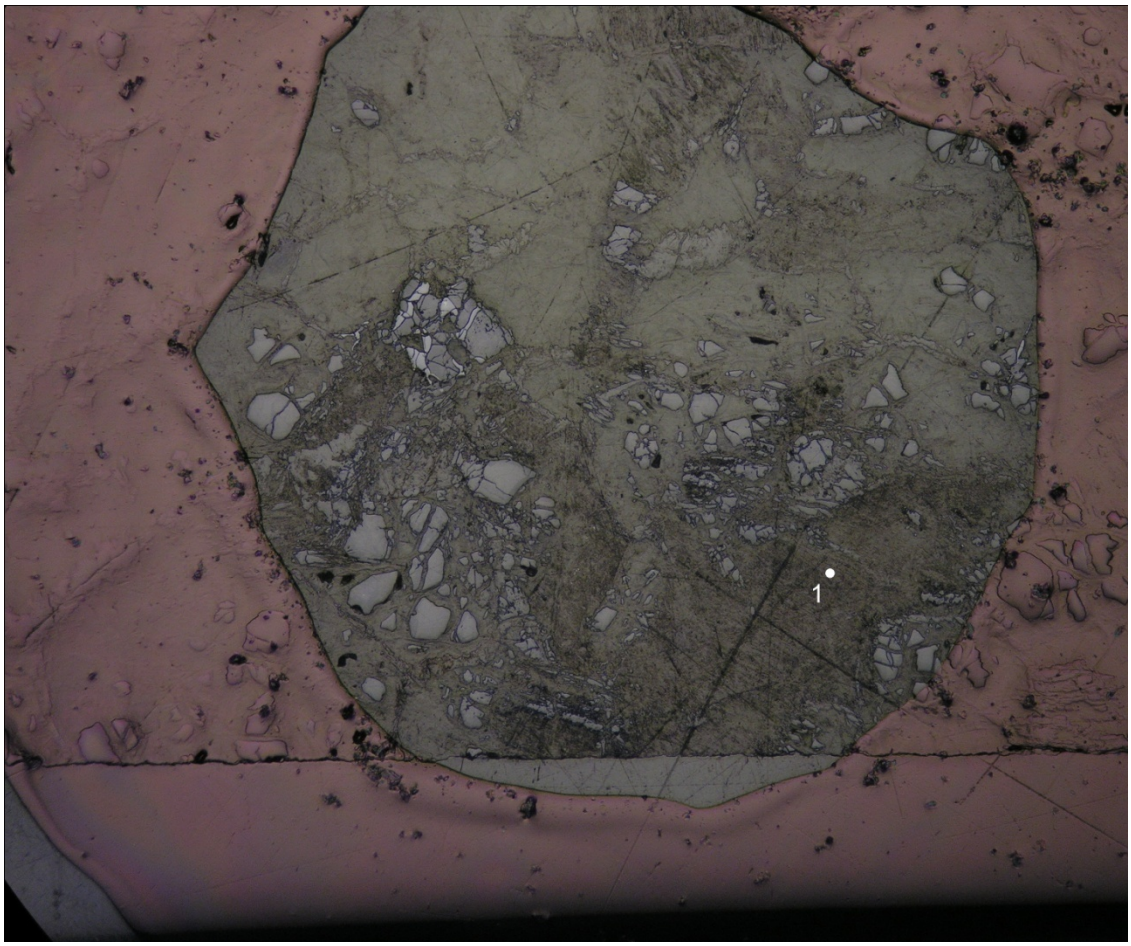

Photomicrograph 21a

Sample No. 147-895D-005R-02W (103-112)

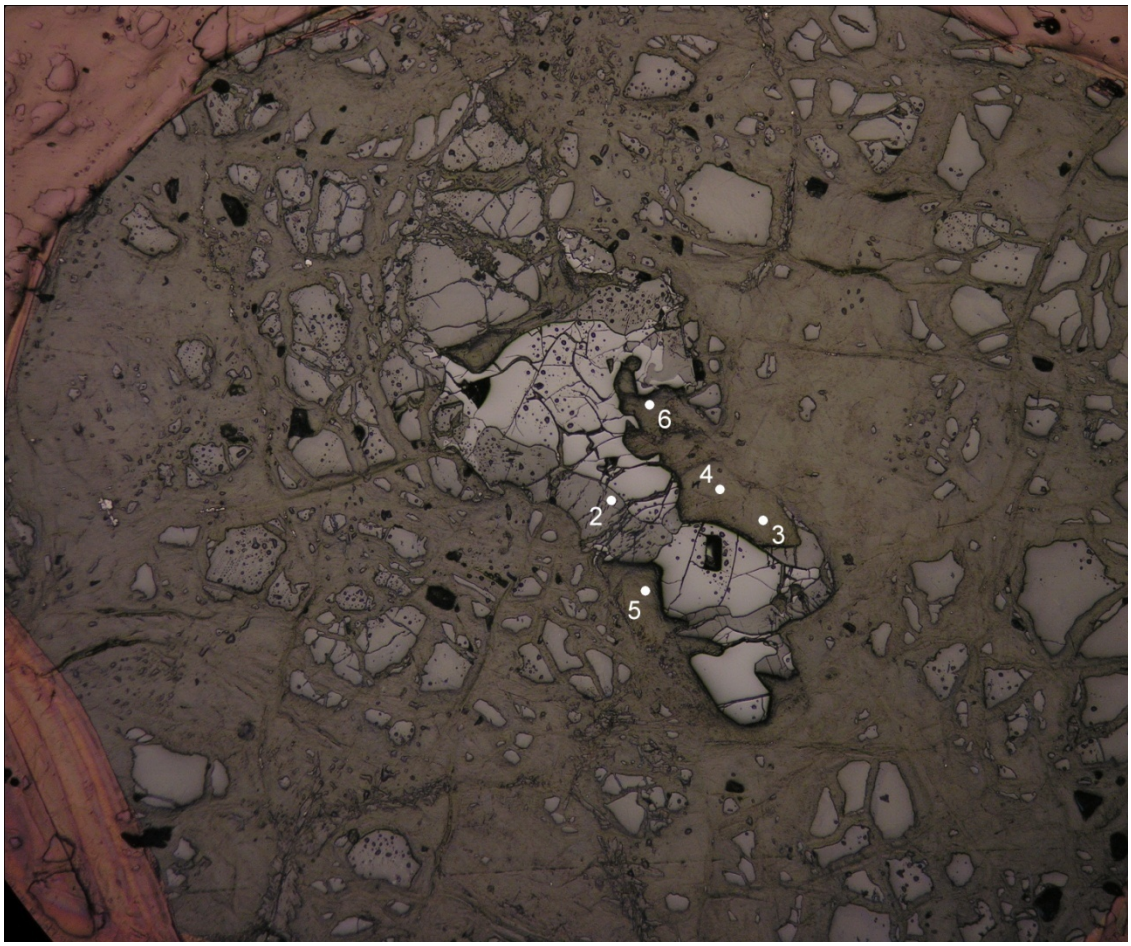

Photomicrograph 22a

Sample No. 147-895D-005R-02W (103-112)

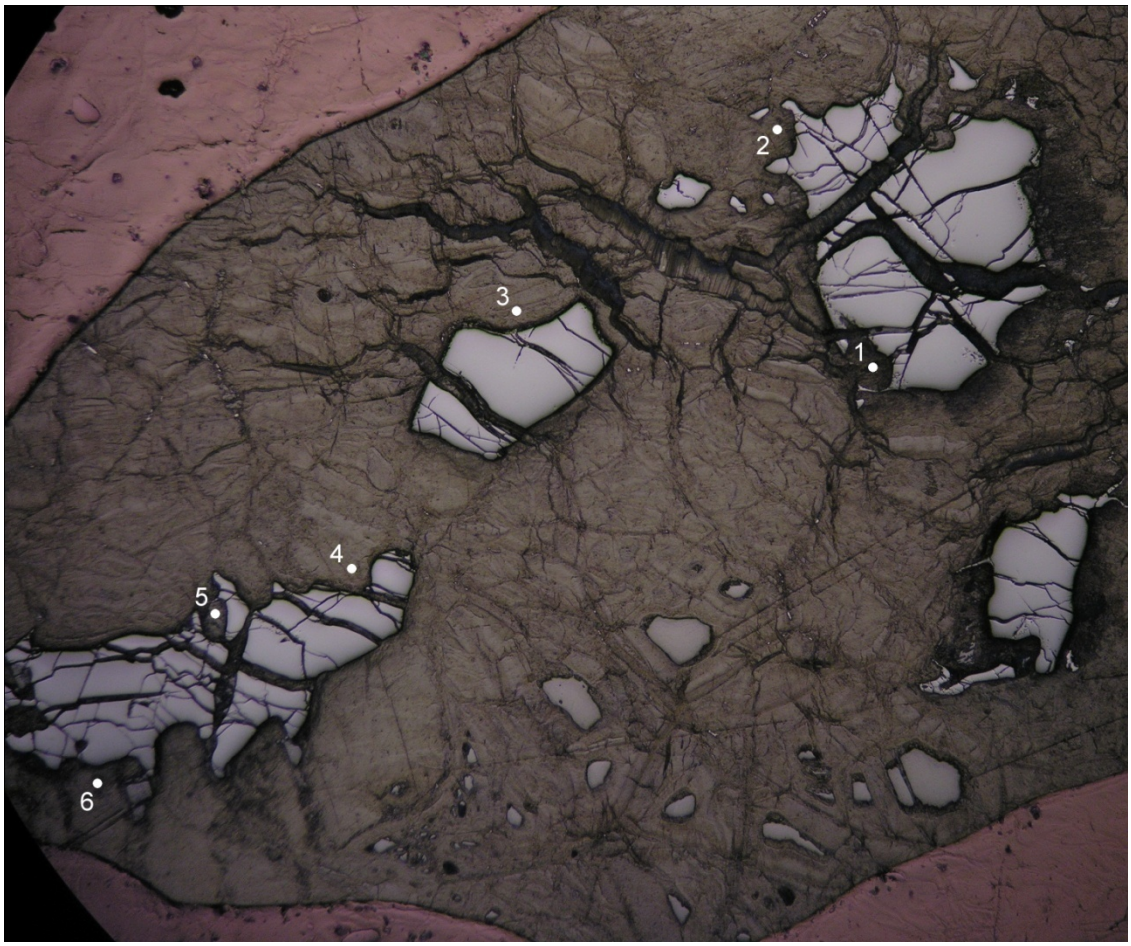

Photomicrograph 23a

Sample No. 147-895D-007R-02W (127-135)

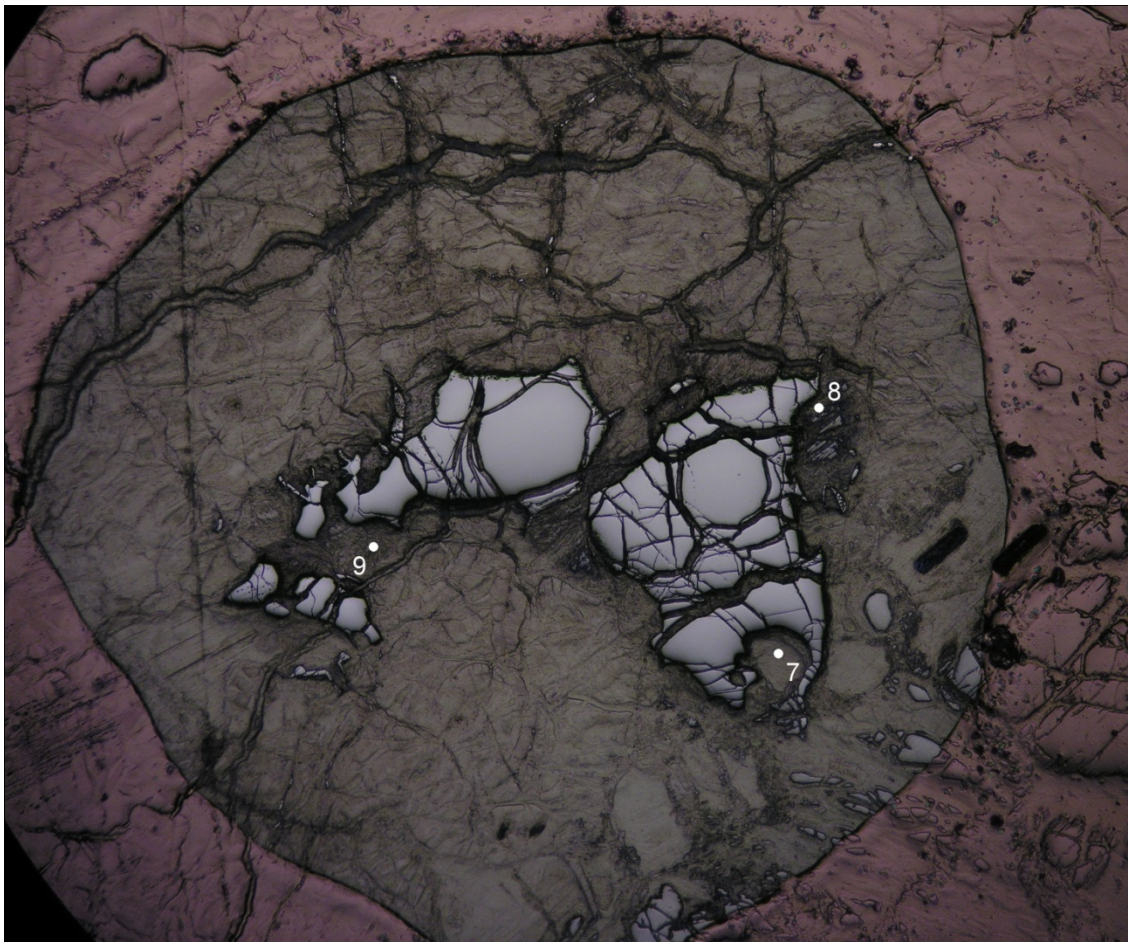

Photomicrograph 24a

Sample No. 147-895D-007R-02W (127-135)

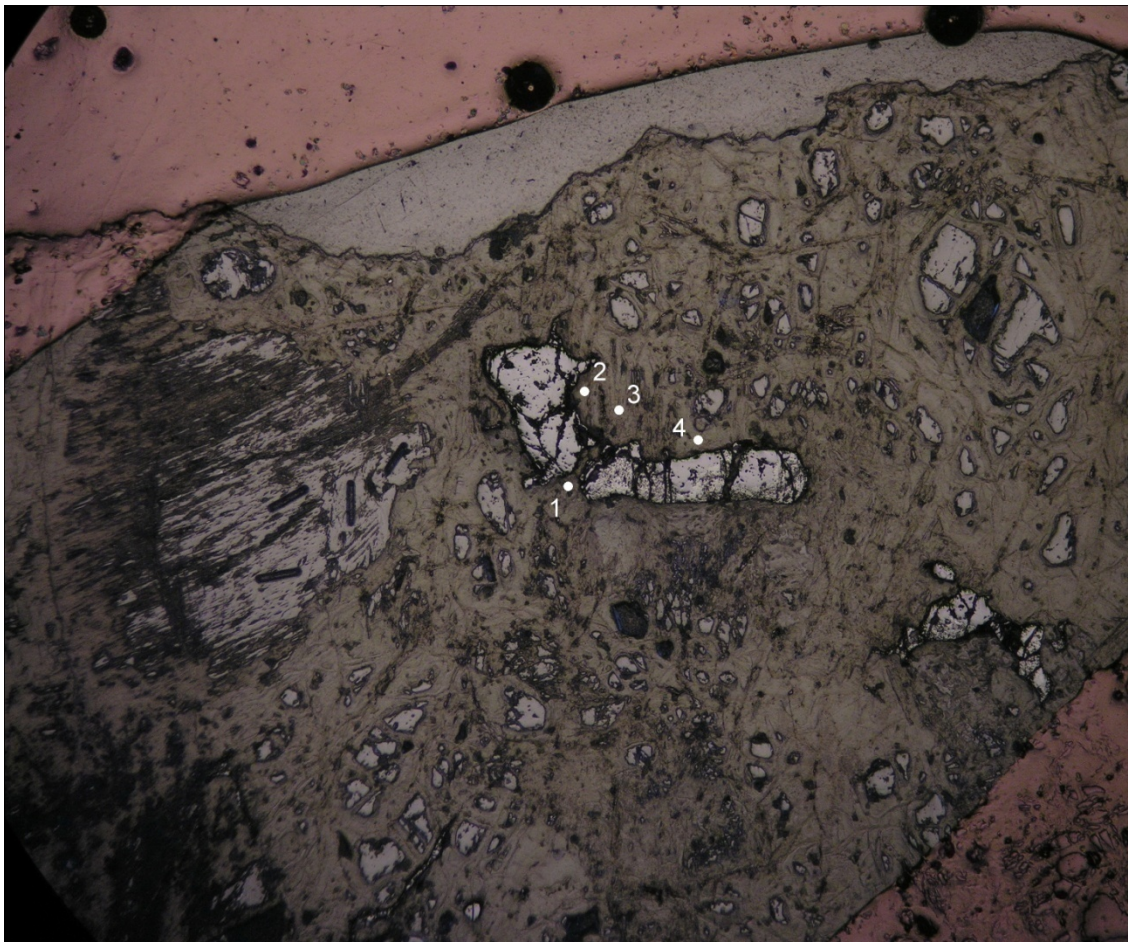

Photomicrograph 25a

Sample No. 147-895E-007R-04W (37-41)

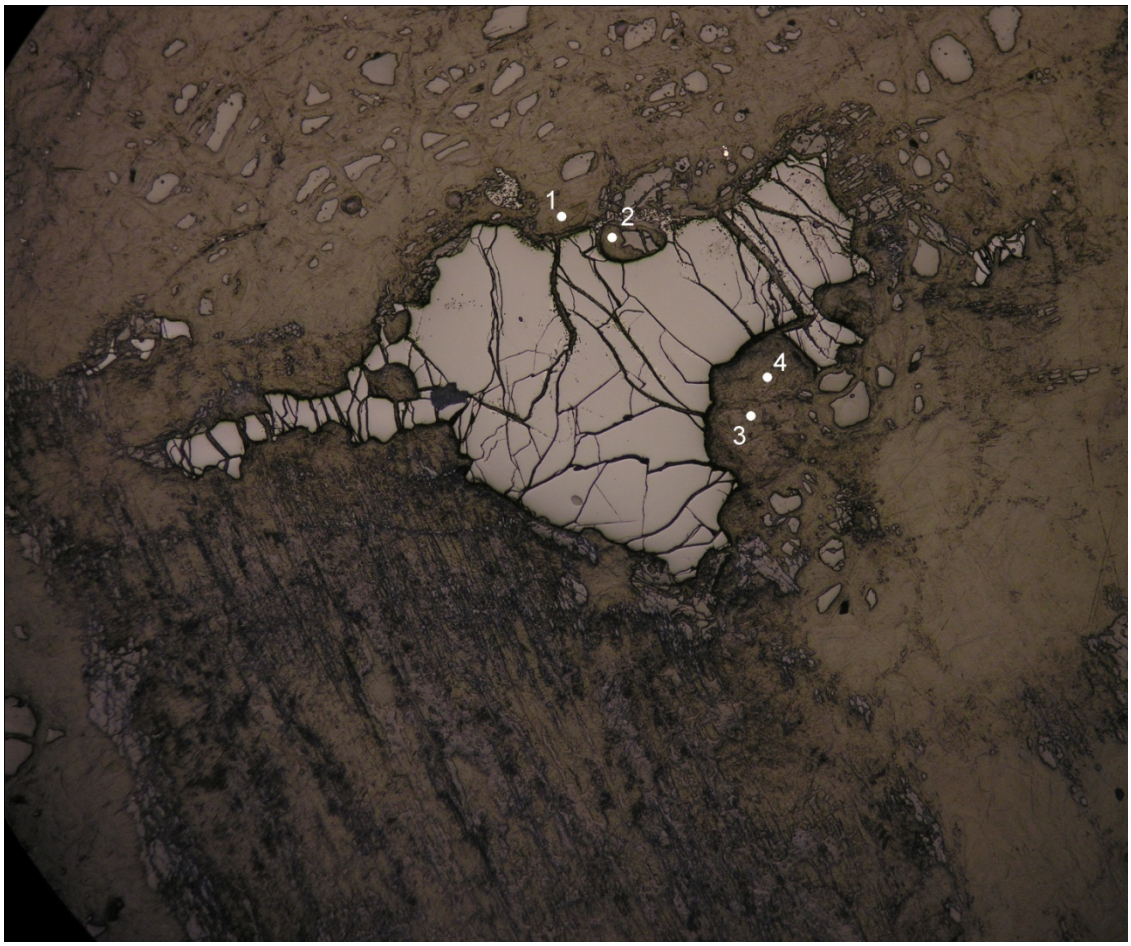

Photomicrograph 26a

Sample No. 147-895E-007R-04W (86-94)

Appendix B

Content description

This appendix contains photomicrographs of select pyroxenes and alteration phases showing the locations of *in situ* electron microprobe (shown as dots or crosses) and LA-ICP-MS (shown as lines) analyses for ocean island xenoliths discussed in Chapter 4. The symbols are colour-coded to match the analysis number. The number in the label for each photomicrograph is included with the analyses results for the respective mineral in Supplementary Table 4.1.

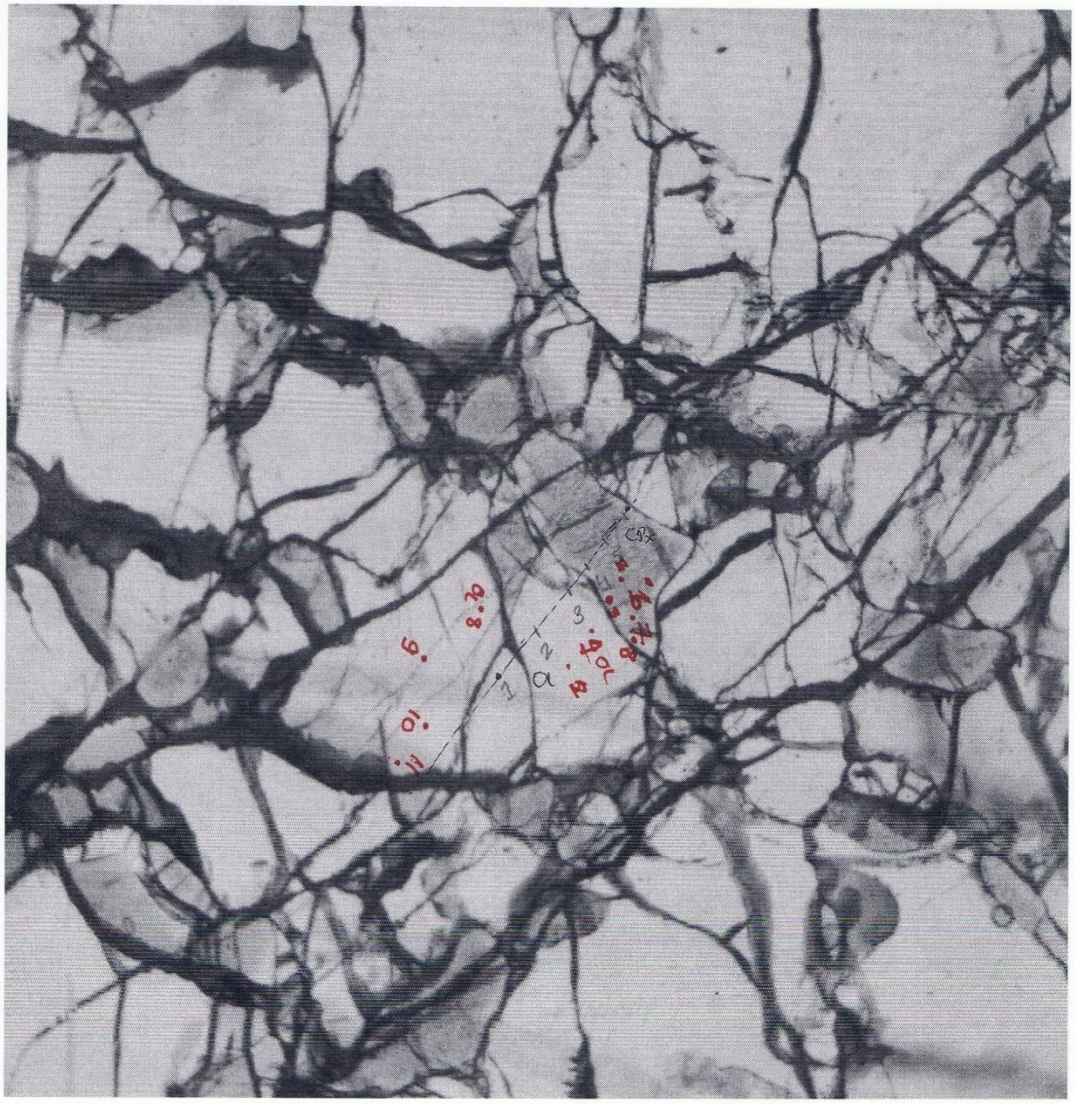

Photomicrograph 123
110035

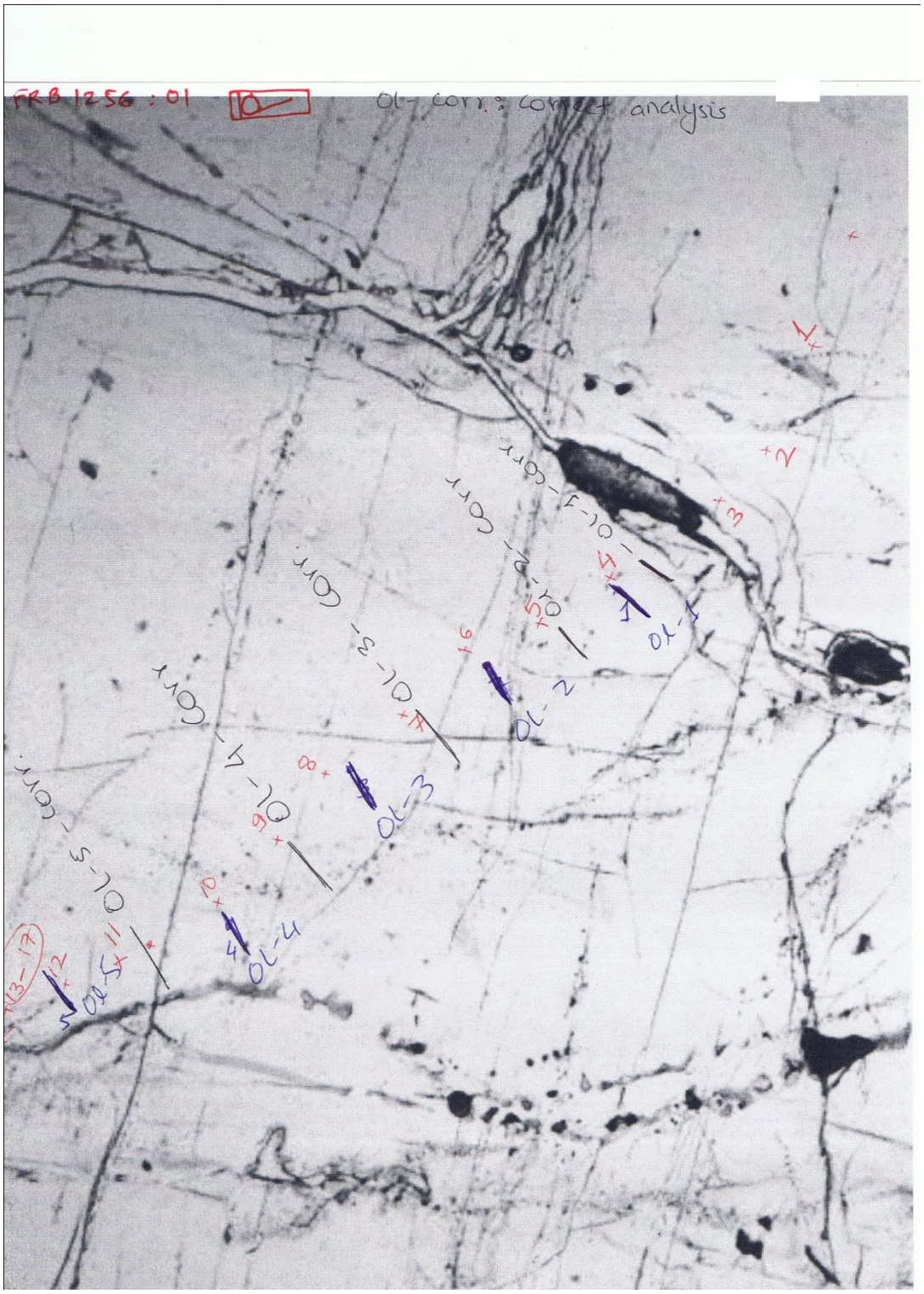

Photomicrograph 124
Sample No. FRB 1256

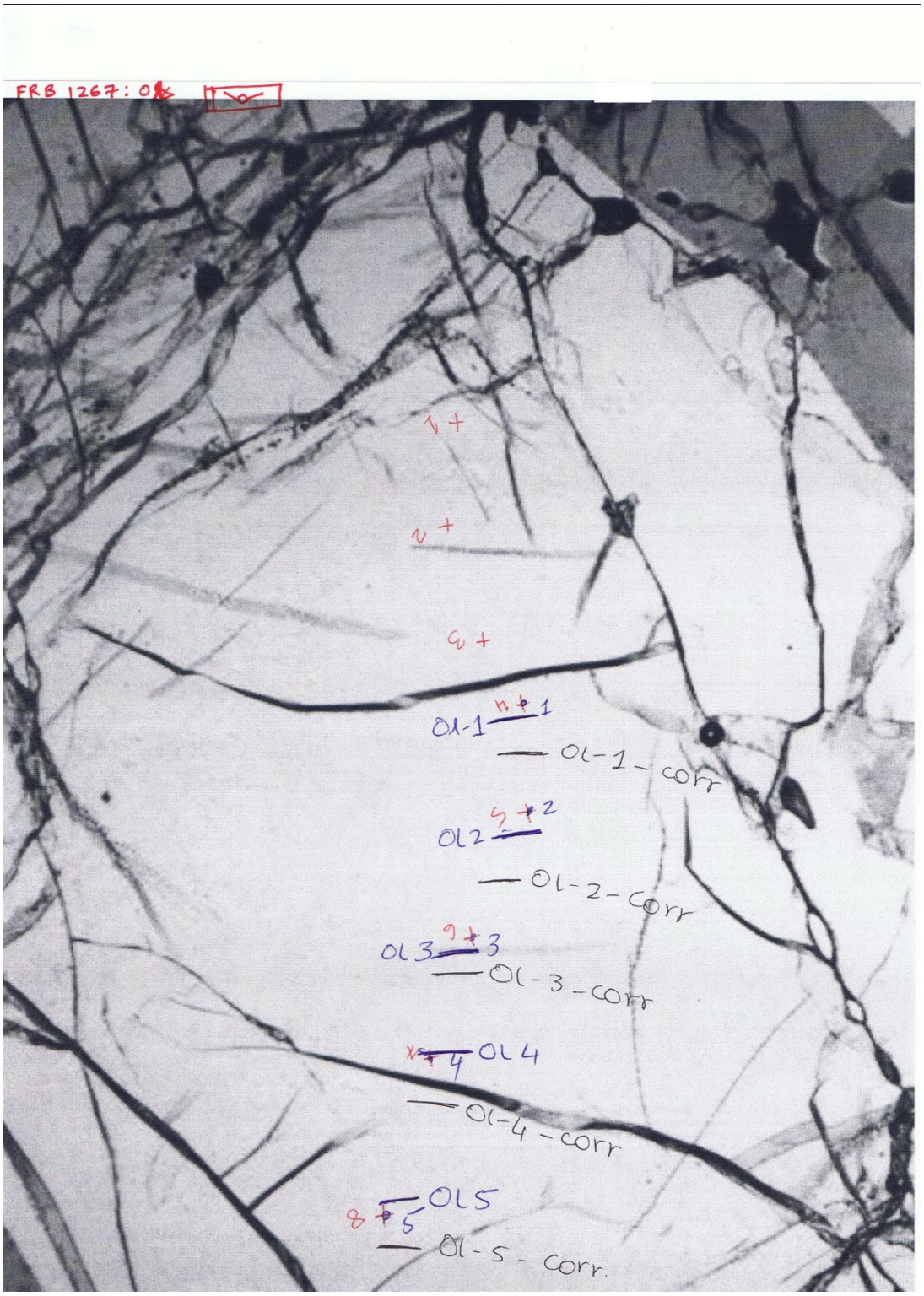

Photomicrograph 125
Sample No. FRB 1267

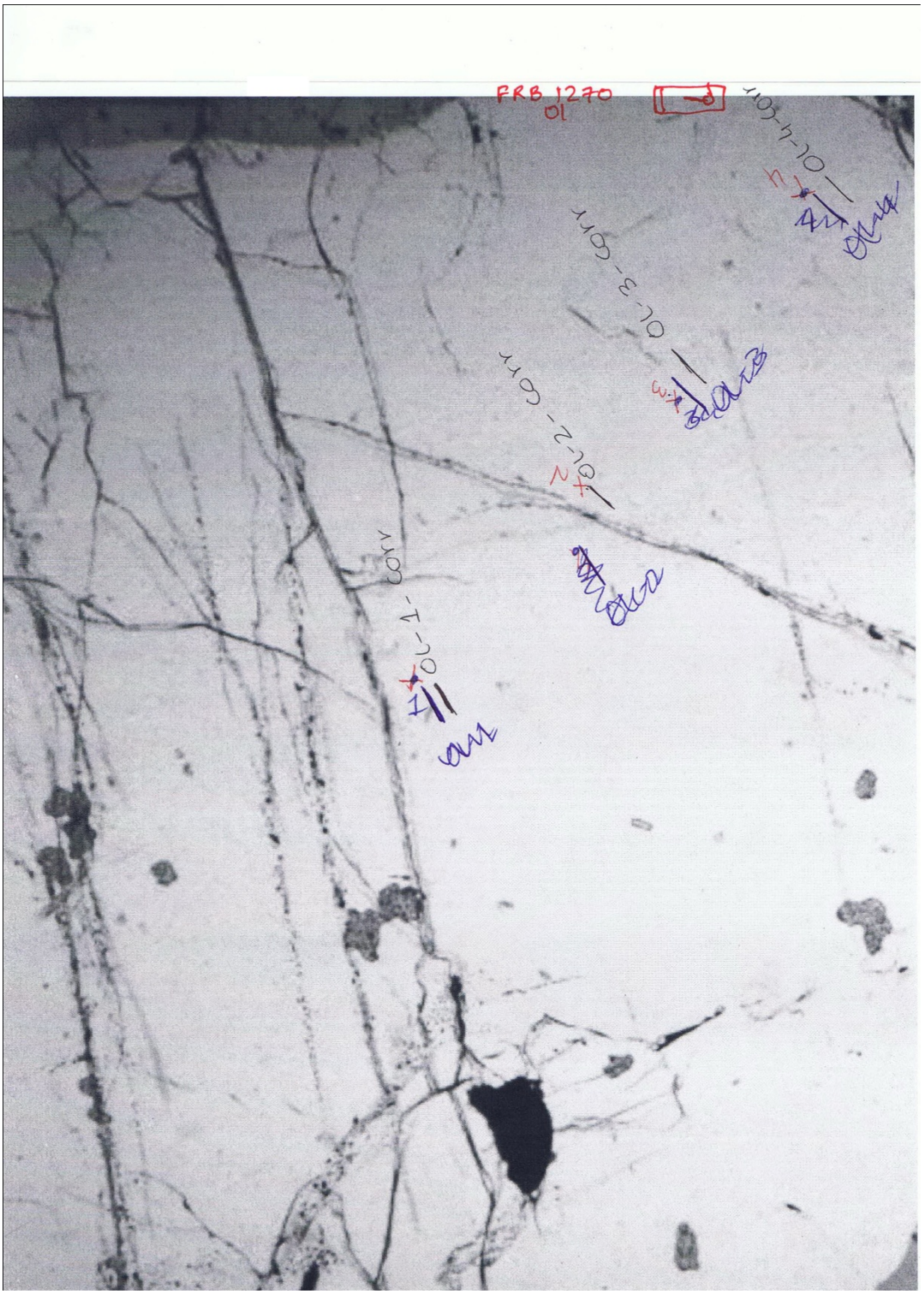

Photomicrograph 126
Sample No. FRB 1270

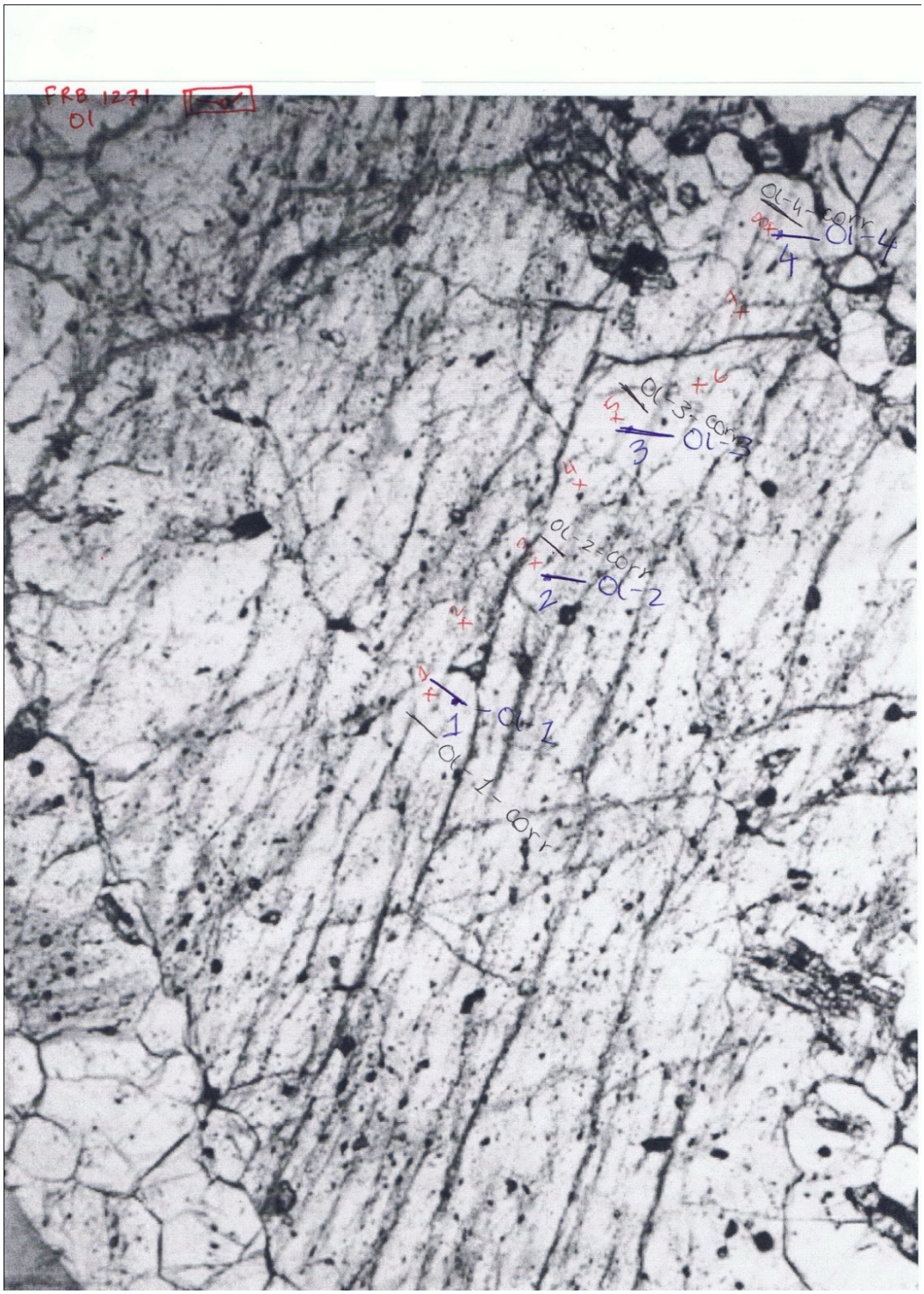

Photomicrograph 127
Sample No. FRB 1271

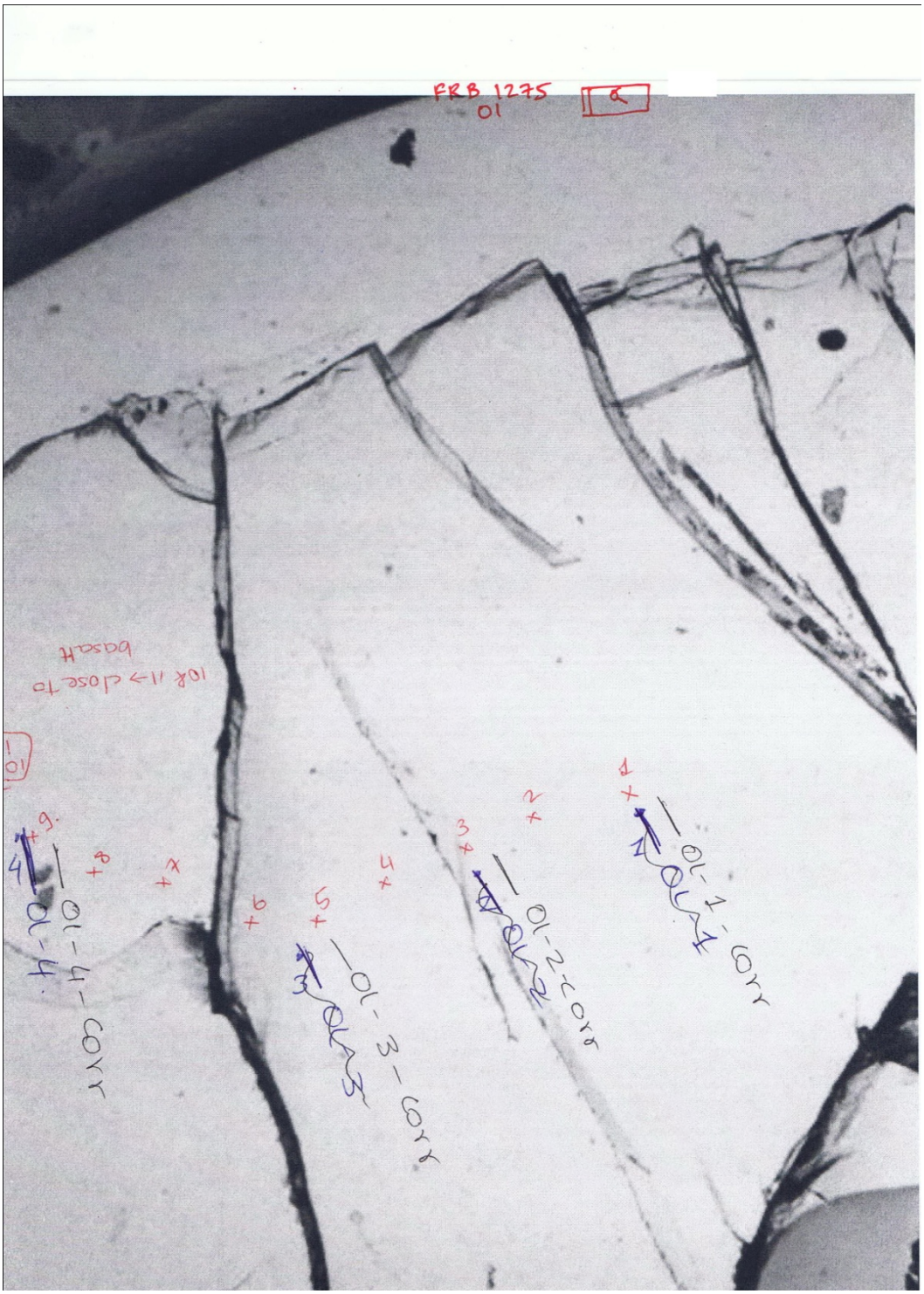

Photomicrograph 128
Sample No. FRB 1275

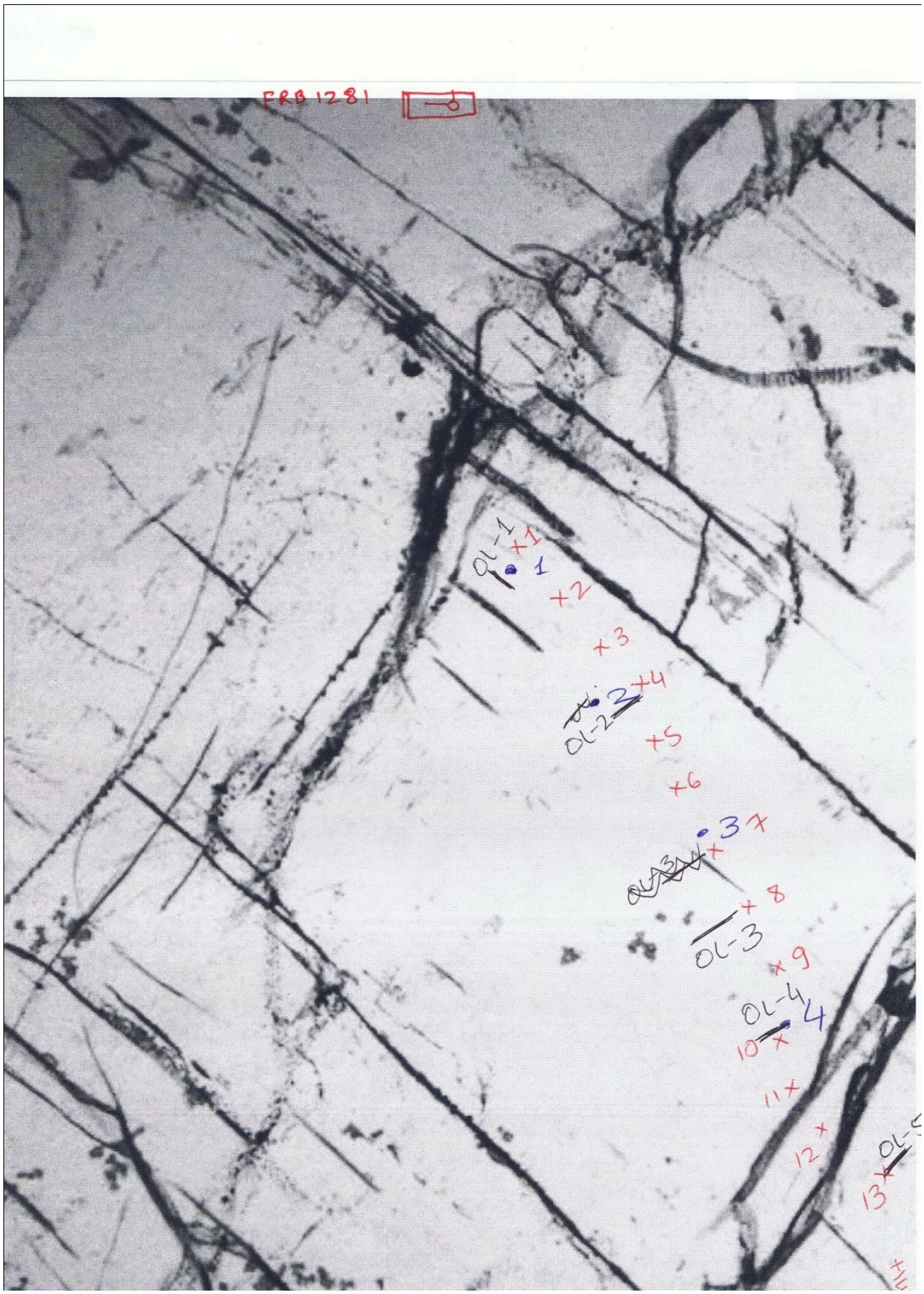

Photomicrograph 129
Sample No. FRB 1281

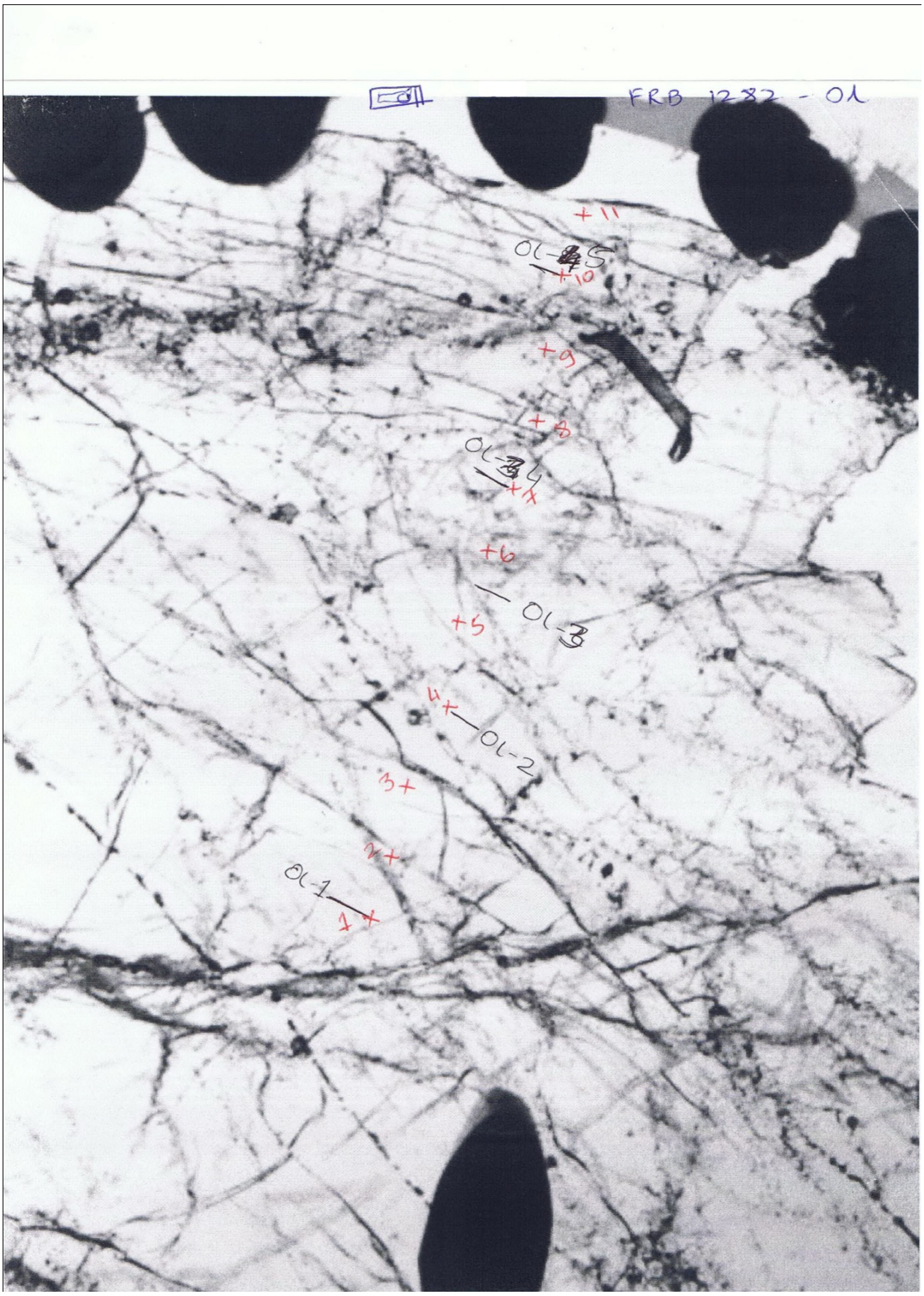

Photomicrograph 130
Sample No. FRB 1282

Photomicrograph 131
Sample No. FRB 1282

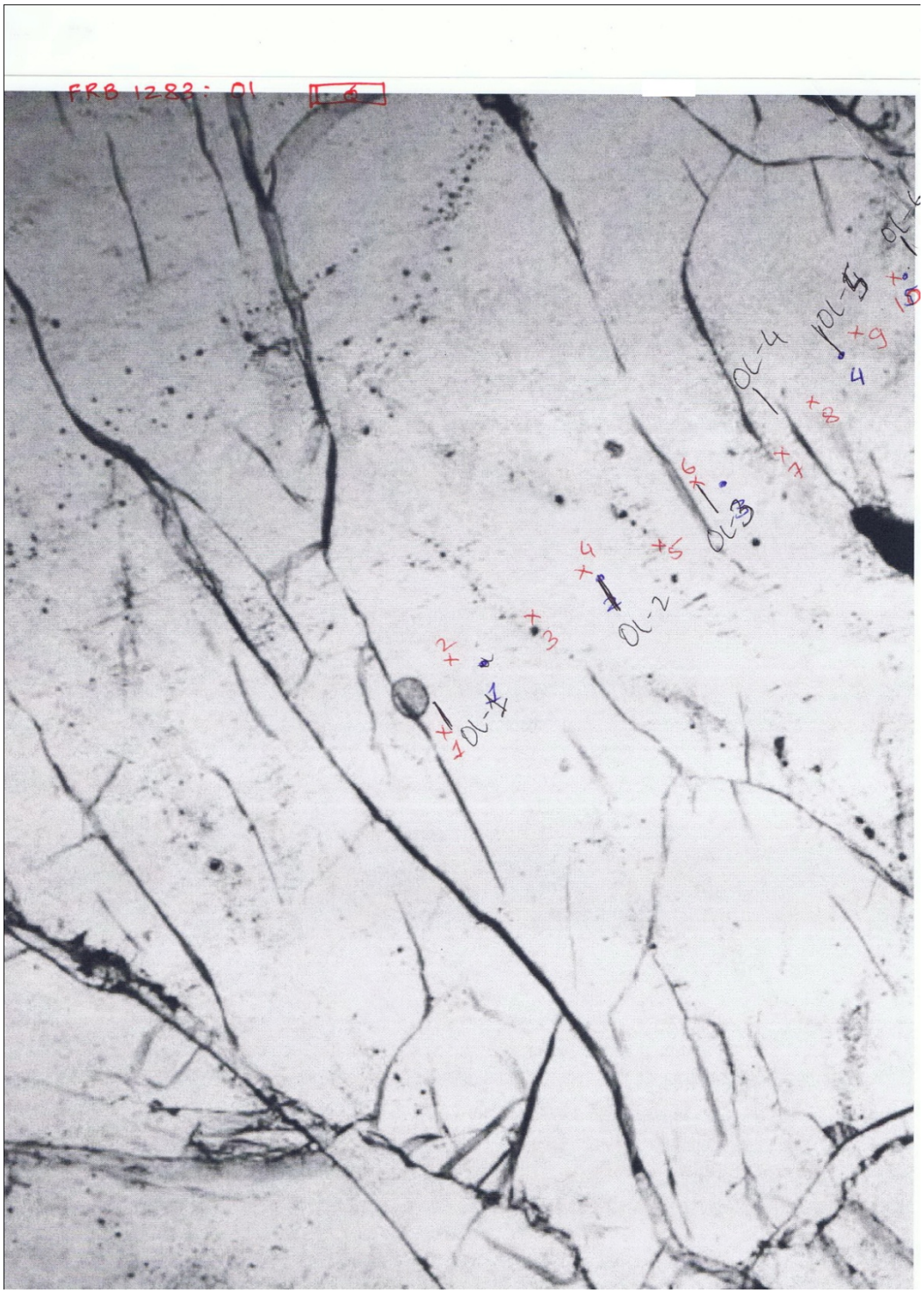

Photomicrograph 132
Sample No. FRB 1283

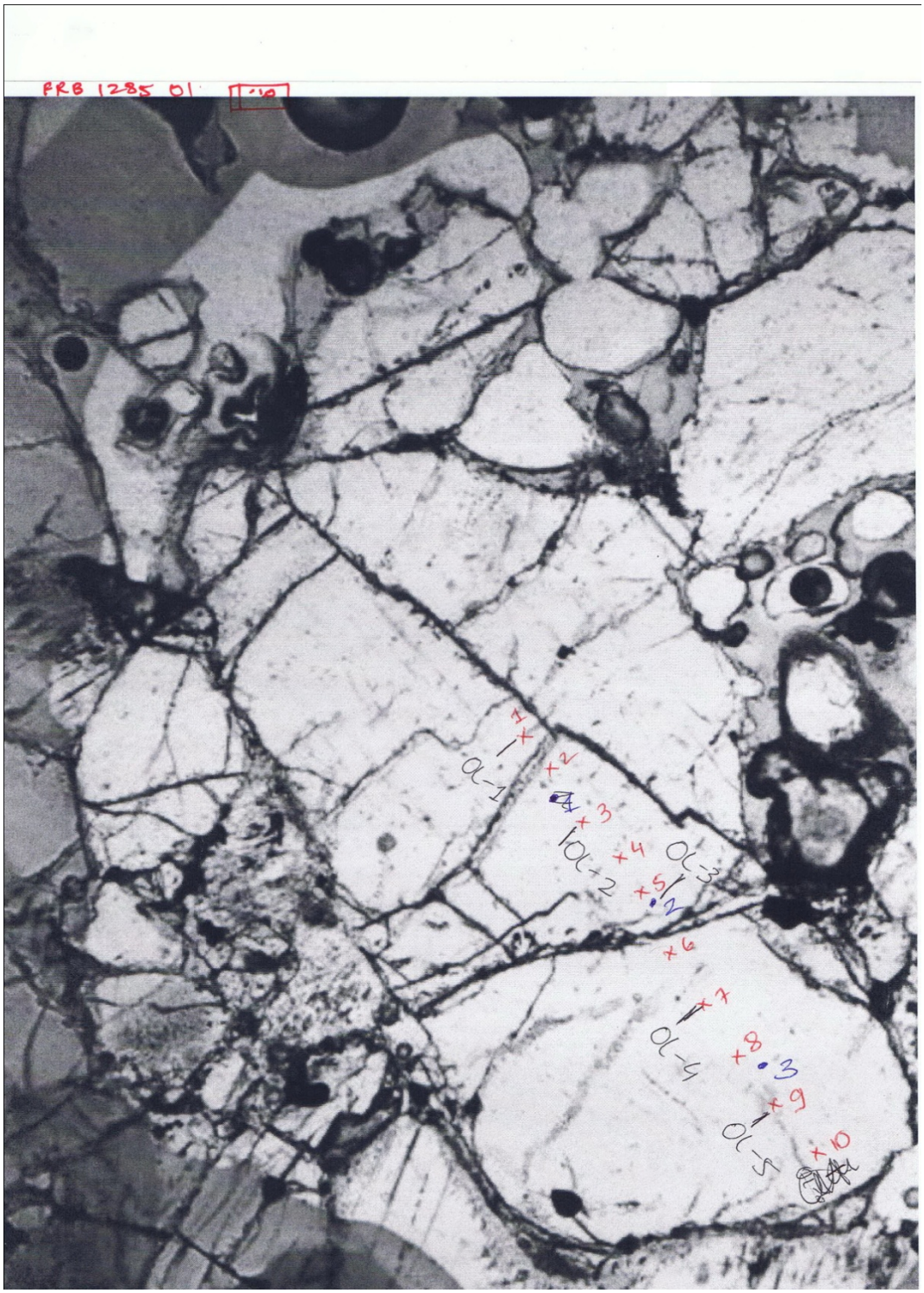

Photomicrograph 133
Sample No. FRB 1285

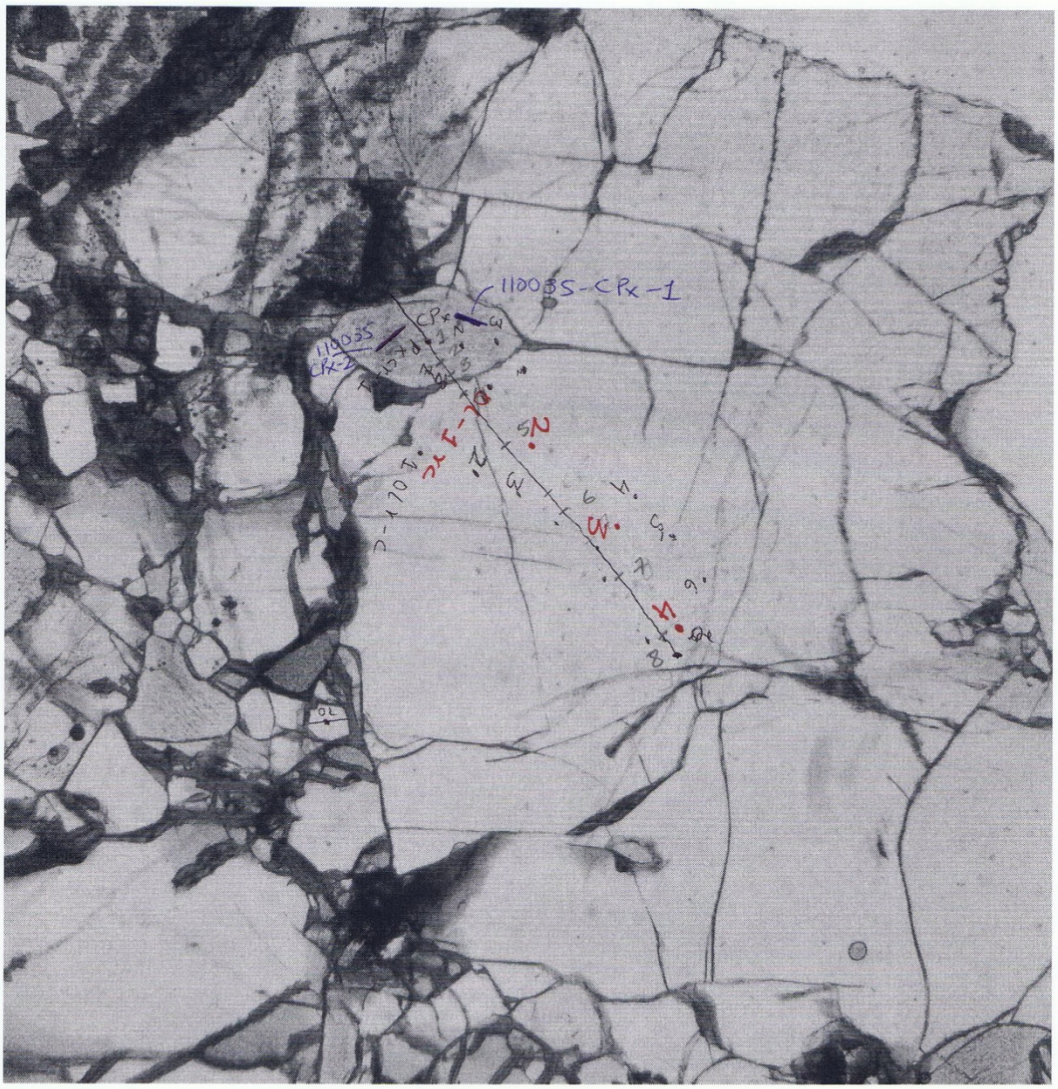

CPx - OL
C - C ~ 8 points.

Photomicrograph 134
Sample No. 110035

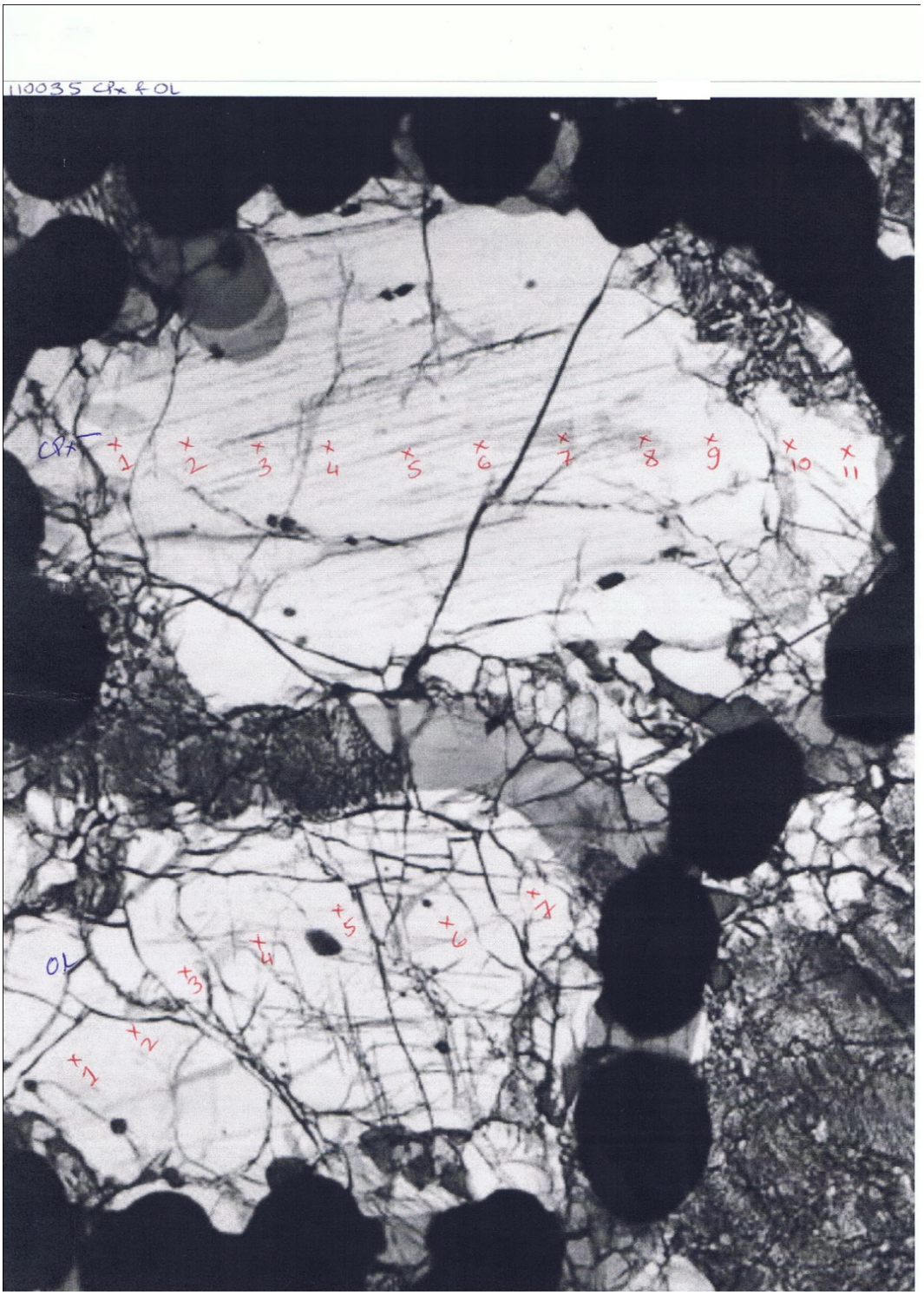

Photomicrograph 135
Sample No. 110035

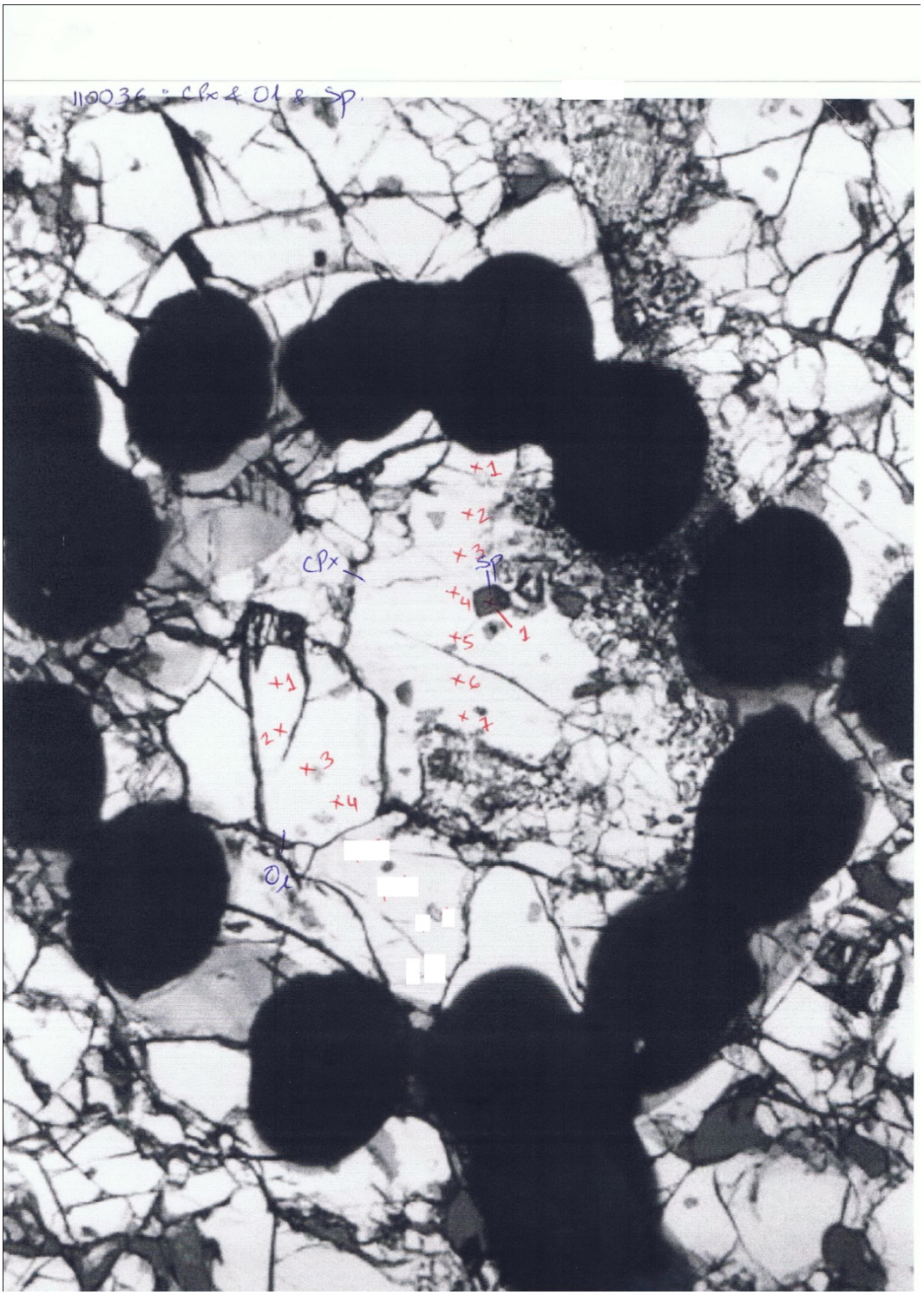

Photomicrograph 136
Sample No. 110036

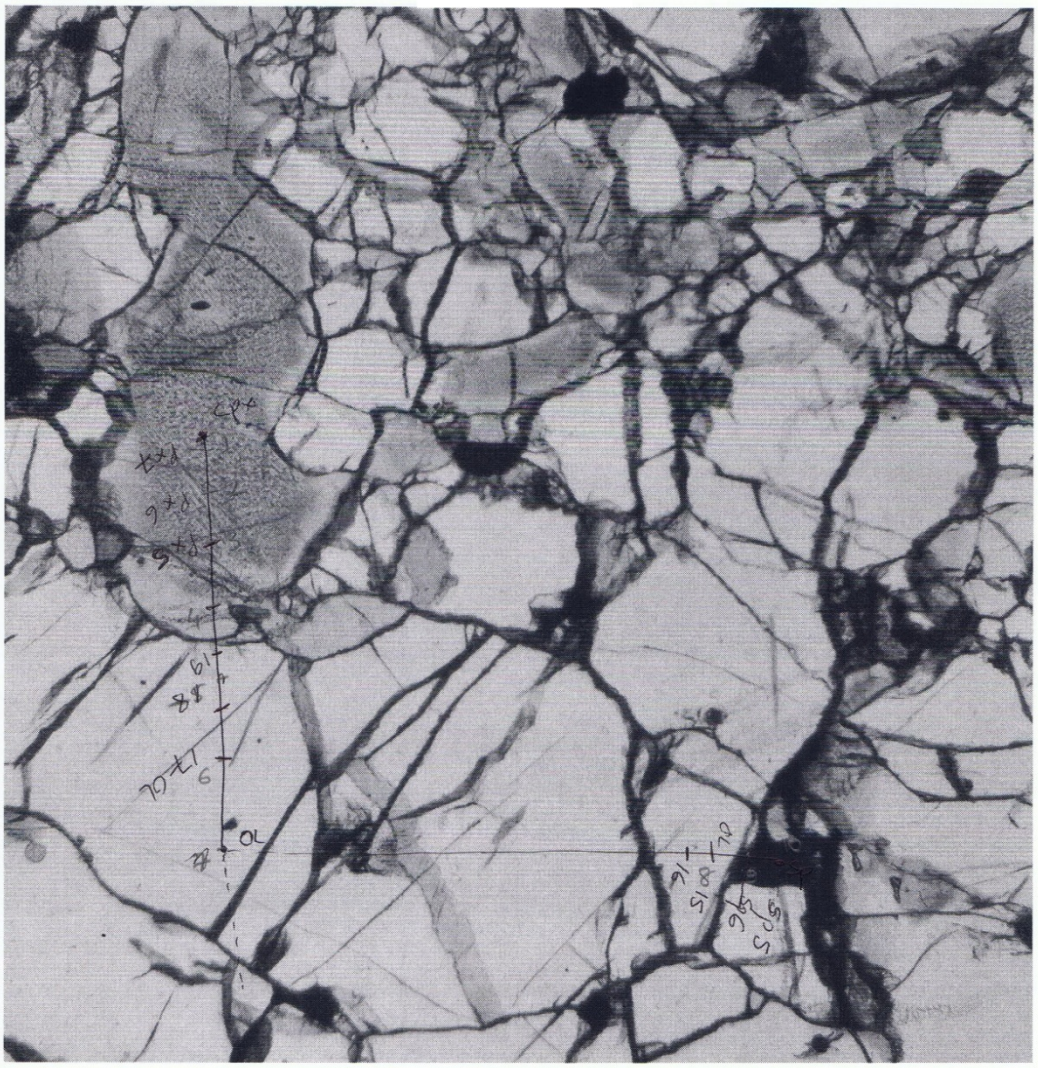

Photomicrograph 137
Sample No. 110037

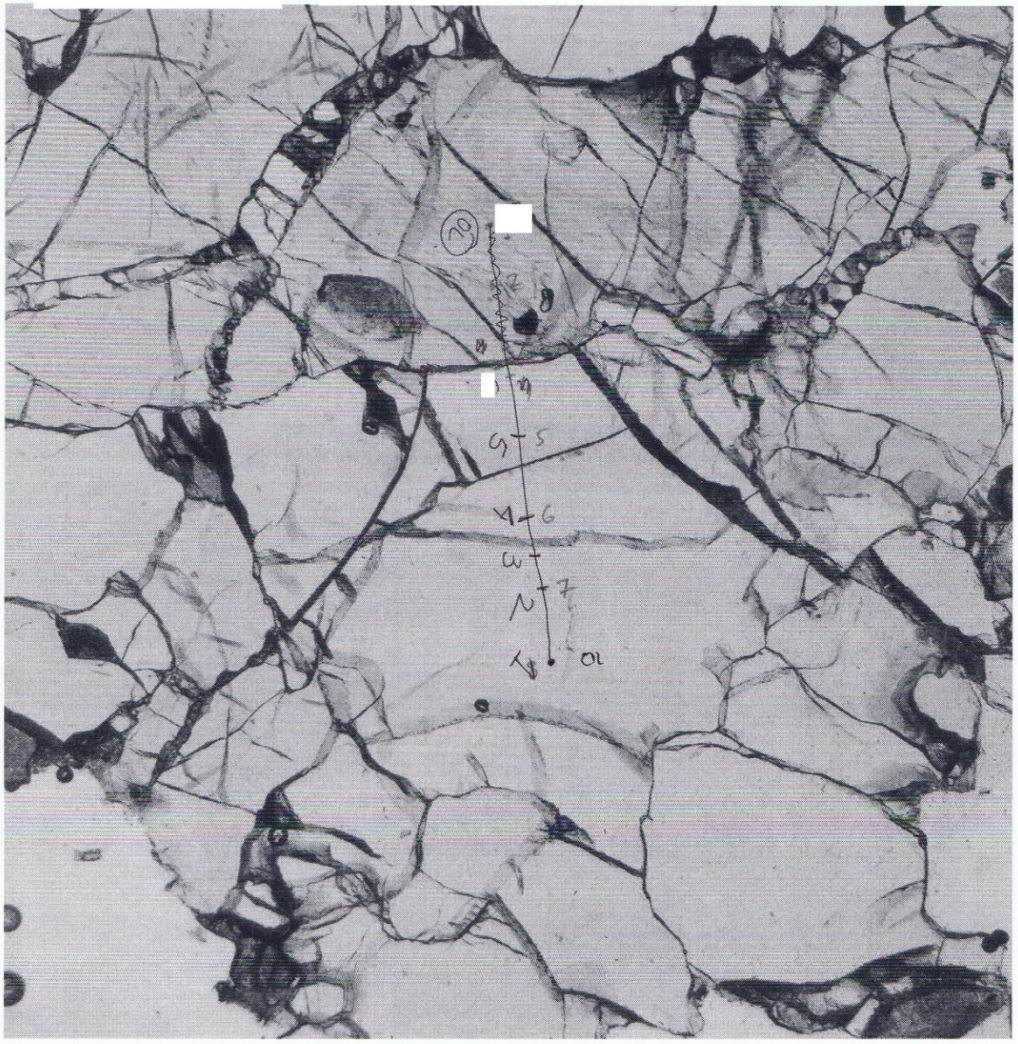

Photomicrograph 138
Sample No. 110037

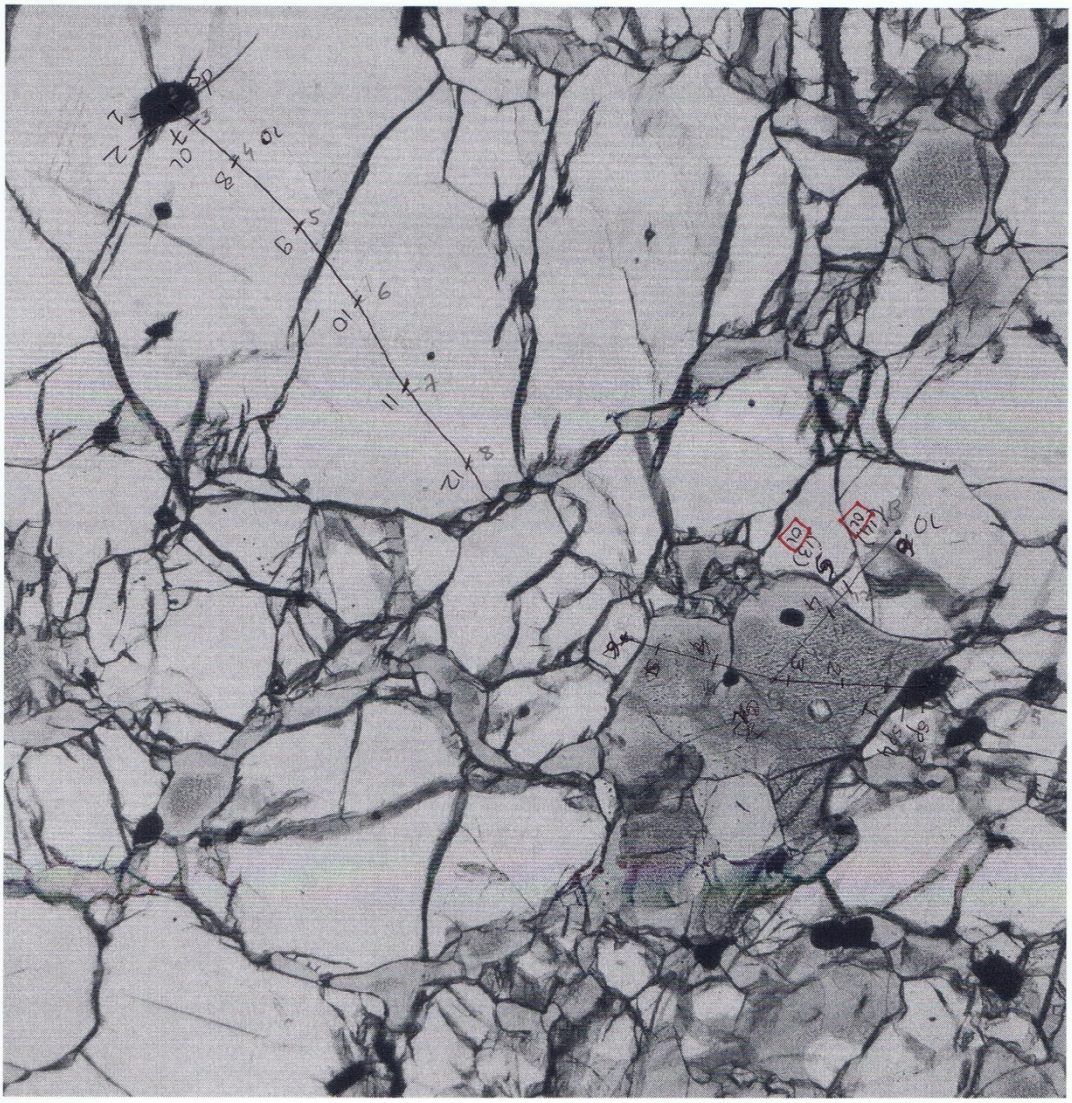

Photomicrograph 139
Sample No. 110037

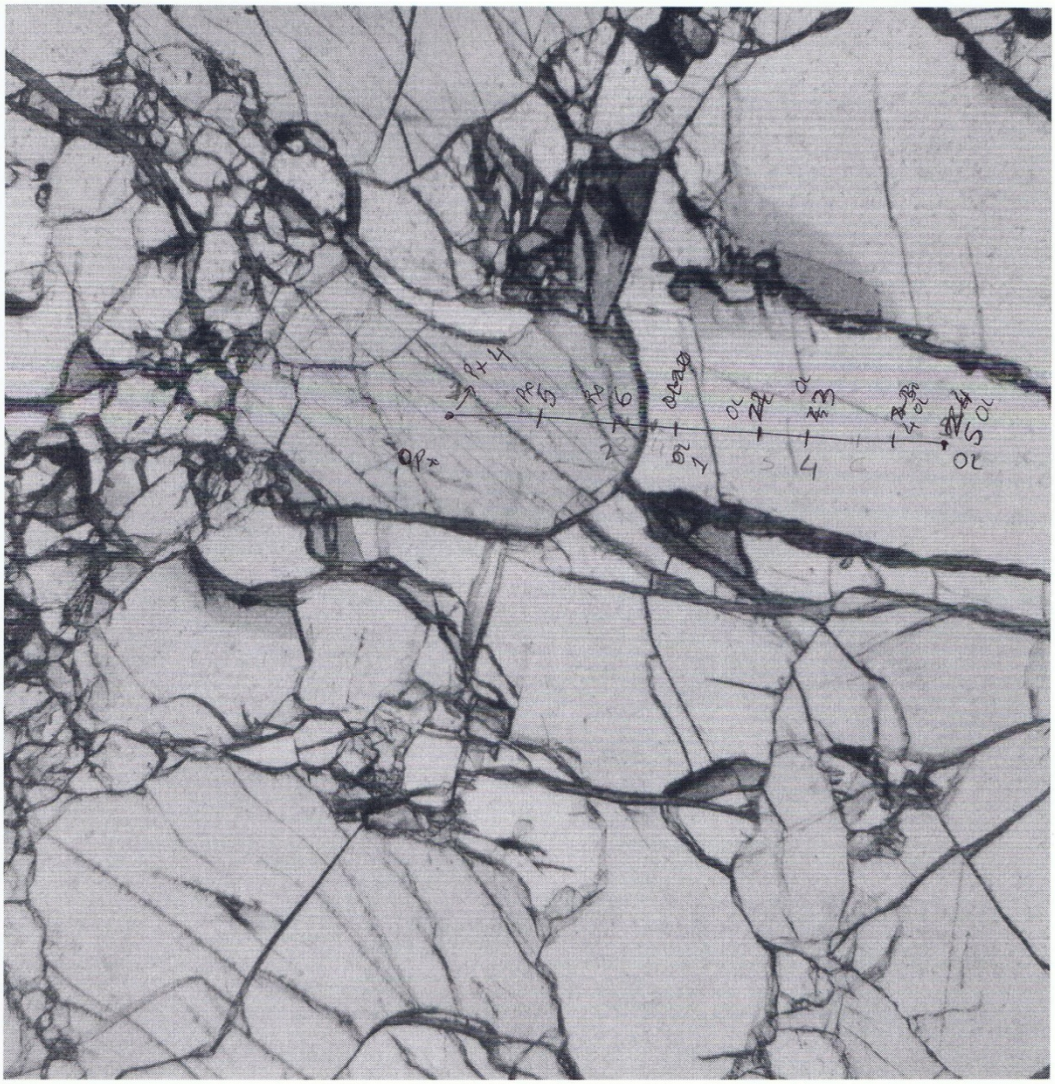

Photomicrograph 140
Sample No. 110038

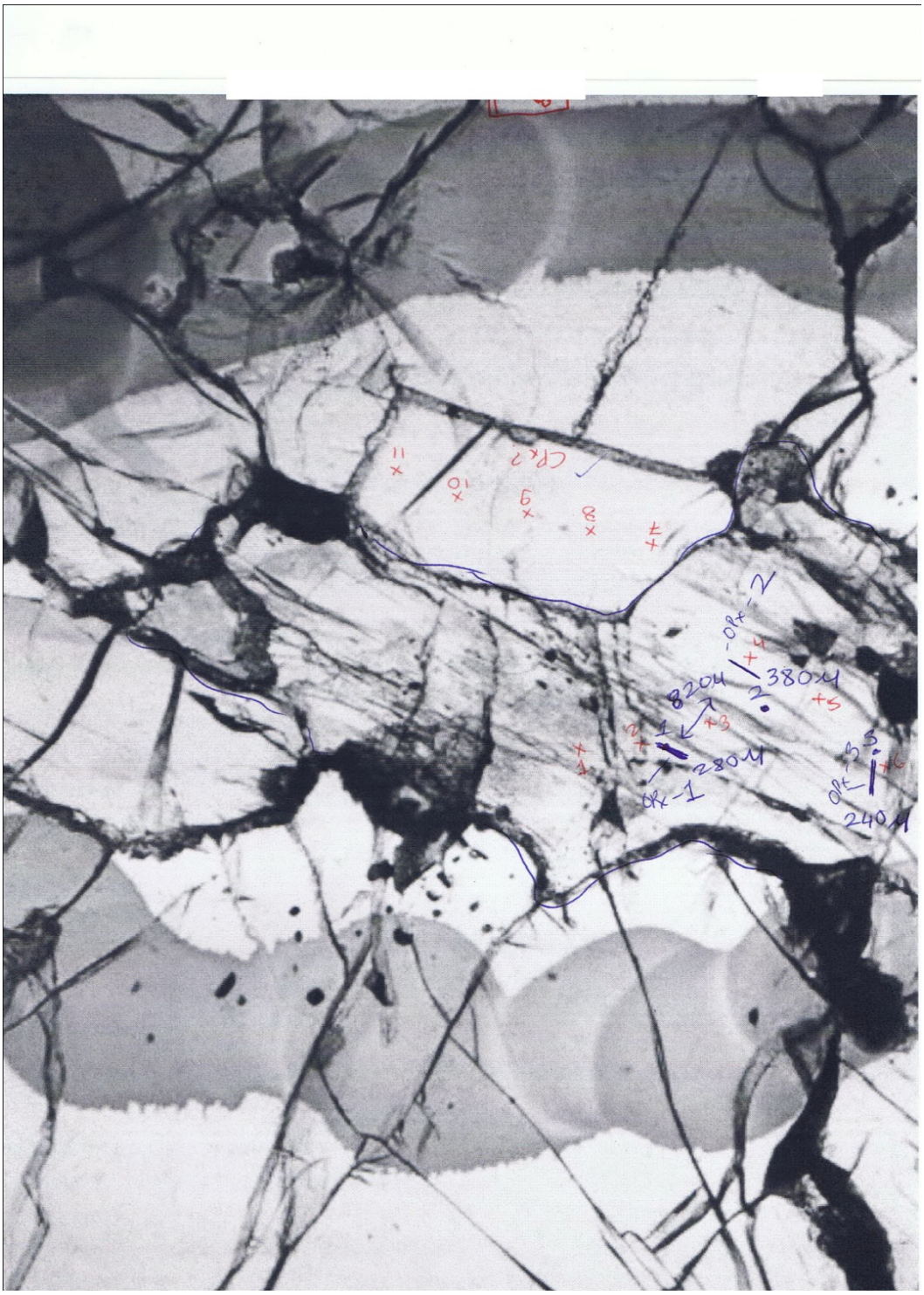

Photomicrograph 141
Sample No. FRB 1275

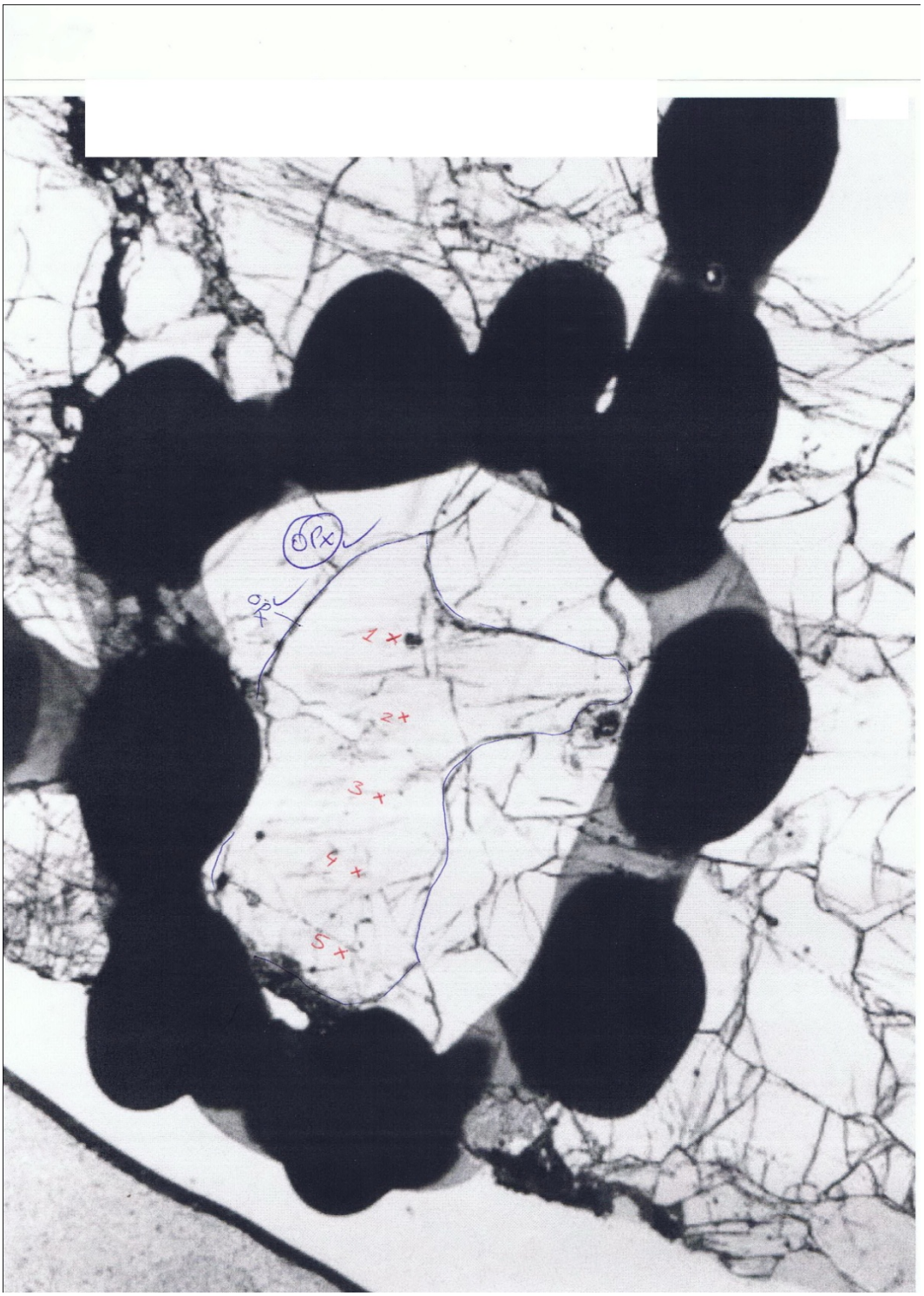

Photomicrograph 142
Sample No. FRB 1267

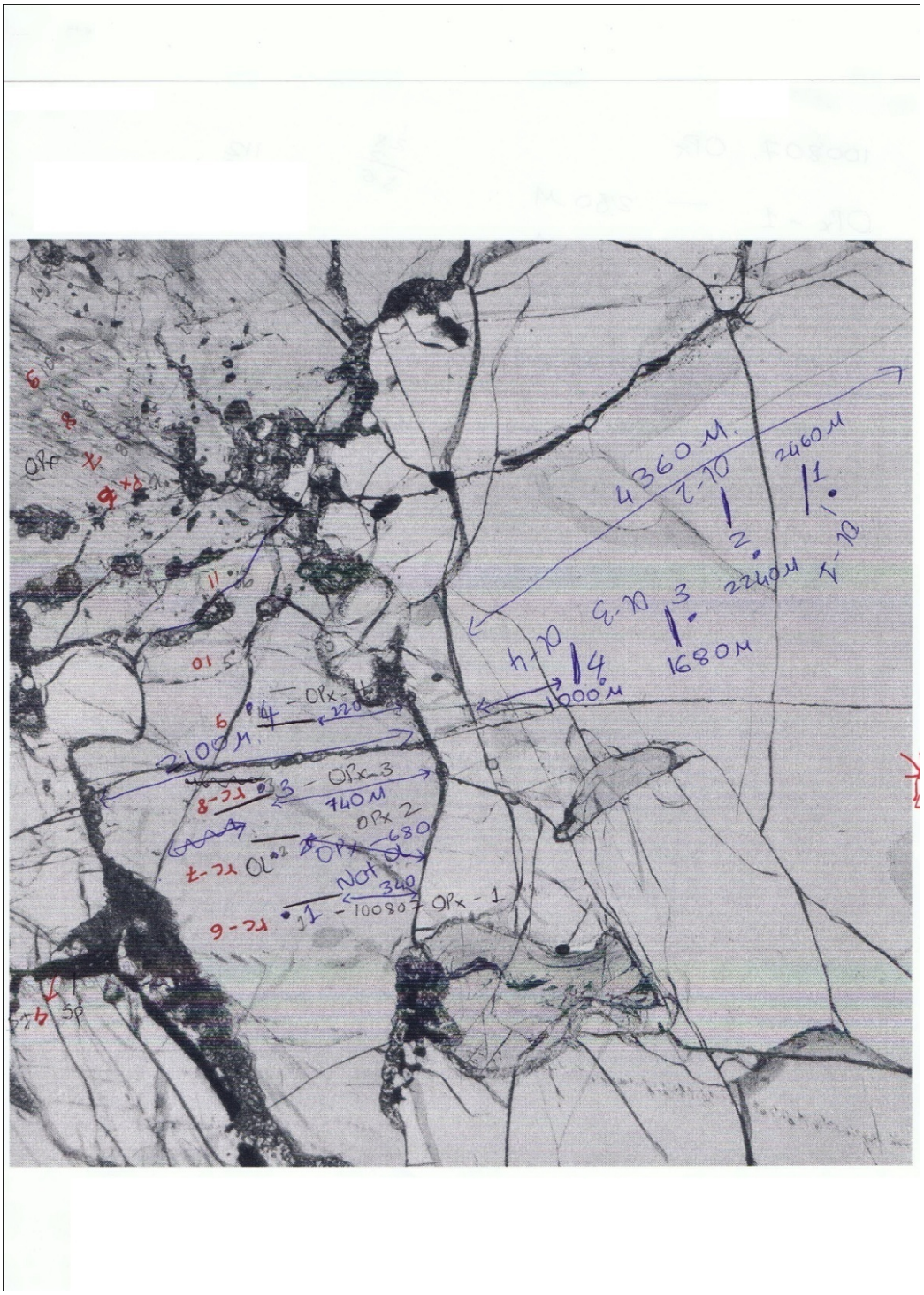

Photomicrograph 143
Sample No. 100807

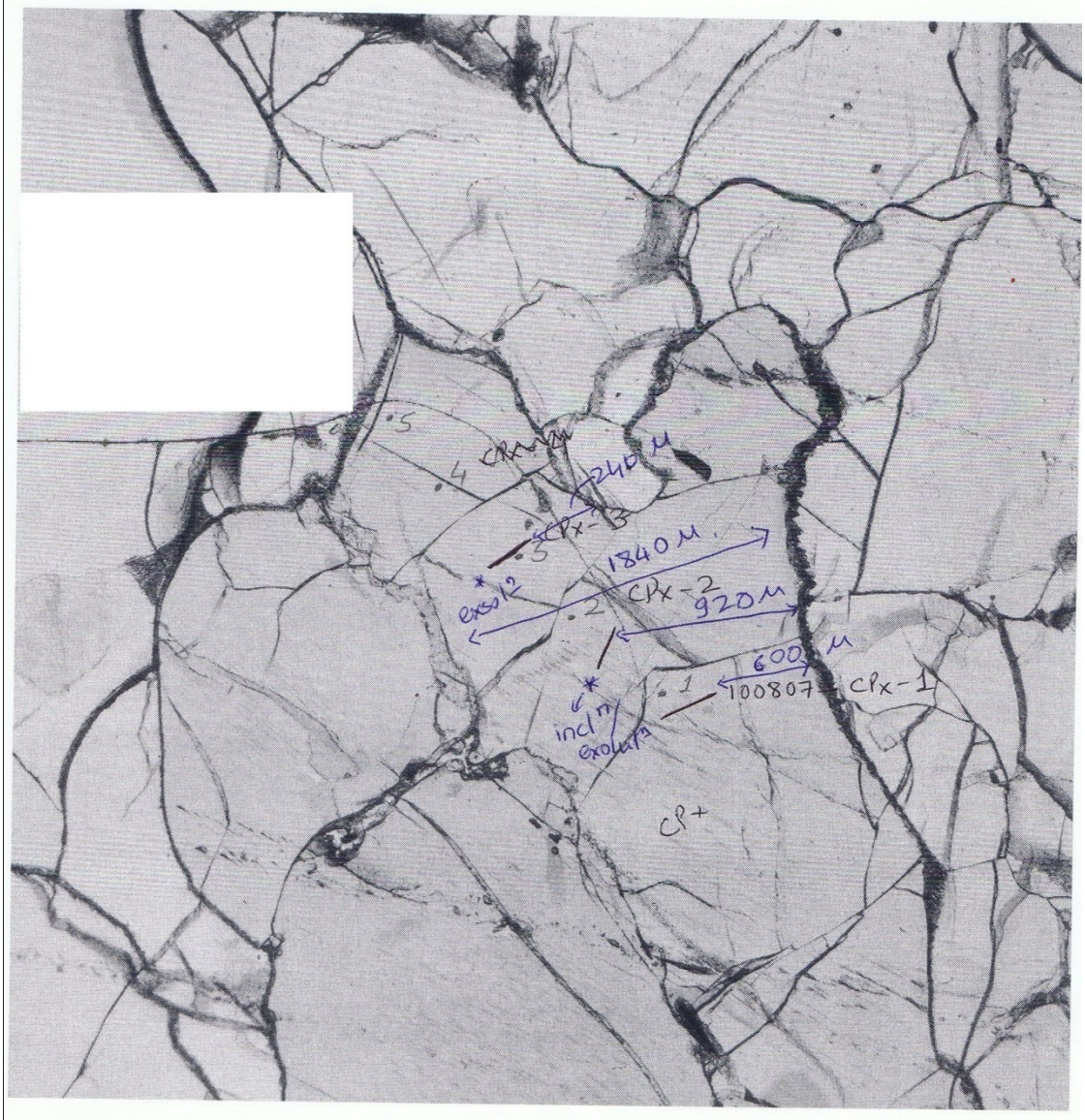

Photomicrograph 144
Sample No. 100807

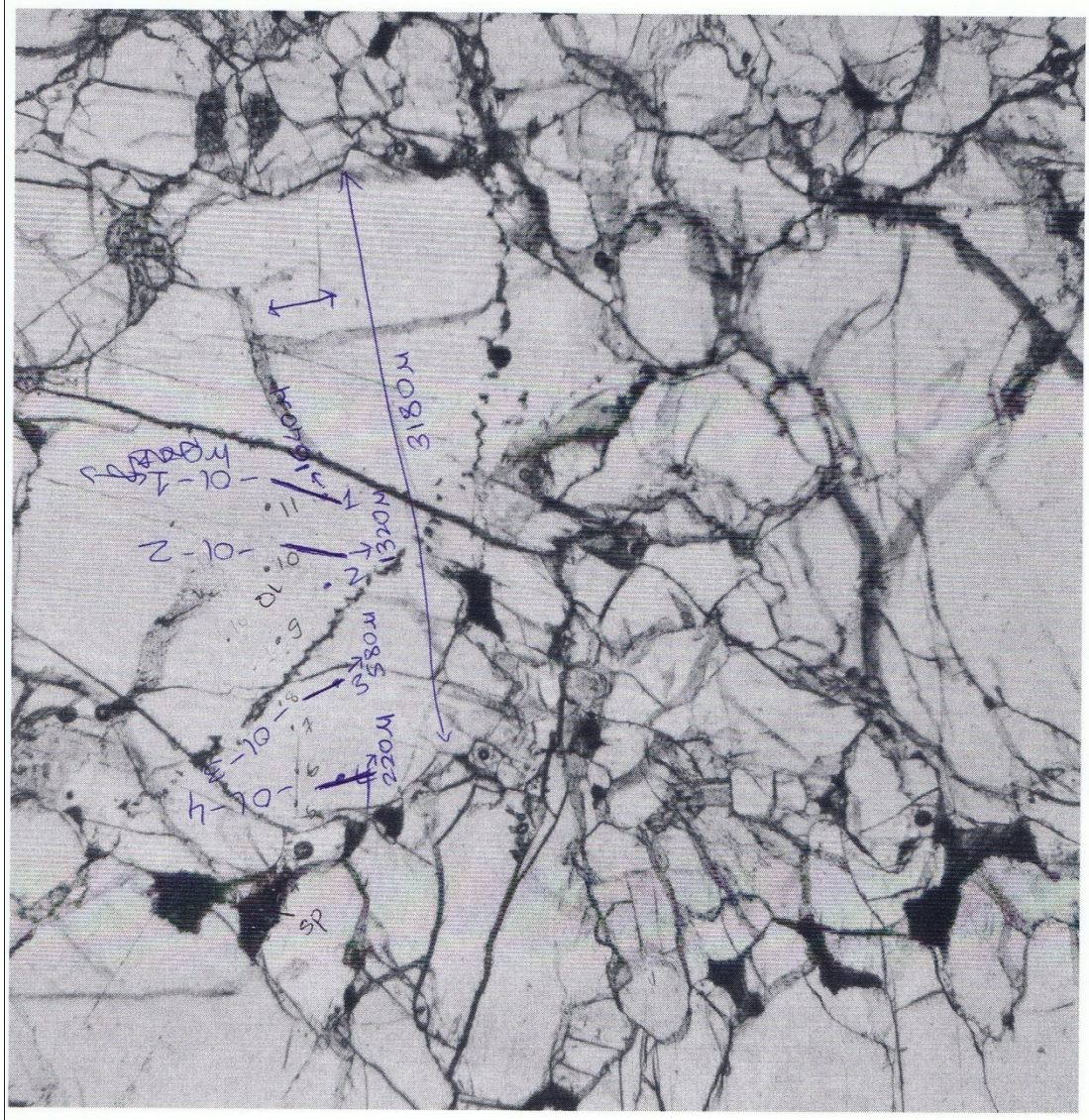

Photomicrograph 145
Sample No. 100818

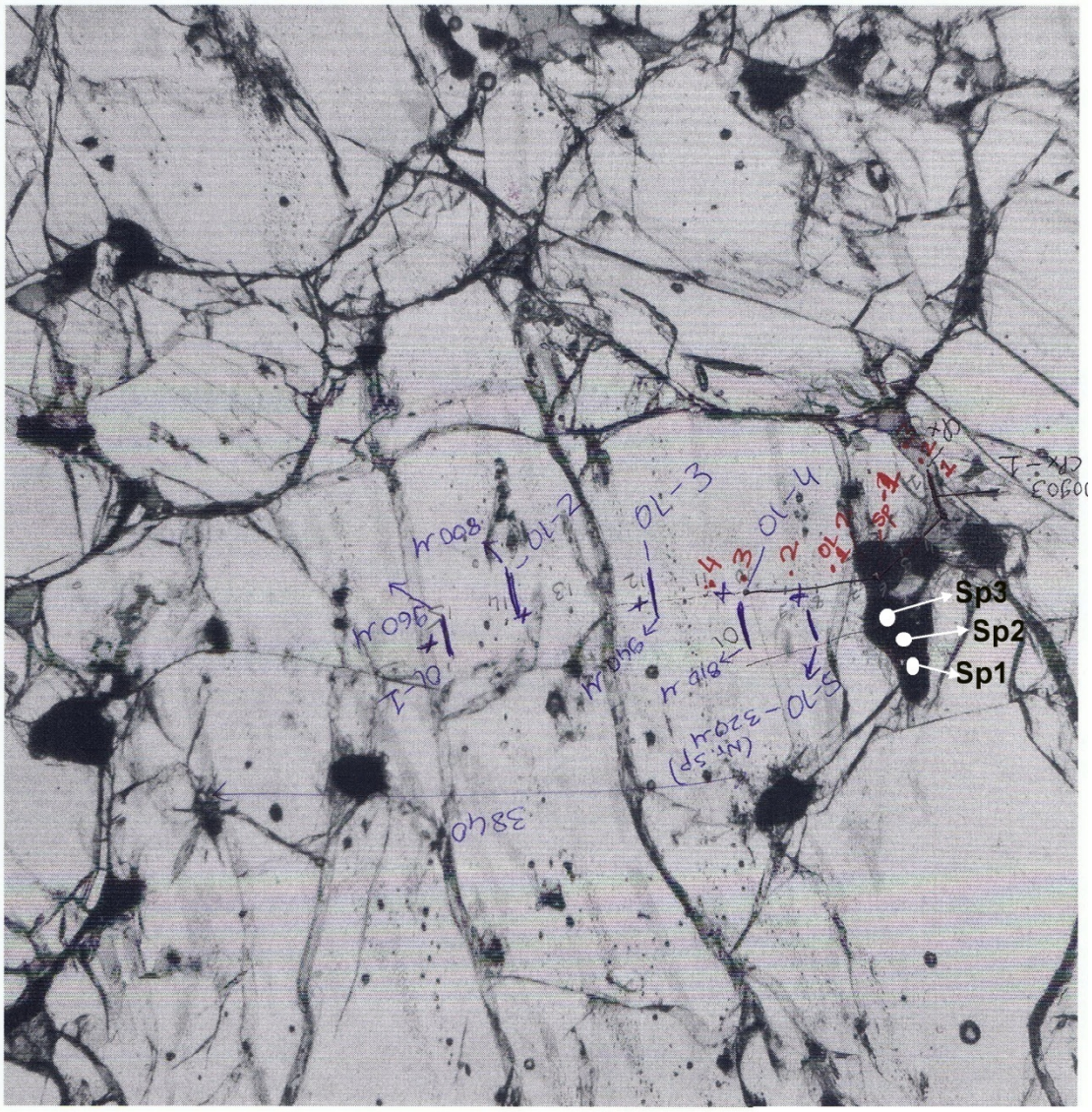

Photomicrograph 146
Sample No. 100903

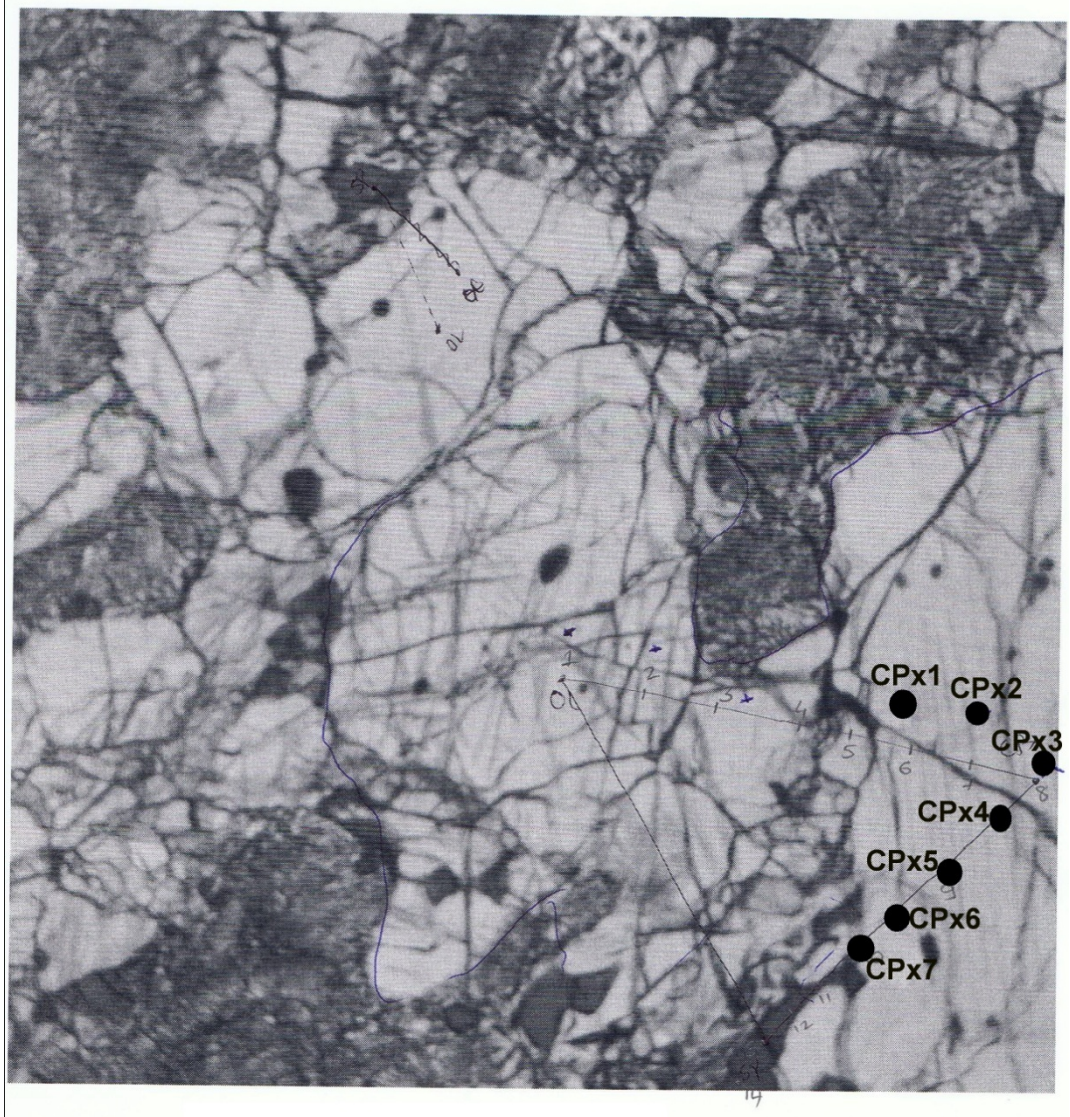

Photomicrograph 147
Sample No. 110035

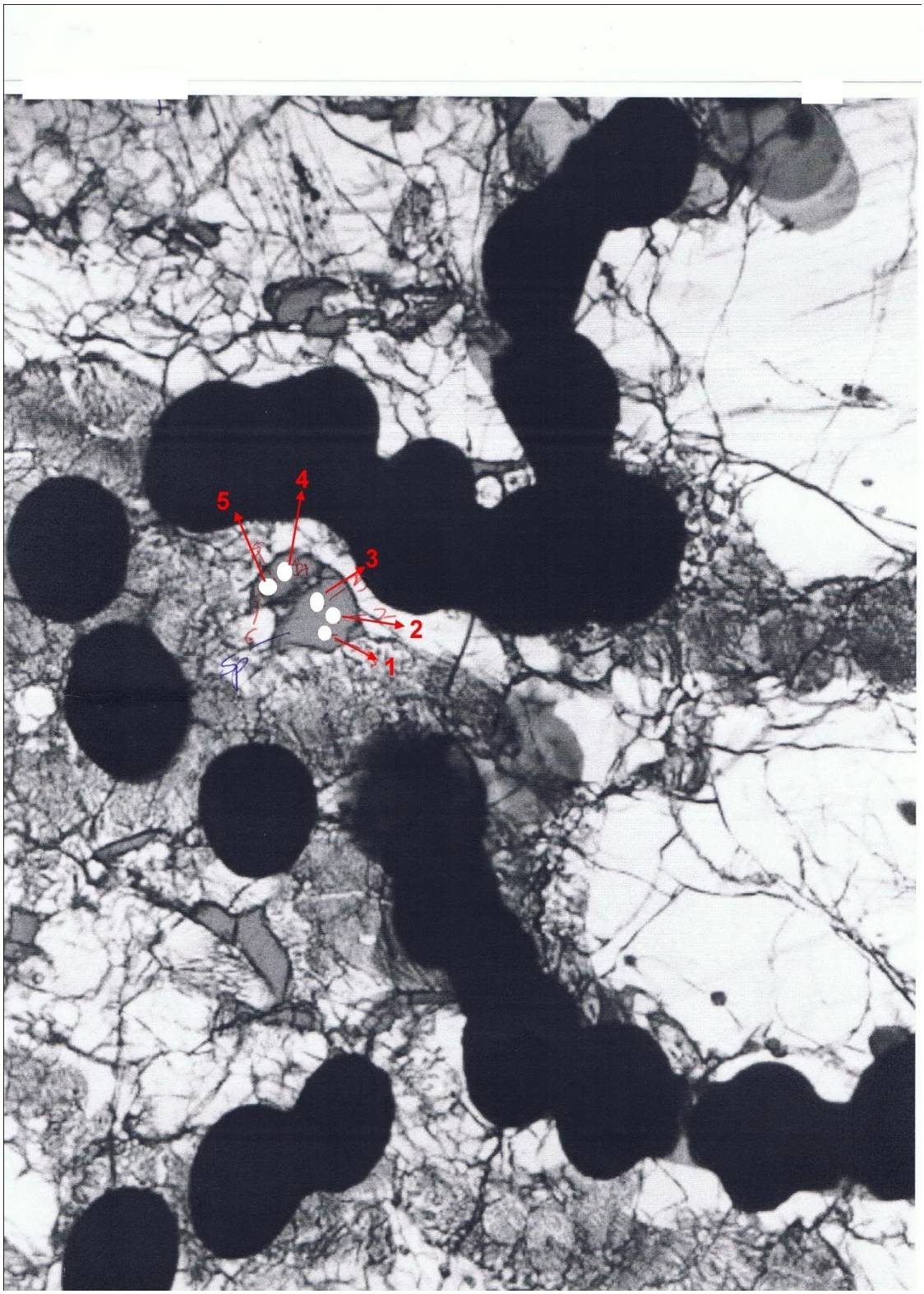

Photomicrograph 148
Sample No. 110035

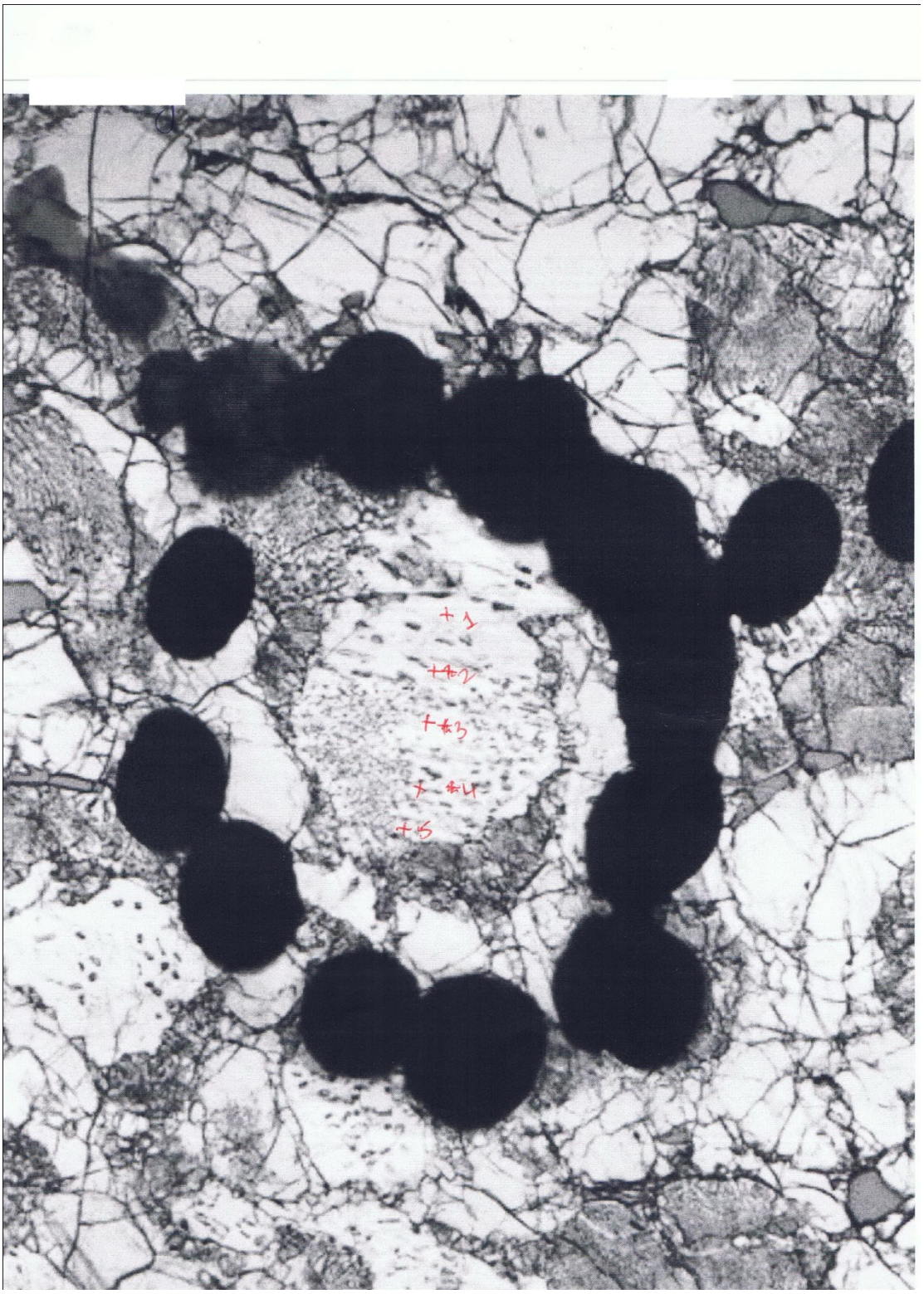

Photomicrograph 149
Sample No. 110035

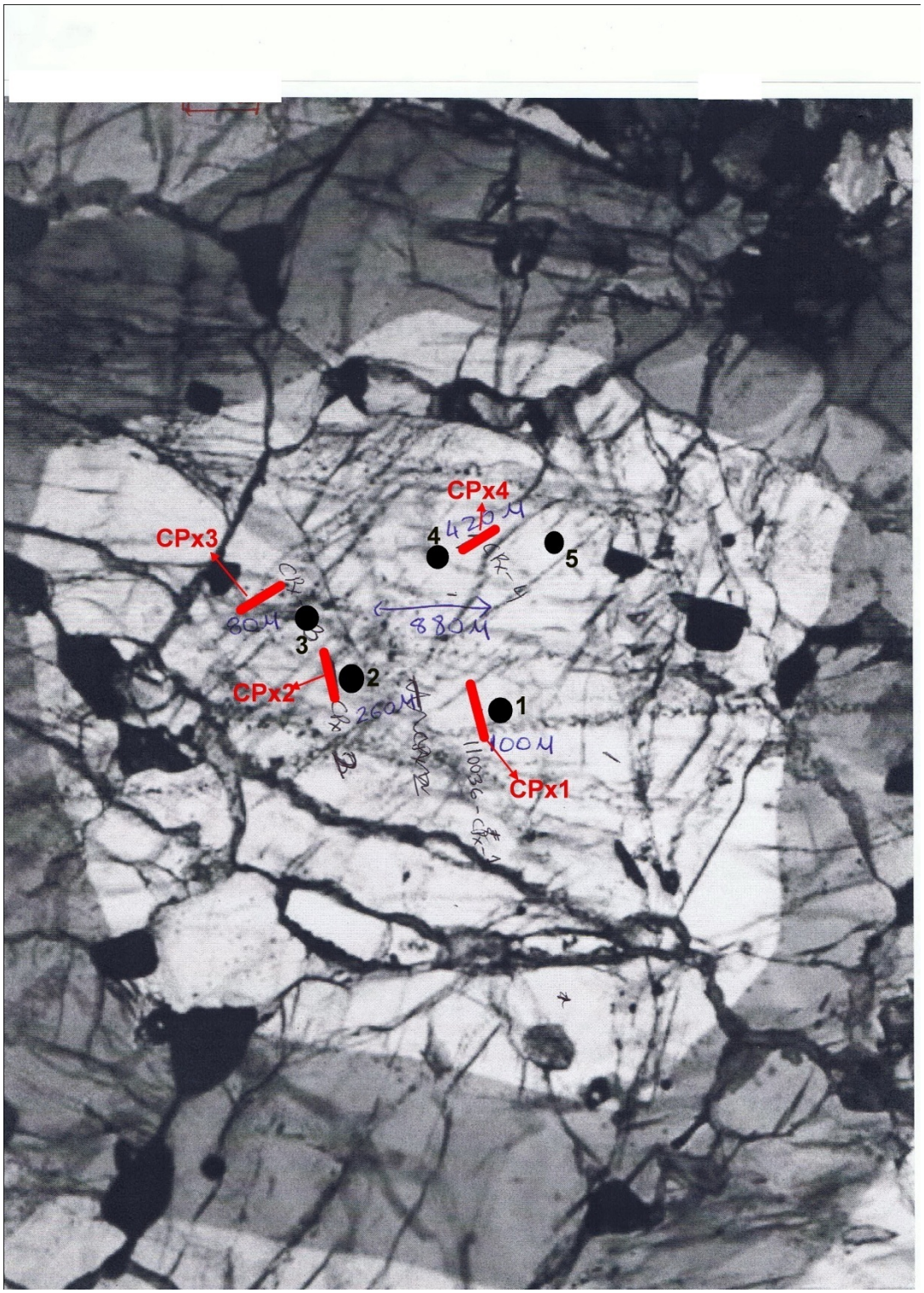

Photomicrograph 150
Sample No. 110036

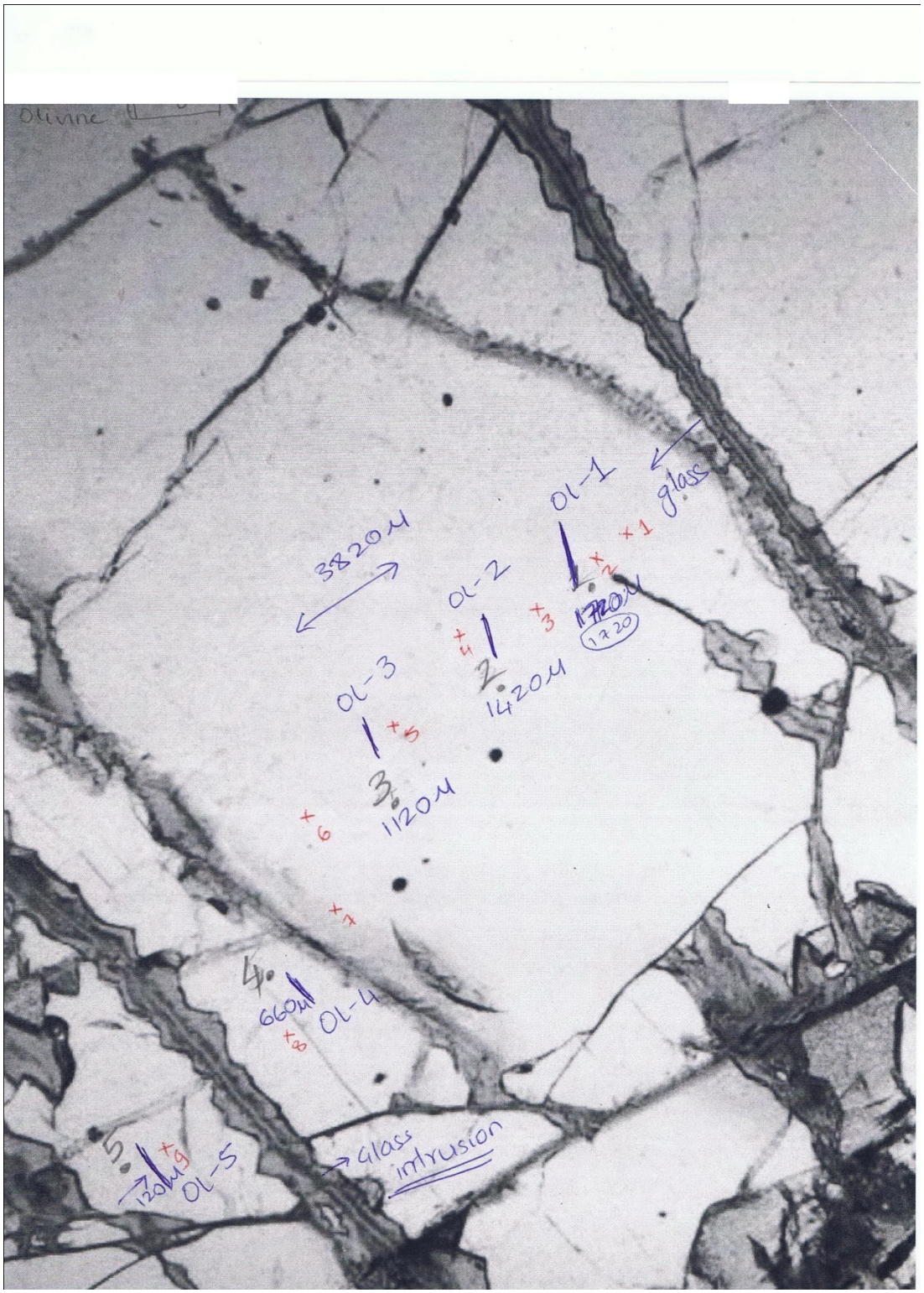

Photomicrograph 151
Sample No. 110045

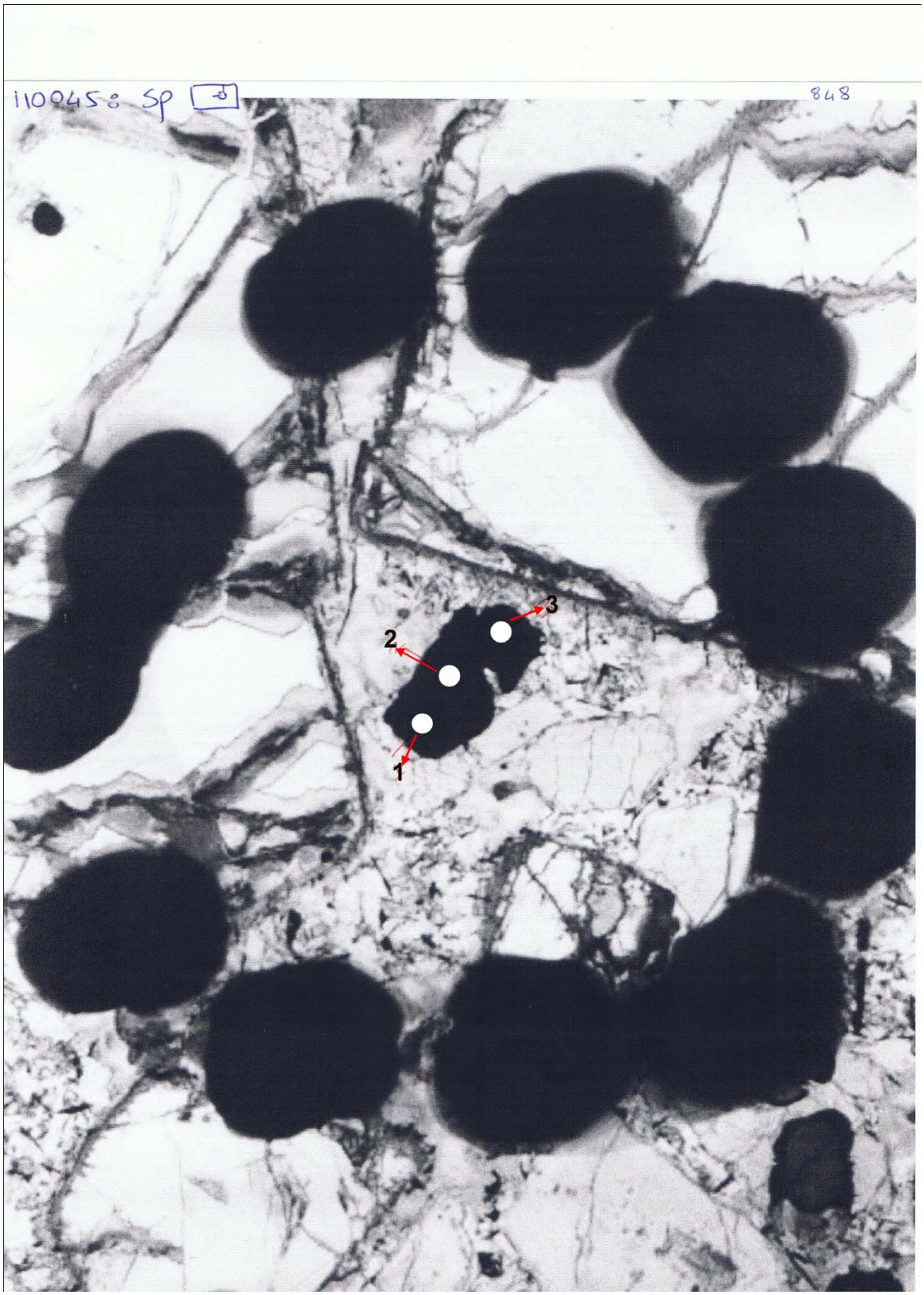

Photomicrograph 152
Sample No. 110045

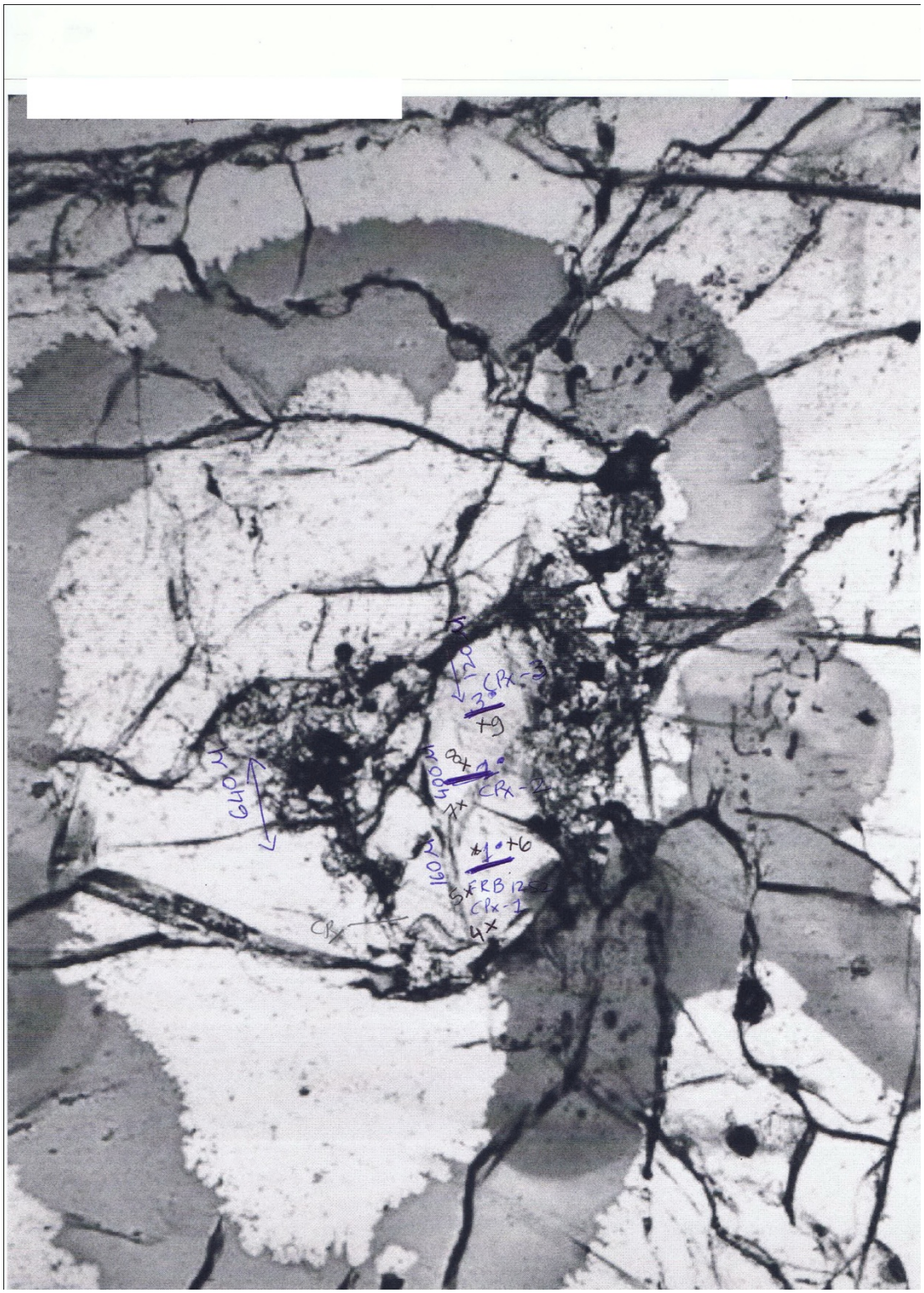

Photomicrograph 153
Sample No. FRB 1252

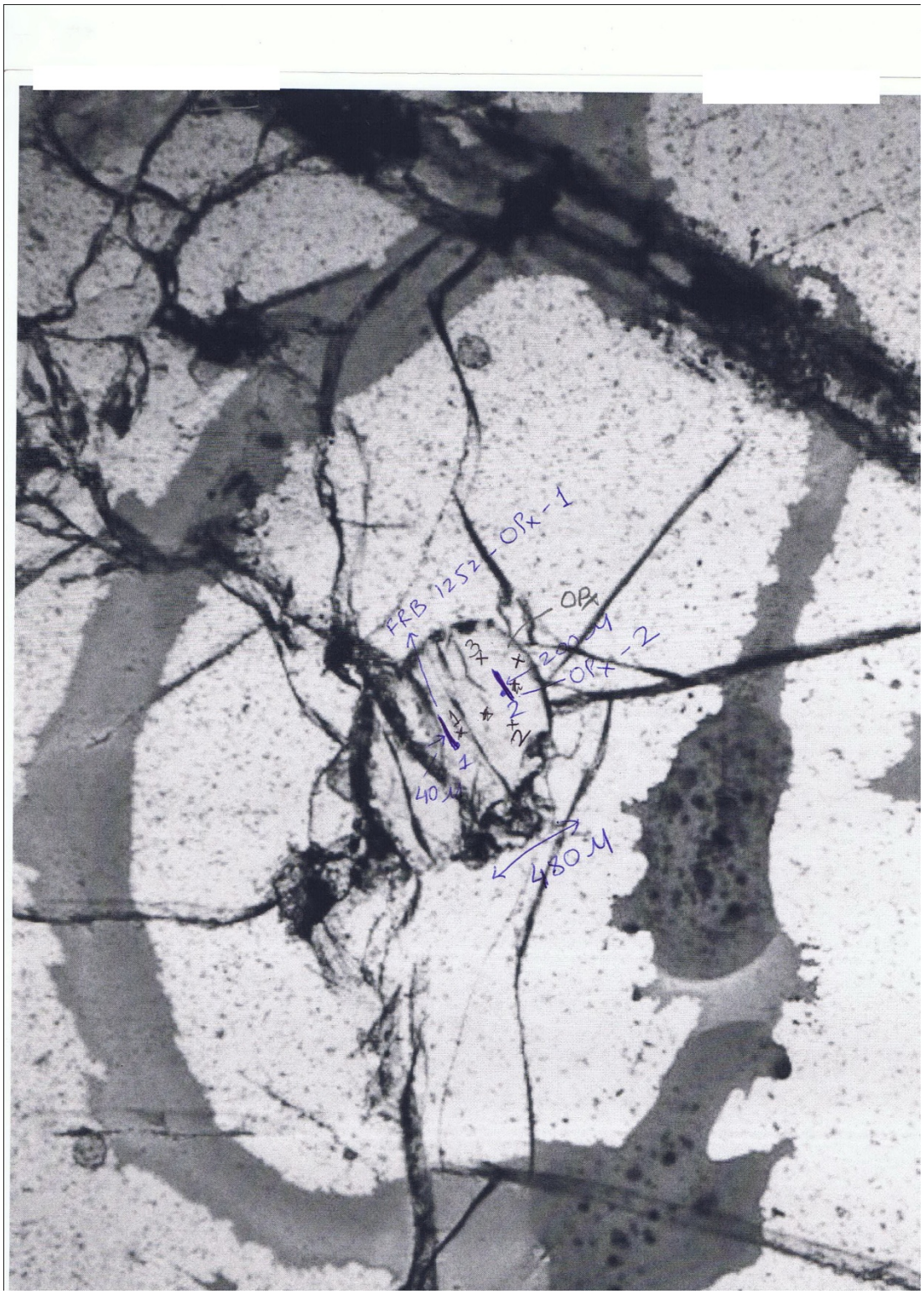

Photomicrograph 154
Sample No. FRB 1252

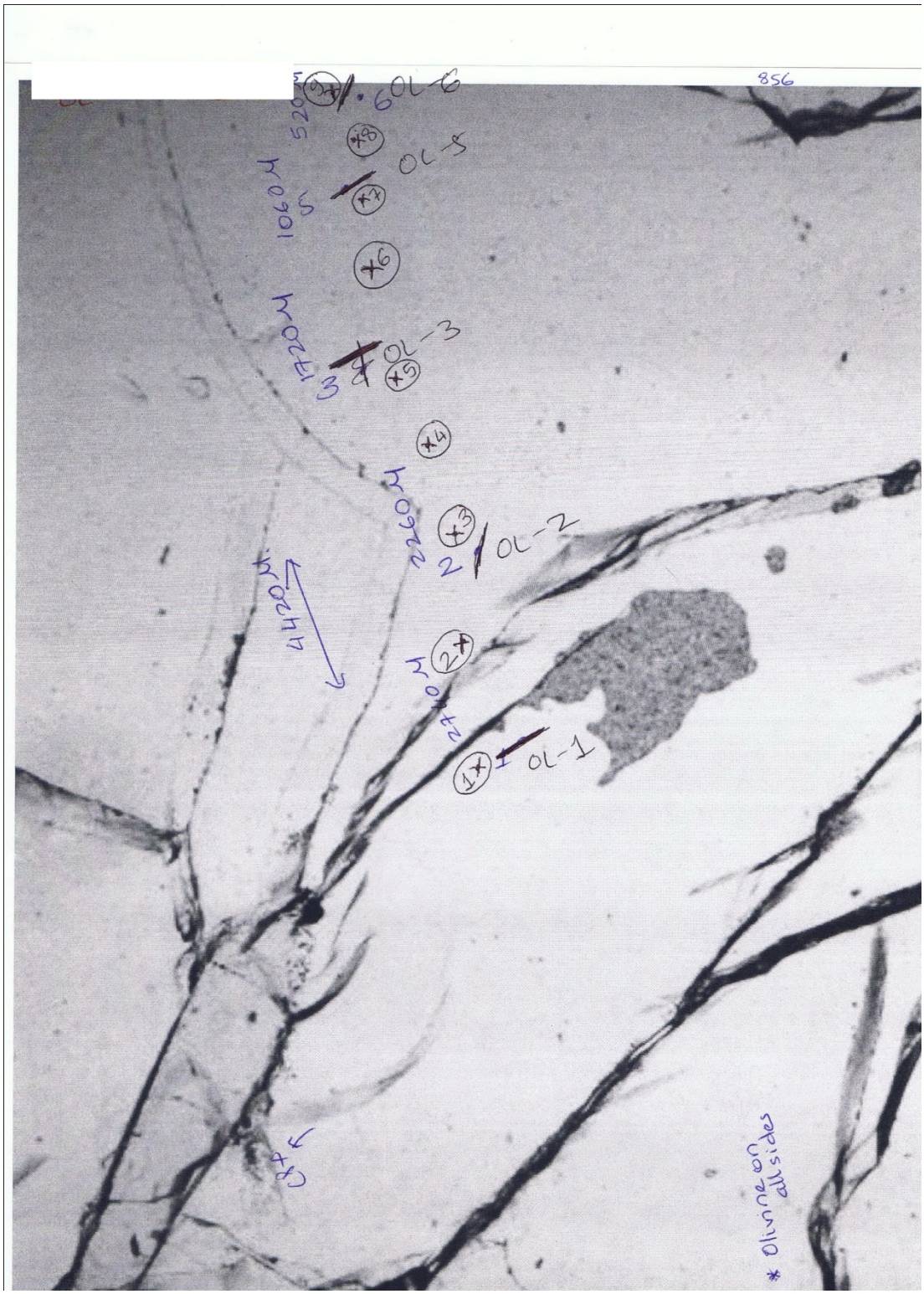

Photomicrograph 155
Sample No. FRB 1252

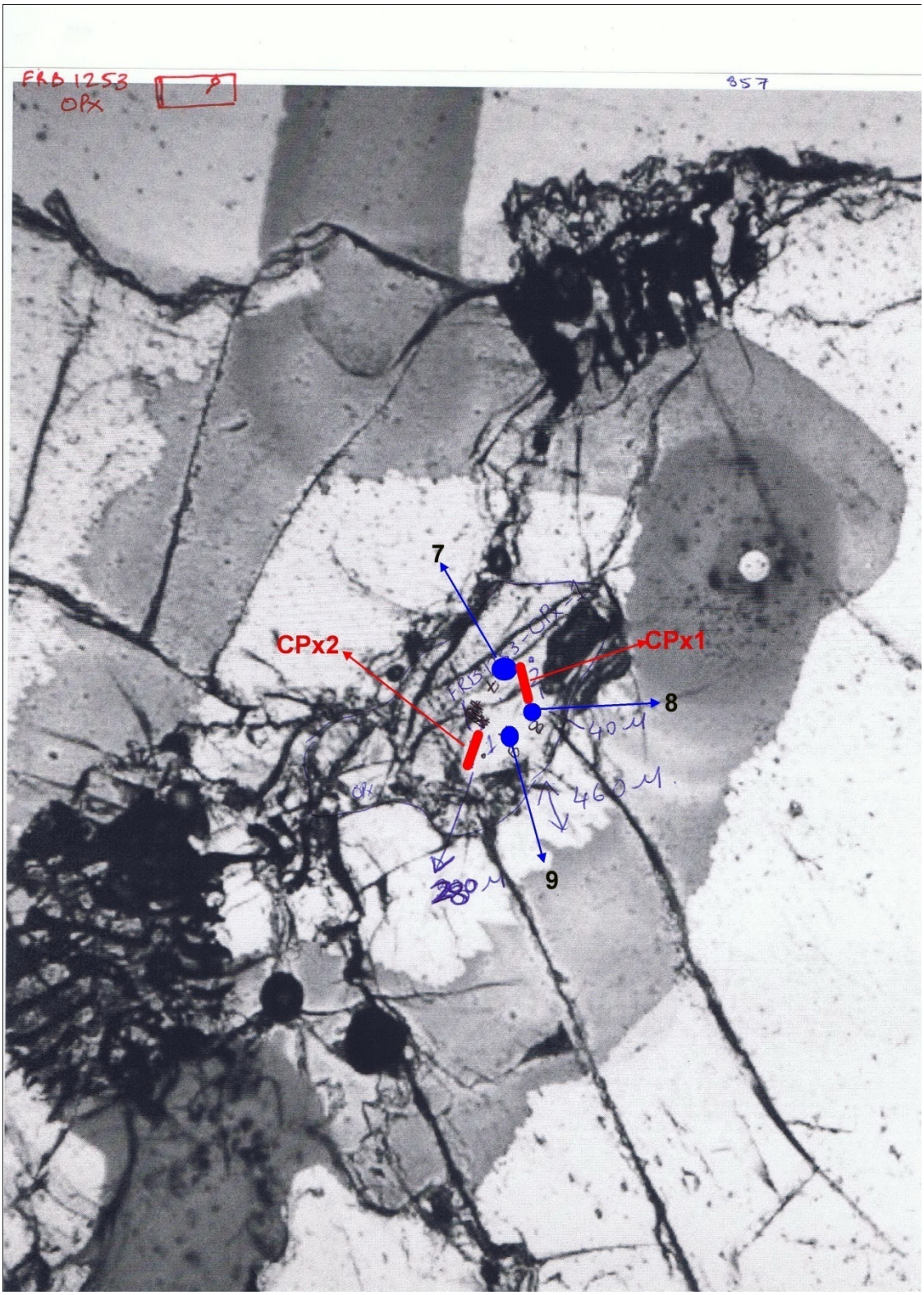

Photomicrograph 156
Sample No. FRB 1253

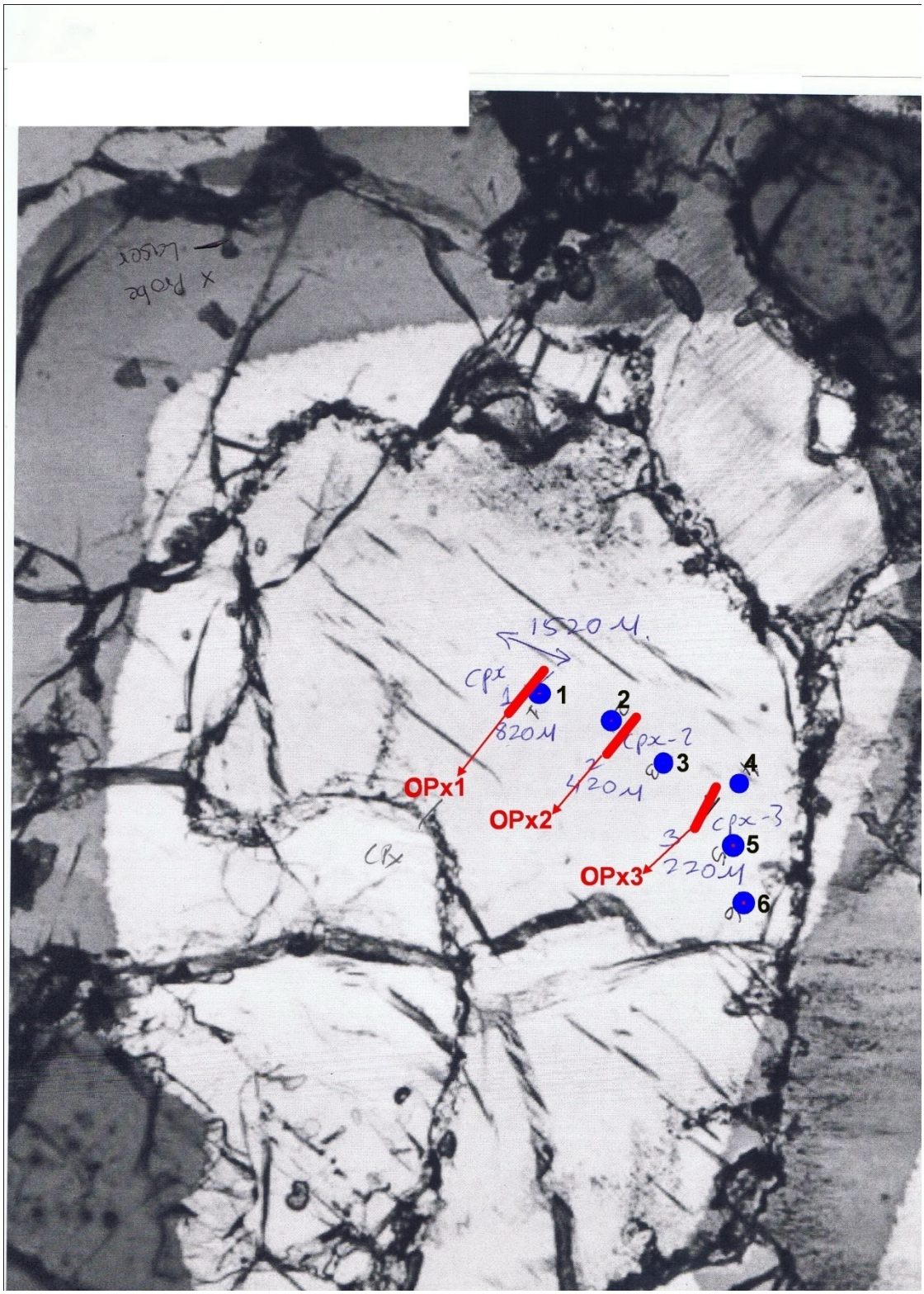

Photomicrograph 157
Sample No. FRB 1253

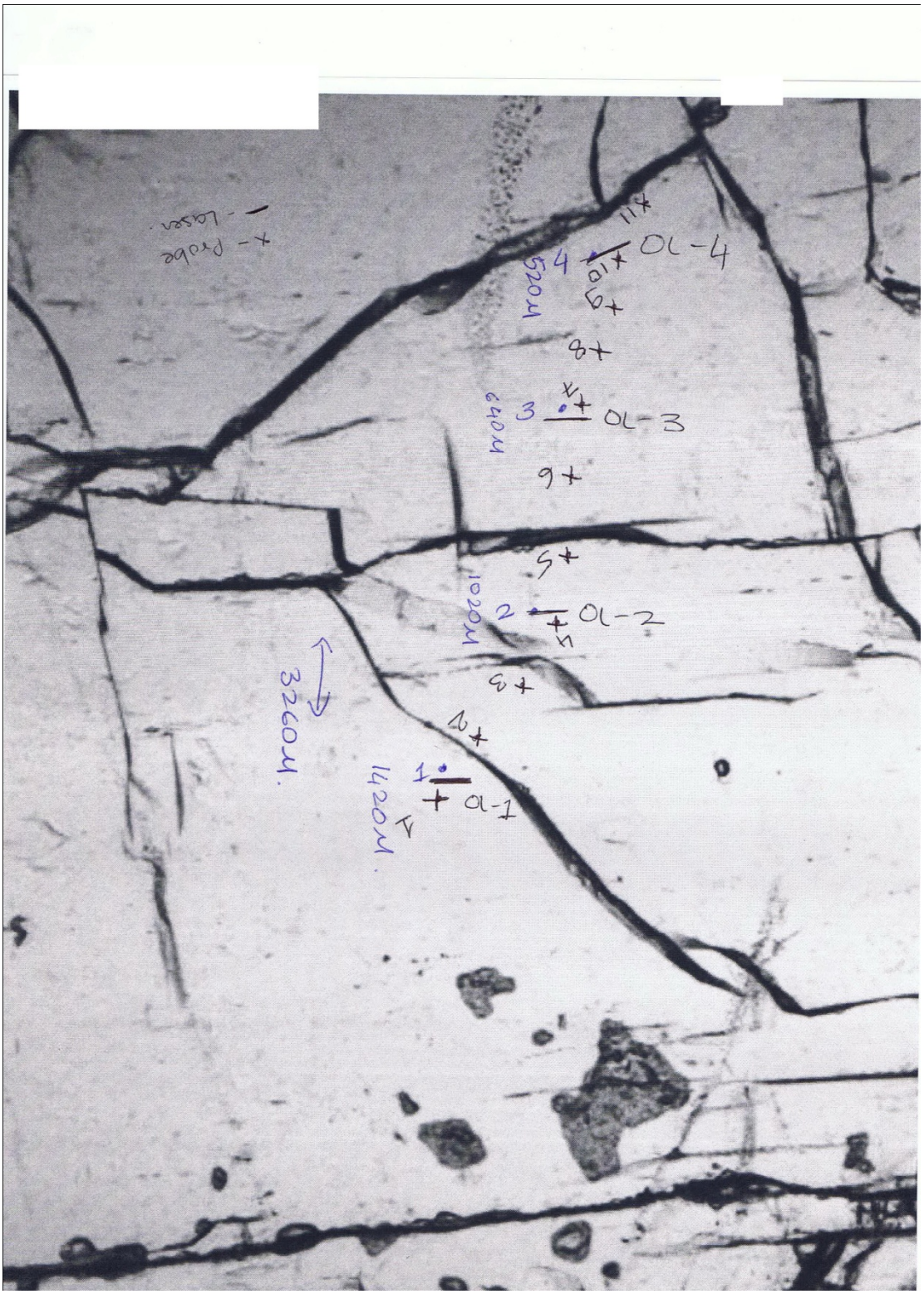

Photomicrograph 158
Sample No. FRB 1253

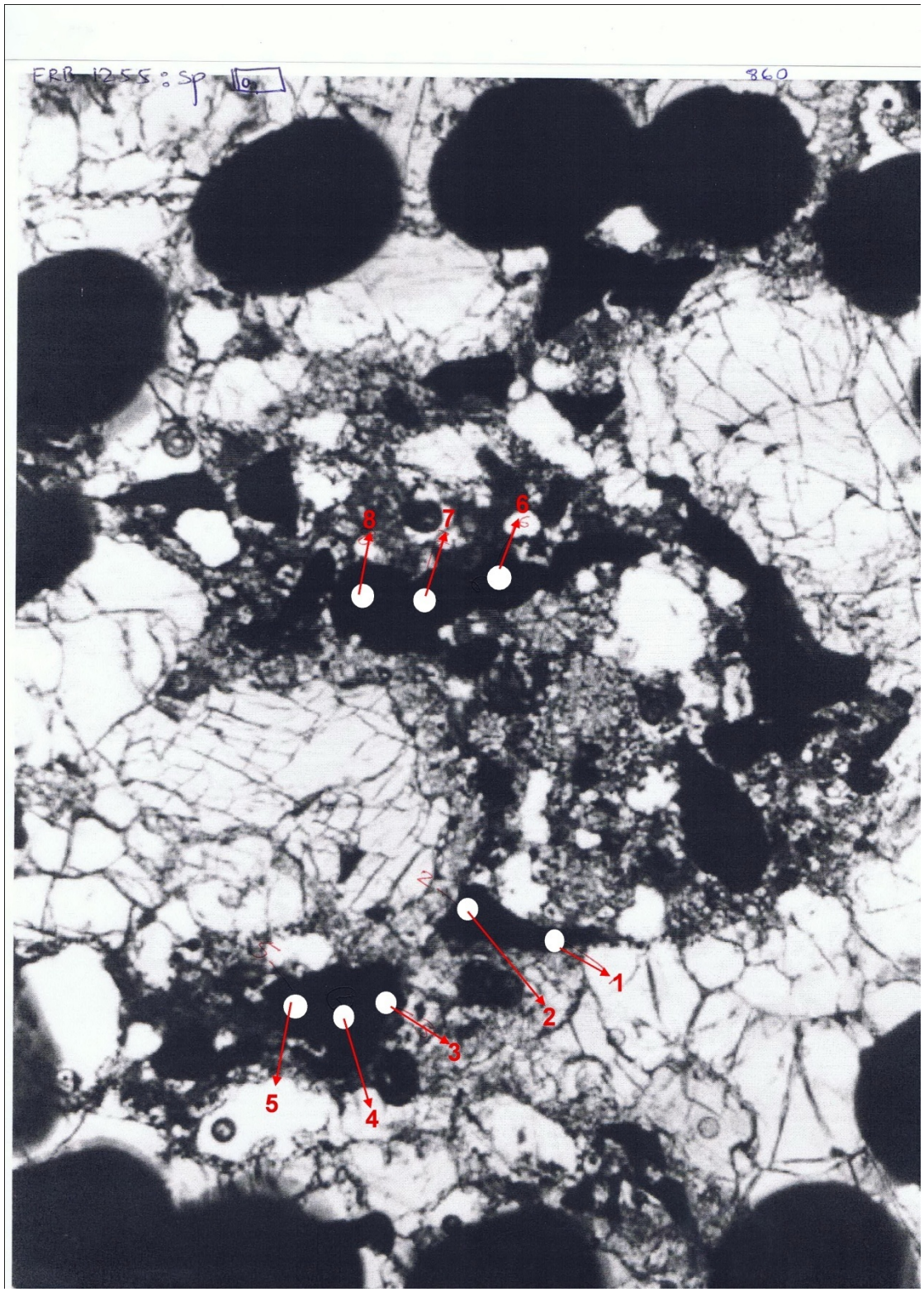

Photomicrograph 159
Sample No. FRB 1255

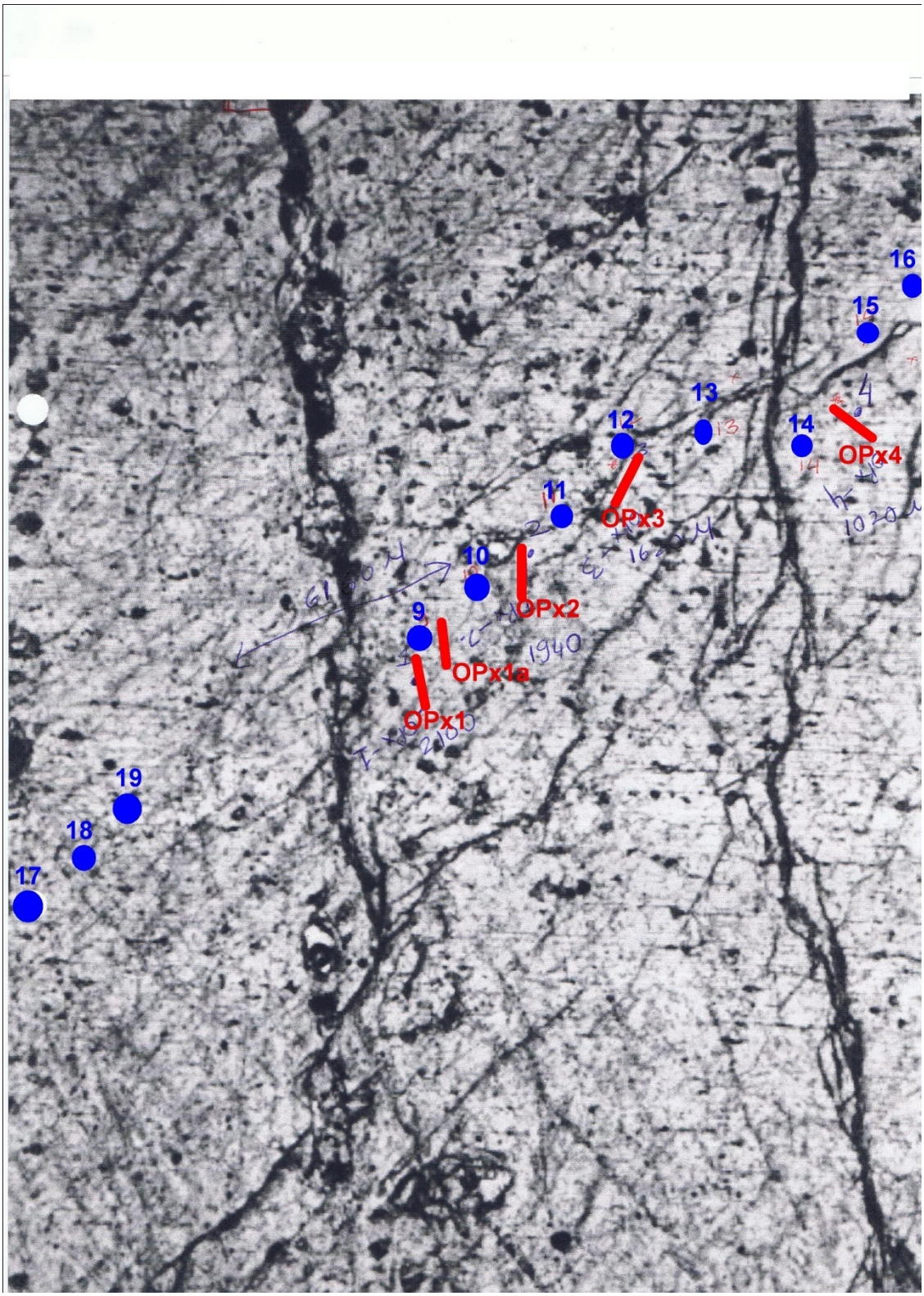

Photomicrograph 160
Sample No. FRB 1255

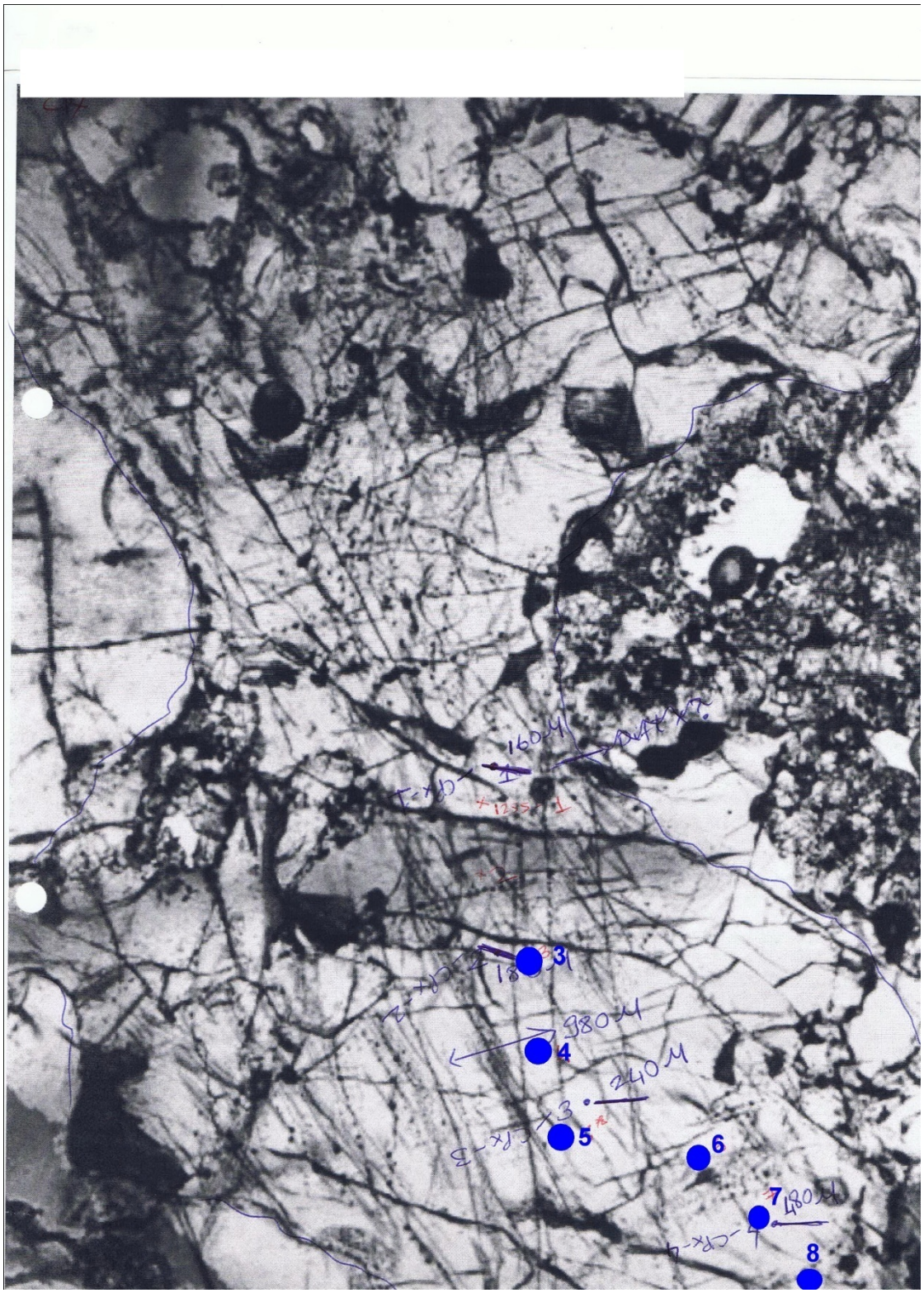

Photomicrograph 161
Sample No. FRB 1255

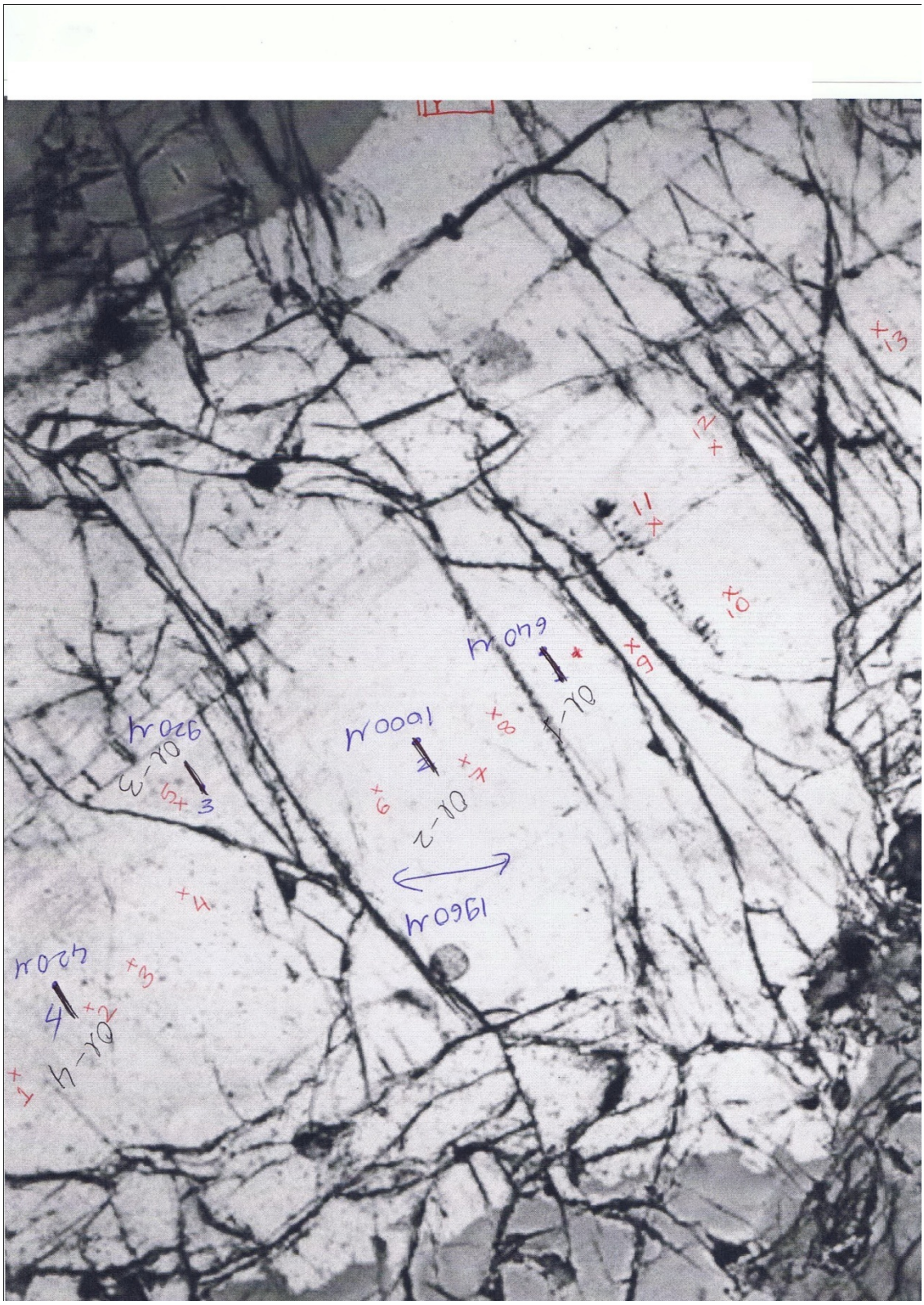

Photomicrograph 162
Sample No. FRB 1255

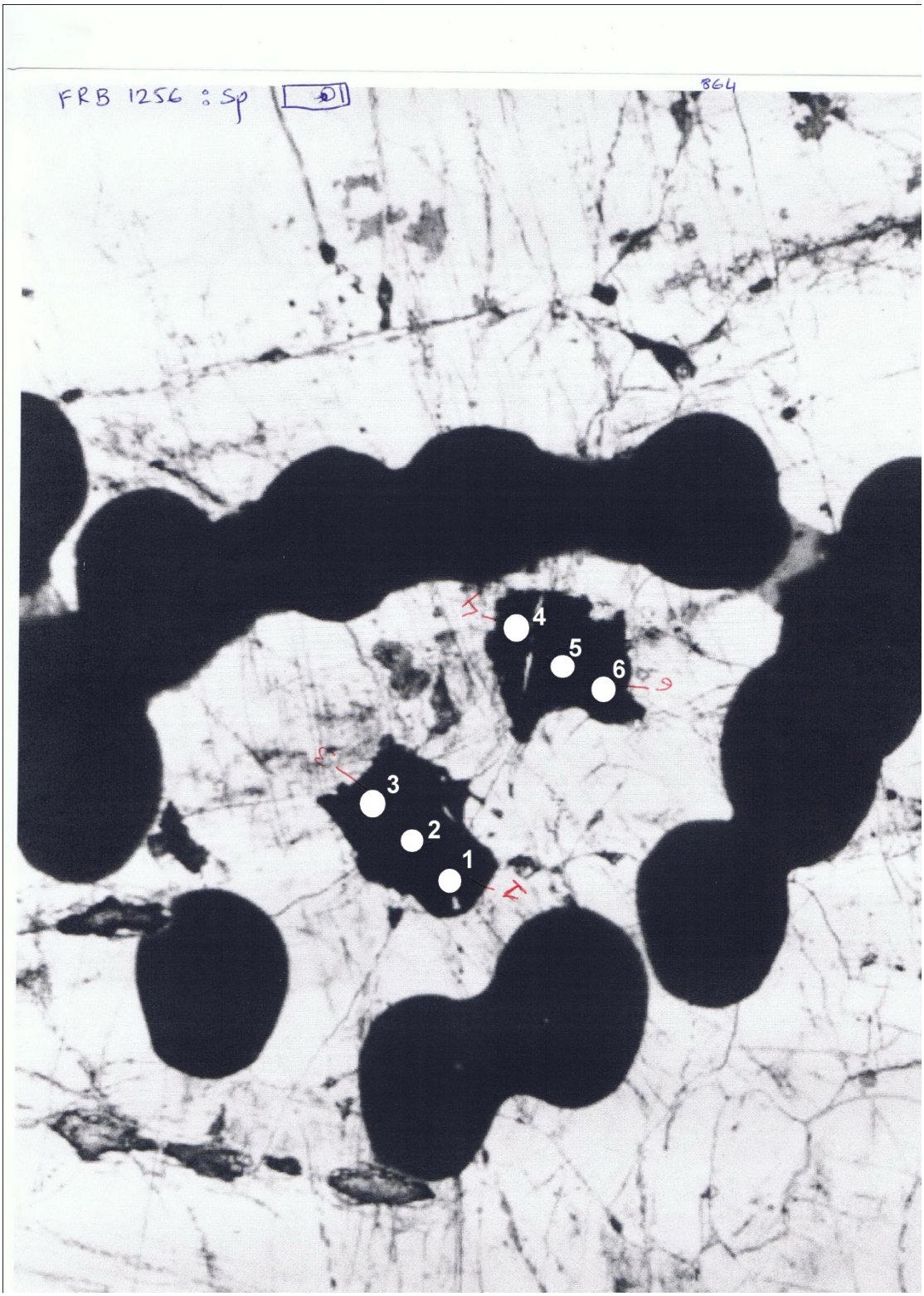

Photomicrograph 163
Sample No. FRB 1256

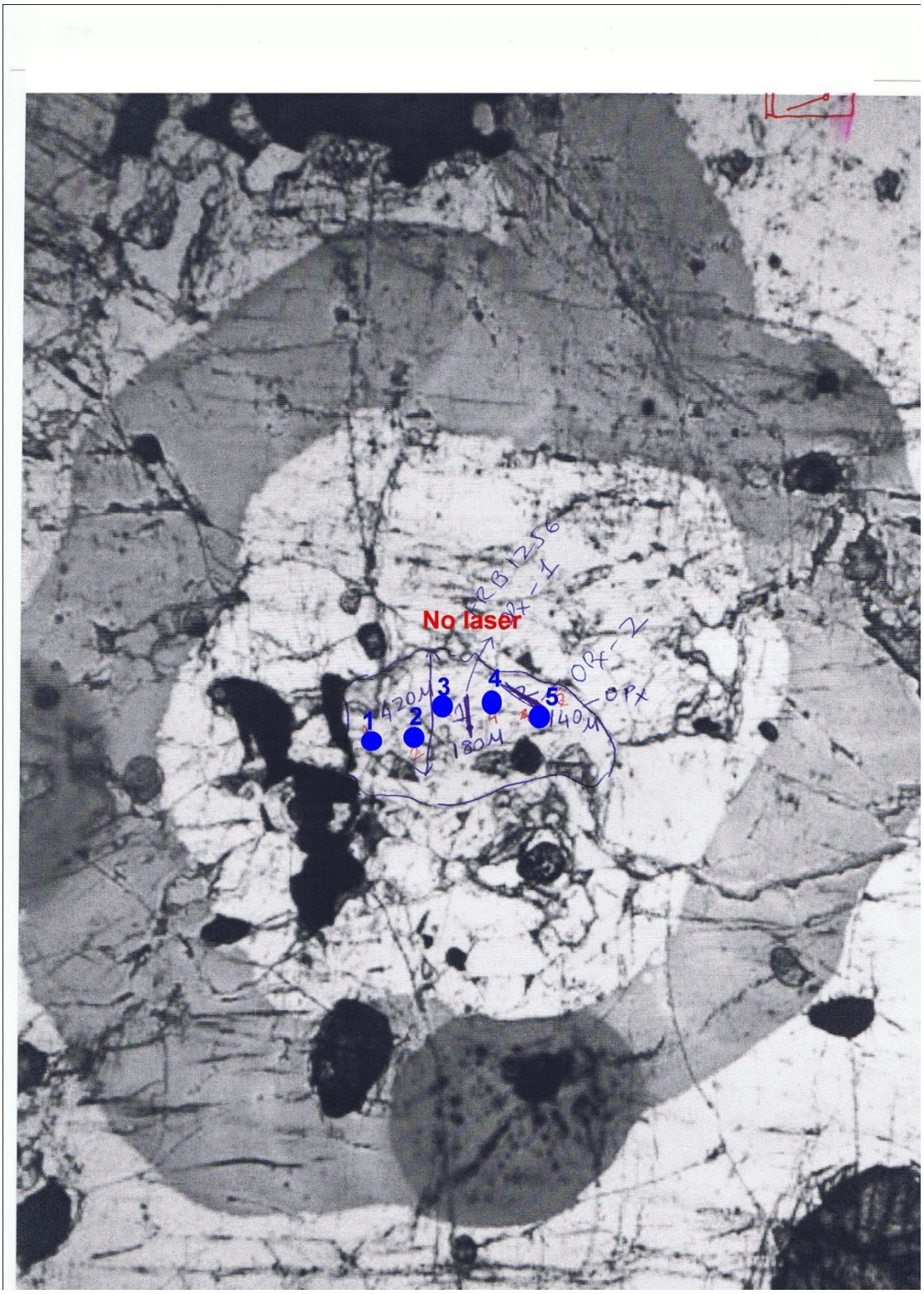

Photomicrograph 164
Sample No. FRB 1256

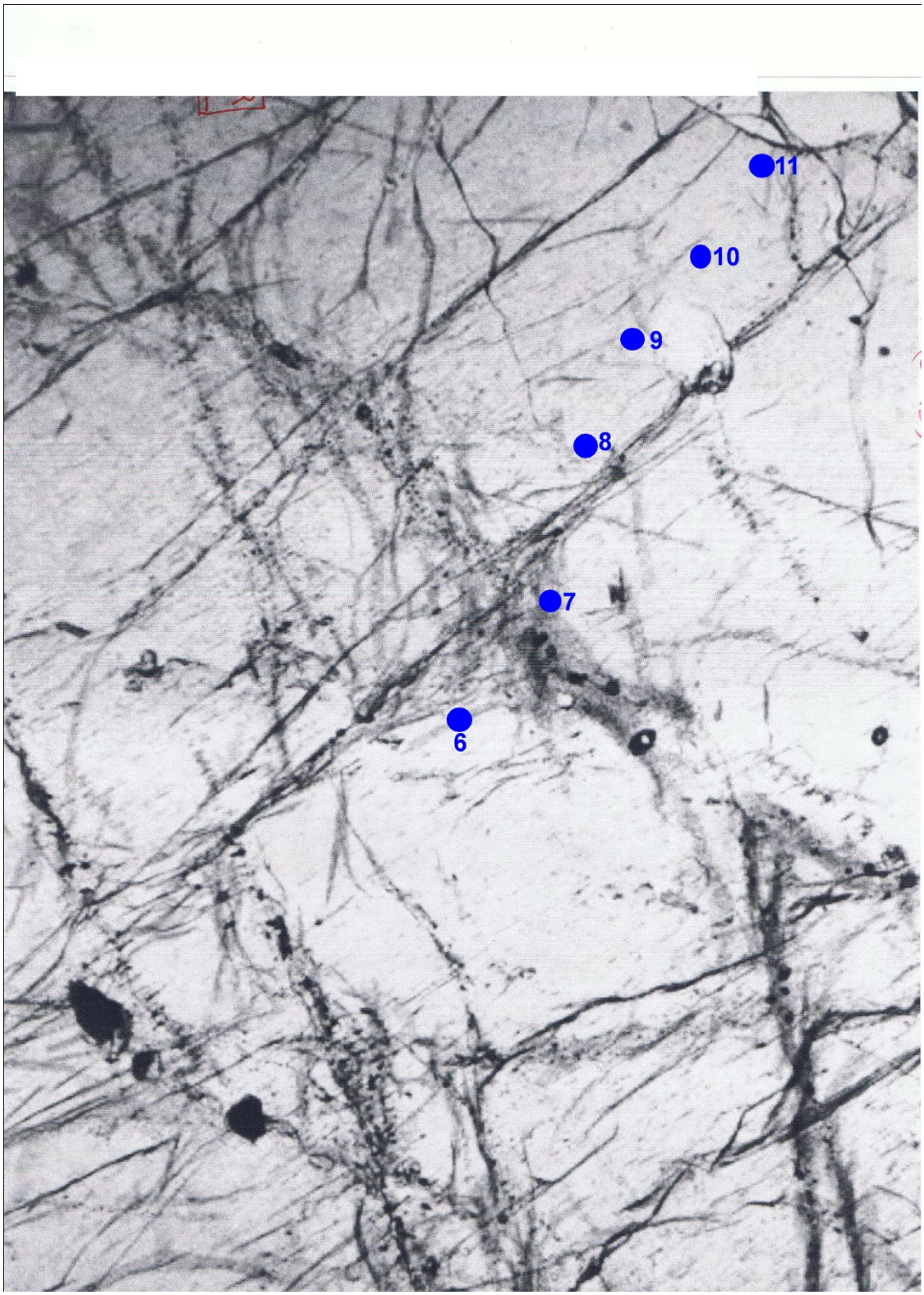

Photomicrograph 165
Sample No. FRB 1267

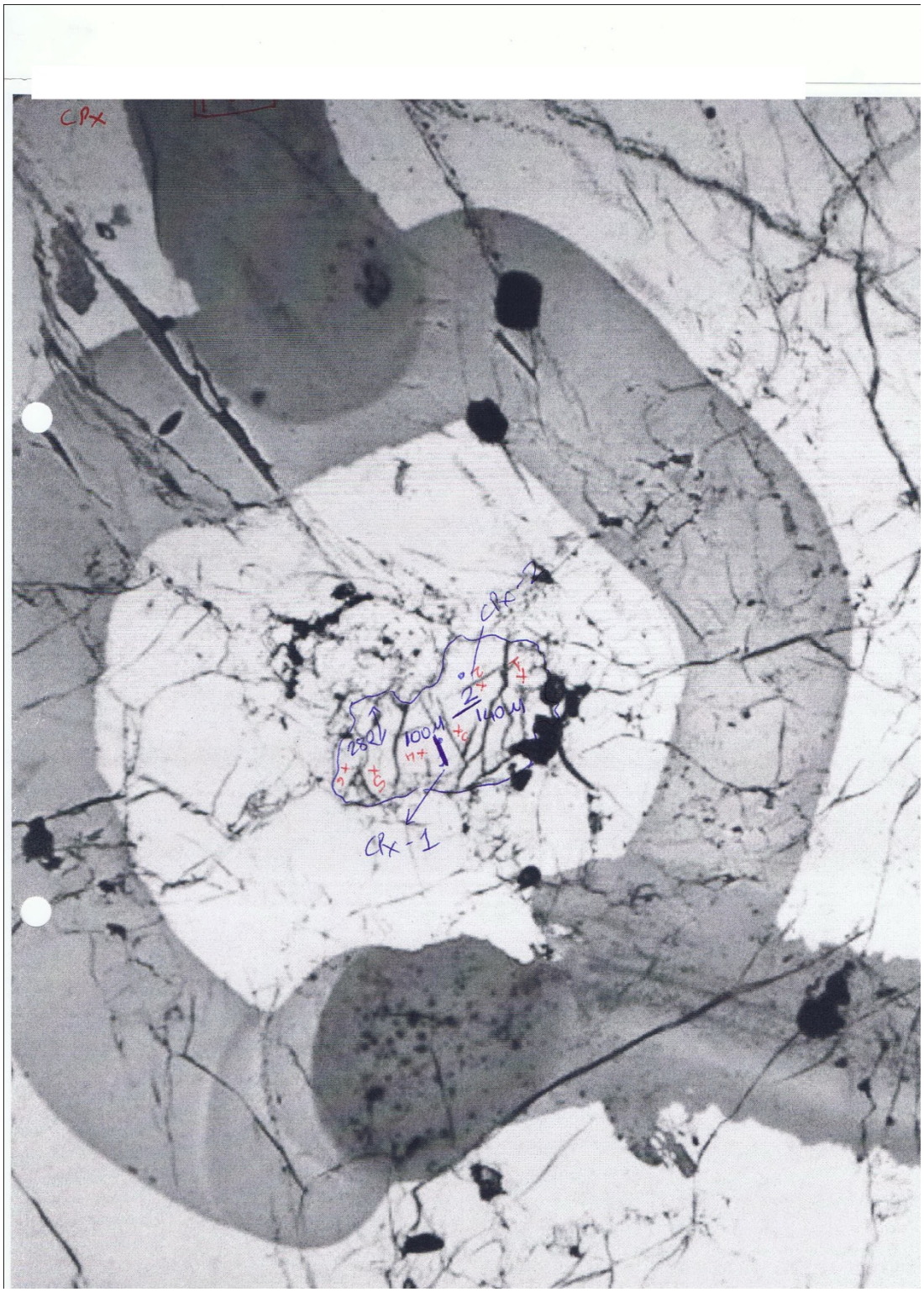

Photomicrograph 166
Sample No. FRB 1270

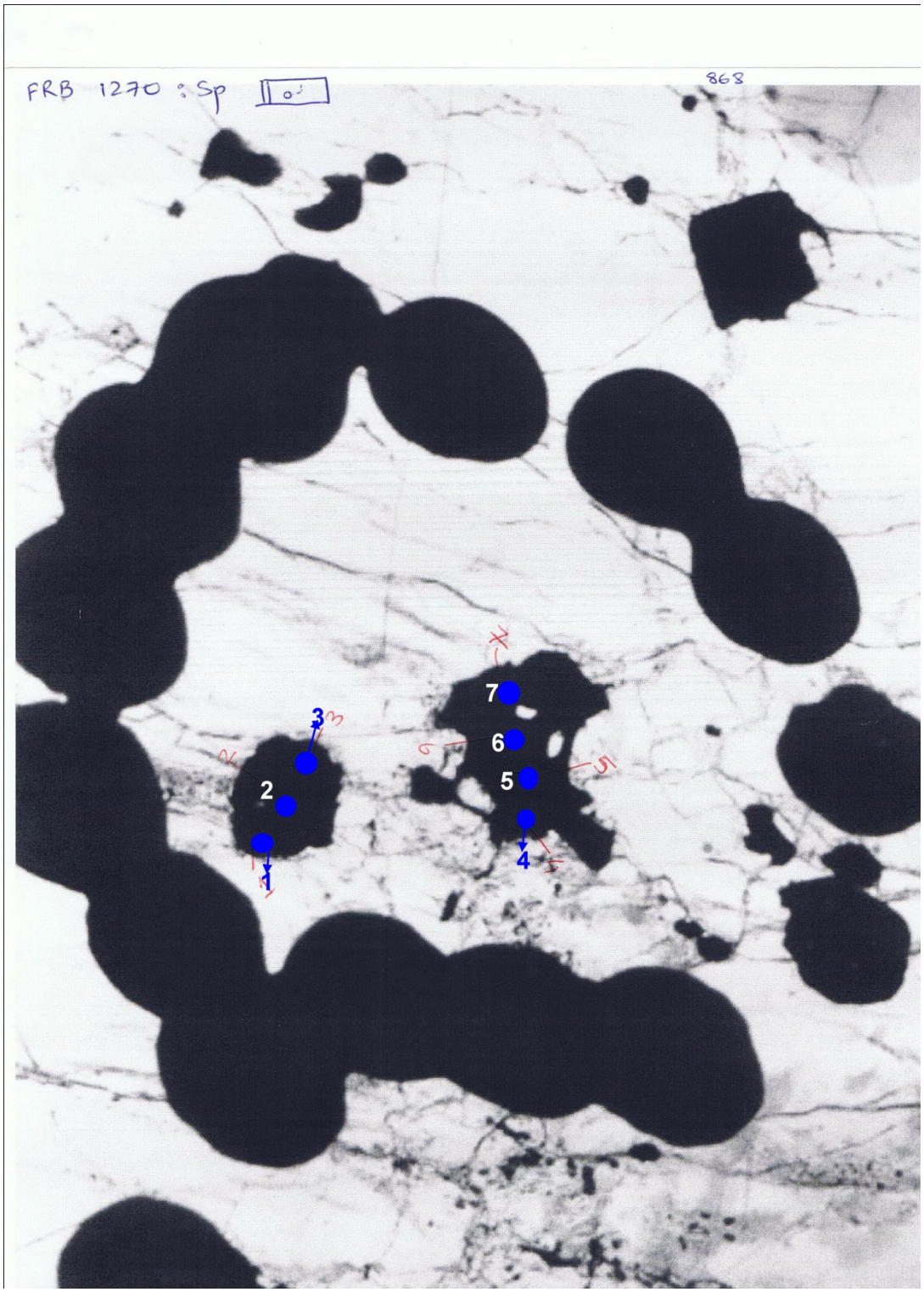

Photomicrograph 167
Sample No. FRB 1270

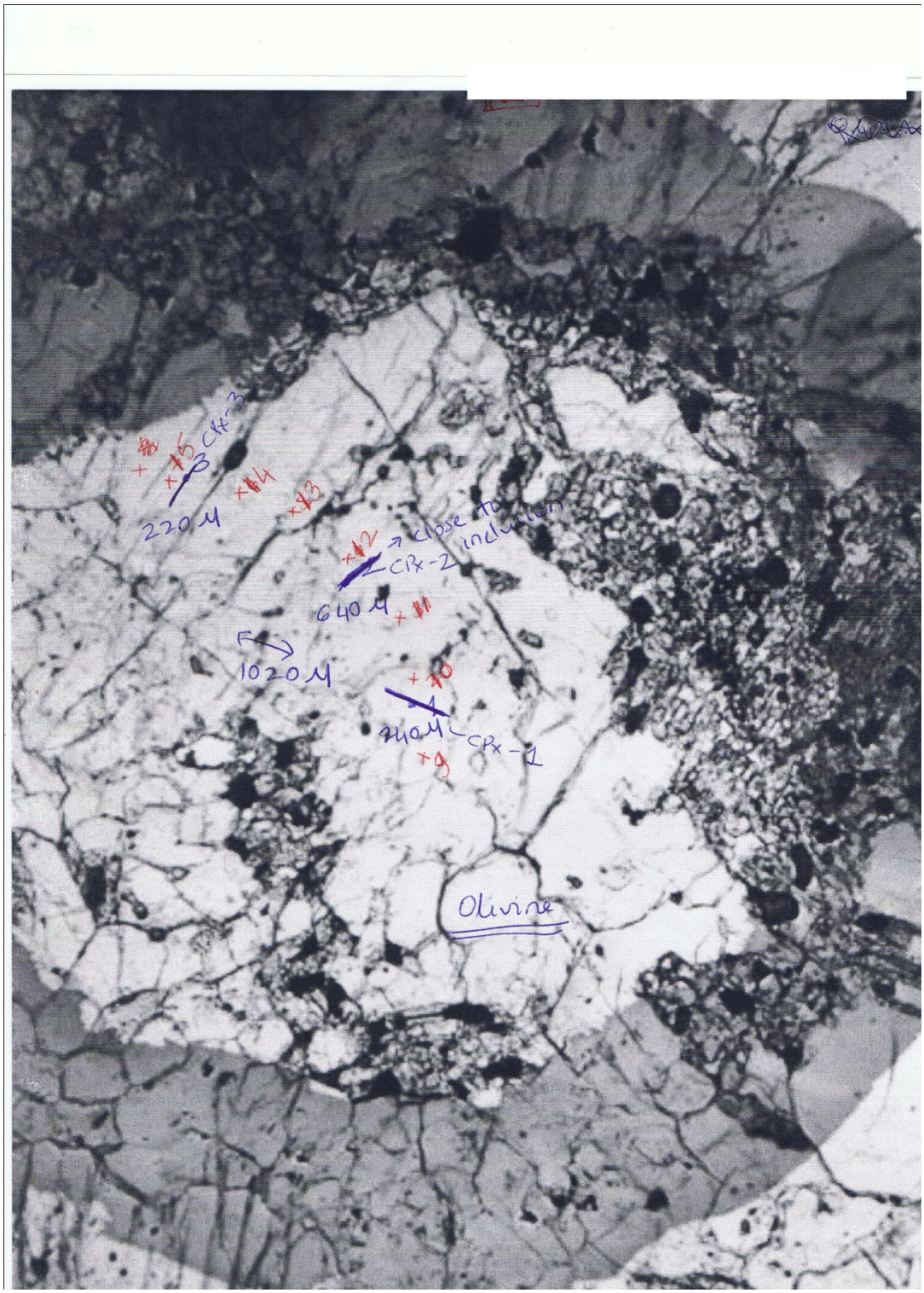

Photomicrograph 168
Sample No. FRB 1271

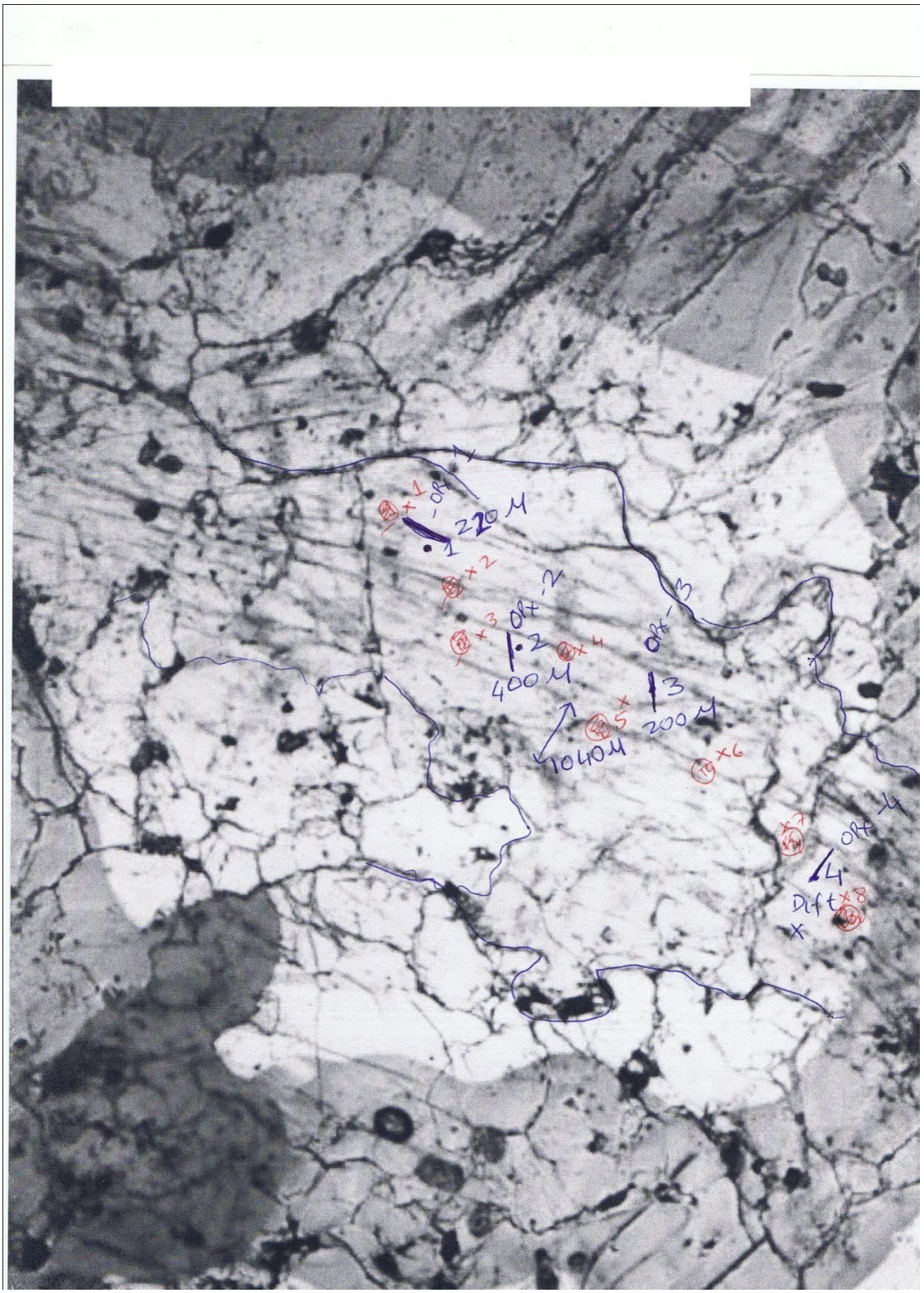

Photomicrograph 169
Sample No. FRB 1271

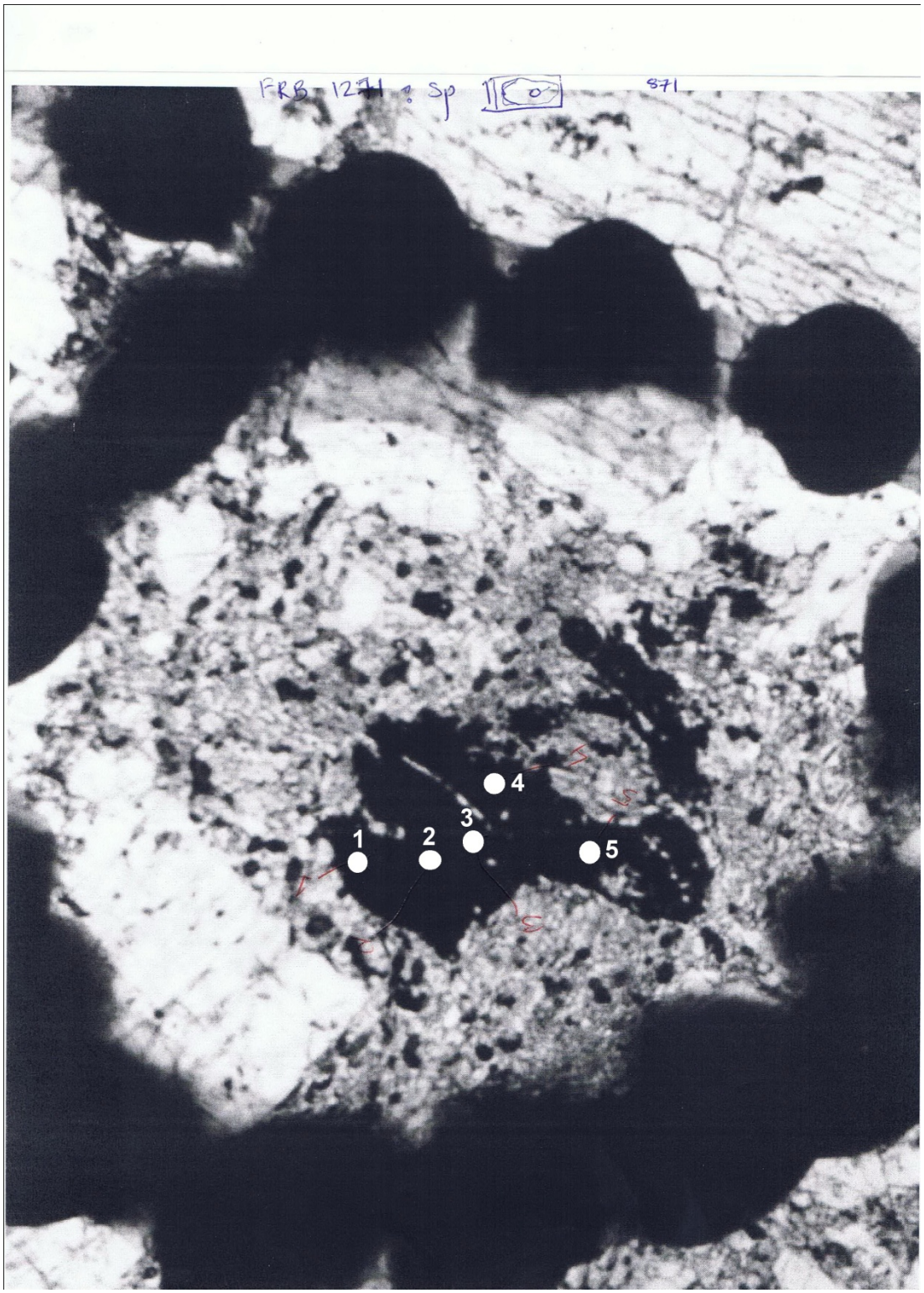

Photomicrograph 170
Sample No. FRB 1271

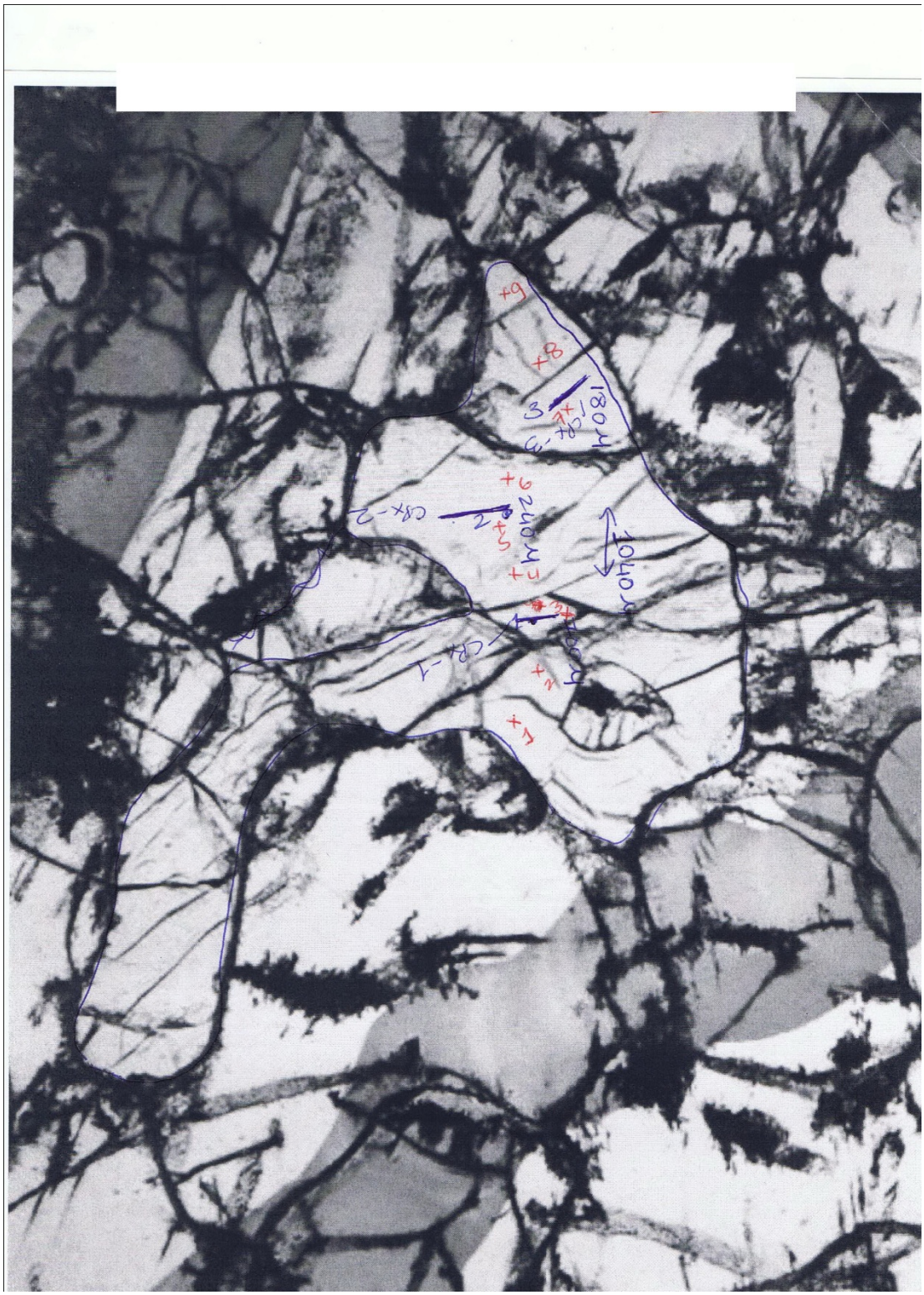

Photomicrograph 171
Sample No. FRB 1277

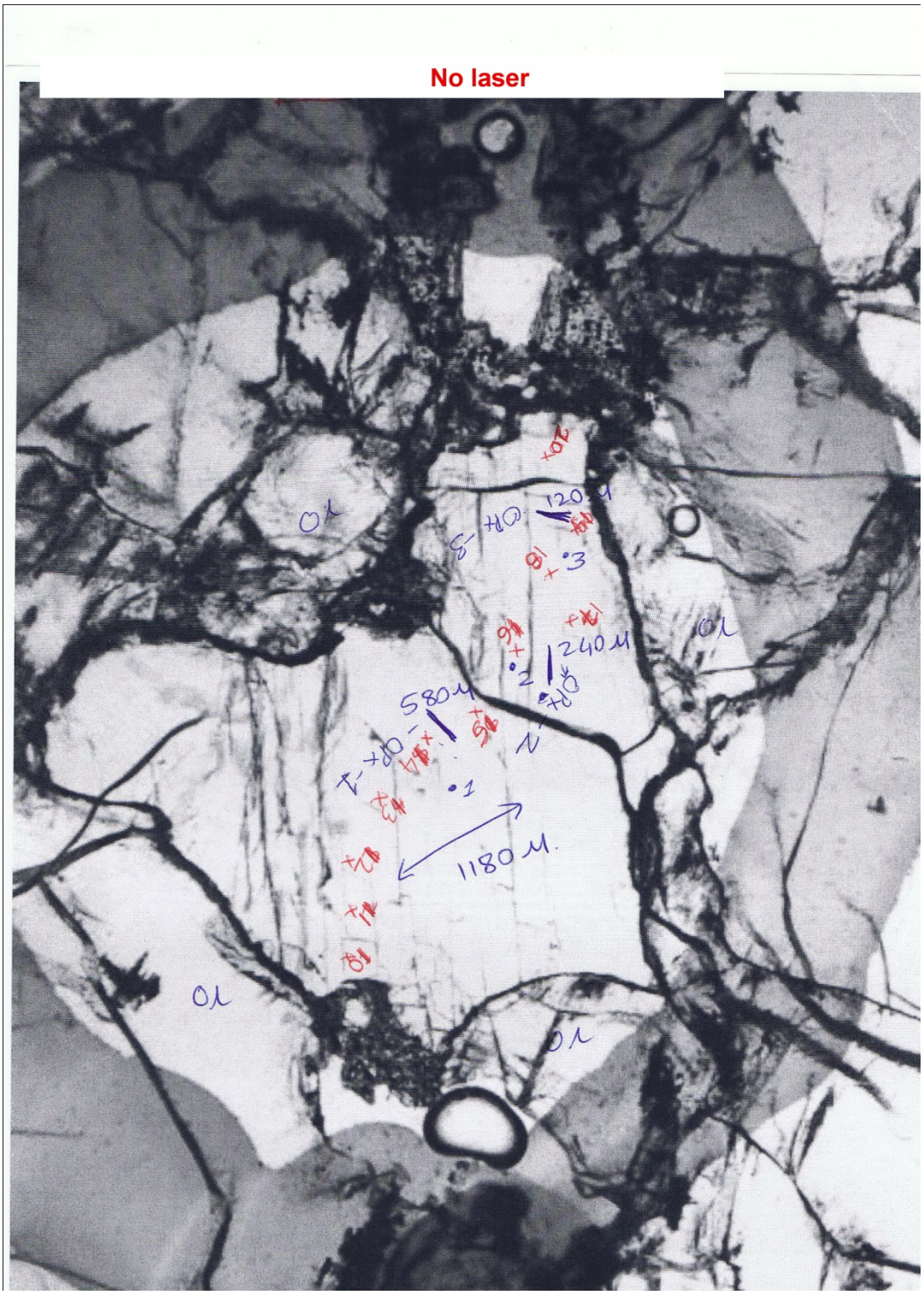

Photomicrograph 172
Sample No. FRB 1277

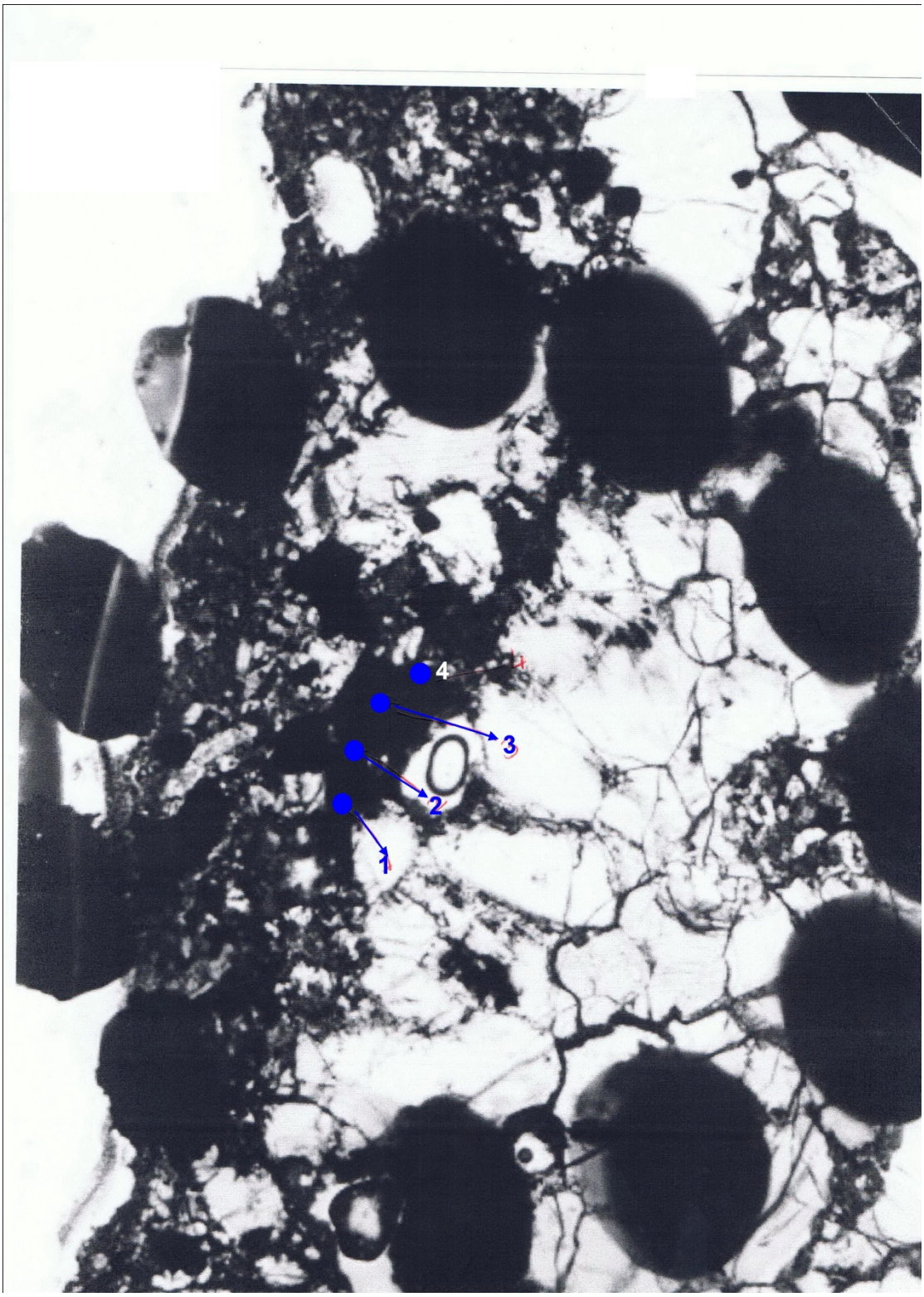

Photomicrograph 173
Sample No. FRB 1277

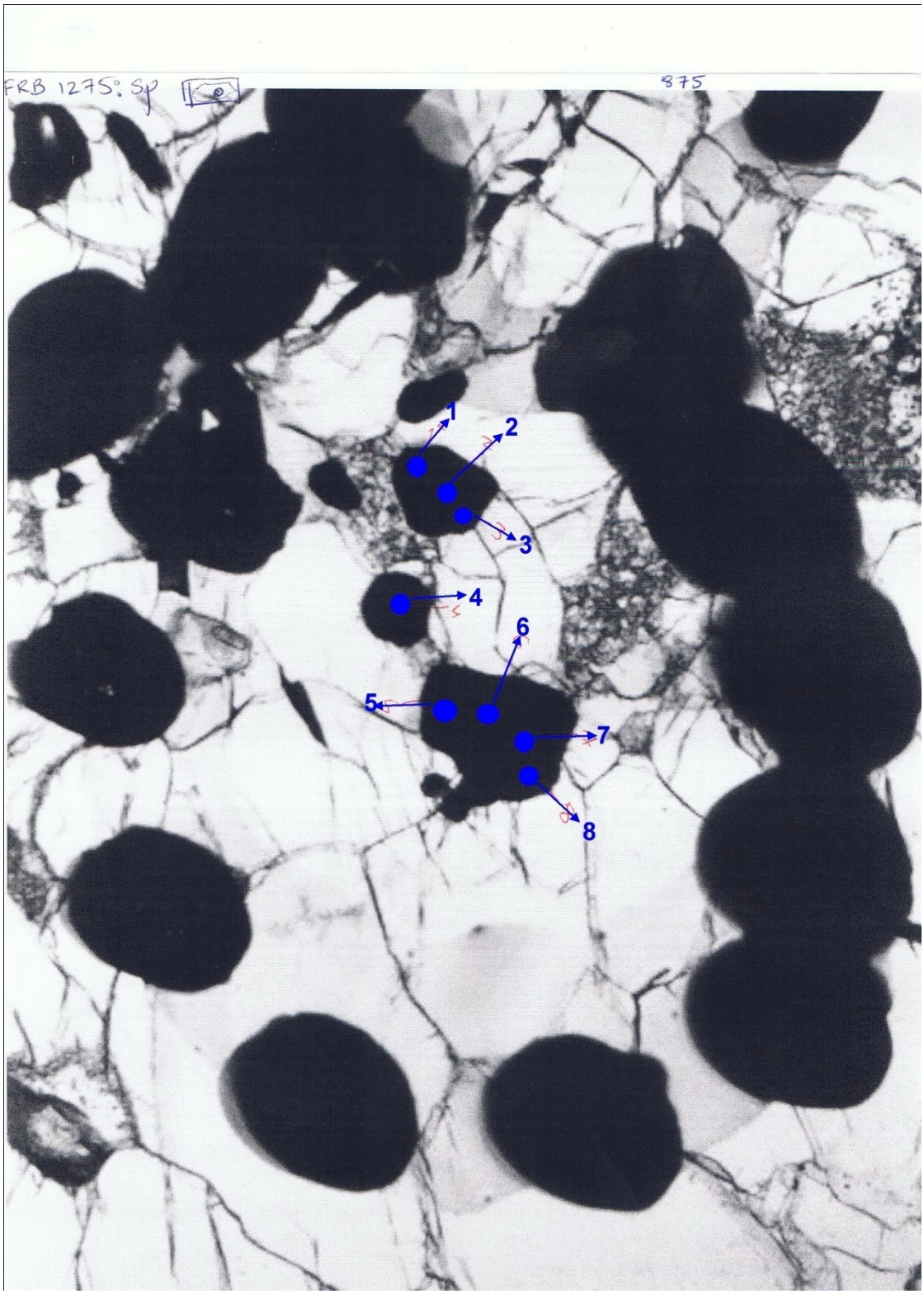

Photomicrograph 174
Sample No. FRB 1275

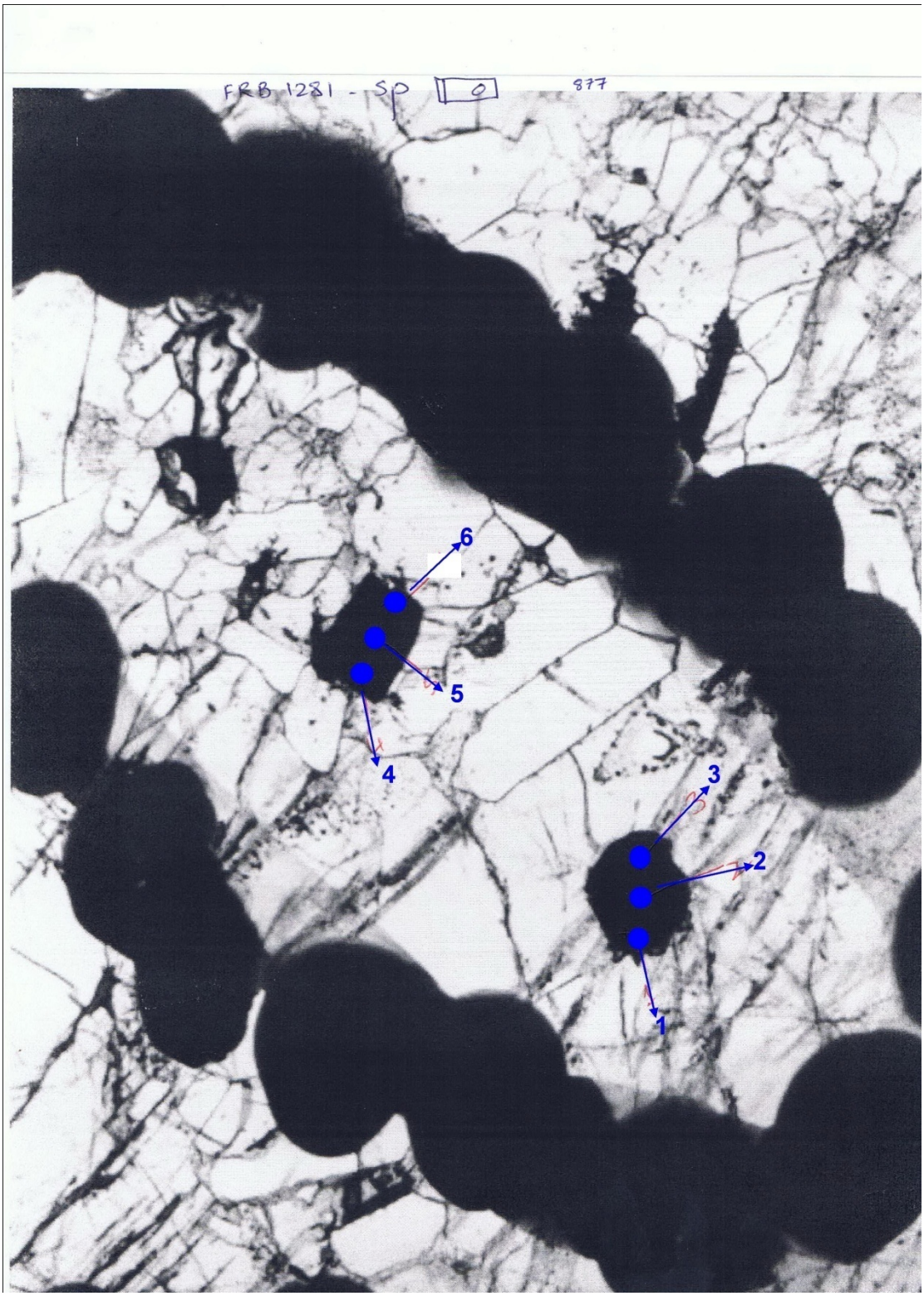

Photomicrograph 175
Sample No. FRB 1281

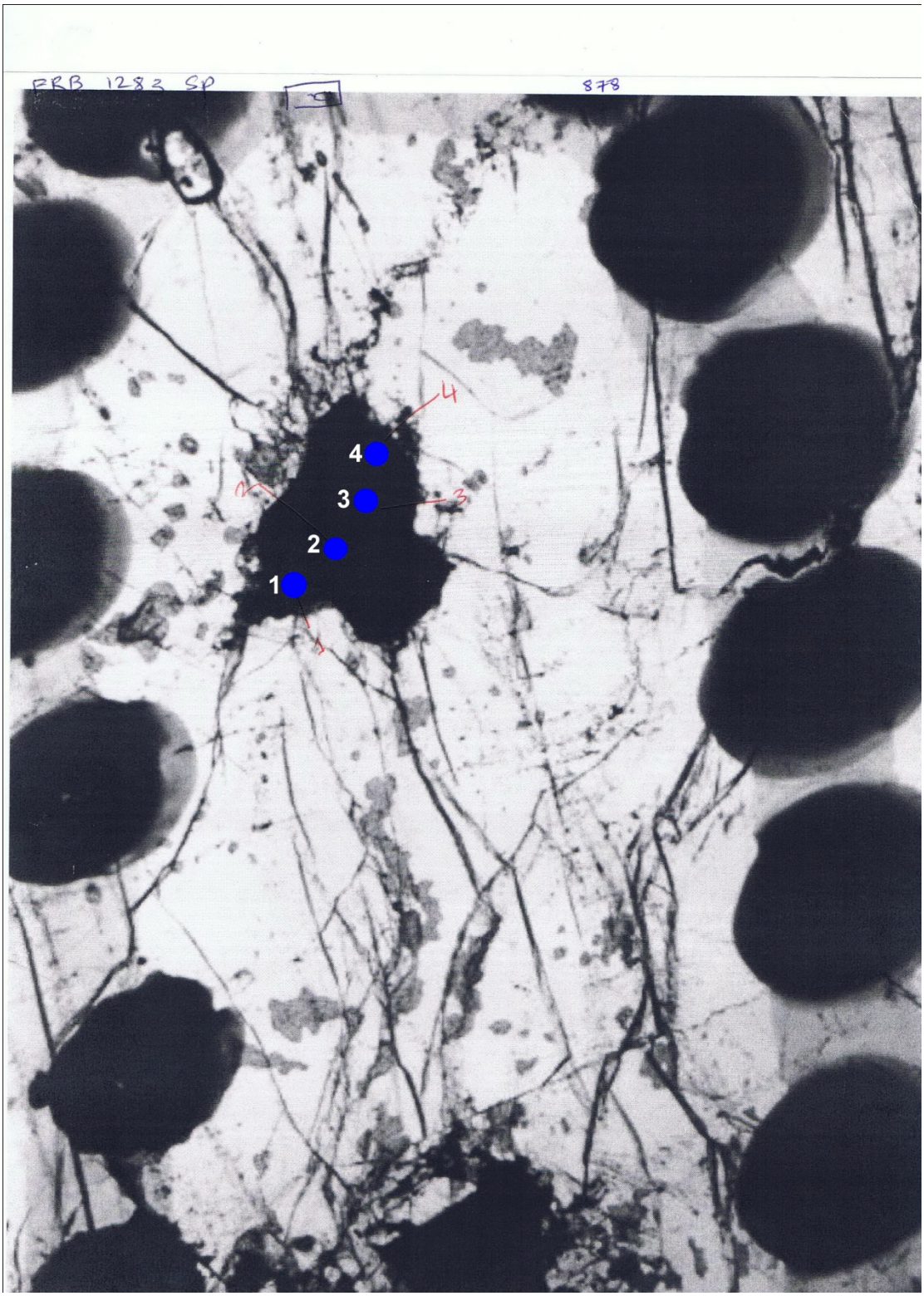

Photomicrograph 176
Sample No. FRB 1283

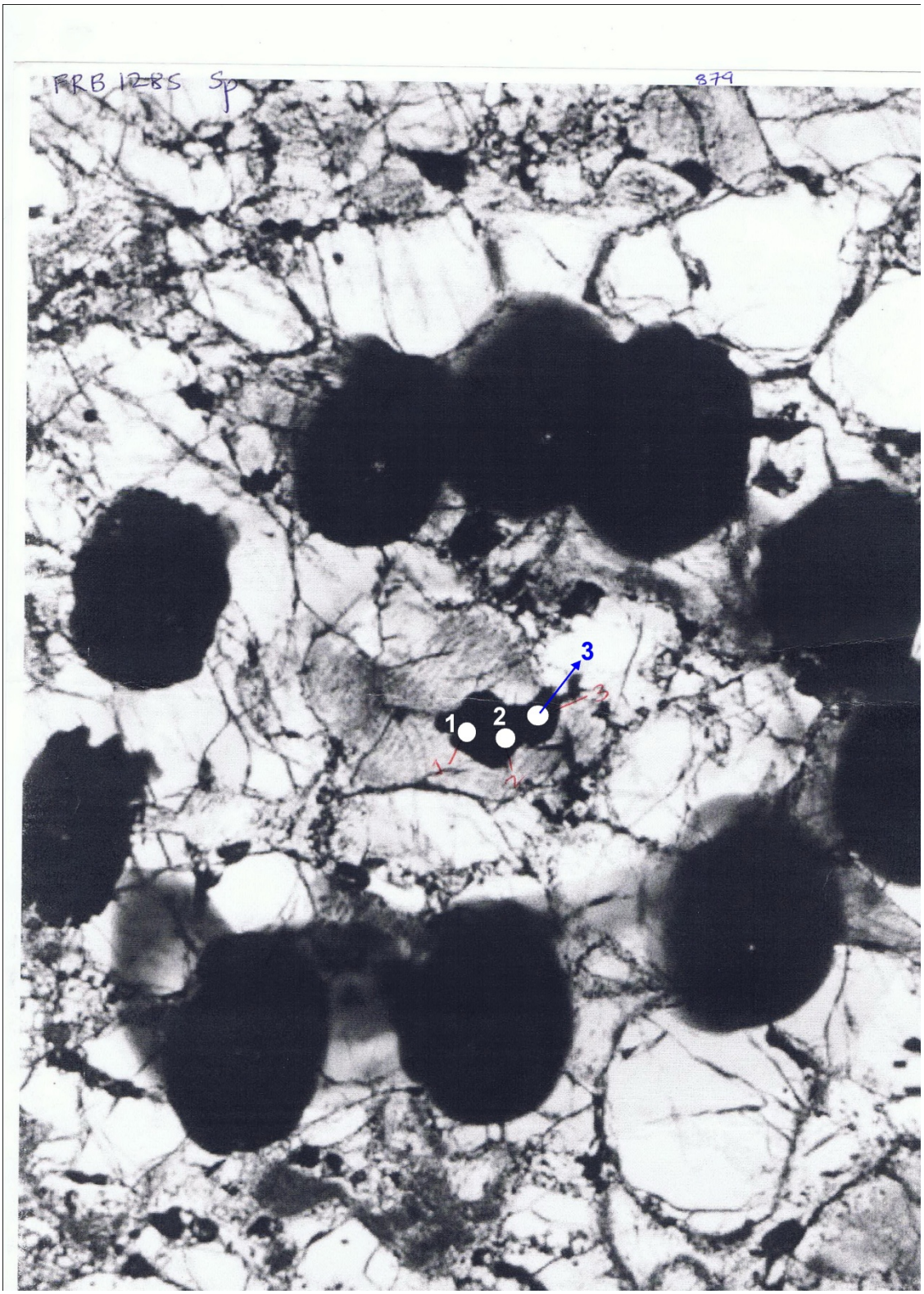

Photomicrograph 177
Sample No. FRB 1285

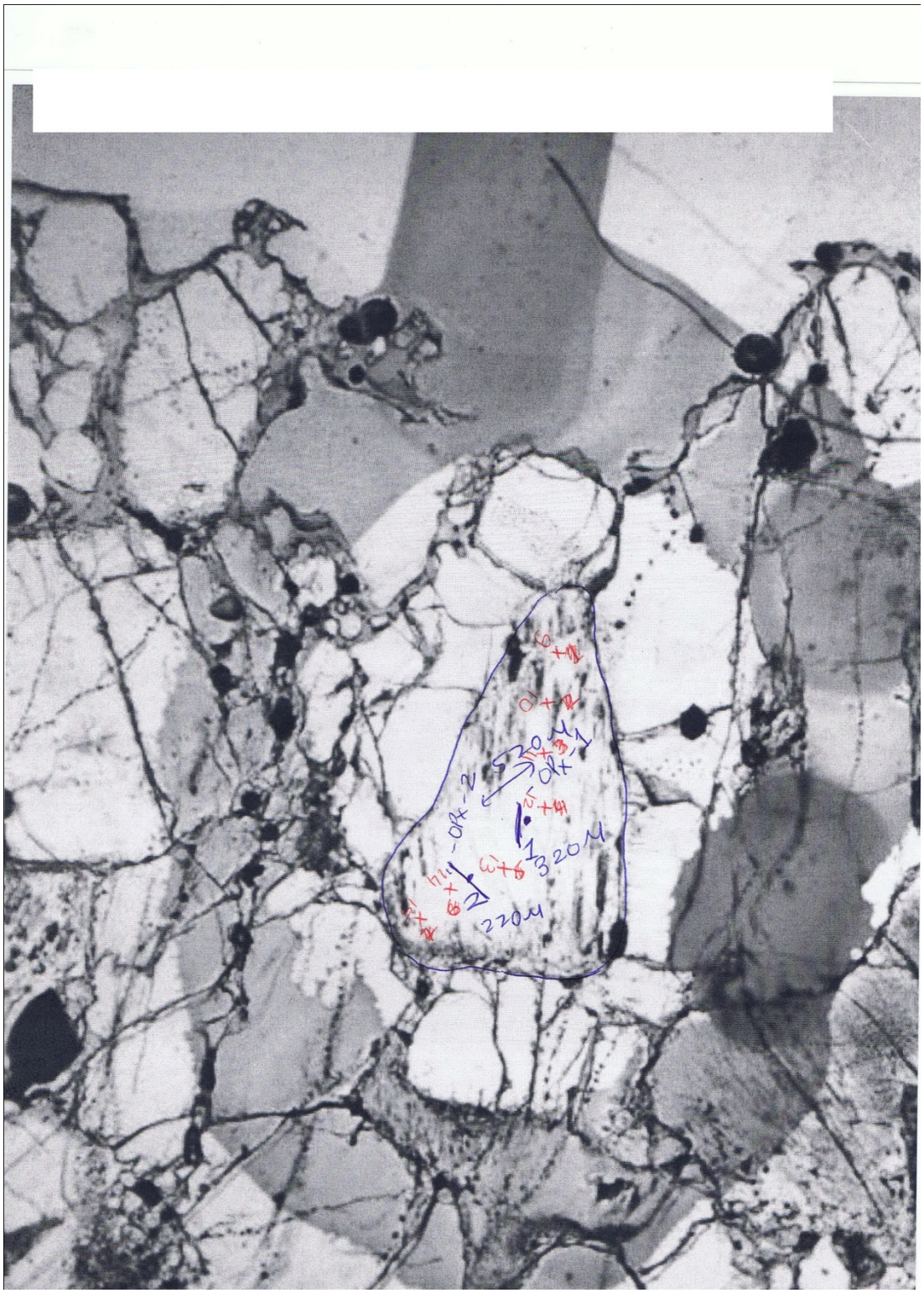

Photomicrograph 178
Sample No. FRB 1285

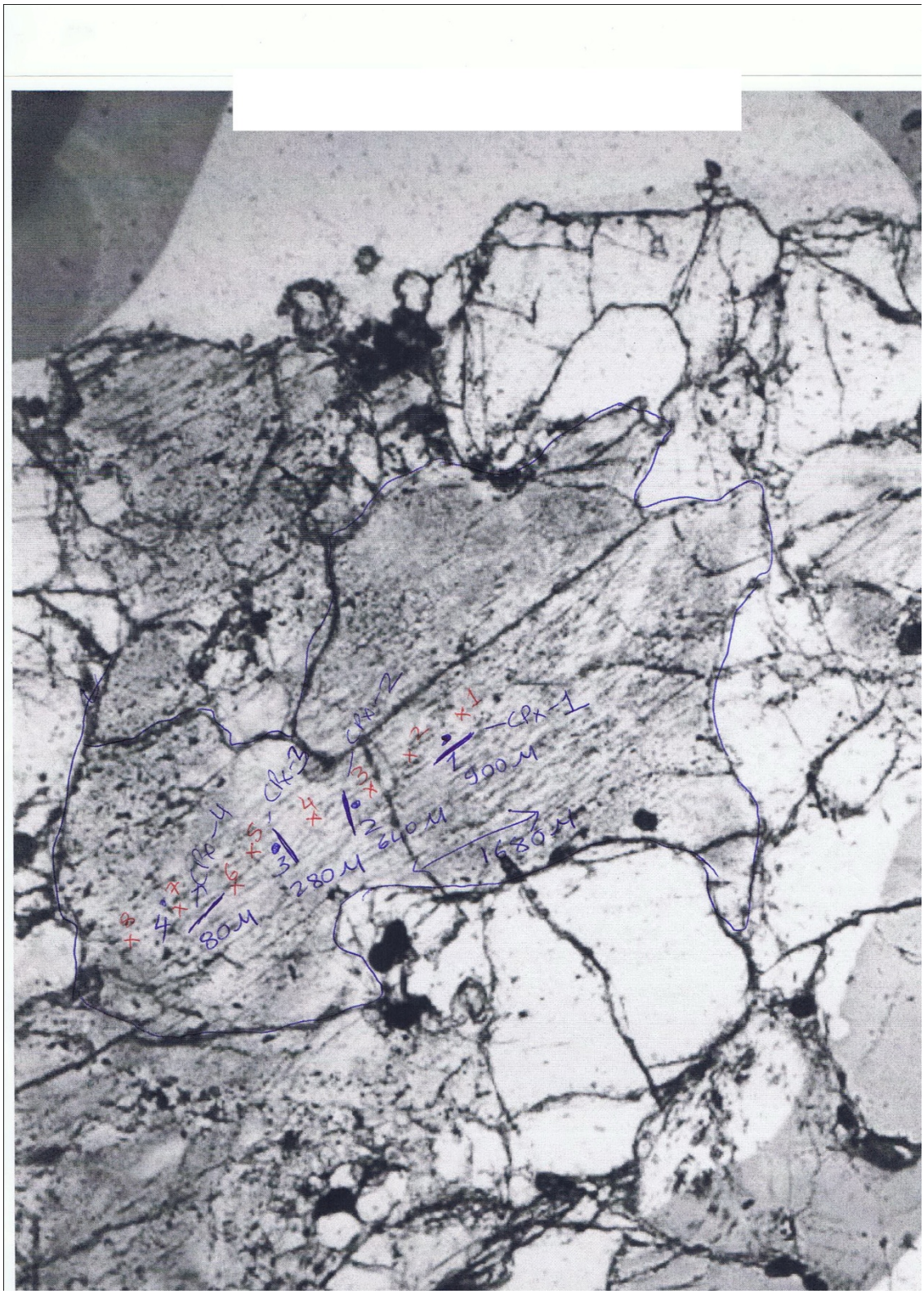

Photomicrograph 179
Sample No. FRB 1285